MULTI-DIMENSIONAL ANALYSIS OF THE CHEMICAL AND PHYSICAL PROPERTIES OF SPIRAL GALAXIES

Thesis submitted for the degree of
Doctor of Philosophy

by

FERNANDO FABIÁN ROSALES ORTEGA

Institute of Astronomy

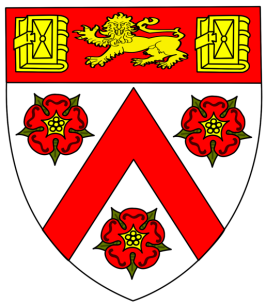

TRINITY COLLEGE

University of Cambridge

November 5, 2009

SUMMARY

The emergence of a new generation of instrumentation in astrophysics, which provide spatially-resolved spectra over a large 2-dimensional (2D) field of view, offers the opportunity to perform emission-line surveys based on samples of hundreds of spectra in a 2D context, enabling us to test, confirm, and extend the previous body of results from small-sample studies based on typical long-slit spectroscopy, while at the same time opening up a new frontier of studying the 2D structure of physical and chemical properties of the disks of nearby spiral galaxies. The project developed in this dissertation represents the first endeavour to obtain full 2D coverage of the disks of a sample of spiral galaxies in the nearby universe, by the application of the Integral Field Spectroscopy (IFS) technique. The semi-continuous coverage spectra provided by this spectral imaging technique allows to study the small and intermediate linear scale variation in line emission and the gas chemistry in the whole surface of a spiral galaxy.

The PPAK IFS Nearby Galaxies Survey: PINGS, was a carefully devised observational project, designed to construct 2D spectroscopic mosaics of 17 nearby galaxies in the optical wavelength range. The sample includes different galaxy types, including normal, lopsided, interacting and barred spirals with a good range of galactic properties and star forming environments, with multi-wavelength public data. The spectroscopic data set comprises more than 50 000 individual spectra, covering an observed area of nearly 100 arcmin^2, an observed surface without precedents by an IFS study. All sources of errors and uncertainties during the reduction process of the IFS observations are assessed very carefully. This methodology contributed not only to improve the standard reduction pipeline procedure for the particularly used instrument, improvements that can be applied to any similar integral-field observation and/or data reduction, but to defining a self-consistent methodology in terms of observation, data reduction and analysis for the kind of IFS surveys presented in this dissertation, as well as providing a whole new set of IFS visualization and analysis software made available for the public domain.

The scientific analysis of this dissertation comprises the study of the integrated properties of the ionized gas of the whole PINGS sample, and a detailed 2D study of the physical and chemical abundance distribution derived from the emission line spectra of four selected galaxies of the sample. Spatially-resolved maps of the emission line intensities and physical properties are derived for each the selected galaxies. Different methodologies are explored in order to study the spatially-resolved spectroscopic properties of the galaxies. Abundance analysis are performed based on a variety of diagnostic techniques using reddening corrected spectra. From this analysis, evidence is found to support that the measurements of emission lines of a "classical" H II region are not only aperture, but spatial dependent, and therefore, the derived physical parameters and metallicity content may significantly depend on the morphology of the region, on the slit/fibre position, on the extraction aperture and on the signal-to-noise of the observed spectrum. On the other hand, the results presented in this dissertation indicate the existence of non-linear *multi-modal* abundance gradients in normal spiral galaxies, consistent with a flattening in the innermost and outermost parts of the galactic discs, with important implications in terms of the chemical evolution of galaxies.

The powerful capabilities of wide-field 2D spectroscopic studies are proven. The chemical composition of the whole surface of a spiral galaxy is characterised for the first time as a function not only of radius, but of the intrinsic morphology of the galaxy, allowing a more realistic determination of their physical properties. The methodology, analysis and results of this dissertation will hopefully contribute in a significant way to understand the nature of the physical and chemical properties of the gas phase in spiral galaxies.

DECLARATION

I hereby declare that this thesis entitled *Multi-dimensional analysis of the chemical and physical properties of spiral galaxies* is not substantially the same as any that I have submitted for a degree or diploma or other qualification at any other University. I further state that no part of this dissertation has already been or is being concurrently submitted for any such degree, diploma or other qualification. This thesis is essentially the result of my own work, and includes nothing which is the outcome of work done in collaboration except where specifically indicated. Those parts of this dissertation which are undergoing review for publication, or included in conference proceedings are as follows:

- **Chapter 3**
  The work presented in this chapter is essentially my own, it has been submitted for publication as: Rosales-Ortega, F. F., Kennicutt, R. C., Sánchez, S. F., Díaz, A. I., Pasquali, A., Johnson, B. D. and Hao, C. N., (2009) *PINGS: the PPAK IFS Nearby Galaxies Survey*, submitted to Monthly Notices of the Royal Astronomical Society, and it was benefited from collaboration with these authors.

- **Chapter 4**
  The work presented in this chapter is essentially my own, a large part of it was submitted for publication in the article mentioned above. The work related to NGC 628 has been partially done within a collaboration, and submitted for publication as: Sánchez, S. F., Rosales-Ortega, F. F., Kennicutt, R. C., Díaz, A. I., Pasquali, A., Johnson, B. D. and Hao, C. N., (2009) *PPAK Wide-field Integral Field Spectroscopy of NGC 628: The largest spectroscopic survey on a single galaxy*, submitted to Monthly Notices of the Royal Astronomical Society. The *Gaussian-suppression* and absolute fux calibration techniques were developed in collaboration with S. F. Sánchez. Their implementation and initial testing were carried out in parallel by both of us, though the final implementation for this dissertation are my own work.

- **Chapter 5**
  The work presented in this chapter is essentially my own. Some parts has been partially done within a collaboration, and submitted for publication in the articles mentioned above.

- **Chapter 6**
  The work presented in this chapter is essentially my own, but benefited from discussions and advice from S. F. Sánchez and A. I. Díaz.

- Some figures of chapter 3 and chapter 6 have been included in *The Promise of Multiwavelength and IFU observations*, Kennicutt, R. C., Hao, C. N., Johnson, B. D., Rosales-Ortega, F. F., Díaz, A. I., Pasquali, A. and Sánchez, S. F., (2009) Proceedings of the IAU Symposium 262, G. Bruzual, S. Charlot, eds.

This thesis is less than 60 000 words in length.

Fernando Fabián Rosales Ortega
Cambridge, November 5, 2009

ACKNOWLEDGEMENTS

I would like to acknowledge all those persons who during these last three years, have provided me with their help, assistance and support, and to whom I will always be indebted.

First and foremost, I cannot thank enough my supervisor, Rob Kennicutt, for his guidance and for all the trust he put on me during the development of this project. I will always remember how his patience with me was first tested after I rejected three or more projects he suggested for my Ph.D., until he came with an obscure if exciting idea that was finally materialised into this dissertation. I hope not to have disappointed him with the outcome. Despite his busy schedule, Rob not only found time to travel abroad with me for observing runs, where the combination of his expertise and teachings made such occasions an invaluable experience, but also had always his door open for my questions and concerns, not to mention the numerous support letters for grants, given my very limited stipend! His warmth, sense of humour, steady support and expertise contributed to make my experience as his student at the Institute of Astronomy a very rewarding one. Thank you, Rob!

I feel especially grateful towards by two closest collaborators, Ángeles I. Díaz Beltran and Sebastián F. Sánchez Sánchez. Without all the hours of your time, effort, encouragement and patience you kindly bestowed upon me, the completion of this thesis would have not been possible. Thank you very much for your support, teachings and hospitality in Spain.

I would like to thank the staff and TAC of the Centro Astronómico Hispano Alemán at Calar Alto, Spain, where the observations for this dissertation were collected. So thanks for the granted observing time and your prompt help and support during the observing nights and training periods spent in your facilities.

My gratitude also towards Paul Hewett and José Vilchez who kindly agreed to be my examiners, despite the short notice and inconveniences thus implied.

On the personal side, my family deserves my fondest gratitude. Their love, patience and support is the fuel that has kept me going through the unexplored, remote and sometimes lonely paths in my life. I hope I can honour all your affections and the sacrifices made for my sake.

Thanks also to all those important persons who made Cambridge a special experience in the last three years. It would take paragraphs and paragraphs to mention you all, but be sure that I will always keep in my heart and memory all the remarkable moments spent together, in so many different circumstances and situations. Thank you for your friendship, company, support, encouragement and even... love.

Finally, this dissertation would not have been possible without the generous sponsorship of several institutions. I want to express my gratitude to the National Council for Science and Technology (CONACYT) in Mexico, which fully sponsored my studies. I would also acknowledge the generosity of the Dirección General de Relaciones Internacionales (SEP) in Mexico, Trinity College, the Cambridge Philosophical Society, and the Institute of Astronomy in Cambridge, as well as the Royal Astronomical Society, who provided me with the financial support to carry out this research.

Fernando Fabián Rosales Ortega
Cambridge, November 5, 2009

A mis padres, Goyo y Zaly.

CONTENTS

LIST OF TABLES

LIST OF FIGURES

‘These earthly godfathers of Heaven’s lights, that give a name to every fixed star, have no more profit of their shining nights, than those that walk and know not what they are.’

Love’s Labour’s Lost, circa 1590
WILLIAM SHAKESPEARE

‘The treasures hidden in the heavens are so rich that the human mind shall never be lacking in fresh nourishment.’

JOHANNES KEPLER

‘Stat rosa pristina nomine, nomina nuda tenemus.’

De contemptu mundi, 12th c.
BERNARD OF CLUNY
(Il nome della rosa, 1980)

1 Introduction

The existence and distribution of the chemical elements and their isotopes in the universe is a consequence of very complex processes that have taken place in the past since the Big Bang and subsequently in stars and in the interstellar medium (ISM) of the present day galaxies, where they are still ongoing. These processes have been studied theoretically, experimentally and observationally. Different theories of cosmology, stellar evolution and interstellar processes have been considered, laboratory investigations of nuclear and particle physics, studies of elemental and isotopic abundances in the Earth and meteorites have also been involved, as well as astronomical observations of the physical nature and chemical composition of stars, galaxies and the interstellar medium.

From the observational point of view, the study of chemical abundances in galaxies, like many other areas of astrophysics, has undergone a remarkable acceleration in the flow of data over the last few years. We have witnessed wholesale abundances determinations in tens of thousands of galaxies from large scale surveys such as the Two Degree Field Galaxy Redshift Survey (2dFGRS, Colless et al., 2001) and the Sloan Digital Sky Survey (SDSS, York et al., 2000), measurements of abundances in individual stars of Local Group galaxies beyond the immediate vicinity of the Milky Way, and the determination of the chemical composition of some of the first stars to form in the Galactic halo. Chemical abundances studies are also increasingly being extended to high redshift, charting the progress of stellar nucleosynthesis over most of the age of the universe. The primary motivation common to all of these observational efforts is to use the chemical information as one of the means at our disposal to link the properties of high redshift galaxies with those we see around us today, and thereby understand the physical processes at play in the formation and evolution of galaxies.

The galactic chemical evolution is dictated by a complex array of parameters, including the local initial composition, star formation history (SFH), gas infall and outflows, radial transport and mixing of gas within disks, stellar yields, and the initial mass function (IMF). Although is difficult to disentangle the effects of the various contributors, measurements of current elemental abundances constrain the possible evolutionary histories of the existing stars and galaxies. Important constraints on theories of galactic chemical evolution

and on the star formation histories of galaxies can be derived from the accurate determination of chemical abundances either in individual star-forming regions distributed across galaxies or through the comparison of abundances between galaxies. Nebular emission lines from individual H II regions have been, historically, the main tool at our disposal for the direct measurement of the gas-phase abundance at discrete spatial positions in low redshift galaxies.

However, in order to obtain a deeper insight of the mechanisms that rule the chemical evolution of galaxies, we require a significantly the number of H II regions sampled in any given galaxy. In this dissertation, I present a new observational technique conceived to tackle the problem of the 2-dimensional coverage of the whole surface of a galaxy. The advent of new spectroscopic techniques provides powerful tools for studying the small and intermediate scale-size variation in line emission and stellar continuum in nearby well-resolved galaxies. In this work, I address the problems and challenges that imply the determination of the chemical composition in galaxies in a 2D context and the subsequent derivation of their physical properties.

I will begin by presenting in this chapter a literature review on the determination of chemical abundances in galaxies. As an introduction to this topic, the physics of gaseous nebulae is discussed in § 1.1, together with a discussion of extra-galactic H II regions in § 1.2. The different methods of abundance determinations are presented in § 1.3. Physical properties derived from the determination of chemical abundances are discussed in § 1.4. These latter sections are partially based on the paper reviews and books about the physics and chemistry of the interstellar medium and H II extragalactic regions by Dinerstein (1990), Pérez-Montero & Díaz (2005), Tielens (2005), and Osterbrock & Ferland (2006). This discussion leads to the presentation of new techniques and methods for the determination of chemical abundances in nearby galaxies as described in § 1.5

1.1 The Physics of Gaseous Nebulae

Gaseous Nebulae are observed as bright extended objects in the sky, some are easily observed on direct images but many others are intrinsically less luminous or are affected by interstellar extinction on ordinary images, but can be resolved on long exposures with special filters and techniques so that the background and foreground stellar and sky radiations are suppressed. The surface brightness of a nebula is independent of its distance, but more distant nebulae have (on average) smaller angular size and greater interstellar extinction.

Gaseous nebula have emission-line spectra. Nebulae emit electromagnetic radiation over a broad spectral range, although only a few wavelengths pass easily through the Earth's atmosphere. Visible light and some infrared and radio radiation can be studied from the ground, but most other wavelengths can only be covered from high-latitude aircrafts or space telescopes. The source of energy that enables normal emission nebulae to radiate is ultraviolet radiation from stars within or near the nebula. There should be one or more stars with effective surface temperature $T_\star \geq 3$ x 10^4 K, the ultraviolet photons of these stars transfer energy to the nebula by photoionization. In all nebulae, hydrogen (H) is by far the most abundant element, and photoionization of H is thus the main energy-input mechanism. Photons with energy greater than 13.6 eV (the ionization potential of H), are absorbed in the process, and the excess energy of each absorbed photon over the ionization potential appears as kinetic energy of a newly liberated photoelectron. Collisions between electrons and between electrons and ions, distribute this energy and maintain a Maxwellian velocity distribution with temperature T in the range 5,000 $< T <$ 20,000 K in typical nebulae. Collisions between thermal electrons and ions excite the low-lying energy levels of the ions. Downward radiation transitions

from these excited levels have very small transition probabilities, but at the low densities ($n_e \leq 10^4$ cm^{-3}) of typical nebulae, collisional de-excitation is even less probable, so almost every excitation leads to emission of a photon, and the nebula thus emits a forbidden-line spectrum that is quite difficult to reproduce under terrestrial laboratory conditions.

Thermal electrons are recaptured by the ions, and the degree of ionization at each point in the nebula is fixed by the equilibrium between photoionization and recapture. In the recombination process, recaptures occur to excited levels, and the excited atoms thus formed then decay to lower and lower levels by radiative transitions, eventually ending in the ground level. In this process, line photons are emitted and this is the origin of the H I Balmer and Paschen line spectra observed in all gaseous nebulae. The recombination of H^+ gives rise to excited atoms of H^0 and thus leads to the emission of the H I spectrum. Likewise, He^+ recombines and emits the He I spectrum, and in the most highly ionized regions, He^{++} recombines and emits the He II spectrum. Recombination lines of trace elements are also emitted; however, the main excitation process responsible for the observed strengths of such lines with the same spin or multiplicity as the ground term is resonance fluorescence by photons, which is much less effective for H and He lines because the resonance lines of these more abundant elements have greater optical depth. Nevertheless, line emission of these rare elements plays a significant role in the physics of the nebula, and permits the determination of the chemical composition inside the nebula.

The spectra of gaseous nebulae are dominated by collisionally excited forbidden lines of ions of common elements, such as [O III] $\lambda\lambda 4959, 5007$ (the famous green nebular lines); [N II] $\lambda\lambda 6548, 6584$ and [S II] $\lambda\lambda 9069, 9523$ in the red; and [O II] $\lambda\lambda 3727$, 3729 in the ultraviolet (which normally appears as a blended $\lambda 3727$ line on low-dispersion spectrograms). In addition, the permitted lines of hydrogen, Hα $\lambda 6563$ in the red, Hβ $\lambda 4861$ in the blue, Hγ $\lambda 4340$ in the violet and so on, are characteristic features of every nebular spectrum, as is He I $\lambda 5876$, which is considerably weaker, while He II $\lambda 4686$ occurs only in higher-ionization nebulae. Long-exposure spectrophotometric observations extending to faint intensities show progressively weaker forbidden lines, as well as faint permitted lines of common elements such as C II, C III, C IV and so on. Nebular emission-line spectra extend into other spectral ranges, in the infrared for example, the [Ne II] $\lambda 12.8$ μm and [O III] $\lambda 88.4$ μm are among the strongest lines measured, into the ultraviolet Mg II $\lambda\lambda 2796, 2803$, C III] $\lambda\lambda 1907, 1909$, C IV $\lambda\lambda 1548, 1551$ and Lyα $\lambda 1216$ are also observed. Is often necessary to obtain spectra outside the traditional visible/near spectral bands to get an accurate picture of the system in question.

Gaseous nebulae have weak continuous spectra, consisting of atomic and reflection components. The atomic continuum is emitted chiefly by free-bound transitions, mainly in the Paschen continuum of H I at $\lambda > 3646$ Å, and the Balmer continuum at 912 Å $< \lambda <$ 3646 Å. In addition to the bright-line and continuous spectra emitted by atomic processes, many nebulae have reflection continua arising from starlight scattered by dust. The amount of dust varies from nebula to nebula, and the strength of this continuum fluctuates correspondingly. In the infrared for example, the nebular continuum is largely thermal radiation emitted by dust particles heated to a temperature of order 100 K by radiation derived originally from the central star.

Gaseous nebula may be classified into two main types: H II regions and planetary nebulae (PNe). Though the physical processes in both types are quite similar, the two groups differ greatly in origin, mass, evolution and age. The objects of study for the chemical composition of galaxies are extragalactic H II regions. These diffuse nebulae are regions of interstellar gas in which the exciting stars are O- or early B-type stars, i.e. young stars which use up their nuclear energy quickly. These hot, luminous stars undoubtedly formed fairly recent from interstellar matter that would be otherwise be part of the same nebula. The effective temperature

of the stars are in the range 3 x $10^4 < T_\star <$ 5 x 10^4 K; throughout the nebula, H is ionized, He is singly ionized and other elements are mostly singly or doubly ionized. Typical densities in the ionized part of the nebula are of the order 10 or 10^2 cm^{-3}, ranging to high as 10^4 cm^{-3}. In many nebulae, dense neutral condensations are scattered through the ionized volume. Internal motions occur in the gas with velocities of order 10 km s^{-1}, approximately the isothermal sound speed. Bright rims, knots, condensations, and so on, are apparent to the limit of resolution. The hot, ionized gas tends to expand into the cooler surrounding neutral gas, thus decreasing the density within the nebula and increasing the ionized volume. The outer edge of the nebula is surrounded by ionization fronts running out into the neutral gas. This original two-phase model of the interstellar medium (the H II /H I region dichotomy) was introduced by Strömgren (1939). He showed that photoionized gas near hot stars is segregated into physically distinct volumes, separated from their neutral environment by sharp boundaries.

1.1.1 Extragalactic H II regions

The spectra of H II regions are strong in H I recombination lines, [N II] , [O II] and [O III] collisionally excited lines, but the strengths of N and O may differ greatly, being stronger in the nebulae with higher central-star temperatures. The brightest H II regions can easily be seen on almost any large-scale image of nearby galaxies, and those taken in a narrow wavelength band in the red (including Hα and [N II] lines) are specially effective in showing faint and often heavily obscured extragalactic H II regions. The H II regions are strongly concentrated to the spiral arms and indeed are the best objects for tracing the chemical composition, structure and dynamics of the spiral arms in distant galaxies. They trace recent star formation and, through the analysis of their chemical composition, previous star formation activity. Typical masses of observed H II regions are of the order 10^2 to 10^4 M$_\odot$, with the lower limit depending largely on the sensitivity of the observational method used.

H II regions are the only form of interstellar material which emits strongly in the optical spectral region; therefore, there is a much longer and richer history of observations and theory for them than for the other thermal phases of interstellar matter. Optical observations of H II regions provide fairly complete information about their elemental composition. From their spectra, abundances relative to hydrogen can be estimated for nearly all of the most common elements, particularly He, N, O, Ne, Ar, and S (note that oxygen alone constitutes nearly 50% by mass of the elements heavier than helium.) Furthermore, ionized nebulae are remarkably efficient machines for converting ultraviolet continuum energy from OB stars, originally diluted over wide bandpasses, into a few narrow, intense, optically-thin emission lines. The intrinsic emissivities of these lines are easy to calculate in principle, although they are sensitive to the local thermodynamic state of the gas (electron density n_e and temperature T_e). On the other hand, the thermal parameters can also be determined from the spectra, using diagnostic line-intensity ratios. In this way, H II regions can be used to measure element abundances in the (present-day) gas of distant galaxies.

The sample of extragalactic H II regions studied so far has metal abundances ranging from about 0.02 to several times solar. This is a useful complement to studies of our own Galaxy, which contains no severely metal-deficient H II regions (except for a handful of planetary nebulae formed by stars of the halo population). In contrast, for many H II regions in the outskirts of late-type spirals and in some dwarf irregular galaxies, the process of metal enrichment by stellar nucleosynthesis is still in its early stages, providing a hint on the early chemical evolution of galaxies. These low-metallicity H II regions are also presumed to have experienced only a small degree of alteration in their helium abundances due to stellar activity. There-

fore, their present He/H ratios should be nearly the same as the primordial value, providing valuable tests for cosmological theories. The various *categories* of extragalactic H II regions are essentially lists of their environments. These include:

1. Disk H II regions in spiral and irregular galaxies.
2. Gassy dwarf irregular galaxies with spectra which are heavily dominated by H II regions.
3. Nuclear and near-nuclear regions sometimes called "starburst" or "hotspot" H II regions (e.g. Kennicutt et al., 1989).

The first two categories have the best abundance data available in the literature. Regions in the third group tend to have relatively strong stellar continua and to be fairly metal-rich, which make it to difficult to obtain accurate measurements of the emission lines from which abundances are determined. On the other hand, members of the first two categories are universally regarded as members of the same family. H II regions in nearby galaxies have been well-catalogued; atlases are available for the Large and Small Magellanic Clouds (LMC, SMC), and a large number of other galaxies (e.g. Hodge & Wright, 1967, 1977; Hodge & Kennicutt, 1983). The star-forming dwarf irregulars are usually found by spectroscopic surveys for emission-line galaxies (e.g. Kinman 1984 and more recently the SDSS data releases).

The statistical properties of the H II region populations in spiral and irregular galaxies were addressed by Kennicutt (1988) and Kennicutt et al. (1989). They find that late-type galaxies have both intrinsically higher-luminosity H II regions, and larger total numbers of H II regions after normalization by galaxy size, than do early-type spirals. Within a galaxy, the differential luminosity function of the H II regions is roughly a power-law, $N \propto L^{-2\pm0.5}$, although some low-luminosity irregulars have an exceptional supergiant complex, and Sa-Sb galaxies are deficient in luminous regions. While the positive correlation between the luminosity of the brightest H II region and that of the parent galaxy can be understood as chiefly a sample-size effect, the dependence on morphological type is a real and separate factor. Typical large galaxies contain hundreds of optically detectable H II regions. It is important to note that of all the regions detected and cataloged in Hα or Hβ, it is usually the nearest and the most luminous "giant" H II regions for which abundances are derived.

Some of the best-studied regions are the 30 Doradus complex in the LMC, NGC 604 in M 33, and NGC 5461 and 5471 in M 101. Selection effects play an important role, necessarily poorer spatial resolution contributes to a tendency to identify larger regions in more distant galaxies. This effect is illustrated by Israel et al. (1975), who compare large-beam radio measurements with optical images of the same H II regions in M 101; at better resolution these regions break up into groups or chains of smaller clumps. Likewise, H II regions in dwarf irregulars are also found to have complex structure when closely examined (e.g. Hodge et al., 1989; Davidson et al., 1989). In more distant galaxies, we will always be looking at more heterogeneous volumes; for example, a typical aperture size (4") for spectrophotometric studies corresponds to 1 pc at 50 kpc (the LMC) and 2 kpc at 100 Mpc.

The morphology of many giant extragalactic H II regions can be characterized to first order as a "core-halo" structure, on the basis of both optical and radio-continuum data. The cores are composed of dense material, often in several distinct clumps, close to the ionizing stars. The diffuse, lower-density envelopes are presumably ionized by photons escaping from the inner regions and represent the radiation-bounded edges of the Strömgren volume. Most giant extragalactic H II regions are believed to be essentially radiation-bounded (e.g. McCall et al., 1985). In addition, the denser regions themselves are inhomogeneous, as seen

in the detailed studies of NGC 5471 by Skillman (1985), and of NGC 604 by Diaz et al. (1987). That there are also inhomogeneities on smaller spatial scales is shown by the discrepancy between (rms) n_e values derived from recombination emission and local values determined from density-sensitive line ratios. The dense clumps are embedded in a much lower-density medium, with typical clump volume filling factors of $0.01 - 0.1$ (e.g. Kennicutt, 1984; McCall et al., 1985). The interclump material is often treated as a vacuum in nebular models, because it does not contribute significantly to the optical emission lines.

Giant extragalactic H II regions display supersonic velocities, which appear to correlate with Hβ luminosity. Terlevich & Melnick (1981) interpret the line-widths as virial and therefore usable for determining the local gravitational field; they also find a secondary dependence on metallicity. An alternative interpretation of the origin of the line-widths is that they are a result of stellar winds from the exciting stars, and possibly also from embedded supernova remnants (e.g Dopita, 1981; Skillman, 1985). For nearby regions, it is possible to actually identify the stars which may be responsible for driving the high-velocity gas.

As mentioned above, luminous extragalactic H II regions are ionized by OB associations. For nearby regions, the members of the stellar cluster can be distinguished individually and HR diagrams can be constructed. The nebular ionization structure and emitted spectrum will evolve as the cluster ages and the UV radiation field diminishes and softens. Wolf-Rayet stars are often present in extragalactic H II regions, the frequency of Wolf-Rayet stars is higher for higher-metallicity regions as proved by Maeder et al. (1980). Wolf-Rayet stars are important in this context because they furnish metal-rich outflows which are capable of altering the chemical composition of their gaseous environment. Giant H II regions are also known hosts of Type II supernovae. Winds and supernovae from the massive stars can contaminate (or enrich) the local gas in H II regions in He, C, O, and other species. Evidence for such local enrichments has been sought and perhaps seen in some regions (Skillman, 1985; Pagel, 1986).

1.2 Determination of chemical abundances in H II regions

H II regions are ideal places to determine the abundance of the elements that are responsible for recombination and fine-structure lines. The list of these elements is generally limited at the present time, although lines of many more elements are observable in several planetary nebulae and high spectral resolution and multi-wavelength studies of nearby H II regions (e.g. García-Rojas et al., 2006). The determination of element abundances in H II regions are given relative to the hydrogen content, which is observed by its recombination lines. Only a few abundant elements give observable recombination lines with similar physics: helium, carbon, nitrogen and oxygen, whose lines are very weak to detect and may suffer problems with fluorescence excitation. The abundances derived from the fine-structure lines in the visible are sensitive to both temperature and density, and the interpretation of the line intensities is a delicate problem. In some cases, the temperature of the emitting zone can be obtained and the abundance determination is safer. However, even in this case temperature fluctuations can yield systematic errors in the abundances.

The abundances derived from the mid-and far-infrared fine structure lines are not sensitive to electron temperature and are little affected by extinction. These are considerable advantages with respect to the optical lines. However, there are important discrepancies between the abundances derived from infrared and from optical lines. These differences may originate in temperature fluctuations or in errors in atomic parameters, but one has to consider that the critical density for infrared lines is generally much smaller than for visible lines, so that the abundances derived from the infrared lines are underestimated if the density is high (this effect can be important for planetary nebulae).

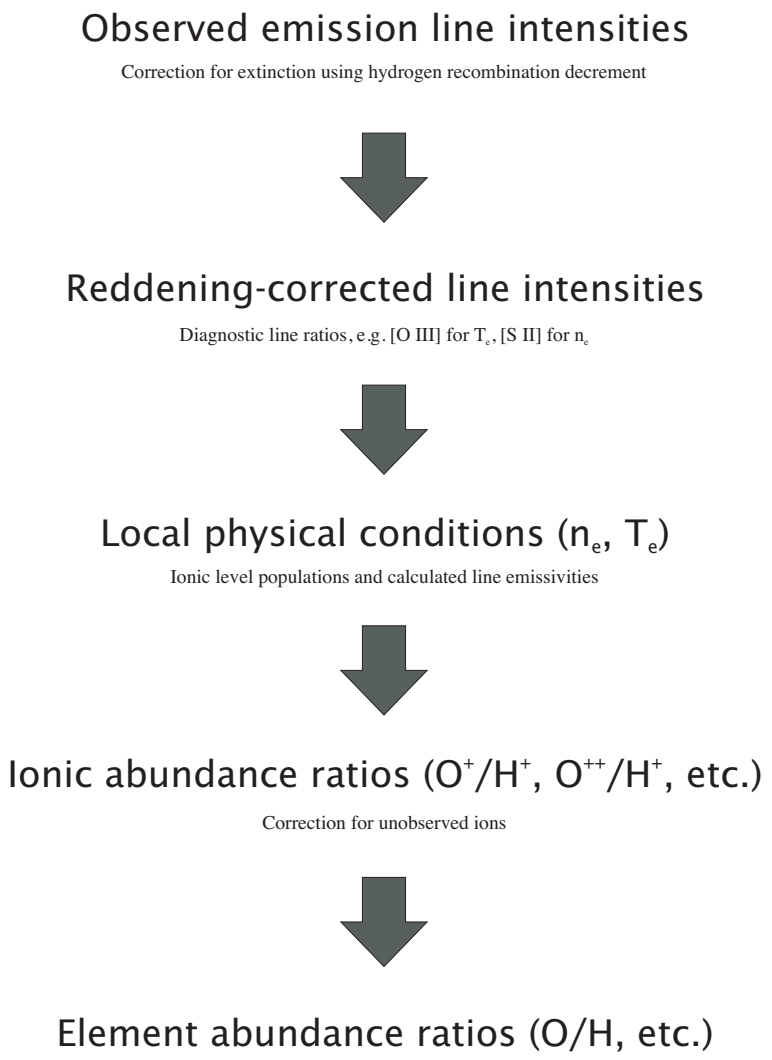

Figure 1.1: The *direct method* of chemical abundance determinations.

All elements (with the obvious exception of H) exist in several ionization states in H II regions. However, only the abundances of those ions that emit observable lines can be determined. If such ions are minor species, they yield no useful information because the physical parameters of H II regions are most often too uncertain to allow an accurate solution of the ionization equilibrium. This is for example the case for O I, C II, S II or Si II. If the observed ion is a major species the situation is more favorable since we can calculate, more or less accurately, the abundances of the unobserved ions of the same element. However, uncertainties remain if a high precision is required, as is the case of helium in a cosmological context. The most favorable case is that of oxygen, whose major ionization states, O II and O III, are observable optically and for which the electron temperature T_e can be determined. For this reason, oxygen is, after helium, the element whose abundance is best determined, at least if the temperature is large enough (or the metallicity is too low) for the temperature-sensitive lines (e.g. [O III] λ4363) to be measured. If this is not the case, we may construct tailored models of the nebular ionization and thermal structure of a H II region to estimate the electron temperatures and ionization correction factors for individual ions.

However, given the difficulty of detecting the T_e-sensitive line and the assumptions made in nebular modeling, a very popular approach is to obtain the abundance of extragalactic H II regions using empirical rela-

tions between the oxygen abundance and the intensity of the [O II] $\lambda\lambda$3726, 3729 and [O III] $\lambda\lambda$4959, 5007 lines relative to Hβ (Pagel, 1997) or by using the [O II] $\lambda\lambda$7320, 7330 as described by Aller (1984) and implemented by Kniazev et al. (2004) in SDSS H II galaxies. This method however, is the less accurate and much discussion about the reliability of the different empirical calibrations is still ongoing in the literature (e.g. see Kewley & Ellison, 2008, for a thorough discussion). A full discussion regarding this topic is beyond the scope of this chapter, however, in chapter 5, I include a small review on the different empirical techniques of abundance determinations (considering their particular advantages and pitfalls), and their implementations in the context of the work carried out in this dissertation. A more complete explanation of the determination of nebular abundances from emission lines can be found in references on the physics of gaseous nebulae such as Aller (1984), and Osterbrock & Ferland (2006).

1.3 Abundance gradients in galactic disks

It has been noticed that certain H II region emission-line ratios, such as [O III]/Hβ, vary across the disks of nearby spiral galaxies. The interpretation of this variation in terms of a metallicity trend was introduced by Searle (1971), in a paper that laid the groundwork for the entire field of abundance gradients. It was soon followed up by further observational studies and a more rigorous analysis involving the construction of realistic nebular models (Shields, 1974). From the start it was recognized that there was a need for a "second parameter" in addition to the O/H ratio, to explain an observed systematic increase in O^{++}/O^{+} with decreasing O/H. Shields & Tinsley (1976) suggested that this secondary effect results from a tendency for the effective temperatures of the ionizing stars to be hotter for lower O/H, and interpreted it as a metallicity-dependent truncation of the top end of the initial mass function (i.e. that the formation of very massive stars is inhibited by higher metallicity). Some form of the idea of a Z-dependent IMF is still a popular interpretation of the "excitation" trend (e.g. Vilchez & Pagel, 1988), but it is also the case that a similar effect can arise from systematic variations in the nebular geometry and/or filling factor (Mathis, 1985; Dopita & Evans, 1986).

An extensive body of literature has been amassed on the subject of abundance gradients in galaxies. Not surprisingly, many works have focused on large, nearby galaxies with many observable H II regions, such as M 33 (Vilchez et al., 1988; Rosolowsky & Simon, 2008) and M 101 (Evans, 1986; Torres-Peimbert et al., 1989; Kennicutt & Garnett, 1996). The gradients are usually expressed as a logarithmic fit to some 5 – 20 regions per galaxy, and have a magnitude of about δlog(O/H)/R = -0.08 ($\pm$ 0.03) dex/kpc. This is similar to the values derived for the solar-neighborhood metallicity gradient in the Milky Way galaxy. The trend of these gradients in the inner parts of galactic disks are difficult to study, both because the H II region samples are often small, and more fundamentally because these are generally the most metal-rich regions, for which [O III] λ4363 is unobservable and therefore the derived abundances are heavily model-dependent.

The steepest abundance gradients were initially seen in late-type spiral galaxies (types Sb-Scd). Irregulars and barred spirals tend to have weak or zero radial gradients. Early type spirals are harder to study because their H II regions are intrinsically fainter, but studies of M 81 (Sab) show it to have an O/H gradient similar to those of M 33 and M 101 (Garnett & Shields, 1987). There is at present no convincing evidence that the O/H gradient depends on morphological type among spiral galaxies. However, there is evidence for a good correlation between mean O/H abundance and the overall galaxy mass or luminosity. This trend resembles the correlation of stellar metallicity with galaxy mass, and probably has its roots in the fundamental processes of galaxy formation and evolution.

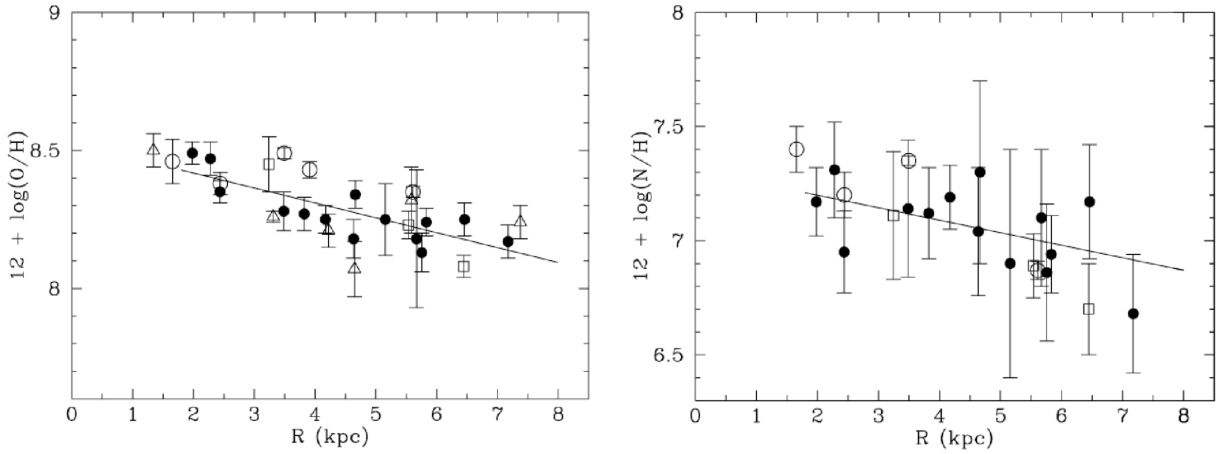

Figure 1.2: The O/H and N/H abundance vs. galactocentric distance in M 33, examples of the radial oxygen and nitrogen abundance gradients. Plots taken from Magrini et al. (2007).

Along with the trend in [O III]/Hβ, a similar radial trend was noted for the ratio [N II]/Hα, which decreases with increasing distance from the centers of spiral galaxies. Although part of this trend is due to the generally lower degree of ionization in the outer H II regions, there also must be a real variation in abundance. Unlike oxygen, for nitrogen one usually can measure the singly-ionized state only; unfortunately, N^{++} has no strong optical lines. As mentioned before, the nitrogen abundance is basically derived from [N II]/[O II]. The relative behavior of O and N is often displayed by plotting N/O vs. O/H. Some studies find that N/O varies almost as steeply as O/H, which has special significance in the context of chemical evolution models, but others claim that N/O varies only slightly or is constant across the disks of galaxies such as M 101, M 33, M 81, and M 83. There also appear to be variations in N/O at a given O/H from galaxy to galaxy (same references as above). Some of these variations may be an artifact of the analysis, especially since N^{+} contains only a small fraction of the nitrogen for the lowest-abundance, most highly ionized regions. For such regions, the ionization correction factors are very large, and the uncertainties in the ionization structure translate into large uncertainties in the elemental abundance of nitrogen. Nevertheless, there is accumulating evidence that nitrogen has a more complicated behavior than does oxygen, with N/O being roughly constant at low values of O/H and increasing at higher O/H (e.g. Pagel, 1985; Torres-Peimbert et al., 1989). Measurements of N/O in metal-poor dwarf irregular galaxies are an important ingredient in this argument.

Scatter in gradient determinations has been seen in various studies (e.g., in the Milky Way Afflerbach et al. 1997 or in M 33 Rosolowsky & Simon 2008), even after accounting for uncertainties in the stellar absorption and reddening corrections, an intrinsic scatter of ~ 0.1 dex has been measured in these very well-studied galaxies which is unexplained by the measurement uncertainties. Regardless of its source, gradient determinations made in the face of significant scatter coupled with a limited number of observations may produce widely varying results. This historical evolution of the gradient determination ranging over nearly an order of magnitude, should serve as a cautionary example. Only large numbers of measurements can overcome the uncertainties engendered by the intrinsic variance, as some observations suggest that the uncertainties in the gradients are systematically underreported.

1.3.1 The Galactic abundance gradient

Because of interstellar extinction, one can use the same techniques as for extragalactic H II regions only for the part of our Galaxy outside a galactocentric distance of about 7 kpc. Studies such as those by Hawley (1978) found gradients similar to those in other spirals, δlog(O/H)/δR = -0.04 to -0.06 dex/kpc and δlog(N/H)/δR = -0.10 dex/kpc. Determination of abundances in the inner galaxy requires the use of other techniques, such as measuring electron temperatures from radio recombination lines. The values of T_e are found to increase systematically with increasing radius, presumably because of a decreasing abundance of oxygen, the primary coolant. The inferred gradient in O/H is δlog(O/H)/δR = -0.07 dex/kpc after the classic paper of Shaver et al. (1983).

The results from optical studies for the other measurable elements are similar to those for other galaxies: N/H varies more steeply than O/H; S/O, Ne/O, and Ar/O do not vary in the outer part of the Galactic disk. Again, the optical studies are restricted to the unobscured portion of the Milky Way galaxy, and therefore do not sample the inner disk where the inferred O/H values are high. A more recent development, made possible by improvements in infrared detectors and the availability of space observatories. The exploration of the infrared spectral region as a tool for studying the galactic abundance gradient. The mid-infrared spectral region (5-30 μm) contains emission lines of the major ions of Ar, S, and Ne: [Ar II] 7.0 and [Ar III] 9.0 μm; [S III] 18 and [S IV] 10.5 μm; and [Ne II] 12.8 μm. These lines have been measured in a number of H II regions in the inner Galaxy, and evidence for abundances elevated by factors of two or three have been found for the Galactic Center and for H II regions in the 5 kpc "ring" region (Pipher et al., 1984).

However, even these mid-infrared lines suffer somewhat from extinction. In particular, the [Ar III] and [S IV] lines fall in the middle of the strong 10 μm silicate absorption feature, where the optical depth is comparable to that in the near-infrared. Another approach to studying abundances in the inner galaxy is to make use of the fine-structure lines of [O III] 52, 88 μm and [N III] 57 μm. By a happy coincidence, these lines from the abundant and (presumably) usually co-extensive O^{++} and N^{++} ions fall close together in wavelength and have fairly similar dependences on the electron density. The line emissivities are also essentially independent of the electron temperature. Measurements of these three lines therefore yield a relatively accurate value for the N/O ratio. A survey of about a dozen galactic H II regions in these lines yielded strong evidence that N/O in the Galactic Center and 5 kpc "ring" is elevated by a factor of 2 or 3 as compared to the solar neighborhood. There remain some unsettled questions regarding N/O determinations from the far-infrared lines, including possible ionization structure effects in H II regions ionized by very cool stars and a systematic discrepancy between values derived from the infrared lines and those derived optically from [N II]/[O II] (Rubin et al., 1988).

More recent observations of IR fine-structure lines of the [S III] 19 μm, [O III] 52 and 88 μm, and [N III] 57 μm in compact H II Galactic regions have found abundance gradients of the form [S/H] = (-4.45 $\pm$ 0.04) - (0.063 $\pm$ 0.006) (kpc), [N/H] = (-3.58 $\pm$ 0.04) - (0.072 $\pm$ 0.006) (kpc), and [O/H] = (-2.85 +/- 0.06) - (0.064 +/- 0.009) (kpc) (Afflerbach et al., 1997). These abundances are consistent with production of sulphur, nitrogen, and oxygen by primary nucleosynthesis. Comparison with abundances in other galaxies implies a Hubble type between Sab and Sb for our Galaxy and an unbarred or mixed galactic structure (Vila-Costas & Edmunds, 1992).

1.4 Comparison with Chemical Evolution Models

The recognition of significant variations in the gas composition within and among galaxies, along with parallel results on the stellar populations, inspired the development of chemical evolution models which attempt to explain these patterns. The so-called "simple model" postulates a closed system of gas and stars, which self-enriches in metals as generations of stars age, die, and seed the ambient gas in the heavy elements (Searle & Sargent, 1972). This model also makes the approximations that the stellar lifetimes and timescale for complete mixing of nucleosynthetic products are negligible in comparison to the timescale on which the metallicity evolves ("instantaneous recycling"). The simple model makes a specific prediction regarding the metallicity and system properties:

$$Z = y \ln(M_{total}/M_{gas}), \tag{1.1}$$

in this equation Z is the metal abundance, y is the fraction of the stellar mass converted to heavy elements (the *yield*), and $M_{total} = M_{gas} + M_{stars}$.

Although this model is most appropriate for the low-mass galaxies, it can also be applied to large disk galaxies if concentric radii are treated as independent zones. However, it does not explain the observed gradients, so modifications such as radial flows, matter exchange with an outside reservoir (infall and outflow), or a variable stellar initial mass function, have been proposed as modifications to the model (Matteucci & Francois, 1989; Dopita, 1990).

The relative abundances of nitrogen and oxygen are of particular interest, since they are synthesized in different astrophysical sites. Oxygen is synthesized in massive stars and distributed into the interstellar medium by Type II supernovae, while the origin of nitrogen is more problematic. A distinction is frequently made between "primary" nucleosynthetic products, which can be synthesized directly from H and He in Population III stars, and "secondary" products, which require a "seed" heavy nucleus to be initially present in the star where its synthesis occurs. By this definition, oxygen is a primary species. Nitrogen is secondary when made as a by-product of CNO-cycle hydrogen burning. According to the simple closed-box model, the abundance of a secondary species is quadratic, so that if N is secondary and O primary, then (N/H) $\propto$ (O/H)^2, or (N/O) $\propto$ (O/H). The N/O ratio does appear to approach this behavior, for H II regions with moderately high O/H values in M 101 (Torres-Peimbert et al., 1989) and in the Milky Way. However, below a certain values of O/H, it appears that N/O is constant; these low-metallicity H II regions occur mostly in low-mass galaxies. Thus, it is becoming clear that nitrogen is not purely a secondary nucleosynthetic product. Indeed, N may be produced within intermediate-mass stars by an effectively primary process, if C synthesized within the star by the triple-alpha reaction is later subjected to the CN cycle. Nitrogen made by this process would be primary, but there might be a time-delay in building up its abundance relative to the nuclear products of supernovae, because of the longer lifetimes of the source stars.

The other elements measured in extragalactic H II regions, S, Ne, and Ar, are not likely to be dominated by secondary processes. They might still, however, vary differently than oxygen, if they were produced in stars of different mass ranges and the IFM varied or the timescales for enrichment differed substantially. There are known variations in the abundance ratios of certain elements. For example the fact that the iron-group is deficient relative to oxygen in Population II stars is thought to reflect an origin for the former chiefly in Type I supernovae, which originate in long-lived progenitors, as opposed to synthesis of oxygen in massive stars and Type II supernovae.

In the context of chemical evolution models, Garnett (2002) studied the metallicity-luminosity and metallicity-rotation speed correlations for spiral and irregular galaxies for a sample of spiral and irregular galaxies having well-measured abundance profiles, distances, and rotation speeds. He finds that the O/H-V_{rot} relation shows a change in slope at a rotation speed of about 125 km s^{-1}. At faster V_{rot}, there appears to be no relation between average metallicity and rotation speed. At lower V_{rot}, the metallicity correlates with rotation speed. This change in behavior could be the result of increasing loss of metals from the smaller galaxies in supernova-driven winds. The idea was tested by looking at the variation in effective yield, derived from observed abundances and gas fractions assuming closed box chemical evolution. The effective yields derived for spiral and irregular galaxies increase by a factor of 10-20 from $V_{rot} \sim 5$ to 300 km s^{-1}, asymptotically increasing to approximately constant y_{eff} for $V_{rot} \sim 150$ km s^{-1}. The trend suggests that galaxies with $V_{rot} \sim$ 100-150 km s^{-1} may lose a large fraction of their supernova ejecta, while galaxies above this value tend to retain metals. The determination of effective yields as function of galactic radius and its interpretation stands as one of the main studies in order to discriminate among different physical effects which may affect the chemical evolution of a galaxy.

1.5 Goals of this dissertation

As described in this chapter, the study of chemical abundances has undergone a remarkable development in the last decades thanks mostly to important observational efforts that have focused on the derivation of physical and chemical properties of emission line H II regions in galaxies by spectroscopic techniques. The main motivation common to all of these observations is to use the chemical information as one of the means at our disposal to understand the physical processes at play in the formation and evolution of galaxies in the universe.

Hitherto, most spectroscopic studies in nearby objects have been limited by the number of objects sampled, the number of H II regions observed and the coverage of these regions within the galaxy surface. In order to increase significantly the number of H II regions sampled in any given galaxy we require the combination of high quality multi-wavelength data and wide field spectroscopy. The advent of multi-object and integral field spectrometers with large field of view now offer us the opportunity to undertake a new generation of observations, based on samples of scores to hundreds of H II regions and full 2-dimensional (2D) coverage. These sort of data would enable to test, confirm and extent the previous body of results from small sample studies, while at the same time open up a new frontier of studying the 2D metallicity structure of disks and the intrinsic dispersion in metallicity, or to test and strengthen the diagnostic methods that are used to measure the H II region abundances in galaxies, among other issues.

The scientific core of this dissertation is based on an observational project conceived to tackle the problem of the 2D spectroscopic coverage of the whole galaxy surface. New techniques in imaging spectroscopy (or integral field spectroscopy, IFS) provide a powerful tool for studying the small and intermediate scale-size variation in line emission and stellar continuum in nearby well-resolved galaxies. We designed a project to take advantage of these new observational techniques in order to assemble a unique spectroscopic sample from which we could study, with unprecedented detail, the star formation and gas chemistry across the surface of a galaxy. The observations consist of Integral Field Unit (IFU) 2D spectroscopic mosaics of a representative sample of nearby galaxies ($D < 100$ Mpc) with a projected angular size of less than 10 arcmin. The mosaics were constructed using the unique instrumental capabilities of the Postdam Multi Aperture Spectrograph, PMAS (Roth et al., 2005) in the PPAK mode (Verheijen et al., 2004; Kelz & Roth,

2006) at the German-Hispanic Astronomical Centre at Calar Alto (CAHA), Spain. The PMAS fibre PAcK (PPAK) is one of the world's widest integral field unit with a field-of-view (FOV) of 74×65 arcseconds that provides a semi-contiguous regular sampling of extended astronomical objects. This project represents the first attempt to obtain 2D spectra of the whole surface of a galaxy in the nearby universe. The spectroscopic mosaicing comprises more than 50 000 spectra in the optical wavelength range.

This observational project was devised as a scientific international consortium, the members are world-leading experts in their respective fields, including star formation and chemical abundances of galaxies, active galactic nuclei, multiwavelength observations of emission line regions and 2D spectroscopy. The project was entitled: the **P**PAK **I**FS **N**earby **G**alaxies **S**urvey, or **PINGS**. The P.I. of this project is Prof. Robert C. Kennicutt Jr. at the Institute of Astronomy, University of Cambridge. The collaborators of the consortium are: Dr. Ángeles Díaz at the Universidad Autónoma de Madrid, Spain; Dr. Anna Pasquali at the Max-Plank Institut für Astronomie in Heidelberg, Germany; Dr. Sebastián S. Sánchez at CAHA, Spain; Benjamin Johnson and Caina Hao at the University of Cambridge, UK.

The primary scientific objectives of this dissertation are to use the PINGS observations to obtain pixel-resolved emission-line maps across the disks of the galaxies to study the 2D abundance distribution and on characterising the relations between these abundance properties and the physical properties of the parent galaxies. By targeting virtually every H II region in the galaxies, as a consequence of the nearly complete spatial coverage of the IFUs, we are able to test for the first time the systematic dependences of the strong-line abundances on the size, luminosity, surface brightness, and other properties of the H II regions. In that respect, the PINGS observations and the subsequent analysis represent a leading leap in the study of the chemical abundances and the global properties of galaxies, information which is most relevant for interpreting observations at all redshift sources accessible with the current technology.

1.5.1 Structure of the dissertation

The structure of this thesis is as follows: In § 2, I discuss the importance of Integral Field Spectroscopy (IFS) in astrophysics, including an explanation of the technique with their advantages and pitfalls, a description of the available instrumentation in the world by the time this project was envisaged, and the selection criteria of the telescope-instrument chosen for this project. I also include a brief review to previous works that have attempted to obtain 3D chemical abundance information in galaxies. In § 3, I present the sample of galaxies and the selection criteria followed according to the scientific objectives established for this dissertation. This chapter also includes a full description of the logistics and observations, explaining the telescope set-up and the particular observing technique adopted for this project. In § 4, I explain the reduction process of the IFS raw data, the additional corrections implemented in this project and the improvements with respect to previous pipelines, particularly regarding the flux calibration and the sky-subtraction. The possible sources of errors and uncertainties are addressed, together with an explanation of the techniques implemented to minimise them. In § 5, I present the integrated spectra of the PINGS sample, obtained by co-adding the spectra from their corresponding mosaics. Comparisons with previously published data are included. An analysis of the ionized gas component is performed, together with the techniques and methodologies implemented in order to derive the physical parameters of the integrated gas-phase of the galaxies sample. In § 6, I present a complete 2D spectroscopic study for a selected number of galaxies from the sample. Selected H II regions previously observed are compared with spectra extracted from the PINGS sample. A set of emission line maps calculated from each galaxy is presented, including a quantitative description of the 2D distribution of

the physical properties inferred from them. Then, a detailed, spatially-resolved spectroscopic analysis of the selected galaxies is performed, based on different spectral samples extracted from the full IFS mosaics of the galaxies. Several diagnostic diagrams and the state-of-the-art abundance diagnostic techniques are used to obtain the 2D distribution of the physical properties and chemical abundances of the selected sample. Finally, in § 7 I present the general conclusions of this dissertation, including some planned paths of future investigation.

2

Techniques and applications of 2D spectroscopy

This chapter is devoted to discuss the importance of 2-dimensional (2D) spectroscopy and in particular of Integral Field Spectroscopy (IFS) as a revolutionary technique in astrophysics and how it can be applied to the determination of chemical abundances. For this purpose, an explanation of the 2D spectroscopic techniques is included, presenting their different advantages and pitfalls, as well as a description of the available instrumentation in the world and the criteria followed in order to select the telescope-instrument combination for the observations presented in this dissertation. Furthermore, I include a brief review to previous works that have attempted to obtain 2D information in nearby galaxies, and the prospects of IFS in future ground and space based observatories.

The term 2D spectroscopy is often used to indicate any technique that produces spatially-resolved spectra over a two-dimensional field. These techniques are known generically as 2D spectroscopy, 3D imaging or spectral imaging[1]. All 2D techniques produce a datacube of a scalar quantity related to flux density as a function of spatial coordinates in the field and wavelength: $I(x, y, \lambda)$. The advantages of 2D spectroscopy arise as a result of the simultaneous capture of spectral and spatial information. Apart from rendering the process more efficient, simultaneity guarantees the homogeneity of the data. 2D spectroscopy also offers practical advantages. It is not necessary to centre on the slit or to adjust the slit width to atmospheric conditions (since the spectral resolution is already defined by the size of the fibres or lenses on the detector). It also allows the spectra to be characterized and corrected for differential atmospheric refraction. These effects can severely influence the classical sequential techniques, especially long-slit observations.

In spite of the obvious advantages of this technique in tackling known scientific problems or in opening up new lines of research, and although there is now an increasing number of instruments available to astronomers, 2D spectroscopy is a technique that is relatively little used. Radio astronomers were making 3D spectral imaging observations long before it was adopted seriously in the optical regime. Nowadays there are very few groups capable of reducing and analysing the huge volume of data generated by observations

[1] The term 3D spectroscopy is also often used, perhaps erroneously.

with a 2D instrument, and these groups tend to be involved with a particular instrument. This implies that most 2D data reduction and analysis procedures and packages are orientated towards and limited to a single instrument so that experience with one instrument does not necessarily guarantee the ability to work on another.

2D techniques are generally preferable to slit spectroscopy for a number of reasons: (a) slit losses are eliminated; (b) accurate target acquisition is not required; (c) the actual target position can be recovered from the data by reconstructing an image also an aid to accurate mosaicing; (d) errors in radial velocity due to differences in the barycenter of the slit illumination obtained from the object and from reference sources can be eliminated; (e) the global velocity field is recovered without bias imposed by the observer's choice of slit position and orientation; (f) atmospheric dispersion effects can be corrected without loss of light by manipulation of the datacube; (g) in poor or variable seeing, most 2D techniques are always optimally matched to the object Point Spread Function (PSF).

2.1 The principles of integral field spectroscopy

Integral Field Spectroscopy (IFS) is that subset of 2D spectroscopy in which all the data for one pointing of the telescope is obtained simultaneously. The other methods, such as Fabry Perot Interferometry (FPI) and imaging Fourier transform spectroscopy (IFTS), use the time domain to step through wavelength space (or a Fourier conjugate). This leaves them potentially sensitive to changes in the instrumental or sky background, but allows a wide field to be covered in one pointing. In contrast, IFS encodes all the spectral and spatial information in the same exposure resulting in a smaller field of view for a given detector format.

Figure 2.1 shows the principle of Integral Field Spectroscopy. A two-dimensional field-of-view on the sky (white frame) is sampled into discrete spatial elements, which can have a round, hexagonal, or (like in this example) square shape. These spatial elements are sometimes called SPAXELS in order to distinguish them from ordinary PIXELS of direct imaging instruments. The peculiar virtue of IFS consists in the ability to create an individual spectrum for each spaxel simultaneously over the whole field-of-view. After data reduction, the set of generated spectra can be rearranged in a computer to form a 3-dimensional data cube of two spatial, and one wavelength coordinates. Alternatively, it is possible to create monochromatic images or co-added quasi-broadband images from slices of the datacube.

2.1.1 Development of 2D spectroscopic techniques

The first attempts to provide 2D spatially resolved spectroscopy consisted in using sequential methods that use time to scan one of the three coordinates. For example taking a series of different exposures, moving the telescope by one slit's width with each exposure in a direction perpendicular to the slit, thus effectively scanning the object with the slit. This is the technique of long-slit or drift scanning. An alternative technique started in 1974 involved Fabry-Perot interferometry in combination with direct imaging detectors (first photographic, later on with images tubes and CCDs), this technique consists in using a filter adjustable in λ, varying the spectral coordinate in successive exposures and obtaining a collection of narrow-band images, introducing in this way the concept of data cubes, which were common use in radio astronomy. Aside from other practical and technical setbacks, one conceptual disadvantage of these techniques is that different parts of the data cube are obtained under different instrumental and atmospheric conditions. Furthermore, both methods involve scanning, which implies a correspondingly large number of exposures, i.e. an overall time

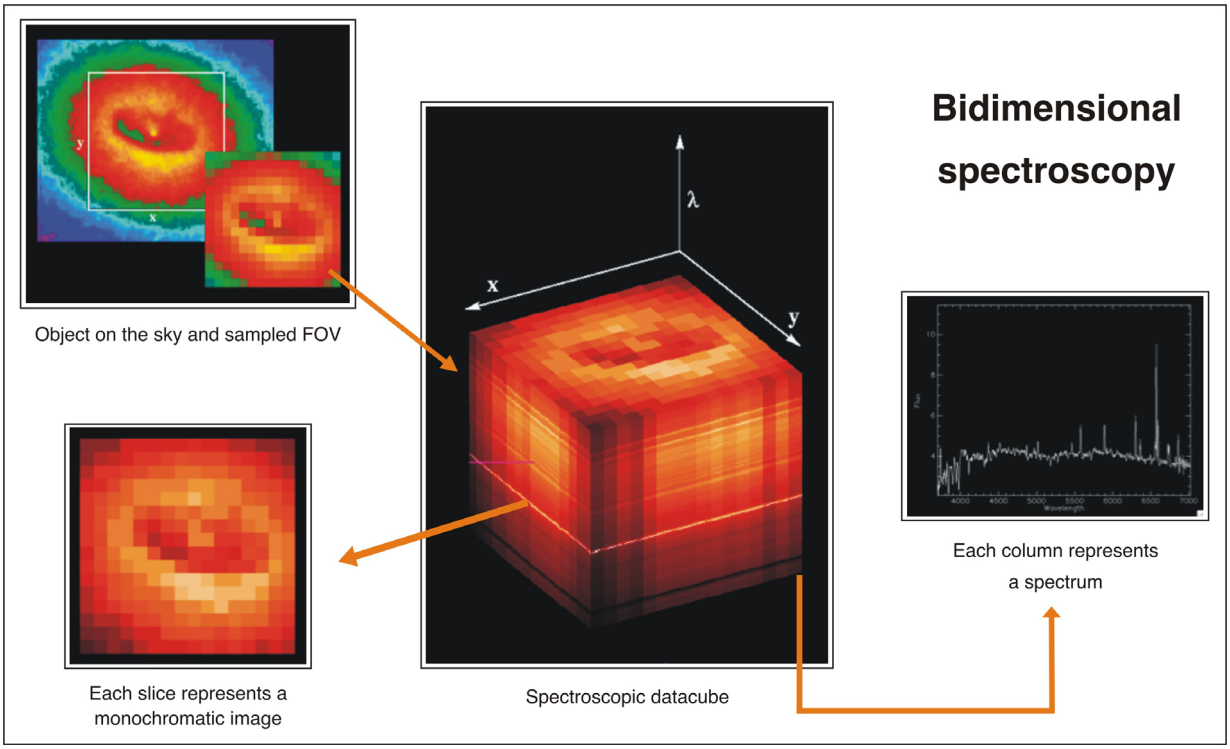

Figure 2.1: Diagram showing the principle of bidimensional spectroscopy. A reduced datacube can be thought as a series of monochromatic images along the spectral range, whereas each column represents an individual spectrum of a discrete spatial position. Figure adapted from an original after M. Roth, `http://tinyurl.com/IFS-principle`.

consuming procedure, an non-simultaneous recording of spectra.

Introduced in 1998, the first true integral field spectrographs were fibre optical instruments, which used a bare fibre-bundle to reformat the 2D focal plane of the telescope into the 1-dimensional geometry of a spectrograph slit. At about the same time, an alternative method was employing a lens array in the focal plane and the so-called micro-pupil principle, to generate a spectrum for each lenslet, similar to a standard multi-object spectrograph. As a variant of the latter two types, the combination of a lens array with a fibre bundle was also used in a number of applications. Another major milestone in the development of 2D spectroscopy was the use of an image slicer, i.e. a stack of long and narrow tilted mirrors to dissect the focal plane, and thus create a family of mini-longslits, which potentially achieves a very high density of spectra. Along with these technical developments, the deployment of various types of 2D spectrographs as common user instruments at major 4 and 8m class telescopes was clearly an important milestone in the history of this technique.

2.2 Choice of instrumentation

Clearly, IFS has an enormous potential advantage over traditional slit spectroscopy since it provides much greater information for extended objects of small or moderate size. But this can be realised only if the system provides adequate performance for a given observational strategy in terms of spatial resolution, field size, spectral resolution, simultaneous wavelength range, and throughput.

From the observational point of view of this dissertation, the objective of the research plan was to obtain

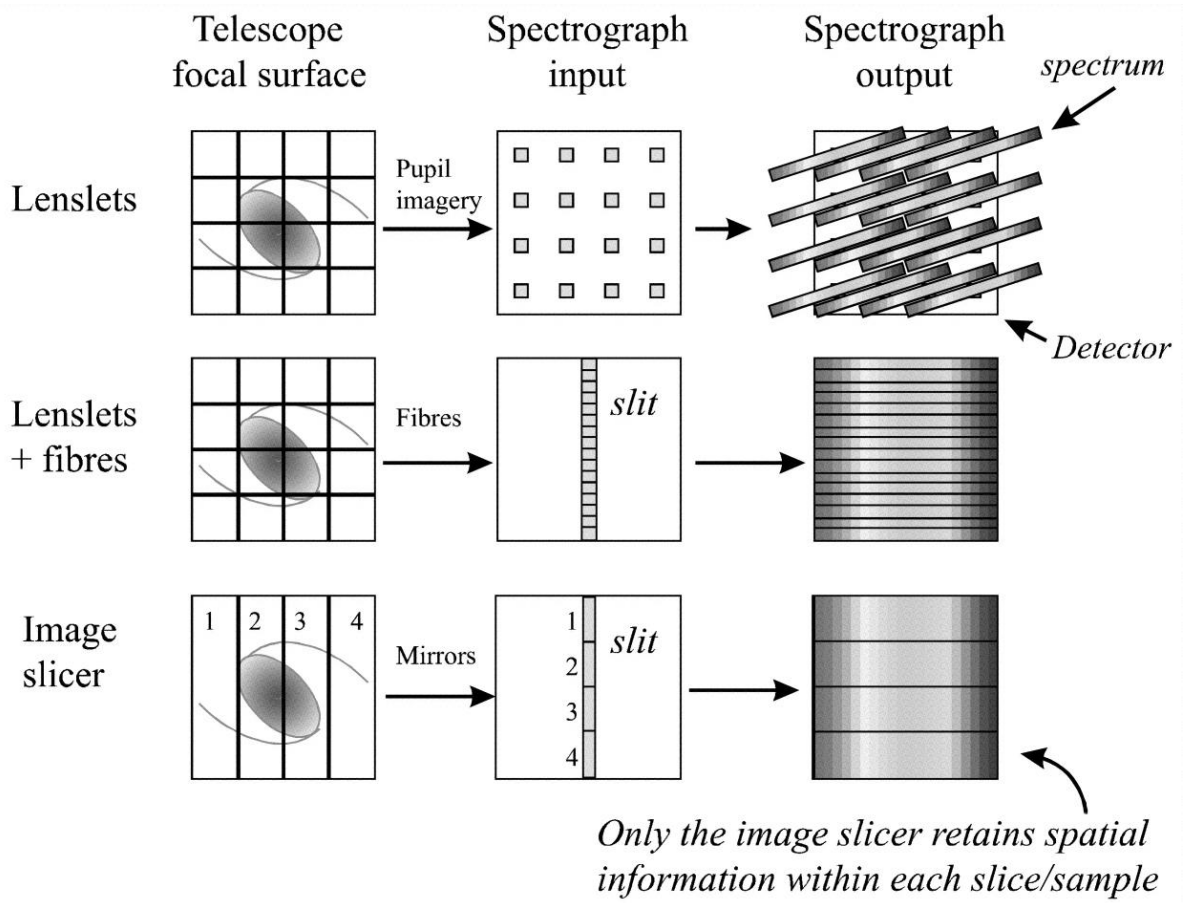

Figure 2.2: The main techniques of integral field spectroscopy, figure adapted from Allington-Smith et al. (1998).

optical IFS of the whole surface area of a sample of nearby galaxies, from which we could construct 2D maps of the chemical composition of stars and gas, and the dust distribution of the galaxy sample. Furthermore, we had to take into account the correct choice of targets, in terms of size, brightness, astrophysical importance, etc. The sample selection contributed significantly to the complex task of finding the right instrumentation. Therefore, we required a correct combination of telescope + instrument that could be optimal for this specific science case.

In the early evolution of this project, different instruments were considered capable of obtaining multi-dimensional spectral coverage in the optical wavelength range. The main characteristic sought at this first stage was that the instruments needed to have a relatively large FoV, required to cover as much surface area as possible per a given pointing and observation. Ideally, a wide spectral window would be necessary in order to cover the main optical diagnostic emission lines used to study the gas in extragalactic H II regions. These include the [O II] $\lambda\lambda$3727,29 ($\sim$ 373 nm) doublet in the blue part of the spectrum, and an the other spectral end, the density sensitive [S II] $\lambda\lambda$6717,31 lines ($\sim$ 672 nm) in the red. The nearby objects considered as potential targets would show practically a zero-redshift, therefore the [O II] doublet would be observable at nearly its rest-frame wavelength.

Among all the instruments available worldwide capable of providing 2D spectral coverage with a close description of the characteristics listed above, we considered the following instruments by the time of the planning of the observational project of this dissertation:

- **VIMOS**
  The VIsible MultiObject Spectrograph (VIMOS), is an optical (360 – 1000 nm) wide field imager and multi-object spectrograph mounted on the UT3 Melipal Very Large Telescope (VLT) in Chile. VIMOS operates in three different modes: i) Imaging (IMG); ii) Multi-Object Spectroscopy (MOS); and iii) Integral Field Unit (IFU). In the case of MOS, the instrument makes use of laser cut masks capable of using between 40 to 200 slits per mask. For the IFU configuration, VIMOS incorporates 6400 fibres (80×80) coupled with microlenses. The total aperture of the FoV ranges between 13×13 and 54×54 arcsec, with element sizes of 0.33 – 0.67 arcsec per fibre depending on spectral resolution and spatial magnification. Reference: Fevre et al. (1998).

- **GMOS**
  The two Gemini Multi-Object Spectrographs instruments (GMOS) at Gemini North (Hawaii) and South (Chile) , provide 400 – 1100 nm long-slit and multi-slit spectroscopy and imaging over a 5.5 arcmin field of view. Each GMOS is also equipped with an Integral Field Unit (IFU) making it possible to obtain spectra of an area of about 35 square arcsec (5×7 arcsec). The IFS mode of GMOS uses a lenslet array of 1500 elements with an element size of 0.2 arcsec. Reference: Allington-Smith et al. (1998).

- **AAOmega-SPIRAL**
  AAOmega is a general purpose instrument providing multi-object and integral field spectroscopy, located at the Anglo-Australian Telescope (AAT), Australia. The instrument has two observing modes: integral field imaging and pupil segmentation imaging. The instrument is fed by 392 fibres in multiple-object spectroscopy mode or by 512 fibres in the SPIRAL (Segmented Pupil/Imaging Array Lenses). For the IFU mode, the FoV is 11×22 arcsec, with an angular size per fibre of 0.7", covering a wavelength range 370 – 950 nm and a limiting magnitude in $B = 22.02$. Reference: Sharp & Team (2006).

- **FLAMES**
  FLAMES: Fibre Large Array Multi Element Spectrograph, is the multi-object, intermediate and high resolution spectrograph of the VLT. Mounted at UT2, FLAMES can access targets over a field of view 25 arcmin in diameter. FLAMES feeds two different spectrograph covering the visual spectral range (370 – 900 nm): GIRAFFE and UVES. GIRAFFE is aimed at carrying out intermediate and high resolution spectroscopy of galactic and extragalactic objects having a high spatial density, it allows the observation of up to 130 targets at the time or to do integral field spectroscopy, with intermediate resolution. UVES provides the maximum possible resolution (R = 47000) but can access only up to 8 objects at the time. Reference: Pasquini et al. (2002).

- **OASIS**
  The optical integral-field spectrograph (OASIS) is installed at one of the science ports of the William Hershel Telescope (WHT) adaptive-optics (AO) system in a dedicated Nasmyth enclosure. Light from the sky is acquire through ~ 1100 hexagonal lenslets in a rectangular array. Three different enlargers can currently be placed in front of the lenslet array in order to change the field of view and corresponding spatial sampling per lenslet. The light from each lenslet is then dispersed using a grism (or prism) and imaged onto the 2k $\times$ 4k detector. 15 different spectroscopic configurations are available, giving a variety of spectral ranges and resolutions. As the spatial sampling and the spectroscopic configuration are independent of each other, this leads to a total of 45 possible configurations for spectroscopy.

The wavelength range of this instrument is 400 – 1000 nm, with a total aperture ranging from 2.4 to 16 arcsec. Reference: Benn et al. (2003).

- **INTEGRAL**
  INTEGRAL is an integral-field spectroscopic facility deployed at the Nasmyth focus of the WHT. The instrument consist of 4 separate IFUs with a nearly contiguous distribution of fibres of different sizes ranging from 7.8×6.4 to 33.6×29.4 arcsec and different fibre core sizes. One of the IFU has the central fibres blanked out (so acting as a coronograph). Different INTEGRAL set-ups offer various spectral resolution, linear dispersions, and wavelength coverage in the range 375 – 660 nm. The IFU and grating can be changed easily throughout the night as targets and conditions change. This instrument is particularly useful for kinematic studies of galaxies. Reference: Arribas et al. (1998).

- **SAURON**
  SAURON (Spectrographic Areal Unit for Research on Optical Nebulae) is a panoramic integral-field spectrograph using a lenslet array. It is a dedicated instrument, mounted on the WHT on La Palma, Spain. SAURON has a relatively large FoV with 41×33 and 11×9 arcsec in low and high resolution modes respectively. The wavelength coverage is 450 – 700 nm with 1431 object lenslets. The instrument was specially designed for a scientific project which main goal is to understand the formation and evolution of elliptical and lenticular galaxies and of spiral bulges from 2D observations. The SAURON survey observed a sample of 72 nearby E, S0, and Sa galaxies drawn from both cluster and field environments. Reference: Bacon et al. (2001).

- **PMAS-PPAK**
  The Potsdam Multi-Aperture Spectrophotometer (PMAS) is an integral-field instrument, developed and built at the Astrophysical Institute Potsdam (AIP) covering the optical wavelength regime of 350 – 1000 nm. PMAS is available as a common-user instrument at the German Spanish Calar Alto observatory. PMAS is mounted at the Cassegrain focal station of the 3.5 m telescope. The instrument was later equipped with an additional IFU, featuring a wider field and higher light collecting power per spaxel. This second unit (called PPak-IFU) is placed 60 off-axis, to by-pass the fore-optics and lens-array IFU. It consists of a focal reducer lens and a densely-packed bare fibre-bundle, that connects to the same spectrograph. The PPak FoV spans 64×74 arcsec, making it by the time this project was envisaged, the world's widest integral field unit. References: Roth et al. (2005); Kelz & Roth (2006).

In the first instance, all the above instruments fulfill the requirements of having instrumental set-ups capable of covering the optical wavelength regime coupled with observational modes able to observe large surface areas on the sky. However, some problems arose when the science case was studied in more detail and it was compared to the specific instrument/configuration. Additionally, we had to consider availability of the instrument for a relatively long-term observational project. Therefore, we had to adopt a final criteria for each of the proposed instruments, based on the best trade-off between spectral coverage and FoV, considering also practical issues in terms of logistic, such as distance to the facility and collaborations.

In the case of twin GMOS instruments, despite of having a wide spectral window (400 – 1000 nm), the [O II] line would not be observable and most importantly, the FoV of the instruments is quite small (5×7 arcsec), preventing a good coverage of the target galaxies on the sky, even with mosaicing mode. Furthermore, being both instruments located at Hawaii and Chile, accessibility for observing runs would have been difficult and costly. The SPIRAL instrument coupled with the AAOmega spectrograph complied with the

wavelength coverage requirement (370 – 950 nm), but again the small FoV of the instrument in the IFU mode (11 × 22 arcsec) would had compromise the observation of a large surface area galaxy. Furthermore, being the instrument physically in Australia, this option would suffer the same problems in terms of logistics as the ones described by GMOS.

The OASIS instrument includes a spatial enlarger capable of providing a larger FoV ($\sim$ 20") than the standard 10.3" × 7.4" at 0.26"/lens sampling. However, this configuration suffers from vignetting and by the time of the observing planning it was undergoing engineering work. Moreover, the wavelength coverage of OASIS (400 – 1000 nm) was not appropriate to observe the [O II] diagnostic blue line. For some other instrument there were important drawbacks that were determinant to do not consider them in the final selection. In the case of INTEGRAL for example, the instrument was a common-user instrument from 1997 to 2004. However, it became a private instrument in 2004, owned by the Instituto de Astronomía de Las Canarias (IAC), Spain. Accessibility to the instrument was therefore compromised in a long-term. Furthermore, given the characteristics of the instrument this is particularly useful for kinematic studies of galaxies, at intermediate and high resolution, being the FoV coverage not an important issue. A similar situation was found for SAURON, being a dedicated instrument for a pre-defined specific project, accessibility was not guaranteed. Furthermore, the wavelength coverage of this instrument starting at 450 nm would make impossible the observation of the [O II] doublet line.

In the case of the VLT instruments, both VIMOS and FLAMES did complied with the optimal wavelength coverage discussed above (360 – 1000 nm). Out of these two instruments, only VIMOS has a relatively large FoV in its low-resolution configuration (54 arcsec^2), while FLAMES was designed for intermediate and high resolution spectroscopy with configurations of a few arcsec in the FoV. However, by the time of defining the observing strategy it was known among the IFS community that the VIMOS instrument suffered from calibrations inaccuracies and additional problems related to the, by itself, intrinsically complex reduction of IFS data. Furthermore, the location of both instruments in Chile presented logistic problems as the ones discussed before.

Fortunately, the technical specifications of the PMAS - PPAK instrument located at the Centro Astronómico Hispano-Aleman de Calar Alto (CAHA), Spain, proved to be optimal for the sort of observations that we planned to develop for the research programme. The PMAS instrument covers the optical wavelength range between 350 – 1000 nm, including therefore the critical diagnostic emission [O II] line in the blue part of the spectrum. In terms of spatial coverage, the IFU fibre bundle PPAK mode, with a FoV of 65 × 74 arcsec, was by the time of the planning of this project the world's widest IFU that provides a semi-contiguous regular sampling of extended astronomical objects. Therefore, both requirements in terms of spectral and spatial coverage were fulfilled. Furthermore, another advantage of this instrument came in terms of logistics: international observing time was offered for this and other common user instruments at CAHA, therefore we could gain access for potential observing runs through this scheme. Additionally, being the instrument physically located at CAHA in Southern Spain, mobility to the site was simpler and cheaper in comparison with the observational facilities mentioned above.

2.2.1 Technical overview of PMAS-PPAK

The Postdam Multi-Aperture Spectrophotometer (PMAS) is a dedicated integral field spectrophotometer. It is based on the lens array-fibre bundle principle of operation. A set of reflective gratings provides low to medium spectral resolution of approximately 1.5, 3.2, and 7 Å in first order, depending on the groove

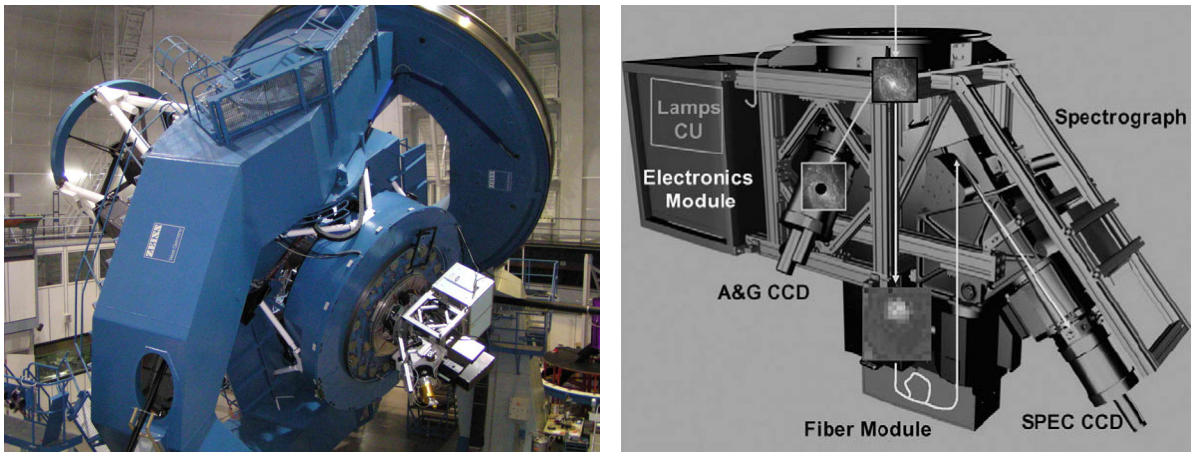

Figure 2.3: Left: The PMAS instrument, attached to the Cassegrain focus of the 3.5-m telescope on Calar Alto, Spain. Right: Overview of the PMAS instrument and how the light (arrows) passes through the instrument towards the two CCD detectors.

density (1200, 600, 300 grooves mm^{-1}). Figure 2.3 presents a view of the instrument and its basic principle of operation. At the focal plane, a mirror intersects the off-axis light and re-directs it to a cryogenic camera for acquisition and guiding (A&G CCD). However, a central, on-axis field-of 25" passes through a magnifying fore-optics towards the lens-array IFU. Short optical fibres, mounted at the backside of the lens-array, re-format the field to form a slit and connect to the Cassegrain-mounted spectrograph. Additionally, the instrument includes a calibration unit, lamps, on-board electronics, and a workstation.

While the standard IFU (originally called LARR-IFU) uses a 16 × 16 arcsec element lens array, which provides seeing-limited sampling in a relatively small FoV in one of three magnifications (8" × 8", 12" × 12", or 16" × 16"), a retrofitted bare fibre bundle IFU called PPAK (*PMAS fibre PAcK*) expands the FoV to an area with a footprint of ~ 1 $arcmin^2$. The PPAK unit features a central hexagonal bundle with 331 densely packed optical fibres to sample an astronomical object at 2.7 arcsec per fibre. Six "mini-IFU's" with all-together 36 active fibres are positioned around these science-fibres to record the sky background. Additionally, 15 fibres can be illuminate directly by internal lamps to calibrate the instrument. Note that contrary to the lens array, which provides a contiguous spatial sampling with negligible edge effects between adjacent lenses, the PPAK bundle has gaps between each fibre and its next neighbours. It is, however, possible to fill these gaps by repeated observations with small offsets (dithering), see Figure 2.4. Contrary to the standard IFU, which would be located in the middle of the dark central spot (field mirror diaphragm), the PPAK IFU is mounted off-axis, outside the field of view of the A&G camera. Accurate pointing is possible by centering the extended target on the PPAK IFU overlay plot, and applying a predefined offset (Pull-down Menu "Pointing"). The target is then no longer visible on the screen. A sufficiently bright star can be selected for offset-guiding. The guide star coordinates can be saved to disk. Restoring these coordinates allows one to repeat observations in another night with sub-arcsec pointing accuracy (note however the importance of A&G camera filter selection and the effects of differential atmospheric refraction). Its pre-optics and fibre-diameter, combined with the efficiency of the PMAS spectrograph, allows PPAK to make a trade-off between total light-collecting power and spectral resolution. A single large PPAK fibre collects more light even with a 3.5-m telescope than a single spatial element of an IFU mounted on a 8-m-class telescope like VIMOS on the VLT. A summary of both IFUs is given in Table 2.1.

The technique of 2D spectroscopic could consist of one or two stages. In the first stage the image is split

COMPARISON OF THE TWO PMAS INTEGRAL-FIELD UNITS

Parameter	LARR-IFU	PPaK-IFU
Design principle	Fore-optics + lens-array + fibres	Focal reducer + fibre-bundle
Plate-scale	Magnified to 0".5 – 1".0/mm	Reduced to 17".8/mm
FoV	8" × 8" or 16" × 16"	74" × 64" (hexagonal)
Fill factor	100%	60%
Spaxel number/shape	256, square	331 + 36 (sky), round
Spaxel size	0".5 – 1".0/mm per lenslet	2".68 per fibre (diameter)
Spaxel pitch	1".0 lens-to-lens	3".5 fibre-to-fibre
Fibre core/length	100 μm, 2 m	150μm , 3.5
Specific grasp[a]	8.2 arcsec^2 m^2	47 arcsec^2 m^2
Total grasp[b]	0.58 arcmin^2 m^2	4.23 arcmin^2 m^2
Slit size	0.1 × 96 mm	0.15 × 94 mm

Table 2.1: Comparison of the technical characteristics of the two PMAS integral-field units.
[a] Specific grasp = spaxel size [arcsec^2] × telescope area [m^2].
[b] Total grasp = spaxel size [arcsec^2] × number of spaxels × telescope area [m^2].

into various elements in the focal plane. In the second, the elements are redistributes in general alignment at the entrance of the spectrograph. In the case of PPAK, the second stage transformation is by means of a matrix of fibres, at the other end of the bundle, the fibres are arranged in a line to form a pseudoslit at the entrance of the spectrograph. In this way, when the telescope is pointed towards an extended object, the bundle of fibres splits it into a matrix of regions in the focal plane and a spectrum is simultaneously obtained for each of these regions in the spectrograph.

The PPAK configuration was found to have a 40 – 50% times higher throughput than the lens-array IFU. The overall instrumental efficiencies have been measured for both IFUs (Kelz & Roth, 2006) using standard star exposures, and are plotted in Figure 2.4. Using an identical spectrograph set-up (no filters and a 300 l/mm grating, blazed at 500 nm) results in a peak efficiency of 20% with the lens-array (LARR-IFU), and of 28 – 30% with the fibre-bundle (PPak-IFU). The fibre-to-fibre response of the PPAK-bundle is more uniform than of the LARR-fibres. For the PPAK-spectra , the maxima of the normalized intensities range between 0.89 and 0.98 with a typical inter-order minimum intensity of 20%of the peak level. As the coupling of both fibre-slits towards the spectrograph is similar and the length difference between the lens-array and PPAK-fibres (3.5 m vs. 2 m) cannot account for these differences, the variation is mainly caused at the input side. At the backside of the lens-array, micro-images of the telescope pupil are fed into the fibres. While the fibre-cores (of 100 μm) are larger than the nominal micro-pupils (of 43 μm), light is lost nevertheless. Due to both diffraction spikes and stray light caused by the lens-array, and the limited accuracy between micro-pupil and fibre alignment, a fraction of the light falls outside the fibre-cores. For PPAK, the focal plane image is directly fed into the fibre-bundle, so that alignment accuracies on a micron scale are not an issue. More technical information on the instrument, telescope and observing configurations are presented below.

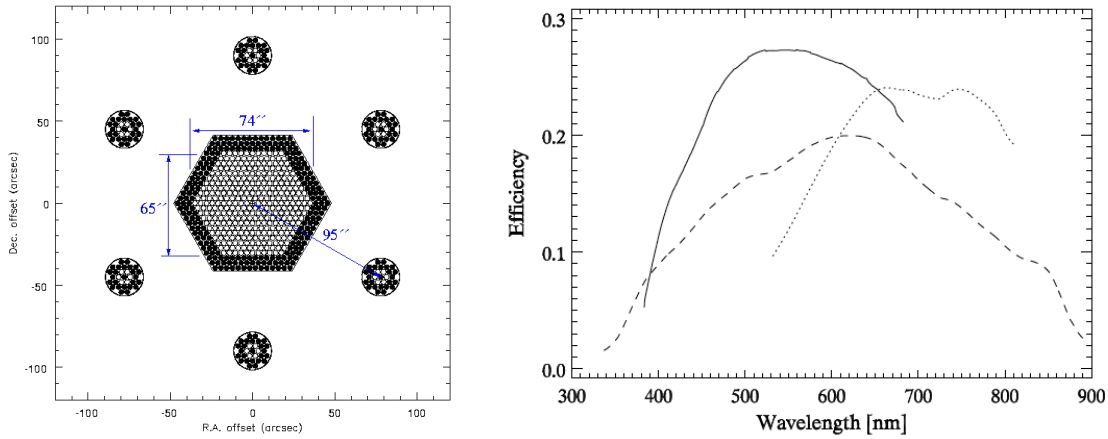

Figure 2.4: Left: Geometrical layout and size of the central hexagonal PPAK - IFU (331 fibres) and six surrounding sky fibre bundles (each consisting of 6 fibres). Only open plot symbols are optically active fibres, filled circles are indicating auxiliary fibres which were employed in the manufacturing process for mechanical reasons. Right: Comparison between the instrumental efficiencies, derived from standard star exposures, using the LARR - IFU (dashed curve) and the PPAK - IFU (solid curve), and an identical spectrograph set-up (V300 grating). The dotted curve was obtained with the LARR - IFU and a grating blazed at *R*. Figure adapted from Kelz & Roth (2006).

Telescope Data

Optics: $f/10.0$ RC focus station, f=35000 mm, effective light-collecting area 8.153 m^2, aperture diameter 3500 mm, diameter of central obscuration 1367 mm, plate scale 5.89 arcsec/mm.

PPAK IFU

Off-axis fibre bundle IFU. Principle of operation: focal reducer + hexagonal packed fibre-bundle. Focal reducer lens: $f10$ to $f/3.3$, platescale: 17.7”/mm. Fibre configuration: 331 object + 36 sky + 15 calibration fibres. Spatial sampling: 2.7 arcsec per fibre (diameter).

Optical fibres

Polymicro, (red response, low OH), core diameter 150 μm.

Fibre Spectrograph and gratings

Dedicated fibre spectrograph with nominal input focal ratio $f/3$, refractive collimator 150/450 mm, pseudo-slit length 96 mm, telecentric input, fibre coupling in immersion to first collimator lens. Reflective diffraction grating 206 mm $\times$ 154 mm on grating rotator, angle position unrestricted from 0 to 360 degrees. Set of interchangeable gratings, stored in cartridges, manually inserted and removed.

Calibration Sources

Internal flatfield exposures from integrating sphere, waveguide-coupled to various continuum and spectral line lamps, each lamp with individual shutter timing allowing for flexible combination of different light sources.

- Lamp 1: tungsten filament continuum lamp.
- Lamp 2: Neon spectral line lamp, ORIEL pencil style type 6032.

- Lamp 3: Neon spectral line lamp (spare for Lamp2, switched-in under remote control).
- Lamp 4: Hg(Ar)spectral line lamp, ORIEL pencil style type 6035.
- Lamp 5: Hg(Ar) spectral line lamp (spare for Lamp4, switched-in under remote control).
- Lamp 6: ThAr hollow cathode spectral line lamp (for special applications).

DETECTORS

Fibre Spectrograph CCD System (acronym spec) : SITe ST002A with 2K $\times$ 4K /15μm pixels, thinned, blue-enhanced AR coating, conversion factor 1.4 *e*/ADU, readout time: 2 min 12 sec (2$\times$2 binned) / 5 min 25 sec(1$\times$1 binned). Each single spectrum is fed from a spaxel of 0.5" $\times$ 0.5" on the sky (default magnification) with recommended 2$\times$2 pixel binning, each fibre projects onto 2$\times$2 = 4 super-pixels CCD readout noise: 5.0 electrons per super-pixel effective dispersion per super-pixel: multiply grating table values by factor of 2.

FORMAT OF FIBRE SPECTRA

Data format of raw data: standard FITS ($\sim$ 17 Mb for single full frame, unbinned).

TOTAL EFFICIENCY ESTIMATES (INCLUDING ATMOSPHERE AND CCD)

360 nm	440 nm	550 nm	700 nm	900 nm
3.8%	12.7%	18.7%	16.9%	7.7%

2.3 Previous applications of IFS to nearby galaxies

2D spectroscopy techniques have reached nowadays a certain maturity, at least in the sense of not being anymore a private tool for a restricted number of astronomers. It is however not so clear if it has yet attained a level of common practice. The complex data reduction and visualisation has imposed a further obstacle to carry out more ambitious projects based on 2D spectroscopy. Nevertheless, the ability to produce 2D maps of physical quantities (e.g., velocity, stellar population age, molecular gas distribution, etc.) is probably the most easily advertised asset of 2D spectroscopy. Long-slit radial profiles allowed in the past to reveal the full extent of a presumed structure that can be now reveal by 2D spectroscopic maps. Although 2D spectroscopy has produced many interesting results, there is a feeling among the scientific community that the full potential of these techniques has yet not been exploited. This section describes some important studies and results of IFS applied to nearby galaxies in the universe, focusing on the IFS surveys and the determination of chemical abundances.

2.3.1 Surveys

A truly remarkable change in the usage of IFUs was the advent of the first surveys of nearby galaxies. Given the limitations of the instrumentation in terms of FoV and acquisition time, surveys consisting of hundreds

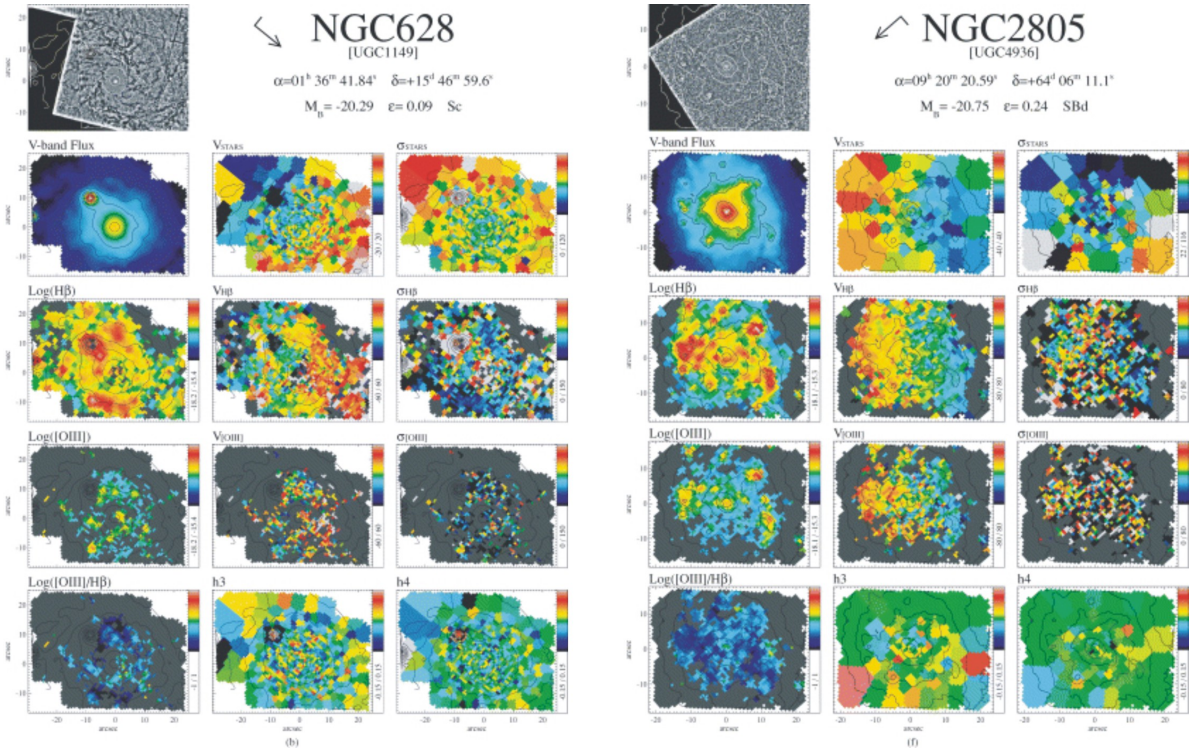

Figure 2.5: IFS maps of NGC 628 and NGC 2805 obtained with SAURON. For both galaxies, the top panel shows an unsharp, masked Hubble Space Telescope (HST) image of the galaxy within the SAURON FoV. Other maps present the stellar + gas distributions and kinematics as well as an emission line ratio map. Figure adapted from Ganda et al. (2006).

of targets have not been done yet, but surveys of a few tens of galaxies are still a remarkable achievement in this context. Heterogeneous samples were already obtained during the last decade with IFUs such as e.g., TIGER and OASIS (CFHT), INTEGRAL (WHT) and with the Multi-Pupil Fibre Spectrograph (MPFS, Russia).

One important attempt is represented by the SAURON project (Lyon/Leiden/Oxford) (Bacon et al., 2001), which is based on a panoramic lenslet array spectrograph with a relatively large FOV of 33×41 arcsec^2. SAURON was specially designed to study the kinematics and stellar populations of a sample of nearby elliptical and lenticular galaxies. The SAURON project was the first to address a representative sample of nearby objects (de Zeeuw et al., 2002), with 72 early-type (E/S0/Sa) galaxies with total luminosity M_B ranging from -18 to -22. Besides the wealth of structures revealed by this unique dataset Figure 2.5, supplemented by higher resolution OASIS (CFHT and WHT) data, this successful observational campaign emphasizes the need to revise our view of these objects (Emsellem et al., 2004; Sarzi et al., 2006; Falcón-Barroso et al., 2006), and bring new constraints on the formation and evolution of galaxies (Cappellari et al., 2006). Bulges of spirals have also been recently examined by Batcheldor et al. (2005) with INTEGRAL (WHT) and SPIRAL (AAT), and later-type spirals were scrutinized with SAURON, providing simultaneous gas, stellar kinematics and line-strengths maps of the central regions of galaxies for a lower range of stellar velocity dispersions.

A SAURON campaign has also been devoted to a sample of active and non-active nearby galaxies to test a presumed link between the inner gravitational potential and the nucleus activity. Chilingarian et al. (2005) obtained MPFS data on 5 dwarf ellipticals, in an attempt to probe the link between the stellar population and

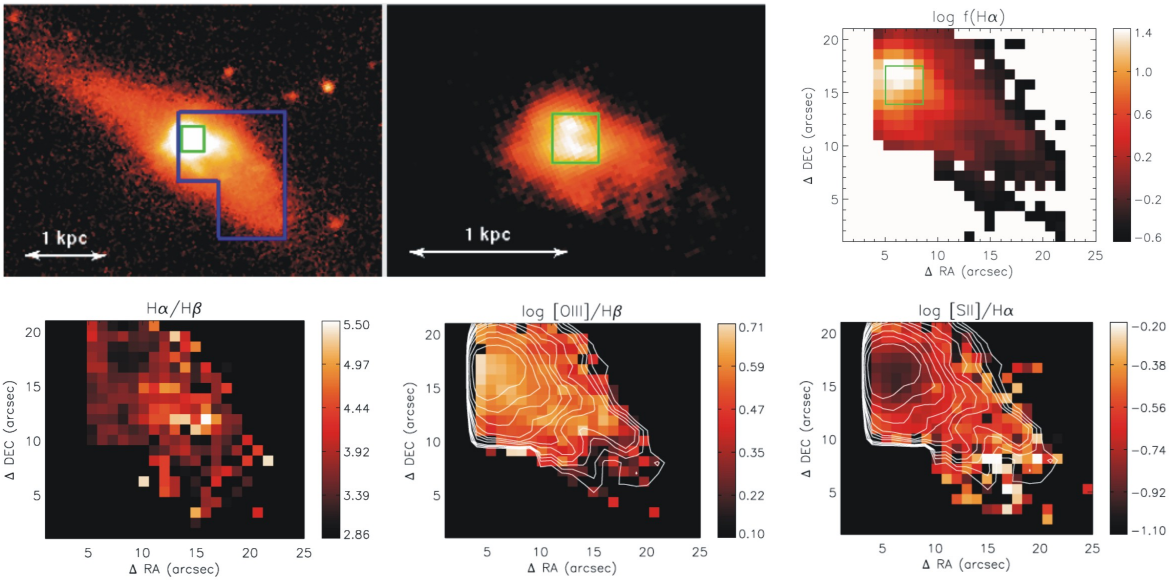

Figure 2.6: On the top left: image of II Zw 70 in the *r* (left) and *u* (right) bands from SDSS. The blue box represents the mosaic field observed with PMAS. Top right: map of the log(F(Hα). On the bottom, Hα/Hβ ratio spatial distribution (left), emission line ratio maps in logarithmic scale for [O III] λ5007/Hβ (middle), and [S II] λ6717.31/Hα (right). Hα emission line fluxes are represented as isocontours. Figure adapted from Kehrig et al. (2008).

kinematical substructures. It is finally worth emphasising a scanning Fabry-Perot Hα study (even though not a true IFU) of the effect of environment on the gas content and kinematics (Chemin et al., 2006) with a survey of 30 galaxies of the Virgo cluster.

2.3.2 IFS and chemical abundances

In spite of the obvious advantages of the IFS technique in tackling known scientific problems and in opening up new lines of research, 2D spectroscopy is a method relatively little used in the determination of chemical abundances in galaxies. Previous works that have attempted to obtain 2D information of the chemical composition have used for example, multi-object instruments to obtain simultaneous spectra of H II regions in a disk galaxy (e.g. Roy & Walsh, 1988; Kennicutt & Garnett, 1996; Moustakas & Kennicutt, 2006b), or narrow-band imaging on specific fields to obtain information of star forming regions and the ionized gas (e.g. Scowen et al., 1996). However small wavelength coverage, fibre optics calibration problems and reduce FOV severely limits the scope of previous studies.

Again, one of the most important attempts was represented by the SAURON project, however this programme was specially designed to study the kinematics and stellar populations of a sample of nearby elliptical and lenticular galaxies; the application to spiral galaxies was restricted to the study of spiral bulges. A recent effort by Rosolowsky & Simon (2008) plans to obtain spectroscopy for $\sim$ 1000 H II regions through the M 33 Metallicity Project, using multi-slit observations. Recently, PPAK was used successfully to map the Orion nebula (Figure 2.7) obtaining the chemical composition through strong line ratios (Sánchez et al., 2007b). Likewise, PMAS in the lens-array configuration was used to map the spatial distribution of the physical properties of the dwarf H II galaxy II Zw 70 (Kehrig et al., 2008, see Figure 2.6), although covering just a small FoV ($\sim$ 32”).

Although the project described in this thesis is not the first attempt to obtain obtain point-by-point spectra

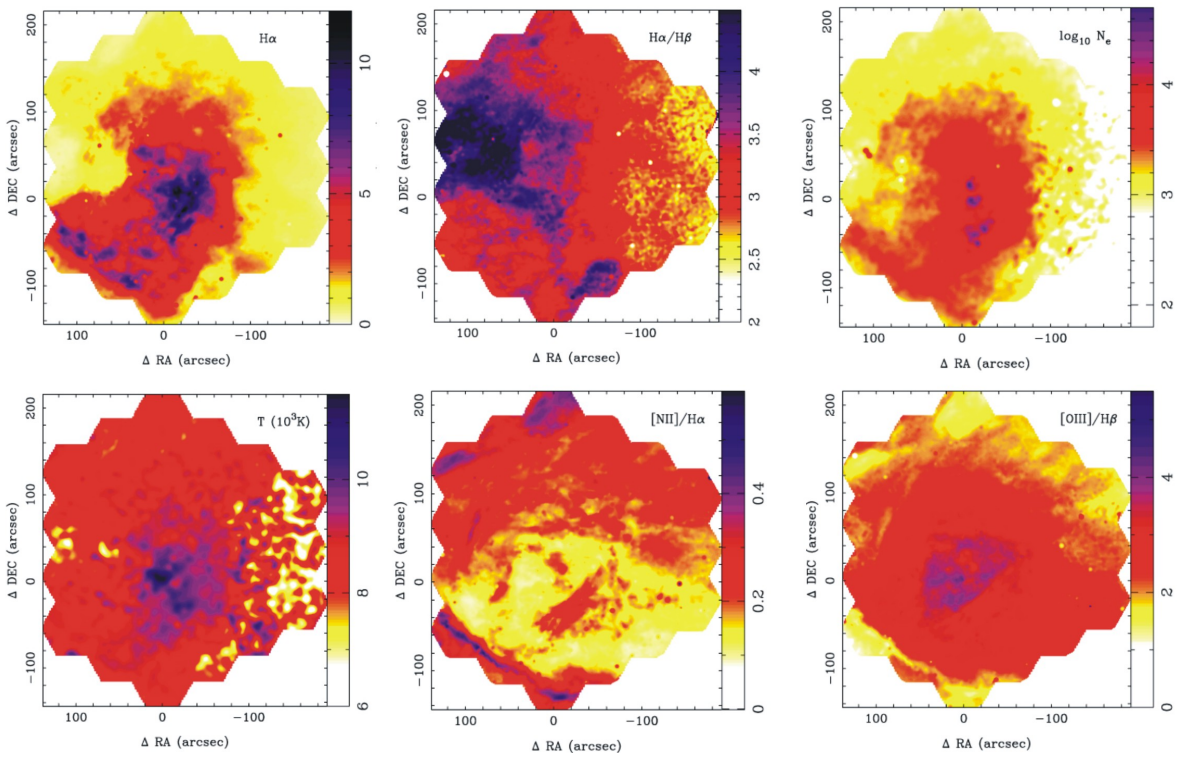

Figure 2.7: IFS survey of the Orion Nebula. The mosaic covers an area of $\sim 5 \times 6$ arcmin centered on the Trapezium region. On the top panels, from left to right: observed Hα line flux map, observed Hα/Hβ line ratio map,electron density map, N_e in cm^{-3}, derived from the [S II] λ6717/λ6731 line ratio, represented in a logarithm scale. Bottom, electron temperature map in units of 10^3 K, derived from the ([N II] λ6548 + λ6583)/λ5755 line ratio, classical diagnostic line ratio maps: [N II] λ6583/Hα line ratio map, [O III] λ5007/Hβ line ratio map. Figure adapted from Sánchez et al. (2007b).

on the surface of a galaxy (e.g. SAURON, VIRUS-P: Blanc et al., 2009), the observations performed for the purpose of this dissertation (the PINGS project, see chapter 3) will provide the most detailed spectroscopic information across a late-type galaxy. This knowledge is most relevant for interpreting the integrated colours and spectra of high redshift sources. In that respect, PINGS could represent a leading leap in the study of the chemical abundances and the global properties of galaxies.

The future of 2D spectroscopy looks very promising. The present inclusion and proliferation of this kind of instrumentation in world-class facilities and in future space and ground based observatories will imply that 2D spectroscopy will not be seen anymore as the exception, but as the rule in terms of spectroscopic observations at all redshifts.

3

Sample selection and observations

Hitherto, most spectroscopic studies in nearby galaxies have been limited by the number of objects sampled, the number of H II regions observed and the coverage of these regions within the galaxy surface. In order to obtain a deeper insight of the mechanisms that rule the chemical evolution of galaxies, we require the combination of high quality multi-wavelength data and wide field spectroscopy in order to increase significantly the number of H II regions sampled in any given galaxy. The observations for this dissertation were conceived to tackle the problem of the 2D spectroscopic coverage of the whole galaxy surface. As described in the previous chapter, the new techniques in imaging spectroscopy provide a powerful tool for studying the small and intermediate scale variation in line emission and stellar continuum in nearby well-resolved galaxies. We designed a project to take advantage of these new observational techniques in order to assemble a unique spectroscopic sample from which we could study, with unprecedented detail, the star formation and gas chemistry across the surface of a galaxy.

The content of this chapter is devoted to present the sample of galaxies considered for this dissertation and to describe the selection criteria that was followed accordingly to the scientific objectives established for this work. Furthermore, a full description of the observations is presented, explaining the telescope set-up and the particular observing technique adopted to fulfill the requirement of the 2D spectroscopic coverage of this work.

3.1 Scientific Objectives

The galactic chemical evolution is one of the many aspects that has an important role in the formation and evolution of galaxies in the universe. The chemical evolution concerns the origin and distribution of nuclear species in stars and gas. In the overall picture, the Big Bang led to a significant initial abundances of H, D, He and Li in the primordial intergalactic medium (IGM). In the scenario of hierarchical galaxy formation, the IGM is assumed to condense into galaxies consisting initially of gas enclosed in dark matter halos, which then cools, collapse and makes stars. In this very oversimplified picture, the star formation may take place

either on a short time-scale (as appears to have happened in the formation of spheroidal systems) or on a long time scale (in the formation of disk components in spirals), while sudden violent star formation may often be triggered by interactions and mergers. In any case, galaxy formation is followed and/or accompanied by star formation leading to synthesis of heavier elements and the modification of primordial abundances by different means, mainly by the life-cycle of the stars and the complex dynamics that galaxies may undergo in their life times. These processes are dictated by different parameters and their inter-relations which include the local initial composition, the initial mass function (IMF), the star formation history (SFH), gas flows, radial transport and mixing of gas within disks, stellar yields, etc.

A deeper understanding of the galactic chemical evolution, the star formation histories and the nucleosynthesis of spiral galaxies can be derived from the accurate determination of chemical abundances, either in individual star-forming regions distributed across galaxies or through the comparison of abundances between galaxies. In this aspect, nebular emission lines from individual H II regions have been historically the main tool at our disposal enabling a direct measurement of the gas-phase abundance at discrete spatial positions in low redshift galaxies. Different studies have shown a complex link between the chemical abundances of galaxies and their physical properties. Such studies have been able to measure the first two moments of the abundance distribution –the mean metal abundances of disks and their radial gradients– and on characterising the relations between these abundance properties and the physical properties of the parent galaxies, for example galactic luminosity, stellar and dynamical mass, circular velocity, surface brightness, colors, mass-to-light ratios, Hubble type, gas fraction of the disk, etc. These studies have revealed a number of important scaling laws and systematic patterns including luminosity-metallicity, mass-metallicity, and surface brightness vs. metallicity relations (e.g. Skillman et al., 1989; Vila-Costas & Edmunds, 1992; Zaritsky et al., 1994; Tremonti et al., 2004), effective yield vs. luminosity and circular velocity relations (e.g. Garnett, 2002), and systematic differences in the gas-phase abundance gradients between normal and barred spirals (e.g. Zaritsky et al., 1994; Martin & Roy, 1994). However, these studies have been limited by the number of objects sampled, the number of H II regions observed and the coverage of these regions within the galaxy surface.

The primary scientific objectives of this dissertation are to study the 2D abundance distribution of a sample of nearby spiral galaxies and to characterise the relations between these abundances with the physical properties of their parent galaxies. We designed a project to take advantage of the new observational techniques described in chapter 2 in order to assemble a unique spectroscopic sample from which we could study, with unprecedented detail, the gas chemistry across the surface of a galaxy. The project is entitled: the **P**PAK **I**FS **N**earby **G**alaxies **S**urvey (PINGS, see section 1.5). The PINGS observations consist of IFU 2D spectroscopic mosaics of a representative sample of nearby spiral galaxies with a projected angular size of less than 10 arcmin. The novel spectroscopic technique implemented in these observations are able to produce pixel-resolved 3D maps of the form $I(x, y, \lambda)$ across the surface area of a given galaxy. This project represents the first attempt to obtain 2D spectra of the whole surface of a galaxy in the nearby universe. By using this technique, we virtually target every H II region in the galaxies as a consequence of the nearly complete spatial coverage of the 2D IFS technique. Therefore, we are able to test for the first time the systematic dependences of the strong-line abundances on the size, luminosity, surface brightness, and other properties of the H II regions.

The resulting spectral maps (together with the information provided by ancillary data) can be used to address a number of important astrophysical issues regarding both the gas-phase and the stellar populations in galaxies. The 2D abundance distributions can help to put constraints on current models of galaxy formation,

chemical evolution and on the star formation history of galaxies. The PINGS observations can be processed and analysed to derive:

1. Oxygen abundance distributions based on a suite of strong-line diagnostics based on absorption-corrected Hα, Hβ, [O II], [O III], [N II], [S II] line ratios.

2. Measurements of ionization structure in H II regions and diffuse ionized gas using the well-known and most updated forbidden-line diagnostics in the oxygen and nitrogen lines.

3. Reddening maps of the galaxies, which can be combined with UV, Hα, and infrared maps to derive robust, extinction-corrected maps of the SFR.

4. Rough fits to the stellar age mix from the stellar spectra.

We intend to test, for example, whether the metal abundance distributions in disks are axisymmetric, this is usually taken for granted in chemical evolution models, but one might expect strong deviations from symmetry in strongly lopsided, interacting, or barred galaxies, which are subject to large-scale gas flow. Another important goal is to place strong limits on the dispersion in metal abundance locally in disks; there is evidence for a large dispersion in some objects such as NGC 925 or M 33 (Rosolowsky & Simon, 2008), but it is not clear from those data whether the dispersion is due to non-axisymmetric abundance variations, systematic errors in the abundance measurements, or a real local dispersion.

On the other hand, although is beyond the scope of this dissertation, the PINGS observations can help to provide a very detailed knowledge of the role played by star formation in the cosmic life of galaxies and their colour bimodality. All the important scaling laws previously mentioned tell us that, once born, stars change the ionization state, the kinematics and chemistry of the interstellar medium and, thus, change the initial conditions of the next episode of star formation. Substantially, star formation is a loop mechanism which drives the luminosity, mass and chemical evolution of each galaxy (leaving aside external agents like interactions and mergers). The details of such a complex mechanism are still not well established observationally and not well developed theoretically, and limit our understanding of galaxy evolution from the early universe to present day. In combination with ancillary data, the flux maps computed from the PINGS data will be used to study both the most recent star formation activity of the targets and the older stellar populations. We will be able to identify the gas and stellar features responsible for the observed spectra, to derive the dependence of the local star formation rate on the local surface brightness, a key recipe for modelling galaxy evolution and the environmental dependence of star formation. These data will also provide an important check for interpreting the integrated broad-band colours and spectra of high redshift sources.

In that respect, the PINGS observations and their subsequent analysis represent a leading leap in the study of the chemical abundances and the global properties of galaxies, information which is most relevant for interpreting observations at all redshift sources accessible with the current technology.

3.2 Sample selection

In order to achieve the scientific goals described above, we tried to incorporate a diverse population of galaxies in terms of their range of properties, rather than their morphology. Given that the primary study would focus on the gas phase of the sample, late-type spirals were preferred given their gas content and

GALAXIES OF THE PINGS SAMPLE

Object	Right Ascension	Declination	Size (arcmin)	Constellation
NGC 628	$01^h\ 36^m\ 41.8^s$	$+15^\circ\ 47^m\ 00.1^s$	10.5×9.5	Pisces
NGC 1058	$02^h\ 43^m\ 30.0^s$	$+37^\circ\ 20^m\ 28.5^s$	3.0×2.8	Perseus
NGC 1637	$04^h\ 41^m\ 28.2^s$	$-02^\circ\ 51^m\ 28.9^s$	4.0×3.2	Eridanus
NGC 2976	$09^h\ 47^m\ 15.4^s$	$+67^\circ\ 54^m\ 59.0^s$	5.9×2.7	Ursa Major
NGC 3184	$10^h\ 18^m\ 17.0^s$	$+41^\circ\ 25^m\ 27.8^s$	7.4×6.9	Ursa Major
NGC 3310	$10^h\ 38^m\ 45.9^s$	$+53^\circ\ 30^m\ 12.2^s$	3.1×2.4	Ursa Major
NGC 4625	$12^h\ 41^m\ 52.7^s$	$+41^\circ\ 16^m\ 26.3^s$	2.2×1.9	Canes Venatici
NGC 5474	$14^h\ 05^m\ 01.6^s$	$+53^\circ\ 39^m\ 44.0^s$	4.8×4.3	Ursa Major
NGC 6643	$18^h\ 19^m\ 46.4^s$	$+74^\circ\ 34^m\ 06.1^s$	3.8×1.9	Draco
NGC 6701	$18^h\ 43^m\ 12.5^s$	$+60^\circ\ 39^m\ 12.0^s$	1.5×1.3	Draco
NGC 7770	$23^h\ 51^m\ 22.5^s$	$+20^\circ\ 05^m\ 47.5^s$	0.8×0.7	Pegasus
NGC 7771	$23^h\ 51^m\ 24.9^s$	$+20^\circ\ 06^m\ 42.6^s$	2.5×1.0	Pegasus
Stephan's Quintet				Pegasus
NGC 7317	$22^h\ 35^m\ 51.9^s$	$+33^\circ\ 56^m\ 41.6^s$	1.1×1.0	
NGC 7318A	$22^h\ 35^m\ 56.7^s$	$+33^\circ\ 57^m\ 55.7^s$	0.9×0.9	
NGC 7318B	$22^h\ 35^m\ 58.4^s$	$+33^\circ\ 57^m\ 57.3^s$	1.9×1.2	
NGC 7319	$22^h\ 36^m\ 03.6^s$	$+33^\circ\ 58^m\ 32.6^s$	1.7×1.3	
NGC 7320	$22^h\ 36^m\ 03.4^s$	$+33^\circ\ 56^m\ 53.2^s$	2.2×1.1	

Table 3.1: Coordinates and projected size of the galaxy sample. Coordinates are equatorial in 2000 Equinox. The major and minor axis data corresponds to the R_{25} isophote (25.0 B-mag arcsec^{-2}) according to de Vaucouleurs et al. (1991). Note: NGC 7770 and NGC 7771 are included in the same mosaic, while NGC 7318A and NGC 7318B were observed in the same pointing.

their intrinsically brighter H II regions compared to earlier types, in that respect the sample was restricted to this particular morphological type. The size and precise nature of the sample was heavily influenced by a set of technical considerations, the principal limiting factor being the FoV of the PPAK unit. We wanted to observe relatively nearby galaxies to maximise the physical linear resolution using the mosaicing technique. However, we also had to take into account the limitations imposed by the amount of non-secure observing time and meteorological conditions for the granted runs (see section 3.3). Therefore, the sample size was dictated by a balance between achieving a representative range of galaxies properties and practical limitations in observing time.

While constructing the sample, we also took into account other properties, such as inclination (with preference to face-on spirals), surface brightness, bar structure, spiral arm structure, and environment (i.e. including isolated, interacting and clustered). The final selection of galaxies also took into account practical factors such as optimal equatorial right ascension and declination for the location of Calar Alto observatory, and the observable time per night for a given object above a certain airmass.

The PINGS sample consists of 17 galaxies within a maximum distance of 100 Mpc; the average distance of the sample is 28 Mpc (for $H_0 = 73$ km s^{-1} Mpc^{-1}). The final sample considers different galaxy types, including normal, lopsided, interacting and barred spirals with a good range of galactic properties and SF environments with multi-wavelength public data. Table 3.1 shows the complete listing of the PINGS sample

GALAXY PROPERTIES OF THE PINGS SAMPLE

Object	Type	Distance (Mpc)	Projected size (arcmin)	M_B	z	$v_\odot$ (km s^{-1})	i	P.A.
(1)	(2)	(3)	(4)	(5)	(6)	(7)	(8)	(9)
NGC 628	SA(s)c	9.3	10.5×9.5	-19.9	0.00219	657	24	25
NGC 1058	SA(rs)c	10.6	3.0×2.8	-18.3	0.00173	519	21	95
NGC 1637	SAB(rs)c	12.0	4.0×3.2	-18.9	0.00239	717	36	33
NGC 2976	SAc pec	3.6	5.9×2.7	-16.9	0.00008	24	63	143
NGC 3184	SAB(rs)cd	11.1	7.4×6.9	-19.9	0.00194	582	21	135
NGC 3310	SAB(r)bc	17.5	3.1×2.4	-20.1	0.00331	993	39	163
NGC 4625	SAB(rs)m	9.0	2.2×1.9	-16.9	0.00203	609	29	30
NGC 5474	SA(s)cd	6.8	4.8×4.3	-17.9	0.00098	294	27	91
NGC 6643	SA(rs)c	20.1	3.8×1.9	-19.8	0.00495	1485	60	37
NGC 6701	SB(s)a	57.2	1.5×1.3	-20.8	0.01323	3969	32	24
NGC 7770	S0	58.7	0.8×0.7	-19.4	0.01414	4242	27	50
NGC 7771	SB(s)a	60.8	2.5×1.0	-20.8	0.01445	4335	66	68
Stephan's Quintet								
NGC 7317	E4	93.3	1.1×1.1	-20.3	0.02201	6603	12	150
NGC 7318A ..	E2 pec	93.7	0.9×0.9	-20.5	0.02211	6633	...	...
NGC 7318B ...	SB(s)bc pec	82.0	1.9×1.2	-20.6	0.01926	5778	...	...
NGC 7319	SB(s)bc pec	95.4	1.7×1.3	-20.8	0.02251	6753	41	148
NGC 7320	SA(s)d	13.7	2.2×1.1	-17.5	0.00262	786	59	132

Table 3.2: Galaxy properties of the PINGS sample. Col. (1): Galaxy name. Col. (2): Morphological type from the R3C catalog(de Vaucouleurs et al., 1991). Col. (3): Distances in Mpc, references: NGC 628, Hendry et al. (2005); NGC 1058, Eastman et al. (1996); NGC 1637, Saha et al. (2006); NGC 2976, Karachentsev et al. (2002); NGC 3184, Leonard et al. (2002); NGC 3310, Terry et al. (2002); NGC 5474, Drozdovsky & Karachentsev (2000); NGC 6643, Willick et al. (1997); NGC 4625, NGC 6701, NGC 7771, & Stephan's Quintet: Galactocentric GSR distances derived from the redshift, assumming a value of H_0 = 73 km s^{-1} Mpc^{-1}. Col. (4): Projected size, major and minor axes at the B_{25} mag arcsec^{-2} from R3C, except NGC 7318 from Jarrett et al. (2003). Col. (5): Absolute B-band magnitude calculated from the apparent magnitude listed in the R3C catalog and the adopted distances to the system. Col. (6): Redshift, references: NGC 628, Lu et al. (1993); NGC 4625, Fisher et al. (1995); NGC 6701, Theureau et al. (1998); NGC 7770, Woods et al. (2006); NGC 1637, NGC 3310, Haynes et al. (1998); NGC 2976, NGC 5474, Falco et al. (1999, The Updated Zwicky Catalog); NGC 1058, NGC 3184, NGC 6643, NGC 7771, Springob et al. (2005); NGC 7317, NGC 7318a, NGC 7318b, Hickson et al. (1992); NGC 7319, NGC 7320, Nishiura et al. (2000). Col. (7): Heliocentric velocities calculated from $v = zc$, with no further correction applied. Col. (8): Galaxy inclination angle based on the B_{25} mag arcsec^{-2} from R3C. Col. (9): Galaxy position angle, measured positive NE, in the B_{25} mag arcsec^{-2} except for NGC 1058, NGC 1637, NGC 7317, NGC 7319, NGC 7770, which are based on the K_s-band (Jarrett et al., 2003), and NGC 3310, NGC 4625, NGC 5474 based on the r-SDSS band.

with coordinates in the J2000 equinox. Some of their relevant physical properties are listed in Table 3.2. A good fraction of the sample belongs to the Spitzer Infrared Nearby Galaxies Survey (SINGS, Kennicutt et al., 2003), which ensures a rich set of ancillary observations in the UV, infrared, H I and radio.

The final sample candidates were given a different observing priority based on the angular size of the

objects, the number of PPAK adjacent pointings necessary to complete the mosaic, and the scientific relevance of the galaxy. The first priority was assigned to medium-size targets such as NGC 1058, NGC 1637, NGC 3310, NGC 4625 and NGC 5474 which are bright, face-on spirals of very different morphological type, with many sources of ancillary data and could be covered with relatively few IFU pointings. The second priority was given to smaller galaxies which fit perfectly in terms of size and acquisition time for the periods during the night when the first priority objects were not observable (due to a high airmass or bad weather conditions) and/or in the case their mosaicing was completed.

NGC 628 (Messier 74) is a special object among the selected galaxies and the most important object of the sample. NGC 628 is a close, bright, grand-design spiral galaxy which has been extensively studied. With a projected optical size of 10.5×9.5 arcmin, it is the most extended object of the sample. Although it could be considered too large to be fully observed in a realistic time, we attempted the observation of this galaxy considering that the spectroscopic mosaicing of NGC 628 represents the real 2-dimensional scientific spirit of the PINGS project. Such a large galaxy would offer us the possibility to test, confirm and extend the body of results from the rest of the small galaxies in the sample and would allow us to study the 2D metallicity structure of the disk and higher order properties of the abundance distribution. Hitherto, NGC 628 represents the largest area ever covered by an IFU observation.

3.3 Logistics

A full observational long-term programme was proposed to the 3.5m-telescope Calar Alto TAC during the first semester of 2007. Observing time was granted for winter of 2007 for a total of four nights. At this point, the objective of the project was to target a set of relatively small galaxies in order to gain expertise with the PPAK instrument, the reduction process, related software, and to obtain the first usable IFS data. With the experience and information gained in this first run, we assessed the scientific scopes for the PhD programme and adjusted the sample and observing strategy accordingly. Further observing time requests were justified on the basis of science results and experience gained from the first and consecutive runs.

During the development of the project we had to bear in mind the amount of time that the processing of the data will take, considering the huge spectroscopic data set that each of these observations implies and the intrinsic complexity of the IFU spectra in terms of reduction and analysis. The observing runs were carried out as follows:

1. **Second Semester 2007**: Pilot programme: Observing time was granted for 4 observing nights (7 – 10 December). We decided the general observing strategy, for small galaxies we used dithering mode to ensure a good surface and depth coverage of the galaxies. In the case of bigger objects, we preferred more surface coverage despite the lose of resolution and depth in our observations, which were compensated by structural information that is relevant in terms of chemical abundance gradients along the spiral arms of big galaxies. During this run we observed a total of six galaxies, namely: NGC 1058, NGC 3310, NGC 1637, NGC 4625, NGC 3184 and NGC 628. We finished the mosaicing for the first four objects and got many pointings for NGC 628 and NGC 3184. We fulfilled the objectives of the first observing run as stated in the application form, where we proposed that we would observe and complete at least four galaxies and would develop the observing technique and gain efficiency for future runs.

2. **First Semester 2008**: Having at this point a clear idea of the scientific scopes and technical difficulties

of the observations, we aimed to observe the remaining small-intermediate size galaxies of the sample and at least two big size galaxies which would require more than one night per object considering the number of PPAK pointings and integration time (see section 3.4). Six nights were awarded in service mode split in two slots: 14th - 17th April and 1st - 2nd June. Unfortunately we lost 5 out of 6 nights due to bad weather, only on the 2nd of June the weather was good enough to observe some positions of NGC 5474 and NGC 6643.

3. **Second Semester 2008**: The priority for this semester is to observe the remaining pointings of NGC 628 (the most important galaxy in the sample) and to obtain the mosaicing of NGC 925. Considering the loss of observing time on the previous run due to weather conditions and problems with the instrumental set-up, we were granted six nights in order to complete all the planned observations. Unfortunately we lost 5 out of 6 nights due to bad weather. However we could observe nine pointings of NGC 628 and we started the mosaicing of NGC 925.

4. **First Semester 2009**: Four nights were granted from the 26th to the 29th of April 2009. The priority for the last run of the project (in the context of the Ph.D. programme) was to finish the mosaicing of NGC 3184 and NGC 5474. Observations could be performed only on the 27th and 28th, completing 9 pointings of NGC 3184 and 2 dithering positions for NGC 5474.

In summary, the project started in December 2007 with the first observing run, three additional runs were granted during 2008-2009 accounting for a total of 20 observing nights, of which 12 were lost due to bad weather or problems with the instrumental set-up, preventing us from acquiring the full PINGS sample of galaxies as first proposed. However, the amount of data collected was sufficiently large for a reasonably good analysis, and the lack of coverage in some galaxies did not compromise the execution of the Ph.D. project. The observing program was adjusted along the way accordingly to the the feasibility of the intended science and the success/failure of the observations during successive observing runs. The total observed sample consist of 17 galaxies (see Table 3.1), covering nearly 100 arcmin^2 on the sky.

3.4 Observations

Observations for the PINGS galaxies were carried out at the 3.5m telescope of the Calar Alto observatory with the Postdam Multi Aperture Spectrograph, PMAS (Roth et al., 2005) in the PPAK mode (Verheijen et al., 2004; Kelz & Roth, 2006), i.e. a retrofitted bare fibre bundle IFU which expands the FoV of PMAS to a hexagonal area with a footprint of 74×65 arcsec, with a filling factor of 65% due to gaps in between the fibres. The PPAK unit features a central hexagonal bundle with 331 densely packed optical fibres to sample an astronomical object at 2.7 arcsec per fibre. The sky background is sampled by 36 additional fibres distributed in 6 mini-IFU bundles of 6 fibres each, in a circular distribution at $\sim$90" of the centre and at the edges of the central hexagon. The sky-fibres are distributed among the science ones in the pseudo-slit, in order to have a good characterisation of the sky. Additionally, 15 fibres can be illuminated directly by internal lamps to calibrate the instrument. PPAK was by the time of the planning of this project the world's widest optical integral field unit that provides a semi-contiguous regular sampling of extended astronomical objects (see subsection 2.2.1 for a technical overview).

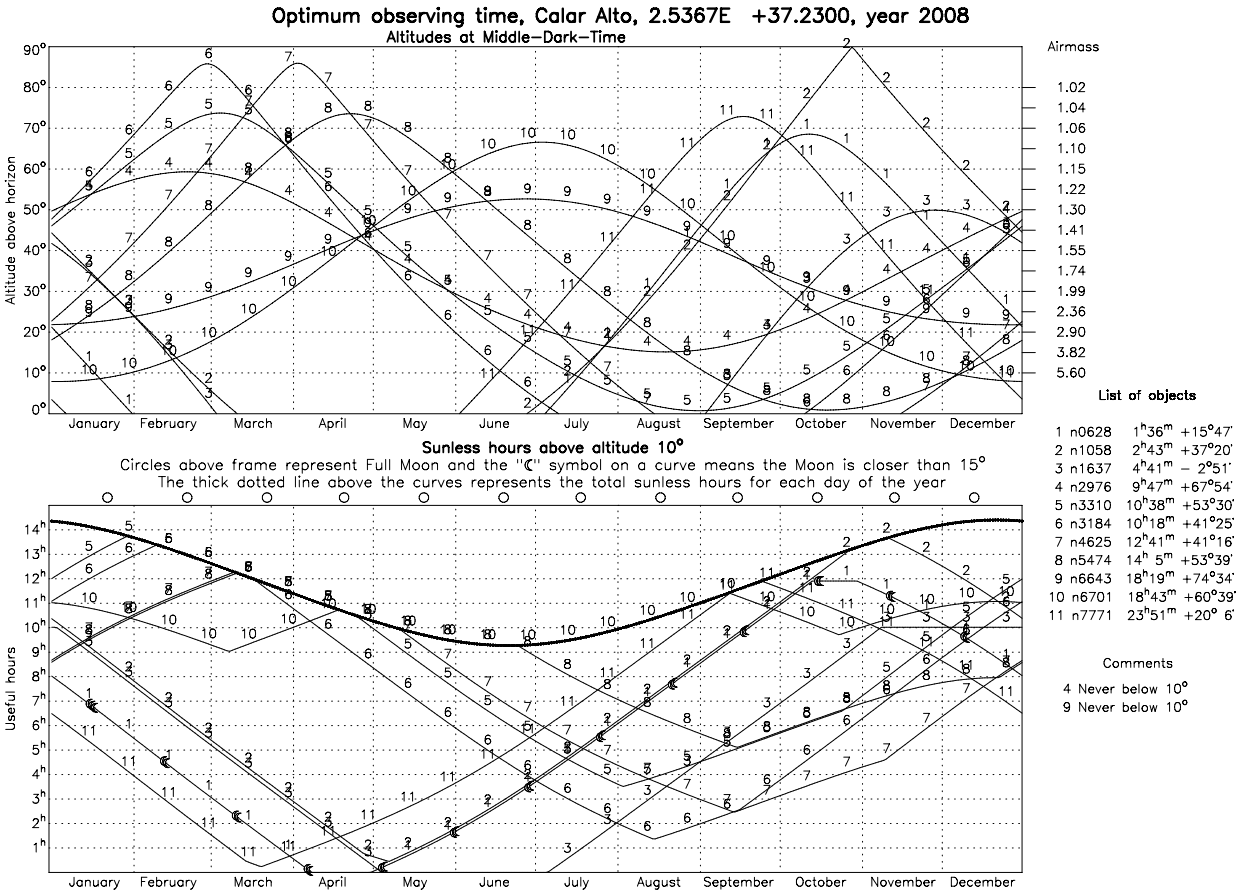

Figure 3.1: Optimum observing times for the sample as explained in the text. The numbers in each line correspond to the labels on the right. Plot obtained using the **Staralt** facility developed by Peter Sorensen and Marco Azzaro.

All sample galaxies were observed using the same telescope and instrument set-up. We used the V300 grating, covering a wavelength between 3700 – 7100 Å with a resolution of ~ 10 Å FWHM, corresponding to ~ 600 km s^{-1}. With this set-up, we cover all the optical strong emission lines used in typical abundance diagnostic methods. The exposure times were calculated from previous experience with the instrument in order to obtain spectroscopy with S/N ≥ 20 in the continuum and S/N ≥ 50 in the Hα emission line for the brightest H II regions with the given grating. For each observation, a value of the monochromatic extinction in the V band was recorded using the CAVEX[1] monitor at CAHA, values are reported in the logs of the observations. When at the time of the observation the CAVEX monitor did not report a value for A_V, the extinction was either inferred from the night trend in the database or assumed to be the average value of A_V at Calar Alto during the corresponding observing season accordingly to Sánchez et al. (2007).

Different observing strategies were implemented depending on the size and priority of the targets. For those objects with relatively small angular size and larger distances, single PPAK pointings would not sample the surface of the galaxy with enough spatial resolution, due to the incomplete filling factor of the fibre bundle. In this case, a dithering method was applied. For each individual position in dithering mode, the first exposure was recorded and then, two consecutive exposures with the same acquisition time were recorded, but with small offsets of Δ(RA, Dec) = (1.56, 0.78) and (1.56, –0.78) arcsec with respect to the first exposure. The advantage of this method is that all gaps of the original exposure are covered, and every single point of

the dithered field is spectroscopically sampled within the resolution. The pitfalls are that the exposure time and the amount of data to be processed is the triple of a normal frame, preventing the possibility to apply this method to large mosaics. We used a mean acquisition time per PPAK field in dithering mode (including set-up + integration time) of 2×600 sec. per dithering position for a total of 60 min. exposure; and 3×600 sec. per non-dithered frames.

For all the objects in the sample, the first exposure was centered in a given geometrical position which, depending on the morphology or a particular mosaicing pattern, may or may not coincide with the bright bulge of the galaxy. Consecutive pointings followed in general a hexagonal pattern, adjusting the mosaic pointings to the shape of the PPAK science bundle as shown for example in Figure 3.2. Each pointing centre lies radially at 60" from the previous one. Due to the shape of the PPAK bundle and by construction of the mosaics, 11 spectra of each pointing corresponding to one edge of the hexagon, overlap with the same number of spectra from the previous pointing. This pattern was selected to maximise the covered area, but to allow enough overlapping to match the different exposures taken under variable atmospheric conditions. Exceptions are NGC 2976, NGC 3310, NGC 6643 and NGC 7770 in which the mosaics were constructed to optimise the galaxy surface coverage as explained in each case in the following sections.

Figure 3.1 displays the optimum observing times along the year for the most important objects of the sample at the geographical location and altitude of the Calar Alto observatory. The top panel shows objects' altitudes above the horizon (airmass). The bottom panel shows the sunless hours above a certain altitude. There are two distinctive groups, one during autumn-winter time (objects 1, 2, 3, 11) and during winter-spring time (objects 4-8). Exceptions are objects 9 and 10 visible along the whole year, with the best observing time during summer.

3.4.1 NGC 628

NGC 628 (or M 74) is an extensively studied isolated grand-design Sc spiral galaxy at a distance of 9.3 Mpc in the constellation of Pisces. The observations for this galaxy extended over a period of three-years in different stages, with a total of six observing nights.

Figure 3.2 shows a Digital Sky Survey [2] (DSS) image of NGC 628 displaying the mosaiced pattern followed for the observation of this galaxy. The central position was observed in dithering mode to gain spatial resolution. Due to the large size of the mosaic, the rest of the 33 positions were observed without dithering. Seven positions were previously observed on the 28th October 2006 by the CAHA staff, and were incorporated as part of the final mosaic, 19 positions were observed in the period 10 – 12 of December 2007, 1 position on August 9th 2008 and the remaining pointings on October 28th 2008, see Table 3.3 for details. Figure 3.2 shows the mosaic pattern covering NGC 628 consisting in a central position and consecutive hexagonal concentric rings. The area covered by the all observed positions accounts approximately for 34 arcmin^2, making this galaxy the largest area ever covered by an IFU mosaicing. The spectroscopic mosaic contains 13571 individual spectra and cover an area of nearly 43 arcmin square.

3.4.2 NGC 1058

NGC 1058 is a well studied Sc spiral with a projected size of 3.0×2.8 arcmin at a distance of 10.6 Mpc, in the constellation of Perseus. The observations for this galaxy were performed on three consecutive nights from the 7th to the 9th December 2007. The mosaic consists of the central position and one concentric ring, covering most of the galaxy surface within one optical radius (defined by the *B*-band 25th magnitude

isophote). Ferguson et al. (1998) found the existence of H II regions out to and beyond two optical radii in this galaxy.

We tried to observe these intrinsic interesting objects by performing a couple of offsets of 2 and 2.5 arcmin north-east from the central position. These 2 additional position were merged to the original 7 tiles for a mosaic with a total of 9 pointings, covering an area of approximately 8.5 arcmin^2 (see Figure 3.3). All positions (with the exception of one blind-offset) were observed in dithering mode, accounting for a spectroscopic mosaic containing 7944 individual spectra. At the time of the observations, we were able to observe the recently discovered supernova 2007gr, a SN type Ic located at 24".8 west and 15".8 north of the nucleus of NGC 1058 between two foreground stars.

3.4.3 NGC 1637

NGC 1637 is a SAB distorted galaxy in Eridanus with a projected size of 4.0×3.2 arcmin. The evident asymmetry of this galaxy is clearly seen in optical images where a third well-defined arm is found. This feature is also visible in H I , CO, near-IR and 20 cm radio continuum maps (Roberts et al., 2001). Some of the unusual features found in NGC 1637 are: an H I envelope which is significantly more extensive than usual $D_{HI}/D_{25} = 3.0$; the optical centre differs from the kinematic centre by 9" (or 435 pc); although there is an H I enhancement associated with the third arm there are even stronger enhancements in regions that lack prominent optical features.

NGC 1637 was observed during December 8th to 10th 2007. The mosaic was built with a central position and one concentric ring of 6 pointings (see Figure 3.4), covering most of the galaxy surface within one optical radius. The mosaic covers approximately 7 arcmin^2. This galaxy has a full spectroscopic mosaic containing 6951 individual spectra.

3.4.4 NGC 2976

NGC 2976 is a SAc peculiar spiral galaxy with strong emission line spectra with a projected size of 5.9×2.7 arcmin in Ursa Major. The observations for NGC 2976 were carried out on October 30th 2008. Given the distorted morphology of the galaxy a more convenient mosaic pattern was tailored designed as shown in Figure 3.5. Unfortunately, due to bad weather conditions, only two pointings were observed for this object, corresponding to the central region of NGC 2976. The fields in dashed lines show the positions that could not be observed. The observations were performed in non-dithering mode. The spectroscopic data for this galaxy consists of 662 individual spectra.

NGC 628

Position	Date	UT	airmass	A_V
1 dith 0	10 Dec 2007	18:30	1.21	0.14
dith 1	”	18:50	1.16	0.14
dith 2	”	19:12	1.13	0.14
1	28 Oct 2006	22:51	1.08	0.24
2	”	00:09	1.09	0.23
3	”	23:30	1.07	0.25
4	10 Dec 2007	19:39	1.09	0.16
5	”	20:15	1.07	0.14
6	”	21:15	1.09	0.14
7	”	21:54	1.14	0.15
8	”	22:37	1.22	0.15⋆
9	28 Oct 2006	01:29	1.23	0.22
10	”	00:52	1.15	0.23
11a	12 Dec 2007	19:05	1.13	0.18⋆
11b	09 Aug 2008	03:25	1.11	0.20
12	12 Dec 2007	18:26	1.19	0.18⋆
13	”	20:43	1.08	0.18⋆
14	11 Dec 2007	21:22	1.10	0.15
15	”	22:01	1.15	0.15
16	”	20:33	1.07	0.15
17	”	19:51	1.08	0.15
18	”	19:00	1.14	0.15
18	”	18:21	1.21	0.15
20	30 Oct 2008	20:45	1.27	0.15⋆
21	”	21:24	1.17	0.15
22	28 Oct 2006	02:44	1.55	0.25
23	”	02:06	1.36	0.23
24	30 Oct 2008	22:02	1.11	0.18
25	12 Dec 2007	19:44	1.09	0.18⋆
26	30 Oct 2008	22:44	1.08	0.16
27	”	23:22	1.07	0.15
28	”	00:02	1.09	0.15
29a	12 Dec 2007	21:20	1.10	0.18⋆
29b	30 Oct 2008	00:47	1.16	0.15
30	11 Dec 2007	22:38	1.24	0.15
31	12 Dec 2007	22:13	1.18	0.18
32	”	22:56	1.31	0.15
33	30 Oct 2008	01:29	1.26	0.15
34	”	02:08	1.41	0.15

Table 3.3: Log of observation for all the PPAK mosaicking positions of NGC 628. The first position (the central one) was observed in dithering mode. Positions 1, 11 and 29 have repeated observations. Entries with the ⋆ flag indicate that the value of A_V, the atmospheric extinction during the observation (mag/airmass), was either inferred from the night trend in the CAVEX extinction database or assumed to be the average value of A_V at Calar Alto during the corresponding observing season as explained in the text.

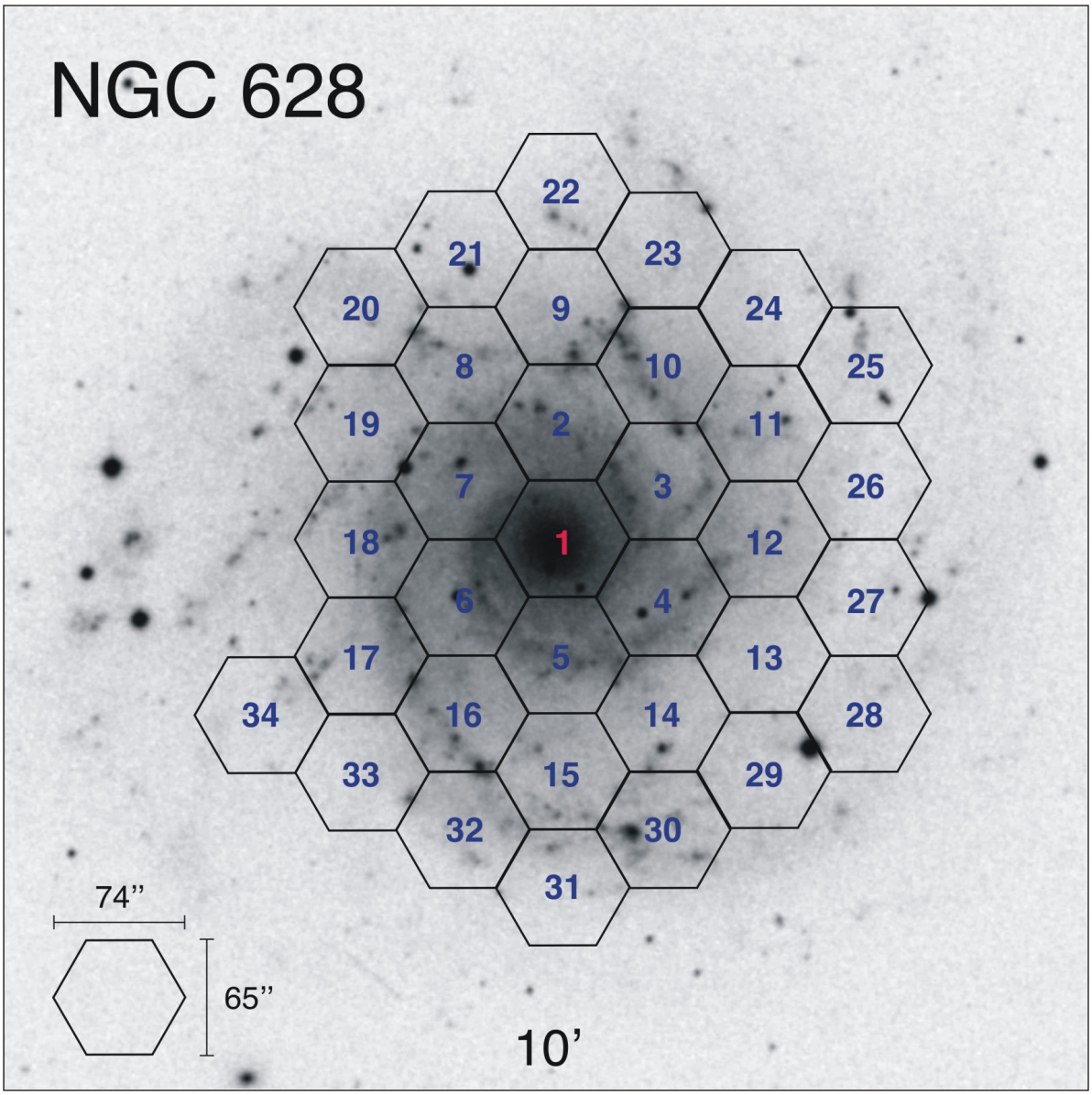

Figure 3.2: Broad *B*-band DSS image of NGC 628. An array of hexagonal, fields each corresponding to the FoV of the PPAK instrument, is superimposed on scale showing the IFU mosaicing technique and all the observed positions. The PINGS mosaicing of NGC 628 covers nearly 34 arcmin^2, which represents the largest spectroscopic survey on a single galaxy in the nearby universe. The positions were observed accordingly to the log shown in Table 3.3. The image is 10’ $\times$ 10’ and it is displayed in top-north, left-east standard configuration.

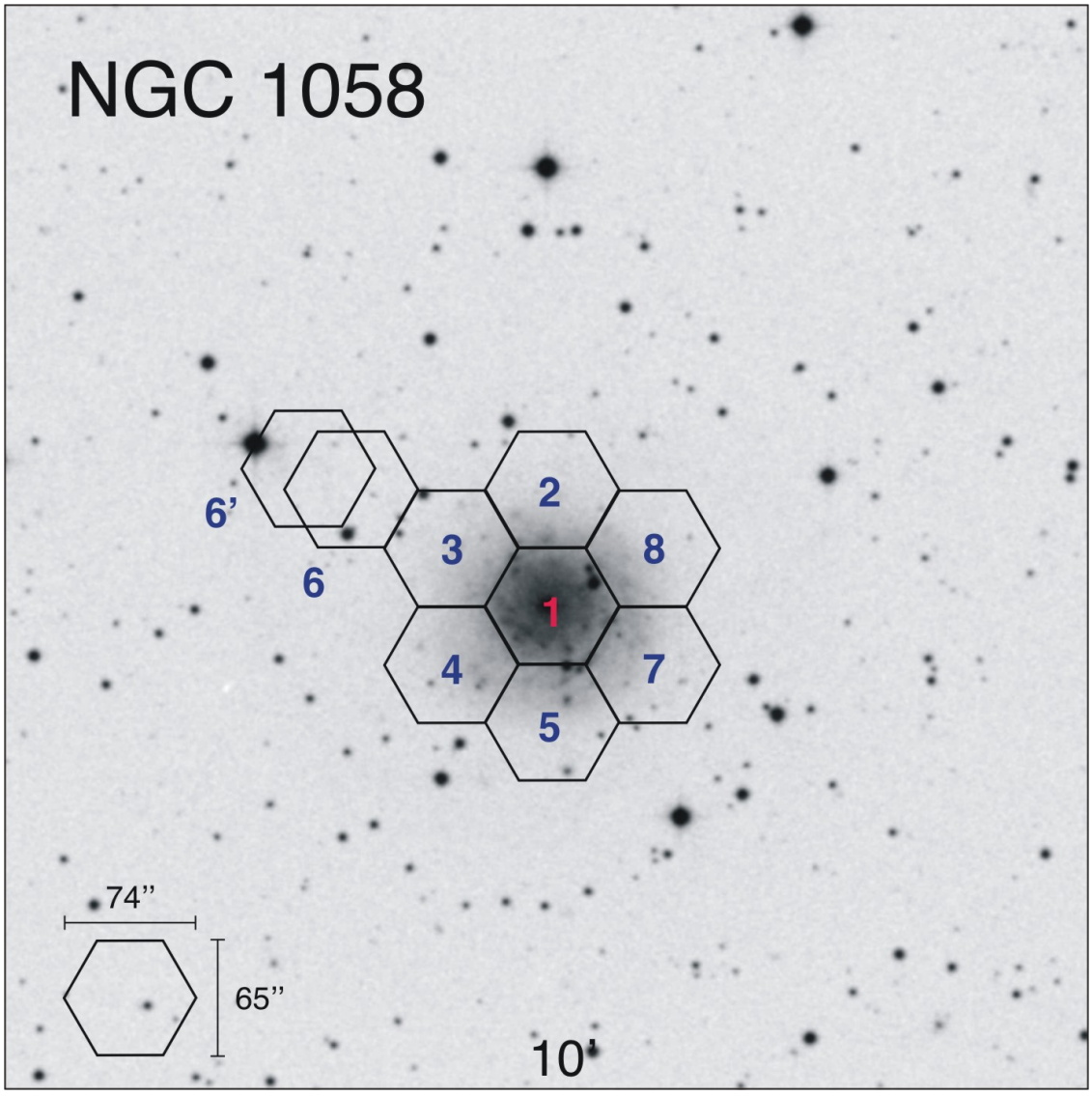

Figure 3.3: DSS image of NGC 1058 with overlaid PPAK pointings. The positions were observed accordingly to the log shown in Table 3.4. The image is 10’ × 10’ and it is displayed in the standard NE configuration.

NGC 1058

Position	Date	UT	airmass	A_V
1 dith 0	07 Dec 2007	19:05	1.19	0.13
dith 1	”	19:33	1.12	0.14
dith 2	”	20:00	1.07	0.15
2 dith 0	07 Dec 2007	20:42	1.02	0.14
dith 1	”	21:07	1.01	0.15
dith 2	”	21:36	1.00	0.13
3 dith 0	07 Dec 2007	22:17	1.01	0.14
dith 1	”	22:46	1.02	0.12
dith 2	”	23:14	1.04	0.12
4 dith 0	07 Dec 2007	23:56	1.10	0.12
dith 1	”	00:25	1.17	0.13
dith 2	”	00:50	1.23	0.16
5 dith 0	08 Dec 2007	18:22	1.30	0.13
dith 1	”	18:49	1.21	0.15*
dith 2	”	19:16	1.15	0.15*
6 —	08 Dec 2007	19:58	1.07	0.15*
6’ dith 0	08 Dec 2007	20:30	1.03	0.15*
dith 1	”	20:54	1.01	0.14
dith 2	”	21:22	1.00	0.14
7 dith 0	09 Dec 2007	18:30	1.25	0.15*
dith 1	”	19:03	1.17	0.15*
dith 2	”	19:27	1.11	0.15*
8 dith 0	09 Dec 2007	20:04	1.06	0.15*
dith 1	”	20:34	1.03	0.15*
dith 2	”	20:59	1.01	0.15*

Table 3.4: Log of observation for all the PPAK moisaicking positions of NGC 1058. All positions in dithering mode except observation number 6, which was a blind offset (104,60) looking for outlying H II regions. Position 6’ has an offset of (130,75). Entries with the $\star$ flag as explained in Table 3.3.

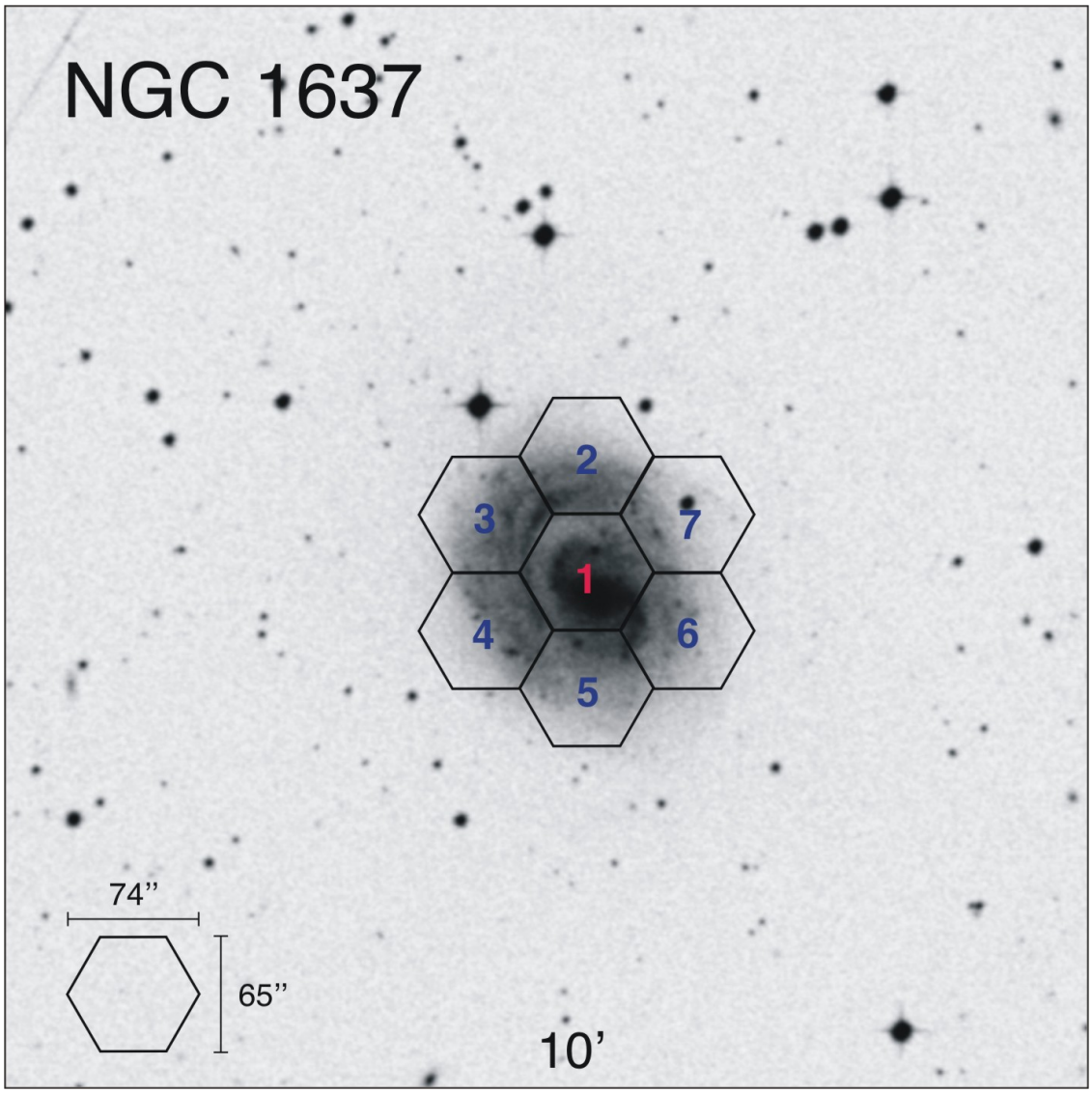

Figure 3.4: DSS image of NGC 1637 with overlaid PPAK pointings. The positions were observed accordingly to the log shown in Table 3.5. The image is 10’ × 10’ and it is displayed in the standard NE configuration.

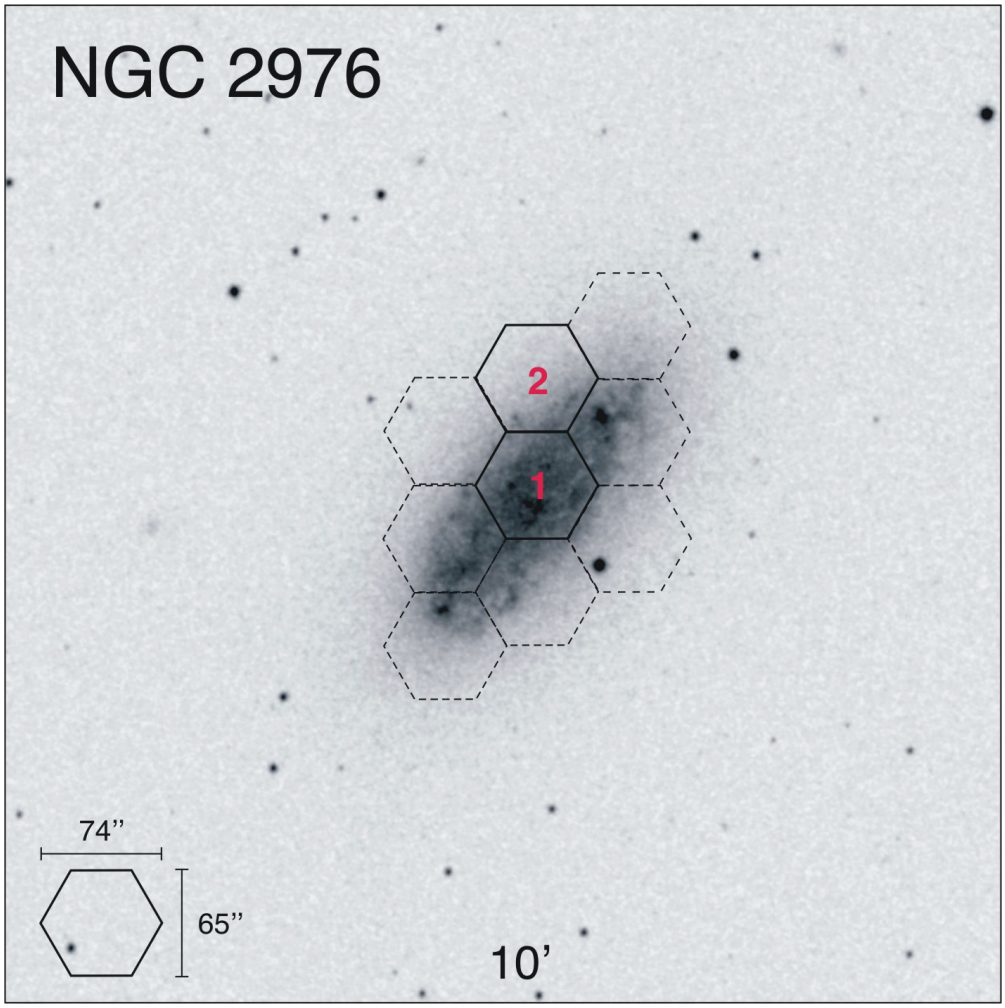

Figure 3.5: DSS image of NGC 2976 with overlaid PPAK pointings. The positions were observed accordingly to the log shown in Table 3.6. The image is 10’ × 10’ and it is displayed in the standard NE configuration.

NGC 1637

Position	Date	UT	airmass	A_V
1 dith 0	08 Dec 2007	22:23	1.39	0.15
dith 1	”	23:07	1.32	0.13
dith 2	”	23:33	1.30	0.12
2 dith 0	08 Dec 2007	00:01	1.31	0.12
dith 1	”	00:27	1.33	0.13*
dith 2	”	00:55	1.37	0.11*
3 dith 0	08 Dec 2007	01:36	1.49	0.13
dith 1	”	02:02	1.60	0.13
dith 2	”	02:29	1.75	0.13
4 dith 0	09 Dec 2007	21:54	1.46	0.14
dith 1	”	22:18	1.39	0.16
dith 2	”	22:44	1.34	0.15
5 dith 0	09 Dec 2007	23:25	1.31	0.13
dith 1	”	23:53	1.31	0.13*
dith 2	”	00:18	1.32	0.13*
6 dith 0	09 Dec 2007	00:52	1.38	0.14
dith 1	”	01:20	1.45	0.15*
dith 2	”	01:46	1.55	0.14
7 dith 0	10 Dec 2007	23:35	1.30	0.13
dith 1	”	00:04	1.31	0.13
dith 2	”	00:31	1.35	0.13

Table 3.5: Log of observation for all the PPAK moisaicking positions of NGC 1637. All positions in dithering mode. Entries with the $\star$ flag as explained in Table 3.3.

NGC 2976

Position	Date	UT	airmass	A_V
1	30 Oct 2008	03:10	1.43	0.15*
2	”	03:56	1.33	0.15*

Table 3.6: Log of observation for all the PPAK moisaicking positions of NGC 2976. Entries with the $\star$ flag as explained in Table 3.3.

3.4.5 NGC 3184

NGC 3184, a SAB face-on galaxy located in Ursa Major, has the 2nd largest angular size in the sample. It covers an area of 7.4 × 6.9 arcmin. This grand-design spiral galaxy is about one degree east of the 3rd magnitude star μ Ursa Majoris. The bright star embedded in the outer parts is about 11th magnitude. Because of errors in the New General Catalog (NGC), this galaxy is also NGC 3180, and is probably the missing objects NGC 3181 and 3182. NGC 3184 is notable for its high abundance of heavy elements (McCall et al., 1985) and a supernova (SN 1999gi) that has occurred there recently (Nakano & Kushida, 1999).

Three concentric rings are necessary to cover the entire optical disk. Observations for this galaxy were performed on December 10th 2007, April 27th and 28th 2009, following the standard mosaicing pattern with a central position and almost two complete ring for a total of 16 IFU pointings as shown in Figure 3.6. The fields in dashed lines show the positions that could not be observed due to bad weather conditions or lack of observing time. The area covered by all the observed positions is approximately 16 arcmin^2. The spectroscopic data for this galaxy totals 5296 individual spectra.

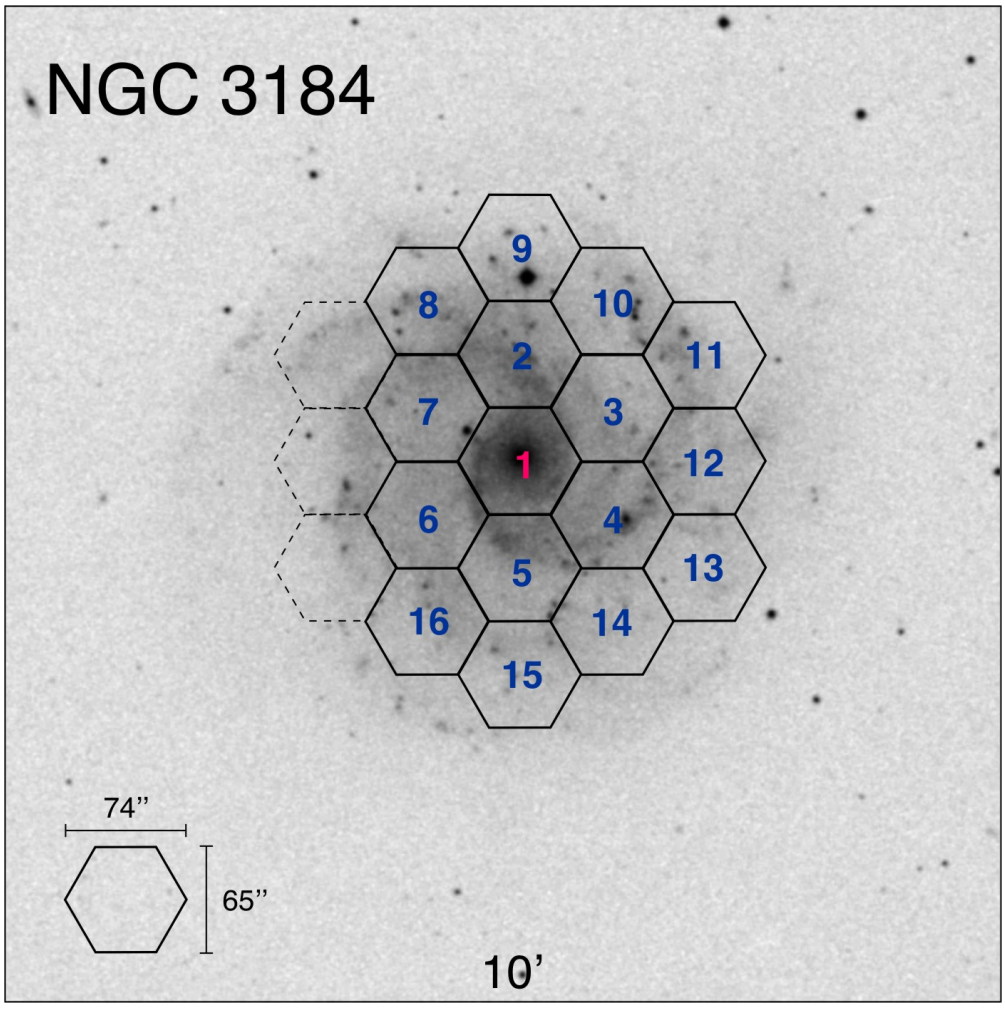

Figure 3.6: DSS image of NGC 3184 with overlaid PPAK pointings. The positions were observed accordingly to the log shown in Table 3.7. The fields in dashed lines show the positions that could not be observed due to bad weather conditions. The image is 10’ × 10’ and it is displayed in the standard NE configuration.

NGC 3184

Position	Date	UT	airmass	A_V
1	10 Dec 2007	01:26	1.36	0.12
2	”	02:21	1.19	0.13
3	”	03:00	1.11	0.14
4	”	03:45	1.05	0.20
5	”	04:23	1.02	0.14
6	”	05:00	1.00	0.14
7	”	05:42	1.01	0.15*
8	27 Apr 2009	21:11	1.03	0.15*
9	”	21:41	1.03	0.15*
10	”	22:10	1.09	0.15*
11	”	22:45	1.17	0.15*
12	”	23:13	1.24	0.15*
13	”	23:42	1.34	0.15*
14	”	00:09	1.45	0.15*
15	28 Apr 2009	20:36	1.01	0.15*
16	”	21:05	1.03	0.15*

Table 3.7: Log of observations for all the PPAK moisaicking positions of NGC 3184. Note the clockwise configuration of the pointings. Entries with the $\star$ flag as explained in Table 3.3.

3.4.6 NGC 3310

NGC 3310 is a very distorted spiral galaxy with strong star formation in the constellation of Ursa Major. It covers an area of 3.1×2.4 arcmin in the optical *B*-band. NGC 3310 likely collided with a smaller galaxy causing the large spiral galaxy to light up with a tremendous burst of star formation. The changing gravity during the collision created density waves that compressed existing clouds of gas and triggered the star-formation activity (Kregel & Sancisi, 2001). Galaxy NGC 3310 is forming clusters of new stars at an unusually high rate. Several hundred clusters of newly formed stars are visible in *B*-band images, as bright blue, diffuse objects that trace the spiral arms of the galaxy. The starburst activity of this galaxy began some 100 million years ago although some of the clusters are quite young, indicating that starburst galaxies may remain in star-burst mode for quite some time.

Given its morphology a different mosaic pattern was constructed for this galaxy (see Figure 3.7). Three pointings cover the surface of NGC 3310 with a central position centered in the galaxy's nucleus and two offsets of (–35, 35) and (35, –35) arcsec in (RA, Dec) in north-west and south-east directions respectively. The observations were carried out on December 8th 2007, and were performed in dithering mode. This galaxy has a full spectroscopic mosaic, which covers an area of approximately 2.8 arcmin^2. The spectroscopic data for this galaxy consists of 2979 individual spectra.

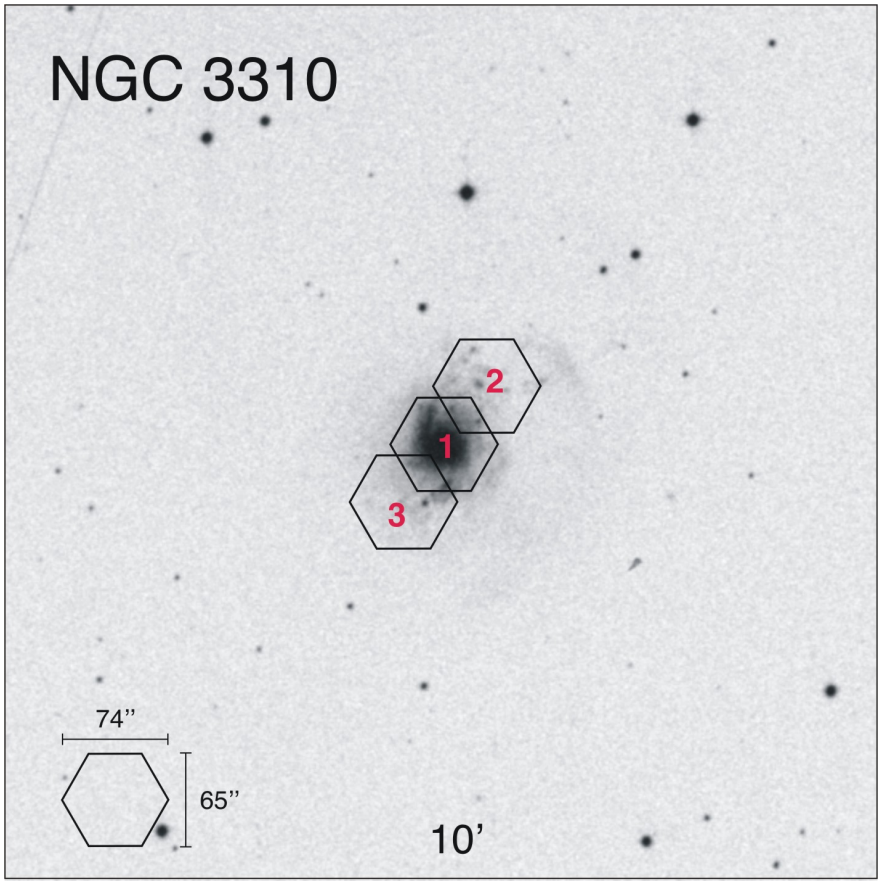

Figure 3.7: DSS image of NGC 3310 with overlaid PPAK pointings. The positions were observed accordingly to the log shown in Table 3.8. The image is 10’ × 10’ and it is displayed in the standard NE configuration.

NGC 3310

Position	Date	UT	airmass	A_V
1 dith 0	08 Dec 2007	03:05	1.17	0.11
dith 1	”	03:25	1.14	0.14
dith 2	”	03:38	1.12	0.13
2 dith 0	08 Dec 2007	04:22	1.07	0.15
dith 1	”	04:37	1.06	0.14
dith 2	”	04:51	1.05	0.15*
3 dith 0	08 Dec 2007	05:19	1.04	0.15*
dith 1	”	05:33	1.04	0.15*
dith 2	”	05:47	1.04	0.15*

Table 3.8: Log of observation for all the PPAK moisaicking positions of NGC 3310. All positions in dithering mode. The offset for position 2 is (–35,35) and for position 3 (35,–35) arcseconds from the mosaick centre reported in Table 3.1 in (RA,Dec). Entries with the $\star$ flag as explained in Table 3.3.

3.4.7 NGC 4625

NGC 4625 is a low-luminosity SAB, one-armed Magellanic spiral galaxy thought to be interacting with the also single-armed spiral NGC 4618 in Canes Venatici. The optical size of this galaxy covers an area of approximately 2.2 × 1.9 arcmin, however de Paz et al. (2005) discovered an extended UV disk reaching to 4 times its optical radius showing evidence of recent star formation. The observation of this galaxy was performed on December 9th 2007 with one single pointing in dithering mode covering the optical radius of NGC 4625. The spectroscopic data for this object totals 993 individual spectra.

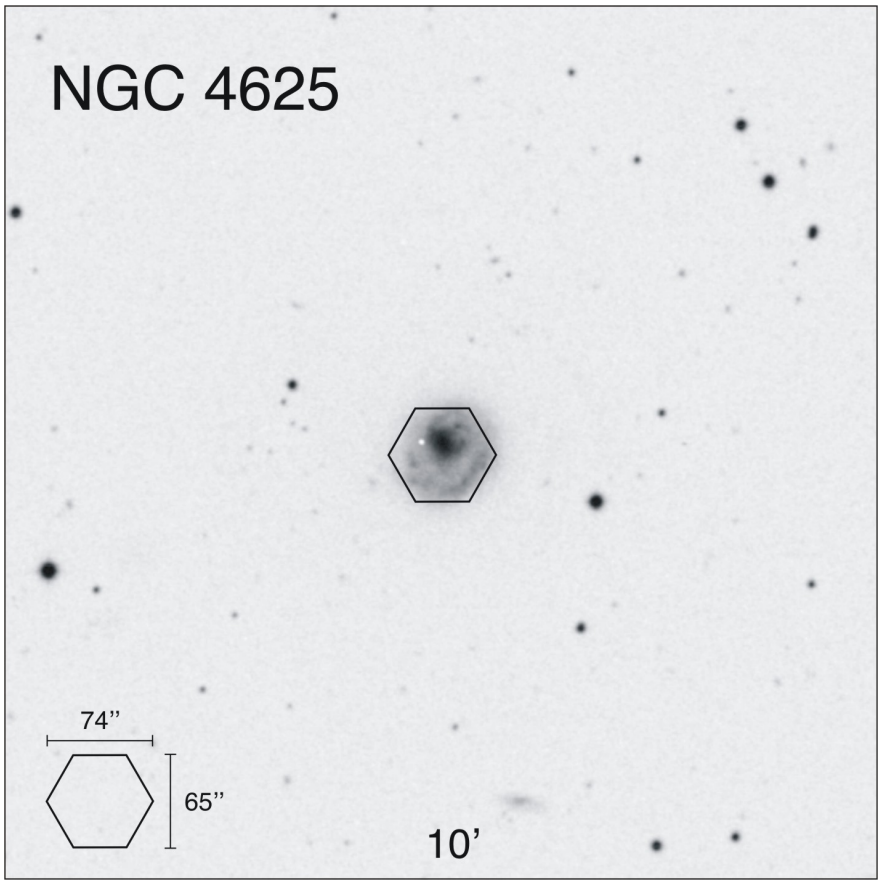

Figure 3.8: DSS image of NGC 4625 with overlaid PPAK pointings. The positions were observed accordingly to the log shown in Table 3.9. The image is 10’ × 10’ and it is displayed in the standard NE configuration.

NGC 4625

Position	Date	UT	airmass	A_V
1 dith 0	09 Dec 2007	04:20	1.27	0.13
dith 1	”	04:44	1.20	0.13
dith 2	”	05:11	1.14	0.12

Table 3.9: Log of observation for all the PPAK moisaicking positions of NGC 4625. All positions in dithering mode.

3.4.8 NGC 5474

NGC 5474 is a strongly lopsided spiral galaxy covering an area of 4.8×4.3 arcmin in Ursa Major. We observed the optical area with a standard mosaic configuration with one central position and one concentric ring. All pointings were observed in dithering mode. Observations were carried out in three different periods, two positions on June 2008, 4 positions during August 9th and 10th 2008 and 2 repeated positions on April 27th 2009, corresponding to the pointings 1 and 2, as the first observations presented low quality problems. The observed positions on June 2008 were discarded. Given the distorted morphology of this galaxy, the central position of the mosaic does not coincide with the bright bulge; a 30" offset in declination was performed towards the south, so that the area covered by the IFU mosaicing includes most of the optical disk of the galaxy in a symmetric way. The fields in dashed lines show the positions which could not be observed due to bad weather conditions of lack of observing time. The area covered by all the observed positions is approximately 6 arcmin^2. The spectroscopic data for this galaxy totals 5958 individual spectra.

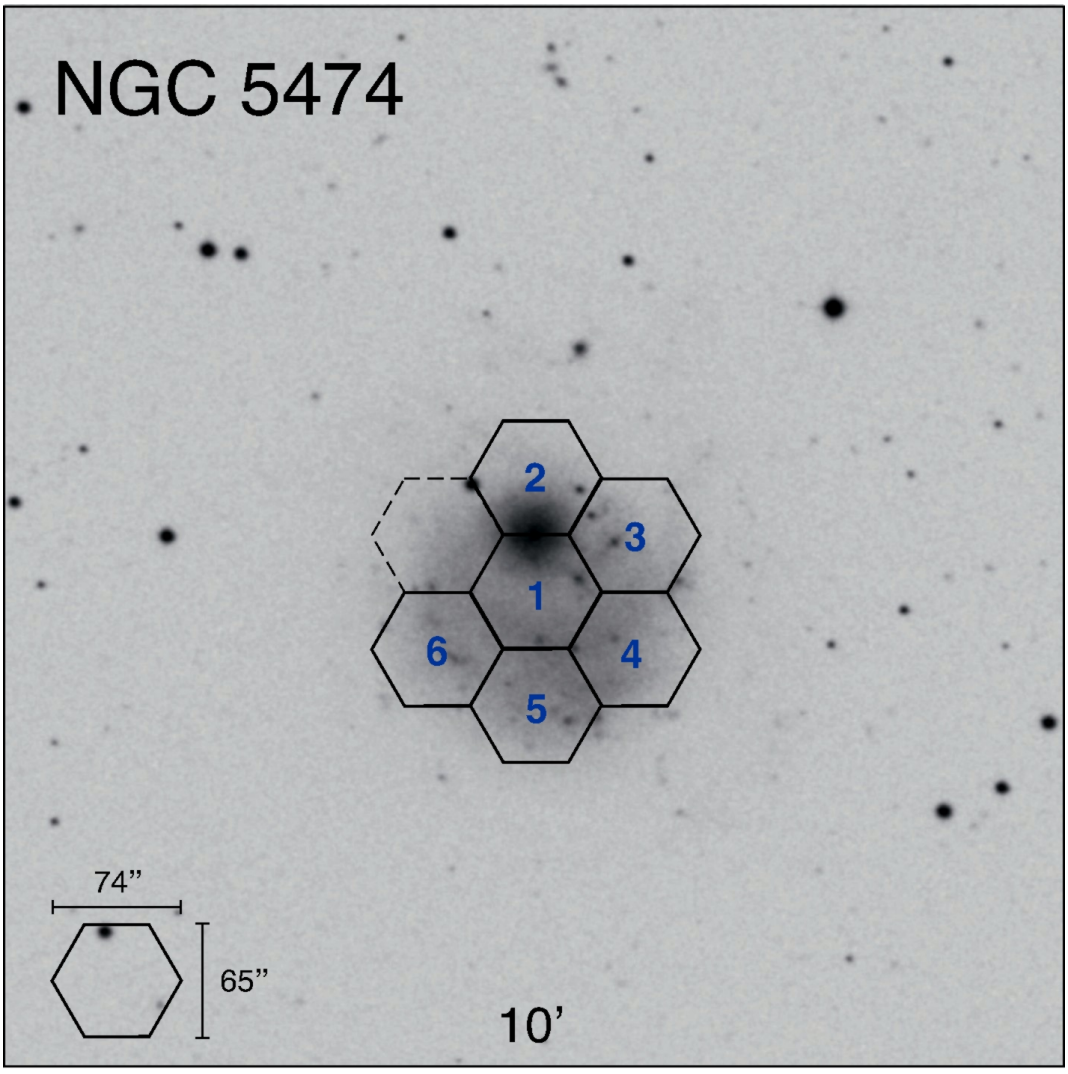

Figure 3.9: DSS image of NGC 5474 with overlaid PPAK pointings. The positions were observed accordingly to the log shown in Table 3.10. The fields in dashed lines show the positions with pending observations. The image is 10' $\times$ 10' and it is displayed in the standard NE configuration.

NGC 5474

Position	Date	UT	airmass	A_V
1 dith 0	27 Apr 2009	00:49	1.06	0.15⋆
dith 1	”	01:15	1.08	0.15⋆
dith 2	”	01:39	1.10	0.15⋆
2 dith 0	27 Apr 2009	02:13	1.15	0.15⋆
dith 1	”	02:38	1.19	0.15⋆
dith 2	”	03:03	1.25	0.15⋆
3 dith 0	09 Aug 2008	20:33	1.30	0.16
dith 1	”	21:02	1.39	0.16
dith 2	”	21:28	1.49	0.17
4 dith 0	09 Aug 2008	22:09	1.69	0.15
dith 1	”	22:36	1.85	0.15
dith 2	10 Aug 2008	20:12	1.25	0.15⋆
5 dith 0	10 Aug 2008	20:51	1.36	0.17
dith 1	”	21:17	1.46	0.17
dith 2	”	21:43	1.57	0.17
6 dith 0	10 Aug 2008	22:16	1.75	0.18
dith 1	”	22:42	1.92	0.18

Table 3.10: Log of observation for all the PPAK mosaicking positions of NGC 5474. All positions in dithering mode. Positions 1 and 2 were repeated in the April 2009 run as the first observations were of bad quality. For position 6, the dithering was not complete due to the low altitude of the object. Entries with the ⋆ flag as explained in Table 3.3.

3.4.9 NGC 6643

NGC 6643 is a SAc galaxy in Draco, with a projected size of 3.8×1.9 arcmin in the *B*-band. NGC 6643 has a very small nucleus separated from the broken remnants of an inner ring that extends into a complex, irregular spiral pattern. Bright knots that are probably H II regions outline the multiple spiral arms.

A tailored mosaic pattern for this galaxy was constructed in order to cover most of its surface. Three pointings cover the surface of NGC 6643 with a central position centered in the bulge and two offsets of $(37, 34)$ and $(-35, -34)$ arcsec in (RA,Dec) in north-east and south-west directions respectively (see Figure 3.10). Observations were performed on June 2nd 2008 for the first 2 positions and on August 10th 2008 for the 3rd position, all of them in dithering mode. At the time of the first observing run, we were able to observe the supernova 2008bo, a SN type Ib located at 31” north and 15” west of the nucleus of NGC 6643. This galaxy has a complete spectroscopic mosaic covering an area of approximately 2.8 arcmin^2. The data for this galaxy consists of 2979 individual spectra. However, due to a technical problem with the instrument set-up, positions 1 and 2 do not cover the usual wavelength range, but are shifted towards the red by approximately 100 Å.

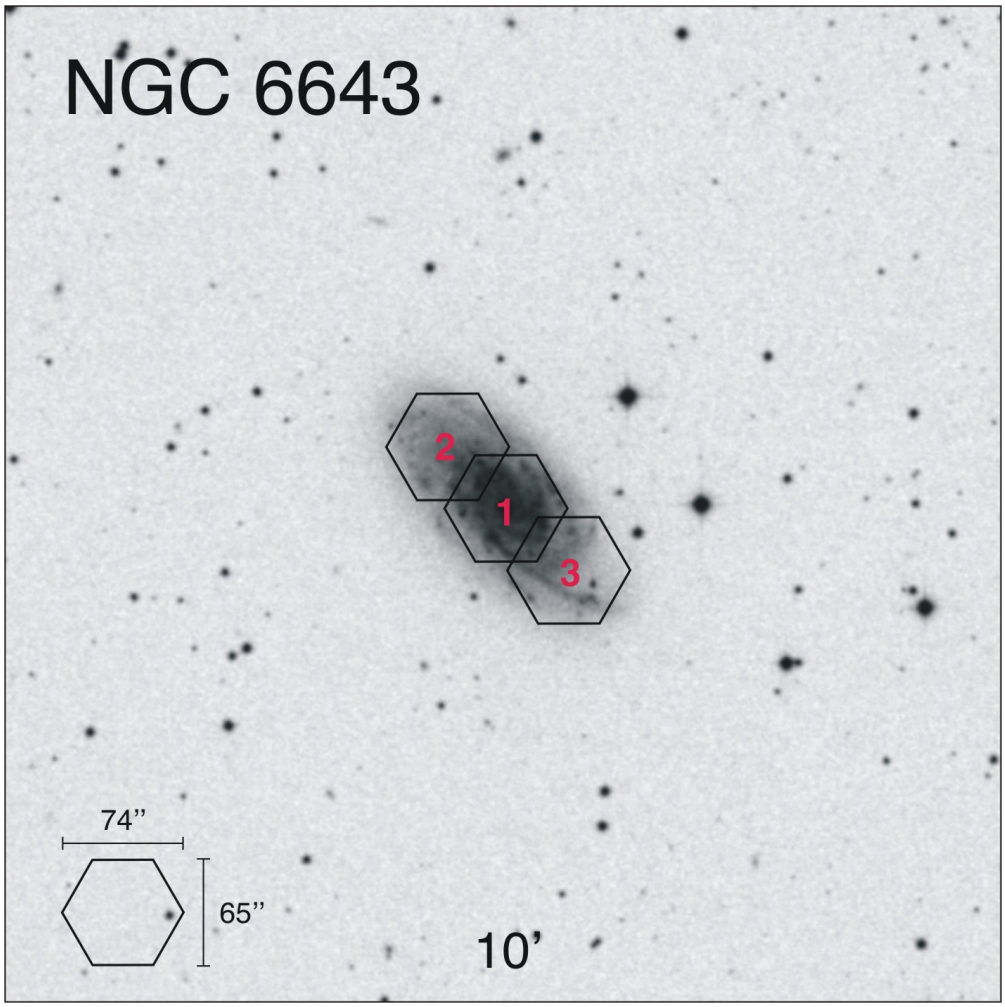

Figure 3.10: DSS image of NGC 6643 with overlaid PPAK pointings. The positions were observed accordingly to the log shown in Table 3.10. The image is 10’ × 10’ and it is displayed in the standard NE configuration.

NGC 6643

Position	Date	UT	airmass	A_V
1 dith 0	02 June 2008	00:52	1.27	0.16
dith 1	”	01:16	1.26	0.16
dith 2	”	01:43	1.26	0.18
2 dith 0	02 June 2008	02:16	1.26	0.18
dith 1	”	02:42	1.27	0.18
dith 2	”	03:07	1.28	0.18
3 dith 0	10 Aug 2008	23:11	1.31	0.20
dith 1	”	00:02	1.35	0.18*
dith 2	”	00:32	1.39	0.18

Table 3.11: Log of observation for all the PPAK moisaicking positions of NGC 6643. All positions in dithering mode. The (RA,Dec) offset for position 2 is (37,34) and for position 3 (–37,–34) in arcseconds from the mosaick centre reported in Table 3.1. Entries with the $\star$ flag as explained in Table 3.3.

3.4.10 NGC 6701

NGC 6701 is a small barred spiral in Draco with an angular size of 1.5×1.3 arcmin. Broad-band images and previous spectroscopic studies argue that the bar of NGC 6701 resembles a dust-lane morphology with a strong decrease of continuum luminosity and the detection of shocks in one of the two dust lanes (Marquez et al., 1996). The age of the bar is inferred to be less than 10^9 years (Martin & Roy, 1994). The prominent bar structure has a diamond-like aspect mainly traced by the two more intense sides. The spiral arms emerge from the bar, with the arm to the north being the more luminous one. The main spiral structure delineates a pseudo-outer ring when the arms close together. Although NGC 6701 had been considered to be an isolated galaxy, a close companion was found at 130 km s^{-1}and 73 kpc in projected distance. Hα images of NGC 6701 show some diffuse emission along the bar and in the spiral arm to the north (Martin & Roy, 1994). The maximum is reached at the galactic center, showing another bright knot just in the vertices of the diamond-like bar structure. Some other features in the south correspond to very recent star forming regions.

The observation for NGC 6701 was carried out on August 9th 2008 with one single pointing in dithering mode covering the optical radius of the galaxy (see Figure 3.11). The spectroscopic data for NGC 6701 contains 993 individual spectra.

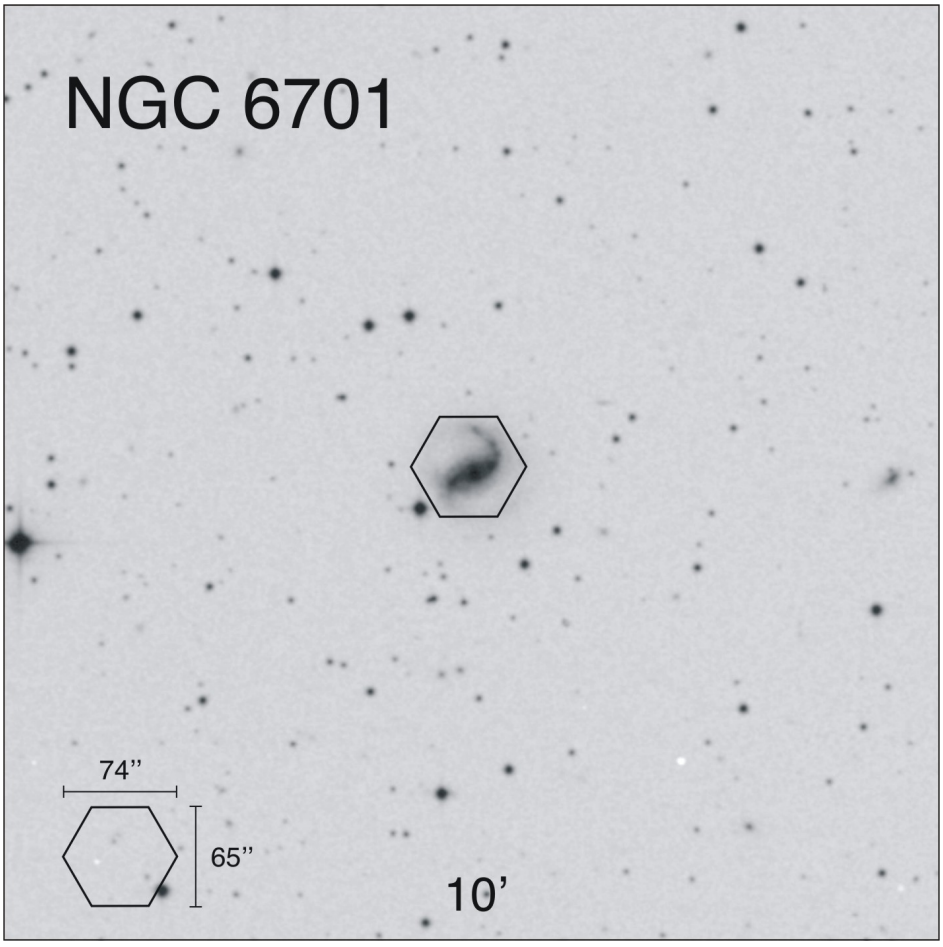

Figure 3.11: DSS image of NGC 6701 with overlaid PPAK pointings. The positions were observed accordingly to the log shown in Table 3.12. The image is 10’ $\times$ 10’ and it is displayed in the standard NE configuration.

3.4.11 NGC 7770 & NGC 7771

The main target for this mosaic was the galaxy NGC 7771, a very luminous, nearby, barred spiral in Pegasus with an optical *B*-band size of 2.5×1.0 arcmin. This galaxy is part of an interactive system containing mainly the face-on spiral NGC 7769 and the faint lenticular NGC 7770 (Nordgren et al., 1997). The optical morphology of NGC 7771 is strongly affected by heavy extinction and prominent dust lanes in the bar. Most of the luminosity of NGC 7771 arises from a massive circumnuclear starburst, which was probably triggered by the interaction with NGC 7770. Nuclear star formation in NGC 7771 is concentrated in an elliptical ring with a major axis of $\sim$ 7" (2 kpc), surrounding the starburst nucleus. This ring is clumpy and contains several emission regions both in radio and in the near-infrared continuum (Smith et al., 1999, and references therein).

Due to the projected size of this galaxy, the mosaic pattern was constructed with three IFU positions. The central position of the mosaic has an offset of (–15, –15) arcsec in (RA, Dec) from the geometrical centre of galaxy (see Figure 3.12). Two more positions were observed with offsets of (37, 33) and (–37, –33) arcsec in north-east and south-west directions respectively. NGC 7770, a small S0 galaxy with an optical size 0.8×0.7 arcmin was observed within the field of the mosaic for NGC 7771. Observations of all 3 positions were performed on October 30th 2008. The spectroscopic data for this galaxy contains 993 individual spectra.

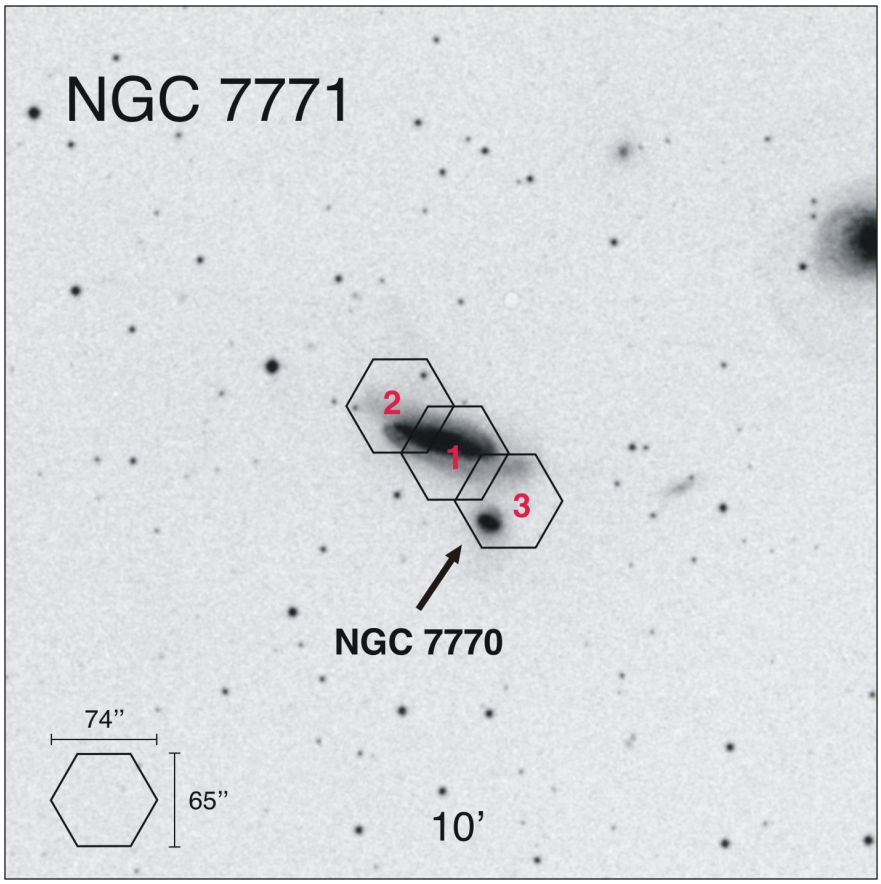

Figure 3.12: DSS image of NGC 7771 with overlaid PPAK pointings. The positions were observed accordingly to the log shown in Table 3.13. The image is 10' $\times$ 10' and it is displayed in the standard NE configuration.

NGC 6701

Position	Date	UT	airmass	A_V
1 dith 0	09 Aug 2008	01:36	1.38	0.15
dith 1	”	02:01	1.45	0.18
dith 2	”	02:36	1.58	0.18*

Table 3.12: Log of observation for all the PPAK moisaicking positions of NGC 6701. Position observed in dithering mode. Entries with the $\star$ flag as explained in Table 3.3.

NGC 7770 & NGC 7771

Position	Date	UT	airmass	A_V
1	30 Oct 2008	18:59	1.23	0.18*
2	”	19:24	1.17	0.18*
3	”	19:54	1.11	0.18*

Table 3.13: Log of observations for all the PPAK moisaicking positions of NGC 7771. The central position shows an offset of (–10.5,–10.5) arcsecs with respect to the coordinates of NGC 7771 shown in Table 3.1. The offsets from this position are (37,33) arcsecs for position 2 and (–37,–33) for position 3 in (RA,Dec). Entries with the $\star$ flag as explained in Table 3.3.

3.4.12 Stephan's Quintet

Stephan's Quintet, is a visual grouping of five galaxies (NGC 7317, 7318A, 7318B, 7319 and 7320) in Pegasus. The group was discovered by Édouard Stephan in 1877 at Marseilles Observatory. The group is the most studied of all the compact galaxy groups. The brightest member, NGC 7320 exhibits smaller redshift than the other members, being therefore a foreground object that happens to lie along the line of sight to the more distant galaxies (see Figure 3.13). Although some controversy prevailed (Balkowski et al., 1974; Kent, 1981), recent observations by HST show that individual stars, clusters, and nebulae are clearly seen in NGC 7320 and not in any of the other galaxies (Gallagher et al., 2001). NGC 7320 shows also extensive H II regions, identified as red blobs, where active star formation is occurring. HST observations showed also that near to the nucleus of NGC 7319 a quasar shines brightly. There is very little absorption of its light due to the effect of the gas and dust of NGC 7319. Therefore the association of this quasar to NGC 7319 is puzzling Galianni et al. (2005). These galaxies are of interest because of their violent collisions. Four of the five galaxies in Stephan's Quintet are on collision courses with one another. Recent studies revealed the presence of a huge intergalactic shock wave (Appleton et al., 2006). The molecular hydrogen seen in this grouping is one of the most turbulent formations of molecular hydrogen known.

Four individual pointings were observed on August 10th 2008, three of which were centered at the bright bulges of NGC 7317, 7319 and 7320, while the last pointing was centered in a configuration to cover NGC 7318A and NGC 7318B (see Figure 3.13). The spectroscopic data for all pointings of the Stephan's Quintet contains 1324 individual spectra.

STEPHAN'S QUINTET

	Position	Date	UT	airmass	A_V
1	NGC 7318	10 Aug 2008	01:12	1.00	0.18
2	NGC 7319	”	01:54	1.01	0.18*
3	NGC 7320	”	02:32	1.03	0.18*
4	NGC 7317	”	03:14	1.08	0.16

Table 3.14: Log of observations for all the PPAK moisaicking positions of the Stephan's Quintet. Entries with the $\star$ flag as explained in Table 3.3.

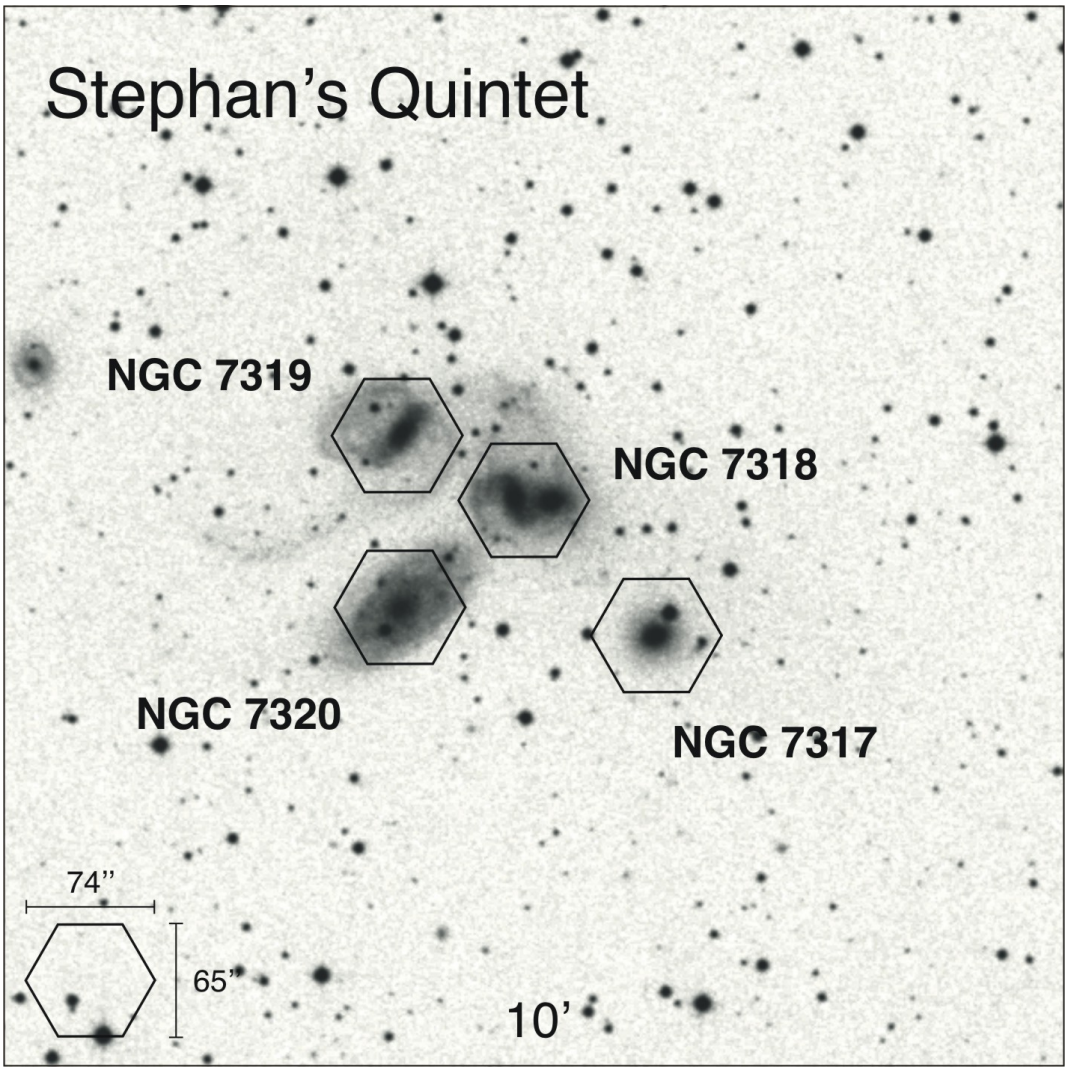

Figure 3.13: DSS image of the Stephan's Quintet with overlaid PPAK pointings. The positions were observed accordingly to the log shown in Table 3.14. The image is 10' $\times$ 10' and it is displayed in the standard NE configuration.

3.5 Summary

The observations of the PINGS project were carefully planned in terms of the science goals, the amount of observing time, the target sample and logistics. The PINGS sample was selected to find a trade off between the size of the galaxies, their morphological type, their physical properties and the practical limitations imposed by the instrument and the amount of observing time. We built a comprehensive sample of galaxies with a good range of galactic properties and available multi-wavelength ancillary data, in order to maximise both the original science goals of this dissertation and the possible archival value of the survey.

The 2D spectroscopic mosaicing technique proved to be feasible. The spectroscopic data accounts for more than 50,000 spectra in the optical wavelength range. As a highlight of the observations, the mosaicing of the largest galaxy in the sample: NGC 628, represents the widest field ever covered by an integral field unit up-to-date. All observations were fully reduced and wavelength/flux calibrated, all the reduction steps and calibration details are explained in the following chapter.

SUMMARY OF OBSERVATIONS OF THE PINGS SAMPLE

Object	Positions	Mosaic	Spectra	Notes
(1)	(2)	(3)	(4)	(5)
NGC 628	34/37	92%	13571	*a*
NGC 1058	9	complete	7944	$\star$,*b*
NGC 1637	7	complete	6951	$\star$
NGC 2976	2/9	20%	662	
NGC 3184	16/19	84%	5296	
NGC 3310	3	complete	2979	$\star$
NGC 4625	1/7	14%	993	$\star$
NGC 5474	6/7	86%	5958	$\star$
NGC 6643	3	complete	2979	$\star$
NGC 6701	1	complete	993	$\star$
NGC 7771	3	complete	993	*c*
Stephan's Quintet	4	complete	1324	*d*

Table 3.15: Summary of observations of the PINGS sample. Col. (1): Galaxy name. Col. (2): Number of individual IFU positions observed for the mosaic of each galaxy. Col. (3): Status of the mosaicking, either in the area percentage or showing the complete mosaics. Col. (4): Total number of spectra for each mosaic. Col. (5): Comments: a) Biggest area ever covered by a IFU mosaicking; b) One position is not in dithering mode, as was performed as a blind offset; c) NGC 7770 in the field. d) NGC 7318A and NGC 7318B in one field.
*All pointings in dithering mode.

Notes

[1] The Calar Alto Extinction monitor CAVEX is an instrument that estimates the monochromatic extinction in the V band continuously along each night. By tracking the location of 15 – 20 stars in a given field of view, it estimates the extinction by measuring their apparent magnitude across a range of 1.1 – 2.4 airmasses every ~ 2 minutes if the night is clear. When the night is cloudy or the extinction has strong fluctuations the instrument does not produce reliable data, flagging it.

[2] The Digitized Sky Survey was produced at the Space Telescope Science Institute under U.S. Government grant NAG W-2166. The images of these surveys are based on photographic data obtained using the Oschin Schmidt Telescope on Palomar Mountain and the UK Schmidt Telescope. The plates were processed into the present compressed digital form with the permission of these institutions.

4

Data reduction, errors and uncertainties

The reduction of IFS observations possesses an intrinsic complexity given the nature of the data and the vast amount of information recorded in a single observation. This complexity is increased if one considers creating an IFU spectroscopic mosaic of a given object for which the observations were performed not only on different nights, but even in different years, with dissimilar atmospheric conditions, and slightly differing instrument configurations. In this chapter I describe the IFS data reduction process for all the observations of the PINGS sample. The reduction process followed the standard steps for fibre-based integral field spectroscopy, already described in detailed in the literature (e.g. Sánchez 2006, hereafter San06). However, the construction of the mosaics out of the individual pointings requires further and more complex reduction steps than for a single, standard IFU observation. These extra steps arise due to the special mosaicing pattern for some of the objects, the differences in the atmospheric transparence and extinction, slight geometrical misalignments, sky-level variations, differential atmospheric refraction, etc. A considerable amount of time was invested in understanding, applying and improving each of the individual reduction steps. New analysis tools and reduction software were developed during this process which contributed to improve the standard pipeline for this kind of IFS data.

Furthermore, I discuss the possible sources of errors and uncertainties that were identified during the data reduction and the basic analysis of the PINGS data set, and the techniques implemented in order to minimise them. All the identified sources of error contribute in a different degree and extent to the overall error budget associated with the observations. Finally, the reduced and calibrated PINGS data set is presented, with some examples of data products extracted from the IFS mosaics.

4.1 Data reduction

All the IFS data reduction steps can be summarised as follows, in sequential order:

a) Pre-reduction.

b) Identification of the location of the spectra on the detector.

c) Extraction of each individual spectrum.

d) Distortion correction of the extracted spectra.

e) Determination of the wavelength solution.

f) Fibre-to-fibre transmission correction.

g) Flux calibration.

h) Allocation of the spectra to the sky position.

i) Cube and/or dithered reconstruction (if any).

j) Additional corrections/calibrations (e.g. DAR, spectrophotometric re-calibration)

Data reduction was performed using a combination of existing software packages specially designed for fibre-fed and IFS data: R3D (San06), E3D (Sánchez, 2004), (written in `perl` and `C` data languages), standard IRAF[1] routines, and custom-built codes written in `perl`, `Shell` and `IDL` data languages, conceived as independent command-line routines which could be merged in order to create general pipelines and scripts so to diminish the number of steps needed during the reduction, and to ensure the homogeneity and repeatability of any reduction step.

4.1.1 Pre-reduction

The pre-reduction of the IFS data consists of all the corrections applied to the CCD that are common to the reduction of any CCD-based data, these comprise:

1. The creation of a master bias.
2. Application of the master bias: Bias subtraction.
3. Application of a master CCD flat: Flat-Fielding.
4. Combination of different exposures on the same pointing.
5. Cosmic ray rejection (if not performed by the previous step).

The pre-reduction processing was performed using standard IRAF packages for CCD pre-reduction steps in combination with the R3D reduction package and the E3D visualization software. A master bias was created using a combination of several bias frames acquired during each observing night, this was subtracted from all raw images. The Flat-Fielding correction was then applied using a master CCD flat provided by the Calar Alto observatory, created using long exposures of scattered light, (in PMAS it is not possible to illuminate the spectrograph CCD without passing through the fibers and the spectrograph). The flat reflect the pixel-to-pixel variation on the CCD and the defect of the CCD itself. For most of the field, the variation ranges between $\pm 1\%$ of the average. Next, different exposures of the same pointing were combined.

[1] IRAF is distributed by the National Optical Astronomy Observatories, which are operated by the Association of Universities for Research in Astronomy, Inc., under cooperative agreement with the National Science Foundation.

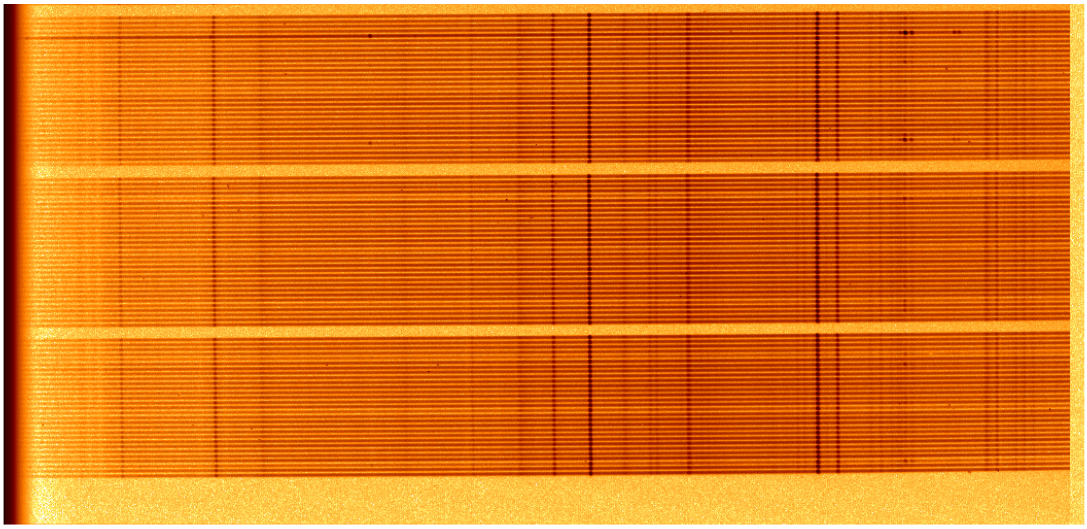

Figure 4.1: View of a section of a PINGS raw data. Each horizontal dark line corresponds to a projection of a spectrum along the dispersion axis. Note the misalignment of the spectra with respect to the CCD frame.

This step also performs the cosmic ray rejection. In the case of the standard stars or individual sky exposures where only one frame was available, the cosmic ray rejection was performed using the `L.A.Cosmic` algorithm after van Dokkum (2001).

4.1.2 Spectra identification

The raw data extracted from a PINGS observation consists of a collection of spectra, stored as 2D frames, aligned along the dispersion axis. As seen in Figure 4.1, the spectra are separated by a certain width, following a characteristic profile which is nearly Gaussian. On a raw data frame, each spectrum is spread over a certain number of pixels along the cross-dispersion axis. The spectra are generally not perfectly aligned along the dispersion axis due to the configuration of the instrument, the optical distortions, the instrument focus and the mechanical flexures. Therefore, the first step of the IFS reduction is to find the location of each spectrum at each wavelength along the CCD and to extract its corresponding flux. This is done by using continuum illuminated exposures taken at each pointing corresponding to a different orientation of the telescope. At any given column on the CCD, the location of the spectra is found by comparing the intensity at each row along the column with those of n adjacent pixels. Then, the location of the peak intensities corresponding to each spectrum in the CCD along the dispersion axis (i.e. the *trace*) is found by looking for maximum values around each original location within a given window. To ensure a continuous behaviour, a low-order polynomial function was fit to the resulting trace.

4.1.3 Spectra extraction and the cross-talk problem

One of the critical reduction steps is to extract the flux corresponding to different spectra at each pixel along the dispersion axis. This is usually performed by co-adding the flux within a certain aperture around the *trace* of the spectra in the science frames. For PMAS/PPAK data, a typical aperture extraction can be performed by co-adding the flux within an aperture of ~ 5 pixels assuming a cut across the cross-dispersion axis. However, this method is not optimal due to the contamination produced by flux coming from the adjacent spectra, i.e. the *cross-talk* problem.

This contamination effect may produce a wrong interpretation of the data. For observations performed with PPAK, and due to the geometrical construction of the instrument, the adjacent spectra on the plane of the CCD may not correspond to nearby locations in the sky plane (Kelz et al., 2006). Furthermore, the position of the calibration fibres (which are located in between the science ones along the pseudo-slit) also contributes to overall contamination. Therefore, the cross-talk effect would potentially mix up spectra from locations that may not be physically related (because of the spectra position on the CCD) or from spectra with completely different nature (i.e. calibration fibres). Given that the cross-talk is an incoherent contamination it is preferable to keep it as low as possible, an average value of $\sim 1\%$ with a maximum of $\sim 10\%$ (San06, and references therein) seems technically as a good trade-off.

Given the limited size of CCDs and the need to record as many spectra as possible within that reduced area, IFS observations will always face a certain level of cross-talk. The FWHM of the projected profile along the cross-dispersion axis is normally defined by the design of the spectrograph and the size of the input fibres, placing a limit in the selected aperture. The PPAK spectra profiles have a FWHM of the order of ~ 2.3 pixels, and Δ peaks of ~ 5 pixels in the 2×2 binning mode (as was the case for all PINGS observations). Selecting an aperture size of the order of Δ peaks seems to be an acceptable compromise between maximising the recovered flux and minimising the cross-talk. Several methods have been implemented to minimise the effect of cross-talk, in particular, San06 developed an efficient technique named *Gaussian-suppression* that reduces the effects of the cross-talk and maximises the recovered flux to within 10% of the original values for any spaxel at any wavelength. However, for certain raw frames which were too crowded or when there were bright sources targeted within the field (e.g. foreground stars, galaxy bulges), some level of contamination was still found that could not be considered negligible.

As part of the meticulous reduction for the PINGS observations, the *Gaussian-suppression* technique was improved to a new method which increases the signal-to-noise ratio of the extracted spectra and reduces the effect of the cross-talk compared to previous extractions. The new technique assumes a Gaussian profile for the projection of each fibre spectrum along the cross-dispersion axis. It performs a Gaussian fitting to each of the fibres after subtracting the contribution of the adjacent ones in an iterative process. First, it performs a simple aperture extraction, using a 5 pixels aperture. This initial guess of the flux corresponding to each spectrum is then used to model the profiles with a Gaussian function, adopting as a centroid the location of the peak intensity described before, and as width the average one of all the fibers profiles ($\sigma \sim 2$ pixels). In the first iteration, the extracted flux is used as the integrated flux of a Gaussian function. This modelled profile is then used, for each spectrum, to remove the contribution of the four adjacent ones. The resulting clean profile is then fitted with a Gaussian function, with the centroid and width parameters fixed, in order to derive a better estimation of the integrated flux. This new flux is stored and used as a new input for the next iteration of the process. The procedure converges in general after three iterations, increasing the signal-to-noise ratio of the extracted spectra and reducing the effect of the cross-talk.

Several tests using simulated and real spectra with a broad range of intensities were performed in order to assess the level of contamination that the extracted spectra show due to the cross-talk. The new method was tested varying the relative intensity of the spectra in the central and adjacent fibres, the pixel extraction apertures and the average width of the Gaussian profiles. It was found that, in the extreme cases (very bright adjacent fibres), the cross-talk was suppressed by 95%, being almost negligible for the range of spectral intensities compared to the instrumental misalignments and distortions found during conventional observations of the PINGS sample (see Figure 4.2).

At this step, the reduced IFS data can be stored using different data formats, all of which should allow

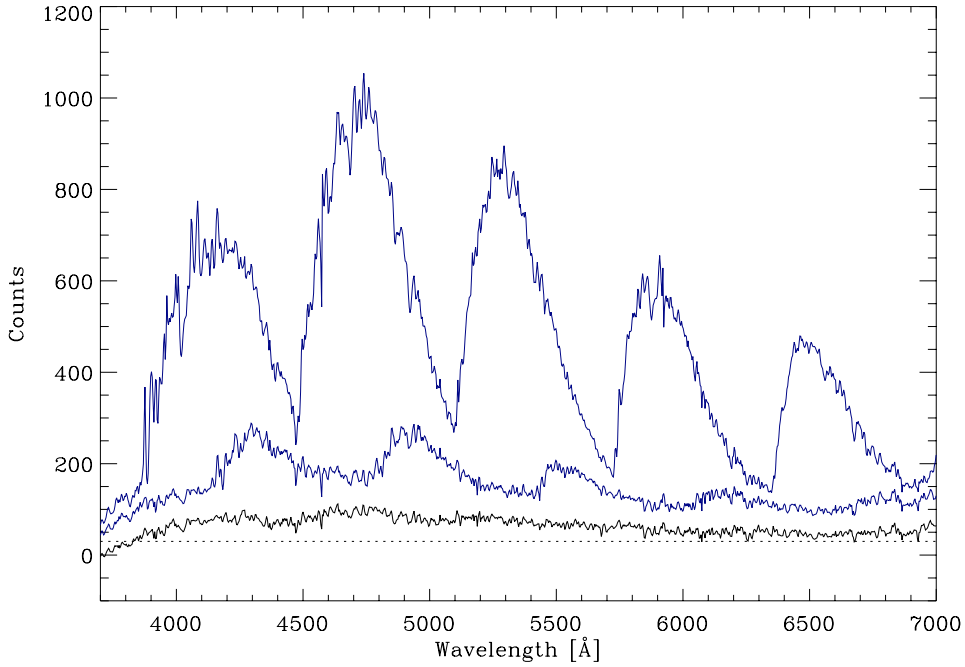

Figure 4.2: Example of a strong cross-talk effect in a fibre adjacent to a very bright source, in this case a standard star with a maximum of 40000 counts. The top spectrum shows the full cross-talk effect when no correction is applied. The middle spectrum shows a first-order correction obtained by minimising the pixel extraction aperture (but losing flux in the process). The bottom spectrum shows the correction of the cross-talk by the improved *Gaussian-suppression* method with an extracted spectrum of the same order of intensity as the average background signal (dotted line) found in the nearby fibres for this particular observation. The apparent periodicity of the cross-talk with respect to the wavelength is just an effect of the spectra misalignments and distortions on the CCD.

to store the spectral information in association with the 2D position on the sky. Two data formats are widely used in the IFS community: datacubes (3-dimensional images) and Row-Staked-Spectra (RSS) files. Datacubes are only valid to store reduced data from instruments that sample the sky-plane in a regular-grid or for interpolated data. In this case the data are stored in a 3-dimensional FITS image, with two spatial dimensions and one corresponding to the dispersion axis. RSS format is a 2D FITS image where the *X* and *Y* axes contain the spectral and spatial information respectively, regardless of their position in the sky. This format requires an additional file (either a FITS or ASCII table), where the position of the different spatial elements on the sky is stored. RSS is widely used by IFUs with a discontinuous sampling of the sky, as it is the case for PPAK. The final reduced PINGS data are stored in the RSS format, with their corresponding position tables.

4.1.4 Distortion correction

Most grating spectrographs do not disperse the light homogeneously along the cross-dispersion axis, the dispersion is distorted, being larger in the edges of the slit than in the centre. This is the so-called C distortion. When the spectrographs are fed with fibres, additional distortions are produced due to the placing of the fibers in the pseudo-slit. The left panel of Figure 4.3 shows an example of extracted spectra where the curvature and distortions are clearly seen. These distortions must be corrected fiber-to-fiber before finding a common wavelength solution.

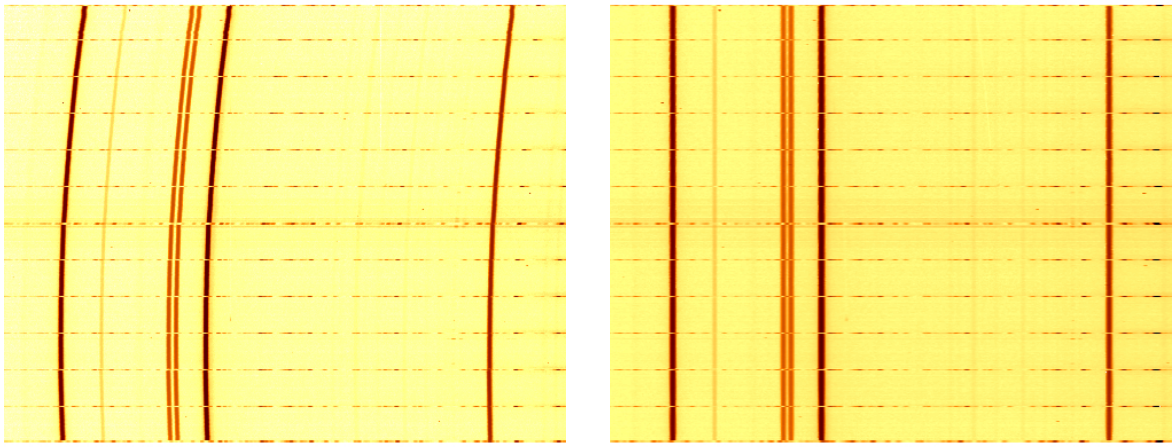

Figure 4.3: Example of extracted spectra from an arc exposure. The left panel shows the frame before the distortion correction, the right panel shows the same frame after wavelength calibration.

The correction is performed by using HeHgCd+ThAr arc lamp exposures obtained at each observed position through the instrument calibration fibres. The peak intensity of a single emission line is traced along the cross-dispersion axis, and then shifted to a common reference by a linear shift. This represents a first order distortion correction. Subsequently, the intensity peak of a set of selected emission lines is traced, and a polynomial distortion correction is determined to recenter all the lines to a common reference. PMAS is a well-behaved instrument in terms of distortion and therefore, just a low-order polynomial function is needed. The second-order distortion correction maps can then be applied to the science exposures. The right panel of Figure 4.3 shows the distortion corrected spectra after applying this technique. A one dimensional spline interpolation algorithm is applied spectrum-to-spectrum in this process.

4.1.5 Wavelength solution

The wavelength solution is determined by identifying the wavelengths of the emission lines in the arc lamps exposures described above. The distortion corrected spectra of the arcs are then transformed to a linear wavelength coordinate system by a one dimensional spline interpolation, assuming a polynomial transformation between both coordinate systems. The required transformation is stored in an ASCII file to be applied over the science data as a first-order wavelength solution. A second-order dispersion correction was applied to the science frames using as a reference the bright sky emission lines present in the observed frames, following the prescription described above. It was found that this second-order correction is important when the altitude of the telescope varies during the observation of a particular target, especially when the telescope moves through the culmination. Without this second order correction, a shift in the dispersion axis is evident when combining different exposures of the same pointing.

The accuracy of the final wavelength solution depends on the selected order of the polynomial function, the number of identified lines, and the coverage of emission lines along the wavelength range. For the instrumental set-up used in the PINGS observations, 6 emission lines and a polynomial function of order 4 are necessary to produce a good dispersion solution (*rms* of the fit ~ 0.2 Å).

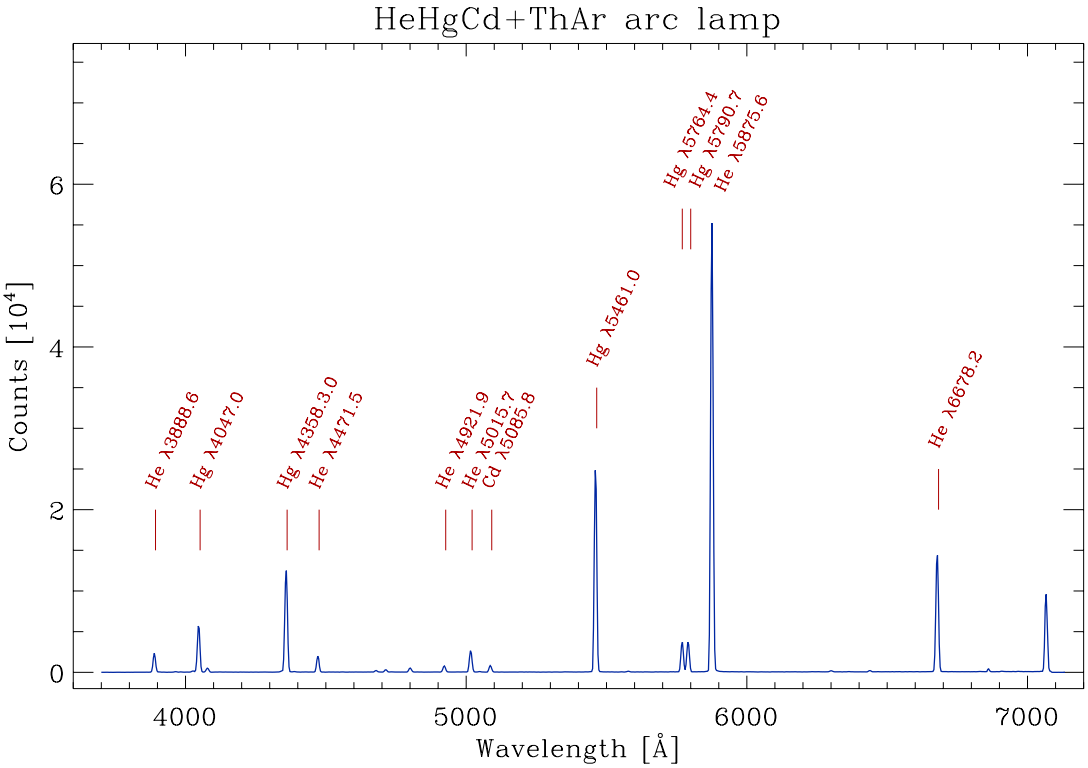

Figure 4.4: Example of a HeHgCd+ThAr arc lamp calibration exposure used to obtain the distortion and dispersion solutions. The most important emission lines are labeled.

4.1.6 Fibre-to-fibre transmission correction

For most IFUs, the transmission varies considerably from fibre-to-fibre. We also have to consider that the optical path through the spectrograph has an impact on the final sensitivity. In order to correct these effects, an exposure of a continuum, well-illuminated, and flat source is required, like a skyflat. Differences in the fibre-to-fibre transmission throughput were corrected by creating a master fibreflat from twilight skyflat exposures taken in every run. The skyflat exposures were reduced following the same procedure as a science frame. Then, a median spectrum is obtained using all the spectra in the frame. Each spectrum is then divided by this median one, obtaining a fibreflat frame. The fibreflat exposures were used to normalize the response of each fibre over the entire wavelength range, assuming that the light input to each fibre is uniform.

4.1.7 Sky subtraction

One of the most difficult steps in the data reduction is the correct subtraction of the night sky emission spectrum. Once the spectra are extracted, corrected for distortions, wavelength calibrated, and corrected for differences in transmission fibre-to-fibre, they must be sky-subtracted and flux-calibrated. The emission from the Earth's atmosphere contributes significantly to the detected signal. The sky emission lines can be easily identified in the RSS frames as bright vertical lines.

In long-slit spectroscopy the sky is sampled in different regions of the slit and a median sky spectrum is obtained by spectral averaging or interpolation. This is possible due to the size of the long-slit compared with the size of the astronomical objects of interest. However, in IFS the techniques vary depending on the geometry of the observed object and on the variation of the sky level for a given observation. As mentioned

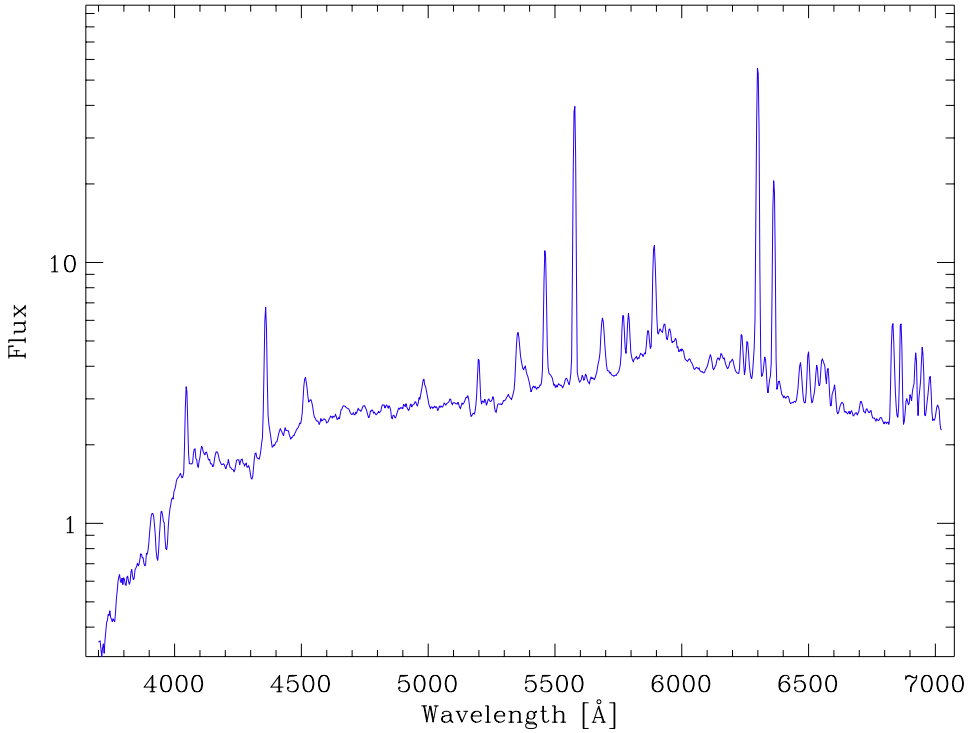

Figure 4.5: Typical night sky-emission spectrum at the Calar Alto observatory. The flux units are: 10^{-14} erg s^{-1} cm^{-2} Å^{-1}. The three more prominent lines correspond to [O I] λ5577, λ6300 and λ6364. In addition, the broad-emission band of Na I centered at $\sim$ 5900 Å is clearly identified.

in chapter 2, PPAK includes additional fibres that sample the sky emission during a given observation. When the target does not fill entirely the FOV of the instrument, these fibres can be used to obtain a reliable sky subtraction by extracting the spectra of the 36 sky fibres, creating a median sky spectrum and then subtracting it from the science exposures. However, caution must be taken as some of the sky-fibres can actually sample nearby objects that could contaminate and alter the resultant median sky-spectrum, e.g. bright foreground stars or H II regions. An individual inspection of all the sky fibres is therefore necessary, in some cases the emission from foreground or background objects can only be identified after a median sky-spectrum is subtracted. If fibres with additional emission other than the sky are found, these should be discarded when obtaining a more refined sky-spectrum.

In order to increase the accuracy of the sky subtraction, a couple of techniques can be applied. The first one determines the sky spectra corresponding to any science fibre by an interpolation of the spectra obtained through the sky lines, this technique takes into account the distortion in the wavelength solution along the cross-dispersion axis. A second method creates a sky spectrum by deriving the median between a certain number of adjacent spectra, clipping those ones with a flux over a certain threshold of the standard deviation. The differences between the two methods in most cases are less than 3%. The application of the method depends on the variation of the transmission during the night or during a specific observation, the position of the pointing with respect to the mosaic (see below), and the brightness of the sky emission. Both results create a better representation of the sky than the simple method, with a lower level of sky residuals.

By construction, many of the positions of the PINGS mosaics (especially those in the galaxy centre) would fill the entire FOV of the IFU, and none of the spaxels (including the sky-fibres) would be completely free of galaxy “contamination”. In this case, we obtained supplementary sky exposures (immediately after

STANDARD STARS

Date	Name	UT	airmass	A_V	t_{exp}
28 Oct 2006	BD+28D4211	22:01	1.18	0.25	100
07 Dec 2007	BD+25d4655	18:47	1.09	0.15⋆	30
	G191B2B	02:21	1.13	0.30	90
08 Dec 2007	BD+25d4655	17:56	1.04	0.14	10
	Feige 34	06:13	1.01	0.17	30
09 Dec 2007	BD+25d4655	17:51	1.04	0.15⋆	20
	HZ 44	03:43	2.96	0.11	120
	Feige 34	05:54	1.01	0.11	30
10 Dec 2007	BD+25d4655	17:56	1.05	0.11	20
	HZ 44	01:15	1.36	0.12	150
11 Dec 2007	BD+28D4211	17:58	1.05	0.15	30
	G191B2B	23:36	1.04	0.15	120
12 Dec 2007	BD+28D4211	18:05	1.06	0.18⋆	60
	G191B2B	23:55	1.04	0.15	120
14 Apr 2008	BD+33d2642	04:33	1.11	0.16	60
	Feige 34	20:11	1.03	0.32	300
02 Jun 2008	HZ 4	20:13	1.01	0.20⋆	120
09 Aug 2008	BD+28D4211	01:10	1.01	0.20⋆	120
10 Aug 2008	BD+28D4211	01:04	1.01	0.18	120
30 Oct 2008	BD+25d4655	17:58	1.08	0.18⋆	30
	G191B2B	02:57	1.04	0.15	90

Table 4.1: Log of observations for standard stars. Entries with the ⋆ flag as explained in Table 3.3.

the science frames) applying large offsets from the observed positions and between different exposures, we then used these "sky-frames" to perform a direct sky subtraction of the reduced spectra using a sky-spectrum obtained following the techniques described above. On the other hand, if the FOV is not entirely filled by the object, it is possible to select those sky-fibres with spectra free of contamination from the observed and foreground/background objects, average them and subtract the resulting sky-spectrum from the science spectra. This technique was used for observations in the last ring of a mosaic or at the edges of the optical surface of the galaxies, where the sky-fibres bundles did actually sample the sky emission.

4.1.8 Flux calibration

Once the sky emission has been subtracted, we need to flux calibrate the observed frames. Absolute spectrophotometry with fibre-fed spectrographs is rather complex; as in slit-spectroscopy, where slit losses impose severe limitations, IFU spectrographs can suffer important light losses due to the geometry of the fibre-arrays.

The flux calibration requires the observation of at least one spectrophotometric standard star during each of the observing nights. A total of six standard stars from the Oke spectrophotometric candles (Oke, 1990) were observed for the purpose of flux calibration during the observing runs. Table 4.1 list the stars name,

date of observation, time of exposure, airmass and the local optical extinction A_V. A star is a point source on the sky, but the image on the detector has characteristic PSF due to the turbulence in the atmosphere the effect of the telescope's optics. Given that the PPAK IFU bundle does not cover the entire FOV due to gaps among the fibres, the observation of calibration standard stars is prone to flux losses, especially when the standards are not well centered in a single IFU spaxel. However, I developed a method which takes into account the flux losses due to the gaps in the fibre-bundle, the pointing misalignments and PSF of the observed standard stars, as well as corrections for minor cross-talk effects, airmass, local optical extinction and additional information provided by broad and narrow-band imaging photometry in order to obtain the most accurate possible spectrophotometric flux-calibration within the limits imposed by the instrumentation.

A standard star frame is reduced following the standard procedure described previously. The sky subtraction is performed by using either a mean sky-spectrum obtained from the sky-fibres or by selecting spaxels in clean regions in the main IFU bundle, e.g. by selecting the external rings of the PPAK FOV.

In order to obtain a calibration sensitivity function from the standard star, a 1D spectrum has to be extracted from the standard frame. Given the relative large size of the PPAK fibres, it is customary to extract the 1D spectrum from the fibre with the higher flux, assuming that the star is well centered in this single fibre and that the size of the fibre is larger than the PSF of the star. However, during the reduction of the PINGS observations I found that in most cases these assumptions are not correct. The amount of light that ends up outside the central fibre depends on several factors: the seeing at the moment of the observation, which determines the PSF of the star on the instrument, and most important if during the observation the standard star was well centred onto the central fibre or there was a small shift and the light falls in between several fibres.

Figure 4.6 illustrate these effects, the figure corresponds to the standard star BD+25d4655 observed in two different nights with different atmospheric conditions. On the top panel, the figure contains 37 spectra corresponding to the brightest fibre and 36 fibres found in three concentric rings. Most of the flux falls in two or three fibres, very small residuals are seen in the rest of the fibres, but the contribution of them are not completely negligible. Furthermore, the amount of flux in the 2-3 brightest fibres is comparable, which shows that if we only take the central fibre we would lose a considerable amount of the flux from the star. The bottom panel shows the integrated flux of the standard star considering all 37 fibres. The bottom panel of Figure 4.6 shows the example of the same star observed during turbulent atmospheric conditions and when the star was not well centred in the fibre bundle. In this case, the flux is spread over a large number of concentric fibres, the individual contribution of the 15 or so closest fibres to the central one is important, up to 50-70% of the total flux of the star would be lost if we would only consider the central fibre.

To counteract the loss of flux, the observed spectrum of a standard star was obtained by adding up the spectra from consecutive concentric spaxel rings centered on the fibre where most of the standard's flux is found, until a convergence limit was found. In all cases, three consecutive rings accounting for 37 fibres would suffice in order to recover most of the flux. Figure 4.7 shows a diagram of the PPAK bundle corresponding the bottom panel of Figure 4.6. The standard star falls between the gaps of the fibres and most of the flux is spread among the three closest fibres, as shown in the top-left panel of Figure 4.7. The rest of the panels show how the selection of fibres is performed by adding up concentric rings centered in the brightest fibre.

A night sensitivity curve as a function of wavelength was obtained for each night by comparing the observed flux with the calibrated spectrophotometric standard spectrum considering the filling factor of the fibre-bundle, the airmass of the observed star, and the local optical extinction. The total extinction in

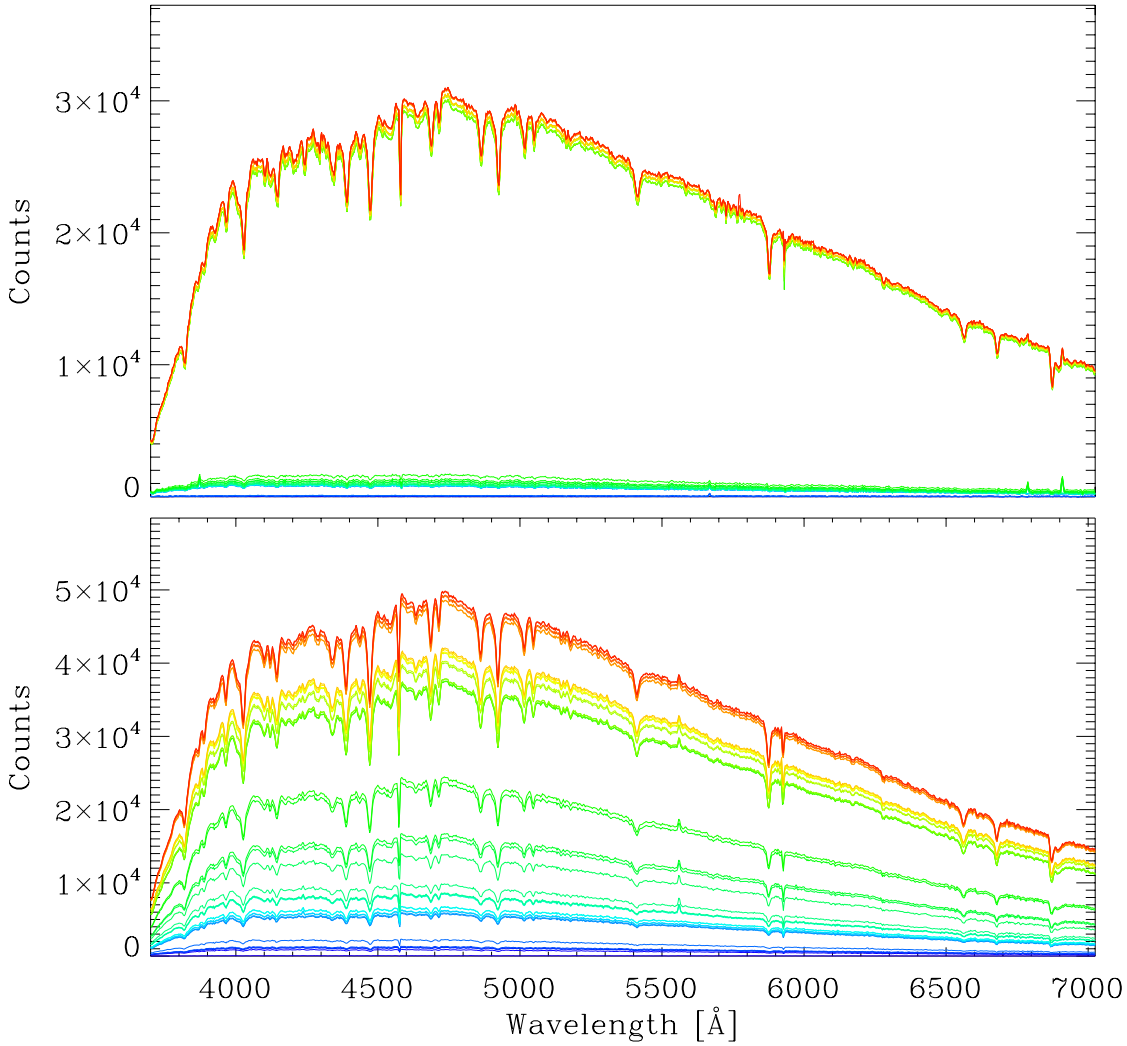

Figure 4.6: Effect of standard star flux loss due to bad seeing and misalignments. On the top panel, the standard star BD+25d4655 was observed during good atmospheric conditions and was well centred on the central fibre of the PPAK bundle. The bottom panel shows the spectra of the same star observed during turbulent atmospheric conditions and when the star was not well centred in the fibre bundle.

Calar Alto observatory has three main contributors: the Rayleigh scattering at the atmospheric atoms and molecules, the extinction due to aerosol particles (mostly dust), and the extinction due to ozone (Sánchez et al., 2007, hereafter San07). According to San07, the ozone absorption has a marginal effect on the total extinction at any wavelength, and the Rayleigh scattering is nearly constant along the year. Therefore, the variations on the extinction are controlled by amount of aerosol particles. Considering that the extinction in the V-band is due to a fix contribution or Rayleigh scattering and a variable contribution due to aerosol extinction, the total extinction can be expressed as:

$$\kappa_\lambda \sim 0.0935 \left(\frac{\lambda}{5450}\right)^{-4} + (0.8\kappa_V - 0.0935)\left(\frac{\lambda}{5450}\right)^{-0.8}, \tag{4.1}$$

which depends on a single parameter, the V-band extinction. This quantity is measured by the Calar Alto Extinction monitor (CAVEX) along the night in a fully automated way. The value of κ_V for a given obser-

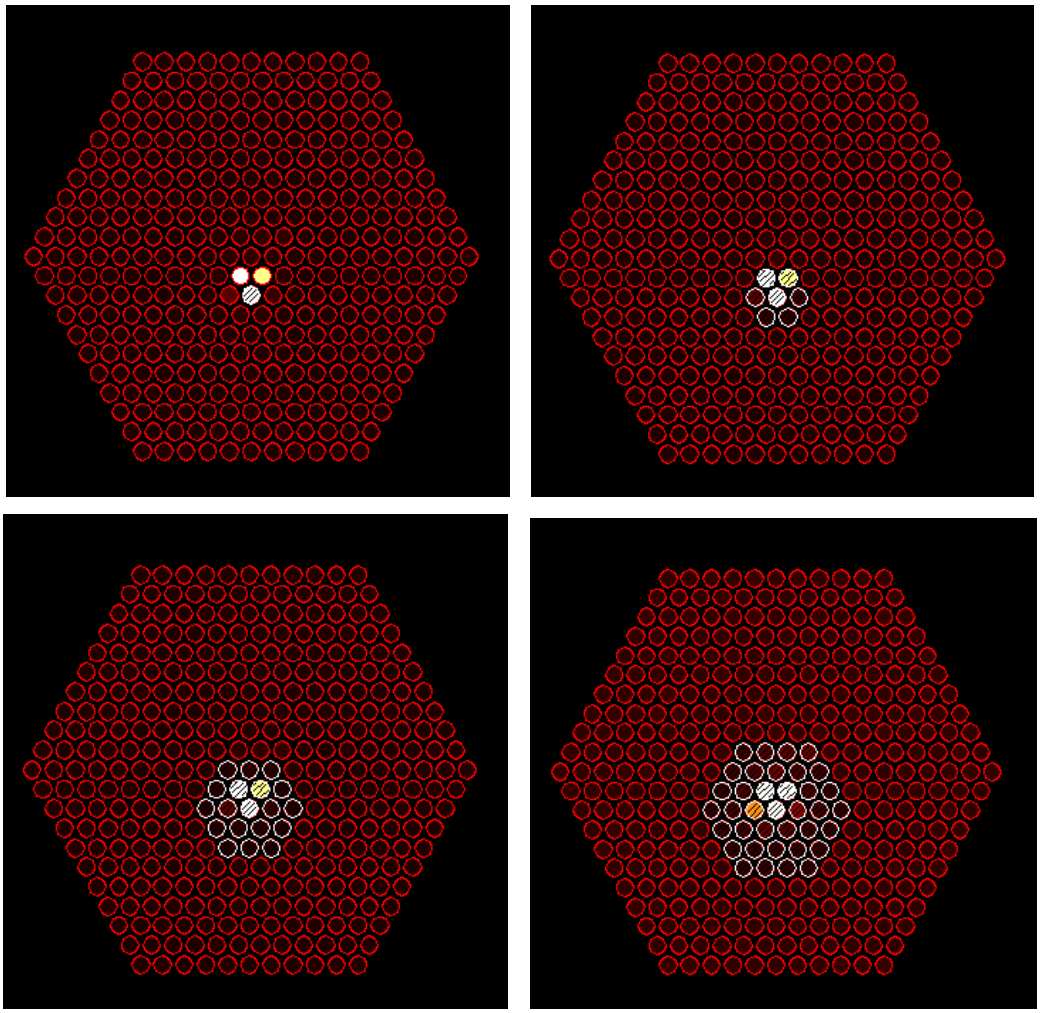

Figure 4.7: PPAK bundle diagrams showing the extraction technique of the 1D spectrum for a standard star by the selection of consecutive rings centered in the brightest fibre. *Top-left*: 1 fibre selected. *Top-right*: 7 fibres corresponding to the central one and 1 concentric ring. *Bottom-left*: 19 fibres, (2 rings). *Bottom-left*: final selection of 37 fibres (3 rings).

vation can be obtain via the CAVEX historic webpage[2]. When no information of the V-band extinction was found due to technical problems of the monitor or bad atmospheric conditions, a value of $\kappa_V = 0.18$ was assumed, corresponding to the mean value of Calar Alto observatory (San07).

It is important to note that several refinements in the standard flux calibration were applied to the general pipeline which improved substantially the accuracy of the sensitivity functions obtained after every standard star observation. During most of the observing runs different standard stars were observed each night at different airmasses in order to asses the variation in transmission and its effect on the relative flux calibration. The sensitivity function was derived by comparing the observed count rate of a star with its absolute calibrated flux as a function of wavelength, i.e. the ratio between the counts per second and the calibrated flux:

$$r_\lambda = \frac{F_\lambda}{f_\lambda \cdot t_{\rm exp} \cdot 10^{0.4\kappa_\lambda z}}, \tag{4.2}$$

[2] `http://www.caha.es/CAVEX/HISTORIC/hcavex.php`

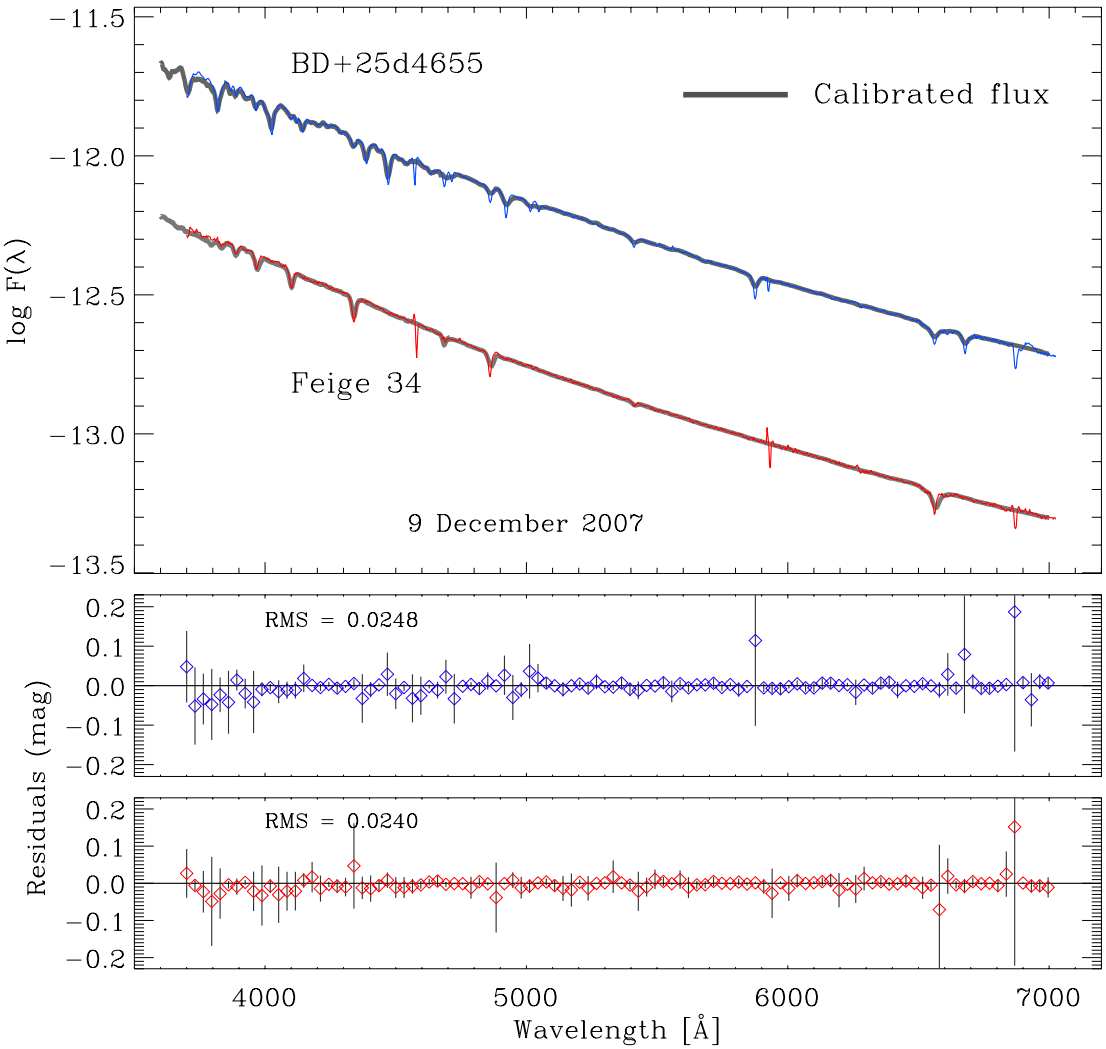

Figure 4.8: Observed standard stars on the 9th December 2007. The top panel figure shows a comparison of the night flux calibration applied to the observed stars (in colour in the online version) and the corresponding calibrated fluxes. The panel below show the residuals in magnitudes as a function of wavelength for each star. The points with relatively large deviations are due to strong sky emission lines and cosmetic defects of the CCD.

where F_λ is the calibrated flux, f_λ is the count rate, z is the airmass, and κ_λ is the extinction. Several sensitivity curves were generated using R3D, changing the key parameters that could affect the accuracy of the derived sensitivity function (e.g. order and type of the fitting function, extinction, airmass, smoothing, etc.). Furthermore, I made a comparison of the response curves obtained through R3D and the ones obtained using standard long-slit flux calibration routines in IRAF, after performing all the appropriate corrections and transformations for the two different kinds of data. I derived whole-run sensitivity curves after the combination of several response curves for a given observing run and applied the derived calibration to the observed standard stars as a proof of self-consistency. Grey shifts were applied when the conditions of the atmosphere changed drastically from the observation of one star to another, which compensates for variable grey extinction due to clouds. In all cases, very similar results were found in the final relative flux calibration.

The best sensitivity function for each night was selected based on the comparison between the flux

calibrated spectra of the standard stars observed that night (using the corresponding sensitivity function derived after each star), and the absolute flux calibrated spectra of the same standards stars[3]. The criterion was to select that sensitivity curve for which the RMS of the residuals between the compared spectra was minimum, as show in Figure 4.8. The selected sensitivity function was then applied to the science frames observed during that night, taking into account the airmass, exposure time and local extinction of each individual pointing as reported in chapter 3. Note that this method yields a *relative* flux calibration, an absolute spectrophotometry can only be achieved using additional information, like the comparison with broad-band photometry, as described in the subsection 4.1.10.

Nevertheless, as shown in detail in chapter 5, it was found that the spectral shape and features of observed targets are reproduced within the expected errors for an IFS observation ($\sim 20\%$ in the absolute sense) along the whole spectral range, with a small increase in the blue region ($\lambda < 3800$ Å) due in part to the degradation of the CCD image quality and instrumental low sensitivity towards the blue ($\sim 2-5\%$, telescope/atmosphere excluded) in this spectral region (Roth, priv. comm.). A formal discussion of the errors in the data sample due to the flux calibration is found in subsection 4.2.2.

4.1.9 Mosaic construction

After all individual pointings for a given galaxy were reduced, sky-subtracted, and flux calibrated (to a first-order), a single RSS file was built for the whole mosaic following an iterative procedure. The process starts with a master pointing chosen for each mosaic, i.e. the pointing that has the best possible sky subtraction and flux calibration, with the best signal-to-noise and the most optimal observing conditions regardless of the geometric position of the pointing in the mosaic. Taking this master pointing as a reference, the mosaic is constructed by adding consecutive pointings following the particular mosaic geometry. The iterative procedure takes advantage of the overlapping fibres between different pointings, as explained in section 3.4. During this process, each new added pointing is re-scaled by using the average ratio of the brightest emission lines found in the overlapping spectra (which is then replaced by the average between the previous pointing and the new re-scaled spectra). In most cases the scale factor is found to be between 0.7 and 1.3 with respect to the master pointing. The difference in the scale between different pointings is due mainly to the relative flux calibration, but other factors such as difference in transmission and a poor sky-subtraction play also a role.

This ratio is wavelength dependent (specially in the cases of variable photometric conditions between the observations). Therefore as a second-order correction, the variations found between the previous pointing and the new re-scaled overlapping spectra were fitted to a low order polynomial function, then all the spectra in the new pointing were divided by the resulting wavelength dependent scale. This correction has little effect on the data when the observations were performed during the same or consecutive nights, as it is the case for the small mosaics. However, there were found variations after all the possible corrections of the order of 10-15% in the extreme cases when the observations were carried out at different epochs (e.g. NGC 628, NGC 3184). This level of error is what it is expected from observations performed during different nights and observing runs, reflecting the variation of the spectrophotometric transmission from night to night (see Figure 4.17).

The procedure was repeated for each mosaic until the last pointing is included (except for the Stephan's

[3] Absolute flux calibrated tables of the spectrophotometric standard stars were obtained from: `http://www.caha.es/pedraz/SSS/sss.html`.

Quintet, where not actual overlapping occurs), ending with a final RSS containing all the individual spectra and the corresponding position table. By adopting this procedure the differences in the spectrophotometric calibration night-to-night are normalized to that of the first frame used in the process. This process ensures a homogenous flux calibration and sky extinction correction for the entire data set.

4.1.10 Absolute flux re-calibration

For those galaxies with suitable multi-band photometric data publicly available (e.g. NGC 628, NGC 2976, NGC 3184, NGC 4625 & NGC 5474), a flux re-calibration was performed to the first-order calibrated mosaics built as described above, by comparing the spectra of the IFS mosaics to the corresponding flux measured by B, V, R broad-band and Hα narrow-band imaging photometry, for the same positions taking into account the fibre apertures and the different filters' response functions.

The mosaics constructed as described in subsection 4.1.9 have a *relative* flux calibration, the additional correction is intended to provide the closest *absolute* flux calibration by finding the difference in the flux level (i.e. a scale factor that should be applied to spectra in the mosaic), without altering the shape of the individual spectra. For this purpose, the flux calibrated broad-band optical images belonging to the ancillary data of the SINGS legacy survey (Kennicutt et al., 2003) were employed. The photometric calibration of these images is claimed to be $\sim 5\%$ for the broad-band imaging and $\sim 10\%$ for the narrow-band ones. They reach a depth of ~ 25 mag/arcsec^2 with a signal-to-noise of $\sim 10\sigma$. Therefore, for the structures included in the FOV of the IFS data, the photometric errors are dominated by the accuracy of the calibration, and not by the noise level of the images.

For each of the galaxy mosaics mentioned before, the IFS position table was registered to the SINGS optical data by matching the coordinates of visible foreground stars in the FOV, and the galaxy bulge. As an example, Figure 4.9 shows the SINGS B-band image of NGC 628 in a N-E positive configuration, the position of each individual fibre of the IFS mosaic is shown overlaid to scale. Once registered, the mosaic position table was used to extract aperture photometry from each broad-band image at the location of each fibre and with an aperture similar to that of the fibres. On the other hand, each spectrum in the mosaic was multiplied with the same transmission curve as the corresponding broad-band filters, in order to extract a similar flux fibre-to-fibre, based on the IFS data.

However, in order to make the right comparison it is important to make sure that position of the fibres correspond to the real observed offsets in the IFS mosaic. Given that the procedure described above provides the same number of photometric points per band per mosaic to compare between the two datasets, it is possible to create an interpolated image of the spectra in the IFS mosaic and a degraded image based on the broad/narrow band imaging. In this way, possible misalignments of individual IFS pointings can be identify and corrected by blinking the two images. Both sets of data were interpolated adopting a natural-neighbor non-linear interpolation scheme, and a final pixel scale of 1"/pixel using E3D. Small misalignments of the order of 2" were found for individual pointings, especially for those mosaics observed over a long period and with a large number of pointings (i.e. NGC 628, NGC 3184). The offsets of these pointings were corrected and a new mosaic was built, updating the corresponding position tables. This mosaic re-centering technique was performed using the Hα narrow band images, as they show regions which are easy to identify and match in both data sets. After this process, the error in the astrometry of the IFS data was estimated to be ~ 0.3", based on the *rms* of the differences in the centroids of foreground stars. The reference coordinates of the Right ascension and Declination in the J2000 equinox were recorded in the FITS headers of the original

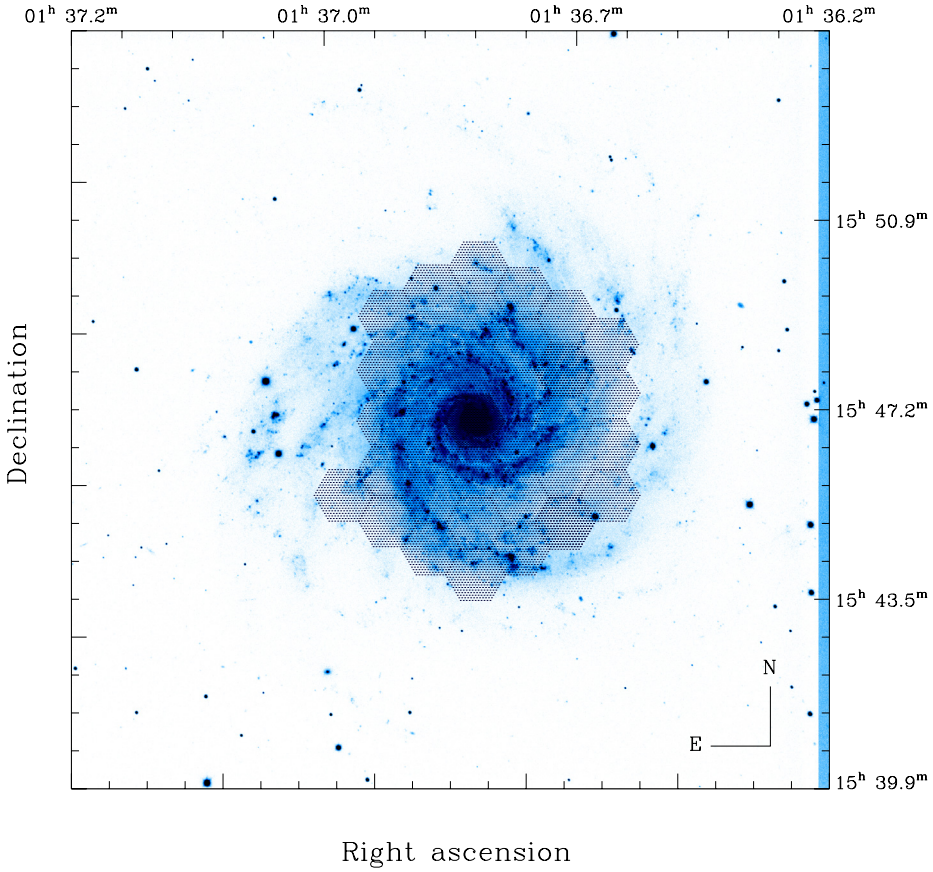

Figure 4.9: SINGS *B*-band image of NGC 628 used to perform the absolute flux re-calibration. The position of each individual fibre of the IFS mosaic is shown overlaid to the real scale.

RSS files, together with the World Coordinate System (WCS) information necessary to recover the position of the centre of each fibre of the mosaics.

Figure 4.10 and Figure 4.11 show examples of the *V*-band and Hα narrow band images of NGC 628 obtained by the interpolation of the aperture extraction in the case of the SINGS images, and the corresponding IFS data with the updated position tables. The SINGS images (top panels) show a degradation in the resolution as expected, while in the IFS images (bottom panels), the hexagonal individual pointings are clearly seen. Note that the main structures of the galaxy are completely reproduced in the IFS images, this is shown more clearly in the Hα images. Those pointings with low signal-to-noise are evident in the *V*-band IFS reconstructed image.

A new aperture photometry extraction to the broad-band imaging was performed with the updated position tables for each mosaic. The photometry was transformed to flux (in cgs units) by using the counts-to-magnitude prescription in the SINGS documentation[4], and the zero-points included in Fukugita et al. (1995). The ratio between the two sets of photometric points was obtain per each band analysed, except for NGC 4625 for which no Hα image was available in the SINGS ancillary data. Only points above a particular flux threshold value (chosen from the IFS data) were considered reliable, a mean value of the ratio was obtained from these points for each band for each galaxy. The flux threshold values ($\sim 10^{-16}$ erg s^{-1} cm^{-2}) were chosen to discard low signal-to-noise fibres. It is important to note that the *B* and *R*-band response

[4] `http://tinyurl.com/SINGS-doc`

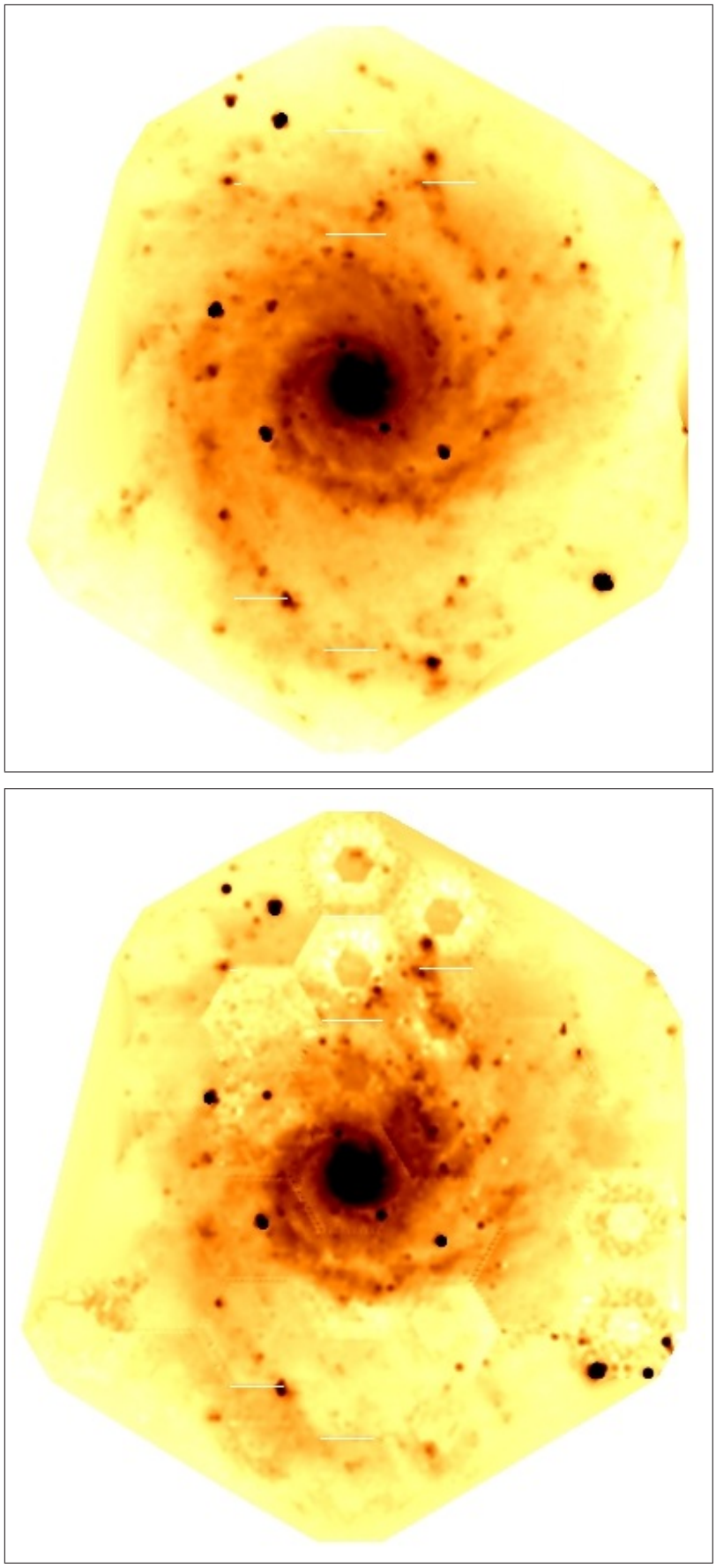

Figure 4.10: Reconstructed V-band images of NGC 628. *Top-panel*: image created after interpolating the aperture photometry extraction of the SINGS broad-band image. *Bottom-panel*: interpolated image derived after multiplying each spectrum of the IFS mosaic with the filter response curve. Both images were created with a regular grid of 1”/pixel. Note the low signal-to-noise pointings in the IFS reconstructed image.

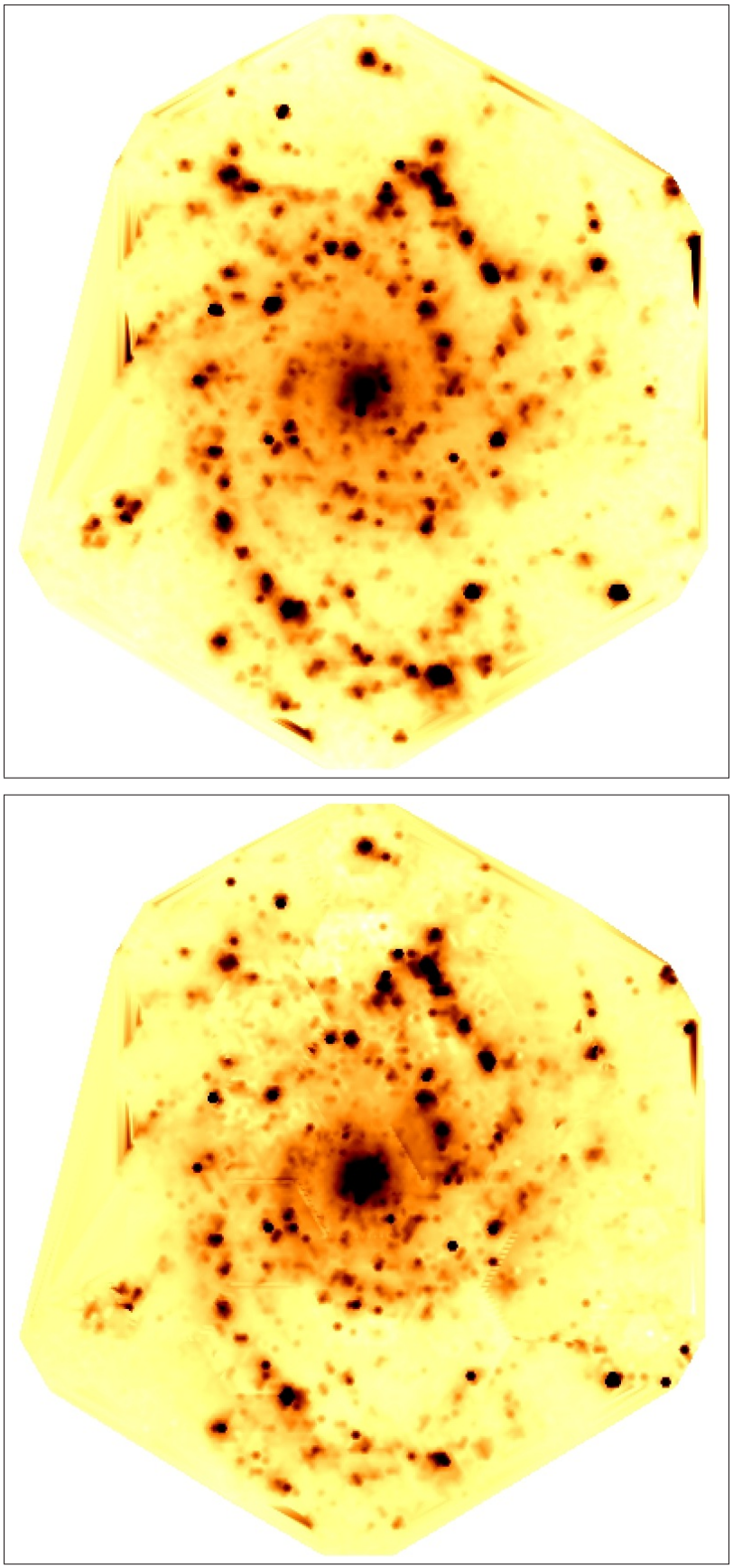

Figure 4.11: Reconstructed Hα narrow-band images of NGC 628. *Top-panel*: SINGS image. *Bottom-panel*: IFS extracted image. Same properties and scale as Figure 4.10. The main structures of the galaxy are completely reproduced in the IFS image.

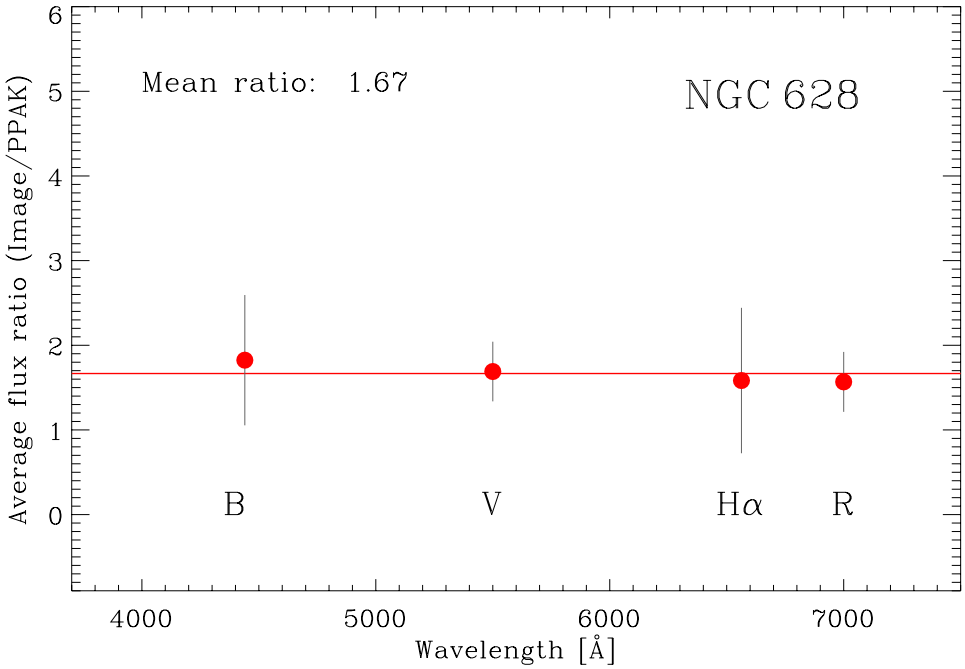

Figure 4.12: Broad-band and narrow-band mean flux ratios of the absolute spectrophotometric analysis of NGC 628.

functions used to multiply the IFS data extend beyond the wavelength range limits of the mosaics spectra, while the V-band and Hα transmission functions fall within the spectral range of the PINGS data. Therefore, more variations in the derived ratio are expected for the B and R-bands. Table 4.2 shows the ratios found between the broad-band aperture photometry and the IFS derived photometry for the analysed galaxies. As an example, Figure 4.12 shows the mean ratios found at each band for NGC 628, all four values are consistent within the errors to a mean value of 1.67, the ratio derived from the B-band is slightly higher than rest of the bands, behavior that is similar for the rest of the galaxies as shown in Table 4.2, except for NGC 5474 where the highest ratio was derived from the R-band, and NGC 2976 for which the B-band ratio is completely inconsistent with the rest of the bands.

In principle, one can derive an absolute spectrophotometric calibration factor solely from the comparison to broad-band imaging, as described above. However, an alternative approach consists of comparing previously published spectroscopic data, which have been spectrophotometrically calibrated. Given the large size of the PINGS mosaics, the comparison cannot be made in terms of individual regions. Therefore, if we want to obtain a calibration factor based on spectroscopy, we need a spectrum which samples a considerable region of the galaxy in order to compare it with the IFS data. This possibility is offered by spatially integrated spectrophotometry, in particular, by spectra obtained using the so-called drift-scanning technique. The PINGS sample contains a number of galaxies for which drift-scan spectra has been obtained previously. In particular, the ancillary data of the SINGS survey contains 20"×20" drift-scan spectra of the central regions of NGC 628, NGC 3184, NGC 4625 & NGC 5474. Additionally, Moustakas & Kennicutt (2006b) obtained spatially integrated optical spectrophotometry for more than 400 nearby galaxies, including NGC 1058, NGC 3310, NGC 4625, NGC 6701 & NGC 7771.

As described in detail in chapter 5, one advantage of 2D spectroscopy is the possibility to use the FOV of an IFS observation as a large-aperture spectrograph, and to obtain the integrated spectrum of a given

ABSOLUTE SPECTROPHOTOMETRIC CALIBRATION FACTORS

Object	*B*-band	*V*-band	Hα	*R*-band	Integ. spectra	Adopted ratio
NGC 628	1.82	1.69	1.58	1.57	1.44	1.56
NGC 1058	...	...	...	...	1.53	1.53
NGC 2976	3.30	1.29	1.45	1.57	...	1.43
NGC 3184	2.23	1.79	1.86	1.81	2.04	1.98
NGC 3310	...	...	...	...	2.17	2.17
NGC 4625	2.49	2.37	...	2.32	2.77	2.40
NGC 5474*	1.47	1.80	1.63	2.17	...	1.77
NGC 6701	...	...	...	...	2.20	2.20
NGC 7771	...	...	...	...	2.56	2.56

Table 4.2: Absolute spectrophotometric calibration factors obtained from the comparison of the IFS data with broad-band, Hα imaging, and integrated spectra as explained in the text. The last column shows the adopted calibration ratio. Only those galaxies for which imaging and/or integrated spectra were available are shown.
* Although a integrated spectrum of NGC 5474 is available in the SINGS ancillary data, a calibration ratio was not obtained due to the bad quality of the spectrum and the unknown position with respect to the galaxy (see subsection 5.1.6).

target. For the purpose of the spectrophotometric calibration described in this section, integrated spectra were obtained for the galaxies mentioned above by co-adding the spectra using different simulated apertures applied to the IFS mosaics, corresponding to the positions, angular sizes and orientations of the drift-scan spectra. All the details of such extractions can be found in chapter 5. Here we only focus on the ratio obtained by comparing the spectrophotometrically calibrated drift-scan spectra and the integrated spectra extracted from the IFS mosaics sampling the same regions. Column 6 of Table 4.2 shows the ratio derived after this comparison for the sample objects. For NGC 628 and NGC 3184, the whole set of calibration ratios, including the four photometric bands and the integrated spectrum are available. The ratios derived from the integrated spectra of these two galaxies (and NGC 4625) are consistent with the broad-band ratios. The final adopted calibration ratio is shown in the last column of Table 4.2, it was derived by the average of the mean value of the broad-band imaging ratios and the integrated spectrum ratio. For NGC 2976, the *B*-band ratio was discarded as it deviates strongly with the rest of the broad-band ratios. For NGC 4625, the broad-band imaging method was given a higher weight in the final adopted ratio due to the difference in the aperture of the drift-scan integrated spectrum.

One important aspect of the comparison with drift-scan spectra is the possibility to obtain a calibration factor for NGC 1058, NGC 3310, NGC 6701 & NGC 7771 galaxies without public, photometrically calibrated, broad or narrow band imaging available. No absolute spectrophotometric calibration was attempted for NGC 1637, NGC 6643 and the Stephan's Quintet, galaxies without broad-band imaging or drift-scan spectra available. The adopted ratio was applied as an absolute spectrophotometric calibration factor, multiplying all the spectra of the mosaic by the corresponding value, correcting in this way for the zero-point of the flux calibration.

Figure 4.13 shows for NGC 628, the ratio between the two sets of photometric points used to perform the absolute flux calibration, along the flux extracted from the IFS mosaic for each of the considered filters, after the spectrophotometric calibration factor was applied. The blue points correspond to the *B*-band,

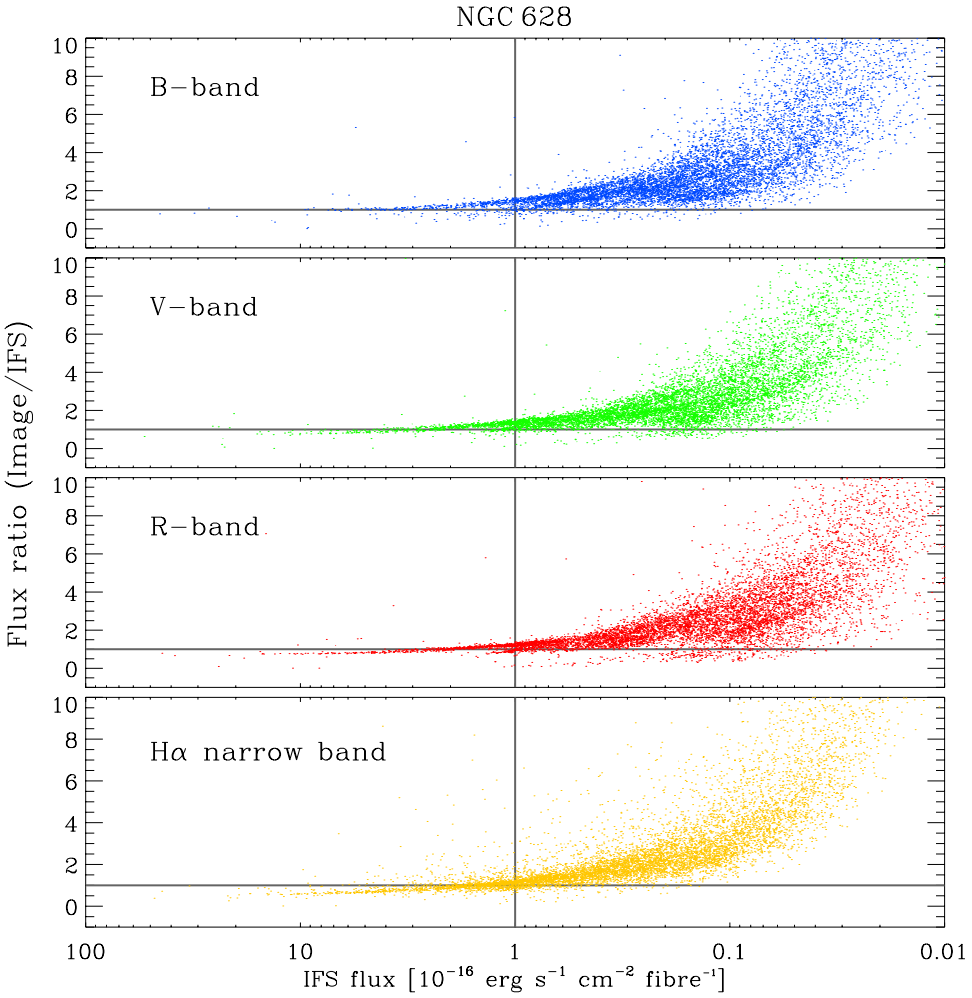

Figure 4.13: Image/IFS flux ratio for NGC 628 as a function of the IFS flux after the absolute flux calibration. The different panels correspond to the four broad/narrow bands used for the comparison. The horizontal lines represents a ratio of one, while the vertical lines correspond to the selected flux threshold as explained in the text.

the green points to the V-band, orange points to the Hα narrow band, and red points to the R-band. The horizontal lines stand for a ratio of one, while the vertical lines represents the selected flux threshold for the determination of mean values. Each filter contains 11094 individual points. The figure shows the typical pattern obtained when comparing the flux ratio between two datasets with different depth, being the broad-band images clearly deeper than the spectroscopic data, as expected. Down to 0.5 erg s^{-1} cm^{-2} ($\sim$ 5000 fibres per band) the ratio is $\sim$ 1.0 for all the fibres, with a standard deviation of $\sim$ 0.2 dex.

Figure 4.14 shows the broad-narrow band mean flux ratios obtained during the spectrophotometric analysis, and the Image/IFS flux ratios after the absolute flux re-calibration for the galaxies reported in Table 4.2. To our knowledge, no other IFS observation has ever attempted to get such (instrument-limited) spectrophotometry accuracy as the one performed for the PINGS sample. As explain in following section, the difference in the zero-point of the flux calibration lies within the expectations based on the estimated accuracy of our spectrophotometric calibration.

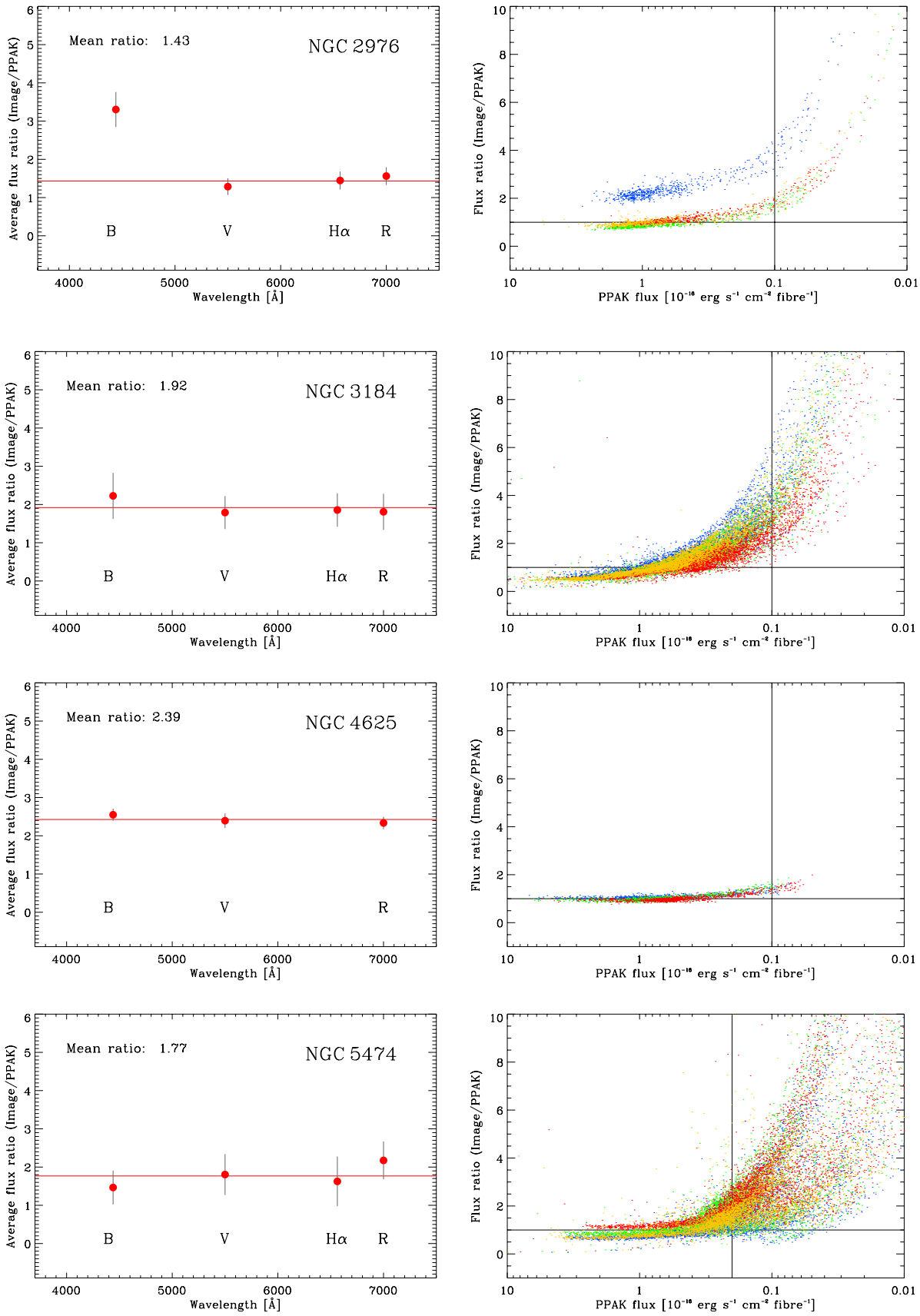

Figure 4.14: Galaxies with broad-narrow band spectrophotometric analysis. For each galaxy, the left plot corresponds to the broad/narrow band mean flux ratios obtained from the aperture photometry comparison. The right plot corresponds to the Image/IFS flux ratio after the absolute flux re-calibration. The colour-coding is equivalent as Figure 4.13. The vertical lines correspond to the flux threshold value.

4.2 Errors and uncertainties in the data sample

During the process of data reduction and basic analysis of the PINGS data set, several possible sources of errors and uncertainties were identified. Each of them contribute in a different way and magnitude to the overall error budget associated with the observations. These are in order of importance: 1) sky subtraction, 2) flux calibration, 3) differential atmospheric refraction (DAR), 4) cross-talk, and 5) second order spectra. In this section I describe the nature of each of these sources of errors, the tests performed in order to understand their effects on the accuracy of the data, and the techniques applied to minimise them.

4.2.1 Sky subtraction

As mentioned previously, sky subtraction is one of the most difficult steps in the IFS reduction process and it is particularly complex for the nature of the observing technique of PINGS. A deficient sky subtraction has several consequences: the contamination of the sky emission lines along the spectra which prevents the detection and/or correct measurement of relatively weak nebular emission lines (e.g. the weak temperature sensitive [O III] λ 4363, which is located in the same spectral region as the strong Hg I λ 4358 sky line), and also affects the shape and intensity of the continuum, which is important for the analysis of the stellar populations and the determination of reddening. In fact, a by-product of the mosaicing method is that it can be used to find the best possible sky subtraction. Due to the shape of the PPAK bundle and by construction of the mosaics in the standard mosaic configuration, 11 spectra of a given pointing (corresponding to one edge of the hexagon) overlap with the same number of spectra from the previous pointing (see NGC 628 or NGC 3184 in Figure 4.19). This allows the comparison of the same observed regions at different times and with different atmospheric conditions.

For a non-standard configuration the number of overlapping fibres is larger (e.g. NGC 3310). These overlapping spectra can be compared and used to correct for the sky emission of the adjacent frame. However, prior to performing the sky subtraction it is required to visually check that no residual of the galaxy is kept in the derived spectrum. This can be the case if the transmission changed substantially during the observation of the adjacent frames. These techniques proved to result in good sky subtraction in most cases. On the other hand, when it was required to obtain supplementary large-angle offset sky-exposures for the inner pointings in the mosaics that were completely filled by the target, it was found that when the sky exposure was taken within a few minutes of the science exposure, this produces a good subtraction. For those cases in which the atmospheric conditions changed drastically and/or the sky subtraction appeared to be poor, different sky frames were combined with different weights to derive a better result.

One way of assessing the goodness of the sky subtraction is to check for sky residuals in the subtracted spectra. The galaxy mosaic more prone to be affected by residuals in the sky subtraction is NGC 628, which as explained in section 3.4, was observed during six nights along four observing runs. Therefore it could be expected that the spectroscopic mosaic of this galaxy would show the most extreme effects due to the sky subtraction to be found in the PINGS sample, given all the variations in transparency and photometric conditions of the night-sky along the three years of observations.

In order to obtain a quantitative assessment of the quality of the sky subtraction, two different data reductions were performed to the spectroscopic mosaic of NGC 628. In the first reduction, the sky subtraction was performed directly with the average spectrum of the sky fibres at each position, without considering the overlapping spectra between pointings, and not accounting for the object contamination in the sky fi-

bres. Therefore, in this first reduction a "poor" sky subtraction was applied. For the second reduction, an individual sky subtraction per mosaic position was applied using the techniques described before, i.e. applying corrections using the overlapping spectra, checking for galaxy residuals in the derived sky spectrum, using the sky exposures obtained by large offsets for the most internal regions of the galaxy, and combining different sky frames with different weights in those cases when there were important changes in the transmission between pointings observed during the same night. I would refer to this reduction as the "refined" sky subtraction.

Airglow is the most important component of the light of the night-sky spectrum at Calar Alto observatory, although a substantial fraction of the spectral features is due to air pollution (Sánchez et al., 2007). The strongest sky line in the Calar Alto night-sky spectrum is the [O I] λ5577 line, followed by the [O I] λ6300 line, both produced by airglow with a notorious stronger effect near twilight. A deficient sky subtraction can be recognised by residual features of the sky lines in the derived spectra, this effect is clearly seen in the [O I] λ5577 sky line which is located in a spectral region without any important nebular emission line. In general terms, (without considering variations in the transparency of the sky), a residual in emission of this line would imply a subtraction of the sky spectrum of slightly lower strength than required, while an absorption feature would imply an over-correction.

In order to make a comparative analysis of the strength of the sky residuals in the two data reductions of NGC 628 described above, the local continuum in the neighbourhood of the [O I] λ5577 sky line was re-scaled to a flux level of 10^{-16} erg s^{-1} cm^{-2} Å^{-1} in every single spectrum of both mosaics. The equivalent width (EW) of the residual features was then measured, centered at the [O I] λ5577 line. EW with negative sign corresponds to residual emission features, while positive EW corresponds to absorption features.

Figure 4.15 shows the value of the EW residuals for the [O I] λ5577 line for both data reductions as a function of the pointing position in the spectroscopic mosaic. Each position *bin* contains 331 values corresponding to the number of spectra per pointing, a total of 11104 values are shown, corresponding to the 34 positions observed for NGC 628. The green dots correspond to the *poor* sky subtraction reduction, while the blue dots correspond to the *refined* sky subtraction. There is a considerable amount of scatter of the EW residual value for the *poor* sky subtraction compared to the *refined* one. In the first two pointings of the mosaic (which correspond to central positions of the galaxy), there are strong residuals in emission for the *poor* reduction, while the residuals have been minimised in the *refined* one. Figure 4.15 shows clear evidence of those pointings in which the sky transparency varied by a considerable amount (positions 4, 5, 11, 12, 23, 24, 28, 29, 33, 34). In all the pointings, the scatter in the residuals is improved in the *refined* reduction with respect to the first one. This effect is more notorious between positions 13 to 22. The *poor* sky subtraction yields very strong sky residuals in emission for positions 33 and 34, while in the *refined* reduction these are minimised.

At the chosen continuum level used for this exercise, a (absolute) value of 5 Å in EW for the [O I] λ5577 residual line in emission corresponds approximately to a flux intensity value of 4×10^{-16} erg s^{-1} cm^{-2}, while a value of 10 Å corresponds to $\sim 11 \times 10^{-16}$ erg s^{-1} cm^{-2}. The average flux intensity of the [O I] λ5577 sky line in Calar Alto is of the order of 33×10^{-16} erg s^{-1} cm^{-2} (Sánchez et al., 2007). However, from a sample of 500 sky spectra acquired during the three years of observation, the measured intensity of the [O I] λ5577 ranges between 30 and 60×10^{-16} erg s^{-1} cm^{-2}, with a mean value of 44. Therefore, a value of 5 Å in EW for a residual emission feature would correspond to $\sim$8–10% of the total emission of the [O I] λ5577 line. Visual inspection of the spectra with emission residual of the order of 5 Å in EW confirms that this value could be considered as the threshold for a good sky subtraction. Spectra with

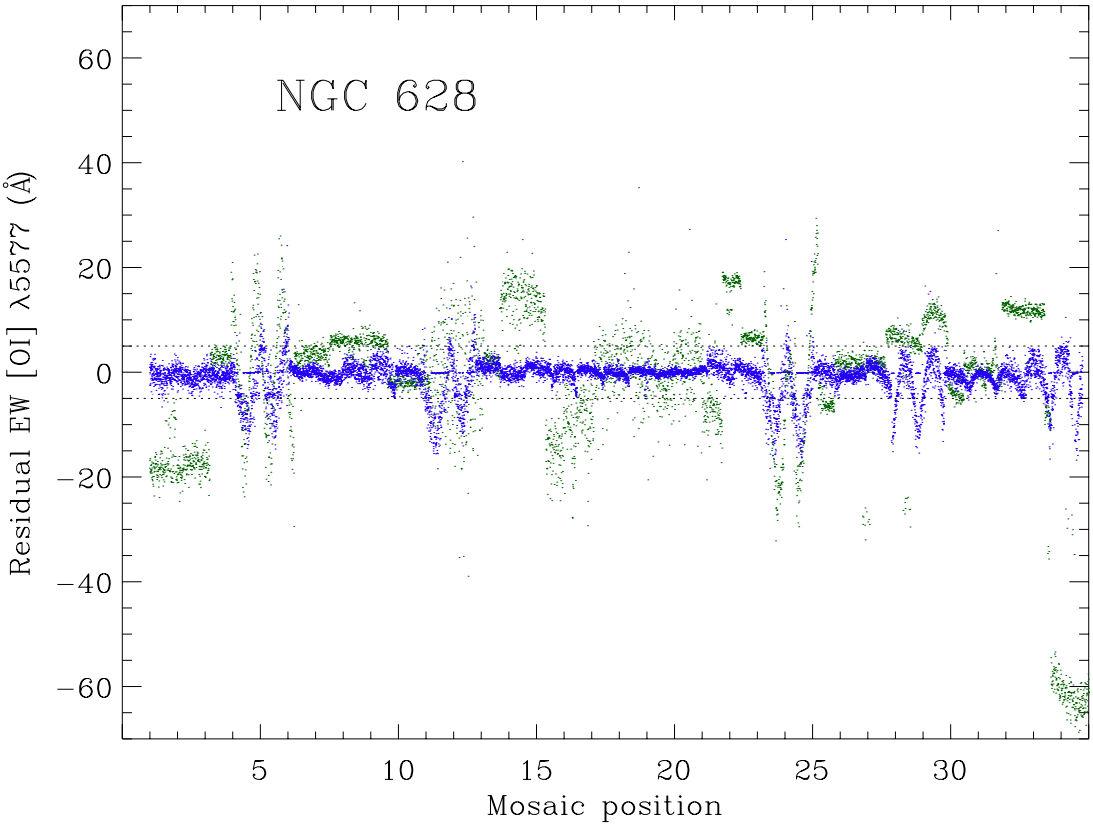

Figure 4.15: Equivalent width values for the emission and absorption residual features of the [O I] λ5577 sky line as a function of the observed position for the spectroscopic mosaic of NGC 628. Positive values correspond to absorption features, while negative values to emission residuals. The local continuum level was re-scaled to the same value in order to make this comparison. The green dots correspond to a *poor* sky subtraction, while the blue dots represent the *refined* reduction as explained in the text. The two horizontal dotted lines mark the threshold EW values of residuals features corresponding to a good sky subtraction.

emission or absorption residuals with absolute EW values less than 5 Å could be considered to have a good subtraction, for features above this value the effects of a deficient sky subtraction are evident.

The two horizontal dotted lines in Figure 4.15 indicate the ±5 EW threshold value for both emission and absorption features. These two lines encompass a region for which the spectra can be considered with a good sky subtraction. The *poor* sky subtraction (green) shows a lot of scatter and a small fraction of the spectra falls within these limits. On the other hand, for the *refined* reduction (blue) a total of 9629 spectra fall within these limits, i.e. 87% of the total mosaic. The number of spectra with sky subtraction problems for which $|\mathrm{EW}| > 5$ Å is 1475, i.e 13% of the mosaic, these spectra are found in those pointings with extreme transparency variations, as expected.

Figure 4.16 shows the histograms of the EW values for both data reductions, the *poor* sky subtraction in green and the *refined* reduction in blue colour following Figure 4.15. The top panels show the distribution of residual emission values, while the bottom panels show the absorption residual features for the [O I] λ5577. The ∼5 Å EW threshold value is shown as the vertical line in the histograms, residual values to the right of this line can be considered a deficient sky subtraction. Visual inspection of the spectra shows that, at the continuum level used for this comparison, emission or absorption features with values of $\log(|\mathrm{EW}|) \leq 0$ could be considered negligible and within the statistical noise of the spectra. The residual emission histograms show that the *poor* sky subtraction produces a large number of strong residuals with values of

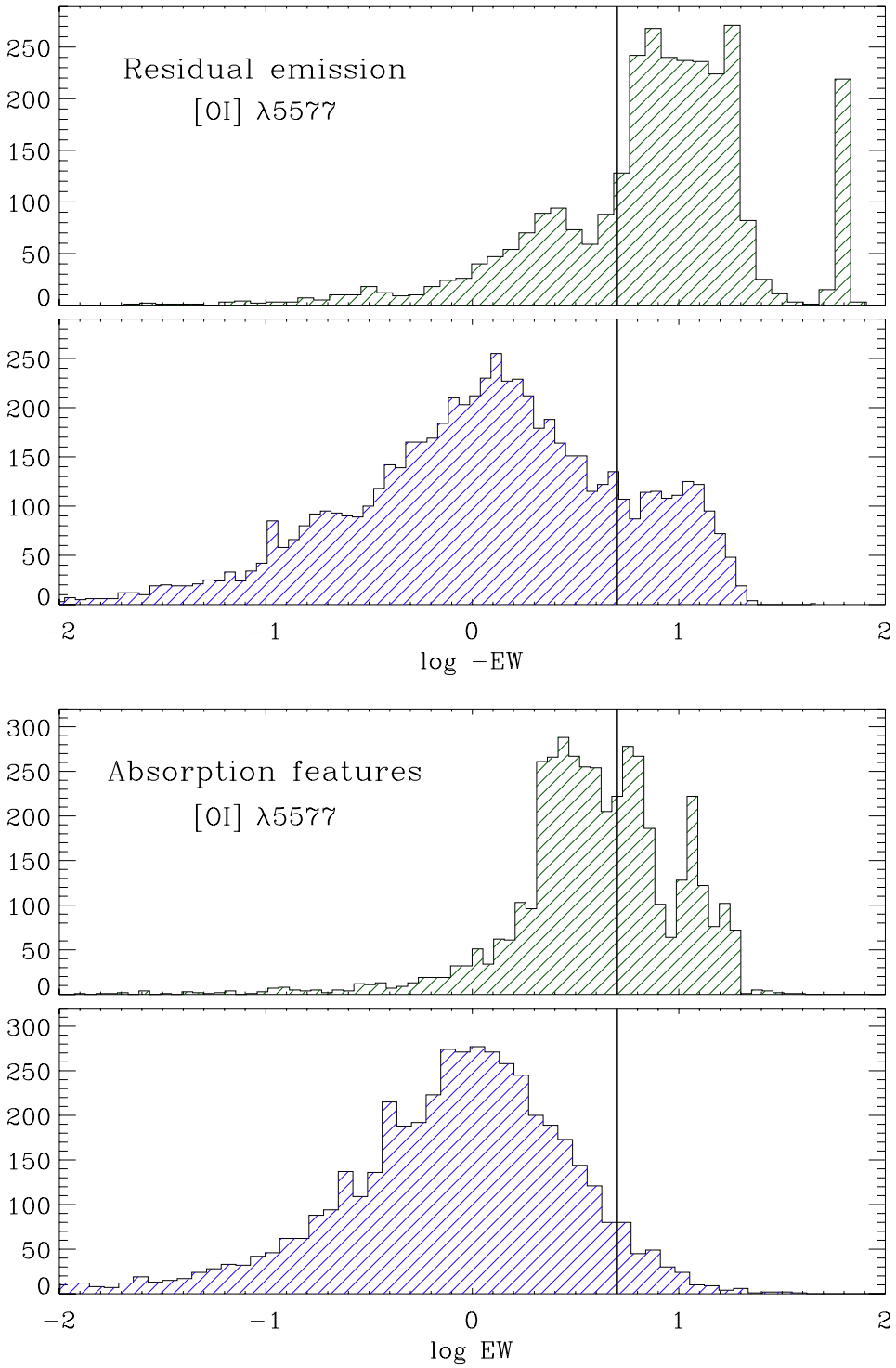

Figure 4.16: Histograms of the EW residual features shown in Figure 4.15. The top panels shows the distribution of EW values for the emission residuals. The bottom panels shows the EW values for the absorption features. All EW values are shown in logarithmic scale (assuming a positive EW value for the emission residuals). The top histograms in both cases correspond to the *poor* sky subtraction, while the bottom histograms correspond to the *refined* reduction. The $\sim$5 Å EW threshold value is shown as the vertical line in all the histograms, residual values to the right of this line can be considered a deficient sky subtraction as explained in the text.

|EW| $>$ 5 Å, even reaching |EW| $\sim$ 60 Å. The majority of the residual values in *refined* sky subtraction are found at log(|EW|) $\sim$ 0, corresponding to negligible residual values, however there is a small tail of strong emission residuals for which |EW| $>$ 5 Å ($\sim$ 18% of the total emission residuals). The distribution of EW values of the absorption features for the *poor* subtraction is approximately centered at the threshold limit, while for the *refined* reduction, the values are nearly normally distributed with a centre value of log(EW) $\sim$ 0 with a small tail of strong absorption values ($\sim$ 7%) due most likely to an over subtraction of the sky spectrum.

The *refined* sky subtraction was the final adopted one for the spectroscopic mosaic of NGC 628. All the sky subtraction techniques implemented showed that the quality of the derived spectra was improved by a considerable amount compared to a standard sky subtraction. Most of the sky residuals are within the limits of a reasonably good sky subtraction. The spectra with strong features are found for those positions in which the photometric conditions changed drastically during the night or observing run. This residual analysis allows to identify those pointings with strong sky variations and thus, to flag the spectral data for future analysis. The sky subtraction for the rest of the PINGS sample was performed similarly to the *refined* technique described above. Therefore the best possible sky subtraction was applied to all the spectroscopic mosaics within the limitations imposed by the IFS data itself.

4.2.2 Flux calibration

Although a particular care has been taken to achieve the best spectrophotometric calibration, there are many effects that can strongly affect it. Among them, the most obvious are the photon-noise from low surface brightness regions of the galaxy, the sky-background noise or variations in the weather conditions between the time when the spectrophotometric standards and the object were observed. This latter effect was reduced by the adopted mosaicing procedure in the data reduction, since the photometric calibration was renormalized to one of a particular good night. Less obvious is the effect of the inaccuracies in the sky subtraction. However, for low surface brightness regions this is one of the most important effects, as described in the previous section.

Figure 4.17 shows the shape and relative magnitude of nine sensitivity curves obtained during the three years of observations. The difference in the vertical scale reflects the variation of the spectrophotometric transmission during different nights and observing runs. However, the differences on the shape from one sensitivity curve to another as a function of wavelength, reflect the intrinsic dispersion of the flux calibration. The bottom panel of Figure 4.17 shows the variation of the sensitivity curves as a function of wavelength after a grey shift with respect to an arbitrary spline fitting normalised at the wavelength of Hβ (4861 Å). This normalisation wavelength was chosen as most spectroscopic studies normalise the observed emission line intensities to the flux in Hβ. The maximum variation from the blue end of the spectrum compared to the red one is of the order of $\sim$ 0.15 mag, corresponding to a maximum calibration error of $\sim$ 15% due solely to the intrinsic dispersion in the relative flux calibration. However, the actual RMS is less than 0.1 mag, corresponding to a typical error in the relative flux calibration of less than 10%.

For those galaxies with available multi-band photometric data, small differences in the transmission curves of the filters and astrometric errors of the built mosaics bring some uncertainties in the derived flux ratios that contribute to the overall standard deviation when applying the photometric re-calibration described before. The errors in the first case are difficult to estimate, however the latter ones were estimated by simulating different mosaic patterns moving randomly the location of the simulated fibres-apertures and

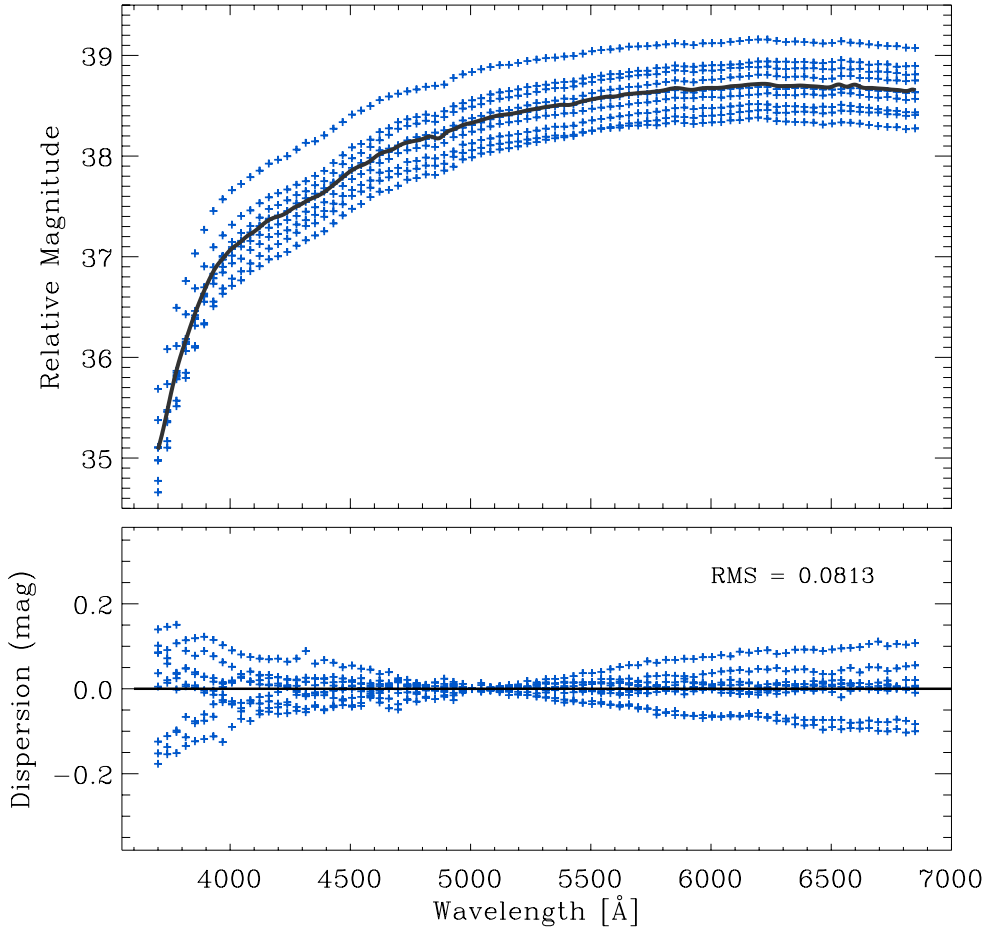

Figure 4.17: Variation of the spectrophotometric transmission as a function of wavelength. The top panel shows nine sensitivity transmission curves using different calibration standard stars. The thick dark line is a 3rd degree spline fitting to the data. The panel below shows the dispersion in magnitudes after a grey re-scaling of all the sensitivity curves with respect to the spline fit normalised at the Hβ wavelength (4861 Å).

then comparing the extracted spectrophotometry. Figure 4.18 shows the result of this exercise, the points correspond to the flux ratio between the extracted V-band photometry of NGC 628 using the original (offset corrected) position table and the extraction with normally distributed random offsets from the same image. The blue points correspond to an offset with a mean value of 0.3 arcsec, the green points correspond to larger offsets with a mean value of 0.5 arcsec, while the grey points correspond to a mean value of 1.3 arcsec, i.e. the radius of the PPAK fibres. The horizontal line corresponds to a flux ratio of one, the vertical line to an arbitrary flux threshold. The standard deviation of the 0.3 offsets (for those points above the threshold flux) is 0.06, while for the larger offsets of 0.5 and 1.3 is 0.16 and 0.29 respectively. Considering that the IFS mosaics were re-centered using the information directly from the aperture photometry, we expect that the location of the fibres lies within 0.5 arcsec, and therefore the error due to the uncertainty in the astrometry would be less than 16%, and more realistically of the order of 10%.

Based on these results, we estimate a spectrophotometry accuracy better than $\sim$0.2 mag, down to a flux limit corresponding to a surface brightness of $\sim$22 mag/arcsec^2 when we apply the re-calibration derived by the flux ratio analysis. In chapter 5 and chapter 6 the PINGS data is compared with previously published spectrophotometrically calibrated data. The spectral shape, the spectral features and emission line intensities match remarkably well, even for those objects for which no re-calibration was performed.

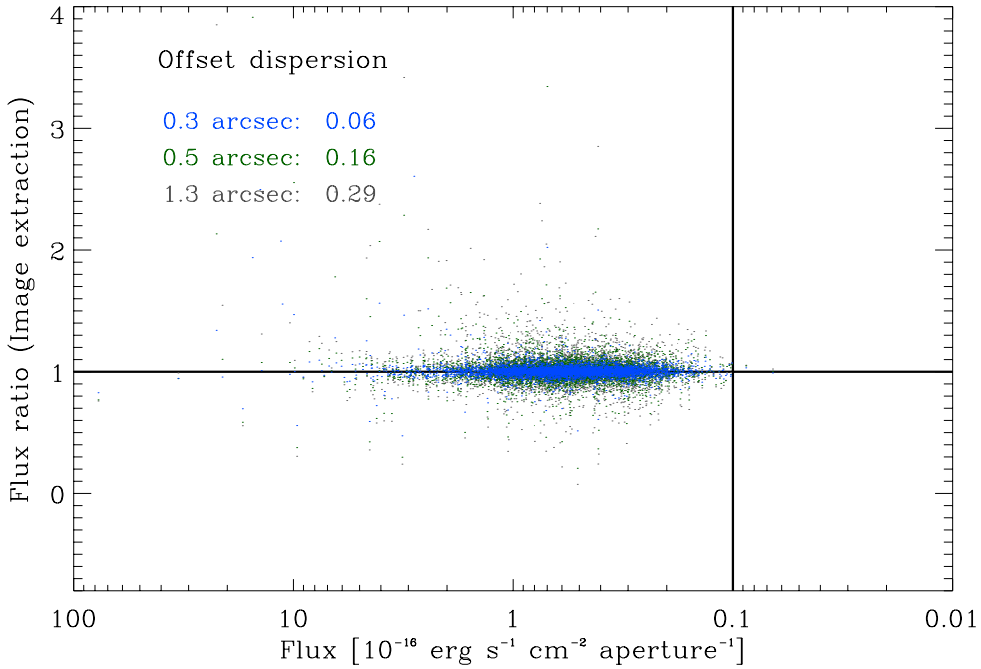

Figure 4.18: Variation of the flux ratio between the extracted V-band photometry of NGC 628 and simulated extractions with normally distributed random offsets from the original position table. The points correspond to an offset with a mean value of 0.3 (blue), 0.5 (green) and 1.3 (grey) arcsec. The standard deviation calculated from the points above an arbitrary flux threshold are shown on the top.

4.2.3 Differential Atmospheric Refraction

An important systematic effect in any spectroscopic observation is due to the refraction induced by the atmosphere, which tends to alter the apparent position of the sources observed at different wavelengths. By definition, there is no refraction when the telescope is pointed at the zenith, but for larger zenith angles the effect becomes increasingly significant. For IFU observations, this has the consequence that, when comparing for example the intensities at two different wavelengths (e.g the emission line ratio of a source), one will actually compare different regions, given that different wavelengths are shifted relative to each other on the surface of the IFU. In theory, one is capable of performing a correction of DAR for a given pointing without requiring knowledge of the original orientation of the instrument and without the need of a compensator, as explained by Arribas et al. (1999). The correction of DAR is important for the proper combination of different IFS exposures of the same object taken at different altitudes and under different atmospheric conditions, and for the proper alignment of a mosaic and dithered exposures, as it is the case of most PINGS observations. An IFS observation can be understood as a set of narrow-band images with a band-width equal to the spectral resolution (San06). These images can be recentered using the theoretical offsets determined by the DAR formulae (Filippenko, 1982) by tracing the intensity peak of a reference object in the FOV along the spectral range, and recentering it. The application of this method is basically unfeasible in slit spectroscopy, which represents one additional advantage of IFS. The correction can be applied by determining the centroid of a particular object or source in the image slice extracted at each wavelength from an interpolated data cube. Then, it is possible to shift the full data cube to a common reference by resampling and shifting each image slice at each wavelength (using an interpolation scheme), and storing the result in a new data cube. A pitfall of this methodology is that the DAR correction imposes

always an interpolation in the spatial direction as described above, a 3-dimensional (3D) data cube has to be created for each observed position, reducing the versatility given by the much simpler and handy RSS files.

It is important to note that the widely accepted formulation summarised by the work of Filippenko and the concept of parallactic angle are just a first order approximation to the problem. All this theoretical body is based on the assumption that all different atmospheric layers have an equal refraction index, are flat-parallel and perpendicular to the zenith. While this approximation is roughly valid, there are appreciable deviations due to the topography and landforms at the location of the telescope, since they alter considerably the structure of the low-altitude atmospheric layers. Therefore, the *a posteriori* correction of the DAR effect, only possible when using IFS, is the most accurate approach to the problem.

In general, the effects due to DAR in IFS are only important for IFUs with small spatial elements (≤ 1.5 arcsec) while for large ones (as it is the case of PPAK), the effect is mostly negligible, as experience with the instruments shows, especially when the airmass of the observations is 1.1 or below (Sandin et al., 2008). According to the DAR formulas one can calculate the angular separation in arcsec due to this effect for two different wavelengths under typical atmospheric conditions for a range of airmasses (Filippenko, 1982, Table 1). If we consider for example the wavelengths of Hα at λ 6563 and [O II] λ 3727 emission lines, the angular separation due to DAR is smaller than the radius of the PPAK fibres (1.35 arcsec) for airmasses below 1.3. Nevertheless, for each object in the sample the pointings which were observed at an airmass > 1.2 were analysed in order to test any effects due to DAR in our data. These individual pointings were transformed into 3D data cubes with a scale of 1"/pixel. Suitable sources within the field were selected (e.g. foreground stars, compact bright emission line regions) to perform a DAR correction creating continuum maps of these bright sources and looking for spatial deviations along the dispersion axis. No significant intensity gradients were found in any of the test fields.

Additionally, I looked for regions in which emission in the blue (e.g. [O II] λ 3727) could be observed, but no emission in the red (e.g. Hα λ 6563) and vice versa. In most cases, no strange [O II]/Hα ratios were found, although for some pointings there were not enough bright H II regions to perform this exercise. However, for a number of pointings peculiar deviations were found from the flux measured in both part of the spectra. All these pointings were observed with an airmass > 1.4 and correspond to: NGC 1637 (all 7 dithered pointings), NGC 6701 (all 3 pointings), and NGC 5474 (pointings 3, 4 & 5). In the case of particular studies which require a degree of spatial precision, one has to bear in mind the significance of the spatial-spectral information derived from the individual fibres of these pointings. However, as shown in chapter 5, integrated spectra over a large aperture (~ 5 arcsec) could be considered reliable.

Considering in general that the effects of DAR are very small given the relatively large size of the spatial elements of PPAK, that $\sim 70\%$ of the observations were performed with an airmass ≤ 1.35, and that no significant evidence of DAR effects were found in the analysis of our data (apart from the flagged pointings described above), no DAR correction was applied when building the final spectroscopic mosaics of the PINGS sample, avoiding the transformation of the RSS files to 3D data cubes and the undesirable interpolation of data. It is important to note that problems caused by atmospheric dispersion cannot be completely avoided in the spectroscopic study of extended objects like any other IFS observation, only for those observations performed in dithering mode a correction for the effect of DAR can be sought.

4.2.4 Second order spectra

In grating spectrometers and depending on the observed wavelength range, short-wave second-order spectra may superimpose on first-order long-wave spectra with wavelength twice as long as the short-wave. Usually the first-order spectra is obtained by preventing the superimposition of short-wave second-order spectra by using cut-off filters. In the PMAS pseudo-slit design the light from each fibre is dispersed by the grating and is projected as a single spectrum on the detector. Since there are many fibres at the pseudo-slit, a family of spectra (and their corresponding orders) is generated simultaneously on the CCD on each exposure. For both the lens array and the PPAK configuration, the IFU is equipped with a special slot inside the fibre spectrograph to use a bandpass filter in the fore optics section, either of which should eliminate the effect for any of the two IFU settings. This filter was used during all the observations of PINGS.

Hitherto, there has been no systematic investigation describing the effects of second-order contamination for the PMAS spectrograph. Such analysis would try to characterise the ratio of short-wave second-order spectra superimposed to a long-wave first-order spectral range for different diffraction grating. A quantitative analysis of the instrumental performance on this matter for a range of setups (including the PINGS setup) is planned for PMAS in the near future (Roth, private communication). No evidence of second-order contamination was found during the analysis of the PINGS data set.

In summary, the two most important sources of error in the data reduction arise from the sky subtraction and the flux calibration. Several tests were performed and new techniques applied in each case in order to minimise the magnitude of the uncertainties. It was found that the sky subtraction cannot be applied as part of any standard reduction pipeline and has to be considered on an individual basis, depending on the observing mode, configuration and strategy. On the other hand, the maximum expected error in the absolute flux calibration for those objects in which a broad-band imaging recalibration was applied is of the order of 20%, being slightly larger in a narrow blue spectral region $\lambda < 3800$ Å. For those objects without broad-band imaging, the absolute flux calibration error is of the order of 30%. However, the absolute error is better than 20% for objects observed during photometric conditions and/or with high S/N. The colors, spectral features and gradients are completely reproduced when comparing our data with previously published long-slit observations (see chapter 5).

DAR effects were found to be negligible due to the large size of the spatial elements of PPAK, no strong evidence of DAR was found in the several test pointings analysed. However all individual IFU positions for which the observations were performed with an airmass > 1.3 were flagged. With respect to cross-talk, the new extraction method described in subsection 4.1.3 proved to suppress this effect to a negligible level for the range of spectral intensities in the PINGS observations. Furthermore, no evidence of any second-order contamination has been found during the data reduction and analysis of the PINGS data set. As explained in chapter 2, the contamination of the 2nd order, up to 7200 Å, is expected to be lower than 1/10000, being negligible for the science case of this dissertation.

4.2.5 The PINGS data set

The final PINGS data set contains more than 50 000 flux calibrated spectra for a sample of 17 galaxies covering in total an observed spectroscopic area of nearly 100 arcmin^2. Table 3.15 shows a summary of the observations, including the number of individual IFU pointings observed for the mosaic of each galaxy, the observational status of the mosaicing, the total number of spectra, and additional individual comments

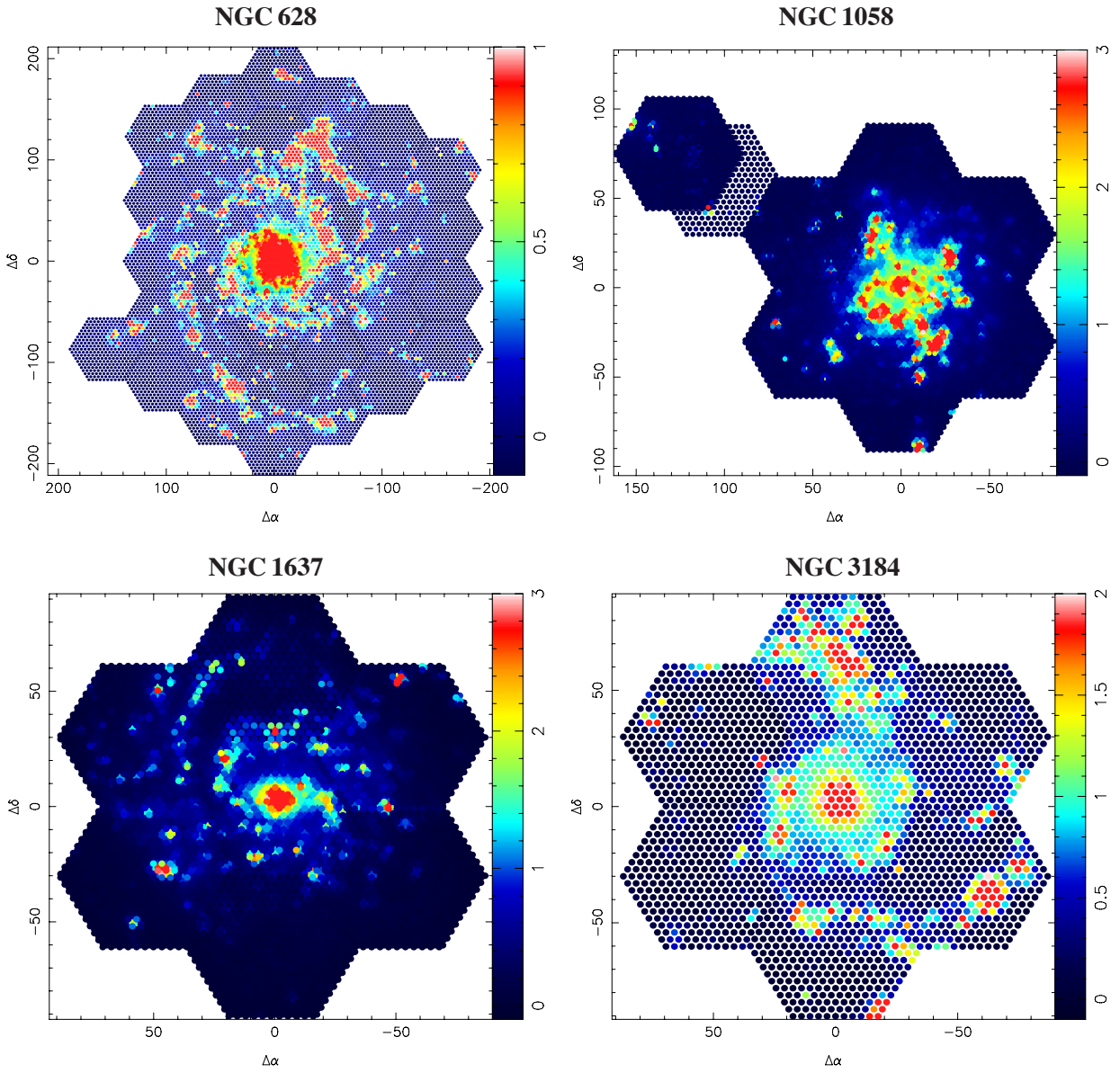

Figure 4.19: Examples of spectroscopic mosaics of NGC 628, NGC 1058, NGC 1637 and NGC 3184. Each panel shows an intensity level *narrow-band* map between 6550 and 6650 Å in units of 10^{-16} erg s^{-1} cm^2 arcsec^{-2}.

on each object. The spectroscopic data set samples the observed objects with fibre circular apertures of ~ 2.7 arcsec in diameter, covering the optical wavelength range between $\sim 3700-7100$ Å, which includes the most prominent recombination and collisionally excited emission lines from [O II] $\lambda\lambda$ 3727, 3729 to [S II] $\lambda\lambda$ 6717, 6731.

Figure 4.19 and Figure 4.20 show examples of the PINGS spectroscopic mosaics. They images represent a *narrow-band* extraction between 6550 and 6650 Å, i.e. corresponding to a map centered at the Hα emission line. The effect of dithered observations is clearly seen in NGC 1058, NGC 1637, NGC 3310 and NGC 67010, while for NGC 628, NGC 3184, NGC 7770-7771 and the Stephan's Quintet, the gaps between the fibres are noticeable. The regions of overlapping fibres between adjacent pointings are seen in the mosaics of NGC 628 and NGC 3184. For NGC 1058, one of the outlying pointings was observed in non-dithered mode, this corresponds to a blind-offset (see section 3.4).

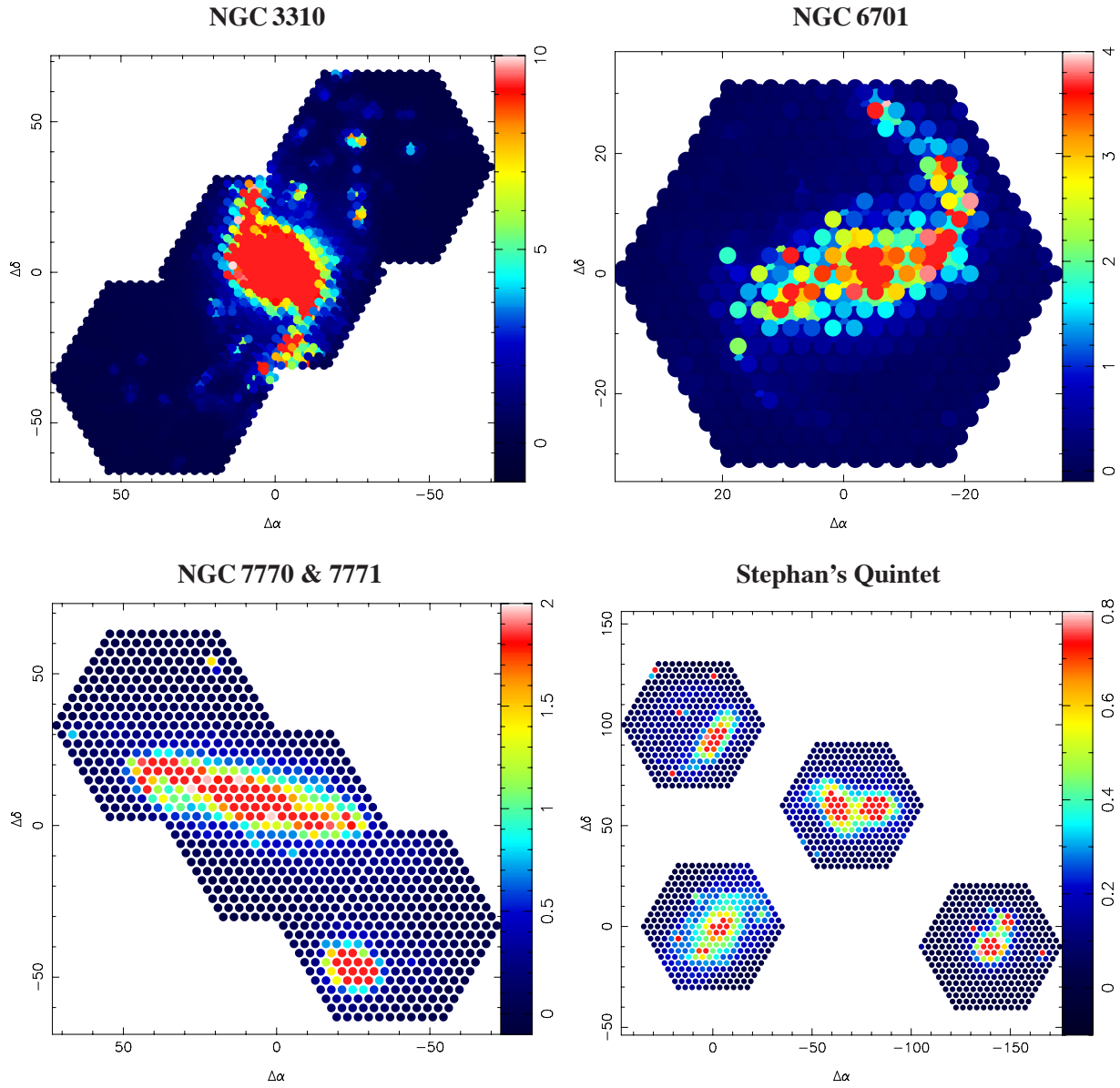

Figure 4.20: Spectroscopic mosaics of NGC 3310, NGC 6701, NGC 7770, and the Stephan's Quintet. Units as in Figure 4.19.

The mosaics obtained after the reduction process described in this chapter represent the first final version of the PINGS data set. Depending on the particular science case, the mosaics can be modified in order to obtain a more convenient sub-sample. In particular, for the study of the gas-phase properties described in the following chapters, the mosaics were further processed to remove regions with low signal-to-noise, foreground stars and SNe.

Given the spatial and spectral information provided by the IFS mosaics of PINGS, it is possible to reconstruct different images of the target by selecting a spectral region at which particular information is sought, e.g. the *narrow-band* maps of Figure 4.19 and Figure 4.20. As an additional example of the potential use of the PINGS data set, Figure 4.21 shows a pseudo-RGB colour image of the IFS mosaic of NGC 628. This picture was generated using the reconstructed images obtained after multiplying the IFS mosaic of NGC 628 with the response functions of the *B*, *V* and *R*-band filters as discussed in subsection 4.1.8. The different band images were separated in RGB channels and merged to produce the image shown in Figure 4.21.

The spiral arms of the galaxy, the bright bulge and foreground stars are clearly seen with their characteristic colours when compared with a real RGB image of the same galaxy obtained from broad-band imaging[5], as Figure 4.22. Pointings of low signal-to-noise are noticeable in the pseudo-RGB image, appearing darker than the adjacent pointings. They correspond to the regions of deficient sky-subtraction identified in subsection 4.2.1. The lines and features at the edges of the image are artifacts due to the interpolation scheme.

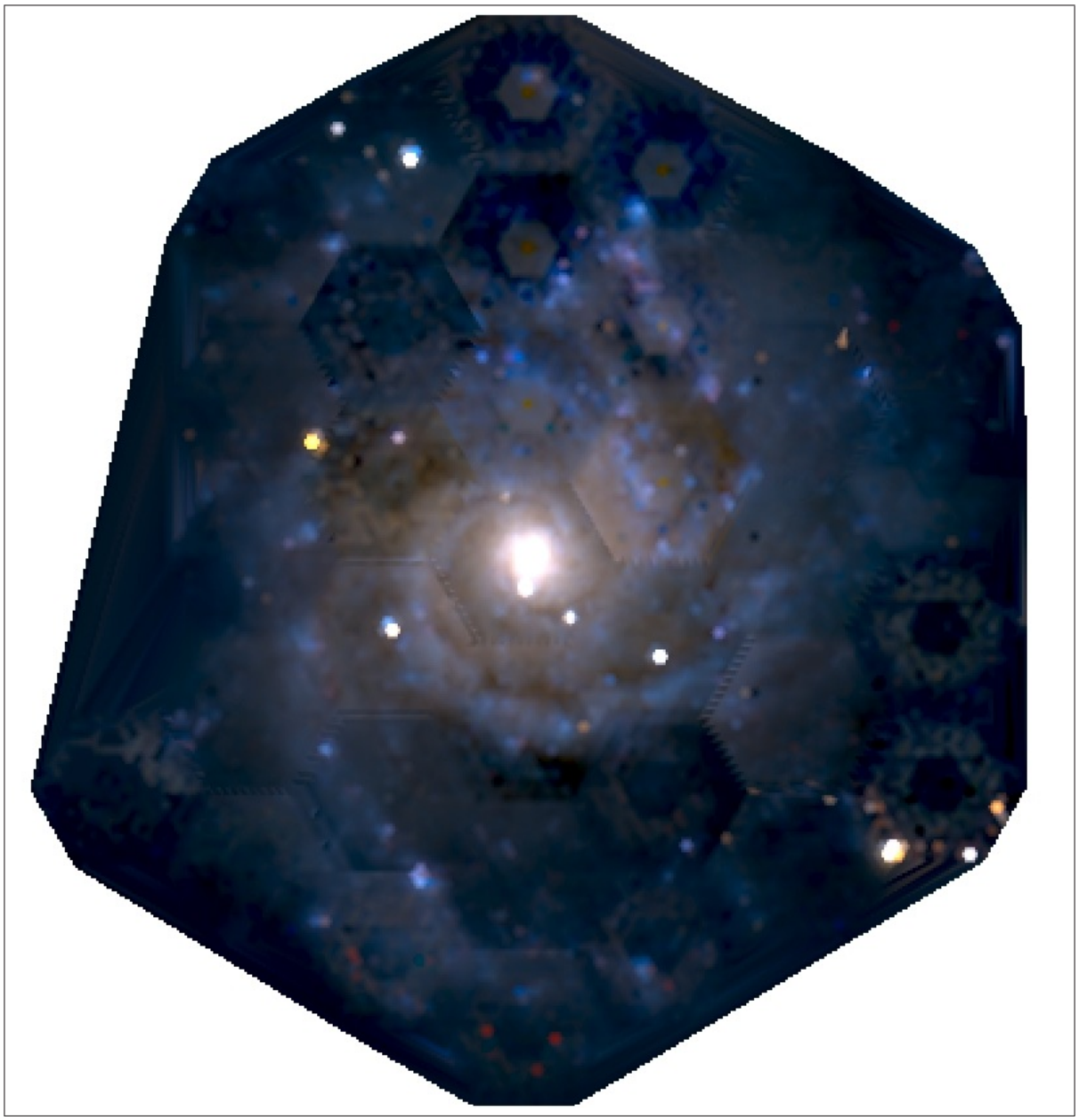

Figure 4.21: Pseudo-RGB image extracted from the IFS mosaic of NGC 628, after multiplying the spectra with the SINGS *B*, *V* and *R*-band filters.

[5] RGB broad-band image obtained at CAHA, original source at `http://www.caha.es/sanchez/`.

Figure 4.22: RGB broad-band image of NGC 628 obtained by the 2.2m telescope of the Calar Alto observatory.

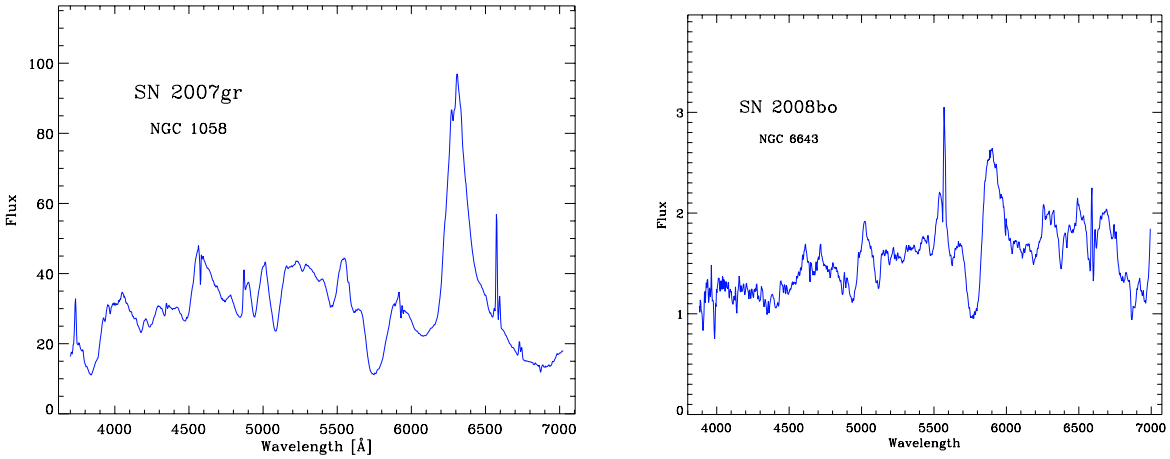

Figure 4.23: Extracted spectra of SN 2007gr in the mosaic of NGC 1058 and SN 2008bo in NGC 6643. The flux units are 10^{-16} erg s^{-1} cm^2 Å^{-1}. Some nebular emission lines are seen superimposed to the SNe spectra.

4.2.6 SN 2007gr and SN 2008bo in the PINGS mosaics

A pair of supernovae were observed during the acquisition of the PINGS sample, these are SNe 2007gr and 2008bo, located in NGC 1058 and NGC 6643 respectively. NGC 1058 was observed during the nights of the 7th and 8th of December 2007. During this period, the Supernova 2007gr, previously discovered by the Lick Observatory Supernova Search on the 15th of August 2007 (Chornock et al., 2007), was still present in the galaxy. On the other hand, SN 2008bo was observed during the mosaicing of NGC 6643 the 2nd of June 2008. This SN was previously discovered by the Taurus Hill Observatory, Finland, on the 1st April 2008.

SN 2007gr was located at 24.8" West and 15.8" North of the nucleus of NGC 1058, with coordinates RA $02^h\,43^m\,27.^s98$ and Dec: $+37^\circ\,20^m\,44.^s7$, between two bright foreground stars. The left panel of Figure 4.23 shows the optical spectrum of the supernova extracted from the IFS mosaic, showing the typical spectrum of a Type Ic core collapse supernova, with the lack of hydrogen, helium and silicon absorption lines. Emission lines of [O II] λ 3727, Hα, [N II] λ 6548, 6584 and [S II] $\lambda\lambda$ 6717, 6731 are clearly seen on top of the SN spectra, probably reflecting the environment of the H II region in which this supernova exploded. As described by Valenti et al. (2008), SN 2007gr showed an average peak luminosity but unusually narrow spectral lines and an almost flat photospheric velocity profile. SN 2007gr motivated an extensive observational campaign for several reasons: it was discovered at a very early stage (5 days after the explosion), it was located in a relatively close distance galaxy, it was the nearest stripped-envelope carbon-rich SNe ever observed, and a suitable candidate for progenitor search (Valenti et al., 2008).

SN 2008bo was discovered at 31" North and 15" West of the nucleus of NGC 6643, with coordinates RA $18^h\,19^m\,54.^s34$ and Dec: $+74^\circ\,34^m\,20.^s9$, with a magnitude of 16.6. The spectrum of SN 2008bo shown in right panel of Figure 4.23 is of type Ib (Navasardyan et al., 2008). Wide-field IFS may become one of the main resources for SNe research groups to find SNe progenitors in previously observed galaxies. The progenitor supergiant stars ($M > 8\ M_\odot$) that at the end of their lives explode as core-collapse supernovae may show a strong stellar spectrum that could be recovered from 2D spectroscopic maps with enough spatial resolution. Furthermore, the nebular emission from the spatially adjacent spectra could provide information on the environment in which these SNe explosions occur.

5

Integrated properties

Optical integrated spectrophotometry provides a powerful means of investigating the physical properties of galaxies at different epochs in the history of the universe. Spectral diagnostics based on integrated optical spectrophotometry can be used to constrain the star formation rate, star formation history, stellar mass, chemical abundance, dust content, and other main drivers of galaxy evolution (e.g. Tremonti et al., 2004). The analysis of the integrated spectra in nearby objects can be used to assess the limitations imposed by high-redshift surveys, such as their limiting magnitude and incomplete spatial coverage (or aperture bias), factors that may be important given that many physical properties of galaxies vary depending on the geometry and position (e.g. stellar populations, metallicity, extinction, etc.).

The study of integrated spectral properties of nearby galaxies poses several observational challenges in classical long-slit spectroscopy. The main limitation resides in obtaining an integrated spectrum of an object that is usually larger than the typical length of a long slit ($\sim 3-5$ arcmin). One by-product of 2D spectroscopy and IFS data sets is the intrinsic capability of adding up all the spectra within an observed field or mosaic into a single spectrum, i.e. using the IFU as a large-aperture spectrograph to obtain the integrated spectra of a given FOV. The PINGS sample is an ideal data set for this purpose given that the spectroscopic mosaics cover, in most cases, the entire optical radius of the galaxy. The integrated spectra derived from PINGS can be used to study the real average spectroscopic properties of a given nearby, large angular size galaxy, as opposed to previous studies that attempted to describe their average properties by the analysis of individual spectra taken from different regions, or by targeting objects with a limited extraction aperture which recovers only a fraction of the total optical light.

In this chapter, I present high signal-to-noise integrated spectra for the whole PINGS sample obtained by co-adding the spectra from their corresponding mosaics, using both simulated apertures and the entire IFS mosaics. Comparisons of these data with previously published integrated spectra are presented for a number of objects in the sample. Furthermore, an analysis of the gas-phase integrated properties of each galaxy in the sample is presented. For this purpose, I describe the techniques implemented in order to decouple the gas

emission from integrated spectra of the galaxies, and the methodology employed to measure the emission line intensities.

5.1 Integrated spectra: comparison with literature

Classically, the spectroscopic studies of nearby galaxies were focused on their nuclear or high surface brightness regions, whose physical properties in general are not representative of the whole galaxy. In recent times, a good deal of effort has gone into obtaining optical spectroscopy of local galaxies that could be compared with observations of distant ones. Examples are large fibre-optic redshift surveys, like the Sloan Digital Sky Survey (SDSS; York et al., 2000), and the Two Degree Field Galaxy Redshift Survey (2dFGRS; Colless et al., 2001), which together provide the opportunity to study the stellar and emission-line properties of nearby galaxies with unprecedented statistical precision. However, they suffer from the incomplete spatial coverage that may be particularly severe, since many physical properties of galaxies vary with galactocentric radius (e.g. Tremonti et al., 2004).

A solution to the incomplete spatial coverage of spectroscopic observations on nearby objects, consists on using sequential methods that use time to scan a target while recording the spectral information. The standard method for obtaining integrated spectra in nearby objects was developed by Kennicutt (1992). The so-called drift-scanning technique consists of moving a narrow, long slit back and forth across the optical extent of a nearby galaxy that may subtend several arcminutes on the sky. This observational technique results in a luminosity-weighted integrated spectrum analogous to traditional (spatially fixed) spectroscopy of distant galaxies. Kennicutt (1992) conducted in this way the first systematic analysis of the integrated spectroscopic properties of nearby galaxies.

As mentioned before, a particular interesting use of IFS datasets is that the observed spectra can be combined in order to produce an integrated spectrum of the object. One advantage of 2D spectroscopy with respect to the drift-scanning is the simultaneous capture of spectral and spatial information. Apart from rendering the process more efficient, simultaneity guarantees the homogeneity of the data. Another advantage is that this technique allows to perform a comparison study between the integrated and the spatially resolved properties of a galaxy. Given that a number of objects in the PINGS sample have been previously observed using the drift-scanning technique, this section is devoted to comparing the spectroscopic data found in the literature with extracted spectra from the PINGS sample. The drift-scan spectra was obtained from the following sources:

1. SINGS ancillary data, Kennicutt et al. (2003).

2. The Integrated Spectrophotometric Survey of Nearby Star-forming Galaxies, Moustakas & Kennicutt 2006b, hereafter MK06.

SINGS: As part of the ancillary data of the SINGS survey, optical spectra were acquired for the sample galaxies in the wavelength range $0.36 - 0.70$ μm, with a resolution of 8 Å. Three different types of spectra were observed: 1) Nuclear spectra (with a 2".5 wide aperture) sampling the brightest central spot of the galaxy; 2) 20" drift scans around the central region; and 3) 55" drift scans, similar to the 20" drift scans. As stated in the reference documentation, absolute spectrophotometric accuracy is not guaranteed. The relative spectrophotometric accuracy ranges from $1 - 4\%$ based on the relative scatter in the derived sensi-

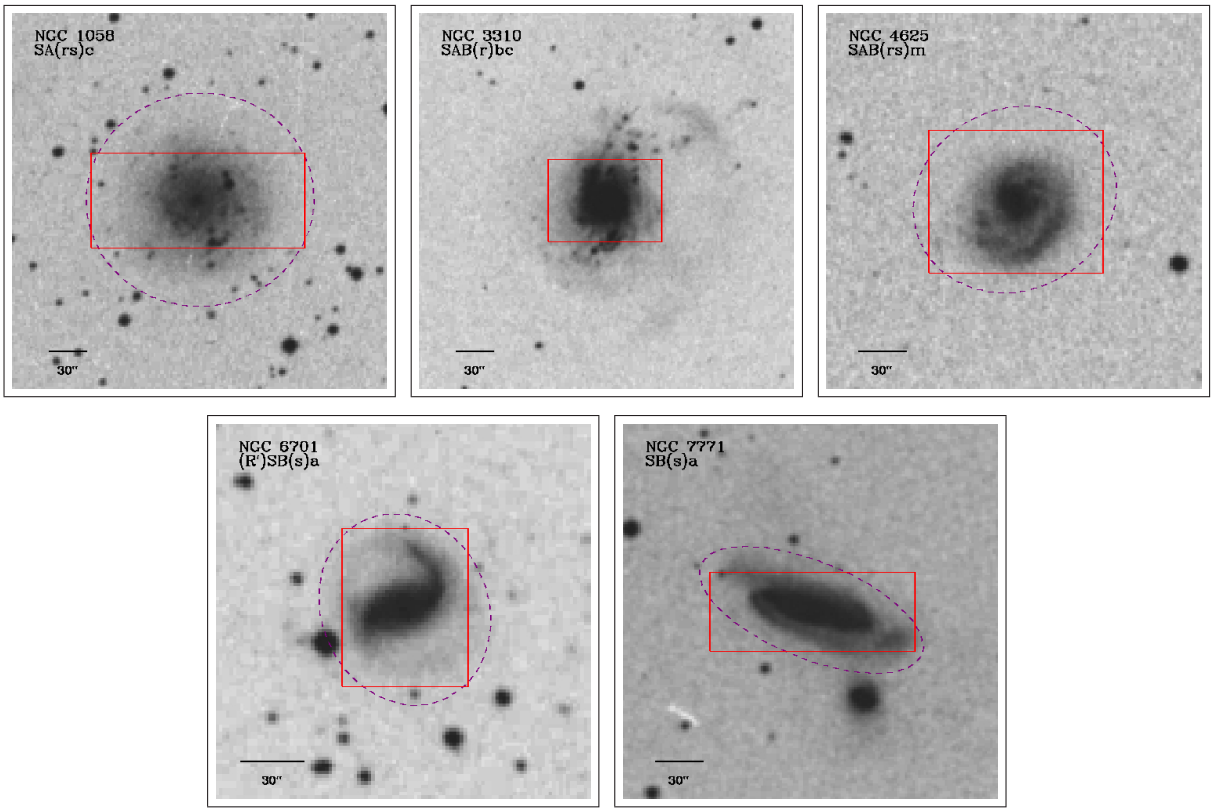

Figure 5.1: Digital Sky Survey images of the PINGS galaxies observed by MK06. The dashed purple ellipse shows the 25 mag arcsec^{-2} surface brightness isophote. The red box delineates the integrated spectroscopic aperture used by the drift-scan. Figures adapted from MK06.

tivity function. The PINGS objects observed by SINGS are: NGC 628, NGC 3184, NGC 4625 & NGC 5474.

MK06: These authors obtained spatially integrated optical ($0.36-0.69\ \mu$m, ~ 8 Å FWHM) spectrophotometry for 417 nearby galaxies of a diverse range of galaxy types, including ultraviolet- and infrared-luminous starbursts, galaxies with enhanced nuclear or circumnuclear star formation, peculiar galaxies, and interacting/merging systems, together with a large number of normal galaxies. The PINGS objects observed by MK06 are: NGC 1058, NGC 3310, NGC 4625, NGC 6701, NGC 7770 & NGC 7771 (see Figure 5.1).

The extraction slits and comparison techniques described in this section were the same used for the analysis of the integrated spectra in order to derive the absolute flux calibration ratios as detailed in subsection 4.1.10. However, the comparison presented here are based on the final absolute flux calibrated mosaics.

5.1.1 NGC 628

Figure 5.2 shows in the upper panel, the comparison between the drift-scan spectrum of the central region of NGC 628 (light-blue colour), and the integrated spectrum extracted from the PINGS mosaic (black-line), after co-adding the spectra within a simulated aperture with the same size, location and PA as the SINGS drift-scan. The SINGS drift-scan corresponds to a 20" aperture and 70º PA. The bottom panel of Figure 5.2 shows a 100 Å width narrow-band map of the mosaic of NGC 628 centered at Hα, the red box in the centre corresponds to the simulated aperture from which the IFS spectrum was extracted. The coordinates, size and PA of the aperture were obtained from the header of the SINGS data file. Given that the PINGS RSS

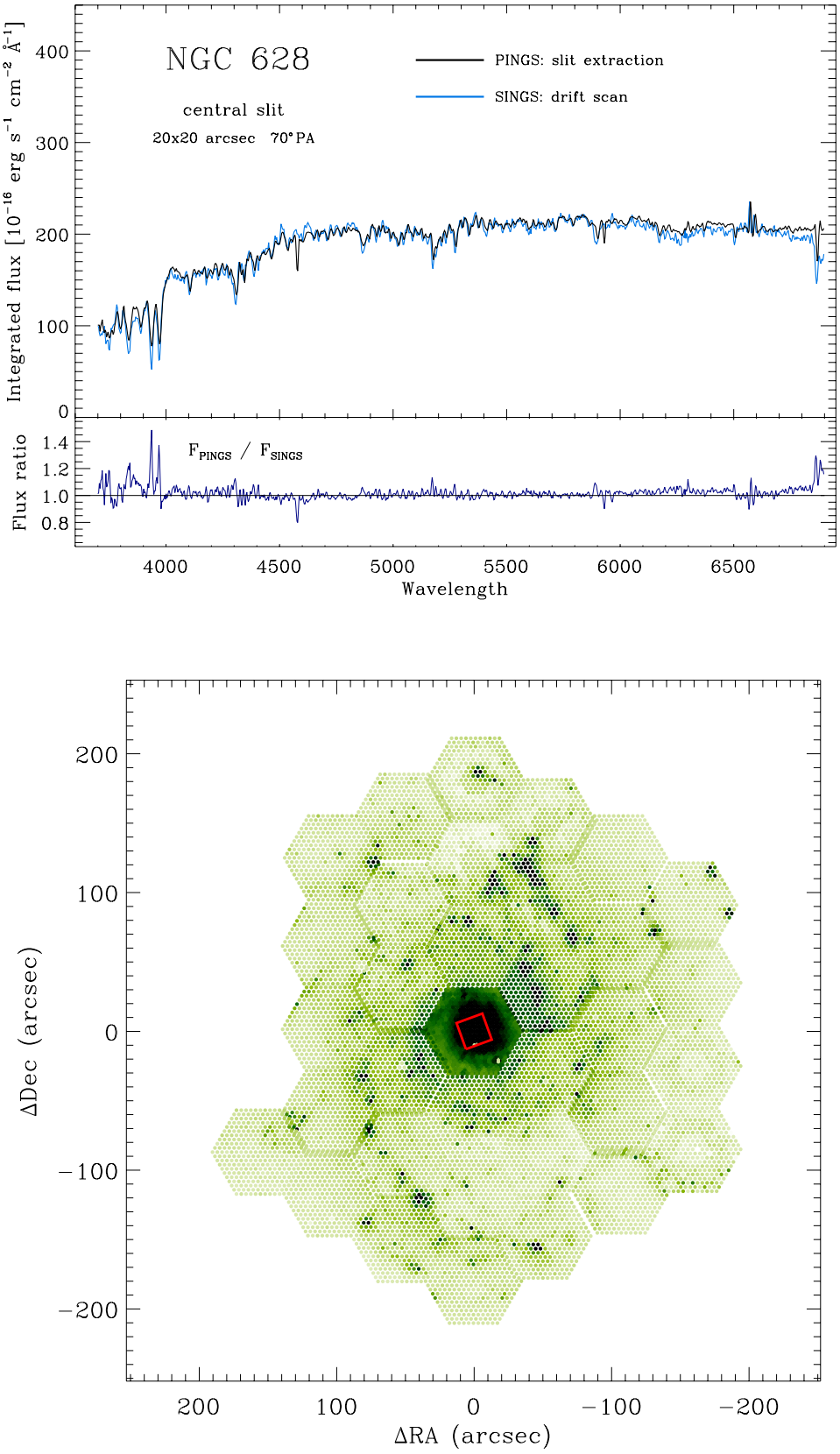

Figure 5.2: Comparison of the integrated spectrum of NGC 628 derived from the PINGS slit-extraction and the drift-scan spectrum of the SINGS ancillary data.

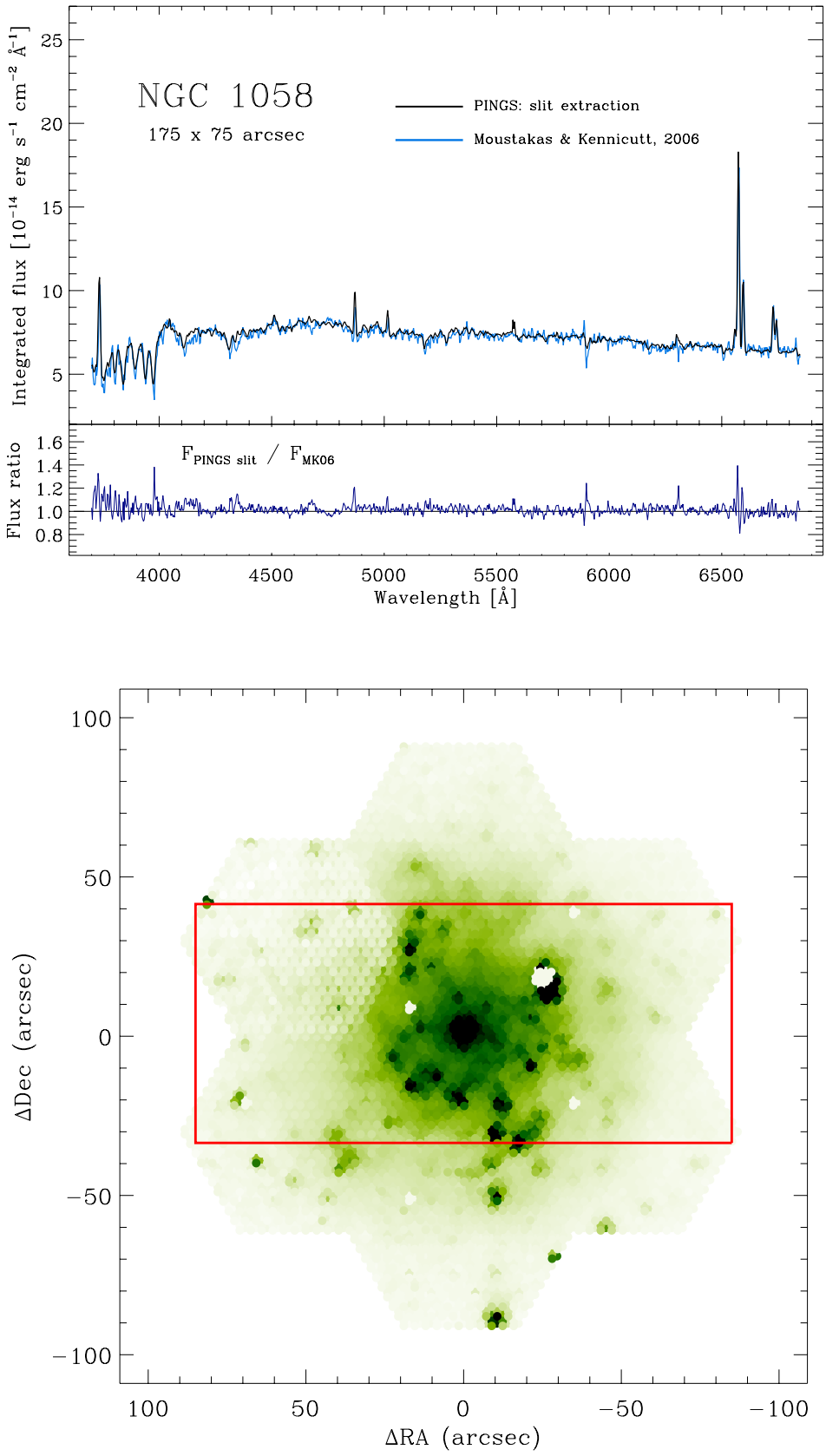

Figure 5.3: Comparison of the integrated spectrum of NGC 1058 derived from the PINGS slit-extraction and the drift-scan spectrum of the MK06 data. The slit-aperture can be compare to the DSS image in Figure 5.1.

files contain the astrometry information, it was possible to centre the aperture very accurately. Some gaps in between the edges of the pointings are seen in the map of NGC 628. They are due to the re-centering of the individual pointings after comparing with the broad-band images as discussed in subsection 4.1.10. Holes in the mosaic (white spots) are due to the removal of foreground stars (10 in total within the FOV of NGC 628). As expected from the spectrophotometric re-calibration of the mosaics, there is a very good agreement between both datasets. The top-panel of Figure 5.2 shows in the lower part the flux ratio between the two spectra, which is consistent to unity and within the 20% error of the absolute flux calibration for most of the spectral range. There is however a small disagreement at wavelengths shorter than 4000 Å. The absorption lines in the SINGS spectrum are deeper than in the PINGS data. The difference in this spectral region is expected due to the degradation of the CCD sensitivity in the blue, as explained in subsection 4.2.2.

5.1.2 NGC 1058

Similarly, Figure 5.3 shows in the upper panel the comparison of the integrated spectrum of NGC 1058 extracted from the PINGS mosaic to the drift-scan spectrum obtained by MK06 from this galaxy. The bottom panel shows the PINGS spectroscopic mosaic diagram of the central region of NGC 1058 (without the outlying positions) with same intensity levels as the map of NGC 628. The rectangular shape shows the slit-aperture used in the drift-scan technique implemented by MK06 to obtain the integrated spectrum of this galaxy, which can be compared to Figure 5.1. The MK06 drift-scan corresponds to a 175×75 arcsec aperture and 90^{o} PA. Three foreground stars and the supernova SN 2007gr (see subsection 4.2.6) were removed from this mosaic. According to MK06, foreground stars were also removed before obtaining the integrated spectrum. The black solid line spectrum in the top-panel was obtained by extracting from the PINGS mosaic all the individual spectra within the area enclosed by the rectangular shape and taking into account the overlapping regions and the covering fraction of the fibres due to the dithering technique applied to this galaxy. The blue line corresponds to the spectrum obtained by MK06 using the drift-scan technique. As in the previous case, there is a very good agreement between the two data sets, the emission lines and the continuum are well matched, even the sky-subtraction seems to be better in the PINGS spectrum (note the Na I λ5893 residual feature in the MK06 spectrum).

5.1.3 NGC 3184

The drift-scan spectrum of NGC 3184 was obtain from the SINGS ancillary data. The SINGS drift-scan corresponds to a 20" aperture and 120^{o} PA. The bottom panel of Figure 5.4 shows the Hα mosaic diagram of NGC 3184 with the red box corresponding to the aperture from which the IFS spectrum was extracted. Note that the slit is not well-centered in the galaxy bulge. The position of the aperture was obtained from the coordinates in the header of the SINGS data file. The top-panel of Figure 5.4 shows the comparison between the two spectra. Although there is a general agreement in the shape of the continuum and the spectral features along the whole spectral range, there is a small shift in the absolute scale, being the PINGS spectrum the one with lower flux. However, this difference is still within the errors of the flux calibration, with a slightly higher difference in the blue part of the spectrum, due to the reasons explained before. Given the difference found in the comparison, as an additional exercise, another spectrum was extracted with the same size and PA as before, but centered at the galaxy bulge with offsets (RA,Dec) = (0,0), presuming that probably the reported SINGS coordinates were wrong. However, this spectrum shows completely different spectral features and intensity levels than the SINGS spectrum.

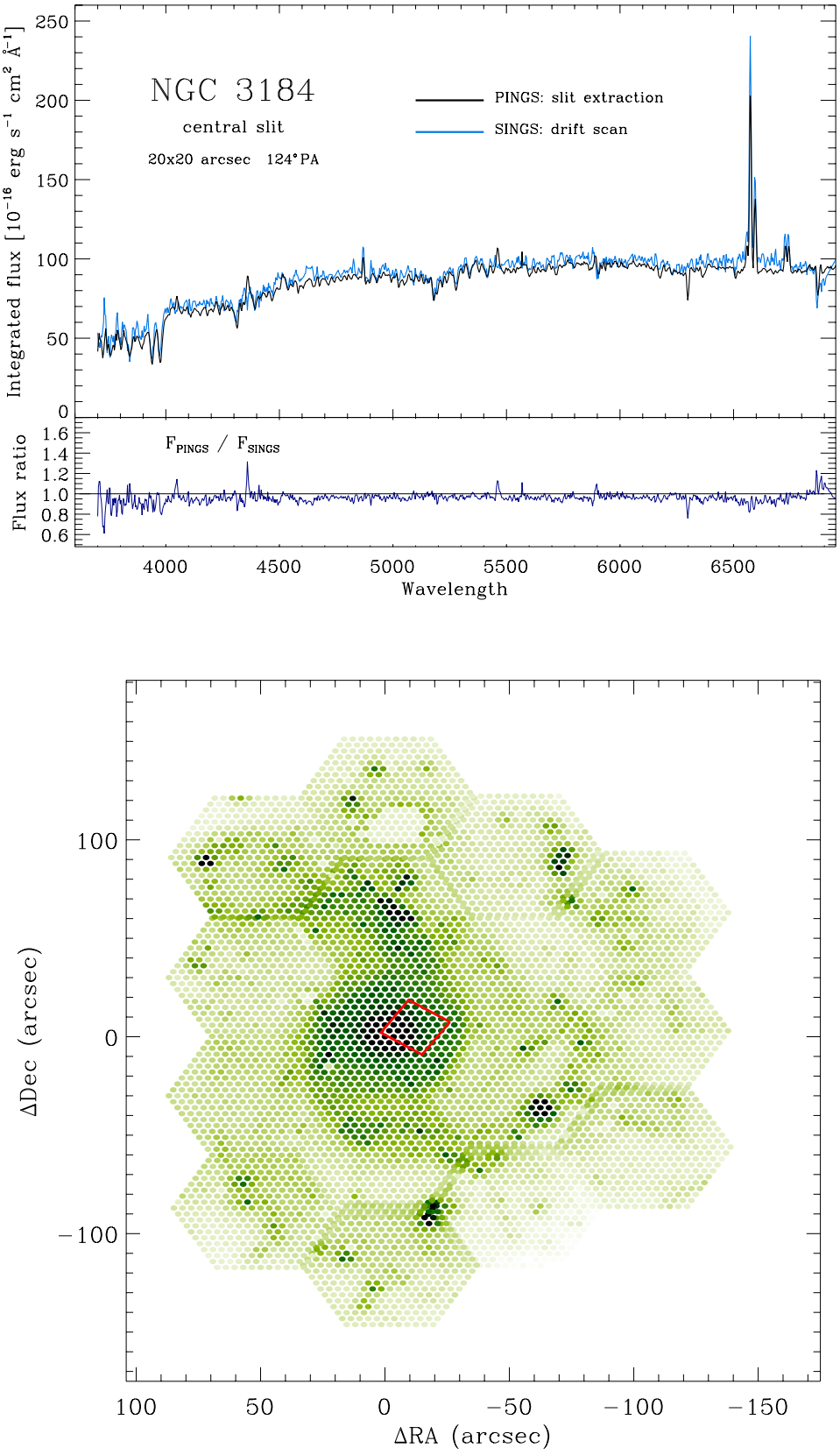

Figure 5.4: Comparison of the integrated spectrum of NGC 3184 derived from the PINGS slit-extraction and the drift-scan spectrum of the SINGS ancillary data. Note that the location of the aperture is not centered in the galaxy bulge.

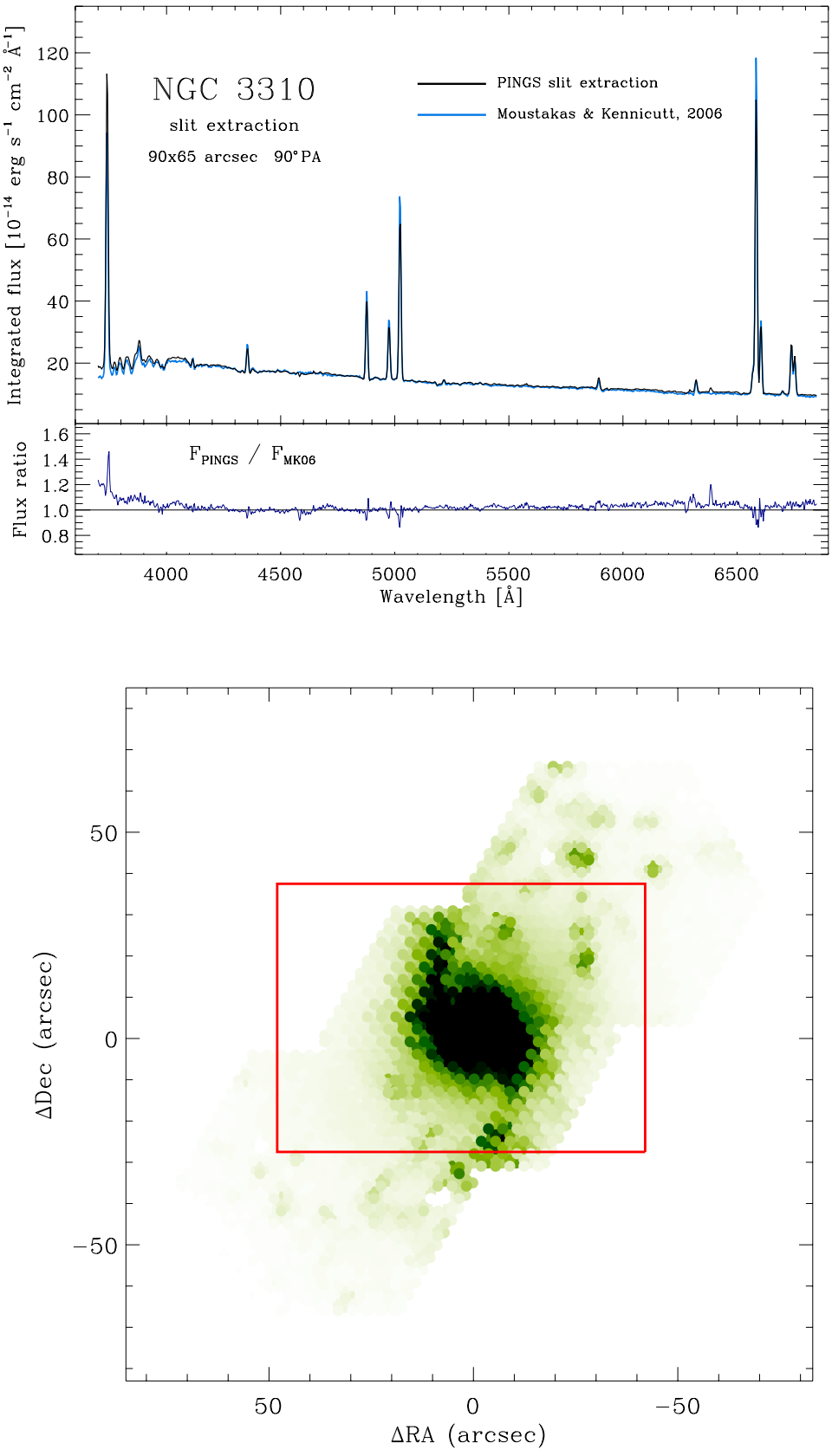

Figure 5.5: Comparison of the integrated spectrum of NGC 3310 derived from the PINGS slit-extraction and the drift-scan spectrum of the MK06 data. The slit-aperture can be compare to the DSS image in Figure 5.1.

Three foreground stars were removed from the mosaic of NGC 3184, a particular large one was found at (RA,Dec) $\sim$ (0,100). The mosaic shows also some white holes not related to foreground objects. These are due to bad fibres detected during the reduction process, associated with a normal degradation in the sensitivity of these fibres in the PPAK bundle. The detection of this problem was not obvious and trivial. Thanks in part to the careful analysis of the PINGS data, this problem was reported to the staff of Calar Alto observatory.

5.1.4 NGC 3310

The top-panel of Figure 5.5 shows the integrated spectra of the starburst galaxy NGC 3310. The blue line corresponds to the MK06 drift-scan integrated spectrum. The black line shows the integrated spectrum obtained after co-adding all the spectra within the rectangular pattern corresponding to the MK06 slit-aperture shown in the bottom-panel of the same figure (which can be compared to Figure 5.1), and considering the overlaps in the mosaic due to the dithering observing method and the non-standard construction of the mosaic. The MK06 drift-scan corresponds to a 90×65 arcsec aperture and 90^{o} PA. No foreground stars were found within this field. In this case, the PINGS extraction is spatially incomplete when compared to the rectangular area of the MK06 aperture. Nevertheless, all the spectral features are reproduced quite well when we compare the PINGS spectrum with the MK06 data. The apparent disagreement seen in some of the emission lines can be explained in part to the different spectral resolution of the data sets (MK06 ~ 8 Å, PINGS ~ 10 Å in FWHM) causing that the peaks of the emission lines differ in height. A stronger effect is seen in the blue spectral region ($\lambda < 3800$ Å) due to the reasons explained before.

5.1.5 NGC 4625

Drift-scan spectra of NGC 4625 is available in both the SINGS ancillary and the MK06 data sets, although each spectrum was obtained using different apertures. The top-panel of Figure 5.6 shows the mosaic diagram of NGC 4625. The red box corresponds to the SINGS 20 arcsec square nuclear aperture (90^{o} PA), while the blue rectangle corresponds to the 110×90 arcsec (90^{o} PA) aperture used by MK06 (see Figure 5.1). The middle and bottom panels of Figure 5.6 show the comparison between the IFS integrated spectra with the SINGS and MK06 spectra respectively. In the first case, the black line corresponds to the integrated spectrum obtained after co-adding the spectra within the aperture SINGS aperture. In the bottom-panel, the black line corresponds to the integrated spectrum of the whole mosaic. In both cases, the overlaps in the mosaic due to the dithering were considered. In both plots, the blue line corresponds to the drift-scan spectrum, note that the units are different in each plot. No foreground stars were found within this field.

In the case of the SINGS aperture, the shape of the continuum and spectral features are well reproduced, with a flux level slightly higher for the PINGS spectrum. Differences of the order of 20% are found for wavelengths shorter than 4000 Å. For the MK06 case, the difference between the spectra is expected, considering the spatially incomplete coverage of the IFS mosaic with respect to the MK06 aperture, although the spectral features in the blue are well reproduced. Note the stronger sky residuals near the [O I] λ6300 region for the MK06 spectrum. This comparison represents an example of how aperture bias may influence the determination of integrated properties for both near and distant galaxies. As a complementary note, the flux calibration ratio for NGC 4625 based on the integrated spectra (see subsection 4.1.10) was derived using the SINGS drift-scan spectrum.

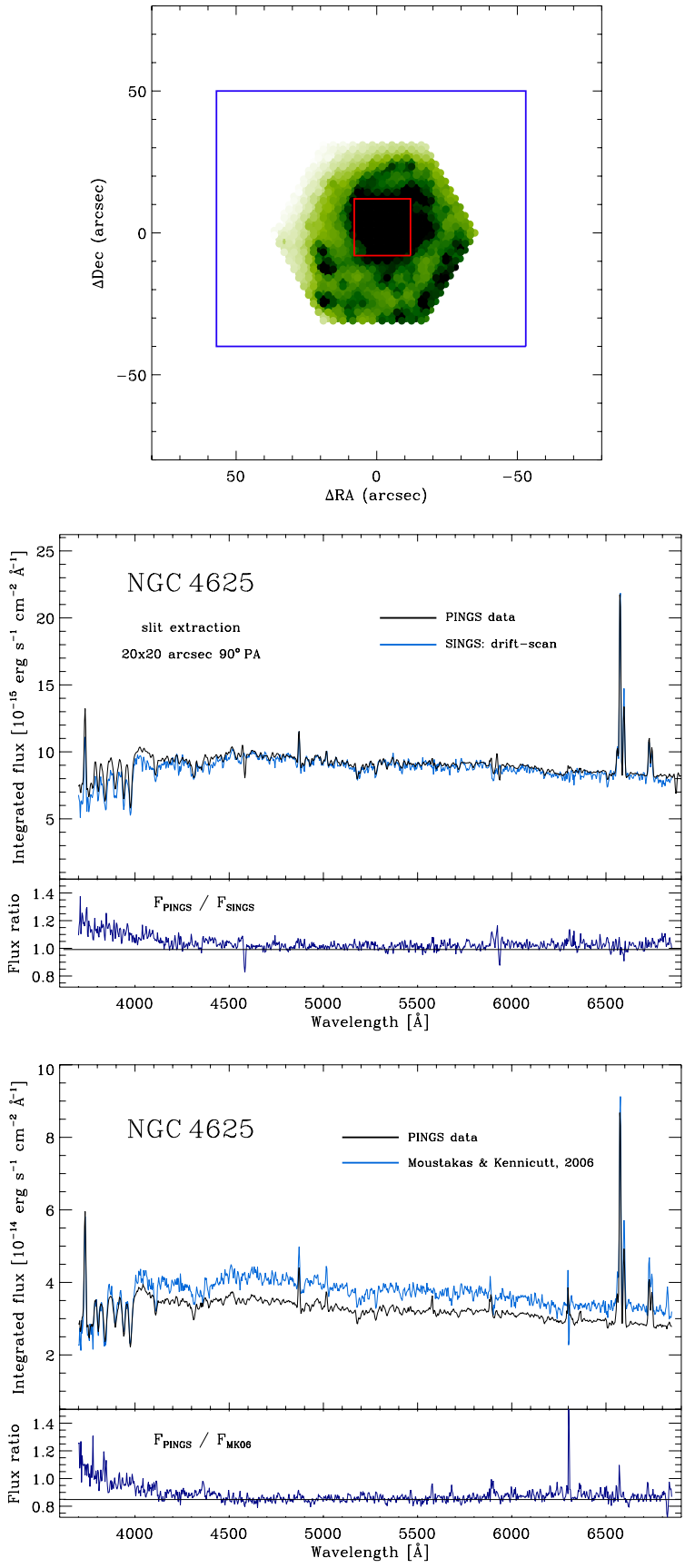

Figure 5.6: Comparison of the integrated spectra of NGC 4625 derived from the PINGS data set and the drift-scan spectra of the SINGS ancillary data (red box and middle-panel) and the MK06 data (blue rectangle and bottom-panel).

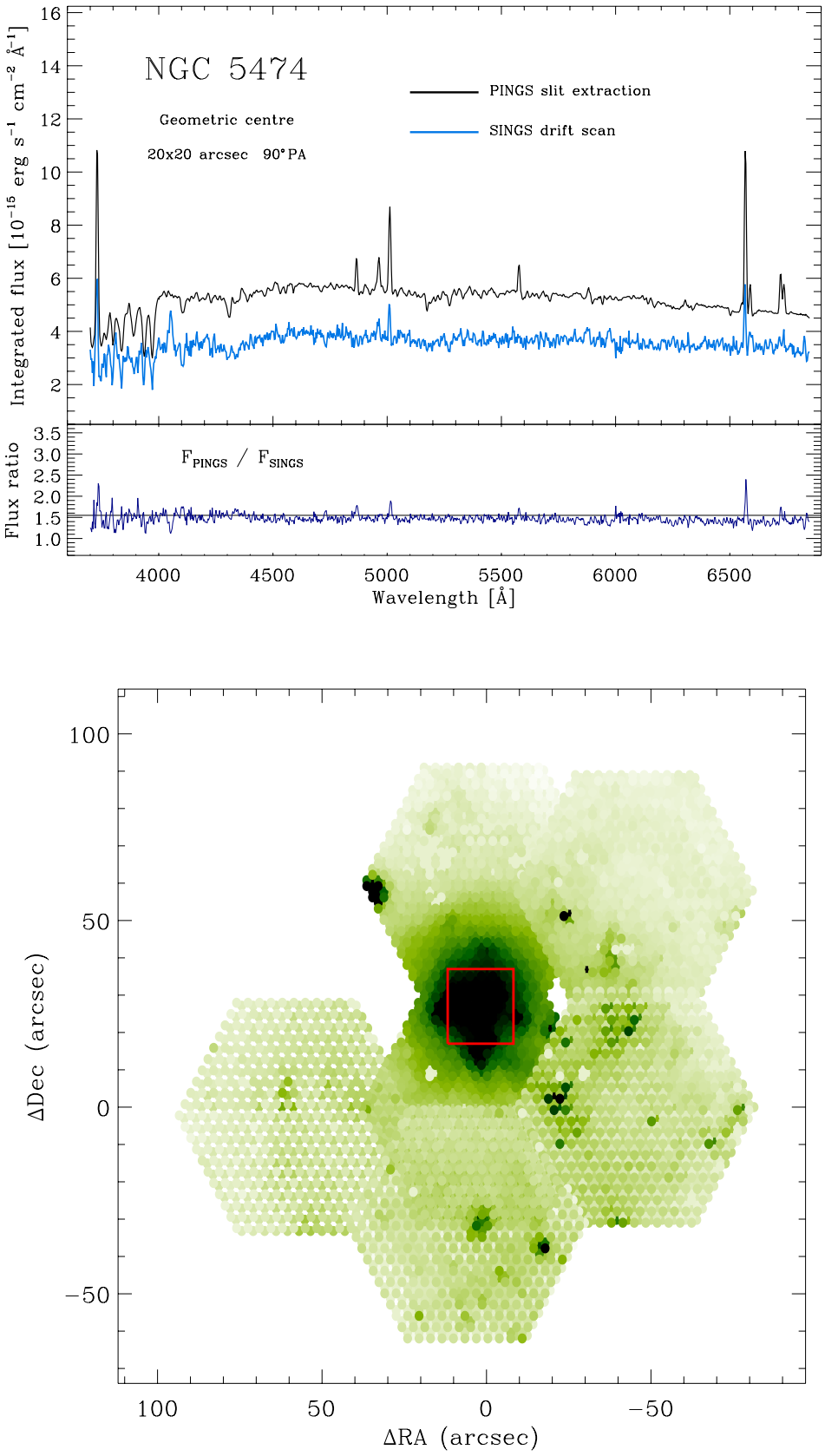

Figure 5.7: Comparison of the integrated spectrum of NGC 5474 derived from the PINGS slit-extraction and the drift-scan spectrum of the SINGS ancillary data.

5.1.6 NGC 5474

The bottom panel of Figure 5.7 shows the mosaic diagram of NGC 5474. Clearly, the pointings do not follow the standard mosaicing scheme with one central pointing and a concentric ring of PPAK positions. Given that this is an asymmetric galaxy, the position of the central pointing was chosen so that the whole mosaic would cover the optical radius of the galaxy, as shown in Figure 3.9. This configuration implies an offset of the central position with respect to the bright bulge of the galaxy. The first two positions were observed following this scheme. However, positions 3 to 6 were observed during service mode, and despite instructions were given clarifying this point, the previous central coordinates were not recovered and the bright bulge was chosen as the reference for the mosaicing. The alignment of these pointings was possible using the comparison with broad-band images, as described in subsection 4.1.10. In this process, the astrometry of the broad-band images was applied to the PINGS mosaic.

The drift-scan spectrum of NGC 5474 was obtain from the SINGS ancillary data, corresponding to a 20" aperture and 90º PA. However, according to the coordinates in the header of the SINGS spectrum, the position does not correspond to the central bulge and/or to the geometric centre of the galaxy disc. The extracted spectrum from the IFS data at this position shows completely different spectral features and intensity levels than the drift-scan spectrum. Given that the reported astrometry of SINGS was wrong, a new extraction was tested, centering the simulated aperture at the bulge of the galaxy, as shown in the bottom-panel of Figure 5.7. The top-panel of Figure 5.7 shows the comparison between the two spectra. There is a difference in the flux level by a factor of 1.5, being the PINGS data with the higher value. However, as shown in the flux ratio panel, there is a very good agreement between the two spectra in terms of the spectral features along whole spectral range. Given that the IFS mosaic of NGC 5474 was re-calibrated using the broad-band imaging technique, I would claim that absolute spectrophotometry of the PINGS data is more accurate than the one of the drift-scan spectrum obtained by SINGS. Two foreground stars were removed from the IFS mosaic, as well as the detected bad fibres described before.

5.1.7 NGC 6701

Another galaxy with a drift-scan spectrum available from MK06 is NGC 6701. However, due to the aperture size and position used by MK06, part of the slit falls outside the observed mosaic for this galaxy, as shown in the bottom-panel of Figure 5.8. An integrated spectrum was obtained from the IFS data by extracting and co-adding the spectra encompassed by the red rectangle of Figure 5.8, which correspond to the MK06 75×60 arcsec aperture (180º PA), which can be compared to Figure 5.1. No foreground stars were found within this field. The whole in the mosaic corresponds to the bad fibres reported before. The top-panel of Figure 5.8 shows the comparison between the integrated PINGS extraction (black line) and the drift-scan spectrum (blue line). Although the flux level is consistent between the two data sets, the PINGS spectrum shows an inclination with respect to the MK06 spectrum, with lower flux values at the blue end of the spectrum, and higher values at the red part. The sky-subtraction residuals are more prominent in the PINGS spectrum, specially the [O I] λ5577 line. A close analysis of the log of observations and reduction of this mosaic shows that, NGC 6701 was observed under non-optimal atmospheric conditions. Due to this fact, only one standard star was observed during the night (as the telescope had to be closed), not allowing a comparison between different flux calibrations and sensitivity curves. Considering these circumstances, and assuming that the MK06 has the right shape in the continuum, we could concluded that the flux calibration of NGC 6701 is somewhat deficient. However, the source of this discrepancy may be due to the incomplete

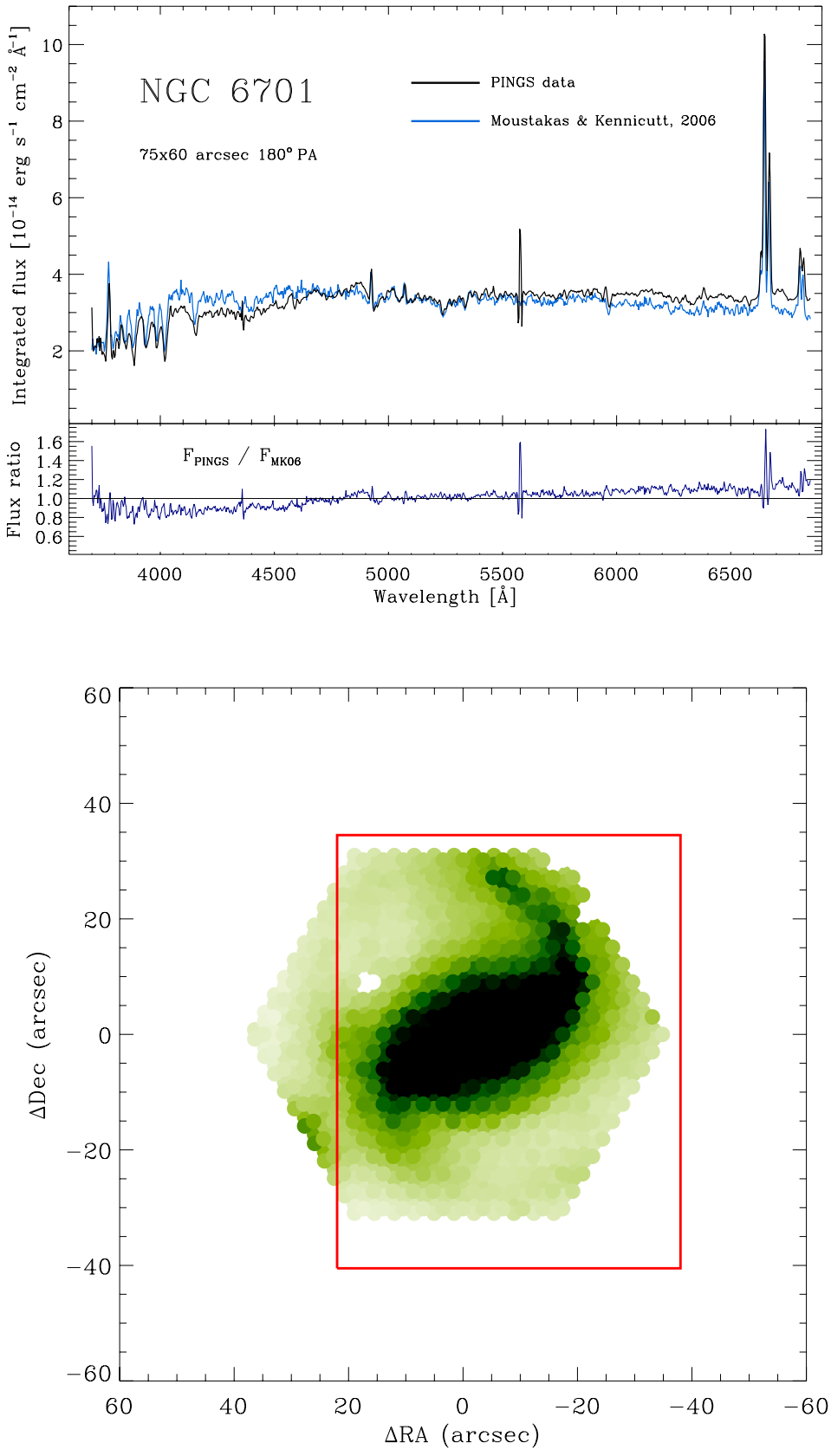

Figure 5.8: Comparison of the integrated spectrum of NGC 6701 derived from the PINGS data set and the drift-scan spectrum of the MK06 data. The slit-aperture can be compare to the DSS image in Figure 5.1.

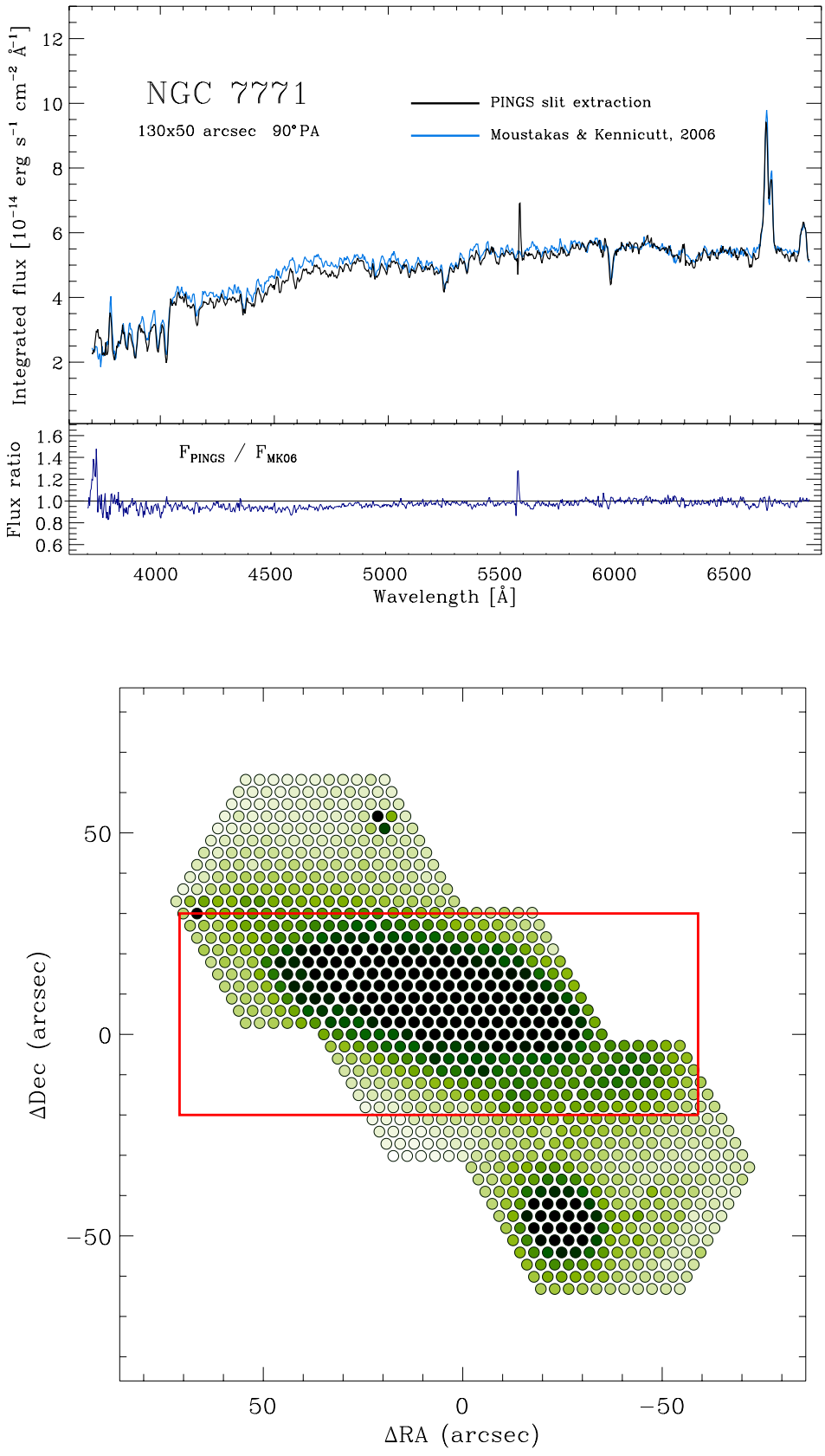

Figure 5.9: Comparison of the integrated spectrum of NGC 7771 derived from the PINGS slit-extraction and the drift-scan spectrum of the MK06 data. The slit-aperture can be compare to the DSS image in Figure 5.1.

spatial coverage of the IFS mosaic, or a combination of the factors mentioned above.

5.1.8 NGC 7771

The last galaxy of the PINGS sample with an drift-scan observation is NGC 7771. The bottom-panel of Figure 5.9 shows the mosaic diagram of this galaxy and overlaid the aperture used by MK06 for the drift-scan. As in previous cases, the aperture size and its position samples regions not covered by the FOV of the PINGS mosaic. MK06 used an aperture 130×50 arcsec and 90^{o} PA (see Figure 5.1). The top-panel of Figure 5.9 shows the comparison of the integrated spectrum extracted from the IFS mosaic within the MK06 aperture (black line) and the drift-scan spectrum (blue line). As in the case of NGC 6701, the PINGS spectrum of NGC 7771 shows a small tilt with respect to the MK06, however to a much lesser degree than the former. Yet, the overall shape of the continuum in the two spectra are consistent, as well as the spectral features in absorption and emission. In fact, the ratio between the two spectra is consistent with unity for wavelengths larger than 5000 Å. The differences in the blue part of the spectrum are within the 20% error. The mosaic of NGC 7771 was observed during a night of slightly better atmospheric conditions than NGC 6701, but not considered optimal. The [O I] λ5577 sky residual is clearly seen in the PINGS spectrum. We also have to consider that the disagreement between the spectra may reside in the larger covering area of the MK06 spectrum.

During the process of extracting the information from the IFS data, the exercise helped to test the accuracy of the astrometry, the mosaics were improved by removing the signal from bad fibres, foreground stars and supernovae within the observed FOV.

Several conclusions can be raised from the comparison of the extracted integrated data from PINGS and previously published drift-scan spectra. Regarding the comparison, when the apertures of both data sets are equal or comparable, there is a very good agreement in terms of the flux intensity level, shape and spectral features of both spectra. All differences are within the errors expected for this kind of spectroscopic data. At wavelengths shorter than $\sim$ 4000 Å, the differences are slightly larger due to the well-known effect of the fall in sensitivity of the CCD detector. The absolute spectrophotometric re-calibration proved to be reliable, as the integrated spectra extracted from PINGS agrees with the spectrophotometrically calibrated drift-scan data.

Differences were found when comparing spectra with incomplete spatial coverage in the IFS mosaic, although some spectral features are well reproduced. Given the 2D nature of the PINGS sample, the comparison of integrated spectra using different apertures for a given object would provide hints on how the aperture bias influences the determination of the galaxies properties, and the consequences of this effect for the study of distant galaxies. This exercise showed the good quality and reliability of the whole the PINGS data set.

5.2 Integrated properties of the ionized gas

Given the confidence acquired in terms of the quality of the data, and the extraction technique described in the previous section, an integrated spectrum for each individual mosaic of the PINGS sample was obtained by co-adding all the spectra belonging to the corresponding RSS file. In this way, 17 high signal-to-noise integrated spectra were obtained. For the galaxies NGC 1637, NGC 2976 & NGC 6643, this was the first

time an integrated spectrum was obtained for these targets. For galaxies such as NGC 628, NGC 1058, & NGC 3184, we obtained integrated spectra covering a much larger area than any previous study. In particular, the integrated spectrum of NGC 628 represents the nearby galaxy with the widest area ever covered by any spectroscopic means.

The single integrated spectrum of each galaxy can be analysed in order to characterise the global properties of the corresponding object. However, in order to extract any physical information from these data, we need first to separate the contribution of the stellar populations and the ionized gas from the observed integrated spectra of the galaxies. Once both contributions are decoupled and for the purpose of this dissertation, I will only focus on the integrated physical properties derived from the study of the emission of the ionized gas in the galaxy sample.

5.2.1 SSP modelling

The flux emitted by the stellar populations in a galaxy affects in several ways the correct determination of the emission spectrum of the ionized gas. The stellar emission is composed of a continuum with features of different species in absorption, especially hydrogen and helium lines. The contribution of the continuum to the overall observed spectrum biases the determination of the age of a certain ionizing population, by affecting the equivalent widths of the emission lines. Furthermore, if the underlying absorptions are not taken into account, the intensity of the hydrogen emission lines (e.g. the Balmer series in the optical wavelength range) are underestimated. For regions of emission lines with small equivalent widths (e.g. Hβ), the correction for underlying stellar absorption may be significant. Inaccurate flux measurements of these recombination lines affect the properties derived from the relative intensities to these emission lines. Therefore, particular care was taken in the subtraction of the underlying stellar populations in order to derive correct emission line intensities.

The decoupling of the stellar population from the emission lines was performed using an improved version of the FIT3D package (Sánchez et al., 2006). This software was specially designed to handle both RSS files and 3D datacubes, but can also be applied to an individual spectrum. FIT3D includes several routines to model and subtract the underlying population of a spectrum using synthetic stellar spectra, and subsequently to fit and deblend the nebular emission lines. This technique results in emission-line measurements corrected (to a first-order) for the stellar absorption. Following Sánchez et al. (2007a), the models were created using the GISSEL code (Bruzual & Charlot, 2003), assuming a Salpeter IMF (Salpeter, 1955), for a range of ages and metallicities. FIT3D includes 72 models covering a discrete grid of 12 ages (5, 25, 100, 290, 640 Myr, 0.9, 1.4, 2.5, 5, 11, 13 and 17 Gyr), and six metallicities (Z = 0.0001, 0.0004, 0.004, 0.008, 0.02 and 0.05).

The adopted scheme to model and decouple the contribution of the stellar population is the following: for each integrated spectrum, the underlying stellar population was fitted by a linear combination of the grid of single-stellar population (SSP) templates described above, after correcting for the appropriate systemic velocity and velocity dispersion (including the instrumental dispersion, that dominates at the considered resolution), and taking into account the effects of dust extinction. A spectral region of 30 Å width around each detected emission line was masked prior to the linear fitting, including regions of sky-subtraction residuals. Once the underlying stellar population was derived, this was subtracted from the original spectrum. The *residual* constitutes a *pure* emission-line spectrum.

However, as discussed thoroughly in the literature, the simple assumption that a single-stellar population

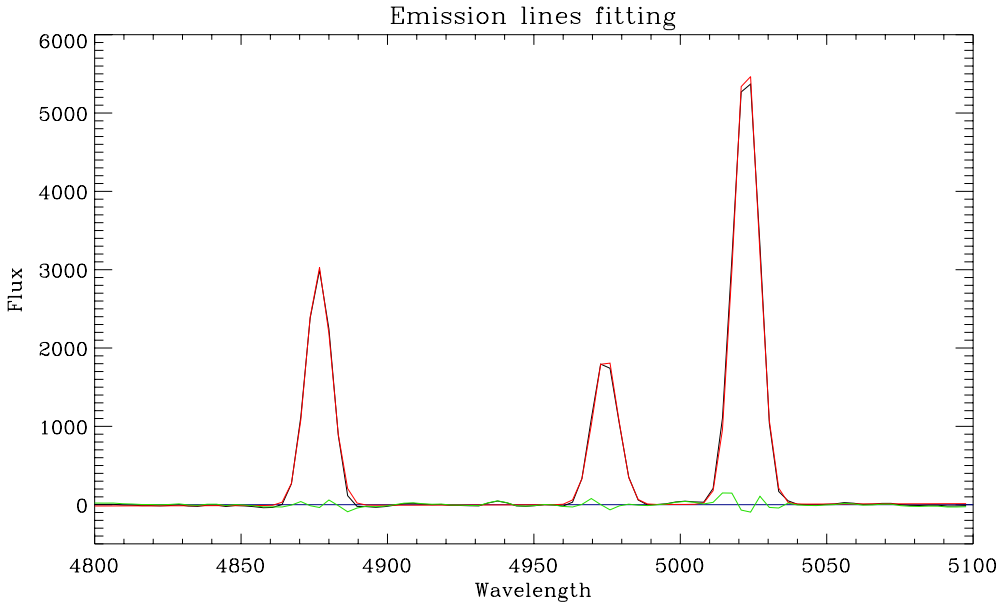

Figure 5.10: Example of the simultaneous multi-component emission line fitting for a residual integrated spectrum of NGC 3310 in the spectral window including the Hβ, and the λ4959 and λ5007 [O III] emission lines (black-line). The red-line shows the best fitted model, comprising three Gaussian functions, assuming a single Gaussian fit to each of the emission lines detected in this wavelength range. The green line is the residual between the fit model and the data.

can describe the SED of a galaxy is not valid for late-type galaxies (e.g. see MacArthur et al., 2009, and references therein). These objects harbour a mixture of young and old stars and present complex star formation histories, with different episodes of activity, of variable intensity and time scale. All these factors lead to undesirable degeneracies between age, metallicity and dust that produce very unstable fits. Different techniques have been proposed in order to reconstruct the stellar populations of late-type spirals (e.g. Fernandes et al., 2005; Ocvirk et al., 2006; Sarzi et al., 2006; Koleva et al., 2009; MacArthur et al., 2009). They require in general a wide wavelength range and a very good spectrophotometric calibration to disentangle the effects of age, metallicity and dust extinction. Nevertheless, they all share the same basis, i.e. the linear combination of multiple stellar populations.

The SSP modelling methodology is very advantageous for statistical and comparative studies, and when dealing with a large number of spectra (as it is the case for the PINGS sample). However, caution must be taken for detailed studies when the errors introduced by the fittings are significant, specially considering weak emission auroral lines. For the particular analysis of this chapter, but in general for the purpose of this dissertation, it is required to get a good representation of the underlying stellar continuum in order to decouple it from the emission lines produced by the ionized gas. Therefore, even in the case that the combination of SSPs is strongly degenerate, and that the fits create models with no physical meaning, they can be partially useful for the purpose of decoupling the nebular emission. Further discussion on the SSP modelling technique can be found in Appendix A, together with a detailed description of the fitting procedure, indicating the basic algorithms adopted, and including estimates of the accuracy of the modeling and the derived parameters based on simulations.

5.2.2 Emission line fitting

After obtaining a *clean* spectrum by the subtraction of the stellar continuum as described in the previous section, a set of emission lines was identified in each of the integrated spectra. Individual emission-line fluxes were then measured in each spectrum by considering spectral window regions of ~ 200 Å. We performed a simultaneous multi-component fitting using a single Gaussian function (for each emission line contained within each window) plus a low order polynomial (to describe the local continuum and to simplify the fitting procedure) using FIT3D (Sánchez et al., 2006). The central redshifted wavelengths of the emission lines were fixed and since the FWHM is dominated by the spectral resolution, the widths of all the lines were set equal to the width of the brightest line in this spectral region. When more than one emission was fitted simultaneously, their systemic velocities and FWHMs were forced to be equal (since the FWHM is dominated by the spectral resolution), in order to decrease the number of free parameters and increase the accuracy of the deblending process (when required).

The program fits the data computing a minimization of the reduced χ^2 and using a modified Levenberg–Marquardt algorithm. The parameters are provided through a configuration file where the model is described. The statistical uncertainty in the measurement of the line flux was calculated by propagating the error associated to the multi-component fitting and considering the signal-to-noise of the spectral region.

5.2.3 Results

Figures 5.11 through 5.22 show the integrated spectra of the PINGS sample. In each figure, the top-panel shows the integrated spectrum of each galaxy, after co-adding all the spectra of its corresponding mosaic. For those cases in which broad/narrow band imaging was available, the red solid squares indicate the integrated flux derived from the B, V, R and/or Hα images after co-adding the aperture photometry extracted for each fibre in the position table of the corresponding object. The middle-panels show the best fit linear combination of SSPs, produced by the procedure described before. In all cases, there is a good agreement between the input data and the fit model, matching within a $\sim 5\%$ level in all the wavelength range. Most the discrepancies are in regions dominated by imperfections in the sky-subtraction. Other spectral regions where the residual is slightly larger than the average are the Ca+H & K-band. The bottom-panels of the same figures show the *residual* emission spectrum after subtracting the model from the original spectrum, the detected emission lines in each case have been labeled, including sky-subtraction residuals. As expected the spectrum is dominated by a set of emission lines, plus a residual continuum, consistent with a null intensity (in average).

Additionally, tables 5.1 to 5.6 list the observed emission line intensities measured using the procedure described in subsection 5.2.2. The tables include the identification of the emission lines and the laboratory rest-frame wavelength. The observed intensities are normalised to the flux of Hβ in units of 10^{-15} erg s^{-1} cm^{-2}. They are shown in the columns labeled as F(λ)/Hβ. The associated 1σ errors are solely due to the statistical uncertainty $\sigma_{\rm stat}$ in the measurement of the flux intensity. Thereafter, the observed line intensities were corrected for reddening using the Balmer decrement according to the reddening function of Cardelli et al. (1989), assuming $R \equiv A_V/E(B-V) = 3.1$. Theoretical values for the intrinsic Balmer line ratios were taken from Osterbrock & Ferland (2006), assuming case B recombination (optically thick in all the Lyman lines), an electron density of $n_e = 100$ cm^{-3} and an electron temperature $T_e = 10^4$ K. The logarithmic reddening coefficient, c(Hβ), was estimated by using the available Balmer lines in each spectrum by a weighted least-square fitting of the measured ratios F(λ)/F(Hβ), with a higher weight given to the value

INTEGRATED LINE INTENSITIES I

		NGC 628		NGC 1058		NGC 1637	
Line	$f(\lambda)$	F(λ)/F(Hβ)	I(λ)/I(Hβ)	F(λ)/F(Hβ)	I(λ)/I(Hβ)	F(λ)/F(Hβ)	I(λ)/I(Hβ)
[O II] λ3727	0.32	1.494 (0.046)	2.138 (0.320)	2.159 (0.057)	2.693 (0.404)	1.506 (0.056)	2.193 (0.331)
[Ne III] λ3869	0.29	...	...	0.141 (0.029)	0.172 (0.043)	0.202 (0.036)	0.283 (0.064)
H8 + He I λ3889	0.29	0.158 (0.032)	0.217 (0.054)	0.122 (0.029)	0.149 (0.041)	0.276 (0.036)	0.385 (0.074)
Hϵ λ3970	0.27	...	...	0.170 (0.029)	0.204 (0.045)	0.326 (0.036)	0.445 (0.079)
Hδ λ4101	0.23	0.165 (0.032)	0.214 (0.051)	0.279 (0.029)	0.326 (0.056)	0.347 (0.036)	0.453 (0.077)
Hγ λ4340	0.16	0.511 (0.023)	0.609 (0.083)	0.434 (0.018)	0.483 (0.066)	0.307 (0.044)	0.368 (0.071)
Hβ λ4861	0.00	1.000 (0.014)	1.000 (0.052)	1.000 (0.020)	1.000 (0.054)	1.000 (0.027)	1.000 (0.057)
[O III] λ4959	-0.03	0.111 (0.010)	0.108 (0.017)	0.183 (0.014)	0.180 (0.026)	0.125 (0.019)	0.122 (0.024)
[O III] λ5007	-0.04	0.329 (0.010)	0.315 (0.040)	0.501 (0.016)	0.488 (0.062)	0.283 (0.019)	0.270 (0.038)
He I λ5876	-0.20	0.299 (0.012)	0.239 (0.031)	0.228 (0.015)	0.198 (0.027)	0.174 (0.019)	0.137 (0.023)
[O I] λ6300	-0.26	...	...	0.141 (0.028)	0.118 (0.027)	0.147 (0.021)	0.108 (0.020)
[N II] λ6548	-0.30	0.383 (0.013)	0.276 (0.035)	0.399 (0.017)	0.326 (0.041)	0.625 (0.026)	0.442 (0.057)
Hα λ6563	-0.30	3.998 (0.041)	2.870 (0.352)	3.520 (0.052)	2.870 (0.340)	4.063 (0.080)	2.870 (0.357)
[N II] λ6584	-0.30	1.111 (0.016)	0.795 (0.098)	1.157 (0.023)	0.941 (0.112)	1.811 (0.041)	1.275 (0.159)
[S II] λ6717	-0.32	0.619 (0.011)	0.435 (0.054)	0.801 (0.014)	0.644 (0.077)	0.833 (0.020)	0.575 (0.072)
[S II] λ6731	-0.32	0.393 (0.010)	0.276 (0.035)	0.529 (0.011)	0.425 (0.051)	0.620 (0.017)	0.426 (0.054)
[O III] λ5007/λ4959		2.96 (0.28)	2.92 (0.58)	2.73 (0.22)	2.71 (0.52)	2.25 (0.37)	2.22 (0.53)
[N II] λ6584/λ6548		2.90 (0.10)	2.88 (0.51)	2.90 (0.12)	2.89 (0.50)	2.90 (0.12)	2.88 (0.51)
[S II] λ6717/λ6731		1.57 (0.14)	1.58 (0.28)	1.52 (0.15)	1.52 (0.25)	1.35 (0.12)	1.35 (0.24)
F(Hβ) λ4861		1549.4		447.8		362.3	
c(Hβ)		0.48 (0.05)		0.30 (0.05)		0.51 (0.05)	
A_V		1.04		0.64		1.09	
Extraction fibres		6949		3976		4133	

Table 5.1: Integrated line intensities for NGC 628, NGC 1058 & NGC 1637. The first column correspond to the emission line identification, with the rest-frame wavelength, the second column to the normalised reddening curve. For each galaxy, the F(λ)/F(Hβ) column corresponds to the observed flux, while the I(λ)/I(Hβ) to the reddening corrected values; normalised to Hβ. The values in parenthesis correspond to the 1σ errors calculated as explained in the text. The observed fluxes in Hβ are expressed in units of 10^{-15} erg s^{-1} cm^{-2}. The last row shows the number of fibres in the *clean* mosaic from which the integrated spectra was extracted.

of derived from the Hα/Hβ ratio. Although for some galaxies high-order Balmer lines were detected in the integrated spectrum, no Balmer lines beyond Hγ were used for the determination of c(Hβ), as the associated error of the measurement of these lines in the residual spectrum yielded high uncertainties in the computed c(Hβ), due to their low signal-to-noise. Appendix B includes a detailed explanation on the determination of the logarithmic reddening correction, c(Hβ), and the visual extinction A_V derived from the Hα/Hβ ratio.

Tables 5.1 to 5.6 show the reddening-corrected emission line fluxes for each integrated spectrum, designated by the I(λ)/I(Hβ) columns, together with the derived values of c(Hβ) and the visual extinction A_V. These flux ratios can be used to derive the average properties of the ionized gas in each galaxy. The adopted reddening curve normalized to Hβ, $f(\lambda)$, is shown in the second column of each table. The observed flux of Hβ is expressed in units of 10^{-15} erg s^{-1} cm^{-2}.

Formal errors in the derived line ratios were estimated through a Monte Carlo simulation by propagating a normal random distribution with a central value equal to the observed emission line intensity, with a width $\sigma_{\rm input}$ equal to

$$\sigma^2_{\rm input} = \sigma^2_{\rm FC} + \sigma^2_{\rm stat} + \sigma^2_{c(H\beta)}, \tag{5.1}$$

where $\sigma_{\rm FC}$ is the uncertainty in the flux calibration, as described in subsection 4.2.2, $\sigma_{\rm stat}$ is the statistical

ERROR BUDGET

Uncertainty source	Case 1	Case 2
Statistical error	5%	1%
c(Hβ)	5%	1%
Flux calibration	15%	3%
Total	$\sim$25%	$\sim$5%

Table 5.2: Error budget in the total uncertainty of the emission line ratios and main derived parameters for the integrated spectra of the PINGS mosaics.

error in the measurement of the line flux, and $\sigma_{c(H\beta)}$ is the error in the c(Hβ) term. The MC propagation was repeated over 200 realisations per each observed emission line intensity. The reported error corresponds to the average standard deviation of the resulting emission line ratio distribution. For a discussion of the total estimated uncertainties of the derived parameters let us consider two IFS data sets of different quality, the first one consistent with large variations of the spectrophotometric conditions along the different observing runs (e.g. large moisacs like NGC 628, NGC 3184) in which the intrinsic variation of the relative flux calibration is relatively large (along the whole spectral range, and without considering the absolute scale, see chapter 4 and Figure 4.17), and a second case in which the mosaic was observed under optimum spectrophotometric conditions and/or during the same observing run (e.g. NGC 1058, NGC 3310), minimising the variations in the relative flux calibration, and in which an absolute flux calibration was performed. Let us call the first example Case 1, and the second Case 2. Table 5.2 shows the estimated contribution of each of the considered uncertainty sources to the total error budget for both cases. In the case of the integrated spectra of the PINGS mosaics, the error budget can be considered to fall between two extreme cases. As it could be expected, the integrated properties of the large mosaics are more prone to larger errors due to the presence of pointings with low spectrophotometric quality,

Some line ratios of interest are also shown in tables 5.1 to 5.6, as a test of self-consistency of the data. In particular, a well-behaved spectrum should possess ratios of [O III] λ5007/λ4959 and [N II] λ6584/λ6548 close to their theoretical values of 2.98 and 2.9 respectively (Storey & Zeippen, 2000; Osterbrock & Ferland, 2006). Furthermore, the value of the [S II] λ6717/λ6731 ratio can be used to place limits on the electron density, n_e, of typical H II regions.

Although particular care was taken in the flux calibration of all the spectra within the PINGS mosaics, the absolute flux intensities listed in tables 5.1 to 5.6 have to be taken with care. As discussed in section 5.1, for some galaxies the spatial coverage of the mosaics is incomplete with respect with the optical surface of the targets. This effect produces an underestimation of the flux intensity in all the lines. On the other hand, given that the PPAK bundle has a filling factor of $\sim$65%, for galaxies without dithered observations, the incomplete sampling underestimates the total integrated flux. Aperture correction factors were estimated for each galaxy, depending on the fraction of the surface covered by the IFS observations (with respect to the 25 mag arcsec^{-2} surface brightness isophote), and considering if the galaxy was observed in dithering mode. These factors are shown in Table 5.7.

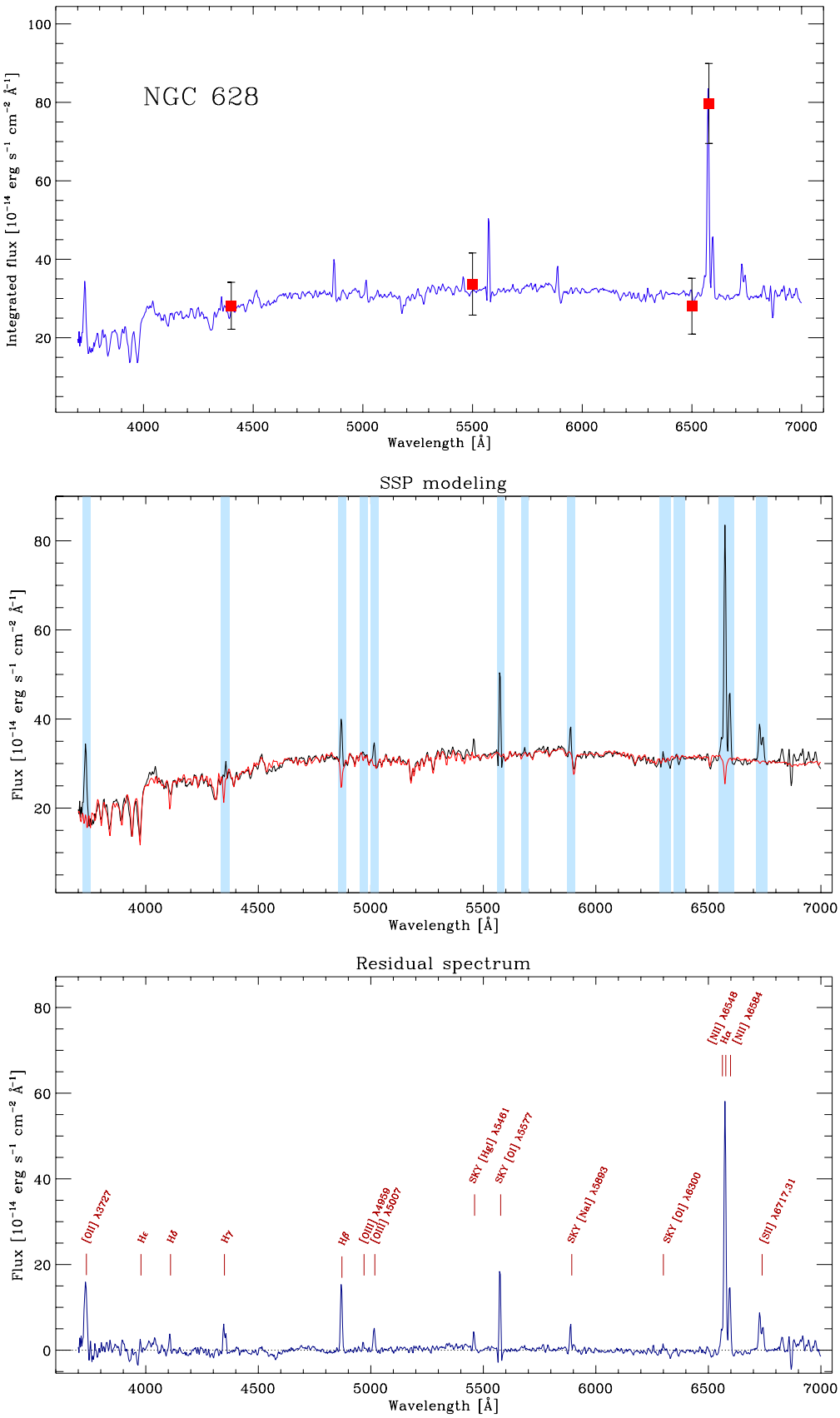

Figure 5.11: Integrated spectrum of NGC 628. The red solid squares in the top-panel indicate the integrated flux derived from the B, V, R and Hα images. The middle-panel shows the SSP model fitting (red line) to the spectrum, the light-blue bands correspond to the spectral regions masked during the fitting. The bottom-panel shows the *residual* after subtracting the model from the original spectrum, the detected emission lines have been labeled.

NGC 628

NGC 628 is the largest object of the sample, the PINGS observation of this galaxy represents the widest spectroscopic survey ever made in a single nearby galaxy. Therefore, the integrated spectrum of NGC 628 shown in the top-panel of Figure 5.11, stands for the largest area of a single object from which an integrated spectrum has been obtained. The spectrum shows a characteristic stellar continuum with absorption features and emission lines superimposed. Hα, Hβ, [O II] λ3727, [O III] λ5007, the [N II] $\lambda\lambda$6548,84 and $\lambda\lambda$6717,31 doublets are clearly identified. Less obvious are the Hγ and [O III] λ4959 lines. Sky residuals are also present in the spectrum, especially the [O I] λ5577 and [Na I] λ5893 lines. The red-solid squares correspond to the integrated flux derived from the *B*, *V*, *R* and Hα images of the SINGS ancillary data, obtained during the spectrophotometric re-calibration explained in subsection 4.1.10. The position of these data-points with respect to the continuum (in the case of the broad-band images) and the peak of the Hα line in the spectrum, corroborates the accuracy of the absolute flux calibration.

The middle-panel of the same figure shows the same spectrum and the best SSP model fit superimposed in red colour. The light-blue bands correspond to the spectral regions masked during the fitting as explained in subsection 5.2.1. They coincide with the position of the strongest redshifted emission lines and regions of bright sky residuals. The SSP model matches accurately the continuum of the integrated spectrum. Note the strength of the underlying stellar absorptions in the Balmer lines. The age of the model corresponds to 8.95 Gyr, with a metallicity index [Z/H] = -0.44 and dust attenuation A_V = 0.4. The bottom-panel shows the *residual* after subtracting the fit model from the original spectrum. This procedure reveals additional emission lines, like Hδ and Hε. The continuum is consistent with a null intensity. All the detected lines have been labeled with their standard notation. The emission line intensities reported in Table 5.1 for this galaxy were measured from this *pure* nebular spectrum. The observed [O III] and [N II] ratios shown in Table 5.1 are consistent with the theoretical values. The c(Hβ) value was derived using the Hα/Hβ ratio only. No auroral lines are detected either in the integrated or residual spectrum. The low strength of the [O III] lines suggests a relatively high metallicity for the integrated abundance of NGC 628.

Different authors have reported on the Hα intensity flux of NGC 628 using different procedures, from photoelectric photometers to narrow-band imaging. Table 5.3 lists a summary of these published values, together with the one derived from the integrated spectrum of this study, after applying the aperture correction factor shown in Table 5.7, which was derived based considering that the PINGS mosaic covers $\sim$ 80% of the galaxy size and the 68% covering factor of PPAK. Despite the different biases introduced by the different methods, there is a substantial degree of agreement between the previously published results and the reported value for the integrated Hα flux of this galaxy.

The derived dust extinction, A_V = 1.04, larger than the one derived from the analysis of the stellar populations ($A_V \sim 0.4$ mag). This result is not surprising, since both methods sample different regions of the galaxy. While the underlying continuum is dominated by the stellar components of the central regions, clearly brighter, the ionized gas spectrum is dominated by the star-forming regions in the spiral arms. These latter regions are known to be more attenuated by dust, due to star forming process (e.g. Calzetti, 2001). Indeed, the extinction law derived by Calzetti (1997) for star-forming galaxies shows that the typical extinction in the emission lines of these objects is approximately double that in their stellar continuum.

The integrated flux of Hα and [O II] λ3727 can be used to determine a rough value of the global star formation rate (SFR) in this galaxy. The intensities of both lines were corrected by dust extinction, adopting the A_V value of Table 5.1 and by the aperture correction shown in Table 5.7. Absolute luminosities were

Hα FLUX OF NGC 628

Flux	Reference
1.07	Kennicutt 1983
0.87	Young et al. 1996
1.51	Hoopes et al. 2001
1.05	Marcum et al. 2001
1.02	Kennicutt et al. 2008
1.14	This work

Table 5.3: Comparison between different Hα fluxes reported for NGC 628 in the literature. Fluxes in units of 10^{-11} erg s^{-1} cm^{-2}.

derived by assuming as a luminosity distance the value reported in Table 3.2. The derived luminosities are $L_{H\alpha} \sim 3.08$ and $L_{[O\,II]} \sim 2.30$, in units of 10^{41} erg s^{-1}. The values of the SFR were derived adopting the classical relations by Kennicutt (1998), obtaining SFR ~ 2.4 and 3.2 M$_\odot$ yr^{-1}, based on the Hα and [O II] luminosities respectively.

NGC 1058

Figure 5.12 shows the integrated spectrum of NGC 1058, the SSP modelling and the residual spectrum in a similar manner as the previous figure. The integrated spectrum was derived after co-adding all the spectra of the seven central position of the mosaic, without the outlying pointings. This spectrum is constructed out of 6951 individual spectra covering 90% of optical B_{25} mag arcsec^{-2} radius of NGC 1058. As in the case of NGC 628, the spectrum shows a stellar continuum and emission lines superimposed, like Hα, Hβ, [O II] λ3727, [O III] λ4959, λ5007 and the [N II] $\lambda\lambda$6548,84 and $\lambda\lambda$6717,31 doublets. Although there are signatures of sky residuals (e.g [O I] λ5577), these are of a much lower extent than the ones shown in the mosaic of NGC 628.

There is a good agreement between the SSP fit model and the spectrum. Balmer absorptions are important, especially in Hβ line. The derived parameters of the SSP fitting are: age of 6.51 Gyr, [Z/H] = -0.46 and $A_V = 0.0$. The subtraction of the model revealed additional emission lines, i.e. Hγ, Hδ, Hε, and marginal detections of H8 + HeI λ3889, and [Ne III] λ3869. The emission line intensities for the detected lines are listed in Table 5.1. The observed [O III] and [N II] ratios are consistent with their theoretical values. No auroral lines are detected either in the integrated or residual spectrum. As in the previous case, the strength of the [O III] lines is consistent with a high metallicity, although the strength of the [O II] λ3727 line is higher with respect to NGC 628. This galaxy shows a relatively low value of dust extinction, $A_V = 0.64$. Luminosities and SFRs were derived following the same procedure as NGC 628, obtaining $L_{H\alpha} \sim 0.65$ and $L_{[O\,II]} \sim 0.61$ (10^{41} erg s^{-1}). These values correspond to SFRs ~ 0.5 and 0.9 M$_\odot$ yr^{-1}, respectively.

NGC 1637

The integrated spectrum of NGC 1637 is shown in the top-panel of Figure 5.13, as in the case of NGC 1058, the spectrum was constructed after considering the seven observed positions, out of 6951 individual spectra and considering the overlapping of the dithered observations. The spectrum does not show as many emission

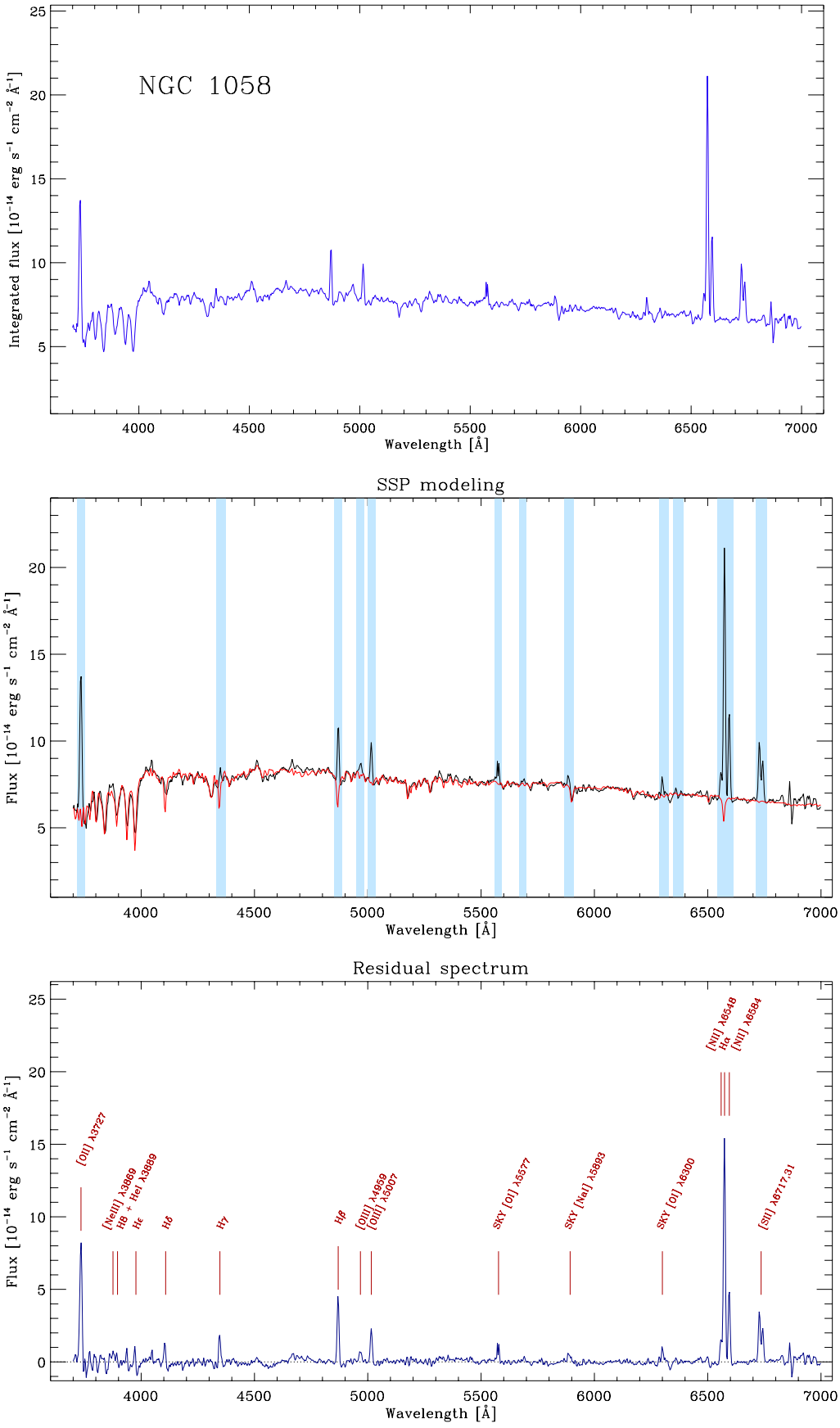

Figure 5.12: Integrated spectrum (top-panel), SSP model fitting (middle-panel), and *residual* spectrum (bottom-panel) of NGC 1058. Full description in the caption of Figure 5.11.

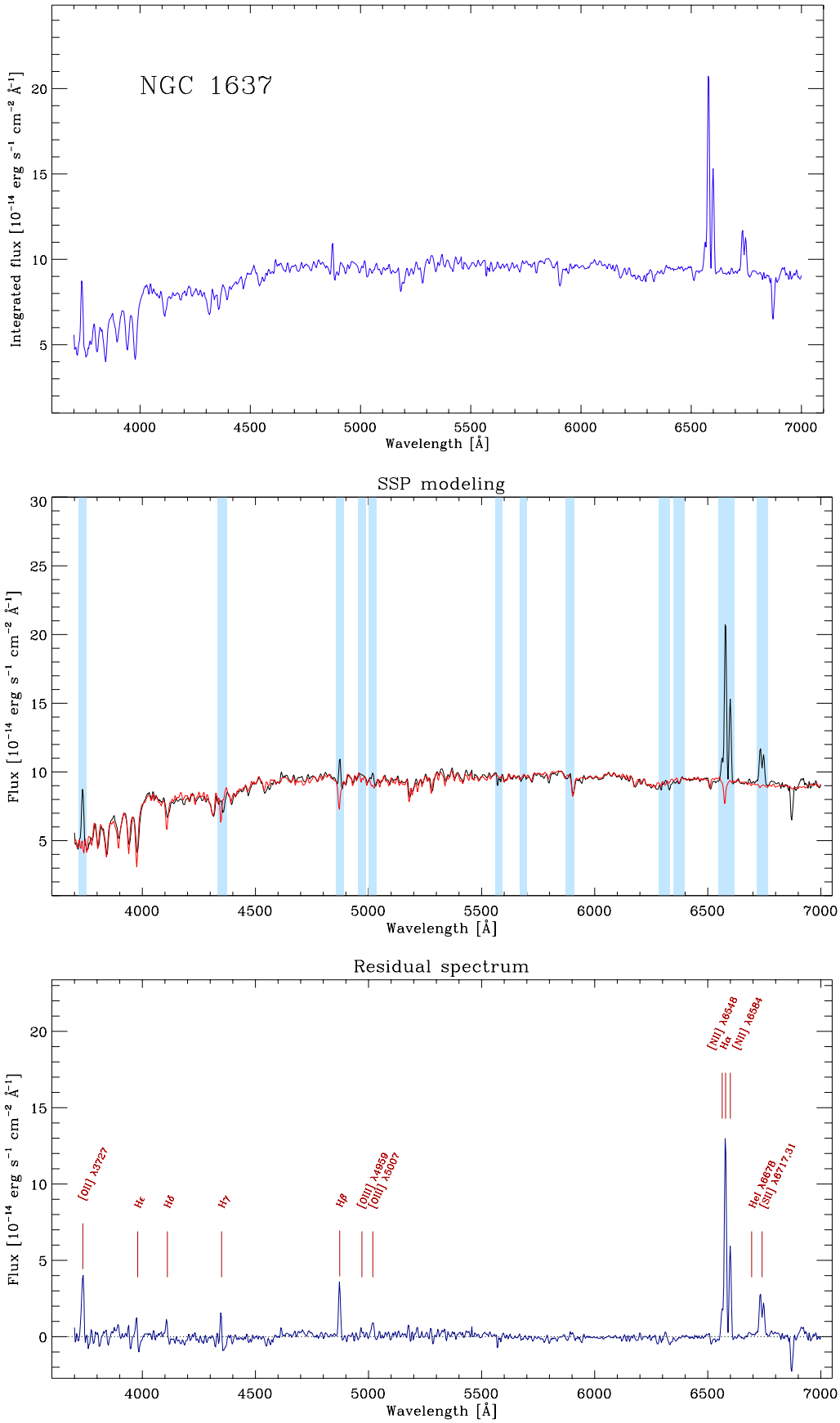

Figure 5.13: Integrated spectrum (top-panel), SSP model fitting (middle-panel), and *residual* spectrum (bottom-panel) of NGC 1637. Full description in the caption of Figure 5.11.

lines an in the previous cases, only Hα, [O II] λ3727, and the [N II] $\lambda\lambda$6548,84, $\lambda\lambda$6717,31 doublets are clearly seen. The strength of the Hβ is very low, no [O III] lines are noticeable in the integrated spectrum. Note that there are practically no residuals of sky subtraction.

The SSP fitting matches well with the observed spectrum. The strength in absorption of the Hβ line is comparable to the emission one. The age of the SSP model is 5.12 Gyr, with metallicity [Z/H] = –0.19 and A_V = 0.2. After subtracting the model, the residual spectrum shows a marginal detection of the [O III] lines, together with Hγ, Hδ, Hε and He I λ6678. Note the high strength of the [N II] doublet with respect to Hα. The emission line intensities for the detected lines are listed in Table 5.1. The observed [N II] ratios is consistent with the theoretical values, but not in the case of the [O III] ratio, which is not surprising given the marginal detection of those lines. The derived value for the extinction is A_V = 1.09. Luminosities and SFRs were derived following the same procedure as NGC 628, obtaining Hα and [O II] luminosities of 1.09 and 0.84 10^{41} erg s^{-1}, respectively, with corresponding SFRs to 0.9 and 1.2 $M_\odot$ yr^{-1}.

NGC 2976

Given the geometry and reduced number of observed positions for NGC 2976, the integrated spectrum shown in Figure 5.14 may not be considered to be representative of the whole galaxy. However, it samples the nuclear region of the galaxy (see Figure 3.5), and it is included in the analysis for completeness. The integrated spectrum was derived from 662 individual spectra, it shows the same spectral features as the previous cases, both [O III] emission lines are clearly seen. Sky residuals (mainly at the [O I] λ5577) are also present.

As in the case of NGC 628, the red-solid squares correspond to the integrated SINGS broad-band imaging fluxes from the *B*, *V*, *R* and Hα bands. There is a very good agreement for the positions of the *V*, *R* and Hα data-points with respect to the continuum and the Hα emission line in the integrated spectrum, but not in the case of the *B* band. This difference may be due to the broad transmission function of the filter, which falls outside the spectral range of PINGS, to problems with the intrinsic image flux calibration, or wrong information in the FITS header of the photometric calibration. The agreement with the rest of the bands suggests that the difference is caused by a problem with the SINGS image.

The SSP modelling in the middle-panel shows a good matching with the observed spectrum, with a small deviation in the continuum near the [O I] λ5577 sky-line region. The underlying absorption in the Balmer lines are significant, specially in the case of Hβ. The derived parameters of the SSP fitting are: age of 2.86 Gyr, [Z/H] = -0.15 and A_V = 0.4, consistent with a young stellar population with solar metallicity. The residual spectrum reveals a whole set of emission lines, including: Hα, Hβ,Hγ, Hδ, Hε, [O II] λ3727, [O III] λ4959,λ5007 and the [N II] $\lambda\lambda$6548,84, $\lambda\lambda$6717,31 doublets. A marginal detection for the H8 + HeI λ3889, and [Ne III] λ3869 lines. Some sky-residuals are also present in the spectrum. The continuum is a bit depleted near the Hβ and Hγ regions, with an enhancement near 5000 Å, due to the deficient fitting mentioned before. The emission line intensities for the detected lines are listed in Table 5.4. The observed ratio of [N II] is consistent with the theoretical values but not for the [O III] ratio, this may be due to the bad SSP fitting of the continuum in this spectral region. The derived extinction from the Hα/Hβ ratio is A_V = 0.99. Values of the luminosities and SFRs derived from the line intensities are included in Table 5.7 for completeness.

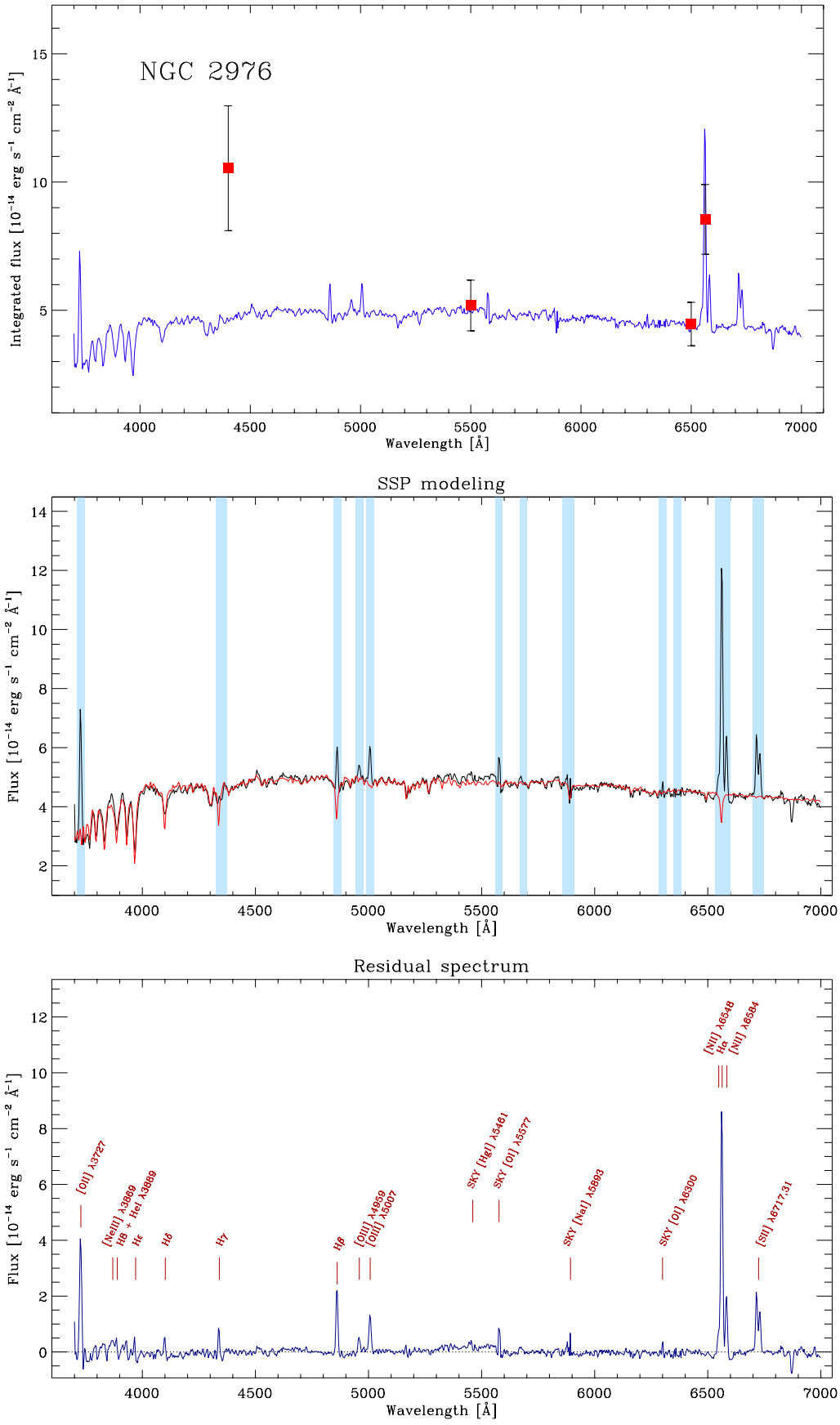

Figure 5.14: Integrated spectrum (top-panel), SSP model fitting (middle-panel), and *residual* spectrum (bottom-panel) of NGC 2976. Full description in the caption of Figure 5.11.

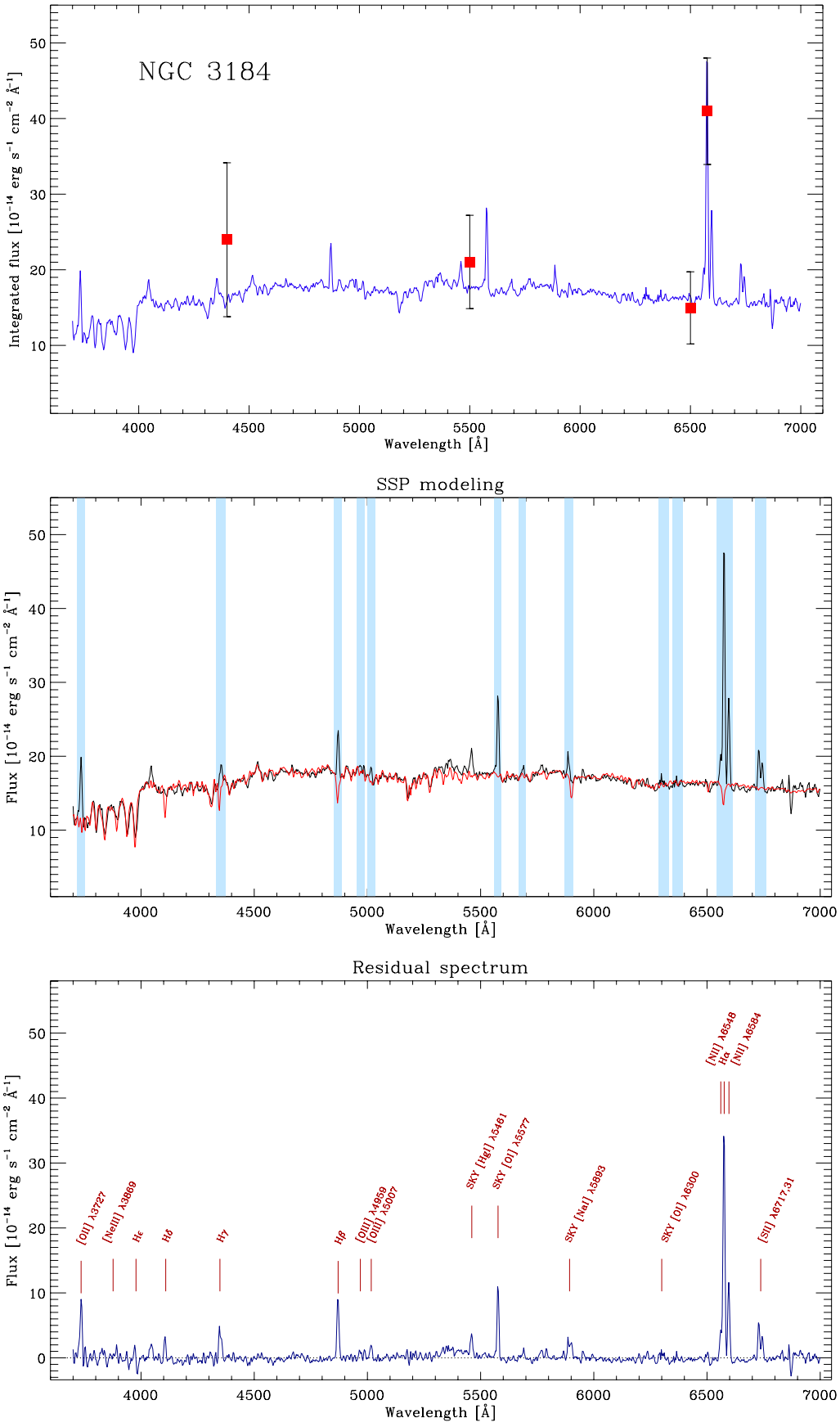

Figure 5.15: Integrated spectrum (top-panel), SSP model fitting (middle-panel), and *residual* spectrum (bottom-panel) of NGC 3184. Full description in the caption of Figure 5.11.

INTEGRATED LINE INTENSITIES II

		NGC 2976		NGC 3184		NGC 3310	
Line	$f(\lambda)$	F(λ)/F(Hβ)	I(λ)/I(Hβ)	F(λ)/F(Hβ)	I(λ)/I(Hβ)	F(λ)/F(Hβ)	I(λ)/I(Hβ)
[O II] λ3727	0.32	2.059 (0.061)	2.897 (0.434)	0.923 (0.040)	1.146 (0.177)	3.543 (0.033)	4.128 (0.615)
[Ne III] λ3869	0.29	0.154 (0.024)	0.209 (0.044)	...	...	0.195 (0.012)	0.224 (0.035)
H8 + He I λ3889	0.29	0.120 (0.024)	0.162 (0.040)	0.141 (0.030)	0.171 (0.043)	0.124 (0.011)	0.142 (0.024)
Hε λ3970	0.27	0.094 (0.024)	0.125 (0.036)	0.120 (0.030)	0.143 (0.041)	0.119 (0.011)	0.136 (0.023)
Hδ λ4101	0.23	0.226 (0.024)	0.288 (0.050)	0.322 (0.030)	0.376 (0.062)	0.181 (0.012)	0.202 (0.031)
Hγ λ4340	0.16	0.305 (0.015)	0.360 (0.050)	0.621 (0.029)	0.690 (0.095)	0.363 (0.006)	0.391 (0.051)
He I λ4471	0.12	...	...	...	...	0.025 (0.005)	0.027 (0.006)
Hβ λ4861	0.00	1.000 (0.019)	1.000 (0.053)	1.000 (0.021)	1.000 (0.054)	1.000 (0.011)	1.000 (0.051)
[O III] λ4959	-0.03	0.237 (0.014)	0.230 (0.032)	0.128 (0.015)	0.126 (0.021)	0.635 (0.010)	0.627 (0.079)
[O III] λ5007	-0.04	0.579 (0.015)	0.556 (0.071)	0.220 (0.015)	0.214 (0.030)	1.902 (0.017)	1.868 (0.232)
He I λ5876	-0.20	0.174 (0.026)	0.140 (0.027)	0.421 (0.029)	0.367 (0.050)	0.151 (0.004)	0.137 (0.017)
[O I] λ6300	-0.26	0.067 (0.015)	0.051 (0.013)	0.131 (0.020)	0.109 (0.021)	0.146 (0.006)	0.129 (0.016)
[O I] λ6363	-0.27	...	...	...	...	0.046 (0.005)	0.041 (0.007)
[N II] λ6548	-0.30	0.324 (0.018)	0.237 (0.032)	0.404 (0.019)	0.331 (0.042)	0.256 (0.008)	0.222 (0.027)
Hα λ6563	-0.30	3.935 (0.055)	2.870 (0.351)	3.508 (0.055)	2.870 (0.340)	3.305 (0.028)	2.870 (0.333)
[N II] λ6584	-0.30	0.938 (0.021)	0.683 (0.084)	1.171 (0.025)	0.956 (0.114)	0.742 (0.010)	0.643 (0.075)
[S II] λ6717	-0.32	0.901 (0.015)	0.643 (0.079)	0.572 (0.014)	0.462 (0.056)	0.569 (0.014)	0.490 (0.058)
[S II] λ6731	-0.32	0.617 (0.012)	0.440 (0.054)	0.354 (0.013)	0.285 (0.035)	0.271 (0.014)	0.233 (0.029)
[O III] λ5007/λ4959		2.44 (0.15)	2.41 (0.45)	1.72 (0.23)	1.70 (0.38)	2.99 (0.04)	2.98 (0.52)
[N II] λ6584/λ6548		2.90 (0.16)	2.89 (0.52)	2.90 (0.14)	2.89 (0.50)	2.90 (0.10)	2.89 (0.48)
[S II] λ6717/λ6731		1.46 (0.13)	1.46 (0.25)	1.62 (0.16)	1.62 (0.28)	2.10 (0.23)	2.10 (0.36)
F(Hβ) λ4861		243.7		1053.3		3687.8	
c(Hβ)		0.46 (0.05)		0.29 (0.05)		0.21 (0.05)	
A_V		0.99		0.63		0.44	
Extraction fibres		485		3645		2535	

Table 5.4: Integrated line intensities for NGC 2976, NGC 3184 & NGC 3310. For a full description see caption of Table 5.1.

NGC 3184

Figure 5.15 shows the integrated spectrum, SSP fitting and residual subtraction of NGC 3184. This spectrum is more affected by the presence of sky-residuals, being for example, the [O I] λ5577 more prominent than the Hβ line. The spectrum was obtained after 5296 individual spectra, corresponding to 16 PPAK positions. This is the 2nd largest area covered by an integrated spectrum of the sample. Comparison with the integrated SINGS broad-band imaging is included. As in the case of NGC 2976, the V, R and Hα bands are in good agreement with the integrated spectrum, while there is a deviation in the B-band, but still consistent with the continuum level within the errors.

There is a good agreement of the SSP modelling, despite that the integrated spectrum is more noisy than in previous cases. The age of the derived model is 5.14 Gyr, with metallicity [Z/H] = 0.08 and A_V = 0.2. The residual spectrum shows the characteristic lines found in previous cases, with marginal detections of the [O III] lines, Hδ, Hε and [Ne III] λ3869. The emission line intensities for the detected lines are listed in Table 5.4. The [N II] ratios are consistent with the theoretical values, which is not the case for the [O III] ratio. The derived value for the extinction is A_V = 0.63, using the Hα/Hβ ratio. Luminosities and SFRs were derived following the same procedure described previously. Hα and [O II] luminosities are 1.66 and 0.66 10^{41} erg s^{-1}, respectively, with derived SFRs of 1.3 and 0.9 $M_\odot$ yr^{-1}.

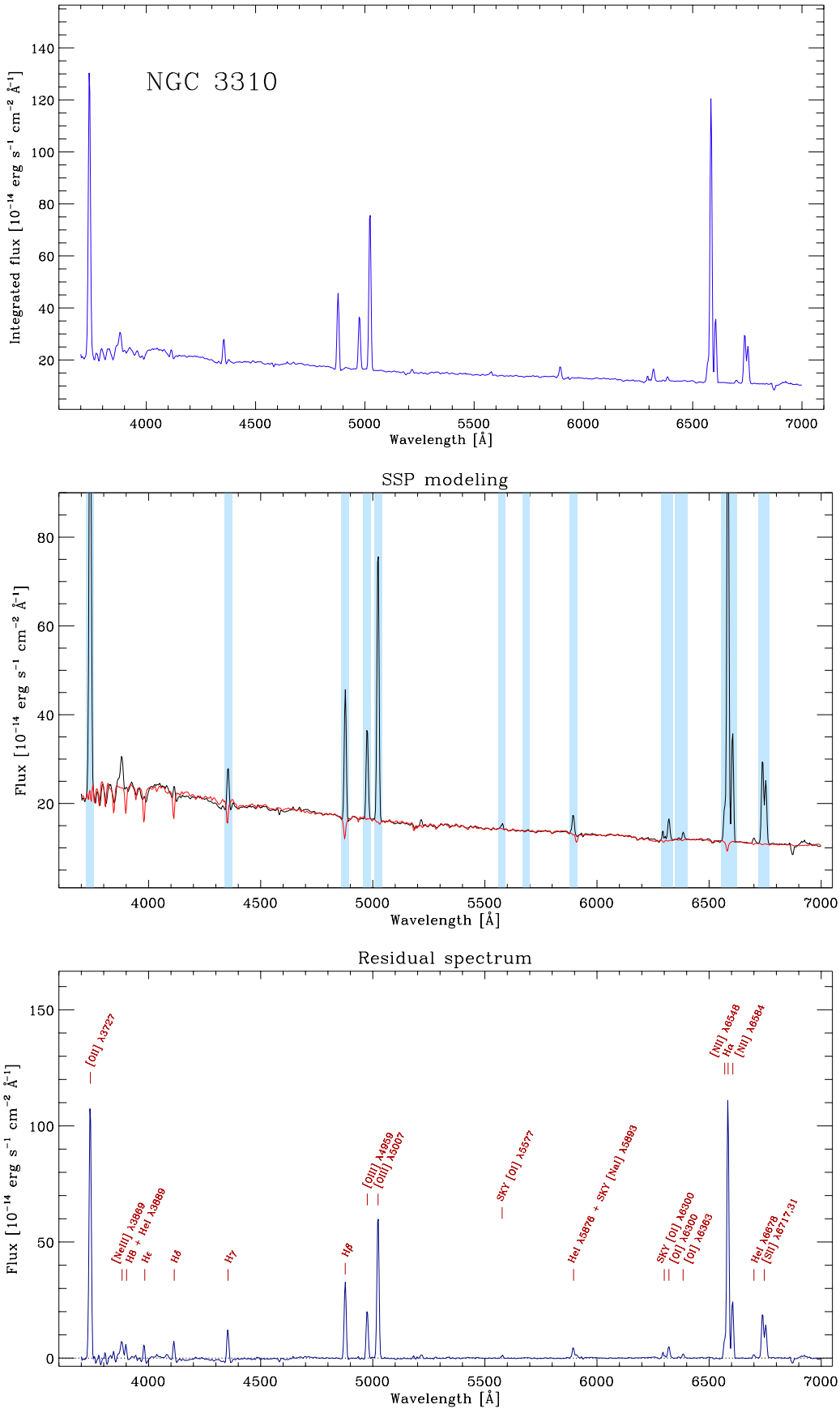

Figure 5.16: Integrated spectrum (top-panel), SSP model fitting (middle-panel), and *residual* spectrum (bottom-panel) of NGC 3310. Full description in the caption of Figure 5.11.

NGC 3310

The integrated spectrum of NGC 3310 is by far the one with the highest signal-to-noise and flux of the whole sample. Figure 5.16 shows the integrated spectrum of NGC 3310, the SSP modelling and the residual spectrum in a similar manner as the previous figure. The spectrum was derived after co-adding 2979 fibres corresponding to the three dithered pointings of the mosaic. In this case, the spectrum is almost entirely dominated by emission lines, and resembles more the spectrum of a H II region or a blue-compact galaxy. The [O II] λ3727 line is more prominent than Hα. The [O I] λ6300 and λ6363 lines in emission are clearly seen, as well as the He I λ5876 and λ6678 lines.

The SSP fitting traces very well the continuum for wavelengths larger than 4500 Å. However, there are disagreements in the region between 4000 Å and the Hγ line, with a SSP continuum slightly higher than the observed one. The derived parameters of the SSP fitting are: age of 0.98 Gyr, [Z/H] = -0.12 and A_V = 0.6, consistent with a very young population with subsolar metallicity. The emission line intensities for the detected lines are listed in Table 5.4. The observed [O III] and [N II] ratios are consistent with their theoretical values. There is a hint of the [O III] λ4363 line detected in the integrated spectrum, which is lost in the residual due to the imperfect SSP fitting. This galaxy shows a relatively low value of dust extinction, A_V = 0.44. The luminosities and SFRs derived for this galaxy are: $L_{H\alpha}$ = 9.60 and $L_{[O\,II]}$ = 13.80 10^{41} erg s^{-1}. These values correspond to SFRs of $\sim$ 7.6 and 19.3 $M_\odot$ yr^{-1}, respectively.

NGC 4625

Despite only one position (dithered) was observed for NGC 4625, sampling the bright central region of this galaxy, the integrated spectrum shown in Figure 5.17 can be considered representative of the whole galaxy, as it covers nearly 80% of its optical surface. The integrated spectrum was derived from 993 individual spectra, it shows a stellar continuum with features in emission similar to previous examples. Small sky-residuals are also present, especially at the [Na I] λ5893 line. As in previous cases, the red-solid squares stand for the comparison with the SINGS broad-band imaging. In this case, there is a very good agreement for the *B* and *V* bands, with the data-point corresponding to the *R* band slightly below the continuum of the integrated spectrum but within the errors, which for this galaxy are larger. No Hα narrow band image was available for this galaxy.

The SSP modelling follows correctly the spectral continuum, with small differences for wavelengths shorter than $\sim$ 4300 Å. The derived parameters of the SSP fitting are: age of 7.04 Gyr, [Z/H] = -0.52 and A_V = 0.4. The residual spectrum reveals some lines of interest, including the marginal detections of the [O III] λ4959 line and [O I] λ6363. Some sky-residuals are also present in the spectrum. The continuum is a bit depleted between the Hδ and Hγ regions. The emission line intensities for the detected lines are listed in Table 5.5. The observed ratio of [N II] is consistent with the theoretical values but not for the [O III] ratio, which is not surprising given the marginal detection of the [O III] λ4959 line. The derived extinction from the Hα/Hβ ratio is A_V = 0.52. The luminosities and SFRs derived for this galaxy are: $L_{H\alpha}$ = 0.23 and $L_{[O\,II]}$ = 0.19 10^{41} erg s^{-1}. These values correspond to SFRs of $\sim$ 0.2 and 0.3 $M_\odot$ yr^{-1}, respectively.

NGC 5474

Figure 5.18 shows the integrated spectrum, SSP fitting and residual subtraction of NGC 5474. The spectrum is of this galaxy is somewhat noisy, an inspection of the log of observations confirms the non-optimal

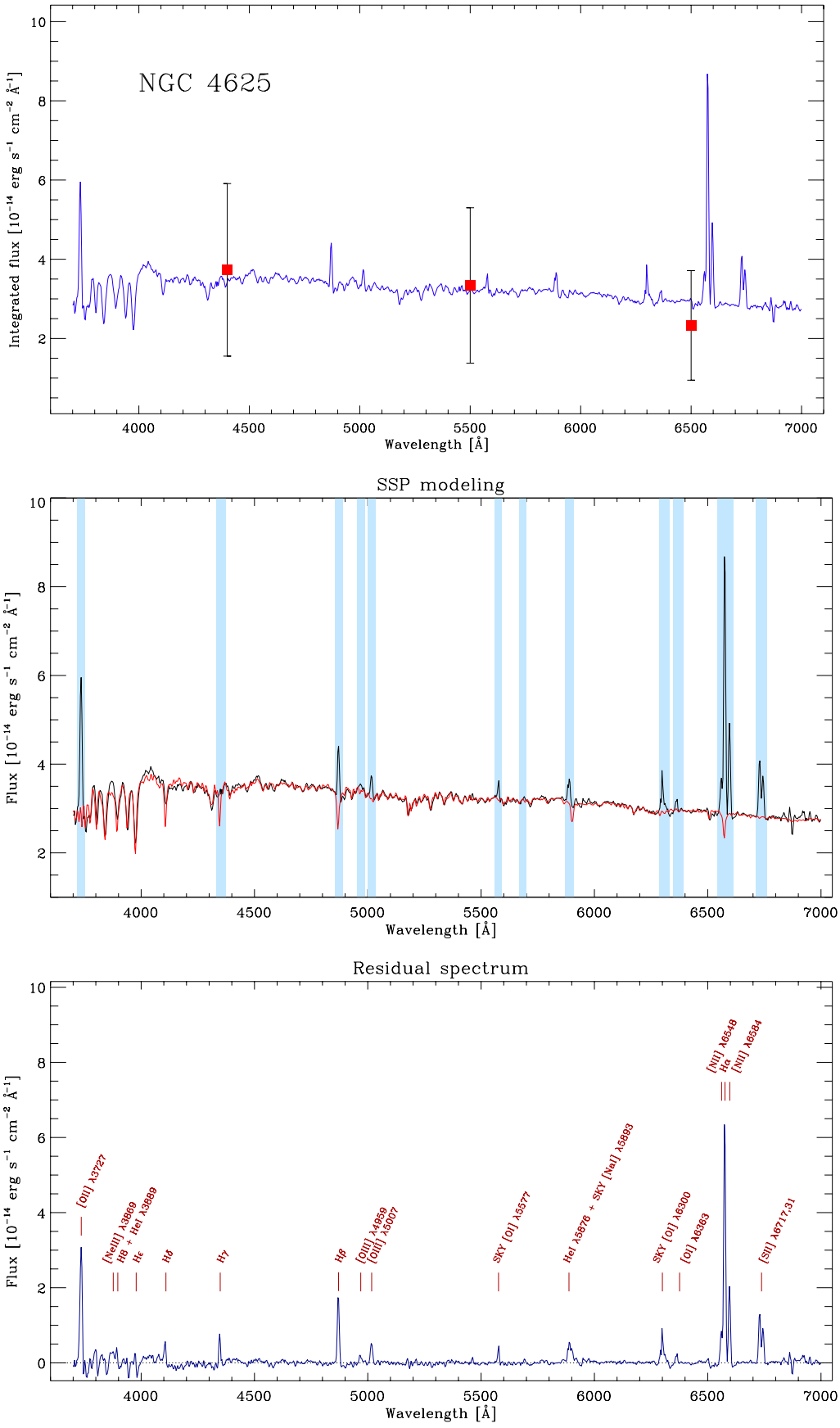

Figure 5.17: Integrated spectrum (top-panel), SSP model fitting (middle-panel), and *residual* spectrum (bottom-panel) of NGC 4625. Full description in the caption of Figure 5.11.

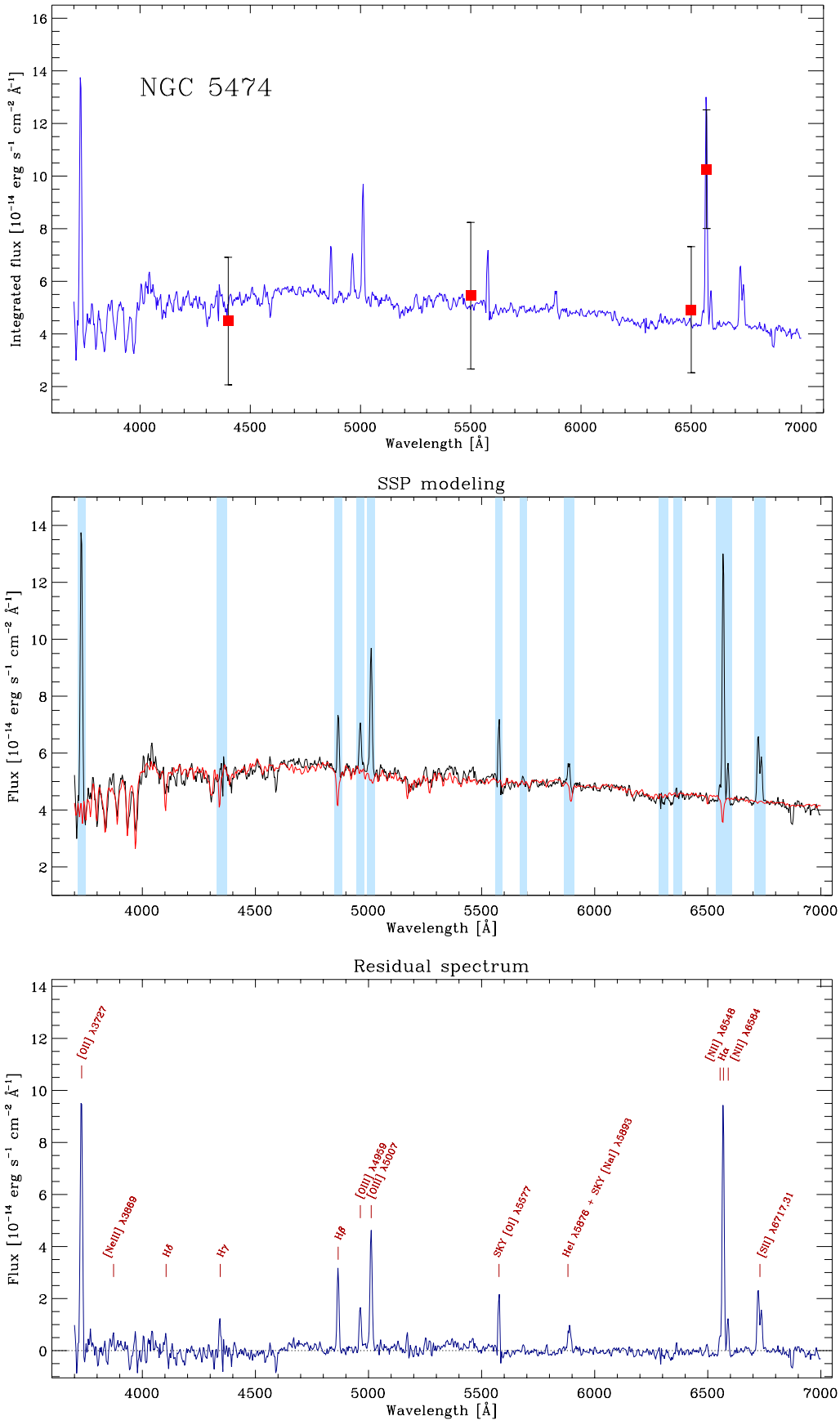

Figure 5.18: Integrated spectrum (top-panel), SSP model fitting (middle-panel), and *residual* spectrum (bottom-panel) of NGC 5474. Full description in the caption of Figure 5.11.

INTEGRATED LINE INTENSITIES III

		NGC 4625		NGC 5474		NGC 6643	
Line	$f(\lambda)$	F(λ)/F(Hβ)	I(λ)/I(Hβ)	F(λ)/F(Hβ)	I(λ)/I(Hβ)	F(λ)/F(Hβ)	I(λ)/I(Hβ)
[O II] λ3727	0.32	1.944 (0.052)	2.328 (0.351)	3.757 (0.108)	4.297 (0.652)	...	...
[Ne III] λ3869	0.29	0.233 (0.032)	0.274 (0.055)	0.203 (0.040)	0.229 (0.056)	0.229 (0.037)	0.436 (0.093)
H8 + He I λ3889	0.29	0.189 (0.032)	0.222 (0.050)	...	...	0.238 (0.037)	0.448 (0.093)
Hε λ3970	0.27	...	...	...	...	0.140 (0.036)	0.252 (0.074)
Hδ λ4101	0.23	0.305 (0.033)	0.347 (0.060)	0.212 (0.040)	0.233 (0.055)	...	...
Hγ λ4340	0.16	0.342 (0.013)	0.373 (0.051)	0.425 (0.030)	0.454 (0.067)	0.288 (0.031)	0.407 (0.068)
Hβ λ4861	0.00	1.000 (0.014)	1.000 (0.052)	1.000 (0.035)	1.000 (0.061)	1.000 (0.030)	1.000 (0.058)
[O III] λ4959	-0.03	0.126 (0.010)	0.124 (0.018)	0.497 (0.028)	0.492 (0.067)	...	...
[O III] λ5007	-0.04	0.301 (0.010)	0.295 (0.038)	1.461 (0.044)	1.438 (0.183)	0.345 (0.022)	0.317 (0.045)
He I λ5876	-0.20	0.440 (0.020)	0.393 (0.050)	0.504 (0.022)	0.463 (0.058)	...	...
[O I] λ6300	-0.26	0.557 (0.024)	0.480 (0.060)	...	...	0.141 (0.014)	0.079 (0.013)
[O I] λ6363	-0.27	0.129 (0.024)	0.110 (0.024)	...	...	...	...
[N II] λ6548	-0.30	0.375 (0.018)	0.318 (0.040)	0.153 (0.017)	0.135 (0.021)	0.628 (0.026)	0.327 (0.047)
Hα λ6563	-0.30	3.391 (0.038)	2.870 (0.335)	3.250 (0.082)	2.870 (0.338)	5.536 (0.119)	2.870 (0.404)
[N II] λ6584	-0.30	1.088 (0.020)	0.919 (0.108)	0.443 (0.019)	0.391 (0.048)	1.822 (0.044)	0.939 (0.133)
He I λ6678	-0.31	0.029 (0.006)	0.024 (0.006)	...	...	0.106 (0.014)	0.053 (0.010)
[S II] λ6717	-0.32	0.715 (0.009)	0.598 (0.070)	0.881 (0.024)	0.771 (0.091)	1.126 (0.028)	0.558 (0.080)
[S II] λ6731	-0.32	0.482 (0.008)	0.403 (0.047)	0.542 (0.017)	0.474 (0.057)	0.828 (0.022)	0.409 (0.059)
[O III] λ5007/λ4959		2.39 (0.20)	2.38 (0.46)	2.94 (0.15)	2.92 (0.54)	...	...
[N II] λ6584/λ6548		2.90 (0.14)	2.89 (0.50)	2.90 (0.32)	2.89 (0.57)	2.90 (0.11)	2.87 (0.57)
[S II] λ6717/λ6731		1.48 (0.15)	1.48 (0.25)	1.63 (0.17)	1.63 (0.27)	1.36 (0.10)	1.37 (0.28)
F(Hβ) λ4861		193.4		313.9		183.1	
c(Hβ)		0.24 (0.05)		0.18 (0.05)		0.96 (0.05)	
A_V		0.52		0.39		2.06	
Extraction fibres		751		2850		1977	

Table 5.5: Integrated line intensities for NGC 4625, NGC 5474 & NGC 6643. For a full description see caption of Table 5.1.

observing conditions during the two runs when the mosaic of this galaxy was observed. Nevertheless, the spectrum shows prominent emission lines superimposed to the stellar continuum. The [O II] and [O III] lines are clearly visible. A strong sky-residual corresponding to [O I] λ5577 is also found, confirming the general quality of the spectra. The integrated spectrum was built after co-adding 5958 individual spectra corresponding to the six observed positions. The comparison with the integrated SINGS broad-band imaging is also included. All the data-points are in good agreement with the continuum level of the spectrum and the Hα peak, within the errors.

The SSP fitting is relatively good considering the noisy shape of the integrated continuum. The age of the derived model is 3.25 Gyr, with metallicity [Z/H] = -0.05 and A_V = 0.0. The residual spectrum shows the lines mentioned previously, plus marginal detections of Hγ, Hδ and [Ne III] λ3869. The emission line intensities for the detected lines are listed in Table 5.5. Both the [N II] and [O III] ratios are consistent with the theoretical values. The derived value for the extinction using the Hα/Hβ ratio is A_V = 0.39, which is consistent with the value found through the SSP modelling. The derived Hα and [O II] luminosities are 0.17 and 0.25 10^{41} erg s^{-1}, respectively, with corresponding SFRs of 0.1 and 0.3 $M_\odot$ yr^{-1}.

NGC 6643

As explained in section 3.4, during the observation of NGC 6643 there was an instrumental problem which affected the observed spectral range, wavelengths shorter than 3800 Å could not be observed. Furthermore,

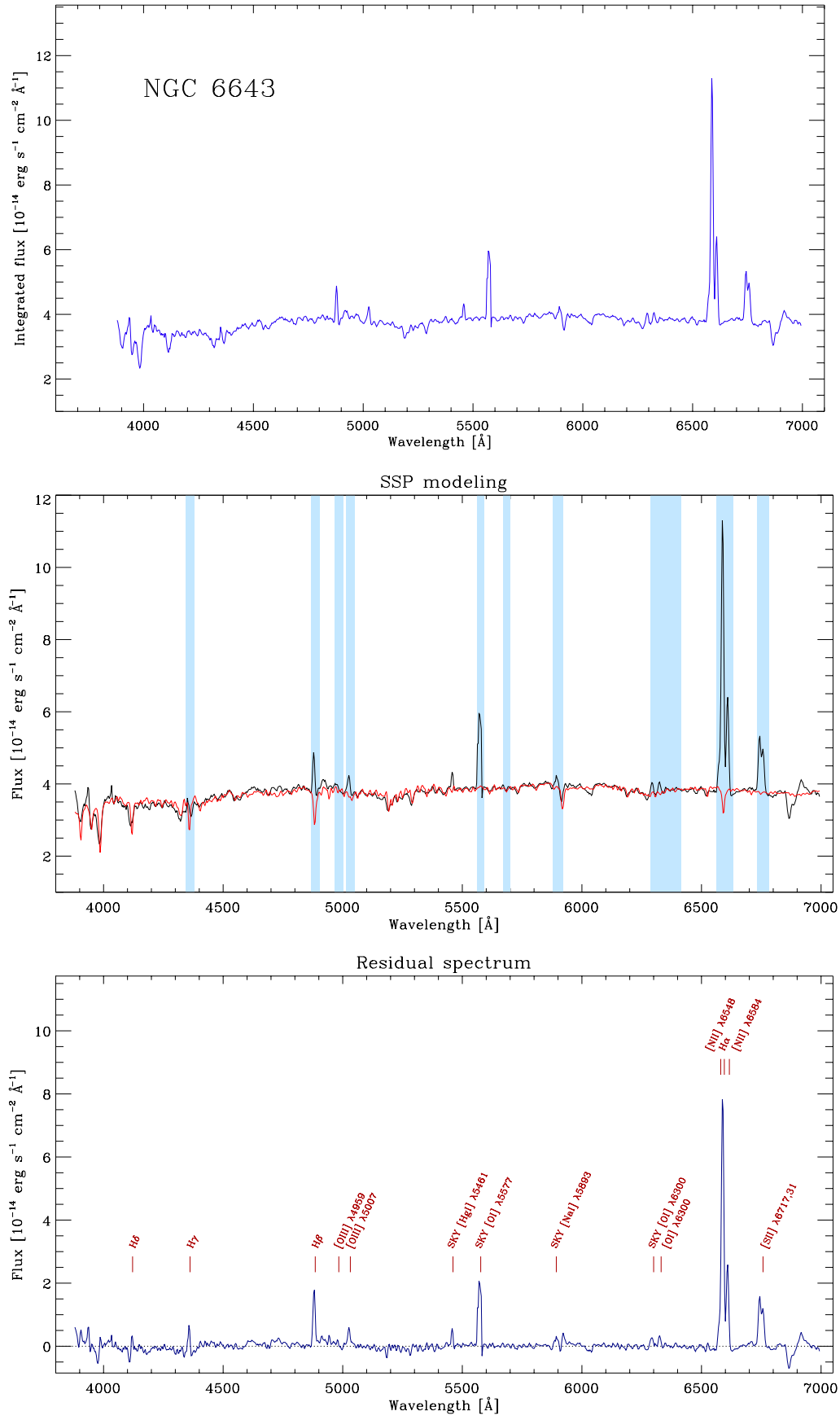

Figure 5.19: Integrated spectrum (top-panel), SSP model fitting (middle-panel), and *residual* spectrum (bottom-panel) of NGC 6643. Full description in the caption of Figure 5.11.

INTEGRATED LINE INTENSITIES IV

		NGC 6701		NGC 7770		NGC 7771	
Line	$f(\lambda)$	F(λ)/F(Hβ)	I(λ)/I(Hβ)	F(λ)/F(Hβ)	I(λ)/I(Hβ)	F(λ)/F(Hβ)	I(λ)/I(Hβ)
[O II] λ3727	0.32	1.307 (0.079)	2.787 (0.436)	1.935 (0.024)	2.810 (0.413)	1.242 (0.097)	2.966 (0.485)
[Ne III] λ3869	0.29	0.234 (0.039)	0.463 (0.101)	0.087 (0.015)	0.122 (0.027)	...	...
H8 + He I λ3889	0.29	...	...	0.120 (0.015)	0.167 (0.031)	...	...
Hε λ3970	0.27	0.191 (0.039)	0.356 (0.088)	0.076 (0.015)	0.104 (0.025)	...	...
Hδ λ4101	0.23	0.178 (0.039)	0.306 (0.078)	0.185 (0.015)	0.241 (0.038)	...	...
Hγ λ4340	0.16	0.355 (0.032)	0.513 (0.080)	0.360 (0.011)	0.432 (0.057)	0.340 (0.041)	0.520 (0.090)
Hβ λ4861	0.00	1.000 (0.045)	1.000 (0.067)	1.000 (0.012)	1.000 (0.051)	1.000 (0.045)	1.000 (0.068)
[O III] λ4959	-0.03	0.128 (0.032)	0.121 (0.034)	0.235 (0.009)	0.228 (0.030)	0.181 (0.033)	0.169 (0.037)
[O III] λ5007	-0.04	0.352 (0.034)	0.322 (0.051)	0.693 (0.011)	0.664 (0.083)	0.368 (0.034)	0.333 (0.052)
He I λ5876	-0.20	0.103 (0.016)	0.064 (0.013)	0.157 (0.007)	0.124 (0.016)	...	...
[O I] λ6300	-0.26	0.254 (0.018)	0.137 (0.021)	0.152 (0.006)	0.112 (0.014)	0.312 (0.038)	0.153 (0.029)
[O I] λ6363	-0.27	0.068 (0.016)	0.036 (0.010)	0.042 (0.006)	0.030 (0.006)	...	...
[N II] λ6548	-0.30	0.982 (0.038)	0.490 (0.072)	0.581 (0.012)	0.412 (0.051)	1.036 (0.089)	0.466 (0.080)
Hα λ6563	-0.30	5.777 (0.185)	2.870 (0.418)	4.052 (0.037)	2.870 (0.353)	6.417 (0.222)	2.870 (0.442)
[N II] λ6584	-0.30	2.849 (0.093)	1.406 (0.205)	1.684 (0.018)	1.189 (0.146)	3.005 (0.127)	1.334 (0.209)
He I λ6678	-0.31	...	...	0.045 (0.012)	0.031 (0.009)	...	...
[S II] λ6717	-0.32	1.125 (0.057)	0.533 (0.082)	0.852 (0.014)	0.589 (0.073)	1.360 (0.131)	0.575 (0.105)
[S II] λ6731	-0.32	0.892 (0.052)	0.420 (0.066)	0.627 (0.013)	0.433 (0.054)	0.870 (0.126)	0.366 (0.078)
[O III] λ5007/λ4959		2.74 (0.72)	2.67 (0.85)	2.95 (0.12)	2.91 (0.53)	2.04 (0.40)	1.97 (0.52)
[N II] λ6584/λ6548		2.90 (0.07)	2.87 (0.58)	2.90 (0.06)	2.88 (0.50)	2.90 (0.24)	2.86 (0.65)
[S II] λ6717/λ6731		1.26 (0.10)	1.27 (0.27)	1.36 (0.12)	1.36 (0.24)	1.56 (0.20)	1.57 (0.43)
F(Hβ) λ4861		153.0		151.0		126.7	
c(Hβ)		1.02 (0.05)		0.50 (0.05)		1.17 (0.05)	
A_V		2.19		1.08		2.52	
Extraction fibres		425		77		384	

Table 5.6: Integrated line intensities for NGC 6701, NGC 7770 & NGC 7771. For a full description see caption of Table 5.1.

the observing conditions were non-optimal, with strong changes in transparency. Both effects can be noticed in the integrated spectrum of NGC 6643 shown in Figure 5.19. The spectrum does not include the [O II] λ3727 line, the continuum is noisy with few emission lines present, while the sky-residual of the [O I] λ5577 line is prominent.

The SSP modelling is relatively good, considering the problems mentioned above. The derived parameters of the SSP fitting are: age of 5.71 Gyr, [Z/H] = -0.02 and A_V = 1.2. In the residual spectrum only few lines are recovered: Hα, Hβ, Hγ, and the [N II] $\lambda\lambda$6548,84, [S II] $\lambda\lambda$6717,31 doublets. The [O III] λ5007 is marginally detected. The emission line intensities for the detected lines are listed in Table 5.5. The observed ratio of [N II] is consistent with the theoretical values, but given that the [O III] λ4959 line was not detected, the [O III] ratio could not be measured. The derived extinction from the Hα/Hβ ratio is quite high, A_V = 2.06, in agreement with the high value of the SSP fitting. Values of the luminosities and SFRs derived from the line intensities are included in Table 5.7 for completeness.

NGC 6701

Figure 5.20 shows the integrated spectrum of NGC 6701. This target is one of the most distant in the PINGS sample, with a much lower surface brightness than the previous galaxies. The spectrum was obtained after 993 individual spectra, corresponding to one pointing and three dithered observations. As in the previous case, it is affected by the presence of the [O I] sky-residual at $\sim$ 5577 Å. This feature is even more prominent

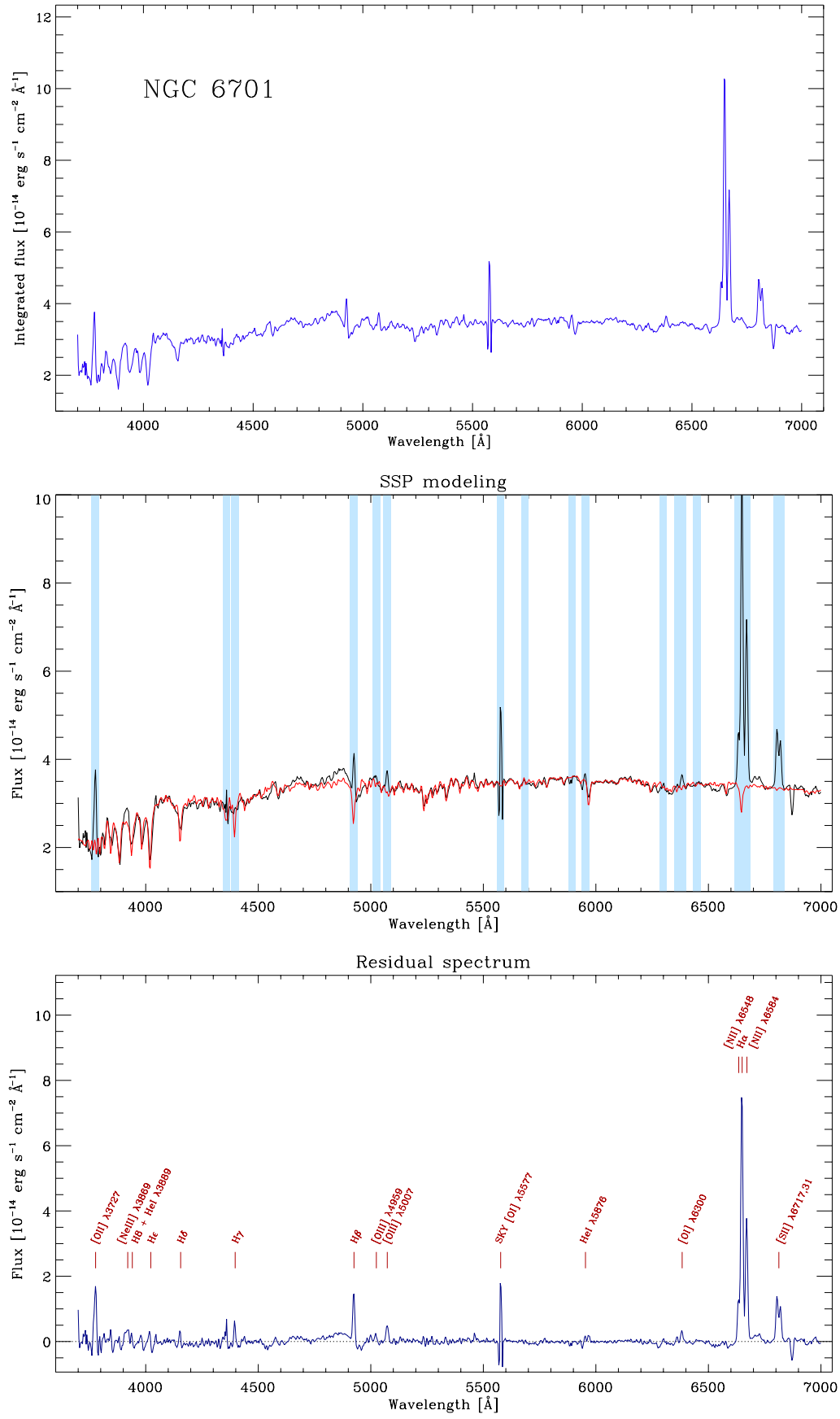

Figure 5.20: Integrated spectrum (top-panel), SSP model fitting (middle-panel), and *residual* spectrum (bottom-panel) of NGC 6701. Full description in the caption of Figure 5.11.

than the observed Hβ emission line.

There is a good agreement of the SSP modelling, with deviations in the region between 4000 and 5000 Å, being the model lower in the continuum level than the observed spectrum. The age of the derived model is 4.78 Gyr, with metallicity [Z/H] = –0.12 and A_V = 0.8. Despite being a more distant object, surprisingly the residual spectrum shows a good number of emission lines, including Hδ, Hε, H8 + He I λ3889, [Ne III] λ3869, He I λ5876 and [O I] λ6300. The [O III] λ4959 line is marginally detected. The emission line intensities for the detected lines are listed in Table 5.6. The [N II] ratios are consistent with the theoretical values, the [O III] ratio is consistent within the errors, considering the marginal detection of the λ4959 line. The derived value for the extinction is A_V = 2.19. The derived Hα and [O II] luminosities are 4.89 and 4.75 10^{41} erg s^{-1}, respectively, with corresponding SFRs of 3.9 and 6.6 $M_\odot$ yr^{-1}.

NGC 7770 & NGC 7771

These two galaxies were observed simultaneously during the mosaic construction of NGC 7771, which was the main target. NGC 7770 & NGC 7771 appear to be in an early stage of interaction, observationally, preference has been given to NGC 7771, classified as a luminous IR bright galaxy, and which previous studies suggest that is going through a period of strong star formation, probably triggered by the close interaction with NGC 7770 (Smith et al., 1999). In fact, they form part of an interacting triplet, with the third member being NGC 7769 (Karachentsev et al., 1988).

The integrated spectra of both galaxies are shown in Figure 5.21 and Figure 5.22. The fibres corresponding to the region of the smaller NGC 7770 were extracted and integrated separately by hand. Interestingly, their integrated spectra show completely different spectral features, in the case of NGC 7770, the spectrum shows practically no signs of stellar continuum and it is dominated by the presence of strong emission lines, as in the case of NGC 3310. On the other hand, the integrated spectrum of NGC 7771 presents a strong stellar continuum with practically no emission lines superimposed, except from the [O II] λ3727, Hα and the [N II] $\lambda\lambda$6548,84, [S II] $\lambda\lambda$6717,31 doublets, with somewhat recognizable broad components.

The SSP fittings for both spectra trace well the continuum for all wavelengths. The derived parameters from the SSP fitting are: 1) NGC 7770; 2.36 Gyr, [Z/H] = -0.52 and A_V = 0.6, consistent with a very young population with subsolar metallicity. 2) NGC 7771; 6.44 Gyr, [Z/H] = -0.05 and A_V = 0.8. The emission line intensities for the detected lines are listed in Table 5.4. The observed [O III] and [N II] ratios are consistent with their theoretical values. There is a hint of the [O III] λ4363 line detected in the integrated spectrum, which is lost in the residual due to the imperfect SSP fitting. This galaxy shows a relatively low value of dust extinction, A_V = 0.44. The luminosities and SFRs derived for this galaxy are: $L_{H\alpha}$ = 9.60 and $L_{[O\,II]}$ = 13.80 10^{41} erg s^{-1}. These values correspond to SFRs of $\sim$ 7.6 and 19.3 $M_\odot$ yr^{-1}, respectively. NGC 7770 shows a very clean residual spectrum, with a continuum consistent with zero in average, all the Balmer lines were detected up to H8, as well as the He I λ5876 and [O I] λ6300 lines. The residual spectrum of NGC 7771 is more noisy, but it reveals emission lines not seen in the integrated spectrum, e.g. Hβ. Marginal detections of Hγ, Hδ, Hε, and the [O III] lines are also present. In both spectra, there is a strong feature at λ5577 corresponding to the sky-residual of [O I] .

The emission line intensities for all detected lines in both galaxies are listed in Table 5.6. The [N II] and [O III] ratios for NGC 7770 are consistent with the theoretical values, while for NGC 7771, the [O III] ratio is not, due to the marginal detection of these lines. The derived values for the extinction are: 1) NGC 7770, A_V = 1.08; 2) NGC 7771, A_V = 2.52, i.e. a very high value, consistent with strong dust attenuation due to

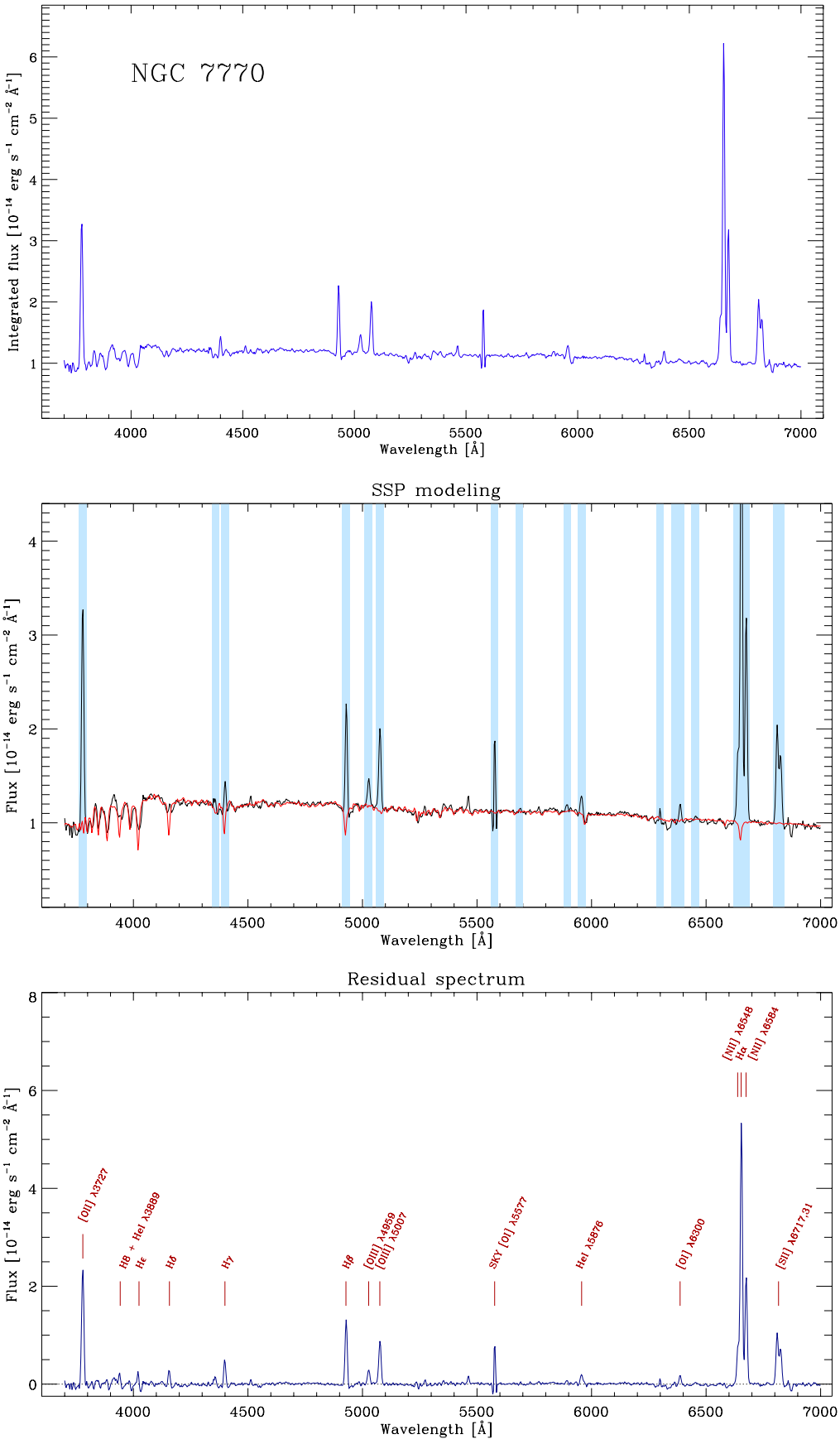

Figure 5.21: Integrated spectrum (top-panel), SSP model fitting (middle-panel), and *residual* spectrum (bottom-panel) of NGC 7770. Full description in the caption of Figure 5.11.

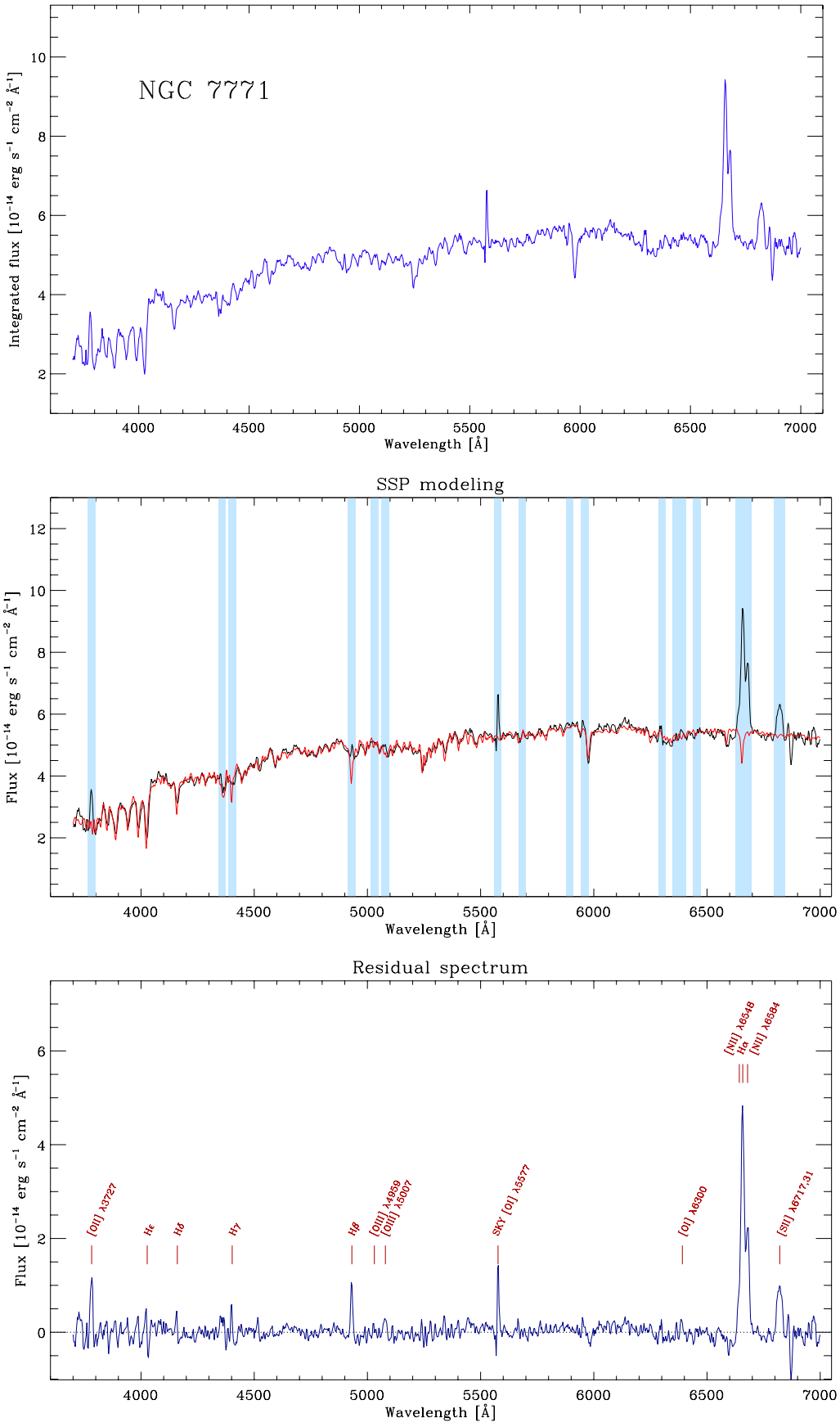

Figure 5.22: Integrated spectrum (top-panel), SSP model fitting (middle-panel), and *residual* spectrum (bottom-panel) of NGC 7771. Full description in the caption of Figure 5.11.

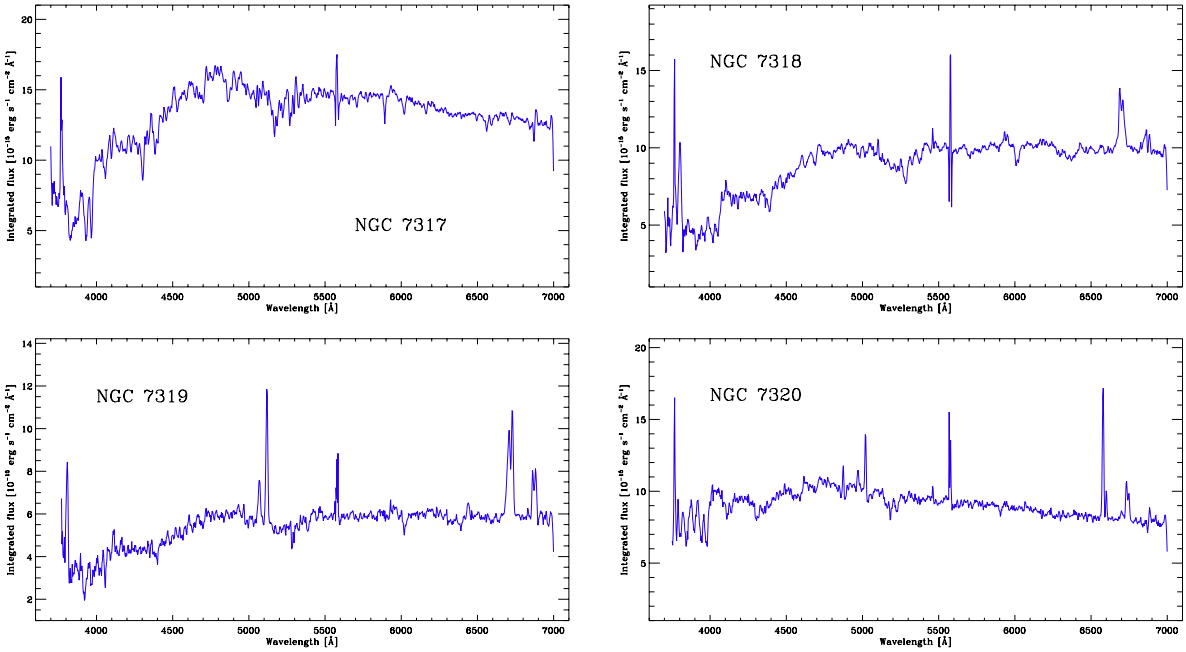

Figure 5.23: Integrated spectra of the Stephan's Quintet. In each panel, the object's name is indicated. No further analysis was performed for these objects (see text).

the nuclear starburst. The derived Hα and [O II] luminosities are: 1) NGC 7770, $L_{H\alpha}$ = 9.31 and $L_{[OII]}$ = 9.11 10^{41} erg s^{-1}; 2) NGC 7771, $L_{H\alpha}$ = 36.64 and $L_{[OII]}$ = 37.86 10^{41}erg s^{-1}, with the following SFRs: 1) NGC 7770, $SFR_{H\alpha}$ = 7.4 and $SFR_{[OII]}$ = 12.8 $M_\odot$ yr^{-1}; NGC 7771, $SFR_{H\alpha}$ = 28.9 and $SFR_{[OII]}$ = 53.0 $M_\odot$ yr^{-1}. These high SFR are consistent with the value of 40 $M_\odot$ yr^{-1} previously derived in the IR by Smith et al. (1999).

Based on recent X-ray studies, NGC 7771 is suspected to be a low-luminosity AGN, (Jenkins et al., 2005). Although no typical AGN broad-components have been previously found in this galaxy (Smith et al., 1999), the slightly broad shape of the Hα + [N II] and [S II] emission lines in the integrated spectrum might indicate a contribution in a very low level of active nuclear activity.

Stephan's Quintet

The four pointings of the Stephan's Quintet were observed as a backup programme during the run of the 10th of August 2008. Figure 5.23 shows the integrated spectrum of each pointing corresponding to NGC 7317, NGC 7318, NGC 7319 and NGC 7320. Each spectrum shows a different contribution of the stellar continuum and emission lines. A prominent sky residual feature of [O I] λ5577 is present in all spectra, specially for the spectrum corresponding to NGC 7318. Although they represent an interesting target for IFS, for the purpose of this dissertation no further analysis was performed on these objects. The integrated spectra shown in Figure 5.23 are presented for completeness.

5.2.4 Ionization and excitation properties

Different possible mechanisms can be responsible for the ionization in emission line galaxies. The source driving the ionization in a given galaxy can be identified by exploring the location of certain line ratios in the so-called diagnostic diagrams (BPT, Baldwin et al., 1981; Veilleux & Osterbrock, 1987). These diagrams

MAIN PROPERTIES OF THE INTEGRATED SPECTRA

	SSP fitting					Luminosity		SFR		
Object	Age	[Z/H]	$A_{V,\star}$	Scale	Factor	Hα	[O II]	Hα	[O II]	log u
	(Gyr)		(mag)	(pc/fibre)		(10^{41} erg s^{-1})		($M_\odot$ yr^{-1})		
(1)	(2)	(3)	(4)	(5)	(6)	(7)	(8)	(9)	(10)	(11)
NGC 628	8.95	−0.44	0.4	121.2	1.84	3.08	2.30	2.4	3.2	–3.58
NGC 1058	6.51	−0.46	0.0	138.3	1.9	0.65	0.61	0.5	0.9	–3.50
NGC 1637	5.12	−0.19	0.2	156.3	1.9	1.09	0.84	0.9	1.2	–3.62
NGC 2976	2.86	−0.15	0.4	47.1	6.9	0.22	0.22	0.2	0.3	–3.47
NGC 3184	5.14	0.08	0.2	144.7	1.9	1.66	0.66	1.3	0.9	–3.44
NGC 3310	0.98	−0.12	0.6	227.6	1.5	9.60	13.80	7.6	19.3	–3.19
NGC 4625	7.04	−0.52	0.4	133.0	1.9	0.23	0.19	0.2	0.3	–3.62
NGC 5474	3.25	−0.05	0.0	88.8	2.2	0.17	0.25	0.1	0.3	–3.30
NGC 6643	5.71	−0.02	1.2	260.5	1.5	3.56	1.38	2.8	1.9	...
NGC 6701	4.78	−0.12	0.8	306.0	1.5	4.89	4.75	3.9	6.6	–3.66
NGC 7770	2.36	−0.52	0.6	770.6	1.5	9.31	9.11	7.4	12.8	–3.42
NGC 7771	6.44	−0.05	0.8	769.5	1.5	36.64	37.86	28.9	53.0	–3.64

Table 5.7: Properties derived from the analysis of the integrated spectra of the PINGS sample. Col. 2, 3 and 4 are derived properties from the SSP modelling, but as discussed in the text, these properties should be taken with caution, as the regressions might create fits with no physical meaning. The $A_{V,\star}$ value corresponds to the model dust attenuation. Col. (3): [Z/H] = $\log(Z)_{SSP}$ - $\log(Z_\odot)$, Z = 27(O/H), and $Z_\odot$ = 0.20. Col. (5): Physical size corresponding to the aperture of the PPAK fibre, assuming an angular distance derived from the information of Table 3.1. Col. (6): aperture correction factor applied to derive the luminosities of Col. (7) and (8), and the SFR of Col. (9) and (10). Col. (11): ionization parameter (not derived for NGC 6643 due to the lack of the [O III] λ3727 line).

can be used as a tool to differentiate objects in which the photoionization is by hot OB stars (H II regions), from objects in which is due to a non-thermal continuum (e.g. LINERs, AGNs). These diagnostics involve two or three strong emission lines with a dependence on the ionization degree and, to a lesser extent, on temperature or abundance. The most common ones are [O III] λ5007/Hβ vs. [N II] λ6584/Hα and vs. [S II] $\lambda\lambda$6717,6731/Hα. Note that these line ratios are not reddening-sensitive.

The spectra of H II region-line galaxies can be distinguished from that of narrow-line AGNs by the weakness of low-ionization lines such as [N II] λ6584, [S II] $\lambda\lambda$6717,31 and [O I] λ6300. The [S II] and [O I] emission lines arise preferentially in a zone of partly ionized hydrogen. This zone is quite extended in objects photoionized by a spectrum containing a large fraction of high-energy photons (e.g. a power-law continuum), but is nearly absent in galaxies photoionized by OB stars. The ionization potentials of S I (10.36 eV) and O I (13.62 eV) are low, while S II has a intermediate value (23.40 eV). Therefore, the emission coming from [S II] λ6717, λ6731 and [O I] λ6300 is related to low ionization and the ratio to Hα will decrease with the degree of ionization.

The behaviour of the [N II] λ6584/Hα is similar to [S II] $\lambda\lambda$6717,31/Hα. A high [N II] λ6584/Hα ratio requires very high N abundances, non-stellar ionizing agents or both. Any galaxy spectrum with a [N II] λ6584/Hα ratio greater than 0.70 suggests a variety of low-level active nucleus (Burbidge & Burbidge, 1965). However, a note of caution must be taken when dealing with gas of very low ionization degree. The

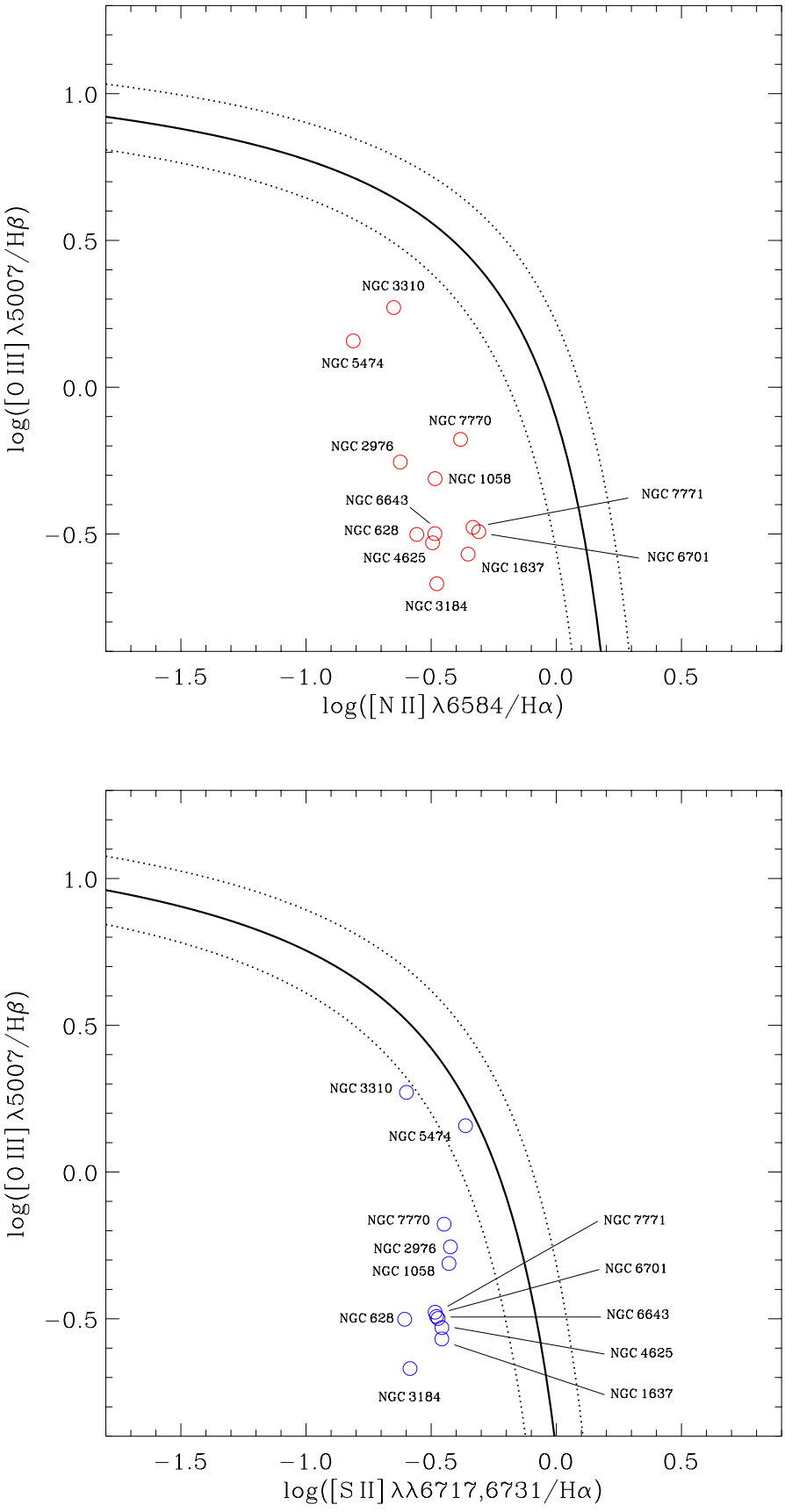

Figure 5.24: Diagnostic diagrams for the integrated spectra of the PINGS sample. Each galaxy has been labeled. The dark-thick lines correspond to the theoretical boundaries for starburst after Kewley et al. (2001), the dashed-lines represent the ± 0.1 dex variation.

ionization potential of N I (14.53 eV) is slightly higher than that of H I , so [N II] λ6584/Hα could decrease when the ionization degree increases. On the other hand, the ionization potential of [O III] is high (54.89 eV) as compared with that of H I (13.6 eV). Thus, the emission of the [O III] λ5007 line is related to highly ionized gas. Summarising, the flux ratio [O III] λ5007/Hβ is a good indicator of the mean level of ionization (radiation field strength) and temperature of the gas, whereas [N II] λ6584/Hα or [S II] $\lambda\lambda$6717,31/Hα are indicators of the number of ionizations per unit volume (ionization parameter).

Figure 5.24 shows the [O III] λ5007/Hβ vs. [N II] λ6584/Hα (top-panel) and vs. [S II] $\lambda\lambda$6717,31/Hα (bottom-panel) diagnostic diagrams for the integrated spectra of the PINGS sample, based on the values listed in tables 5.1 to 5.6. In each diagram, the dark-thick line corresponds to the theoretical boundaries for starburst, dividing the region from objects of other types of excitation, based on the parametrization given by Kewley et al. (2001), the dashed lines represent the $\pm$ 0.1 dex variation. Line ratios below and to the left of these boundaries correspond to the expected values for star-forming galaxies and/or H II regions. All galaxies are located within these regions, indicating that the dominant ionization mechanism in the integrated spectra of the galaxy sample is due to hot OB stars. The position of the suspected low-luminosity AGN NGC 7771 shows one of the highest [N II] λ6584/Hα ratios, but it is consistent with a starburst ionizing mechanism. The positions of NGC 3310 and NGC 5474 in the [O III] λ5007/Hβ vs. [S II] $\lambda\lambda$6717,31/Hα diagram lie very close to the boundary of non-thermal ionization. However, their position in the [O III] λ5007/Hβ vs. [N II] λ6584/Hα diagram correspond to a H II -region like galaxy.

The (volume-averaged) ionization parameter, defined as the ratio of the density of ionizing photons to the particle density:

$$u = \frac{Q_{H^0}}{4\pi R_s^2 nc}, \tag{5.2}$$

where Q_{H^0} is the flux of ionizing photons produced by the exciting stars above the Lyman limit, R_s is the radius of the Strömgren sphere, n the number density of hydrogen atoms, and c the speed of light. This parameter determines the degree of ionization at any particular location within the nebula. An alternative definition, considering S_{H^0}, the *local* ionizing photon flux through a unit area:

$$\mathscr{U} = \frac{S_{H^0}}{nc}, \tag{5.3}$$

can be physically interpreted as the maximum velocity of an ionization front that can be driven by the local radiation field (Kewley & Dopita, 2002). As discussed in the next section, many of the empirical methods commonly used to derive the chemical abundance of a star-forming region are sensitive to this parameter, and for some ranges of metallicity, they are not useful unless the ionization parameter can be constrained within a small range of possible values.

The ionization parameter is best determined using the ratios of emission lines of different ionization stages of the same element. In general, the larger the difference in ionization potentials of the two stages, the better the constrain. A commonly used ionization parameter diagnostic is based on the ratio [O II]/[O III] = λ3727 / (λ4959 + λ5007). However, this ratio is not only sensitive to the ionization parameter, but is also strongly dependent on metallicity. Another possibility is to use the [S III] λ9069 and/or [S III] λ9532 together with the [S II] λ6717, λ6731 emission lines. The [S II]/[S III] ratio provides a more reliable useful ionization parameter diagnostic (Diaz et al., 1991). Alternatively, it can also be determined from [O II]/Hβ

or [S II]/Hα if the metallicity of the region is known (Diaz, 1994). Table 5.7 lists the derived ionization parameter log u for the integrated spectra, estimated via:

$$\log u = -0.80 \log([\text{O II}] / [\text{O III}]) - 3.02, \tag{5.4}$$

after Díaz et al. (2000). Their uncertainty is estimated to be ± 0.2 dex. In all cases, the derived $\log u$ correspond to low values of the ionization parameter ($\sim 10^{-4}$), with the highest value corresponding to NGC 3310 ($\log u$ = –3.19), and the lowest to NGC 6701 ($\log u$ = –3.66). Some studies have suggested than the ionization parameter derived from [O II]/[O III] is systematically lower than the one obtained from the [S II]/[S III] ratio, implying a low effective temperature of the ionizing stars (Castellanos et al., 2002).

5.3 Chemical abundance analysis

Galaxies in the local universe have been used as an anchor point to determine the evolution of the metallicity along different cosmological periods. The global metallicity of a given galaxy is represented by its oxygen abundance. The rest of the elements vary with it in solar proportions. However, while the determination of this observable at high redshift normally describes their average values across the galaxies (due to aperture effects), at the local universe most of these determinations are based on studies of a number of discrete H II regions. Previous works which have studied the integrated abundances of spiral galaxies found that integrated spectroscopy provides a fairly reliable measure of the gas-phase abundance (e.g. Kobulnicky et al., 1999; Pilyugin et al., 2004, and references therein). However, these studies synthesized integrated spectra by co-adding observations of individual H II regions; therefore, they could not investigate the systematic effects of diffuse emission and dust reddening.

The integrated spectra presented in this chapter allow us to derive the real-global emission line spectrum for a nearby galaxy, and to perform an integrated abundance analysis in a consistent way as the studies performed over high redshift galaxies, with the advantage than the results of the integrated study can be compared with the abundances of resolved regions within each galaxy, considering the effects mentioned above. In this section, I present a chemical abundance analysis of the integrated spectra of the PINGS sample, together with a summary of the different abundance diagnostic methods used to perform such analysis.

5.3.1 The *empirical method* for abundance determination

As previously explained in chapter 1, the analysis of nebular spectra from diffuse H II regions in the Galaxy, to extragalactic H II regions and H II galaxies, has been the main source of information regarding the metal content of regions of recent star formation. In principle, recombination lines would provide the most accurate determination of the abundance, due to their weak dependence on nebular temperature. However, most of the observed emission in nebulae correspond to collisionally excited lines, and their intensities depend exponentially on the temperature of the gas.

Electron temperature is useful as an abundance indicator since higher chemical abundances increase nebular cooling, leading to lower H II region temperatures. This temperature can be determined from the ratios of auroral lines like [O III] λ4363 to lower excitation lines such as λ4959, λ5007, or [N II] λ5755 to λ6548, λ6584. In practice, however, these ratios involve the detection and measurement of one intrinsically weak line, which in objects of low-excitation and/or low surface brightness, result too faint to be observed. Giving these limitations, empirical methods based on the use of strong, easily observable optical lines have

been developed throughout the years. Although abundances derived in this way are recognised to suffer considerable uncertainties, they are believed to be able to trace large-scale trends in galaxies.

The so-called *empirical method* is based on the cooling properties of ionized nebulae which ultimately reflect on a relation between emission line intensities and oxygen abundance. When the cooling is dominated by oxygen, the electron temperature depends inversely on oxygen abundance. Since the intensities of collisionally excited lines depend exponentially on temperature, a relation is expected to exist between these intensities and oxygen abundance. According to Pagel et al. (1979), the main underlying assumptions behind the method are:

(a) The nebula is ionization bounded.

(b) The region can be represented by small clumps of gas with a given electron density surrounded by much less dense material, so that the degree of ionization is proportional to $(\varepsilon^2 n_e Q_H)^{1/3}$, where n_e is the clump electron density, Q_H is the number of hydrogen ionizing photons and ε is the filling factor.

(c) The cooling is fixed by oxygen abundance.

under this assumptions, the emission-line spectrum of the nebula will depend on: the energy distribution of the ionizing radiation field, the ionization parameter and the oxygen abundance. Therefore, if a single relation between the chosen calibrator and the oxygen abundance is sought, further assumptions are needed, implying that either the hardness of the radiation field or the degree of ionization or both depend on oxygen abundance.

Following these ideas, several abundance calibrators have been proposed involving different emission-line ratios and have been applied to determine oxygen abundances in objects as different as individual H II regions in spiral galaxies, dwarf irregular galaxies, nuclear starburst, and emission-line galaxies. By far, the most commonly used such ratio is ([O II] λ3727 + [O III] λ4959, λ5007)/Hβ, known as the R_{23} method (Pagel et al., 1979). The logic for the use of this ratio is that it is not affected by differences in relative elemental abundances, and remains essentially constant within a given giant H II region despite variations in excitation (Diaz et al., 1987). The R_{23} is double-valued (see Figure 5.28), the lower branch increases with increasing abundance, while the upper branch shows an opposite behavior, i.e. R_{23} decreases with increasing abundance. There is an ambiguity inherent to the method since there are two values of abundance corresponding to a given value of R_{23}. The turn-over in the relation is located around $12 + \log(\mathrm{O/H}) \sim 8.1$, however this is ill-defined zone where regions with the same R_{23} value have oxygen abundances which differ by almost an order of magnitude. The origin of this behavior is because at low abundance the intensity of the forbidden lines scales roughly with the chemical abundance, while at high abundance the nebular cooling is dominated by the infrared fine-structure lines and the electron temperature becomes too low to collisionally excite the optical forbidden lines. Another drawback of using R_{23} (and many of the other emission-line abundance diagnostics) is that it depends also on the ionization parameter. Some calibrations have attempted to take this into account (e.g. McGaugh 1991, hereafter M91; Kewley & Dopita 2002; hereafter KD02; Kobulnicky & Kewley 2004, hereafter KK04; Pilyugin & Thuan 2005, hereafter PT05), with different levels of success.

Among the empirical methods for the determination of chemical abundances, we find theoretical methods based on photoionization models (e.g. M91; KK04; Zaritsky et al. 1994, hereafter Z94), empirical methods based on measurements of the electron temperature of the gas (e.g. Pilyugin 2001a; Pettini & Pagel 2004;

hereafter PP04), or a combination of the two (e.g. Denicoló et al. 2002, hereafter D02). The advantages and drawbacks of the different calibrators have been thoroughly discussed in the literature (e.g. Pagel et al. 1980, Kennicutt & Garnett 1996, KD02, Pérez-Montero & Díaz 2005, Kewley & Ellison 2008). Regrettably, comparisons among the metallicities estimated using these methods reveal large discrepancies. They are usually manifested as systematic offsets in metallicity estimates, with high values corresponding to theoretical calibrations and lower metallicities estimated by electron temperature metallicities, with offsets as large as 0.6 dex in log(O/H) units (Liang et al., 2006).

5.3.2 Abundance diagnostics

The abundance calibrations developed from measurements in individual extragalactic H II regions seem to be fairly robust when applied to the integrated light of galaxies (Kobulnicky et al., 1999; Pilyugin et al., 2004; Moustakas & Kennicutt, 2006a). A principal assumption of this method is that the observed emission lines arise via photoionization from massive stars. As discussed in subsection 5.2.4, there seems to be no contamination from nuclear activity in our integrated emission-line spectra. A set of these empirical calibrators were applied to the integrated spectra of the galaxy sample, in order to derive their characteristic chemical abundance. In order explore the effect of a particular calibration depending on the physical properties of the galaxies, different abundance estimators were chosen corresponding to each of the categories described above. A subset of these estimators correspond to R_{23} based calibrations. From this category, three methods were applied:

1. The M91 calibration based on detailed H II region models, using the photoionization code Cloudy (Ferland et al., 1998), which includes a correction for ionization parameter variations. The analytical expressions of Kobulnicky & Zaritsky (1999) for this calibrator were used for the lower and upper branches of R_{23}. The estimated accuracy of M91 is $\sim \pm 0.15$ dex.

2. The Z94 calibration, which was derived from the average of three previous calibrations by Edmunds & Pagel (1984), Dopita & Evans (1986) and McCall et al. (1985). Z94 provided a polynomial fit that is only valid for the upper R_{23} branch. They do not consider explicitly a solution for the ionization parameter. The estimated accuracy is equal to the difference between the different methods.

3. The KK04 calibration used stellar evolution and photoionization grids to produce a fit to each of the R_{23} branches. They propose an iterative method which takes into account the ionization parameter to produce an estimate of the metallicity. The estimated accuracy of the method is $\sim \pm 0.15$ dex.

Given the double-valued nature of R_{23}, additional information is necessary in order to discriminate between the different branches. A commonly method to break this degeneracy is based on the use of additional line ratios such as [N II]/Hα or [N II]/[O II] (Kewley & Ellison, 2008). Following previous works (e.g. KD02), the [N II]/[O II] ratio was used to differentiate between the two branches for the M91 and the Z94 R_{23}-based calibrations. The [N II]/[O II] ratio is not sensitive to the ionization parameter to within ± 0.05 dex, and it is a strong function of metallicity above $\log([\mathrm{N\,II}]/[\mathrm{O\,II}]) \gtrsim -1.2$ (KD02), the division between the upper and lower branches occurs at ~ -1.2.

Figure 5.25 shows the location of the galaxies in a [N II]/[O II] vs. log R_{23} diagram. All of them are situated in the upper-branch of R_{23} as a first visual inspection of their spectra suggested. Another hint of the right placement of the objects in this branch is that, for some galaxies, their R_{23} values would correspond

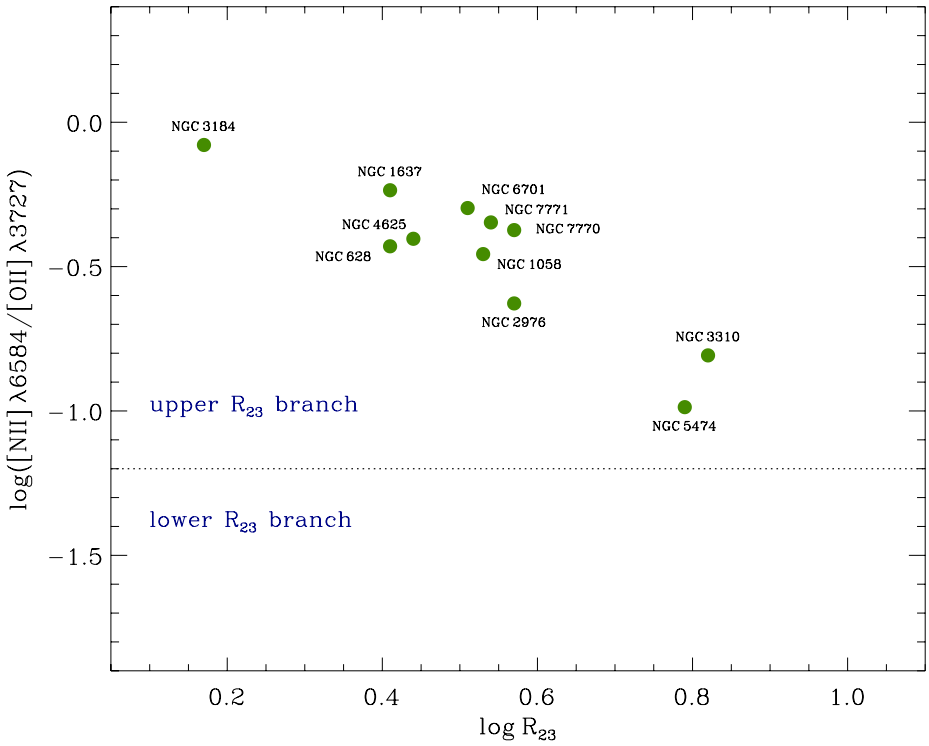

Figure 5.25: [N II] / [O II] vs. log R_{23} relation for the integrated spectra of the PINGS sample. The horizontal line corresponds to the empirical boundary between the upper and lower branch of the R_{23} relation.

to very low oxygen abundances in the lower branch (e.g. NGC 3184, NGC 1637, NGC 628), which is not expected given the strength of the oxygen lines in each individual residual spectrum. The closest galaxy to the boundary is NGC 5474, but still in a region in which it can be considered upper-branch with confidence.

Another subset of estimators was chosen from the category of empirical strong-line methods, the correspond to:

1. The N2 calibration (first proposed by Storchi-Bergmann et al. 1994), after D02, based on a fit to the relationship between electron-temperature metallicity estimates (T_e) and the N2 $\equiv$ log([N II] λ6584/Hα) index. D02 provided a linear fit valid in the regime $\sim$ –2.5 $\lesssim$ N2 $\lesssim$ –0.5. PP04 revised this calibration with an updated database, finding a better fit by a third-order polynomial, valid in the regime –2.5 $<$ N2 $<$ –0.3. The N2 metallicity value derived in this section is an average of these two N2 diagnostic versions. The estimated uncertainty of the derived metallicities is $\sim \pm$ 0.2 dex.

2. The O3N2 calibration (first proposed by Alloin et al. (1979)), using the definition by PP04, where O3N2 $\equiv$ log{[O III] λ5007/Hβ)/([N II] λ6584/Hα)}, valid for O3N2 $<$ 2.

These two indices have the virtue of being single-valued, however, they are affected by the low-excitation line [N II] λ6584, which may arise not only in bona-fide H II regions, but also in the diffuse ionized medium. According to Thilker et al. (2002), the emission from the diffuse ionized gas might contribute to up to 50% of the total Hα emission in galaxies. Therefore, calibrations of these indices based on giant H II regions may not be relevant for the interpretation of integrated spectra of galaxies.

The PT05 calibration is based on an updated version of the Pilyugin (2001b) estimator, obtained by empirical fits to the relationship between R_{23} and T_e metallicities for a sample of H II regions. This calibration includes and excitation parameter P that takes into account the effect of the ionization parameter. The PT05 calibration has two parametrizations corresponding to the lower and upper branches of R_{23}. This estimator was also considered in the present work. As in the case of the M91 and Z94 calibrators, the [N II]/[O II] ratio was used to discriminate between the two branches of the R_{23} relation.

The last strong-line "empirical" method considered is combination of the flux-flux (or ff-relation) found by Pilyugin (2005) and parametrised by Pilyugin et al. (2006), the $t_2 - t_3$ relation between the O^+ and O^{++} zones electron temperatures for high-metallicity regions proposed by Pilyugin (2007), and an updated version of the T_e-based method for metallicity determination (Izotov et al., 2006). The ff-relation links the flux of the auroral line [O III] λ4363 to the total flux in the strong nebular lines [O II] λ3727 and [O III] λ4959, λ5007. This relation is metallicity-dependent at low metallicities, but becomes independent at metallicities higher than 12+log(O/H) $\sim$ 8.25, i.e. the regime of high-metallicity H II regions. Using this relation, an inferred value of the [O III] λ4363 line can be derived, which translates to an electronic temperature of the high-ionization zone $t_3 \equiv t$([O III]). The $t_2 - t_3$ relation proposed by Pilyugin (2007) is based on the assumption that there is no one-to-one correspondence between t_2 and t_3, and that instead the $t_2 - t_3$ is a function of the excitation parameter P. This temperature, coupled with the t_3 obtained via the ff-relation, are used together with the strong-line intensity ratios in order to derive the chemical abundance using the revised T_e direct method by (Izotov et al., 2006). According to these authors, the combination of these methods solves the problem of the determination of the electron temperatures in high-metallicity H II regions, where faint auroral lines are not detected. However, the abundances determined through this method rely on the validity of the classic T_e method, which has been questioned for the high-metallicity regime in a number of studies by comparisons with H II region photoionization models (Stasińska, 2005). The abundances derived through this method (which will be called from this point the ff–T_e method), will be referred as $(O/H)_{ff}$ or ff–T_e abundances.

Finally, a *pseudo-direct* abundance determination was considered, by using the t_3 temperature derived through the ff-relation, and the "classic" prescriptions for a direct abundance determination (when the [O III] λ4363 auroral line is detected and measured). The physical conditions of the gas were obtained using the same procedures as Pérez-Montero & Díaz (2003), ionic abundances were obtained from the functional forms of Pagel et al. (1992). The nitrogen abundance was also considered under this scheme. The abundances derived through this method will be referred as $(Z/H)_D$ abundances.

Appendix C includes all the definitions and explicit equations involved in each of the empirical calibrators used in this analysis, together with the direct method prescriptions employed for the pseudo-*direct* abundance determination.

5.3.3 Integrated chemical abundances

Table 5.8 shows the value of log R_{23} and the oxygen abundance (in units of 12+log(O/H)) derived for each integrated spectrum of the sample, using the abundance diagnostics listed above. They correspond to the R_{23} methods (M91, Z94, KK04), to the index-empirical methods (N2, O3N2), and the PT05 calibrator. Given that the [O II] λ3727 line was not observed in NGC 6643, only the N2 and O3N2 abundances are given for this galaxy. Table 5.9 shows the results obtained by applying the combination of the ff–T_e methods in order to derive the $(O/H)_{ff}$ abundances. The second column corresponds to the excitation parameter P as defined

INTEGRATED ABUNDANCES: VARIOUS CALIBRATIONS

Object	log R_{23}	M91	Z94	KK04	N2	O3N2	PT05
NGC 628	0.41	8.90 ± 0.14	9.07 ± 0.14	9.06 ± 0.11	8.62 ± 0.16	8.71 ± 0.11	8.30 ± 0.19
NGC 1058	0.53	8.81 ± 0.18	8.98 ± 0.19	8.99 ± 0.14	8.68 ± 0.25	8.67 ± 0.11	8.24 ± 0.23
NGC 1637	0.41	8.90 ± 0.14	9.07 ± 0.15	9.06 ± 0.11	8.79 ± 0.24	8.80 ± 0.13	8.28 ± 0.17
NGC 2976	0.57	8.78 ± 0.19	8.94 ± 0.20	8.96 ± 0.16	8.58 ± 0.14	8.61 ± 0.10	8.21 ± 0.15
NGC 3184	0.17	9.02 ± 0.08	9.20 ± 0.10	9.13 ± 0.09	8.68 ± 0.31	8.79 ± 0.13	8.53 ± 0.11
NGC 3310	0.82	8.53 ± 0.18	8.59 ± 0.17	8.66 ± 0.12	8.56 ± 0.15	8.44 ± 0.11	8.07 ± 0.25
NGC 4625	0.44	8.88 ± 0.15	9.05 ± 0.16	9.04 ± 0.12	8.67 ± 0.33	8.74 ± 0.11	8.25 ± 0.20
NGC 5474	0.79	8.55 ± 0.16	8.64 ± 0.13	8.70 ± 0.18	8.41 ± 0.31	8.40 ± 0.09	8.03 ± 0.15
NGC 6643	...	...	...	...	8.68 ± 0.31	8.73 ± 0.13	...
NGC 6701	0.51	8.82 ± 0.17	8.99 ± 0.18	9.00 ± 0.14	8.82 ± 0.22	8.79 ± 0.13	8.16 ± 0.19
NGC 7770	0.57	8.78 ± 0.19	8.94 ± 0.20	8.96 ± 0.15	8.76 ± 0.08	8.66 ± 0.11	8.25 ± 0.20
NGC 7771	0.54	8.79 ± 0.20	8.97 ± 0.21	8.98 ± 0.17	8.80 ± 0.25	8.78 ± 0.13	8.14 ± 0.23

Table 5.8: Integrated oxygen abundances for the PINGS sample in units of 12+log(O/H). The columns designations correspond to following abundance calibrators: M91, McGaugh (1991); Z94, Zaritsky et al. (1994); KK04, Kobulnicky & Kewley (2004); N2, Denicoló et al. (2002); O3N2, Pettini & Pagel (2004); PT05, Pilyugin & Thuan (2005).

INTEGRATED ABUNDANCES: ff–T_e AND *DIRECT* METHODS

	ff–T_e method						*Direct* method	
Object	P	t_2	t_3	(O^+/H^+)	(O^{++}/H^+)	$(O/H)_{ff}$	$(O/H)_D$	$(N/H)_D$
NGC 628	0.17	0.77	0.75	8.50 ± 0.09	7.56 ± 0.14	8.55 ± 0.09	8.52 ± 0.07	7.58 ± 0.04
NGC 1058	0.20	0.81	0.84	8.47 ± 0.07	7.55 ± 0.12	8.52 ± 0.08	8.49 ± 0.04	7.58 ± 0.02
NGC 1637	0.15	0.77	0.75	8.51 ± 0.08	7.52 ± 0.14	8.56 ± 0.08	8.53 ± 0.06	7.78 ± 0.03
NGC 2976	0.21	0.83	0.87	8.46 ± 0.07	7.55 ± 0.10	8.51 ± 0.07	8.48 ± 0.03	7.41 ± 0.02
NGC 3184	0.23	0.70	0.59	8.45 ± 0.14	7.96 ± 0.25	8.57 ± 0.17	8.54 ± 0.14	7.87 ± 0.08
NGC 3310	0.38	0.96	1.13	8.31 ± 0.06	7.67 ± 0.07	8.40 ± 0.06	8.37 ± 0.00	7.24 ± 0.00
NGC 4625	0.15	0.78	0.77	8.51 ± 0.08	7.49 ± 0.13	8.55 ± 0.08	8.52 ± 0.06	7.62 ± 0.03
NGC 5474	0.31	0.93	1.12	8.37 ± 0.06	7.56 ± 0.07	8.43 ± 0.06	8.41 ± 0.00	7.03 ± 0.00
NGC 6701	0.14	0.80	0.84	8.53 ± 0.07	7.37 ± 0.13	8.56 ± 0.07	8.53 ± 0.04	7.76 ± 0.01
NGC 7770	0.24	0.83	0.86	8.44 ± 0.07	7.62 ± 0.10	8.50 ± 0.07	8.47 ± 0.04	7.66 ± 0.02
NGC 7771	0.14	0.81	0.87	8.52 ± 0.07	7.37 ± 0.11	8.55 ± 0.07	8.52 ± 0.03	7.72 ± 0.00

Table 5.9: Integrated abundances for the PINGS sample using the ff–T_e and seudo–*Direct* methods, as explained in the text, units are 12+log(Z/H). For the ff–T_e method, P corresponds to the excitation parameter, t_2 and t_3 to the electronic temperatures of the O^+ and O^{++} regions, in units of 10^4 K.

by PT05, the next two columns show the t_2 and t_3 temperatures derived from the $t_2 - t_3$ and ff-relation respectively, in units of 10^4 K. The following three columns show the ionic and total abundances of oxygen derived from the T_e method. The last two columns show the results of the (pseudo) *direct* determination by using the t_3 temperature derived from the ff–T_e method and the classic prescriptions of direct abundance determination. NGC 6643 is not included in this table for the reasons given above. In both tables, the uncertainties correspond to the 1σ error found by propagating the errors through a Monte Carlo simulation by using Gaussian distributions with a width equal to the errors of the emission line intensities, modulated by recomputing the distribution 500 times.

The calculated oxygen abundances shown in tables 5.8 and 5.9 are plotted in Figure 5.26 and Figure 5.27 for the different abundance calibrations and methods employed. The red-solid points correspond to the R_{23} methods, the green points to the index-empirical methods, and the blue points to the different methods proposed by Pilyugin and collaborators, including the pseudo-*direct* determination. The red-open circles correspond to an arbitrary –0.5 dex offset of the R_{23} methods.

As a general trend, the R_{23} methods result in higher oxygen values than the rest of the empirical methods. Among them, the M91 value is always less than Z94 and KK04 values. These two last calibrations show very close oxygen values in all cases. For all galaxies, except NGC 3310 and NGC 5474, all the R_{23} methods derive super-solar metallicity values. In all cases (except NGC 3184), the PT05 oxygen value correspond to the lowest metallicity derived for a given galaxy. The $(O/H)_{ff}$ and *Direct* abundances are very similar (within 0.1 dex) as expected, since they were calculated using the same electronic temperature[1]. The index-empirical methods, N2 and O3N2, stand in between the metallicities derived through the R_{23} and the PT05 + ff-T_e methods. It is interesting to note that, the R_{23} calibrations metallicities which were shifted to a lower value (red-open circles), considering the well-known systematic offset of theoretical-based calibrations, are in close agreement (within the errors) to the ff–T_e based metallicities. This effect is clearly seen in most cases, with the exceptions of NGC 3184, NGC 3310 and NGC 5474.

For NGC 3184, the R_{23} integrated metallicities are super-solar, with values of 12+log(O/H) $\geq$ 9.0, while the rest of the methods (and the R_{23} offsets) are closer to a solar metallicity. For NGC 3310, the R_{23}-based calibrations are consistent with the index-empirical based metallicities, with a slightly lower O3N2 oxygen abundance, but coincident with the ff–T_e determination. Only for NGC 5474, the oxygen abundance derived from the index-empirical calibrations are basically the same than the $(O/H)_{ff}$ abundance.

Given the relative large projected-size of the PINGS galaxies, practically no information on integrated abundances is available in the literature for this sample. The only comparable analysis was performed by Moustakas & Kennicutt (2006a) for 14 spiral galaxies from the MK06 sample of drift-scan integrated spectra. From this reduced number of galaxies, only NGC 1058 is a common object in both samples. Using the M91 and PT05 abundance calibrators, they found an integrated oxygen abundance of 8.86 ± 0.03 using the M91 method, and 8.23 ± 0.04 using the PT05 calibration. From Table 5.8, the integrated oxygen metallicities calculated in this work are: 8.81 ± 0.18 and 8.24 ± 0.23, respectively. Both abundance determinations agree remarkably within the errors, specially for the PT05 determination. Considering all the uncertainties and sources of systematic errors, in both the observations and reduction of the IFS data, and the intrinsic scatter of the empirical methods, the larger errors reported for the PINGS integrated abundances seem more realistic.

Figure 5.28 shows the O/H vs. R_{23} relation for the oxygen abundances found in this work, for a given

[1]The main difference relies on the way that the t_2 temperature and the electronic density are calculated, plus small variations due to different atomic parameters.

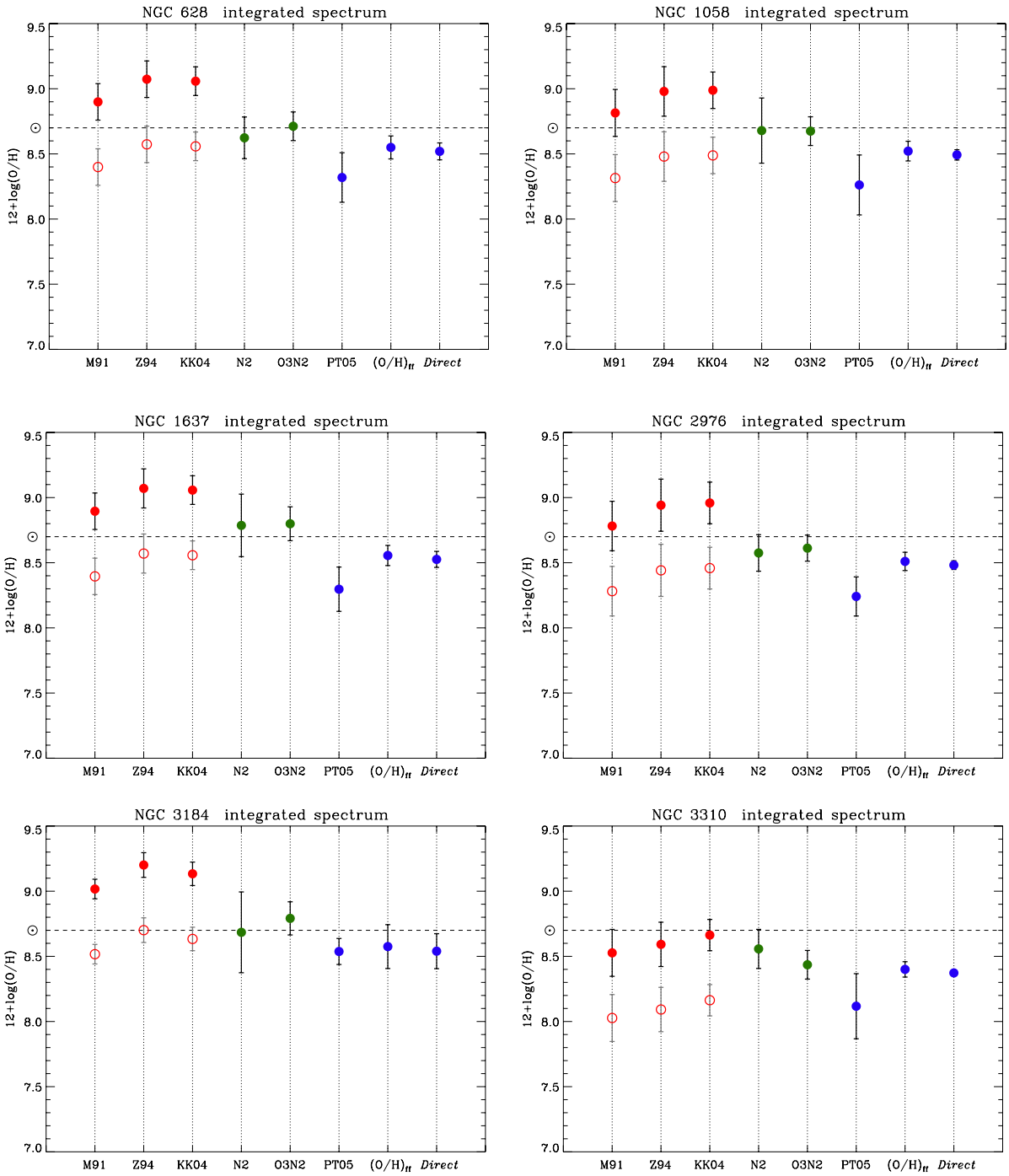

Figure 5.26: Comparison of the integrated oxygen abundances for different estimators. Red-solid points correspond to R_{23} calibrators, green-points to index-empirical methods, and blue-points to the different methods proposed by Pilyugin and collaborators. The open circles correspond to an arbitrary –0.5 dex offset of the R_{23} based methods. The horizontal dashed-line correspond to the oxygen solar value.

set of calibrators. The position of each galaxy can be inferred from the Z94 labels (orange-full diamonds) The solid lines correspond to a family of $O/H = f(\mathrm{R}_{23}, P)$ labeled for different values of the excitation parameter P. The horizontal dashed lines show the (arbitrary) transition zone between the two R_{23} branches, corresponding to 8.0 < 12+log(O/H) < 8.3. Taking as an example NGC 3184, we see that the spread in the derived oxygen abundance for different estimators can be as large as ~ 0.7 dex. The higher values correspond to the Z94 calibrator, followed (in average) by the M91, O3N2, ff–T_e and PT05 methods. As in figures

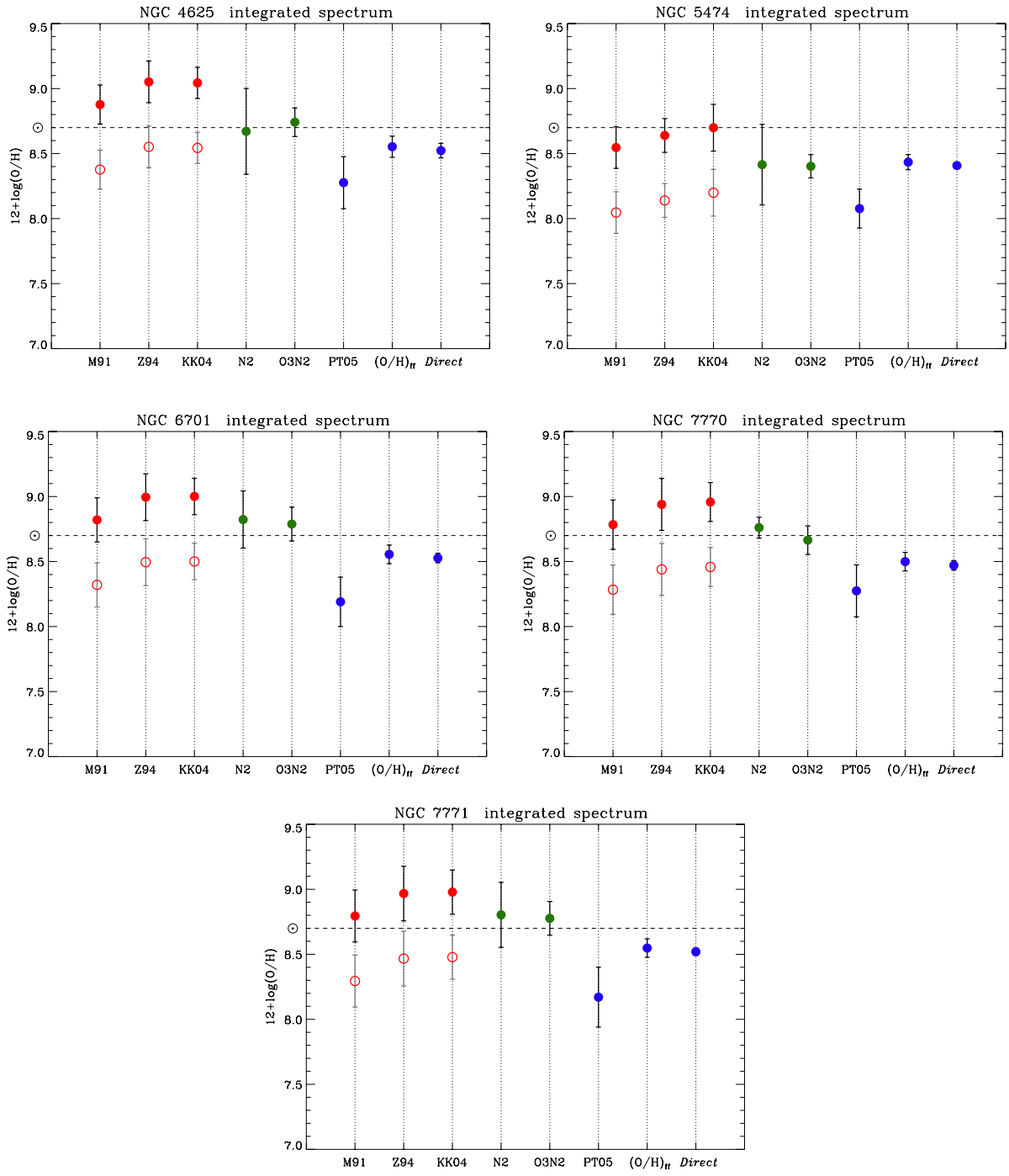

Figure 5.27: Comparison of the integrated oxygen abundances for different estimators. Same description as Figure 5.26. NGC 6643 is not included in these diagrams.

5.26 and 5.27, the open symbols correspond to the –0.5 dex offset of the theoretical-based calibrations based on R_{23}. The differences between the calibrators is reduced for decreasing metallicities (take as an example NGC 3310 and NGC 5474), where there seems to be a "convergence" of the different calibrators. For all galaxies (except NGC 3184), the PT05 derived metallicity falls within the transition zone. According to PT05 the validity of this method has been tested for regions belonging to a definite branch, the PT05 relation may be unreliable in the transition zone domain. In the case of NGC 3184, there is a very good agreement between the metallicity found by PT05 and the ff–T_e method.

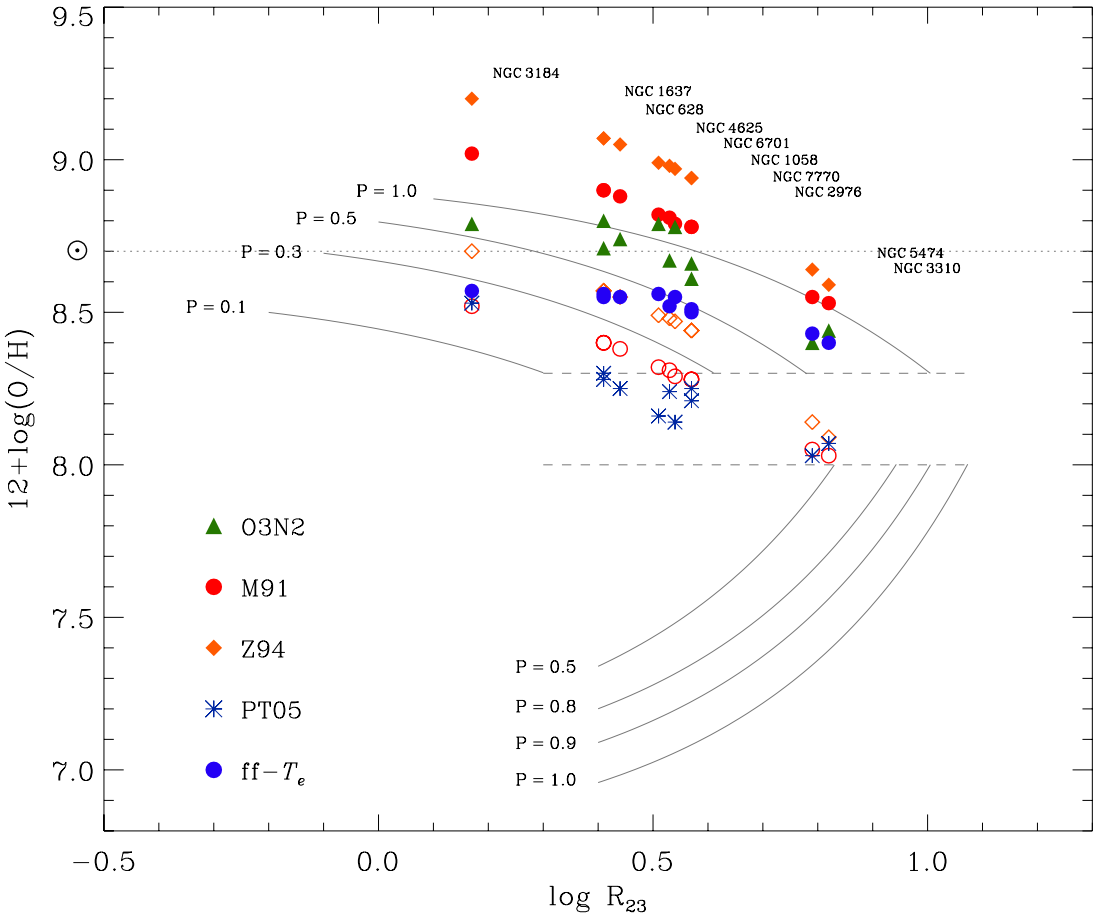

Figure 5.28: 12+log(O/H) vs. log R_{23} diagram for the integrated oxygen abundances. The different calibrators are labeled in the graph. The position of each galaxy is marked for the Z94 calibrator (orange-closed diamonds). The solid lines correspond to predictions of empirical calibrations in both branches for different values of the excitation parameter P. The horizontal dashed lines show the transition zone between the two R_{23} branches. The horizontal dotted line corresponds to the oxygen solar value. Open symbols stand for an arbitrary –0.5 dex offset of the M91 and Z94 calibrators.

5.4 Summary

In this chapter I have analysed integrated extracted spectra from the PINGS sample in different contexts. First, I obtained extractions corresponding to different apertures, varying in sizes and location within the mosaic in order to compare them with previously published integrated spectra from the drift-scan technique. These comparisons proved that the quality of the spectrophotometric calibration of the PINGS mosaic is comparable to that obtained for the drift-scanning method. After this sanity check, the integrated spectra of all the galaxies in the sample was obtained by co-adding all the individual spectra from each mosaic.

For the purpose of this dissertation, these spectra were analysed in order to derive the integrated properties of the ionized gas. For that purpose, it was necessary to decouple the emission of the stellar populations from the emission of the gas in the integrated spectrum. This was achieved by using a multi-SSP modelling algorithm which fits a linear, non-negative combination of single stellar populations in order to derive a continuum spectrum which can then be subtracted from the observed spectrum. After this method was applied, a pure-nebular emission line spectrum was obtained for each of the galaxies. This method accounts for the underlying stellar population which affects the intensity of the Balmer lines with small equivalent widths.

The intensity of all detected emission lines were measured and corrected for interstellar reddening. The techniques for decoupling the stellar continuum and the emission line fitting were explained in this chapter, detailed information can be found in the appendices of this dissertation.

The ionization and excitation properties of the derived spectra were analysed by means of diagnostic diagrams, which helped to confirm that the ionization source of the detected emission lines was due to thermal radiation (i.e. young-hot stars), and not by AGNs or LINERs. Subsequently, I outlined the method applied in order to analyse the integrated chemical abundance of each galaxy, by means of different empirical diagnostic abundance calibrators, based on the intensities of strong-lines in the spectrum. I confirmed the validity of the determination of the integrated chemical composition of a galaxy through the analysis of the global-emission line spectra. From the set of calibrators used for this purpose, the R_{23} methods based on photoionization modelling provide higher values of the oxygen abundance (M91, Z94, KK04), followed by those methods which consider one of two emission-line indices (N2, O3N2). The most stable and reliable abundance determination seems to be the ff–T_e method, although this technique gives the impression to vary very little from a mean oxygen value. The differences between different calibrators are as large as $\sim \pm 0.7$ dex, especially for the high values of O/H derived from the R_{23} methods compared to the other ones. If an arbitrary negative offset is applied (as suggested by different results in the literature), the values seems to be consistent for galaxies with R_{23} super-solar O/H values > 9.0. It was found that the validity of the abundance determination depends mainly on the chosen calibrator used to derive the chemical composition, and to a second order, on the SSP fitting decoupling.

The integrated properties of the ionized gas derived in this chapter need to be compared with the resolved properties of the same galaxies in order to analyse the validity of the results obtained from the integrated analysis, taking into account different effects, such as the extinction or the contribution of the diffuse interstellar emission. These points will be addressed in the following chapter.

6

Spatially resolved properties

Hitherto, most spectroscopic studies in nearby galaxies have focused on the derivation of physical and chemical properties of bright-individual H II regions in order to understand the physical processes at play in the formation and evolution of galaxies in the universe. However, these studies have been limited by the number of objects sampled, the number of H II regions observed and the coverage of these regions within the galaxy surface. The IFS data presented in this dissertation was conceived to tackle the problem of the 2D spectroscopic coverage of the whole galaxy surface. This information can be used to investigate the small and intermediate scale-size variation in line emission, to study the gas chemistry across the surface of a galaxy, and to characterise the relations between the 2D abundance properties and the physical properties across the disks of the parent galaxies.

In this chapter, I present a complete 2D spectroscopic analysis of the area covered by the IFS observations for four galaxies of the PINGS sample: NGC 628, NGC 1058, NGC 3184 and NGC 3310. This subset of galaxies was chosen given that they correspond to the largest objects of the sample, with the largest observed mosaics, covering a large percentage of the optical disk of the galaxies; therefore, more spatial information can be recovered from the IFS mosaics. Furthermore, they are the closest and brightest objects of the sample, combination which, in principle, would alleviate problems in the analysis due to observations of low signal-to-noise regions. These four galaxies have individual properties that make them interesting in the context of the 2D study presented in this chapter. NGC 628 is the largest object in the sample, and intrinsically interesting given its proximity, brightness and the large amount of studies based in this *normal*, grand-design, late-type galaxy. NGC 1058 is a nearly face-on galaxy with bright H II regions across its surface, but somehow lacking an evident spiral structure. These two galaxies have particularly extended disks of neutral hydrogen and present extreme outer disk star formation. NGC 3184 is another *normal* spiral with the 2nd largest IFS mosaic of the sample, claimed to be one of the oxygen-richest objects observed so far. Finally, NGC 3310 is a very bright and very distorted starburst galaxy, with a possible recent merging episode. Although by no means complete, these galaxies possess a good range of morphological and physical properties for a comparative analysis in the 2D context.

The analysis starts with a comparison of selected spatially resolved H II regions previously observed to spectra extracted from the PINGS mosaics. In the previous chapter, the comparison to previously published spectra was restricted to a qualitative basis, while in the following section the comparison will be performed in a quantitative manner, focusing on the origin of any discrepancy between different observations. Next, I present the emission line maps derived from the spectroscopic mosaics with a qualitative description of the 2D distribution of the physical properties inferred from the line intensity maps. Subsequently, a detailed, spatially-resolved spectroscopic analysis of the selected galaxies is performed, based on different spectral samples extracted from the full IFS mosaics of the galaxies. Diagnostic diagrams, radial trends of different physical parameters and metallicity gradients are then derived and analysed, comparing the results with previously published data, when appropriate.

6.1 Emission line ratios: comparison with literature

As mentioned previously, several galaxies in the PINGS sample have been spectroscopically targeted by different authors, not only for obtaining integrated spectra of the central regions as described in chapter 5, but by observing spatially resolved bright H II regions performing a variety of studies from the observed spectra. However, many of these studies have focused on outlying H II regions, and a relative few number of inner regions have been observed within the FOV of the PINGS mosaics. As an additional consistency test of the quality of the data, in this section I present a comparison of the emission line ratios measured from the PINGS data with three selected H II regions from the literature, two belonging to NGC 1058 and one for NGC 3310, for which the authors published comparable information. The emission line ratios were measured by the procedure described in the previous chapter. Table 6.1 shows a comparison of the PINGS emission line intensities for the H II regions: FGW 1058E and FGW 1058H, analysed by Ferguson et al. (1998) (hereafter FGW98), and the Jumbo H II region in NGC 3310 observed by Pastoriza et al. 1993, (hereafter Pas93).

FGW98 observed a total of 8 H II regions in NGC 1058, however, regions FGW 1058A to D are located in the inner part of the galaxy and their identification is somewhat unclear (see Figure 2 from FGW98). Regions FGW 1058F and FGW 1058G fall outside the observed FOV of PINGS. On the other hand, FGW 1058E is a bright H II region located at $\sim$ (–10, –88) arcsec in (ΔRA, ΔDec) with respect to the galaxy centre (see Figure 6.46), while FGW 1058H is an outlying H II region located at $\sim$ (140, 90) in the PINGS mosaic. For the purpose of this comparison, these two objects were selected as both fall within the FOV observed by PINGS and are uniquely distinguishable from the Hα maps/images.

In the case of FGW 1058E, a 4 arcsec circular aperture centered was applied on the fibre with the strongest emission in Hα, assuming that the long-slit observation was placed in this region as FGW98 did not give details of the observation of each specific object and their given offsets are only approximate with respect to the centre of the galaxy (even the extraction aperture is uncertain as they only quote a size range from 3 to 15 arcsec depending on the seeing and on the size of the object in question). In the case of FGW 1058H, the identification was relatively simple as this is a small and well-defined outlying H II region. The emission line ratios for this region were obtained from a single fibre at the quoted position. FGW98 published the observed and reddening corrected emission line intensities for 9 spectral lines, in Table 6.1 we compare our results with the observed un-corrected emission line fluxes only. Additional spectral lines and atomic species detected and measured in the PINGS data are also included in Table 6.1.

On the other hand, Pas93 performed an optical and near-IR spectroscopic analysis of circumnuclear

		NGC 1058				NGC 3310 JUMBO H II REGION		
		(–10.6, –87.9)		(140.6, 90.0)		PINGS		Pas 93
Line	$f(\lambda)$	PINGS	FGW 1058E	PINGS	FGW 1058H	F(λ)/F(Hβ)	I(λ)/I(Hβ)	I(λ)/I(Hβ)
[O II] λ3727	0.32	3.033 ± 0.262	2.739 ± 0.064	2.261 ± 0.130	1.950 ± 0.052	2.388 ± 0.132	3.028 ± 0.352	2.59 ± 0.040
[Ne III] λ3869	0.29	0.170 ± 0.018		0.188 ± 0.026		0.180 ± 0.020	0.223 ± 0.048	0.18 ± 0.040
H8 + He I λ3889	0.29	0.164 ± 0.018		0.111 ± 0.021		0.126 ± 0.021	0.156 ± 0.044	0.13 ± 0.039
Hε λ3970	0.27	0.162 ± 0.018		0.173 ± 0.025		0.115 ± 0.020	0.140 ± 0.043	0.17 ± 0.053
Hδ λ4101	0.23	0.209 ± 0.022		0.228 ± 0.029		0.184 ± 0.020	0.218 ± 0.039	0.21:
Hγ λ4340	0.16	0.386 ± 0.039		0.447 ± 0.046		0.406 ± 0.018	0.455 ± 0.046	0.40:
[O III] λ4363	0.15	...		...		0.017 ± 0.004	0.019 ± 0.006	0.018 ± 0.005
He I λ4471	0.12	0.029 ± 0.004		0.052 ± 0.012		0.034 ± 0.004	0.037 ± 0.009	0.036 ± 0.009
Hβ λ4861	0.00	1.000 ± 0.050	1.000 ± 0.033	1.000 ± 0.051	1.000 ± 0.037	1.000 ± 0.038	1.000 ± 0.082	1.000 ± 0.053
[O III] λ4959	-0.03	0.745 ± 0.038	0.786 ± 0.026	1.137 ± 0.057	1.148 ± 0.042	0.936 ± 0.048	0.919 ± 0.067	0.740 ± 0.007
[O III] λ5007	-0.04	2.301 ± 0.115	2.298 ± 0.076	3.227 ± 0.163	3.282 ± 0.117	2.857 ± 0.060	2.779 ± 0.143	2.310 ± 0.009
He I λ5876	-0.20	0.109 ± 0.011		0.223 ± 0.024		0.133 ± 0.011	0.114 ± 0.013	0.099 ± 0.005
[O I] λ6300	-0.26	0.050 ± 0.006		0.069 ± 0.009		0.060 ± 0.008	0.050 ± 0.010	0.051 ± 0.004
[S III] λ6312	-0.26	...		...		0.011 ± 0.004	0.009 ± 0.006	0.011 ± 0.003
[O I] λ6363	-0.27	...		...		0.021 ± 0.006	0.017 ± 0.008	0.014 ± 0.005
[N II] λ6548	-0.30	0.142 ± 0.023	0.135 ± 0.005	0.065 ± 0.013	0.099 ± 0.009	0.189 ± 0.018	0.152 ± 0.020	0.150 ± 0.005
Hα λ6563	-0.30	3.114 ± 0.156	3.231 ± 0.106	3.135 ± 0.158	2.980 ± 0.106	3.574 ± 0.056	2.870 ± 0.179	2.880 ± 0.004
[N II] λ6584	-0.30	0.413 ± 0.045	0.414 ± 0.014	0.187 ± 0.022	0.179 ± 0.009	0.548 ± 0.038	0.439 ± 0.055	0.460 ± 0.003
He I λ6678	-0.31	0.037 ± 0.004		0.020 ± 0.006		0.045 ± 0.006	0.035 ± 0.008	0.032 ± 0.003
[S II] λ6717	-0.32	0.373 ± 0.028	0.362 ± 0.012	0.190 ± 0.020	0.238 ± 0.011	0.315 ± 0.014	0.249 ± 0.032	0.270 ± 0.006
[S II] λ6731	-0.32	0.270 ± 0.023	0.257 ± 0.009	0.134 ± 0.014	0.148 ± 0.008	0.248 ± 0.015	0.196 ± 0.025	0.220 ± 0.006
I(λ5007)/I(λ4959)		3.09 ± 0.15	2.92 ± 0.14	2.83 ± 0.20	2.85 ± 0.15	3.05 ± 0.05	3.02 ± 0.08	3.12 ± 0.03
F(Hβ) λ4861		236.2	210.5	11.6	19.5		1096	1690

Table 6.1: Comparison of the PINGS emission line intensities for two H II regions in NGC 1058 and one in NGC 3310 with previous observations and published line ratios. For NGC 1058 we compare with the regions E and H by Ferguson et al. (1998), and the Jumbo H II region in NGC 3310 observed by Pastoriza et al. (1993). For NGC 1058, the coordinates shown represent approximate offsets of the H II regions with respect to the galaxy nucleus in the PINGS mosaic in the format (ΔRA, ΔDec) with NE positive. All values for NGC 1058 are the observed line ratios. In the case of the NGC 3310 Jumbo H II region, the observed and redenning corrected ratios for PINGS are shown as Pas 93 only shows corrected line intensities (see text for details). All line ratios are normalised to Hβ. * Observed Hβ flux in units of 10^{-16} erg s^{-1} cm^{-2}.

H II regions (at less than 400 pc from the nucleus) and the Jumbo H II region in NGC 3310. The identification of the circumnuclear H II regions is somewhat difficult in the PINGS mosaic given the linear scale of the regions and the size of the fibres. Therefore we chose to analyse the bright Jumbo H II region for which emission line intensities were measured by Pas93. The slit position, aperture and PA are well described by these authors, however we did not choose to simulate an aperture in the PINGS mosaic as the aperture of the slit used by Pas93 (1.5 arcsec) is smaller than the size of a single PPAK fibre. Instead, we chose the fibre within this region with the strongest emission in Hα, which corresponds to an offset (–10.6, –2.2) in (ΔRA, ΔDec) with respect to the galaxy centre in the PINGS mosaic.

Pas93 quoted only the reddening corrected line intensities, therefore for this comparison, Table 6.1 shows the observed and reddening corrected line ratios obtained from the PINGS spectrum extracted for this region. The PINGS observed line intensities listed in Table 6.1 were corrected for reddening in the same way as the integrated spectra of chapter 5, i.e. using the Balmer decrement according to the reddening function of Cardelli et al. (1989), assuming $R \equiv A_V/E(B-V) = 3.1$. Theoretical values for the intrinsic Balmer line ratios were taken from Osterbrock & Ferland (2006), assuming case B recombination, an electron density of $n_e = 100$ cm^{-3} and an electron temperature $T_e = 10^4$ K. We have used only the Hα/Hβ ratio to deduce the logarithmic reddening constant c(Hβ), obtaining a value of 0.32 for the PINGS spectrum, whereas Pas93 obtained c(Hβ) = 0.29 for the same region. Emission line fluxes were not corrected for underlying stellar absorptions. Formal errors in the derived line ratios were estimated by summing in quadrature the uncertainty in flux calibration, the statistical error in the measurement of the line flux and the error in the c(Hβ) term.

Despite the ambiguity due to the exact location and extraction aperture of the observed spectra, from Table 6.1 there is a very good agreement between the previously published emission line ratios and the PINGS observations for these three H II regions. The strongest deviation is found in the [O II] λ3727 as expected, since this line falls in the spectral region at which the instrumental low sensitivity increases the flux calibration error. The comparison with the NGC 1058 regions is more straightforward as these are the observed values without any further correction. The comparison of the emission intensities with the NGC 3310 Jumbo H II region has to be made carefully since the values of Pas93 were corrected for underlying absorption and using a different reddening curve. Nevertheless, the reddening corrected values of PINGS are in good agreement with the values derived by Pas93, even the very faint [O III] λ4363 line was detected and measured correctly, showing the good quality of the sky subtraction despite the presence of the Hg λ4358 sky-line. The line strength of the [O III] λ4363 line combined with the redshift of NGC 3310 cause that this line falls in the region of "detectability" as described in the simulation presented in subsection 6.1.1.

An additional assessment of the quality of the data is given by the value of the I(λ5007)/I(λ4959) ratio which can be predicted from atomic theory and observed in high signal-to-noise astronomical spectra. According to current atomic computations, the theoretical value for this intensity ratio is 2.98 (Storey & Zeippen, 2000). In Table 6.1 we show this ratio for the three H II regions. The observed central values for the region FGW 1058E in both datasets are in good agreement with the theoretical value. In the case of FGW 1058H both values are quite similar but differ within the errors from the theoretical value. For the NGC 3310 Jumbo H II region, the central value observed by PINGS is closer to the theoretical value for both uncorrected and corrected line ratios compared to the Pas93 value.

The flux observed by PINGS in the Hβ line for FGW 1058E is slightly higher than the one measured by FGW98, contrary to the case of FGW 1058H, where the flux in PINGS for the same line is somehow smaller, reflecting the unknown aperture extraction for the FGW98 long-slit spectrum. In the case of the

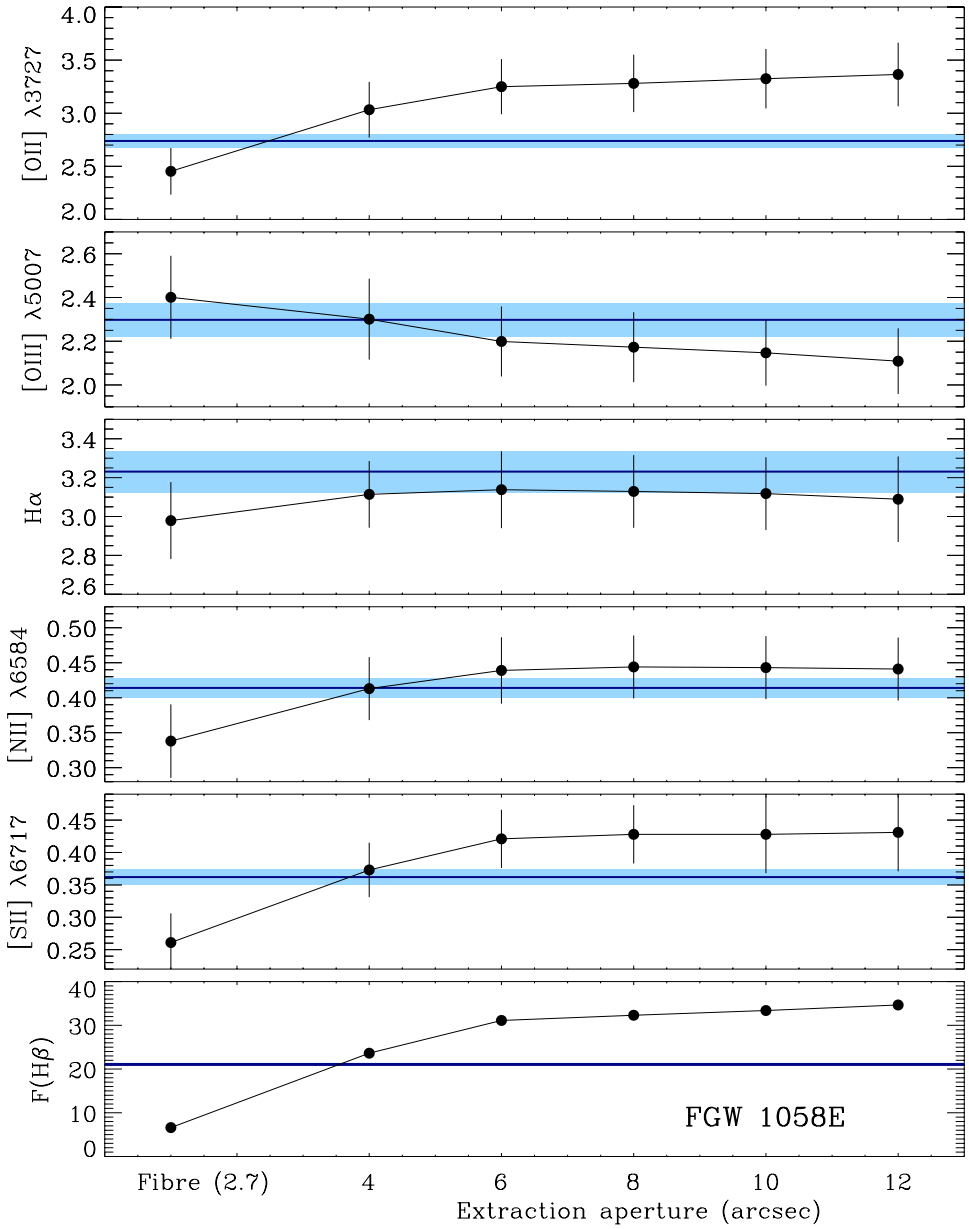

Figure 6.1: Variation of the emission line ratios as a function of integration aperture of the H II region FGW 1058E. The horizontal line/band in each panel shows the value/error derived by FGW98. All emission line intensities are normalized to Hβ. The observed integrated fluxes of Hβ are in units of 10^{-15} erg s^{-1} cm^{-2}.

NGC 3310 Jumbo H II region, the flux measured by PINGS is somewhat smaller than the one measured by Pas93.

The 2D character of the PINGS data allows us to study the variation of the spectra within a given area that would be otherwise taken as a single H II region. In Figure 6.1 we show the effect of the extraction aperture on the emission line intensities for the H II region FGW 1058E. FGW98 considered 1058E as a single H II region, however a closer look using the dithered spectroscopic mosaic shows that this region is actually a complex composed of several knots and substructures with varying emission fluxes in the most prominent lines. In order to examine the difference in the emission line ratios in this region, we take as a central position the fibre with the strongest emission in Hα within this area, with an integration aperture

of 2.7 arcsec diameter. We then take concentric circular apertures of different sizes (ranging from 4 to 12 arcsec in diameter), we integrate the spectra within these apertures to obtain spectra from which we measure a different set of emission line intensities.

The five top panels of Figure 6.1 show the variation of the emission line ratios obtained at different extraction aperture sizes for some relevant lines (normalised to Hβ). The second data point corresponds to the value shown in Table 6.1 (4 arcsec aperture), the horizontal line in each panel shows the central value and the error bar obtained by FGW98 (the dark/light blue colour line/band in the online version). The bottom panel shows the integrated flux of Hβ at each aperture. From Figure 6.1 we can see that the emission line ratios measured using different extraction apertures vary considerably as a function of the aperture size, and that in most cases the dispersion of the central values is larger than the error of the measurements, reflecting that this is a physical effect. All emission line ratios tend to converge to a certain value as the aperture size increases. Note that at the flux level in Hβ measured by FGW98 for this region, all the emission line intensity ratios, as measured by PINGS, are basically the same (within errors) as the values derived by FGW98.

From this exercise we note that, to a first-order, the emission line ratios measured for a given H II region may significantly depend on the morphology of the region, on the slit (fibre) position, on the extraction aperture and on the signal-to-noise of the observed spectrum. All these effects should be taken into account when deriving physical quantities from spectroscopic studies of H II regions, as will be discussed further in the following sections.

6.1.1 Detection of the [O III] λ4363 line

The Hg λ4358 sky line strongly affects any attempt to measure precisely the emission of the faint [O III] λ4363 line in any object with a low redshift. The temperature-sensitive line [O III] λ4363 is usually very weak in extragalactic H II regions and decreases in strength rapidly with increasing abundance. Faint H II regions coupled with the low resolution of the spectroscopy severely limit the detectability of this key diagnostic line.

In order to assess the significance of the detection of the [O III] λ4363 given the contamination of the Hg λ4358 sky line in the PINGS data, a simulation of the detectability of the [O III] λ4363 line was performed for a given range of redshifts and line intensity strengths. We simulated a pure emission line spectrum including the Hγ λ4340 and [O III] λ4363 lines at the same spectral resolution of the PINGS observations; we assumed a normally distributed I(λ4363)/Hγ ratio with a mean value of 0.10 ± 0.05, corresponding to typical values found in previous spectroscopic studies where the [O III] λ4363 line was detected in H II regions within the metallicity range of the PINGS sample (e.g. McCall et al., 1985); we did not consider higher ratios ($\sim 0.25 \pm 0.10$) which are representative of extremely low metallicity objects (e.g. Pagel et al., 1992; Izotov & Thuan, 2004). We added a random statistical noise of 0.02 RMS at the continuum level constructed from the observed spectroscopic data. A sample of 540 sky spectra were selected among all the observing runs during the three years of observations. A flux calibrated sky spectrum was created out of 20 randomly selected spectra from the total sample. This sky spectrum was added to the previous emission line plus the noise described above to create a simulated "observed" spectrum. An average sky spectrum from the total sample of 540 sky spectra was then subtracted from the simulated "observed" spectrum to obtain a "sky-free" spectrum.

Emission line intensities were then measured simultaneously for both lines in the simulated "sky-free"

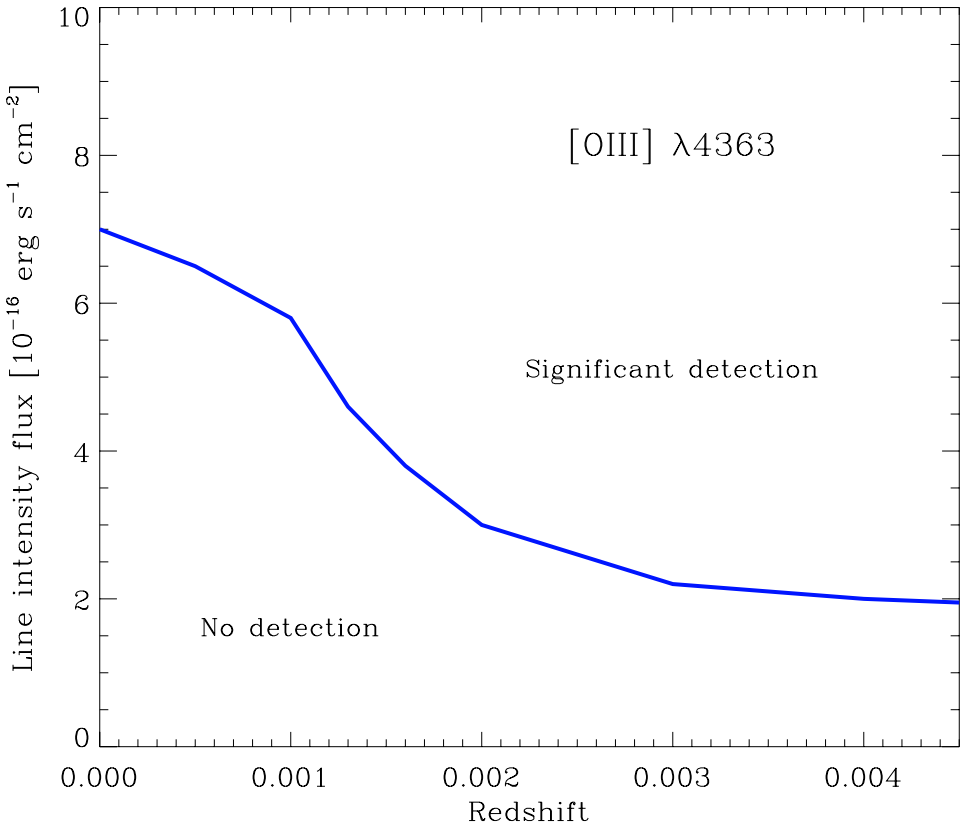

Figure 6.2: Detectability of the [O III] λ4363 line as a function of redshift and line strength according to the simulation described in subsection 6.1.1. For a given redshift, the [O III] λ4363 can be significantly detected for flux values above the thick line, which marks the region at which the difference between the observed and simulated line intensity is of the order of 15%. The contamination effect of the Hg λ4358 disappears for redshift values larger than 0.004.

spectrum using the techniques described in subsection 5.2.2. These line intensities were then compared with the flux of the pure emission lines. For a given redshift, we varied the emission line strengths of the simulated spectrum from high to lower values until the significance of the detection of the [O III] λ4363 fell drastically. We performed 100 realisations of the emission line intensity measurements for a given redshift and for a given line strength. Figure 6.2 shows the results of the simulation, the thick line represents the region at which the difference between the line intensity measured from the simulated "sky-free" spectrum and the flux from the pure emission line is of the order of 15%. According to the simulation, observed flux values of the [O III] λ4363 above this line can be significantly detected at a given redshift. For flux values below this region the significance of the detection is negligible as it is mostly affected by the statistical noise of the data. The contamination effect of the Hg λ4358 disappears for redshift values larger than $\sim$ 0.004, where the detectability of the [O III] λ4363 depends on the signal-to-noise of the spectrum at low line-intensity levels. With the aid of this simulation, we can discriminate the reliability of any detection of the [O III] λ4363 in the PINGS data, as will be discussed in the following sections.

6.2 Emission line maps

One of the main objectives of the PINGS project is to obtain complete maps of the emission-line intensities which could then be analysed to describe the 2D spatially-resolved distribution of the physical properties of the sample. The PINGS spectroscopic mosaics allow us to obtain for the first time a complete 2D view in the optical wavelength range of the main emission lines used in typical abundance diagnostics methods, and important spectral features useful for the analysis of the underlying stellar populations.

The ionized gas in spiral galaxies exhibits a complex structure associated morphologically with star-forming regions located mainly along the spiral arms. Previous attempts to perform a wide-field 2D analysis have made use of narrow-band and Fabry-Perot imaging at different spectral widths. However, in some cases the narrow-band imaging includes the contribution of more than one single emission line, such as the case of the Hα imaging, which includes the [N II] $\lambda\lambda$ 6548, 6584 doublet, or the [S II] density sensitive doublet at $\lambda\lambda$ 6717, 6731. This factor limits the utilization of these techniques to study just the basic parameters of the ionized gas, under the assumption of fixed line ratios. The great advantage of IFS arises from the fact that we are able to deblend emission lines at any discrete spatial location, and to ultimately produce maps of individual emission lines.

6.2.1 SSP fitting and emission line measurements

As in the case of the integrated spectra, in order to extract any physical information from the data set, we need first to identify the detected emission lines of the ionized gas and to decouple their emission from the stellar continuum. The population synthesis modelling method described in detail in subsection 5.2.1 was used to subtract the stellar continuum underlying the nebular emission lines. However, as opposed to the integrated case where only one spectrum was fit for a given galaxy, this method has to be applied to each individual spectrum of the IFS mosaic. Considering that the large mosaics of the galaxies presented in this chapter contain thousands of observed spectra, the SSP fitting technique is a lengthy process that has to be applied to each observed IFS mosaic. The amount of time of the SSP fitting depends on the number of templates used, but mainly on the number of spectra to be fit within a single RSS file. A good amount of the fibres in each mosaic do not contain enough signal-to-noise or do not contain signal at all (i.e. spectra with a flat continuum consistent with zero-flux), as they were sampling regions where the intrinsic flux from the galaxy is low or null (e.g. borders of the mosaic, intra-arms regions, etc). In order to speed up the SSP fitting process and to get rid of spectra where no information could be derived, a flux threshold cut was applied to each mosaic choosing only those fibres with an average flux along the whole spectral range greater than 10^{-16} erg s^{-1} cm^{-2} Å^{-1}, obtaining thus a *clean* mosaic for each of the objects.

After this (relatively conservative) flux threshold was applied, the number of fibres remaining in each mosaic was (in most cases) considerably reduced. Table 6.2 shows the number of original fibres observed per each mosaic and the number of remaining fibres after the flux cut. For the largest mosaics (e.g NGC 628), the final number of spectra in the clean mosaics accounts for $\sim$ 50% of the total number of fibres in the original RSS files. This first exercise suggests that, despite the large number of spectra obtained for a single galaxy, fibres with useful information represent only a reduced percentage of the total area sampled by the IFS observations.

The SSP fitting method was then applied to each individual spectrum of the clean mosaics. The details of this process are described in subsection 5.2.1 and Appendix A. Nevertheless, here I present briefly the

NUMBER OF FIBRES PER MOSAIC

Object	Original mosaic	Clean mosaic	Percentage
NGC 628	13571	6949	51%
NGC 1058	7944	3976	50%
NGC 3184	5296	3645	69%
NGC 3310	2979	2535	85%

Table 6.2: Number of fibres in different mosaic versions, the number in the "original" mosaic column refers to the total number of spectra considering all the pointings for a given object. The "clean" mosaic number corresponds to the remaining fibres after the flux threshold cut. The percentage stands for number of "clean" fibres with respect to the original number.

scheme followed to decouple the stellar population and the emission lines in the clean mosaics: i) For each spectrum in the data set, the underlying stellar population is fitted by a linear combination of a grid of Single Stellar Populations (SSP), masking all the nebular and sky emission lines. The effects of dust extinction are considered by varying A_V from 0 to 1 mag at $\Delta 0.2$ mag. ii) The fit stellar population is subtracted from the original spectrum to get a residual pure emission-line spectrum. This technique results in emission-line measurements corrected (to a first-order) for stellar absorption. To give an idea of the amount of time that it takes to perform the SSP fitting, let us take the example of the largest mosaic: NGC 628. For this galaxy, the 6949 spectra were fitted in 16 hours and 6 minutes, for an average of 7.2 spectra fit per minute, using a Sun ultra 40 workstation[1] running Red-Hat Linux v9.0.

In general, this process results in a good stellar continuum subtraction and accounts for the underlying stellar population in the derived intensities for each Balmer line in the spectrum. However, the automatization of this process could lead to bad fittings which might result in totally erroneous residual spectra, which will produce the measurement of non-physical emission line ratios. Considering the large number of fittings, individual inspection by eye is not practical. In order to quantify the goodness of a given fit, five spectral regions were analysed by comparing the difference between the observed spectrum and the model. The spectral windows were chosen at regions where no strong emission lines or sky residuals are expected to be found, i.e. they correspond to "continuum bands" where deviations between the model and the original spectrum can be traced. The five continuum bands are: 1) 3780–3830 Å, 2) 4200–4300 Å; 3) 4730–4830 Å; 4) 5200–5400 Å; and 5) 6100–6200 Å; where the wavelengths correspond to rest frame values. The top-panel of Figure 6.3 shows an example of a bad SSP fitting for a given spectrum of the mosaic of NGC 3310. The red part of the spectrum ($\lambda \gtrsim 5000$) shows a reasonable fit, but in the blue part there are important deviations between the model (red-line) and the observed spectrum. The five spectral windows are shown as light-blue vertical bands in the same figure, the bottom-panel shows the residuals between both spectra in terms of the RMS. The dots within each band correspond to the difference between the spectra in the way: $F(\lambda)_{\rm observed} - F(\lambda)_{\rm model}$, e.g. in the case of the Band 5, the dots are above the null-reference line, while in the Band 4, the majority of the dots are below this line.

The criterion to decide if a spectral band shows evidence of a bad fitting is the following. For a given continuum window, we compare the intrinsic scatter of the input (observed) data within the spectral window (in terms of its RMS), with the RMS of the residual spectrum within the same region. If the $\rm RMS_{residual}$

[1] With two dual-core AMD Opteron processors and 8 Gb RAM memory.

is greater than the RMS_{input} by more than 20%, then the continuum band is flagged. If 3 or more bands are flagged for the same spectrum, then the latter is flagged as a possible "bad fit". The vertical bars in the bottom-panel of Figure 6.3 correspond to the values of the input data RMS in black, and the residual RMS in red. For a given band, a good fitting would correspond to the black bar (i.e. RMS_{input}) being proportional or larger than the red bar (i.e. $RMS_{residual}$). This is the case for example of Band 4 at $\sim$ 5300 Å. However, for the rest of the bands, the red bar corresponding to the scatter in the residual spectrum is larger the black bar, by more than 20%. Therefore, this spectrum was flagged as a bad fit. Although the above methodology for identifying a bad fit might seem slightly intricate, experience with the SSP fitting proved that the criterion based on the RMS was a better option than a standard residual analysis because it is less sensitive to the effect of the intrinsic signal-to-noise of the input observed spectrum, that could lead to a erroneous flagging of spectra as a bad fit.

The number of bad fittings vary depending on the mosaic, but they range between dozens (e.g. NGC 1058) to hundreds (e.g NGC 628). Figure 6.4 shows the histograms of the ratio between the the $RMS_{residual}$ and the RMS_{input} for each spectral window of the SSP fitting of NGC 3310. In this context, a good fitting would correspond to a value of 1, while a reasonable fitting would be around this number within 20%. Bad fittings correspond to ratios $\gtrsim$ 1.2, ratios $\lesssim$ 0.8 correspond in general to spectra of very low signal-to-noise. As shown by Figure 6.4, all histograms are distributed around a central value of 1, with few spectra with ratio values $\gtrsim$ 1.2. As a test of the goodness of the SSP fitting, similar histograms were constructed for each of the mosaics in the sample. All of them show the same behavior, i.e. ratio values centered at unity, with small tails of ratios corresponding to bad fittings ($\gtrsim$ 1.2) and a more pronounced tail of lower ratio values corresponding to spectra of low signal-to-noise.

The spectra flagged as bad fits were then checked individually for each mosaic. In some cases, despite that the statistics flagged a particular spectrum with a bad fit, visual inspection showed that the fitting was reasonable good considering the intrinsic noise of the observed spectrum. However, in most cases, the flagged spectra did correspond to bad fittings. In those cases, one of two options were followed depending on the signal-to-noise of the observed spectrum: 1) If the input spectrum was of low signal-to-noise, the corresponding residual spectrum was left untouched in the residual RSS file. This decision was made considering that further threshold cuts and quality checks would be performed as part of the analysis presented in the following sections. These regions will be automatically discarded in this process, and therefore they would not represent a set of non-physical residual spectra. 2) On the other hand, if the input spectrum showed a good signal-to-noise, the SSP fitting was repeated with a modified set of templates (e.g reducing the range of metallicity); however, as experienced proved, in most cases the resultant fitting was also bad. Two alternatives were considered for those spectra with a bad fit after the second fitting was attempted, depending on the shape of the spectrum. If the input spectrum showed a strong stellar-dominated continuum with few emission lines, the corresponding residual spectrum was discarded from the residual RSS file. The reason for this is that the derived residual spectrum would be prone to large errors in the measured strengths of the emission lines. Given the large number of spectra within a single RSS mosaic, the rejection of one or two spectra within a small region would not be important from a statistical point of view. On the other hand, if the spectrum was dominated by strong emission lines with a weak, flat and/or power-law like stellar continuum (as in the case of the spectrum shown in Figure 6.3), the original observed spectrum was replaced instead of the residual spectrum in its corresponding position within the residual RSS file. For spectra of this type, the contribution of the stellar continuum is relatively small, and therefore the emission line intensities can be derived directly from the observed spectra (e.g. FGW98). The effect of the underlying stellar

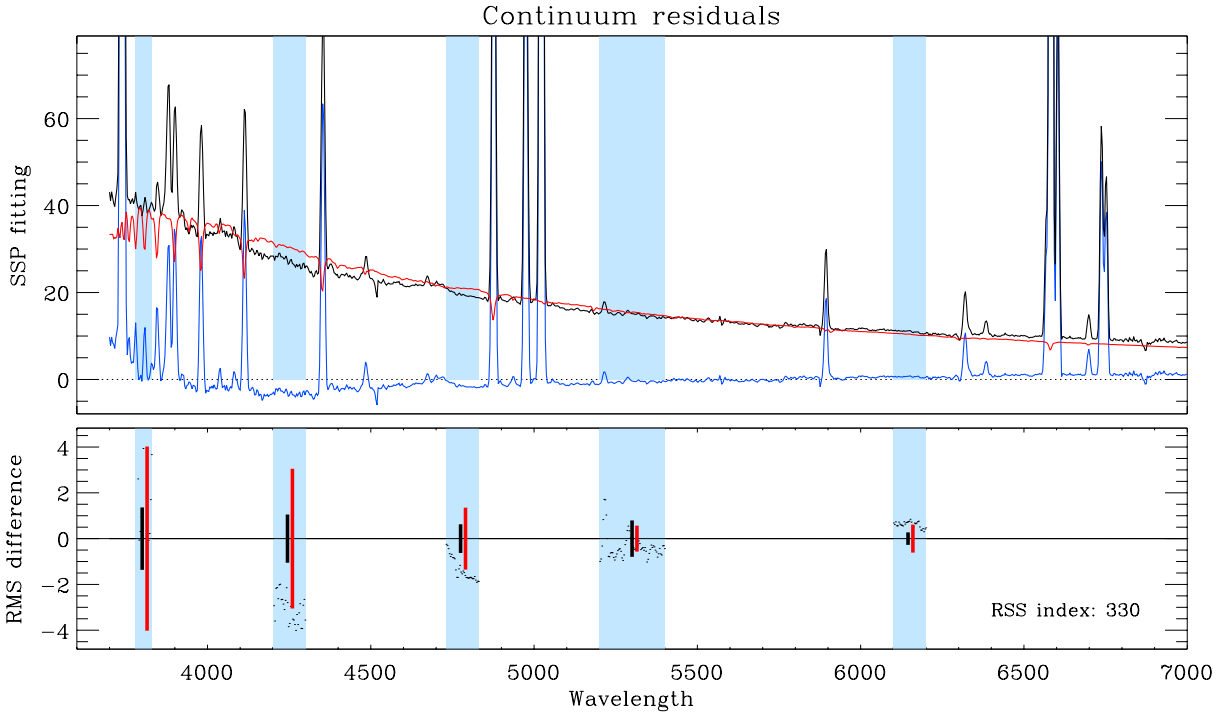

Figure 6.3: Example of a bad SSP fitting for a given spectrum of NGC 3310. The model (red) does not trace correctly the continuum of the observed spectrum (black), this effect leads to an amorphous residual spectrum (blue). The vertical bands in light-blue correspond to the continuum bands used to derive the residual statistics as explained in the text. The bottom panel shows the difference in RMS between the observed (black) and residual spectra (red) for each continuum band.

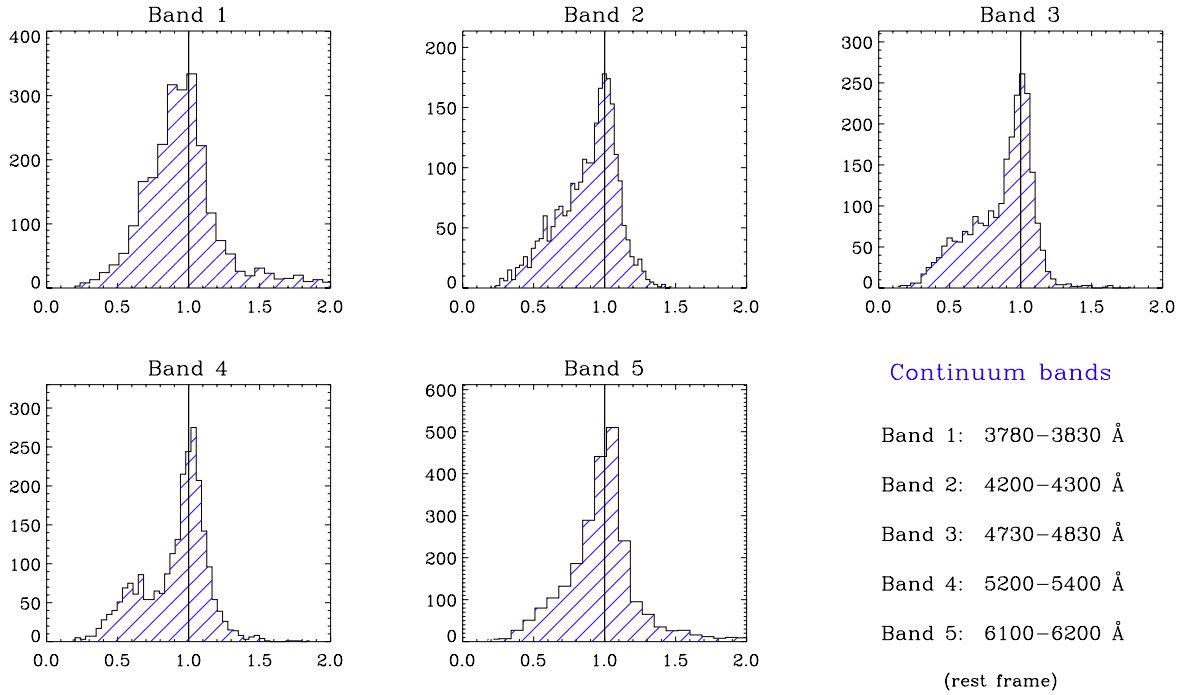

Figure 6.4: Histograms of the ratio between the the $RMS_{residual}$ and the RMS_{input} for each spectral window of the SSP fitting of NGC 331. A good fitting corresponds to a value of 1 $\pm$0.2 as explained in the text.

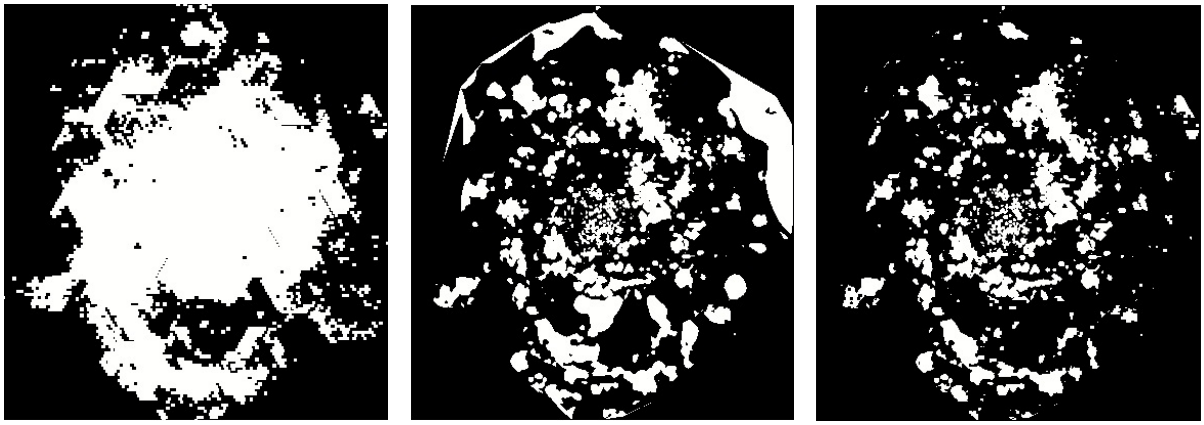

Figure 6.5: Masks constructed for NGC 628 in order to correct for the effects of interpolation on the mosaic borders (left) and for low signal-to-noise regions (middle). The final mask applied to the data is shown on right-panel. Regions in black correspond to values of zero, while regions in white to values of one.

absorption was considered by applying a 2 Å correction to the measured equivalent widths of the Balmer lines, which is a standard approach when the absorption equivalent widths cannot be derived directly (e.g. McCall et al., 1985; Oey & Kennicutt, 1993).

After the residual spectra was obtained for each of the mosaics, the intensities for each detected emission line were measured following the technique described in detail in subsection 5.2.2. As a summary, individual emission-line fluxes were measured in each spectrum by considering spectral window regions of ~ 200 Å. A simultaneous multi-component fitting was performed using a single Gaussian function (for each emission line contained within each window) plus a low order polynomial (to describe the local continuum and to simplify the fitting procedure) using FIT3D (Sánchez et al., 2006). Line intensity fluxes were then measured by integrating the observed intensity of each line. The statistical uncertainty in the measurement of the line flux was calculated by propagating the error associated to the multi-component fitting and considering the signal-to-noise of the spectral region.

As a result of the elaborated processes described above, a set of measured emission line intensities (plus associated errors) was obtained for each observed spectrum of the final clean mosaics of the whole sample (including the galaxies not considered in this chapter). From these sets of emission line intensities, emission line maps were created by interpolating the intensities derived for each individual line in each individual spectrum, based on the position tables of the clean mosaics, and correcting for the dithering overlapping effects when appropriated. The interpolation was performed using E3D, adopting a natural-neighbour, non-linear interpolation scheme, with a final scale of 1"/pixel in the resulting maps. Regions in the borders of the mosaics and/or large regions in between the mosaic without signal are prone to artifacts created by the interpolation scheme, special masks were created in order to deal with those regions. Further, as many of the derived maps are based on a reliable measurement of Hβ, a flux threshold mask was created for each mosaic for those regions with an integrated Hβ flux per fibre below 10^{-16} erg s^{-1} cm^{-2} (i.e. 0.2×10^{-16} erg s^{-1} cm^{-2} per pixel), which corresponds to a detection limit of $\sim 5\sigma$.

Figure 6.5 shows as an example, the masks employed for NGC 628, the first left-panel correspond to the mask which corrects for the effects of interpolation artifacts, while the middle one corresponds to the Hβ flux threshold mask. The right panel is the combination of both masks, which is the one applied to the data. Therefore, the resulting maps show only those regions within the area defined by this masking scheme.

Practically any emission line map (or a combination of them) can be constructed from the detected emission lines in each mosaic. In this section, I present a number of maps corresponding to the most important emission lines and derived quantities of interest. These emission line maps are presented and discussed for each galaxy in the following sections.

It is important to mention that at each step of the process we tried to avoid an over-automatization of the method, as this could lead to errors in the derived physical parameters from the resultant spectra. However, given the large amount of data, several steps were completely automated, and despite our best efforts to check and confirm at each point the consistency of the data, we might expect problems with individual fibres, pointings or regions, or in the derived quantities from the measured line intensities. Nevertheless, the methodology applied in this dissertation is very advantageous for a statistical and comparative studies and when dealing with a large number of spectra.

6.2.2 NGC 628

Figure 6.6 shows the emission line maps calculated for NGC 628. They correspond to Hα, Hβ, the doublet-blended [O II] λ 3727, [O III] λ4959 + λ5007, [N II] λ6548 + λ6584 and the [S II] λ6717 + λ6731 emission lines in units of 10^{-16} erg s^{-1} cm^{-2} arcsec^{-2}, orientated in the standard configuration North-East positive. These maps show the distribution of pure nebular emission, continuum subtracted, line intensities for each of the different species.

The top panels show the distribution of the star-forming regions in the galaxy traced by the Hα and Hβ line intensity maps. They display a distinctive spiral structure with multiple H II regions and H II complexes of different sizes and morphology along the spiral arms. The brightest sources are located at the outer regions of the galaxy, with a particular giant region located at (ΔRA, ΔDec) $\sim$ (–40,120) arcsec. From these maps we can also note the presence of diffuse emission along the spiral arms and in the intra-arms regions. The two middle panels correspond to the the line intensity distribution of [O II] λ 3727 (left), and [O III] λ 4959 + λ 5007 (right). Both maps show the same star-forming regions as those traced by the Hα and the Hβ maps. However, we can note that the line intensities of the [O II] map are stronger than the [O III] map, and that there is practically an absence of emission in the inner regions of the galaxy. This is specially important in the case of the [O III] map. Furthermore, a closer analysis of H II regions along the spiral arms show that we can identify regions with [O II] emission but with significantly less or null [O III] emission, take as an example the complexes located at (ΔRA, ΔDec) $\sim$ (40,–120) and at (–60,20).

The bottom panels display the combined emission of [N II] λ6584 + λ6584 (left) and [S II] λ6717 + λ6731. A typical (continuum subtracted) Hα narrow band image would correspond to the sum of the [N II] map plus the Hα image of the top-left panel. Again, the distribution of the [N II] and [S II] line intensities follows the spiral pattern outlined by the Hα and Hβ maps, being the nitrogen lines relatively more intense than the sulfur ones. The distribution of this element is important given its secondary nature in the nucleosynthesis process. The [S II] lines are useful to derive limits on the electron density of a particular emission line region. Both ionic species are also important to understand the degree of ionization for a given region, as explained in subsection 5.2.4.

Figure 6.7 shows an alternative visualization of the emission line maps presented in Figure 6.6, which correspond to a 3D rendering in which the *XY* plane corresponds to the RA-Dec plane, and the *Z*-axis corresponds to the emission line intensity for a particular map. The top panels show the distribution of the Hα emission line at two different projections rotated along the *Z*-axis. The height of the individual peaks

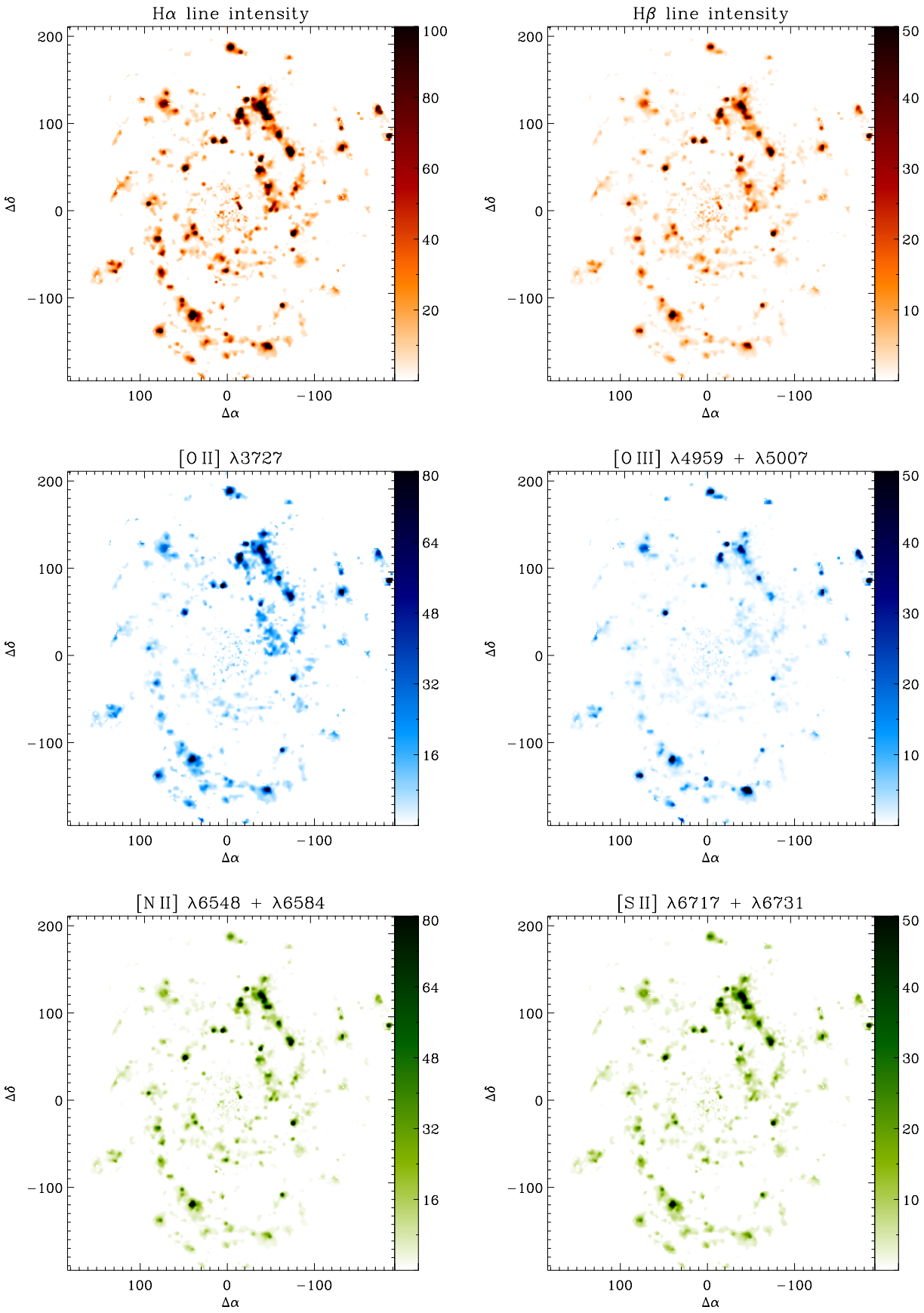

Figure 6.6: Emission line maps calculated from the IFS mosaic of NGC 628. The top panels (red) correspond to the line intensity maps of the Balmer lines Hα and Hβ; the middle panels (blue) to the [O II] and [O III] line intensity maps; the bottom panels (green) to the [N II] and [S II] emission maps. All maps are in units of 10^{-16} erg s^{-1} cm^{-2} arcsec^{-2} with a standard orientation north-east positive. No correction for dust extinction was applied to these maps.

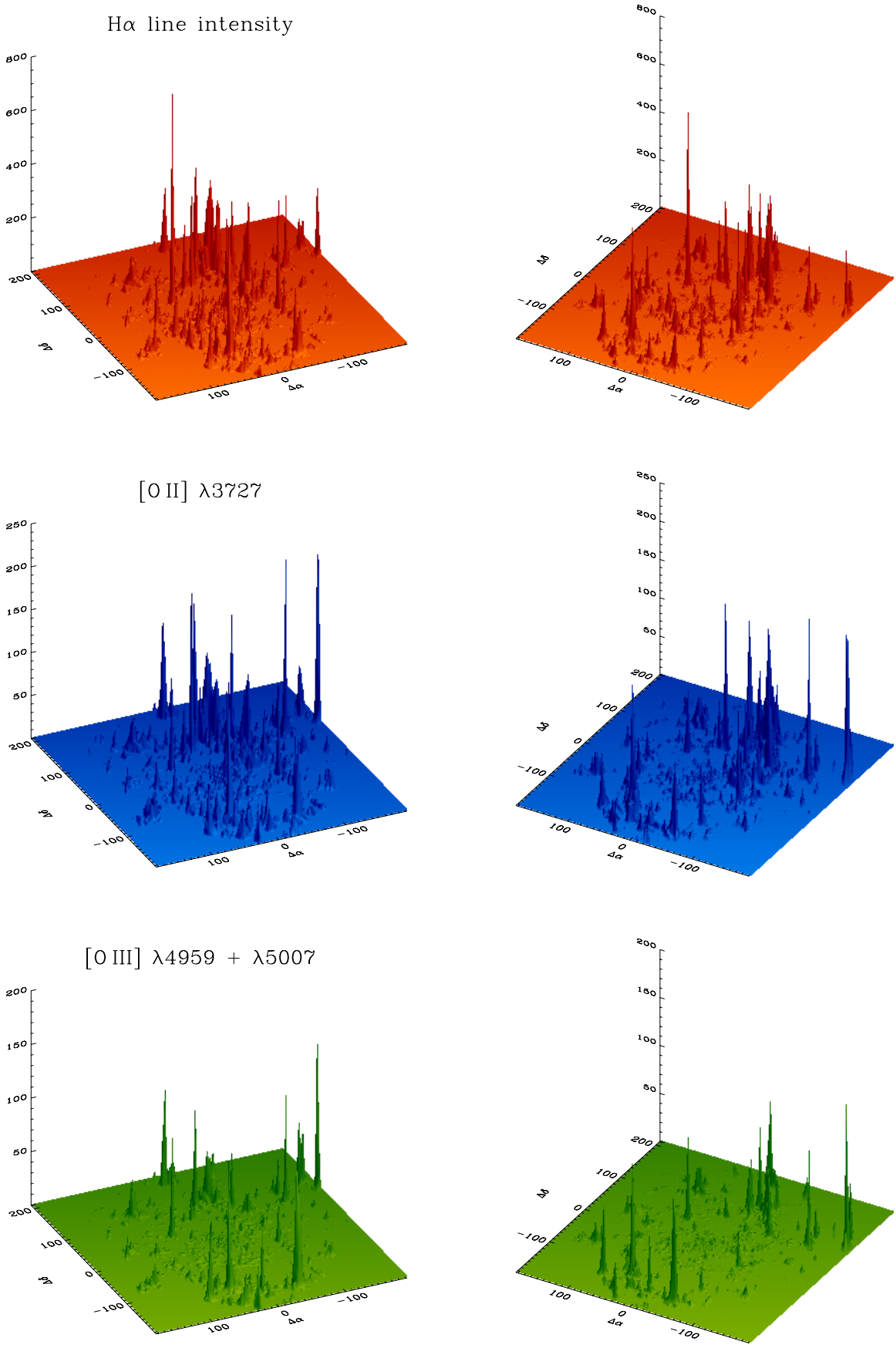

Figure 6.7: 3D visualisation of the emission line maps of NGC 628 corresponding to Hα, [O II] and [O II] emission lines. The XY-plane correspond to the RA-Dec plane, while the Z-axis corresponds to the measured interpolated intensity. Two projections are shown for each line at different angles.

correspond to the real intensity of the emission lines at that particular region. The limits shown in the color bars of Figure 6.6 were chosen to display properly, in a linear scale, within the limitations imposed by the visualization method, the different regions and the diffuse emission in each map, much in the style of typical narrow band images. The Hα 3D visualization in Figure 6.7 shows that the most intense emission is originated from the northern part of the galaxy, with a very prominent region located at (ΔRA, ΔDec) $\sim$ (50,50)

The middle panels of Figure 6.7 show a similar 3D rendering for the [O II] λ3727 line intensity. As previously described in the maps of Figure 6.6, the [O II] emission follows the regions traced by Hα, the most prominent regions are found at the northern-west part of the galaxy, coincident with the giant complex at (ΔRA, ΔDec) $\sim$ (–40,120). Interestingly, the most intense region is located at the edge of the mosaic, at $\sim$ (–190,90), which corresponds to a real emission and it is not an artifact of the interpolation at the edge of the map. The bottom panels display the rendering of the [O III] λ4959 + λ5007 intensity. In this panels the absence of emission in the central region of the galaxy is more evident, with the strongest emission corresponding to outer regions along the spiral arms and the very intense [O II] region previously mentioned.

2D SPATIAL PROPERTIES

Besides the intrinsic significance of the emission line maps presented previously, the most interesting application of the 2D distribution of the different line intensities resides in the calculation of well-known line ratios that can be translated to physical properties of the emitting gas. With the IFS data provided by PINGS we can investigate for the first time, the point-to-point variation of these physical properties over a considerable area on the surface of a galaxy. Figure 6.8 shows the spatial distribution of several key diagnostic indices commonly used in order to derive the dust extinction, the ionization conditions and the chemical abundance of typical H II regions. In each map, two perpendicular lines are drawn centered at the reference point of the mosaic, dividing the map in four quadrants.

The top-left panel of Figure 6.8 shows the distribution of the dust extinction derived from the Hα/Hβ line ratio, in terms of the visual extinction A_V (in magnitudes), assuming, as in the case of the analysis of the integrated spectrum, case-B recombination with an electron temperature of $T_e \sim 10^4$ K, and adopting the Cardelli et al. (1989) extinction law with R_V, the total to selective extinction ratio, equal to 3.1. Although other Balmer lines were detected at different locations in the galaxy, Hα and Hβ are obviously the lines with the highest signal-to-noise and therefore are the most adequate for the determination of A_V. The details on the calculation of this quantity can be found in Appendix B. The dust extinction map was derived for those locations where the intensity of the Hβ line was above the adopted flux threshold. These regions clearly follow the spiral arm structure. The dust shows a clumpy distribution, a rich structure and large variations even within the same H II region or complex. There is no apparent trend of the extinction along the spiral arms or in any radial direction. The average extinction derived from the values shown in the map is $A_V \sim 1.24 \pm 0.76$ mag, which is slightly larger but comparable to the value derived using the integrated spectrum ($A_V \sim 1.04$). The reason for this discrepancy may reside in the fact that the ionized gas component of the integrated spectrum is dominated by the spectra of the outer regions, where the intensity of the emission lines is stronger (e.g. Figure 6.6 and Figure 6.7) and the extinction is somewhat lower. Extinctions greater than 2.5 are found in specific regions, e.g. the central zone of the giant H II complex at $\sim$ (–40,120), while others are found in compact H II regions along both spiral arms. Previous studies have estimated the extinction at

different locations within this galaxy targeting individual H II regions (e.g. McCall et al., 1985; Petersen & Gammelgaard, 1996), the derived extinctions from these studies are consistent with the range of A_V values found in this work.

As discussed previously in subsection 5.2.4, the source and structure of the ionization can be in principle investigated by exploring the line ratio maps of typical diagnostic indices. The top-right panel and middle-left panel of Figure 6.8 show the line ratio maps of [N II] λ6584/Hα (N_2H_α) and [O III] λ5007/Hβ (O_3H_β), respectively, in logarithmic scale. Note that, given the proximity of the emission lines, these indices are almost reddening-independent. The N_2H_α shows a very homogeneous behaviour, with small variations in individual regions, some of them showing lower values in the central part of the regions (e.g the knot at $\Delta\alpha, \Delta\delta \sim$ 40,–130). The average ratio derived from this map is –0.55 $\pm$ 0.12 dex, which is excellent agreement with the value derived from the integrated spectrum (N_2H_α = –0.56). However, some regions at the outer part of the galaxy show lower ratios consistent with values ~ -0.75, e.g ($\Delta\alpha, \Delta\delta$) $\sim$ (–50,–160), (0,200), which might suggest a gradient of this index decreasing from the inner to the outer regions of the galaxy. On the other hand, the O_3H_β shows a clear gradient along the spiral arms with lower ratios towards the inner regions and greater values at the outer part of the galaxy. The average value of this index derived from the map is -0.50 $\pm$ 0.25 dex, which again is in good agreement with the integrated value of –0.48. It is interesting to note that the regions with the highest values of O_3H_β are coincident with the zones of the lowest N_2H_α ratios. Given that the [N II] emission originates in the singly ionized regions, between the fully ionized and the partially ionized zones, the N_2H_α ratio traces the changes in the local ionization, while the [O III] originates in the fully ionized zones, tracing the strength of the ionization. Therefore, the distribution found in these diagnostic maps may indicate that the ionization is stronger in the outer parts of the spiral arms, than in the central regions. The values of both ratios at any location in the galaxy are consistent with ionization produced by hot OB stars, as expected. In particular, there is no evidence of ionization due to shocks and/or nuclear activity.

The differences in the line ratios at different locations in the galaxy may be driven by the strength of the ionization field, being stronger in the regions with higher N_2H_α line ratio, and lower O_3H_β one. In order to investigate this point, the middle-right panel of Figure 6.8 shows the distribution of the ionization parameter in logarithmic scale, $\log u$, calculated accordingly to 5.4 (Díaz & Pérez-Montero, 2000), which is based on the dust-corrected [O II]/[O III] ratio. Both lines were corrected by extinction using the A_V map discussed previously. Note that the colour-bar is inverted compared to the rest of the maps of Figure 6.8. The $\log u$ map shows that the ionization is indeed stronger in the outer parts of the spiral arms, as the previous maps suggested. However, we can also distinguish a good degree of ionization structure in individual regions within the spiral arms, with higher values of $\log u$ corresponding to the geometrical centroids of the H II regions, as one might expect in the scenario of a central star cluster or association embedded within an H II region. Given that the dominant source of the ionization is radiation from OB stars, this result indicates that the star-formation rate is stronger in the outer regions of the galaxy. A striking feature of this map is the presence of regions with low values of the ionization parameter (blue colour) located mainly in an specific region, corresponding to the first quadrant, north-west part of the galaxy. These low $\log u$ regions are found mainly at the edges of giant H II complexes, but they are also found as individual regions. The nature of these low ionization regions will be investigated thereinafter. The mean value of $\log u$ derived from this map is –3.50 $\pm$ 0.26 dex, which is 0.08 dex higher than the value derived from the integrated spectrum of NGC 628.

A particular interesting use of the dataset is to study the metallicity content of the galaxy. As discussed

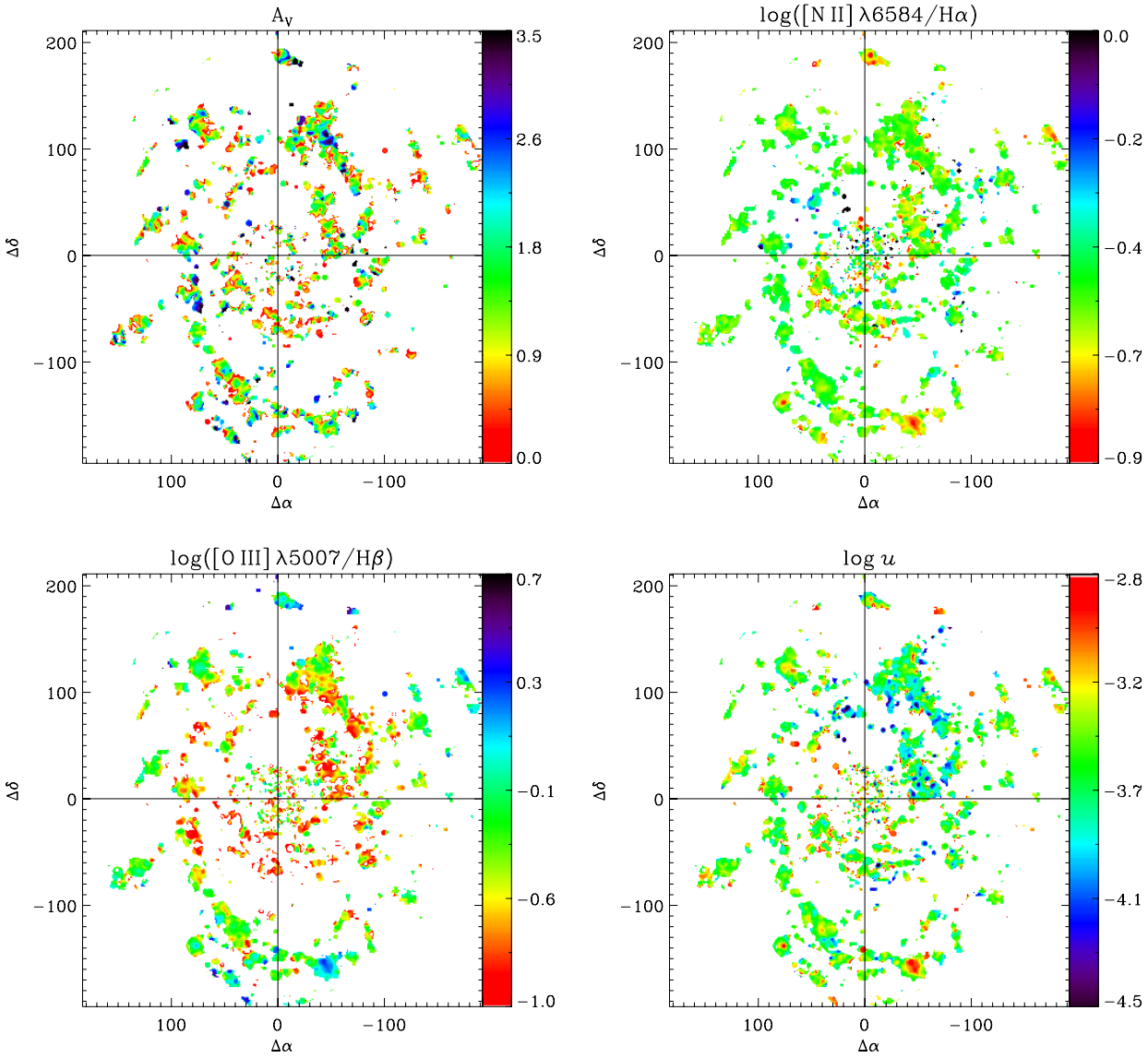

Figure 6.8: 2D spatial properties of NGC 628. The top-left panel corresponds to the A_V extinction map (in mag) derived from the Hα/Hβ ratio; the top-right panel shows the N_2H_α line ratio in logarithmic scale; the bottom-left panel corresponds to the O_3H_β line ratio in logarithmic scale; the bottom-right panel shows the distribution of the ionization parameter $\log u$. Note that the colour-bar for $\log u$ is inverted compared with the other panels. The perpendicular lines are centered at the mosaic's reference point. Offsets are in arcsec.

previously, the oxygen abundance is normally derived using a variety of diagnostic methods based on strong lines, from which the most common one is the R_{23} indicator. The logic for the use of this ratio is that is not affected by differences in relative elemental abundances, and according to the literature (e.g. Diaz et al., 1987), remains essentially constant within a given giant H II region. However, the main drawback of R_{23} is represented by its double-valued nature, as discussed in subsection 5.3.1. Nevertheless, the dust-corrected emission line maps of [O II] and [O III] provide the means to explore the behavior of this indicator. The left panel of Figure 6.9 shows the R_{23} map for NGC 628. From a first visual inspection it is evident that the map presents a clear gradient of lower values of R_{23} in the inner regions of the galaxy, to higher values to the outer parts, specially along the spiral arms. The average R_{23} value derived from the map is 2.41 ± 1.37, which is in good agreement with the value inferred from the integrated spectrum ($R_{23} = 2.57$). The lower values of R_{23} in the central regions of the galaxy are expected, given the low emission of [O II] and (especially) [O III] ,

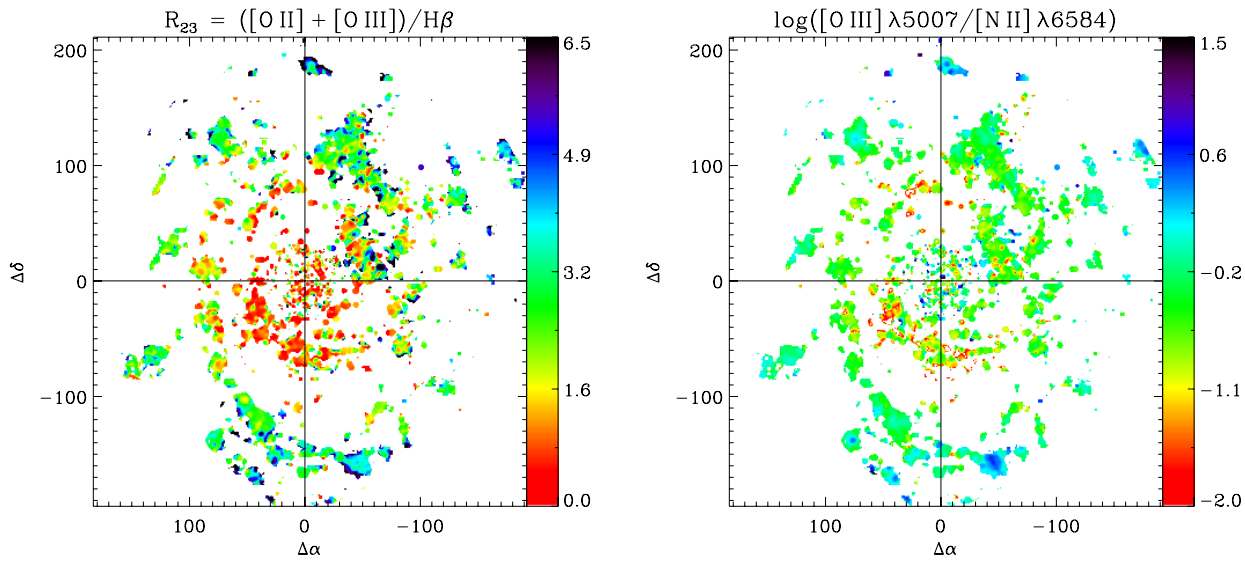

Figure 6.9: 2D distribution of the R_{23} and [O III]/[N II] metallicity indices for NGC 628. Both maps show a gradient of lower values in the inner regions to higher values to the outer part of the galaxy.

as shown in figures 6.6 and 6.7. For well-defined H II regions, the value of R_{23} seems to be constant in the majority of the cases; however, there are regions for which the value of R_{23} varies within the H II region or complex, showing some level of structure. Considering the O/H values derived after different calibrators from the integrated spectrum of NGC 628 in subsection 5.3.3 (12+log(O/H) $\sim$ 8.6), and previous abundance determinations from individual H II regions in this galaxy (e.g. McCall et al. 1985; FGW98), may suggest that the average oxygen abundance of NGC 628 corresponds to the high metallicity regime. In this scenario, the double-valued nature of the R_{23} index can be broken, and the gradient of higher-to-lower values of R_{23} from the inner to the outer parts of the galaxy shown in this map would correspond to the decrement of the R_{23} ratio in the upper-branch of a O/H vs. R_{23} diagram, and therefore, to a true metallicity gradient of the galaxy, as previous studies based on individual H II regions have shown.

Another popular, metallicity-sensitive index is given by the [O III] λ5007/[N II] λ6584 ratio. As discussed previously in subsection 5.3.1, PP04 suggested the use of this ratio (in a modified version) as abundance indicator suitable for the analysis of high-redshift galaxies. However, the direct application of this indicator may be too simplistic, the reasons being that the [O III]/[N II] ratio is strongly dependent on the excitation of the nebula, and it is also sensitive to both the ionization parameter and to the age of the cluster of exciting stars (Dopita et al., 2000). As suggested by Dopita et al. (2006), the [O III] λ5007/[N II] λ6584 ratio can only be used as an abundance indicator only when a characteristic age of the exciting clusters can be assumed, and its application in single galaxies should be taken with caution. However, the combination of this ratio with, for example, the [N II] λ6584/[O II] λ3727 ratio, can provide a good diagnostic of both metallicity and age of the ionizing source (Dopita et al., 2006). The right panel of Figure 6.9 shows the map of the [O III] λ5007/[N II] λ6584 ratio of NGC 628 in logarithmic scale. It is worthy to note that this ratio spans for more than two orders of magnitude. Similarly to the R_{23} map, this panel shows a gradient of lower values of the [O III]/[N II] ratio from the inner part of the galaxy, to higher values in the outer parts. The average value derived from the map is –0.35 $\pm$ 0.36 dex, compared to –0.40 obtained from the integrated spectrum. The map show a smoother distribution within individual regions compared to the R_{23} map. With the corresponding cautions considering the known dependences of this index with the functional parameters of the H II regions, the [O III]/[N II] gradient found for NGC 628 would correspond to a metallicity gradient

of the galaxy, with some level of inhomogeneity in individual regions as shown in this map. In order to determine the existence of abundance variations within the same region of the galaxy, it would be required to co-add the spectra corresponding to regions with similar ionization conditions, and then perform an analysis based on single regions. This detailed analysis will be presented in section 6.3.

6.2.3 NGC 1058

Figure 6.10 shows the emission line maps of Hα, Hβ, [O II], [O III], [N II], [S II] for NGC 1058, constructed in the same way as in the case of NGC 628. These maps were calculated using all the eight pointings observed for this galaxy, including the outlying position at $(\Delta\alpha, \Delta\delta) \sim$ (120,80). This is the reason of the large blank areas seen in the different panels.

The star formation in this galaxy is traced by the Hα and Hβ line intensity maps displayed in the top panels. Although many of the most intense emission regions are located along the inner spiral arms of the galaxy, some of them lie in outer regions not associated with any spiral structure (e.g. to the south of the galaxy, at $\Delta\alpha \sim$–10, $\Delta\delta \sim$–90 arcsec, which corresponds to the FGW 1058E H II region previously discussed). Two faint outlying H II regions are found at $(\Delta\alpha, \Delta\delta) \sim$ (140,80). The Hα emission is primarily coming from well-defined H II regions and there is no clear evidence of diffuse emission. The two middle-panels corresponding to the maps of the oxygen lines follow the structures traced by the Hα and Hβ maps, the intensity of the [O II] emission lines is somewhat stronger than the [O III] map, this latter is confined to well-defined regions without much diffuse emission. In both cases, we notice strong emission regions along $\Delta\alpha \sim$ –20 arcsec, and again several outlying emission regions that do not follow the spiral pattern of the galaxy. In fact, the [O III] map does not resemble a spiral pattern like the one showed by the maps of NGC 628. The green bottom panels correspond to the [N II] and [S II] emission lines. In these maps the structure traced by the Hα map is recovered, but with a lower level of detail. Furthermore, we note that the outlying H II regions are not visible in these two maps, reflecting a very low or null emission of these lines from these outlying regions.

As in the case of NGC 628, Figure 6.11 shows the 3D rendering of the Hα, [O II] and [O III] emission maps. From the Hα panels, we can note that there is a very intense Hα emission coming from the central H II regions of the galaxy. The relatively weak outlying regions are also visible in the upper-left corner. On the other hand, the [O II] emission is relatively flat in the inner part of the galaxy compared with strong peaks coming from the very bright regions at the edge of the mosaic at $\Delta\alpha \sim$ –10. In this case, the [O II] emission from the outlying regions are comparable to the [O II] flux from the inner regions of the galaxy. The [O III] panels show that there is practically no emission in the central regions of the galaxy, the strongest signal correspond to the outlying regions at $\Delta\alpha \sim$ 140 and the FGW 1058E region.

2D SPATIAL PROPERTIES

Similar line ratios as the previous galaxy were calculated for NGC 1058 in order to derive the spatial distribution of the physical properties of this galaxy. The top-left panel of Figure 6.12 shows the NGC 1058 A_V extinction map (in mag) calculated from the Hα/Hβ ratio. The map shows a clumpy distribution consistent with low extinction values. There is no evident trend or gradient of the extinction. The average A_V calculated from the map is 0.68 ± 0.51, which is in agreement with the A_V value derived from the integrated spectrum, (0.64, see subsection 5.3.3). Higher extinction values ($\sim$ 1.5) are found in small regions spread over the

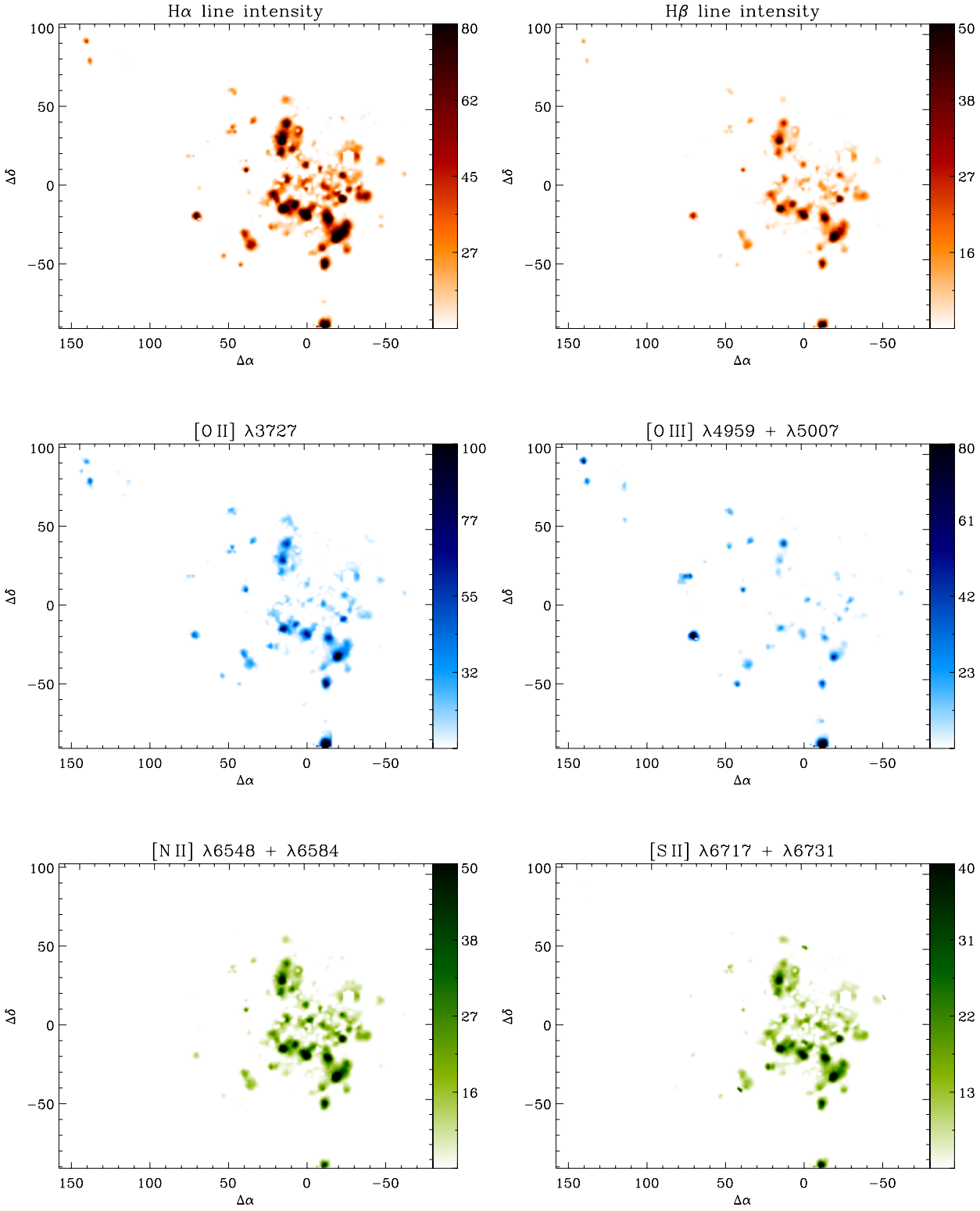

Figure 6.10: Emission line maps of NGC 1058 in units of 10^{-16} erg s^{-1} cm^{-2} arcsec^{-2}. No correction for dust extinction was applied to these maps.

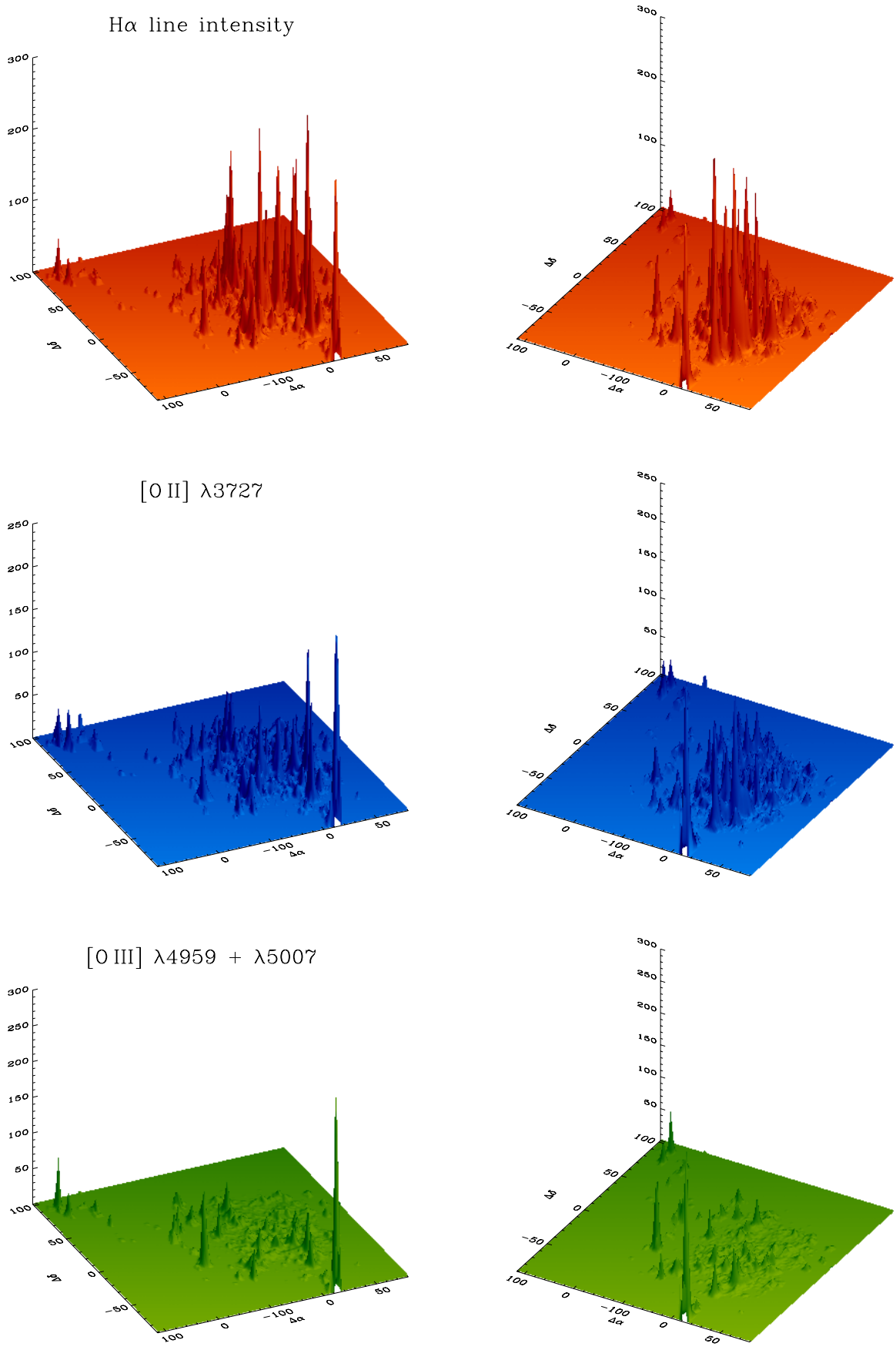

Figure 6.11: 3D emission line maps visualisation for NGC 1058.

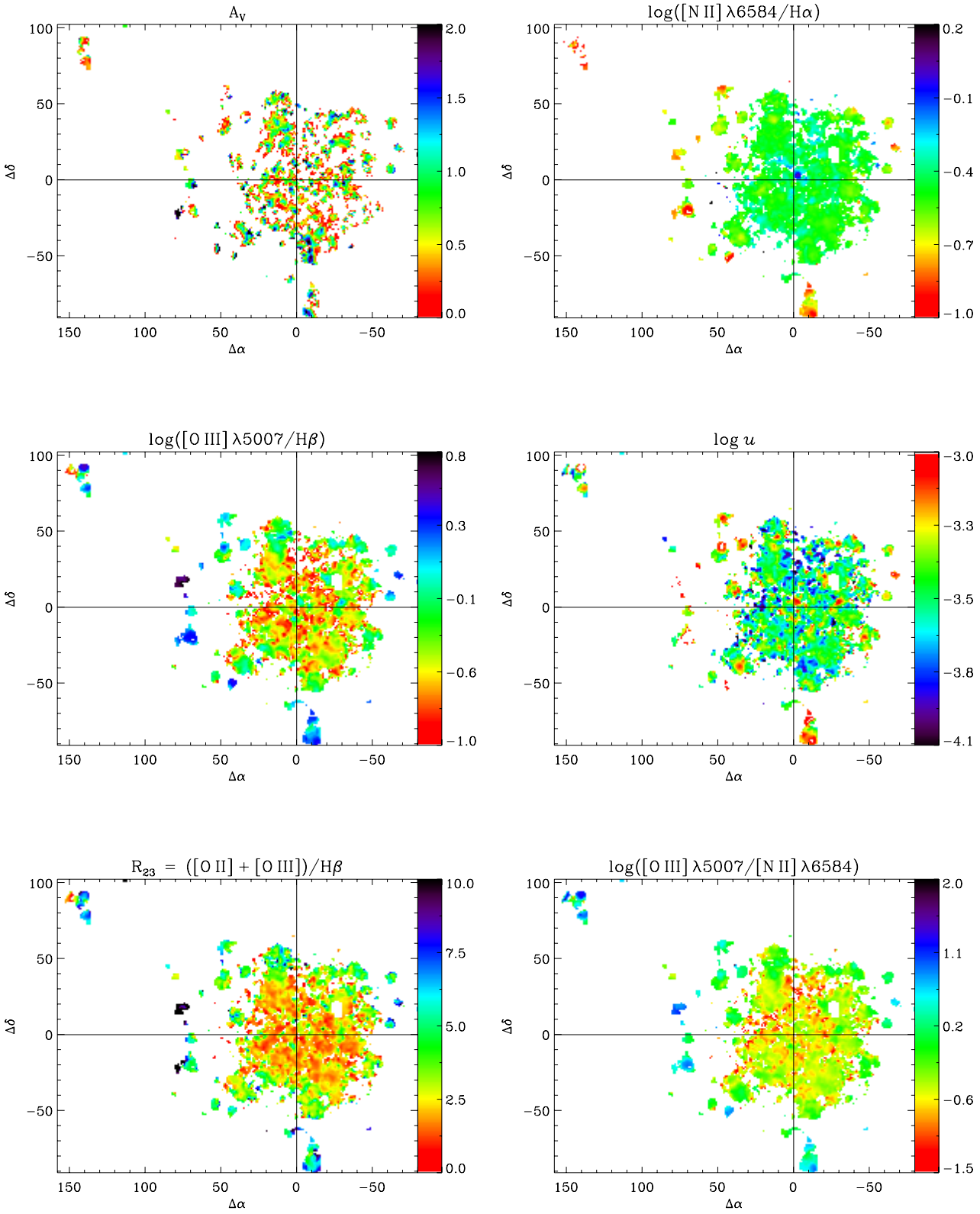

Figure 6.12: 2D spatial properties of NGC 1058. Note that the colour-bar of $\log u$ is inverted with respect to the rest of the panels.

surface of the galaxy, especially in the regions along $\Delta\alpha$ –10, including the FGW 1058E H II region. The outlying regions at $\Delta\alpha \sim$ –140 have low extinction values corresponding to $A_V \sim 0.3$ The apparent blank gaps in the central regions of the galaxy are an artifact of the visualization, they do correspond to A_V values of zero. Although is not evident from the maps shown in Figure 6.10, an inspection of the raw images show that these blank regions possess low-intensity diffuse emission, as it will be evident in the following maps. On the other hand, some wholes in the mosaic are real, and correspond to the regions where foreground stars and the SN 2007gr were removed, as previously described.

The top-right panel of Figure 6.12 shows the N_2H_α ratio map, which presents a very homogenous distribution over most of the surface of the galaxy. The average N_2H_α value derived from the map is –0.49 $\pm$ 0.12 dex while the value derived from the integrated spectrum is –0.50. Higher values of this ratio ($\sim$ 0.1) are only present at some positions in the central region of the galaxy. Lower values are found at the outer parts of the galaxy, e.g. the outlying H II regions and FGW 1058E, with N_2H_α ratios $\sim$ –0.8. Therefore, the distribution of this ratio is consistent with a high peak in the centre, a nearly flat distribution over most of the area of the galaxy, with a drastic drop at the outer parts.

This distribution in the ionizing properties of the galaxy is confirmed by the O_3H_β map presented in the middle-left panel of Figure 6.12. Although in the central regions the distribution of this ratio is quite inhomogeneous as compared to the N_2H_α map, it is consistent with values between –0.1 and –0.6. The average O_3H_β ratio derived from the map is –0.49 $\pm$ 0.22 dex, which is a bit lower than the obtained after the integrated spectrum (–0.38). Higher values are found in the outer regions, which coincide with the regions of lower values of the N_2H_α map. The gradients of both maps suggest that there is higher level of ionization in the outer regions of the galaxy, as it is confirmed by the middle-right panel of the same figure, showing the distribution of the ionization parameter $\log u$. This map, based on the reddening corrected [O II]/[O III] ratio, shows that in general the outer regions present a higher ionization than the central ones. However, there are many high ionization regions embedded in the central regions of the galaxy. Low ionization (blue) regions are also found at the edges of some structures in the galaxy, associated with H II regions after a visual comparison with the Hα emission line map. The average value of the ionization parameter derived from the map is –3.49 $\pm$ 0.22 dex, which is in excellent agreement with the $\log u$ value calculated from the integrated spectrum ($\log u$ = –3.50).

As in the previous galaxy, the distribution of the R_{23} and the [O III]/[N II] indices is investigated as potential metallicity indicators. The bottom-left panel of Figure 6.12 shows the calculated map of R_{23}. A gradient of lower to higher values from the inner to the outer parts of the galaxy is clearly seen, although the distribution is quite homogeneous for the central regions (yellow-red colours). The average R_{23} map value is 2.82 $\pm$ 1.29, which is lower than the value derived from the integrated spectrum, i.e. R_{23} = 3.39. The [O III]/[N II] ratio map shown in the bottom-right panel of Figure 6.12 shows a similar behavior, most of the central regions are consistent with low [O III]/[N II] values, but not showing a clear raising trend. The outer regions show higher values, the average [O III]/[N II] ratio derived from the map is –0.30 $\pm$ 0.42 dex, which is in agreement with the integrated value of –0.29. The distribution of these metallicity indices suggests the presence of a metallicity gradient in this galaxy, although the almost constant values found in most of the surface of NGC 1058 might be a sign of a not very steep gradient.

6.2.4 NGC 3184

Figure 6.13 shows the emission line maps derived for NGC 3184. These are the second largest maps of the

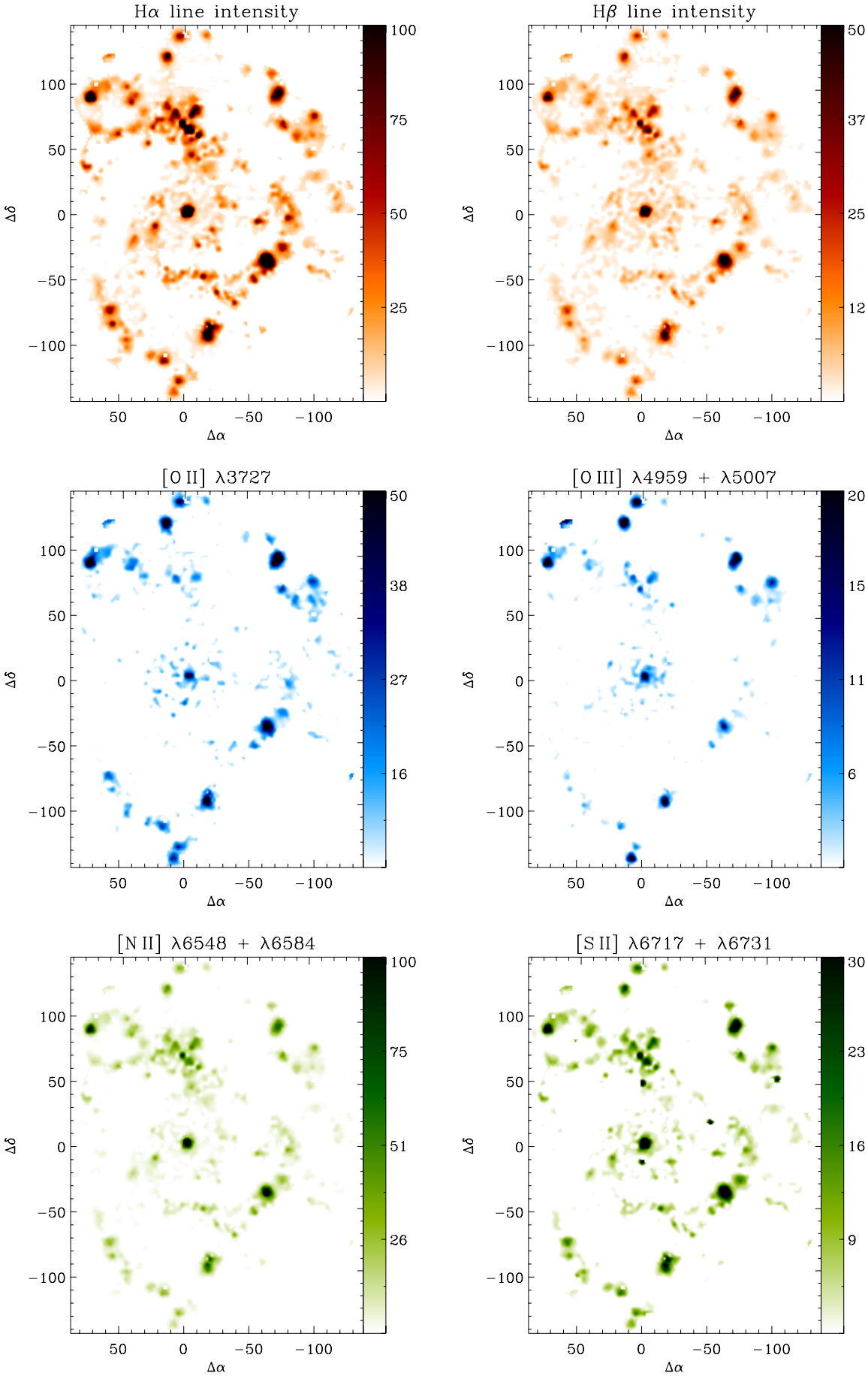

Figure 6.13: Emission line maps of NGC 3184 in units of 10^{-16} erg s^{-1} cm^{-2} arcsec^{-2}. No correction for dust extinction was applied to these maps.

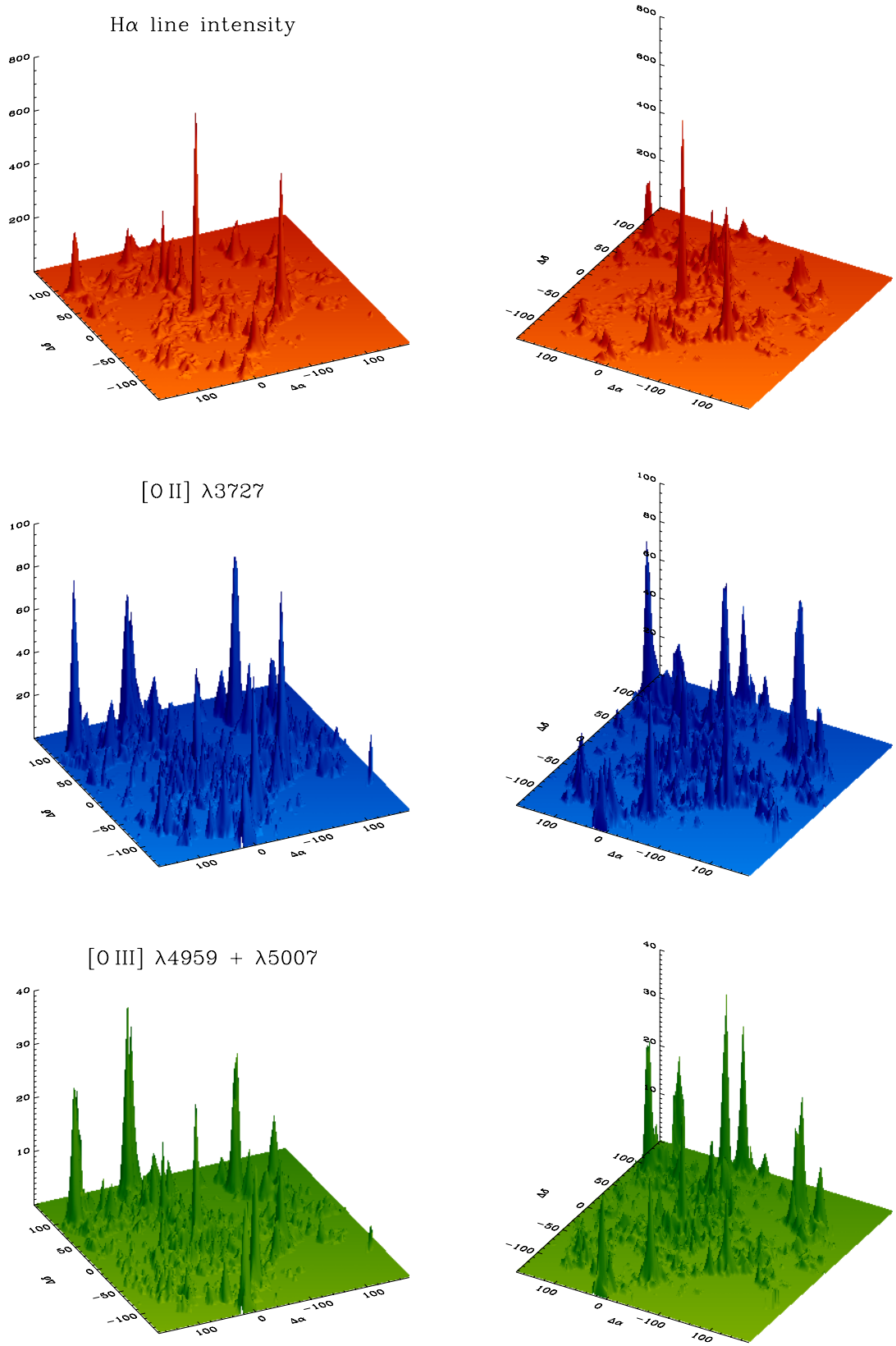

Figure 6.14: 3D emission line maps visualization for NGC 3184.

sample in terms of the area covered by the IFS observations. All positions were observed in non-dithering mode. The top panels of this figure show the Hα and Hβ maps, tracing the regions of star formation. They display a recognizable spiral structure, with a bright centre and several H II regions along the spiral arms. Some prominent features are located at $(\Delta\alpha, \Delta\delta) \sim$ (–20,–90), (–70,–40), (–70,100), (70,90) and a giant H II complex located at (0,70). Diffuse emission from the intra-arms regions is also visible, as well as smaller H II regions following the spiral structure of the galaxy. The [O II] map in the middle-left panel displays emission from the H II regions traced by the Hα and Hβ maps, although the emission in the central region of the galaxy is much lower than in the spiral arms, the nucleus is the only bright source in this region of the galaxy. This feature is more evident in the [O III] map, where practically no emission, apart of the nucleus, is originated from the centre of the galaxy. The very bright complex shown in the Hα and Hβ maps at $(\Delta\alpha, \Delta\delta) \sim$ (0,70) shows a low level of emission in the oxygen maps, specially in the [O II] panel.

The bottom panels of Figure 6.13 show the [N II] and [S II] maps of NGC 3184, the spiral pattern is distinguishable again, although the number of bright regions is lower than in the Hα and Hβ maps. The nucleus is very bright in both maps. The [S II] map shows a higher level of structure, while the [N II] map shows more low-level emission along the spiral arms

Figure 6.14 shows the 3D rendering of the Hα, [O II] and [O III] emission lines maps of NGC 3184. The Hα visualization shows a similar feature as NGC 1637, i.e. a very bright nucleus compared with the rest of the emission in the galaxy, although not as high as compared to NGC 1637. Low-level Hα emission is present in the centre of the galaxy, the second stronger emitting region is the one located at $(\Delta\alpha, \Delta\delta) \sim$ (–70,–40), as suggested by the Hα map of Figure 6.13. The rest of the bright regions in Hα are located in the outer part of the galaxy, along the spiral arms. The [O II] and [O III] 3D visualizations are quite similar in terms of the distribution of line intensities in the galaxy. Contrary to the case of NGC 1637, the bright nuclear region in Hα is not an important feature in the [O II] and [O III] maps. The brightest regions are located at the outer part of the galaxy, with low level emission in the centra region, which is more evident in the [O III] visualization.

2D SPATIAL PROPERTIES

Figure 6.15 shows the 2D distribution of the physical properties of NGC 3184, with similar panels as presented for the previous two galaxies. The top-left panel shows the distribution of the dust extinction traced by A_V (in magnitudes). As in previous cases, the blank areas correspond to zero A_V values, regions deleted in the original mosaic due to foregrounds objects or regions masked by the Hβ flux threshold. The extinction shows a very clumpy distribution with no apparent trends along the spiral arms of any radial direction. Some regions of high extinction ($\sim$ 3 mag) are found as compact knots along the spiral arms and as isolated regions. The average value of A_V calculated from the map is 1.02 ± 0.71 mag, which is higher than the value of 0.63 mag derived from the integrated spectrum.

The top-right panel of Figure 6.15 displays the N_2H_α ratio map of this galaxy, which displays a very homogeneous distribution over the whole surface of the galaxy. Regions with high N_2H_α values are found at third south-east quadrant of the mosaic, corresponding to compact knots at the edges or in between the regions. The average value of the N_2H_α ratio from the map is -0.46 ± 0.14 dex, which coincides exactly with the value of the integrated spectrum. On the other hand, the middle-left panel of Figure 6.15 shows the distribution of the O_3H_β ratio. In this case, the galaxy shows a mixture of high and low values within the same regions and along the spiral arms, this is more evident in the same third south-east quadrant, which can

be compared to the nearly homogeneous distribution of O_3H_β values in the spiral arm found at the fourth south-west quadrant. The average value of the O_3H_β ratio from the map is –0.58 $\pm$ 0.24 dex, compared to –0.64 obtained from the integrated spectrum. As a general trend, there seems to be gradient of lower to higher values from the inner to the outer part of the galaxy, although the differences in the N_2H_α and O_3H_β ratios suggest that the ionization is different for different morphological regions of the galaxy and not related to the galactocentric distance.

This idea is supported by the $\log u$ map shown in the middle-right panel of Figure 6.15, showing the distribution of the ionization parameter calculated from the dust-corrected [O II]/[N III] ratio as explained before. In general, the regions of the galaxy in the fourth south-west quadrant are consistent with lower $\log u$ than the regions in the central part of the galaxy and/or in the third south-east quadrant. This might suggest that the ionization is higher in these latter regions than in the portion of the spiral arm within the fourth south-west quadrant. This possibility will be investigated further in following sections. The average value of the ionization parameter in the map is –3.46 $\pm$ 0.26, while the ionization derived from the integrated spectrum is –3.44.

The bottom panels of Figure 6.15 show the distribution of the metallicity indices R_{23} and [O III]/[N II]. In the first case, most of the galaxy shows a very low value of R_{23}, even for those regions where [O II] and [O III] are prominent, therefore these values are not due to missing [O II], [O III] emission or very high values of Hβ, but seem to be reflecting the intrinsic oxygen content of the galaxy. The region of the spiral arm along $\Delta\alpha \sim 0$ to the north of the nucleus shows particularly low R_{23} values. Few regions in the centre of the galaxy and in the outer parts show higher values, e.g. the region at $(\Delta\alpha, \Delta\delta) \sim$ (10,–140). The average value of R_{23} derived from the map is 1.87 $\pm$ 1.18. This value is consistent with the R_{23} figure found from the integrated spectrum, which is 1.48. On the other hand, the [O III]/[N II] map distribution shows also a homogeneous distribution but with high values corresponding to compact knots along the spiral arms (specially in the third south-east quadrant) which are coincident with the regions of high ionization shown in the O_3H_β and $\log u$ maps, reflecting the dependence of this ratio on the ionization and its application to different regions of a single galaxy. The average value of the [O III]/[N II] ratio from the map is –0.51 $\pm$ 0.32, which is higher than the –0.65 value derived from the integrated spectrum of NGC 3184. Given the double-valued nature of R_{23}, the very low values found in most regions of the galaxy suggest that either the galaxy is very metal deficient or very metal rich. Previous studies have found that the metal content of this galaxy is particularly high (e.g. McCall et al., 1985; van Zee et al., 1998), and considering the high O/H values found in subsection 5.3.3 from the integrated spectrum of NGC 3184 using different calibrators (12+log(O/H) $\sim$ 8.7), the low R_{23} values shown in the corresponding map should reflect the high metallicity content of this galaxy.

6.2.5 NGC 3310

The last emission line maps presented in this section correspond to NGC 3310. Figure 6.16 shows in the top panels the Hα and Hβ maps of this galaxy. Note the very high intensities compared to similar maps of the rest of the sample. These maps show basically the nuclear part of the galaxy and the two spiral arms extending to the north and south of the galaxy. The centre of the galaxy is dominated by three features, a bright nucleus which appears as a compact knot in both maps, a bright circumnuclear region with a half-ring or *C*-shape to the left of the nucleus, and a compact H II complex to the south-west of the nucleus, which includes the previously mentioned *jumbo* H II region of NGC 3310. Some other bright regions are seen along the short spiral arms, as well as isolated H II regions to the north-west of the galaxy nucleus at $(\Delta\alpha, \Delta\delta) \sim$

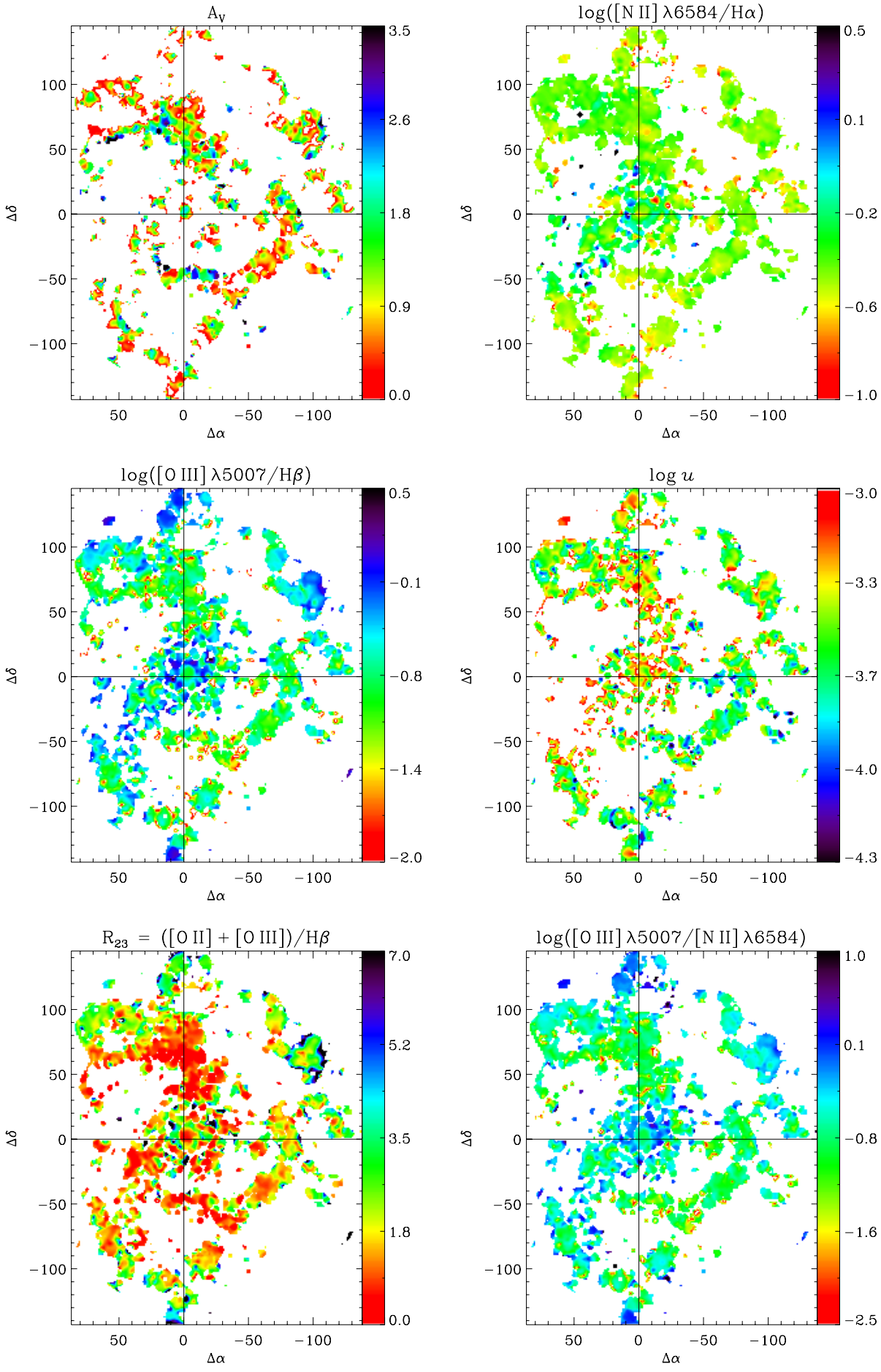

Figure 6.15: 2D spatial properties of NGC 3184. Note that the colour-bar of $\log u$ is inverted with respect to the rest of the panels.

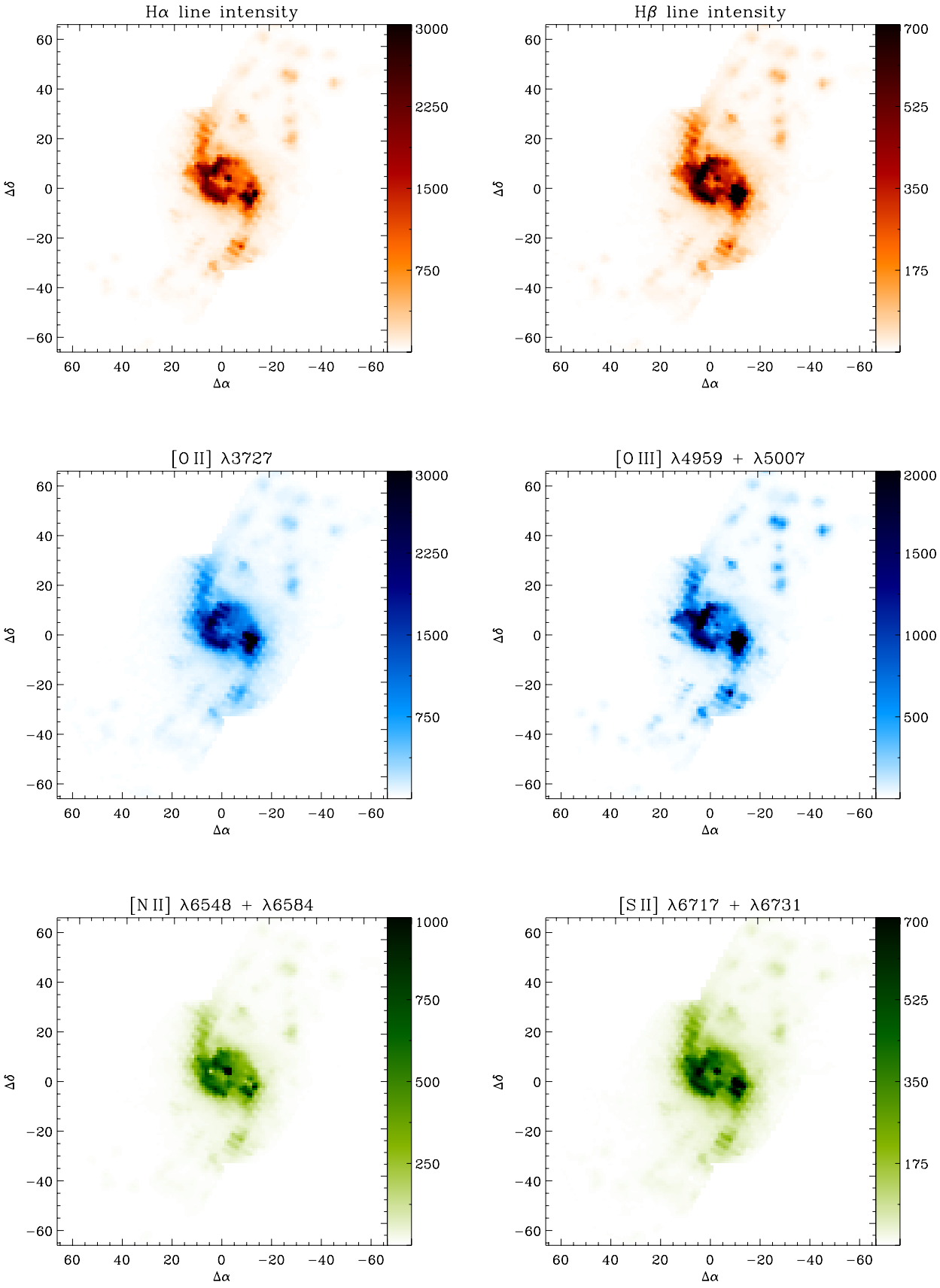

Figure 6.16: Emission line maps of NGC 3310 in units of 10^{-16} erg s^{-1} cm^{-2} arcsec^{-2}. No correction for dust extinction was applied to these maps.

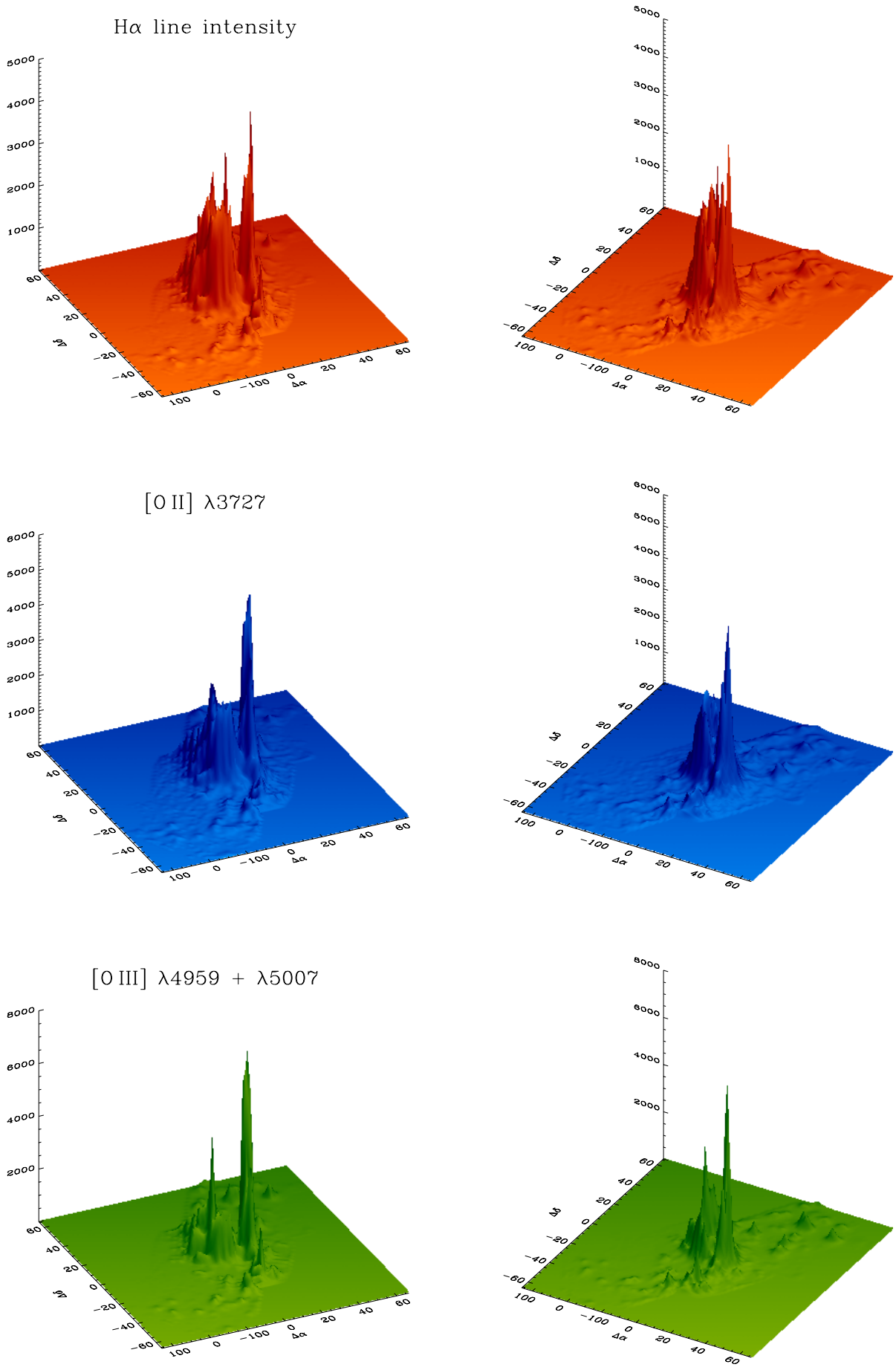

Figure 6.17: 3D emission line maps visualisation for NGC 3310.

(–30,30). The Hα and Hβ maps do not show much evidence of diffuse emission, however, given the high intensity level of these maps, the contrast is not sufficient to appreciate this effect. In that case, the level of diffuse emission, which could be considered negligible in this galaxy, would be important for the total Hα or Hβ flux in other galaxies.

The middle panels of Figure 6.16 show the [O II] and [O III] maps. The circumnuclear region and the *jumbo* complex are the most prominent features, the nucleus is not particularly bright in the [O II] map, but the intensity levels are comparable to those of the Hα map. The [O III] map shows more structures in the central region of the galaxy than the [O II] map. The circumnuclear region appears with additional knots. Several intense regions appears in the [O III] map which are not that evident in the [O II] map, e.g. at $(\Delta\alpha, \Delta\delta) \sim$ (–10,–25) and to the north-west of the nucleus at $\sim$ (–30,40). The bottom panels of the same figure show the [N II] and [S II] maps. Again, the most prominent features are located at the central region of the galaxy, with "weak" emission originating from the spiral arms. The [N II] map shows a very bright nucleus, with comparable intensity of the *jumbo* H II complex. The *C* circumnuclear regions is less evident in this map. On the other hand, the [S II] map resembles to a good level the Hα map, with the three prominent features in the central region showing similar structure and intensity levels.

The 3D rendering of NGC 3310 is shown in Figure 6.17. The panels corresponding to the Hα emission show the difference in intensity between the central region of the galaxy and the rest of the area covered by the IFS observations. Note the very high intensities compared to similar figures of the other galaxies in the sample. The emission structure is completely concentrated in the nuclear region, although the H II regions found in the rest of the mosaic are of considerable signal-to-noise. The brightest region corresponds to the *jumbo* H II complex and not to the nucleus of the galaxy. The 3D map of [O II] shows a similar structure, here the *jumbo* H II complex is even more prominent than in the case of Hα. The intensity levels are also very high compared with similar figures of previous galaxies. The [O III] 3D visualization shows a lower intensity level from the central region, the *jumbo* complex is still the brightest source in the field, while the emission from the *C*-circumnuclear region is lower than in the case of [O II] .

2D SPATIAL PROPERTIES

As in the previous cases, the top-left panel of Figure 6.18 shows the distribution of the dust extinction, A_V (in magnitudes), for NGC 3310. Despite the fact that the map displays a very clumpy structure all over the observed mosaic, the actual values correspond to a low extinction (red-yellow). Some regions present values of $A_V \sim 1.0$ (green), and very few, very compact knots of $A_V \sim 2.0$. As in previous galaxies, most of the blank areas in the mosaic's field correspond to values of A_V equal to zero, limitations with the visualization prevented the correct rendering of these zones. However, blank areas at the edges of the mosaic do correspond to masked zones due to low signal-to-noise regions, as evident in the rest of the panels of Figure 6.18. The average A_V derived from the map is 0.68 ± 0.48 mag, which is higher than the value calculated from the integrated spectrum (0.44 mag).

The N_2H_α map shown in the top-right panel of Figure 6.18 displays a very homogeneous distribution of this ratio over most of the surface of the mosaic. The average value derived from the map is -0.64 ± 0.12, which is in very good agreement with the value derived from the integrated spectrum (–0.63). High values of the N_2H_α ratio are found at the centre of the mosaic, corresponding to the nucleus of the galaxy, and in small clumps, particularly at the third (south-east) quarter. The lower N_2H_α values coincide with the position of H II regions which can be identified in the maps shown in Figure 6.16. The *C*-shape circumnuclear feature

is not evident in this map, but the *Jumbo* complex shows a slightly higher N_2H_α value than the surrounding regions. The middle-left panel of the same figure shows the map of the O_3H_β ratio. As in the previous case, the map shows in general terms a homogeneous distribution of this ratio. However, regions of high O_3H_β values are more evident in this map, specially in the top-right and bottom left parts of the mosaics. A careful inspection shows that the regions with higher O_3H_β values coincide in general with regions of low N_2H_α values, including the *Jumbo* H II complex region. The nucleus shows also an inverse behavior with respect to the N_2H_α, with a lower O_3H_β ratio than the surrounding regions. The average value of the O_3H_β ratio derived from the map is 0.20 ± 0.17, which is slightly lower than the value calculated from the integrated spectrum, which is 0.28. The coincidence of regions with low N_2H_α with high O_3H_β ratios would suggest that these zones present a higher ionization than the rest of the galaxy. The ionization parameter map presented in the middle-right panel of Figure 6.18 reinforces this idea. A visual comparison of this map with the N_2H_α and O_3H_β maps shows that the regions with higher values of the ionization parameter correlate with the regions previously described in the other maps, including the *Jumbo* complex. The nucleus of NGC 3310 does not show a significant amount of ionization and it is consistent with the values in its surroundings. The average value of $\log u$ derived from the map is -3.30 ± 0.17, which is 0.11 dex lower than the value derived from the integrated spectrum (–3.19). An interesting feature present in the O_3H_β and $\log u$ maps is the presence of large low-ionization regions, the most prominent ones are located at $(\Delta\alpha, \Delta\delta)$ $\sim$ (10,–15) and (–20,20). This particular last region has a curved shape, resembling somehow a shell. Given the suspected recent merging history of this galaxy, these structures might be related to those episodes of the galaxy formation.

Finally, the bottom panels of Figure 6.18 show the distribution of the R_{23} and [O III]/[N II] metallicity indicators. The R_{23} shows a very smooth distribution over the whole field covered by the IFS mosaic. Slightly lower values are found at the centre of the galaxy, with higher values found at particular locations as compact knots, specially at the top-right of the map. This might be an indication of a weak R_{23} gradient, however, we also found lower R_{23} values at the bottom-left part of the map. It is interesting to note that the high values of R_{23} in the first (north-west) quadrant form a sort of ring around a high ionization region, as shown in the O_3H_β and $\log u$ maps. The average R_{23} derived from the map is 5.51 ± 1.06, while the value derived from the integrated spectrum is 6.60. Similarly, the [O III]/[N II] map shows also a quite homogeneous distribution over the field, with some particular regions showing either higher or lower values of this ratio. The nucleus shows a relatively lower ratio than the average values found in its surroundings. Regions of higher [O III]/[N II] values are located mainly in the top-right quadrant of the map. However, a comparison of this map with the O_3H_β and N_2H_α maps show that these regions coincide with the high ionization zones previously described. The "shell" features discussed in the $\log u$ map are also visible in this map. The *Jumbo* H II region also appears with a high [O III]/[N II] ratio. The average value of the [O III]/[N II] ratio derived from the map is 0.40 ± 0.23 dex, in agreement with 0.46, which is the value calculated from the integrated spectrum. The higher values of [O III]/[N II] corresponding to higher ionization regions manifest the high sensitivity of this ratio to the ionization parameter, which is a drawback if we are to measure the metallicity from the [O III]/[N II] indicator.

The emission line maps and derived properties presented in this section proved to be very useful in describing the 2D properties of the galaxy sample. General trends, gradients and particular interesting regions were found by comparing different maps, corresponding to different line ratios, which test some of the most important physical properties of the galaxies, including the extinction by dust, the ionization and

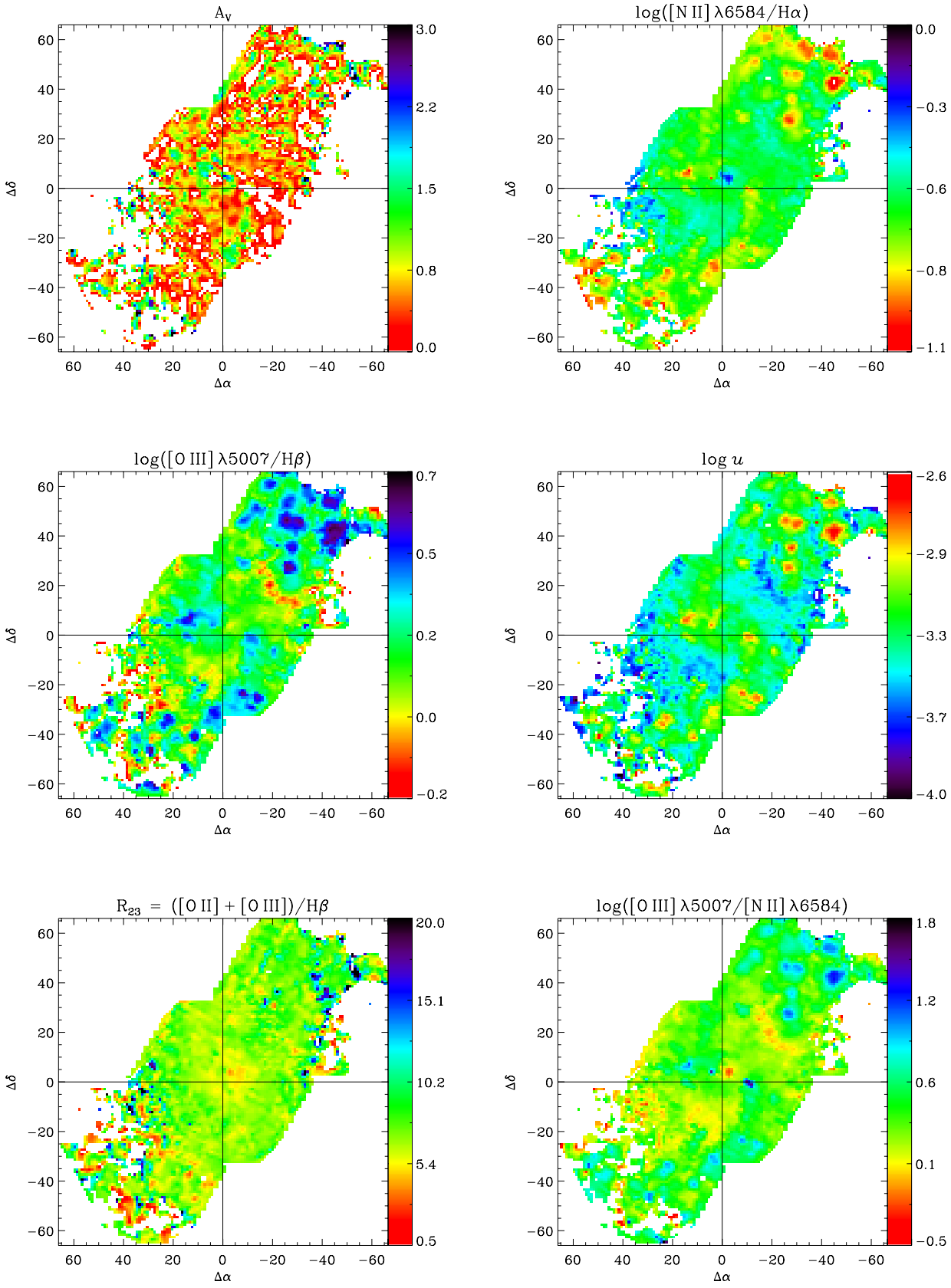

Figure 6.18: 2D spatial properties of NGC 3310. Note that the colour-bar of $\log u$ is inverted with respect to the rest of the panels.

excitation structure, and the metallicity content. However, more specific conclusions can only be drawn by analysing individually certain regions of a galaxy, or by co-adding spectra of regions with the same physical properties and comparing the results in the 2D context. The following sections will address a detailed 2D spectroscopic study in accordance with these concepts, so that we could derive a quantitative description of the 2D distribution of the physical properties of the galaxies, with a special focus on their chemical abundance content.

6.3 2D spectroscopic analysis of NGC 628: a case study

The nearly full IFS coverage of the objects presented in this chapter offers the possibility to undertake a detailed, spatially resolved, spectroscopic analysis of the sample based on thousands of individual spectra. Small and intermediate-scale variations of the physical properties of these nearby galaxies could be, in principle and within the limitation of the spatial resolution of the instrument, studied with an unprecedented degree of detail. The emission line maps method presented in the previous chapter could be considered a valid procedure in order to study the 2D distribution of the physical properties of a galaxy. However, the conclusions raised from these maps are based on general trends and depend, to a certain level, on the interpolation scheme applied in order to derived the pixel-resolved maps. On the other hand, classical spectroscopy on the objects has typically targeted a handful of bright individual H II regions per galaxy, especially from the outer regions and along the spiral arms, where (in general) the contribution of the stellar population to the observed spectrum is not significant. The spectroscopic dataset presented in this dissertation poses a challenge with respect to classical spectroscopy, a right methodology has to be found in order to handle and analyse, in a homogeneous and meaningful way, this huge spectroscopic database.

Different analysis possibilities were investigated, these took into account the signal-to-noise of the data, the 2D spatial coverage, the physical sense of the derived results, and the final number of analysed spectra. From all the options explored, three different methodologies were tested. They differ mainly in the way to select a subsample of spectra from the IFS mosaics, from which a similar spectroscopic analysis is later performed. The three different methods are presented in this section using the most representative galaxy of the sample, NGC 628, as a case study. Each method is explained in detailed for this galaxy, and the results of the analysis based on each subsample are also presented. The pros and drawbacks of each method are discussed, and a final methodology is adopted for the rest of the galaxies considered in this chapter.

6.3.1 Method I: FIBRE-BY-FIBRE ANALYSIS

Considering that, at the adopted distances of the galaxies presented in this chapter, the 2".7 aperture of a single PPAK fibre covers more than 100 pc (in diameter) in physical scale on each galaxy, the spectrum obtained from each fibre would sample, in principle, a large-enough region to subtend a small H II region and/or a fraction of a larger one. With this assumption as a premise, the first proposed method is based on considering every single fibre of the mosaic as a source of an individual analysable spectrum. This method will be referred as the *fibre-by-fibre* analysis. In the case of NGC 628, at the assumed luminosity distance ($D_{\rm L}$ = 9.3 Mpc) and redshift ($z = 0.00219$) of this galaxy, the angular distance D_θ would be equal to 9.26 Mpc, which translates to a scale of 44.9 pc/arcsec, assuming a standard ΛCDM cosmology (WMAP 5-years results: $H_0 = 70.5$, $\Omega = 0.27$, $\Lambda = 0.73$, Hinshaw et al. 2009). This linear physical scale implies that the fibre diameter of PPAK samples $\sim$ 121 pc on NGC 628, a region from which, in principle, one would expect

enough signal-to-noise in the observed spectrum.

The process of the *fibre-by-fibre* method starts with the *residual* RSS file corresponding to the *clean* mosaic obtained after discarding all those fibres with an average flux level less than 10^{-16} erg s^{-1} cm^{-2} Å^{-1} (along the whole spectral range), as explained in section 6.2. In the case of NGC 628, this mosaic corresponds to 6949 fibres, i.e. 51% of the total number of originally observed fibres as shown in Table 6.2. As mentioned in the analysis of the previous section, not all the fibres in this mosaic have detectable emission lines and/or enough signal-to-noise in order to derive meaningful physical parameters. The rejection criterion applied to the emission line maps was based on a flux threshold cut to the Hβ line intensity, which proved to be a reasonable approach. A similar strategy was followed in the case of the *fibre-by-fibre* method, with some additional requirements. The subsample selection was split in three steps, each with different quality criteria conditions based on different assumptions, explained as follows:

1. An analysable spectrum would have to include several detected lines in order to perform a basic analysis. One obvious line is represented by Hβ, as the typical line ratios used in any spectroscopic analysis are normalised to the flux intensity of this line, and as it is required to derive a first-order correction for interstellar extinction based on the Hα to Hβ ratio. Furthermore, a well-defined region from which we could derived with physical meaningful properties would have to include both the [O III] λ4959 and λ5007 lines. The λ4959 line is weaker than the λ5007 by a theoretical factor of 2.98 (Storey & Zeippen, 2000), therefore the detection of the [O II] λ4959 line would also assure the detection of the λ5007 line. It is important to note that the detection of the λ4959 and λ5007 lines does not imply necessary their correct measurement, as it will be discussed below. Given the theoretical constrain on the observed ratio of these two lines, the requirement of the detection of [O III] λ4959 (and consequently of λ5007) will help to characterise the quality of the subsample spectra and their physical meaning. Therefore, the first criterion applied to the *clean* mosaic was to select those fibres where both, the Hβ and [O III] λ4959 line intensities were greater than zero, i.e. meaning that the lines were detected in the automated line intensity calculation. In the case of NGC 628, the total number of fibres for which this criterion was fulfilled is 2659, i.e. 38% of the 6949 fibres contained in the *clean* mosaic and 20% of the original number of fibres in the observed, unprocessed mosaic.

2. During the data processing of the line intensities and their subsequent manipulation into reddening corrected line flux ratios, there were found problems of non-floating numbers among the thousands of derived figures. A careful inspection showed that the reason of the appearance of these values was due to an incorrect determination of the logarithmic extinction coefficient c($H\beta$), which produced Not-a-Number (NaN) or infinite values in some specific cases. Therefore, the second selection criterion was based on purely computational reasons, considering only those fibres for which the calculated c($H\beta$) value was a finite-floating number, regardless of its value (including negative, non-physical ones). The c($H\beta$) coefficient was calculated from the Hα/Hβ ratio, accordingly to the prescriptions outlined in Appendix B. Generally speaking, the number of fibres with non-finite c($H\beta$) values was small in all galaxies. In the case of NGC 628, the account for 97 spectra, reducing the number of selected fibres after this step to 2562.

3. After applying the previous selection criteria, the data subsample consisted in a set of fibres with line intensities greater than zero for Hβ and [O III] λ4959 and finite values of the derived c(Hβ). Based

on the experience learned from the emission line maps analysis, an additional signal-to-noise cut had to be applied in order to obtain a subsample of spectra from which meaningful information could be obtained. As in the previous case, the flux threshold was based on the line intensity of the Hβ line. The Hβ flux cut was chosen instead of the probably more common Hα because, as experience with the data manipulation proved, in some cases a certain line intensity threshold on Hα did not mean the correct detection and measurement of Hβ, and a high cut in Hα would eliminate many regions of low intensity but with physical meaning. Furthermore, as the main focus of this dissertation is to characterise the chemical abundance of the galaxy sample, we required the presence on the spectrum of typical strong lines from which we could obtain information on the abundance for a given region. Thus, a further requirement applied at this point to the spectra was the detection of the [O II] λ3727 line, given that many of the most important abundance calibrators are based on the line strength of this line (e.g. R_{23}). Therefore, the last selection criteria applied to the spectra sample obtained in the previous steps was, to select those fibres where the line intensity of the Hβ line was greater than or equal to a given flux limit threshold, *and* that the line intensity of [O II] λ3727 was greater than zero, i.e. the emission line was detected. The value of the flux threshold was chosen individually for each galaxy, based on several factors: 1) The final number of spectra after the flux cut was applied; 2) The "quality" of the spectra as shown by certain line flux ratios and their histograms (discussed below); 3) The position of the derived spectra in some of the most common BPT diagrams (also explained below). The flux threshold in Hβ was always found in the range $4-8\times10^{-16}$ erg s^{-1} cm^{-2}. In the case of NGC 628, the flux limit applied in Hβ was equal to 8×10^{-16} erg s^{-1} cm^{-2}. The final number of spectra after applying this last selection criteria was 376 fibres, i.e. $\sim$ 6% of the number of fibres in the *clean* mosaic and $\sim$ 3% of the original fibres in the full NGC 628 mosaic.

All the selection criteria could had been merged into a single step, however the steps were separated for the following reasons: 1) In order to check the number of fibres kept and removed at each step; 2) For an easier manipulation of the data in computational terms; and 3) The different data sets could be analysed independently in order to check for systematic errors and trends due to the different quality selection criteria.

Figure 6.19 shows the histograms of three different line ratios from which the quality of the selected spectra at each step can be gauge. They correspond to the ratios of Hα/Hβ, Hγ/Hβ and [O II] λ5007/λ4959. The first two correspond to the most important Balmer recombination ratios used to derive the reddening extinction in spectroscopic studies. Their values should be close to the theoretical ones (which depend mainly on the characteristic T_e) and, in high signal-to-noise spectra, the deviations from these values correspond to the effect of interstellar reddening, which tends to increase (Hα/Hβ) or decrease (Hγ/Hβ) these ratios depending on the amount of extinction. For case-B recombination, and assuming a $T_e = 10^4$ K, the theoretical values for the Hα/Hβ and Hγ/Hβ ratios are 2.87 and 0.466 respectively (Table 4.2, Osterbrock & Ferland, 2006). The third ratio corresponds to the forbidden line emission of [O III] λ5007/λ4959, which corresponds to the ratio of the line strengths for the magnetic-dipole $^1D_2 - ^3P_2$ and $^1D_2 - ^3P_1$ transitions. According to theoretical work, the transition probability for this ratio is 3.01, implying a fixed intensity ratio of 2.98 (Storey & Zeippen, 2000). Therefore, the line ratio of this [O III] doublet is an excellent indicator of the quality of the spectra.

The first row of Figure 6.19 shows the histograms of these three line ratios after the 1st selection criteria was applied, i.e. all those fibres with Hβ and [O III] λ4959 greater than zero. The vertical lines in all plots show the position of the theoretical values mentioned above. Ratios of Hα/Hβ greater than the theoretical

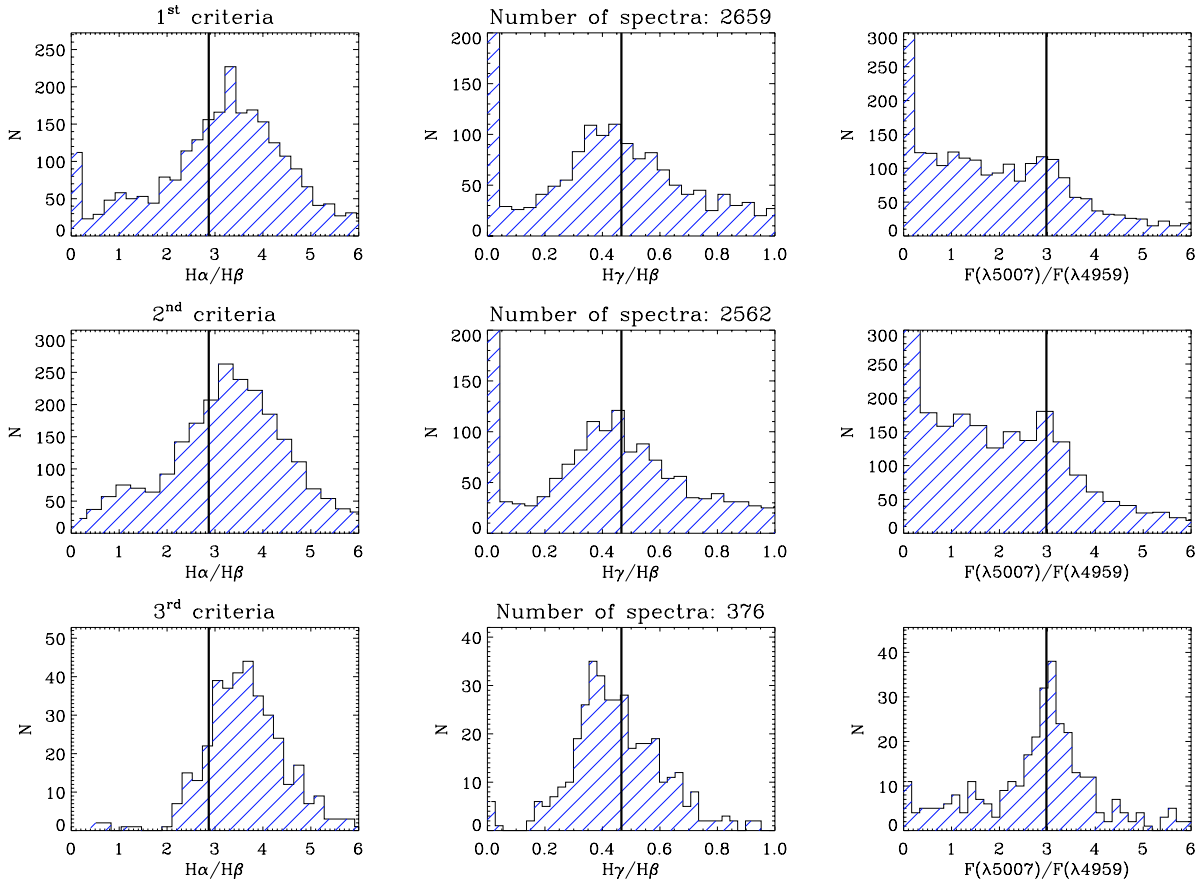

Figure 6.19: Selection criteria histograms for the *fibre-by-fibre* analysis of NGC 628. In each panel, the vertical lines correspond to the theoretical values of the given line ratio.

value are consistent with spectra affected by a certain amount of extinction, values to the left of vertical line would correspond to a negative non-physical extinction. The Hα/Hβ histogram of the first subsample shows a nearly Gaussian distribution centered at values slightly higher than the theoretical ones. It shows a tail of higher values corresponding to spectra affected by interstellar reddening, however, there is a considerable tail of non-physical spectra with negative extinction values, with a strong peak near the Hα/Hβ ~ 0 ratios. The second histogram corresponding to Hγ/Hβ shows that the ratios are nearly centered around the theoretical value, but with a broader dispersion than the case of the Hα/Hβ ratio. A strong peak is also found at Hγ/Hβ ~ 0, reflecting the spectra for which there was no enough signal-to-noise to detect the Hγ line. The last histograms shows the distribution of the [O III] λ5007/λ4959 ratio. The values are clearly not centered at the theoretical value, although the histogram shows a peak at that position. Most of the fibres are consistent with values lower than the theoretical one, with a strong peak near the null ratio values. The total number of selected spectra after this selection criteria is shown above the Hγ/Hβ histogram.

The second row of Figure 6.19 shows the same set of histograms after the 2nd selection criteria, i.e. where only spectra with finite values of c(Hβ) are considered. All three histograms are basically the same as the previous case, however, we can notice that the peak of low Hα/Hβ values in the first row disappear in the corresponding plot, i.e. those spectra produce non-finite c(Hβ) values. The third row of histograms shows the distribution of the line intensity ratios for the final *fiber-by-fibre* sample after the 3rd selection criteria was applied.

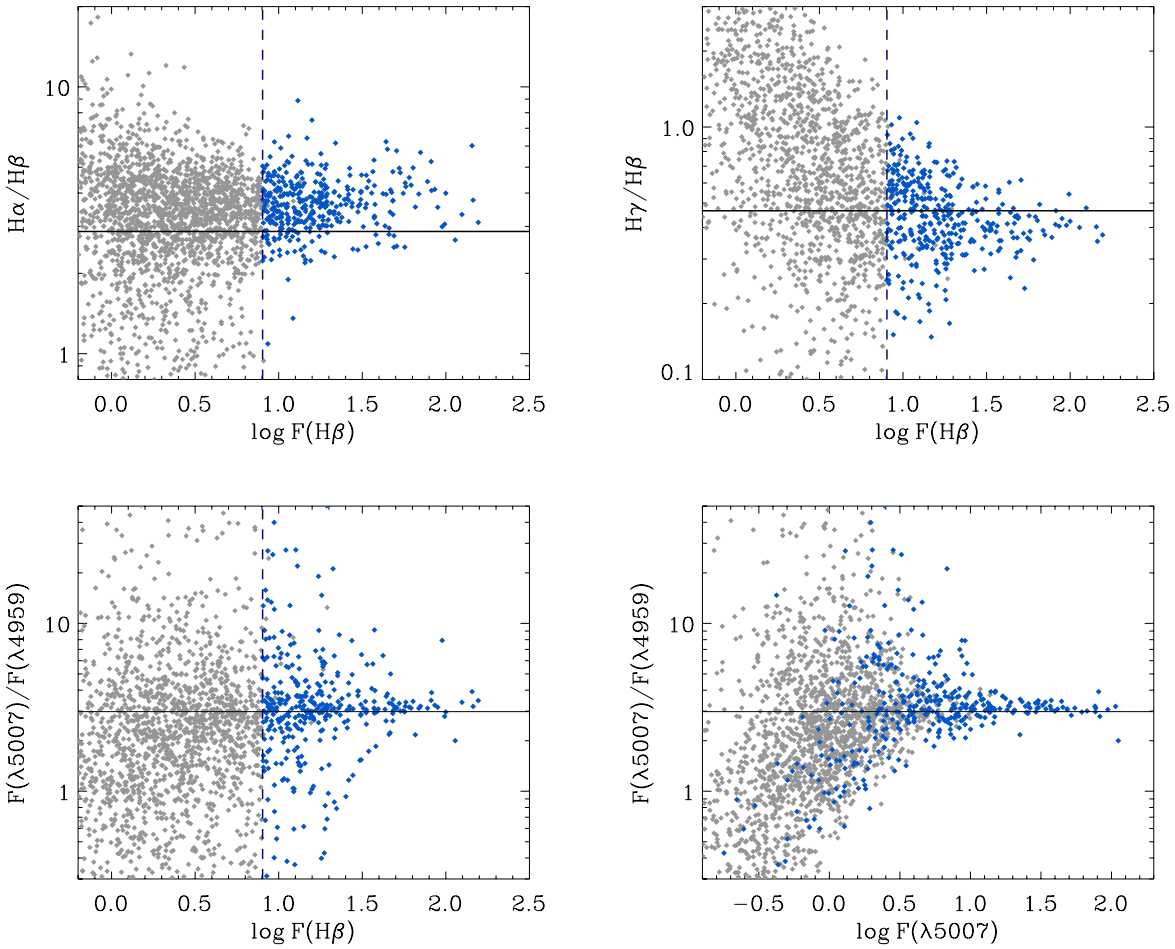

Figure 6.20: Hα/Hβ, Hγ/Hβ and [O III] λ5007/λ4959 ratios as a function of observed flux in Hβ and F(λ5007) for the *fibre-by-fibre* analysis of NGC 628. Grey and blue symbols correspond to the 2nd and 3rd selection samples, respectively. The horizontal lines correspond to the theoretical values for each ratio. The vertical dashed line stands for the flux threshold in Hβ.

The Hα/Hβ shows the expected, nearly-Gaussian distribution, with a tail of values higher than the theoretical one consistent with spectra suffering from the effects of interstellar reddening, and a small number of spectra with "non-physical" extinction towards the left of the theoretical value. The peak of the distribution is centered at Hα/Hβ $\sim$ 3.8. Similarly, the Hγ/Hβ plot shows the expected distribution with a concentration of values lower than the theoretical one, which again is consistent with reddened spectra. The prominent peak of low Hγ/Hβ values present in the previous histograms disappeared. In the case of the [O III] ratio, the histogram shows a well-defined distribution centered at the theoretical value. However, some very low and high values of the [O III] ratio are still present in the distribution, but representing a low number compared to the main body of the data.

A better understanding of the quality of the selected spectra can be inferred by Figure 6.20. The top panels show the Hα/Hβ and Hγ/Hβ ratios as a function of observed flux in Hβ, i.e. the variation of these ratios due to the intrinsic signal-to-noise of the data. The grey symbols correspond to the 2562 spectra selected after applying the second selection criteria, the blue symbols are overlaid on the previous data, showing the position of the selected spectra after the third selection criteria was applied. The horizontal lines correspond to the theoretical values as explained before. The vertical dashed lines correspond to the

Hβ flux threshold value. For larger observed fluxes in Hβ, the scatter of the Hα/Hβ and Hγ/Hβ ratios is smaller. As the signal-to-noise diminishes (exemplified here by the flux in Hβ), the scatter of the ratios increases to a considerable level. Ideally, in the case of the Hα/Hβ ratio, a good signal-to-noise sample would be located above the theoretical line (consistent with physical reddening) and to the right of a certain flux limit. Conversely, in the case of the Hγ/Hβ ratio, an optimal sample would be located below the theoretical line and to the right of the flux ratio threshold. The value of the latter has to be chosen in order to find a good trade-off between the number of physically meaningful selected spectra, and the point at which the noise starts to dominate the measured ratios. As the Hα/Hβ vs. log F(Hβ) diagram shows, the flux threshold is located exactly at the value when the scatter in the Hα/Hβ ratio increases significantly for lower values of the Hβ flux. A similar behaviour is found in the Hγ/Hβ diagram, although the scatter is in general higher, this would be expected as the Hγ line is more prone to errors the measurement, due to its relatively low strength and because it is more affected by the correction for underlying absorption.

The bottom panels of Figure 6.20 show the distribution of the [O III] λ5007/λ4959 ratio as a function of the observed flux in Hβ (left) and of the observed flux in λ5007 (right). The colour-coding is similar to the previous plots, the horizontal lines show the theoretical F(λ5007)/F(λ4959) ratio value. In both cases, an ideal spectroscopic sample would lie horizontally along the theoretical value over most of the intensity range, with a very small scatter around this value. The F(λ5007)/F(λ4959) vs. log F(λ5007) plot shows this behaviour for a range of observed values log F(λ5007) $\sim$ 1.0–2.0, for lower log F(λ5007) values (i.e. lower signal-to-noise) the scatter increases considerably, even for the blue symbols corresponding to the final selected sample. In the case of the F(λ5007)/F(λ4959) vs. F(Hβ) diagram, most of the final selected sample lie near the theoretical value, however, a significant scatter in the F(λ5007)/F(λ4959) ratio is found even for relatively large Hβ fluxes (i.e. higher signal-to-noise). The large dispersion found in the [O III] λ5007/λ4959 ratio might suggest that, despite the quality selection criteria and the low number of final selected fibres with respect to the original ones, many of the selected fibres do not correspond to spectra of physical meaning. This possibility will be discussed later on in this chapter.

Figure 6.21 shows examples of spectra discarded at different stages of the selection criteria, the top panels correspond to spectra of nearly null continuum, strong sky residuals and without signatures of Hβ or any other important emission line, these sort of spectra were discarded after the first selection criterion. The rest of the panels show spectra with the signature of Hα and Hβ but strong sky residuals and low signal-to-noise (middle panels) or without the presence of the [O II] λ3727 line (bottom panels). These spectra were also discarded after the second and third selection criteria. On the other hand, Figure 6.22 shows a series of three different individual fibres showing different ranges of signal-to-noise for the final selected *fibre-by-fibre* sample. For each fibre, the left column corresponds to the observed spectrum, plus the SSP fit model overlaid as a red line, the right column shows the residual spectrum from which the selection criteria was applied. Note that all three spectra show the most important emission lines, including Hα, Hβ, [O II], [O III], etc.

Figure 6.23 shows the histogram of the logarithmic extinction coefficient c(Hβ) (derived from the Hα/Hβ ratio), for the final *fibre-by-fibre* spectral sample. The details on the derivation of this coefficient are given in Appendix B. The vertical line corresponds to a null extinction. The values follow a well-defined, nearly Gaussian distribution with the centre shifted to a relatively low value of extinction $\sim$ 0.4. The average value of c(Hβ) derived from this distribution is 0.34 ± 0.32, which can be compared to the value calculated from the integrated spectrum, which is 0.48 ± 0.05. A small tail of negative (non-physical) values of c(Hβ) is present in this histogram, which correspond to the spectra below the theoretical line and to the right of the

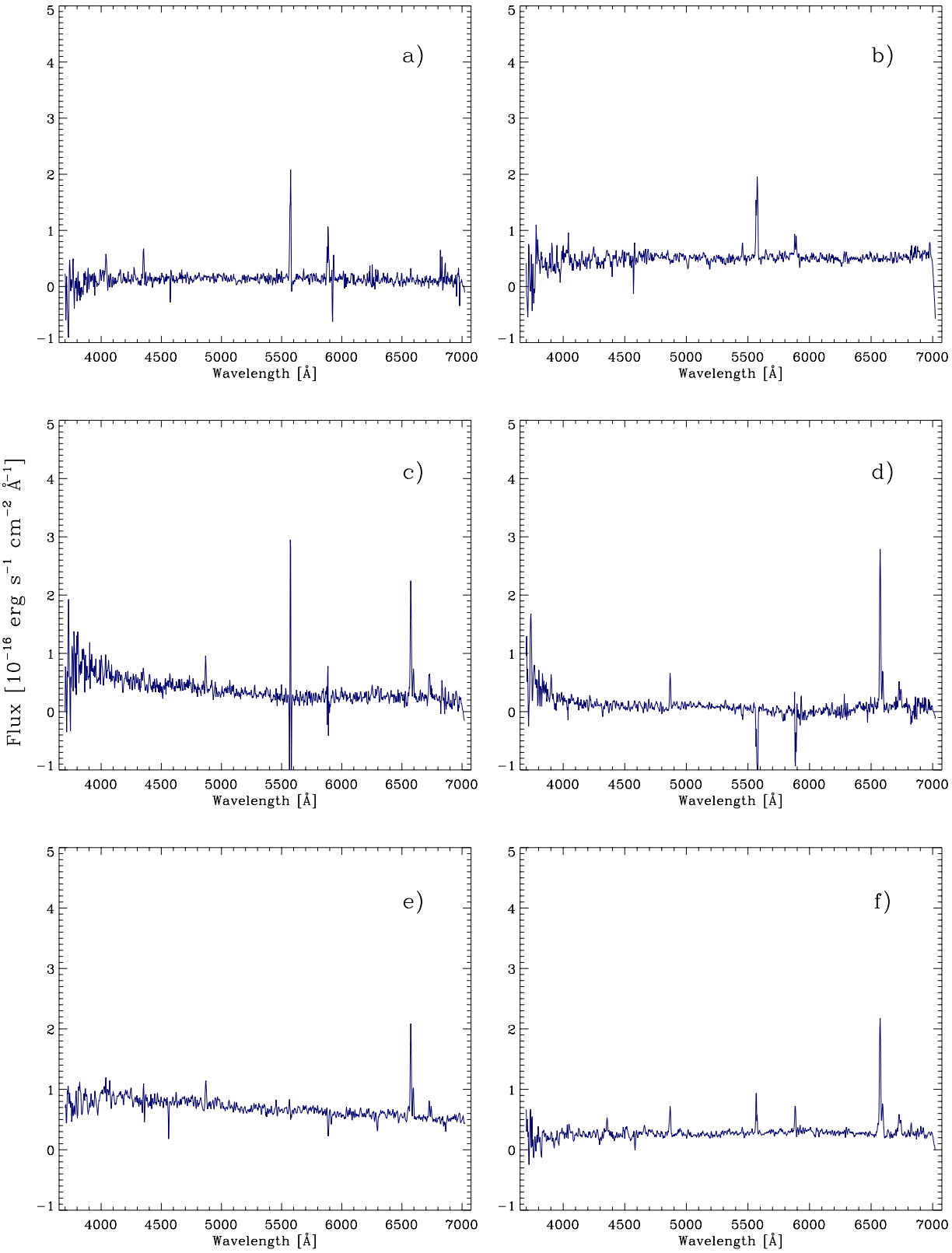

Figure 6.21: Examples of discarded spectra after the selection criteria: a) & b) spectra without the presence of Hβ; c) & d) spectra with Hα, Hβ, but with low S/N and strong sky residuals; e) & f) spectra without [O II] λ3727.

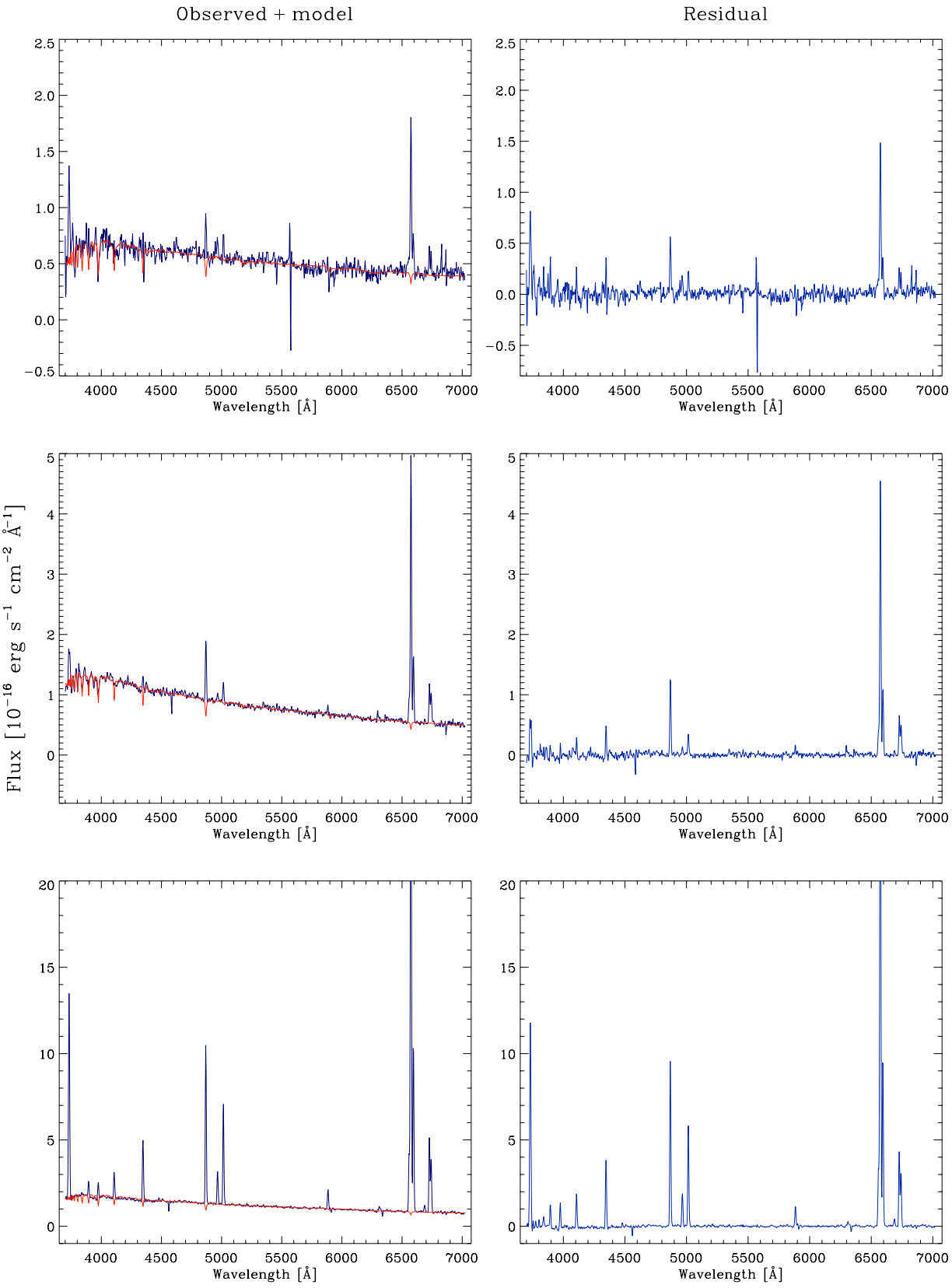

Figure 6.22: Examples of spectra with different S/N extracted from the final *fibre-by-fibre* sample. For each fibre, the left column corresponds to the observed spectrum, plus the SSP fit model overlaid as a red line, the right column shows the residual spectrum from which the selection criteria was applied.

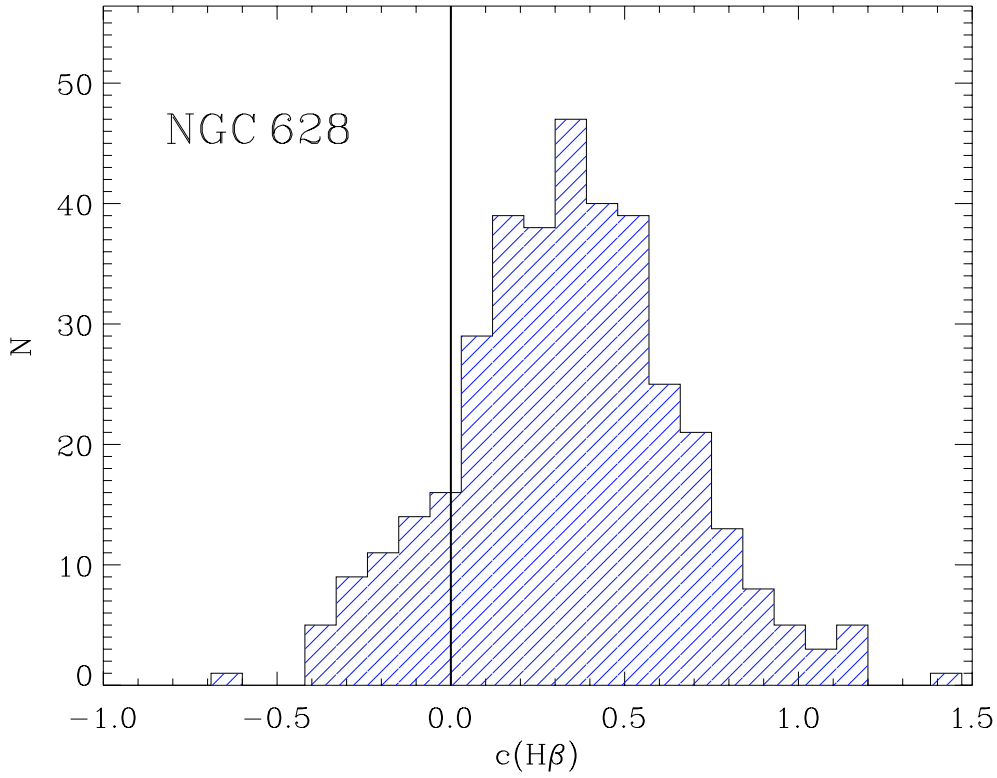

Figure 6.23: Fibre-by-fibre c(Hβ) histogram for NGC 628.

flux limit shown in the top-left panel of Figure 6.20. This small negative tail would be is expected within the statistical framework of the analysis performed in this section. The line intensities of the final *fibre-by-fibre* sample were corrected by interstellar reddening using the c(Hβ) value together with the extinction law of Cardelli et al. (1989), assuming a total to selective extinction ratio $R = 3.1$, following the same procedures as the analysis of the integrated spectra in chapter 5. Formal errors were derived by propagating in quadrature the uncertainty in the flux calibration, the statistical error in the measurement of the line intensities and the error in the c(Hβ) term. The c(Hβ) value was restricted to 4 significant figures throughout the calculation. A detailed description on the correction for dust extinction can be found in Appendix B.

Figure 6.24 shows the spatial positions of the different selected spectra, in a ΔRA–ΔDec plane in the standard orientation (north-east positive), for the *fibre-by-fibre* analysis. The colour-coding is identical to Figure 6.20, i.e. the grey fibres correspond to the subsample selected after the first and second selection criteria, the blue fibres are overlaid on the diagram, showing the position of the final selected sample after applying the third selection criteria. The colour intensity of each fibre has been scaled to the flux intensity of Hα for that particular spectrum. In that way, Figure 6.24 would correspond to a Hα *emission line map* obtained from the *fibre-by-fibre* data sample. The perpendicular lines intersect at the reference point of the mosaic's position table. A visual comparison with the interpolated Hα emission line map of Figure 6.6 shows that the grey fibres correspond mainly to the edges of the H II regions and to regions of diffuse emission along the spiral arms and in the intra-arms regions. Some grey fibres are also found as isolated regions all over the surface of the mosaic. On the other hand, the blue fibres correspond mainly to the central areas of H II regions along the spiral arms, as well as some other bright sources over the surface of the galaxy. This behaviour would be expected, since the third selection criteria was based mainly on a Hβ flux threshold, which separates the brightest fibres (i.e. the centre of H II regions) from the weaker

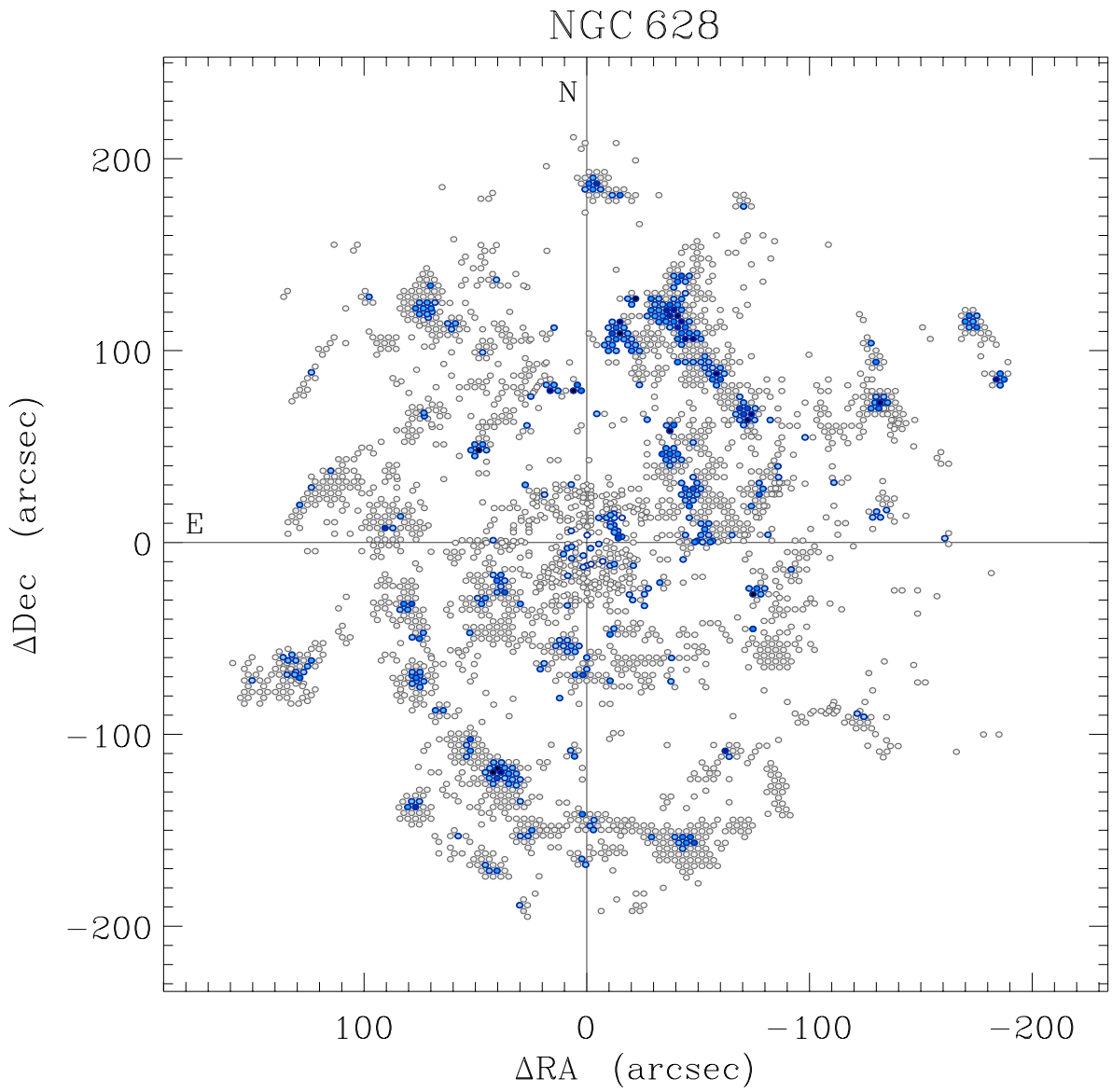

Figure 6.24: Spatial map of the *fibre-by-fibre* (blue) sample and the *diffuse* (grey) sample for NGC 628. The colour intensity of each fibre has been scaled to the flux intensity of Hα for that particular spectrum.

ones, which correspond mainly to regions of diffuse emission. The fibres selected after the first and second selection criteria, corresponding to the grey fibres in Figure 6.24, would be referred as the *diffuse* sample.

An additional way of studying the 2D distribution of the galaxy properties consist in obtaining azimuthally-averaged radial spectra, from which radial average properties can be derived. Taking the (blue) *fibre-by-fibre* sample shown in Figure 6.24 as a base, radial average spectra were obtained by co-adding all the spectra of this sample within successive rings of 10 arcsec, starting from the central reference point. An average spectrum was obtained for each single annulus at a given radius. Annulus with less than 5 fibres were excluded and skipped in the process. The radial average spectra were then analysed using the same fitting procedures described before. Although the derived spectra present more signal-to-noise than the single-fibre case, the measured emission lines were corrected by extinction using only the Hα/Hβ ratio, for consistency with the *fibre-by-fibre* analysis.

Figure 6.25 shows a collection of different diagnostic diagrams for the spectral samples considered in

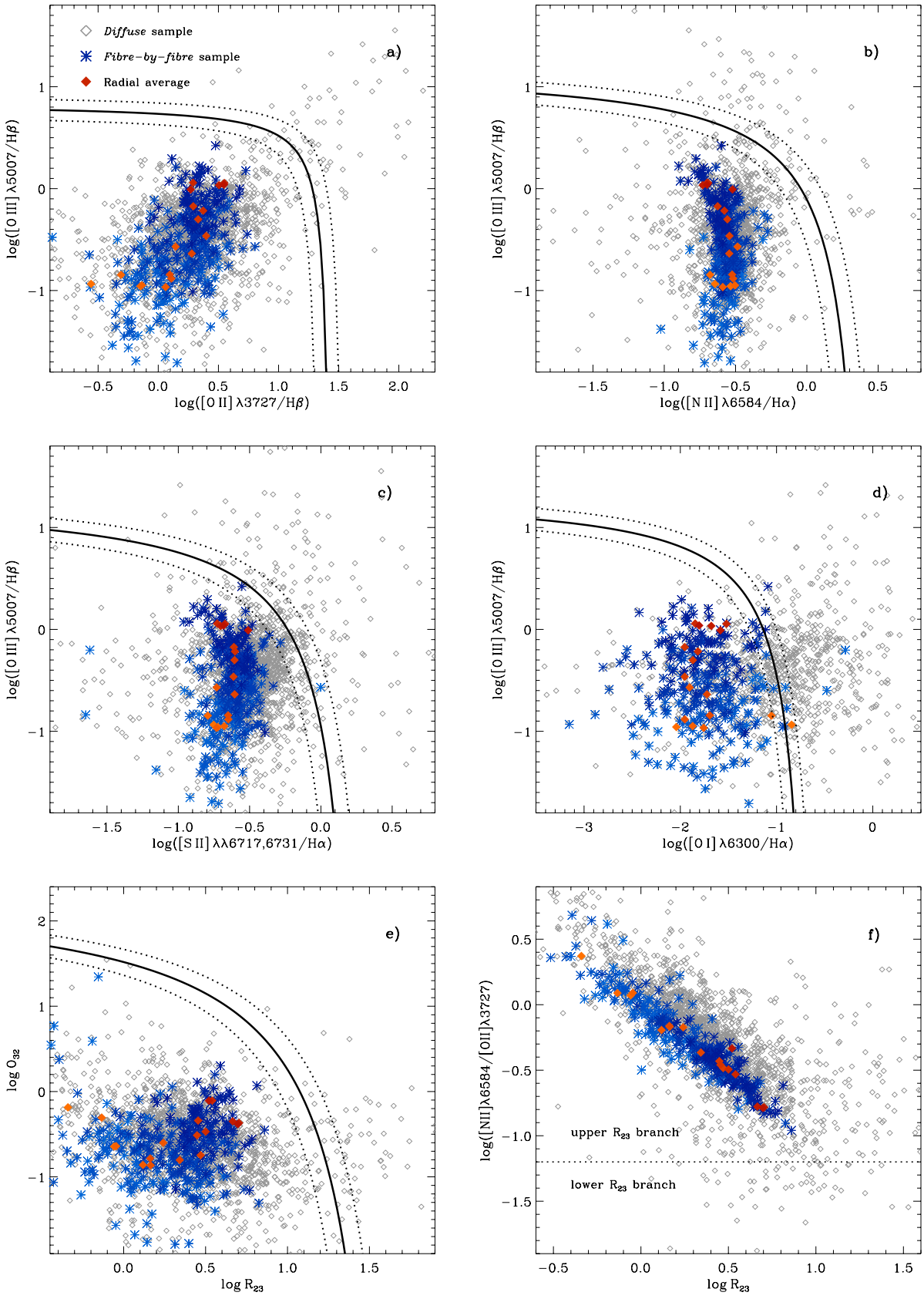

Figure 6.25: Diagnostic diagrams for NGC 628. The grey open diamonds correspond to the *diffuse* sample, the blue symbols to the final *fibre-by-fibre* sample and the filled diamonds to the azimuthally-averaged radial values. Lighter tones correspond to inner regions of the galaxy, darker colours to increasing galactocentric distance.

this section, including the *diffuse* sample (grey open diamonds), the final *fibre-by-fibre* sample (bluish symbols), and the radial average sample (reddish diamonds). Panel a) corresponds to the classical BPT diagram [O III] λ5007/Hβ vs. [O II] λ3727/Hβ. Panels b) and c) were introduced previously in subsection 5.2.4 and correspond to [O III] λ5007/Hβ vs. [N II] λ6584/Hα and vs. [S II] $\lambda\lambda$6717,31/Hα. Panel d) corresponds to [O III] λ5007/Hβ vs. [O I] λ6300/Hα, while the panel e) shows the [O III]/[O II] = $\lambda\lambda$4959,5007/[O II] λ3727 vs. R_{23}, in logarithmic scale. In all diagrams (except [O III]/[O II] vs. R_{23}), the dark-thick line corresponds to the theoretical boundaries dividing the starburst region from other types of ionization using the parametrization provided by Kewley et al. (2001). The theoretical boundary for the [O III]/[O II] vs. R_{23} diagram was obtained from the parametrization of Lamareille et al. (2004). The dashed lines represent the $\pm$0.1 dex variation.

As it can be seen in these diagnostic diagrams, the *diffuse*, low signal-to-noise spectra is scattered all over the diagrams, including those regions outside the boundaries which correspond to ionization sources different than OB stars. On the other hand, the line ratios corresponding to the *fibre-by-fibre* sample are, in general, encompassed by the theoretical H II regions boundaries. The line ratios of the radial averaged spectra are overlaid on each plot as filled diamonds. The colour-coding of both samples is related to the spatial position of a given fibre/annulus. Lighter tones correspond to the inner regions of the galaxy, while darker colours correspond to positions with increasing galactocentric radius. Clear trends can be noticed in each of the diagrams, in the case of panel a) the spectra corresponding to the inner regions, both for the *fibre-by-fibre* and radial average sample, tend to have lower line ratios for both indices; for regions at the outer part of the galaxy, the ratios increase approaching the theoretical boundary. The reason for this behaviour can be understood from the emission line maps of the previous section, the inner parts of the galaxy lack emission in [O II] and [O III] , while towards the outer parts, the emission from these species is prominent, increasing the two line ratios involved in this diagram. A slightly different trend is shown by the radial average spectra, which stay with a nearly constant [O III]/Hβ value and increasing [O II]/Hβ ratio, with increasing galactocentric distance up to [O II]/Hβ $\sim$ 0.2, where the [O III]/Hβ ratio increases considerably.

In the case of panels b) and c), the behaviour of both samples is quite similar. The [O III]/Hβ ratio increases with galactocentric distance (for the reasons given above), but the [N II]/Hα and [S II]/Hα ratios do not vary much (except for some outlying blue fibres) and are concentrated along a vertical pattern centered log [N II]/Hα $\sim$ –0.6 and log [S II]/Hα $\sim$ –0.7, with the [S II]/Hα showing a slightly higher scatter. The radial average values follow the same trend in both cases, i.e. the azimuthally-average values of the [N II]/Hα and [S II]/Hα ratios do not change appreciably with increasing galactocentric distance. Panel d) shows the [O III]/Hβ vs. [O I] λ6300/Hα diagnostic diagram, which presents a large scatter along the [O I]/Hα values for a given value of [O III]/Hβ ratio. The [O I] λ6300 is a weak emission line located in a region with strong sky emission. The redshift of NGC 628 is not large enough to avoid the contamination of the [O I] λ6300 sky-line, and therefore, the measurement of this line in the IFS data is prone to large errors due to the combined effect of its intrinsic low strength and the quality of the sky-subtraction. This would explain the large scatter seen in panel d). However, despite a couple of outliers of very small radii, the radial average values follow a vertical trend centered at [O I]/Hα $\sim$ –1.9, i.e. the azimuthally-average value of the [O I]/Hα ratio does not vary significantly with galactocentric radius.

Panel e) of Figure 6.25 shows the O_{32} vs. R_{23} diagnostic diagram. As it was previously noticed in the emission line maps section, the value of R_{23} increases with galactocentric distance. On the other hand, the O_{32} ratio (which is also a measure of the ionization degree) does not show a clear trend with respect

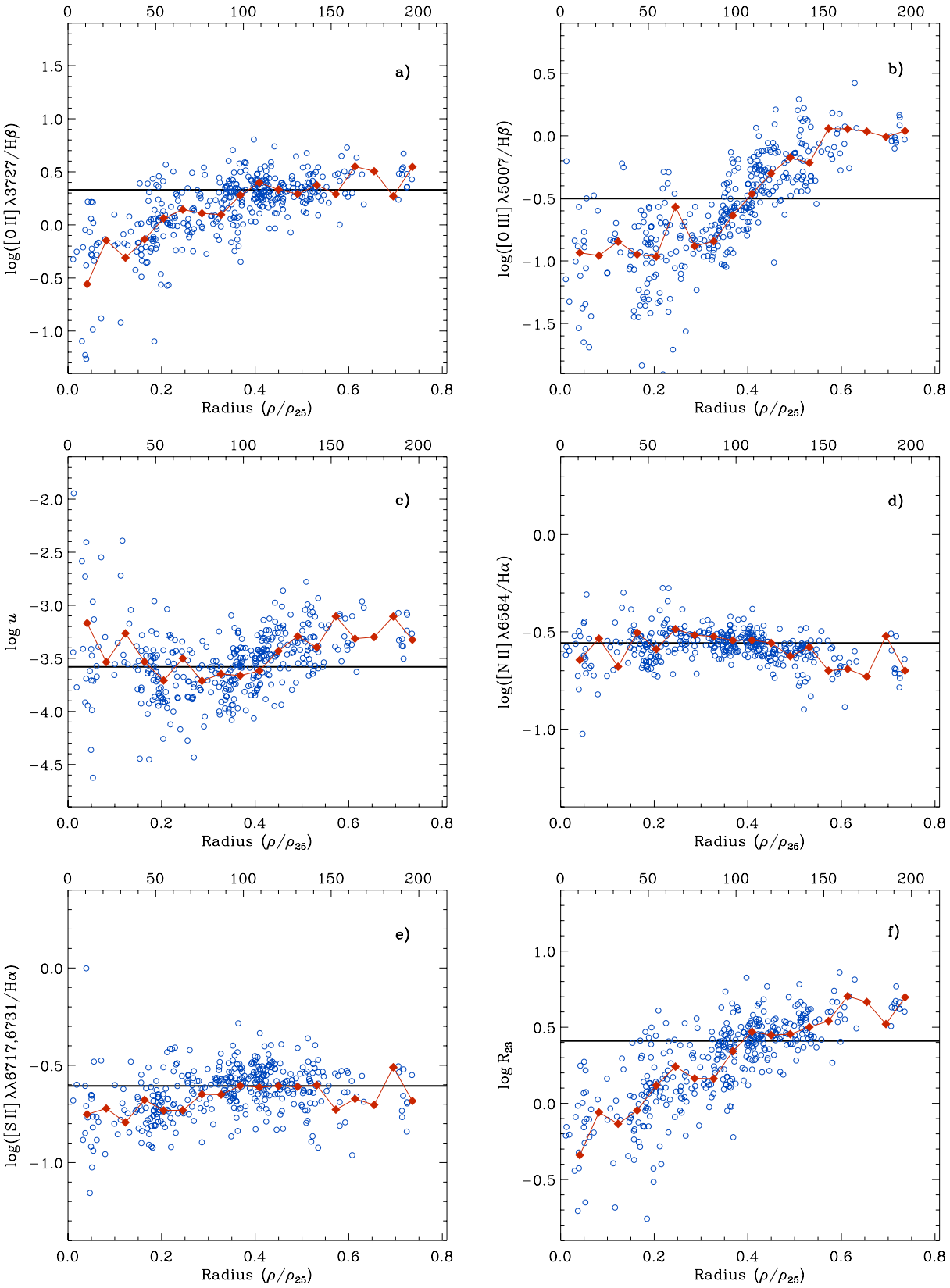

Figure 6.26: Radial variation of different line ratios and physical properties of NGC 628 for the *fibre-by-fibre* sample (blue circles) and the azimuthally-averaged spectra (red diamonds). The deprojected radial position for the blue symbols has been normalised to the size of the optical disk at the 25 mag arcsec^{-2} isophote. The radial position of the red diamonds correspond to the projected outer radius of the corresponding annulus. The top values on the X-axes show the linear-projected galactocentric radius in arcsec. The horizontal lines in each diagram correspond to the values derived from the integrated spectrum of NGC 628.

to the spatial position of the spectra, which is evident from the radial average values, inner regions show similar O_{32} values than the outer regions, with a drop at intermediate R_{23} values, producing a U shape. It is important to note that, apart from very few outliers in the [O I]/Hα diagram (due to the reasons explained above), the *fibre-by-fibre* sample in all diagnostic diagrams is consistent with regions in which the dominant ionization mechanism giving rise to the line emission of these spectra is a thermal continuum (i.e. hot OB stars). Therefore, the selection criteria applied in order to obtain the *fibre-by-fibre* sample, did in fact extract those regions with spectra showing features of real H II regions.

The last panel of Figure 6.25 corresponds to the N_2O_2 vs. R_{23} diagram, which as explained in subsection 5.3.3, it is usually used to differentiate between the two branches of R_{23} and it is a strong function of metallicity for log [N II]/[O II] $\gtrsim$ –1.2 (KD02). As in the previous diagrams, the *diffuse* sample is spread over most regions of the plot, while the *fibre-by-fibre* sample and the radial average values are found along a well-defined pattern consistent with inner regions of the galaxy having higher N_2O_2 values and outer regions showing lower N_2O_2 ratios, which combined with the opposite behavior of R_{23}, create a correlation with a negative slope. All N_2O_2 values for the *fibre-by-fibre* sample correspond to the upper branch of the R_{23} calibration, as it was implied in the analysis of the emission line maps for this galaxy.

The radial trends of the line ratios inferred from Figure 6.25 can be seen clearly in Figure 6.26. Panel a) corresponds to the variation of [O II] λ3727/Hβ; Panel b) to [O III] λ5007/Hβ; Panel c) to the ionization parameter $\log u$ (which is a calibration of the [O II]/[O III] ratio); Panel d) to [N II] λ6584/Hα; Panel e) to [S II] λ6717,31/Hα; and Panel f) to R_{23}. The blue circles correspond to the *fibre-by-fibre* spectra, while the red-connected diamonds correspond to the values derived from the radial averaged spectra. The deprojected radial position for the blue symbols has been normalised to the size of the optical disk at the 25 mag arcsec^{-2} isophote. The radial positions of the red diamonds correspond to the projected outer radius of the corresponding annulus from which the spectra were obtained. The values shown on the top X-axes correspond to the linear projected galactocentric radius in arcsec. In each panel, the horizontal lines correspond to the value derived from the integrated spectrum of the galaxy.

The [O II] and [O III]/Hβ ratios on panels a) and b) increase as a function of the radius, with a somewhat steeper increase for the [O III]/Hβ ratio from a normalised radius $\sim$ 0.3, for lower radii this latter ratio shows some level of scatter, but consistent with a constant value log([O III]/Hβ) $\sim$ –1.0, as already noticed in Panel a) of the BPT diagrams shown in Figure 6.25. The ionization parameter shows quite a lot of scatter for radii lower than 0.3, probably due to the lack of oxygen emission (from which this parameter is derived) in these inner regions. From $\rho/\rho_{25} > 0.3$, $\log u$ increases slightly with increasing radius. On the other hand, the [N II] and [S II]/Hα ratios shown in Panels d) and e) confirm the very small variation of these ratios over the surface of the galaxy. However, the [N II]/Hα ratio shows a slightly negative gradient towards larger radii. The log([S II]/Hα) ratio is consistent with a value of $\sim$ –0.3 $\pm$ 0.2 dex along all the radii range covered by the spectral sample. The R_{23} shows the increasing radial pattern inferred previously, extending for more than one order of magnitude from the inner ($\log R_{23} \sim$ –0.5) to the outer regions ($\log R_{23} \sim$ –0.7). Note that all the indices and parameters in which the oxygen [O II] and/or [O III] lines are involved show a larger dispersion for normalised radii lower than 0.3.

The radial average values traced by the red diamonds follow quite well the trends shown by the blue symbols in all the radial plots. The higher signal-to-noise of the average spectra allows a better determination of the line ratios, specially for the regions in the inner part of the galaxy. Note also that the *fibre-by-fibre* spectra cover practically all radii values up to $\rho/\rho_{25} \sim 0.75$, with one small gap at $\rho/\rho_{25} \sim 0.65$. Interestingly, the values of the ratios and parameters derived from the integrated spectrum are consistent in

all cases with the radial values found at $\rho/\rho_{25} \sim 0.4$.

The reddening corrected line ratios of both samples were used to derived the oxygen abundance for each individual spectrum, using a subset of the abundance diagnostics employed in the case of the integrated spectra. They correspond to two R_{23} calibrators, namely M91 and KK04, which take into account the effects of the ionization parameter and provide parametrizations for both branches of the R_{23} relation. Two "index-empirical" methods: $N2$ and $O3N2$; and two more methods based on the use of the strong oxygen lines combined with the excitation parameter P, i.e. PT05, and the ff–T_e method, as explained in detailed in subsection 5.3.3.

Radial abundance gradients were derived for NGC 628 based on the *fibre-by-fibre* analysis sample for the different abundance diagnostics mentioned above. In each plot, the blue symbols correspond to the spectra of the final sample, the red diamonds correspond to the azimuthally-averaged radial spectra, as in Figure 6.26. All values show 1σ error bars derived through a Monte Carlo simulation by propagating Gaussian distributions with a width equal to the errors of the emission line intensities, modulated by recomputing the distribution over 500 times. For the R_{23} methods, M91 and KK04, the open symbols correspond to an arbitrary offset of –0.5 dex (no error bars are drawn in these cases). The blue and red thick lines correspond to the linear least-squares fit to the *fibre-by-fibre* and radial average data points, respectively. In each panel, the horizontal line correspond to the oxygen abundance value obtained from the integrated spectrum of the galaxy for that particular calibrator. The vertical line corresponds to the radius at which the *fibre-by-fibre* linear fit (blue line) equals the integrated abundance value. The solar abundance ($12+\log(\mathrm{O/H})_\odot = 8.70$, Scott et al. 2009) is shown with the $\odot$ symbol in the Y-axes. The scale in both axes is the same for all diagrams, so that the differences and offsets can be compared among the calibrators.

All the oxygen abundances derived using the R_{23} methods were based on the corresponding upper branch parametrizations, based on the results of the [N II]/[O II] ratio, shown on Panel f) in Figure 6.25. As in the integrated spectra case, the R_{23} methods (top-panels) show a higher oxygen abundance than the rest of the diagnostic methods, with the KK04 method providing the highest values. However, the shape and slope of both methods is quite similar. The gradient derived from the M91 method is -0.52 ± 0.05 dex ρ_{25}^{-1}, slightly steeper than the gradient obtained from the KK04 method, which is -0.46 ± 0.04 dex ρ_{25}^{-1}. The maximum oxygen values at $\rho = 0$ inferred from these gradients are: $12 + \log(\mathrm{O/H}) = 9.10$ and 9.23, for the M91 and KK04 methods respectively, which translate to 8.6 and 8.73 for the –0.5 dex offsets. In both cases, the oxygen abundance derived from the integrated spectrum matches the linear fit for radius ρ/ρ_{25} very close to 0.4 ($\sim$ 100 arcsec). The scatter of the data points is somewhat larger than the intrinsic errors of the derived abundances, specially for regions located between 0.2 and 0.6 in normalised radius units. On the other hand, the radial average spectra shows in both cases a very linear relationship, with a low level of scatter. The gradients derived from the linear fits of these samples correspond to -0.67 ± 0.06 and -0.58 ± 0.06 dex ρ_{25}^{-1} for the M91 and KK04 cases respectively, with corresponding central oxygen abundances of 9.16 and 9.27 (8.66, 8.77 for the offsets).

The $N2$ gradient (middle-left panel of Figure 6.27) shows a very different behaviour. Although the dispersion along the radius is reduced compared to the previous cases, the oxygen abundance shows a nearly flat dependence with galactocentric radius. The derived slopes correspond to -0.08 ± 0.02 and -0.11 ± 0.06 dex ρ_{25}^{-1} for the *fibre-by-fibre* and radial average samples respectively, with a common central oxygen abundance of 8.64. The integrated oxygen abundance for this calibrator equals the spatially resolved gradient at $\rho/\rho_{25} \sim 0.2$, i.e. at $\sim$ 60 arcsec in linear projection.

The $O3N2$ derived gradient (middle-right panel in Figure 6.27) presents a similar trend to the R_{23} meth-

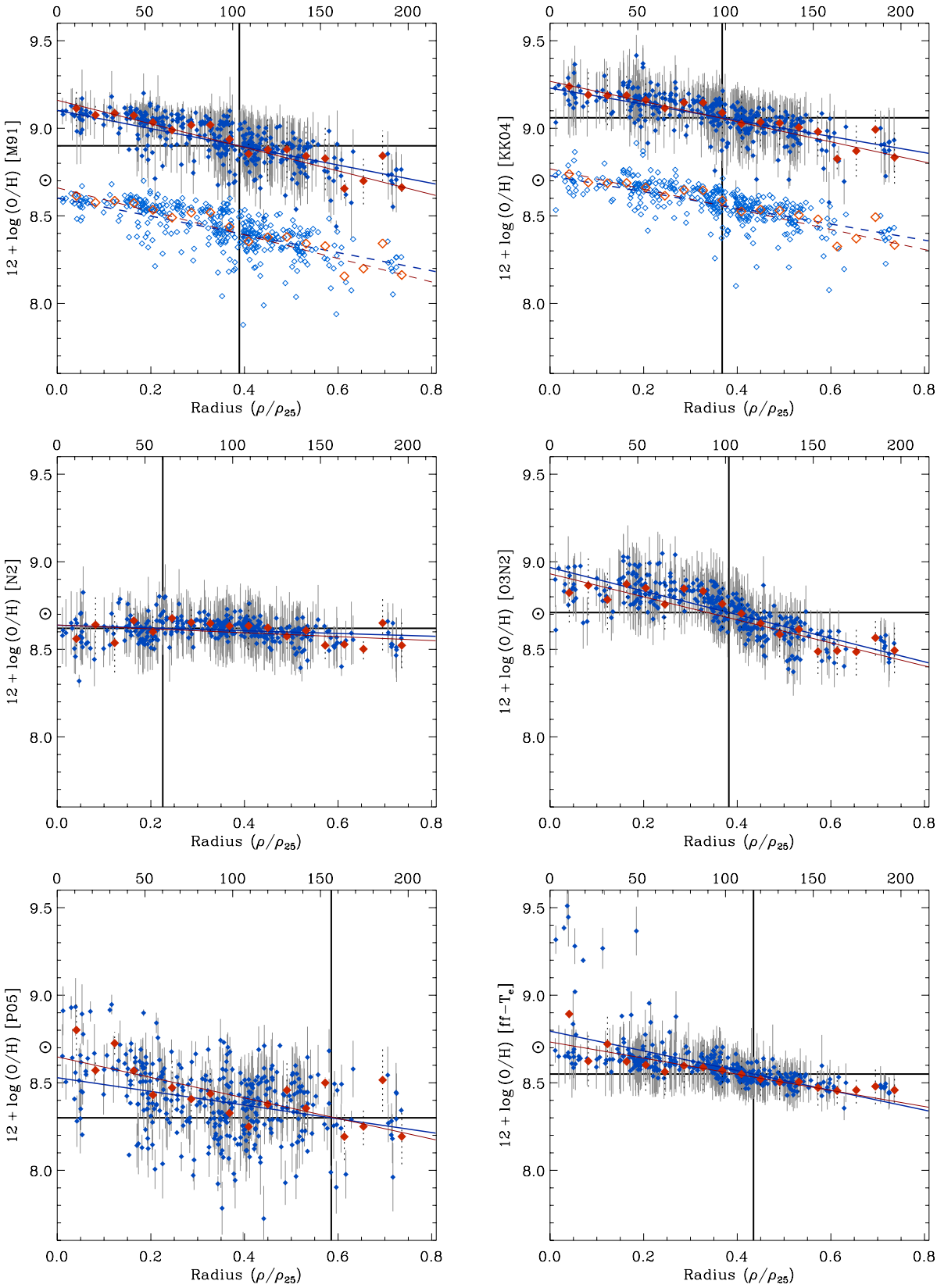

Figure 6.27: Radial abundance gradients derived for NGC 628 based on the *fibre-by-fibre* analysis for different abundance diagnostics. In each plot, the blue symbols correspond to the spectra of the final sample, the red diamonds correspond to the azimuthally-averaged radial spectra. For the R_{23} calibrators, the open symbols correspond to an arbitrary offset of –0.5 dex. The top X-axis values correspond to the projected radii in arcsec for the radial average data. The assumed solar abundance is shown in the Y-axis. See the text for a full explanation.

RADIAL ABUNDANCE GRADIENTS FOR NGC 628: *fibre-by-fibre* ANALYSIS

	M91		KK04		N2	
	Fibre-by-fibre	*Radial*	*Fibre-by-fibre*	*Radial*	*Fibre-by-fibre*	*Radial*
$12+\log(\mathrm{O/H})_{\rho=0}$	9.10 ± 0.02	9.16 ± 0.03	9.23 ± 0.02	9.27 ± 0.02	8.64 ± 0.01	8.64 ± 0.03
$12+\log(\mathrm{O/H})_{\rho=0.4\rho_{25}}$	8.89 ± 0.02	8.89 ± 0.03	9.05 ± 0.02	9.04 ± 0.02	8.61 ± 0.01	8.59 ± 0.03
$\log(\mathrm{O/H})_{(\mathrm{dex}\ \rho_{25}^{-1})}$	-0.52 ± 0.05	-0.67 ± 0.06	-0.46 ± 0.04	-0.58 ± 0.06	-0.08 ± 0.02	-0.11 ± 0.06
$\log(\mathrm{O/H})_{(\mathrm{dex\ kpc}^{-1})}$	-0.037 ± 0.004	-0.048 ± 0.004	-0.033 ± 0.003	-0.041 ± 0.004	-0.006 ± 0.001	-0.008 ± 0.005
	O3N2		PT05		ff–T_e	
	Fibre-by-fibre	*Radial*	*Fibre-by-fibre*	*Radial*	*Fibre-by-fibre*	*Radial*
$12+\log(\mathrm{O/H})_{\rho=0}$	8.97 ± 0.01	8.93 ± 0.03	8.53 ± 0.03	8.65 ± 0.06	8.79 ± 0.01	8.73 ± 0.03
$12+\log(\mathrm{O/H})_{\rho=0.4\rho_{25}}$	8.70 ± 0.01	8.67 ± 0.03	8.37 ± 0.03	8.41 ± 0.06	8.57 ± 0.01	8.55 ± 0.03
$\log(\mathrm{O/H})_{(\mathrm{dex}\ \rho_{25}^{-1})}$	-0.67 ± 0.03	-0.66 ± 0.07	-0.39 ± 0.07	-0.59 ± 0.14	-0.56 ± 0.04	-0.46 ± 0.07
$\log(\mathrm{O/H})_{(\mathrm{dex\ kpc}^{-1})}$	-0.048 ± 0.002	-0.047 ± 0.005	-0.028 ± 0.005	-0.042 ± 0.010	-0.040 ± 0.003	-0.033 ± 0.005

Table 6.3: Results from the oxygen abundance gradient analysis of NGC 628 based on the *fibre-by-fibre* sample. The columns correspond to the different calibrators employed, differentiating between the results from the individual fibres and the radial average samples. The rows correspond to: the central abundance at galactocentric radius $\rho = 0$; the *characteristic* abundance at $\rho = 0.4\rho_{25}$; and the slope of the abundance gradients in dex ρ_{25}^{-1} and dex kpc^{-1}, respectively.

ods, although it does not show a very linear relationship as in the previous cases. The patterns is more consistent with a semi-sinusoidal trend. This feature is more notorious for inner regions where the *O*3*N*2 abundances show the more level of scatter. This may be due to the combined effect of the high dispersion of the [N II]/Hα and [O III]/Hβ ratios observed for normalised radius lower than 0.3, as shown in Figure 6.26. Nevertheless, the scatter of the data is somewhat within the calculated error bars. The abundance gradients derived from the *O*3*N*2 calibrator are -0.67 ± 0.03 and -0.66 ± 0.07 for the *fibre-by-fibre* and radial average samples respectively, with central oxygen abundances of 8.97 and 8.93 in each case. Similarly to the R_{23} methods, the oxygen abundance obtained from the integrated spectrum matches the *O*3*N*2 linear fit at normalised radius ~ 0.4.

The gradient corresponding to the PT05 calibrator (bottom-left panel of Figure 6.27) shows the highest level of dispersion among all different metallicity indicators. Also, the oxygen abundances derived from this method are, in average, the lowest ones, consistent with subsolar values. Although an abundance gradient can be inferred from the use of this calibrator, the scatter is so large that a linear correlation may not represent a radial trend of the oxygen abundance. The linear fit to the data results in a gradient of -0.39 ± 0.07 dex ρ_{25}^{-1} in the case of the *fibre-by-fibre* sample and -0.59 ± 0.14 dex ρ_{25}^{-1} for the radial average spectra. The corresponding oxygen central abundances are 8.53 and 8.65. The integrated abundance equals the radial trend of the PT05 derived abundances at a large normalised radius ~ 0.6, i.e. ~ 150 arcsec.

The abundance gradient based on the ff–T_e method is shown in the bottom-right panel of Figure 6.27. It presents a clear linear trend of the oxygen abundance with the galactocentric radius. The scatter of the data points falls within the error bars for normalised radius greater than 0.3. However, for the inner regions of the galaxy, the dispersion increases considerably, with a number of outlying data points approaching oxygen values of $12+\log(\mathrm{O/H}) \sim 9.5$. Considering that the signal-to-noise of the [O II] and [O III] emission lines for the inner regions of the galaxy (i.e. $\rho/\rho_{25} \lesssim 0.3$) is relatively low, this behaviour suggests that this method is sensitive to the signal-to-noise of the strong oxygen lines used in the determination of the oxygen abundance. The abundance gradient derived from the *fibre-by-fibre* sample is -0.56 ± 0.04 dex ρ_{25}^{-1}, while

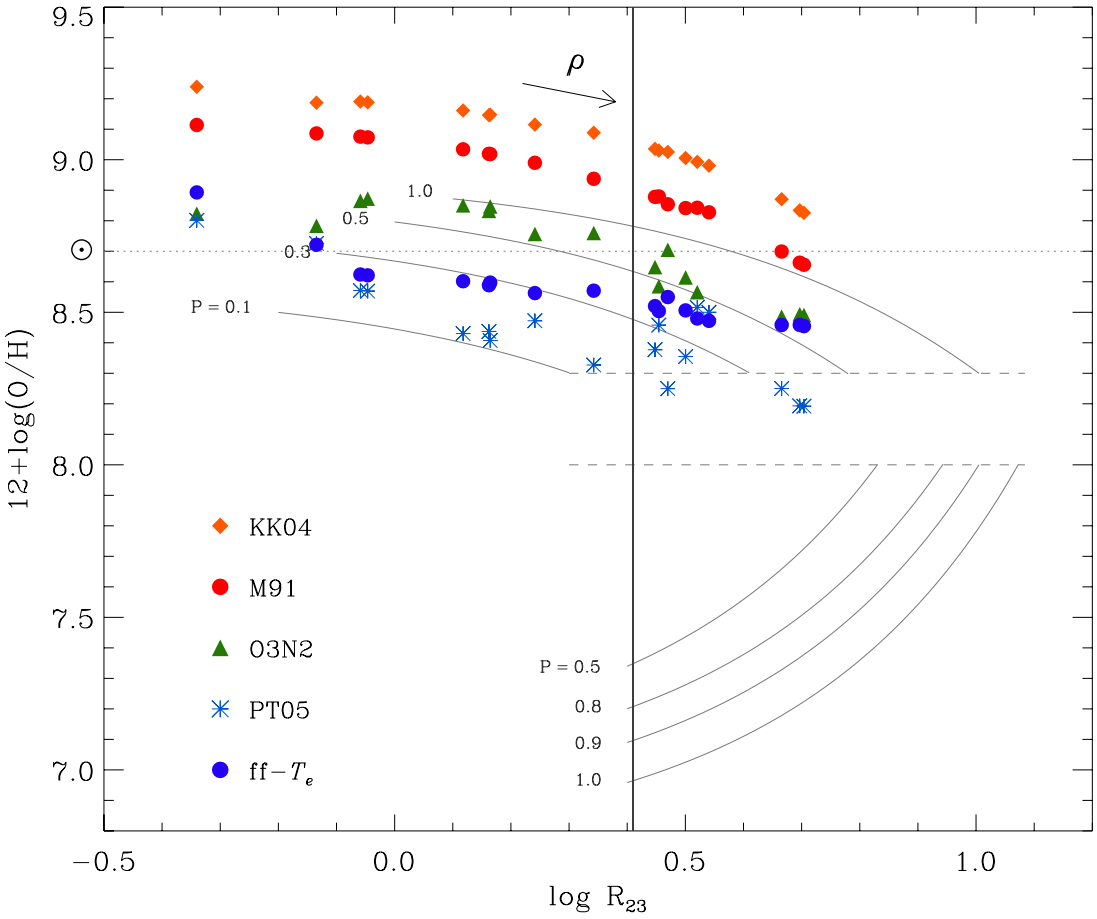

Figure 6.28: $12+\log(\mathrm{O/H})$ vs. $\log R_{23}$ diagram for the radial average sample extracted from the *fibre-by-fibre* analysis. The solid lines correspond to predictions of the empirical calibrations in both branches for different values of the excitation parameter P. The horizontal dashed lines show the transition zone between the two R_{23} branches. The arrow shows direction of increasing galactocentric radius. The vertical line shows the value of $\log R_{23}$ derived from the integrated spectrum of NGC 628.

the slope obtained from the radial average is –0.46 ± 0.07 dex ρ_{25}^{-1}, values consistent with the derive from the R_{23} methods. The central abundances are 8.79 and 8.73 respectively. The oxygen abundance determined from the integrated spectrum matches the ff–T_e radial trend for a normalised radius ~ 0.45 (i.e. ~ 115 arcsec), slightly larger than in the R_{23} cases.

From the analysis of the abundance gradients discussed above we might conclude that, despite the scale offsets and small pattern variations among the calibrators, the R_{23} methods (M91, KK04), the $O3N2$ and the ff–T_e methods are quite similar in qualitative terms. They show a well-defined linear correlation between the oxygen abundance and galactocentric radius, the slopes derived from the *fibre-by-fibre* and radial average samples are equivalent within the errors, although the $O3N2$ and ff–T_e methods suggest somewhat a flattening of the gradient for the innermost regions. Obviously, the central oxygen abundances are different considering the offsets of the calibrators, specially in the case of the R_{23} methods based on photoionization models, as the M91 and KK04 employed here. An interesting common feature is that for all these calibrators, the integrated abundance coincides with the H II region abundance gradient for a normalised radius $\rho/\rho_{25} \sim 0.4$, i.e. that the integrated abundance correlates with the spatially resolved abundances, independent of the abundance calibration used. This effect was previously indicated by Moustakas & Kennicutt

(2006a), who observed that, to a first order, the abundance inferred from the integrated spectrum of a galaxy is representative of the gas-phase oxygen abundance at $\rho = 0.4\rho_{25}$, i.e. the *characteristic* abundance of a galaxy, even in the presence of an abundance gradient, emission from the diffuse medium or variations in dust reddening. They reached this conclusion based on the M91 calibrator, the use of the PT05 calibrator showed a similar behaviour in their sample but a much higher dispersion. Here we confirm this result for the case of NGC 628, extending the number of calibrators which also show this trend, i.e. $O3N2$ and the ff–T_e method. The generalization of this result for the rest of the considered galaxies will be discussed thereafter in this dissertation.

Table 6.3 shows the results from the abundance gradients analysis of NGC 628 for the *fibre-by-fibre* sample. Different columns present the values of the extrapolated central abundance at galactocentric radius $\rho = 0$, of the *characteristic* oxygen abundance at $\rho = 0.4\rho_{25}$ (in $12 + \log(\mathrm{O/H})$ units), and the slope of the abundance gradients in dex/ρ_{25} and dex/kpc for the different abundance calibrators considered in the analysis, separating the values derived from the *fibre-by-fibre* and the radial average samples.

In Figure 6.28, we present the O/H vs. R_{23} relation for the *fibre-by-fibre* analysis discussed in this section. As the values derived from the azimuthally-averaged radial spectra are representative of the abundances obtained using the full *fibre-by-fibre* sample at any galactocentric radius of the galaxy (and for the sake of clarity), only these values are presented in Figure 6.28. The different calibrators employed in this analysis are labeled in the graph.

As previously mentioned through the analysis of the emission line maps and in the present section, the R_{23} value increases from the inner regions to the outer parts of the galaxy. Therefore, different values of the R_{23} correspond to different spatial positions for a given calibrator. The arrow in the upper part of the graph shows the direction of increasing galactocentric radius. In that respect, the O/H vs. R_{23} diagram of Figure 6.28 can be analogous to an abundance gradient as a function of R_{23}. The trends and scales of the different calibrators can be clearly noticed, with the KK04 and M91 calibrators corresponding the higher oxygen determinations, following a curved shape as expected, considering the parametrization of these diagnostics in terms of R_{23} and $\log u$ (see Appendix C). The rest of the calibrators show a more irregular pattern, but consistent with a linear relationship in the $\log - \log$ space, specially in the case of the ff–T_e relation. In the case of the PT05 calibration, many radial points fall within the transition zone between the two different branches. As suggested by PT05, the oxygen abundances derived by the PT05 relation may be unreliable in this domain. The vertical line shows the value of $\log R_{23}$ derived from the integrated spectrum of NGC 628.

Finally, in Figure 6.29 we present the oxygen abundance 2D map of NGC 628 based on the $O3N2$ calibrator, obtained by the manipulation of the emission line maps based on the *diffuse* sample (see Figure 6.24 for a comparison). The reason for the use of this sample (and not the final *fibre-by-fibre* sample) is due to the interpolation scheme employed in order to generate the maps. Large blank areas produce convergence problems which limits the application of any interpolation routine. No other 2D abundance maps were attempted since the parametrizations of the different calibrators do not allow a simple image manipulation. However, as discussed previously in this section, the $O3N2$ abundance determination follows qualitatively the same pattern as the other more elaborated calibrators based on R_{23} and the ff–T_e relation. The map of Figure 6.29 shows a clear gradient of higher oxygen metallicity values from the inner part to the outer part of the galaxy, and along the spiral arms. The most metal deficient regions are found at the extremes of the spiral arms, a prominent region is found at ($\Delta\alpha$,$\Delta\delta$) $\sim$ (–40,–60). The average value of the oxygen abundance derived from this map is 8.75 ± 0.17, which is equivalent to the oxygen abundance derived from

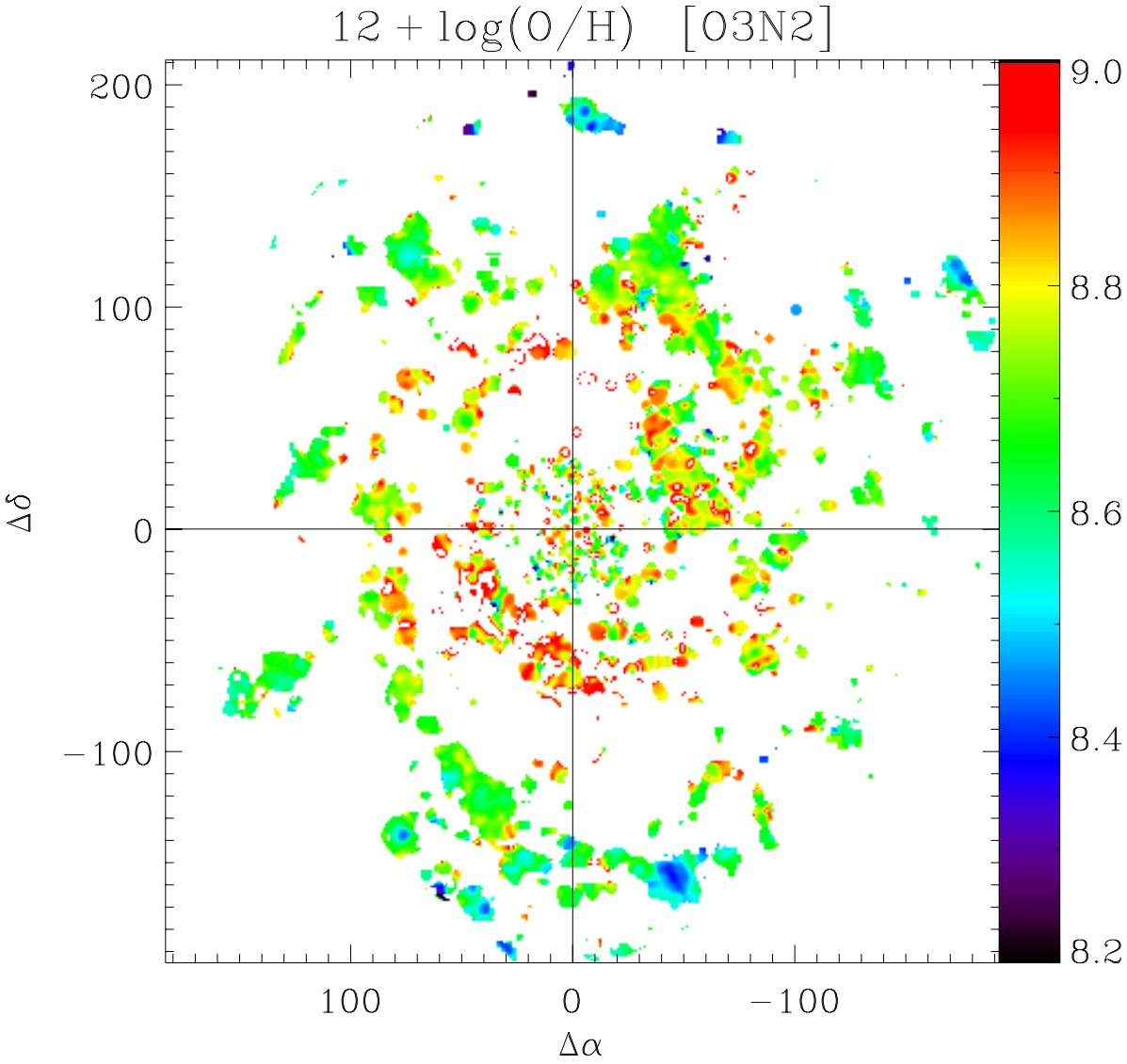

Figure 6.29: Oxygen abundance map of NGC 628 derived by applying the *O3N2* calibrator to the emission line maps of the galaxy.

the integrated spectrum using the same calibrator, i.e. 8.71 ± 0.11.

In this section I have presented a thorough analysis of the 2D spectroscopic properties of NGC 628 based on the first proposed analysis method, by considering that each individual fibre samples a considerable physical region of the galaxy, and therefore, contains enough information for a further analysis. The quality sanity checks, figures and methodology presented in this section will be taken as a reference to compare the results and samples obtained from the other analysis methods presented in the following sections.

6.3.2 Method II: [O III] LIMITED SAMPLE

The previous analysis demonstrated that, the assumption that a single fibre contained enough signal-to-noise to be analysed in individual basis was, to a first order, correct. However, among the final selected spectra in the *fibre-by-fibre* sample there were found many spectra not showing characteristic signatures of a "physical" H II region, i.e. fibres with a [O III] $\lambda 5007/\lambda 4959$ ratio not consistent with the constraints

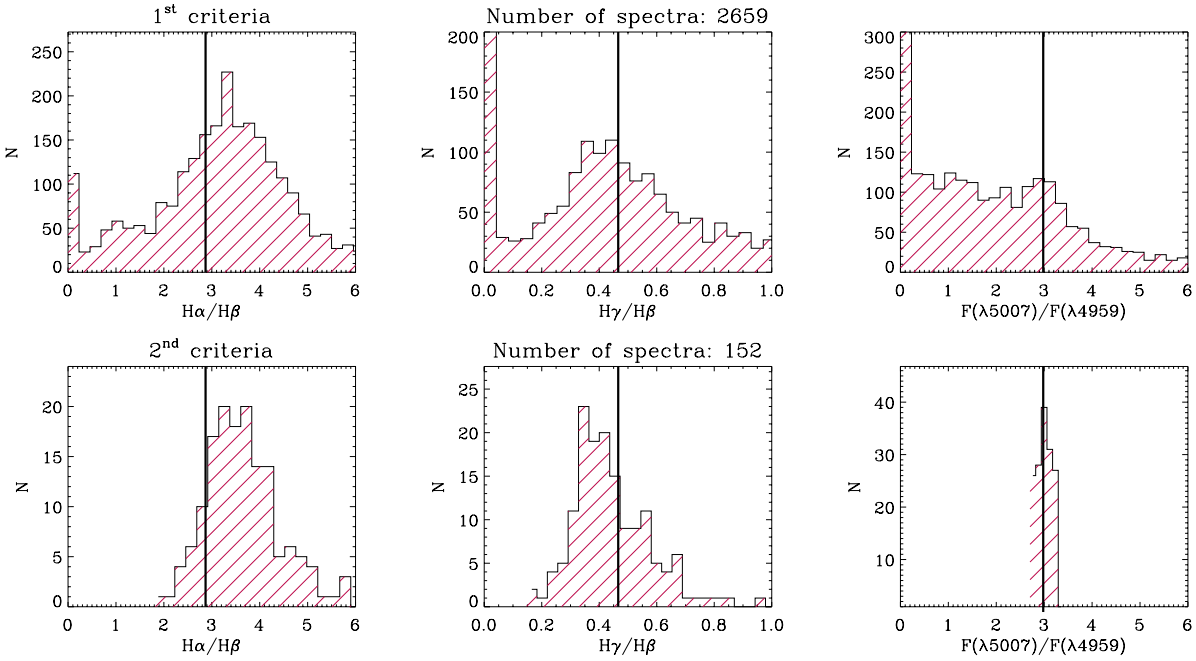

Figure 6.30: Selection criteria histograms for the $O_3 - limited$ analysis of NGC 628. In each panel, the vertical lines correspond to the theoretical values of the given line ratio.

imposed by the theoretical value (~ 3) and/or regions with a Hα/Hβ ratio less than the theoretical value for case-B recombination, implying a negative value of the logarithmic extinction coefficient c(Hβ), and therefore a negative correction for extinction.

Therefore, a second analysis method was proposed in order to restrict the sample to only those regions showing "physical" features in their spectra. The *clean* mosaic was taken again as the starting point of the sample selection. The first selection criteria was exactly the same as in the case of the *fibre-by-fibre* sample, i.e. to select those fibres where both, the Hβ and [O III] λ4959 line intensities were greater than zero, i.e. implying detectability of those lines. As in the previous case, this selection criteria reduced the number of fibres to 2659. The second selection criteria was applied in order to extract "physical" regions from this latter sample. The criteria consisted on two parts:

1. To select only those fibres for which the [O III] λ5007/λ4959 ratio was consistent with the theoretical value, within a very small range of observed ratios. Therefore, only fibres with [O III] λ5007/λ4959 = 2.98 ± 0.3 were selected.

2. As the above criterion does not suffice to discard those regions with low signal-to-noise, a flux threshold cut was applied to the data, taking a lower limit than in the *fibre-by-fibre* case, hoping that the restriction of the [O III] line ratio would provide better quality spectra even for fibres with low observed intensity. The flux threshold was based (as in the case of the *fibre-by-fibre* sample), on the intensity of the Hβ line, for NGC 628 the chosen value was 5×10^{-16} erg s^{-1} cm^{-2}, compared with the the 8×10^{-16} erg s^{-1} cm^{-2}, applied to the *fibre-by-fibre* sample.

The two criteria mentioned above were applied at the same step in the analysis, reducing the number of selected fibres to 152, i.e. only 2% of the total number of fibres in the *clean* mosaic and a factor of $\sim$2.5 lower fibres than the *fibre-by-fibre* sample. As in the previous method, the sample was checked for

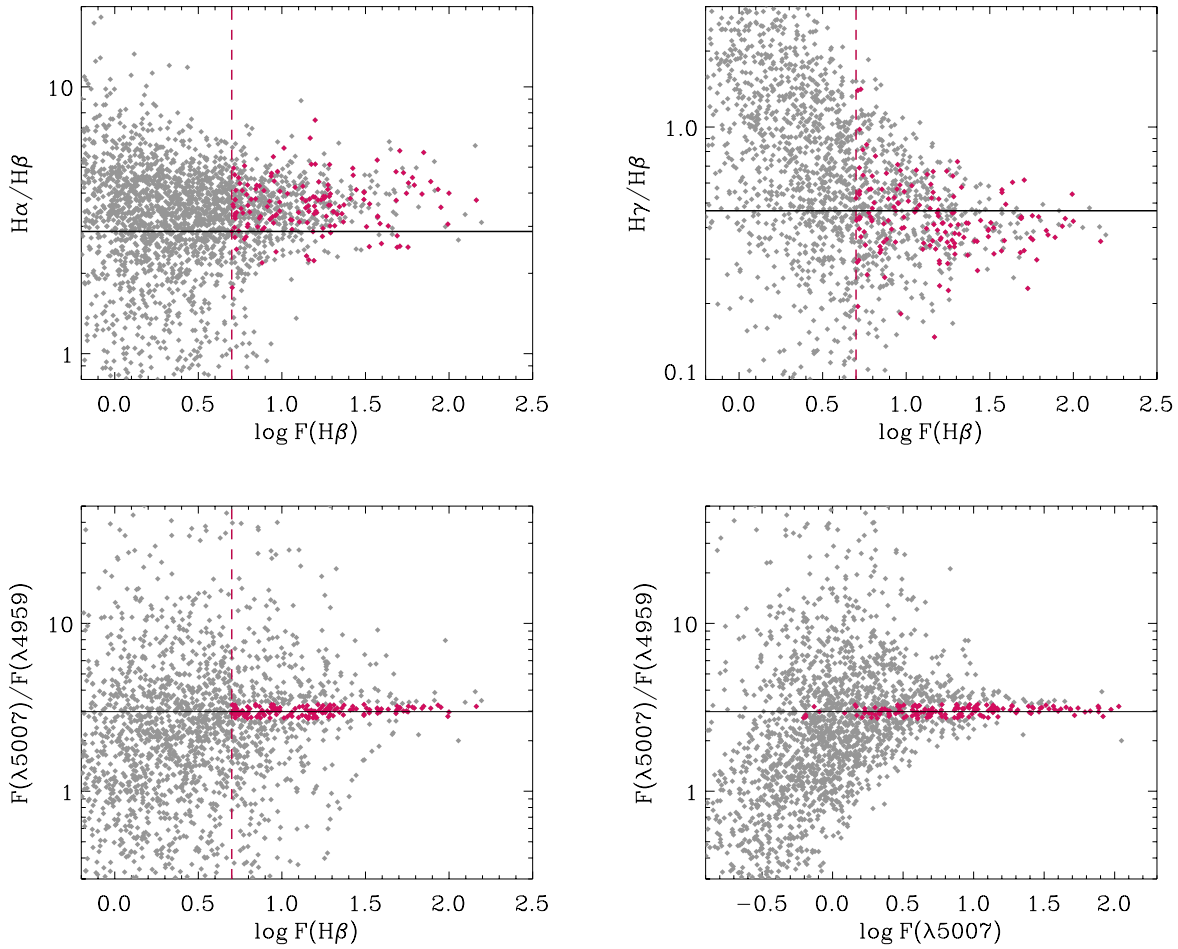

Figure 6.31: Hα/Hβ, Hγ/Hβ and [O III] λ5007/λ4959 ratios as a function of observed flux in Hβ and F(λ5007) for the $O_3 - limited$ analysis of NGC 628. The grey symbols correspond to the 1st selection sample, the magenta symbols to the final $O_3 - limited$ sample. The horizontal lines correspond to the theoretical values for each ratio. The vertical dashed lines stand for the flux threshold in Hβ.

non-finite numbers in the derived logarithmic extinction coefficient. However, all of the values were finite and no further selection was necessary. The final sample selected through the method described above will be referred as the $O_3 - limited$ sample.

Figure 6.30 shows the histograms of the $O_3 - limited$ selection steps, similarly to Figure 6.19 in the case of the *fibre-by-fibre* sample. The top panels corresponds to the first selection criteria (which is identical to the *fibre-by-fibre* case). The bottom panels show the distribution of the different line ratios for the final $O_3 - limited$ sample. The Hα/Hβ and Hγ/Hβ are somewhat similar to the final sample of the *fibre-by-fibre* analysis, showing the expected distribution of reddened spectra with values greater than the Hα/Hβ ratio, and lower than the Hγ/Hβ ratio. The tail of values greater than the theoretical one for the Hγ/Hβ ratio is smaller than in the case of the *fibre-by-fibre* case, and both distributions do not show extreme lower vales as in the previous case. However, a small tail of Hα/Hβ values lower than the theoretical are still found in the sample. On the other hand, the [O III] λ5007/λ4959 distribution reflects the selection criteria applied to the data, showing a narrow distribution centered at the theoretical value with a width equal to the predefined variation in this ratio (i.e. ±0.3).

The distribution of the line ratios as a function of line flux is presented in Figure 6.31 in a similar way as Figure 6.20. The grey symbols correspond to the 1st selection criteria, i.e. fibres with Hβ and [O III] λ4959

greater than zero, the magenta symbols to the final $O_3 - limited$ sample. The horizontal lines correspond to the theoretical values for each ratio. The vertical dashed lines stand for the flux threshold in Hβ. The selected fibres in the Hα/Hβ and Hγ/Hβ show a very similar trend as in the case of the *fibre-by-fibre* sample, i.e. most of the data points are above the theoretical line in the case of the Hα/Hβ ratio. The Hγ/Hβ values show more dispersion around the theoretical value. The real difference with respect to Figure 6.20 resides in the bottom panels showing the distribution of the [O III] ratio, showing the narrow distribution of data points along the theoretical value.

The line intensities of the selected spectra were corrected for dust-extinction following the same procedure as described before. As in the case of the *fibre-by-fibre* sample, an azimuthally-average radial spectra was obtained from the final spatial distribution of the $O_3 - limited$ sample, by co-adding the spectra found within successive rings of 12 arcsec. Given the low number of fibres at some galactocentric radius, a minimum number of fibres per annulus was not required when co-adding the radial spectra. Emission line intensities were obtained for each radial average spectrum and corrected with the derived value of extinction (using only the Hα/Hβ ratio).

Figure 6.32 shows similar diagnostic diagrams as presented in Figure 6.25 for the *fibre-by-fibre* analysis, but without the background *diffuse* sample for the sake of clarity. The colour-coding of the data points is equivalent to the previous case, i.e. lighter tones corresponding to the inner regions of the galaxy, and darker colours to the outer parts. Obviously, the number of data points has been reduced drastically compared with the previous case. However, there are some important differences between the two sets, for example, in panels a), b), c) and d) where the Y-axis corresponds to [O III] λ5007/Hβ, Figure 6.32 shows practically no points for values log([O II]/Hβ) below –1. In the *fibre-by-fibre* case, these data points are present and correspond to the inner regions of the galaxy. Similarly, panels e) and f) corresponding to R_{23} in the X-axes shows practically no spectra for $\log R_{23} < -0.3$. From these results we may infer that the selection criteria has discarded the most inner regions of the galaxy consistent with low values of oxygen as shown in the previous analysis.

The [O III]/Hβ vs. [O II]/Hβ diagram of panel a) shows basically the same trend as its counterpart of Figure 6.25, this is specially noticeable in the radial average trend which shows the same behaviour of a constant [O III]/Hβ for a range of [O II]/Hβ ratios with an increase at log [O II]/Hβ $\sim$ –0.2. The [O III]/Hβ vs. [N II]/Hα diagram shows a lower level of scatter but still the same narrow range of [N II]/Hα values as in the *fibre-by-fibre* case. The radial spectra follows quite well the trend of the sample, with one notorious outlier at log [N II]/Hα $\sim$ –1.0 The situation is slightly different for panel c), showing the [O III]/Hβ vs. [S II]/Hα diagram. Despite the reduced number of spectra in the new sample, the scatter seems to be equal or larger than its counterpart shown in Figure 6.25. Data points emerged near the theoretical boundary, the reason for this being the lower flux threshold applied to the data. The radial spectra shows a similar behaviour to the *fibre-by-fibre* case, and a clear vertical trend of narrow values of [S II]/Hα. In the case of panel d), showing the [O III]/Hβ vs. [O I]/Hα, the scatter is comparable to that of the same figure in the *fibre-by-fibre* sample, the lower flux threshold results in more spectra falling outside the theoretical boundary for starburst ionization. Opposite to the previous case, the radial trend in this diagram does not show a trend, and instead it is scattered along a good range of [S II]/Hα values. The [O I] λ6300 presents intrinsic measurement problems as discussed previously, but it was expected that the more restricted selection criteria would diminish the scatter and show a better trend for this particular diagram.

Panel e) shows basically the same trend as the *fibre-by-fibre* sample, for both the full $O_3 - limited$ and radial average samples, but with a lower number of data points for low values of R_{23} as previously

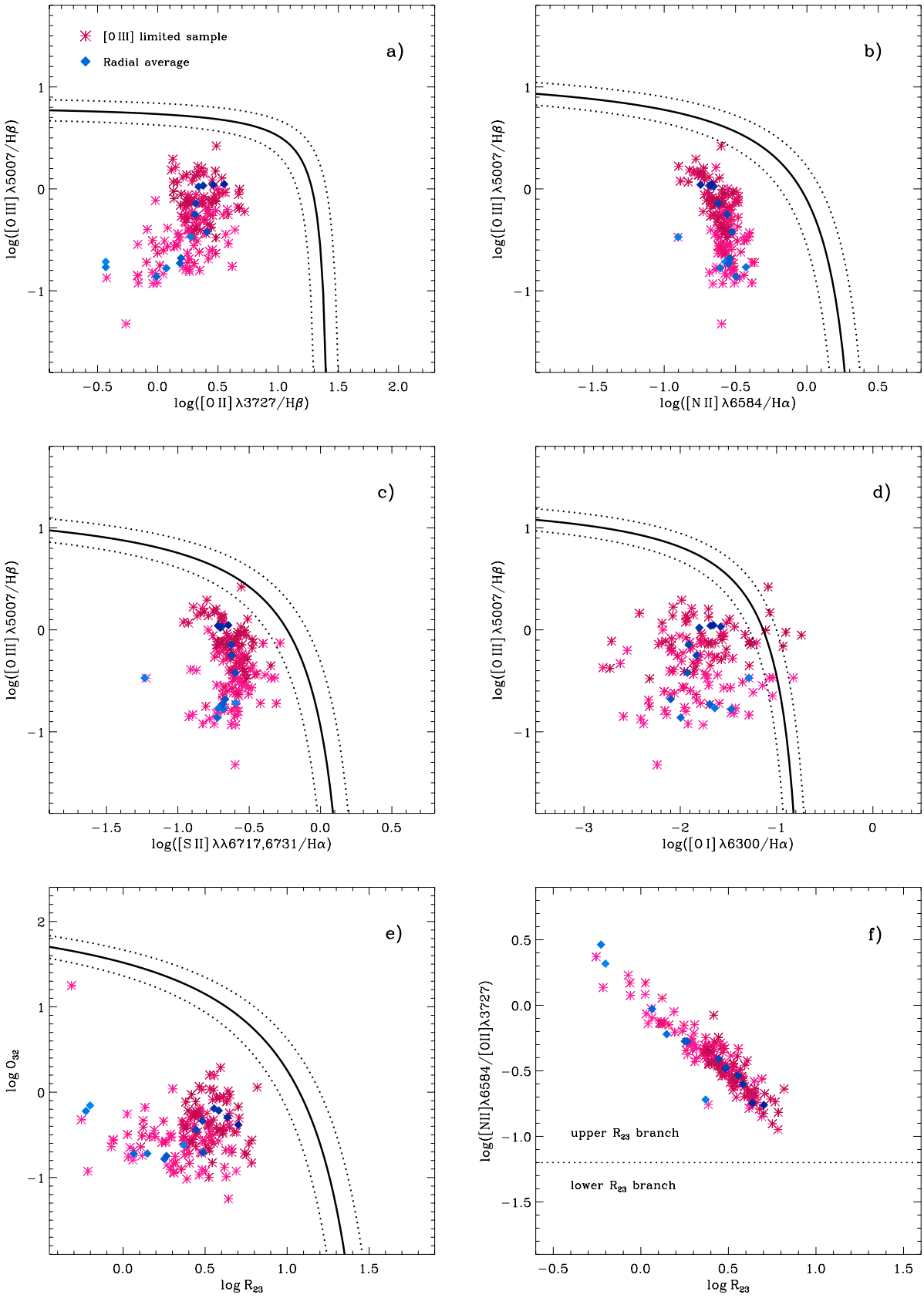

Figure 6.32: Diagnostic diagrams for NGC 628 based on the $O_3 - limited$ sample (magenta symbols). The filled diamonds correspond to the azimuthally-averaged radial values. Lighter tones correspond to inner regions of the galaxy, darker colours to increasing galactocentric distance.

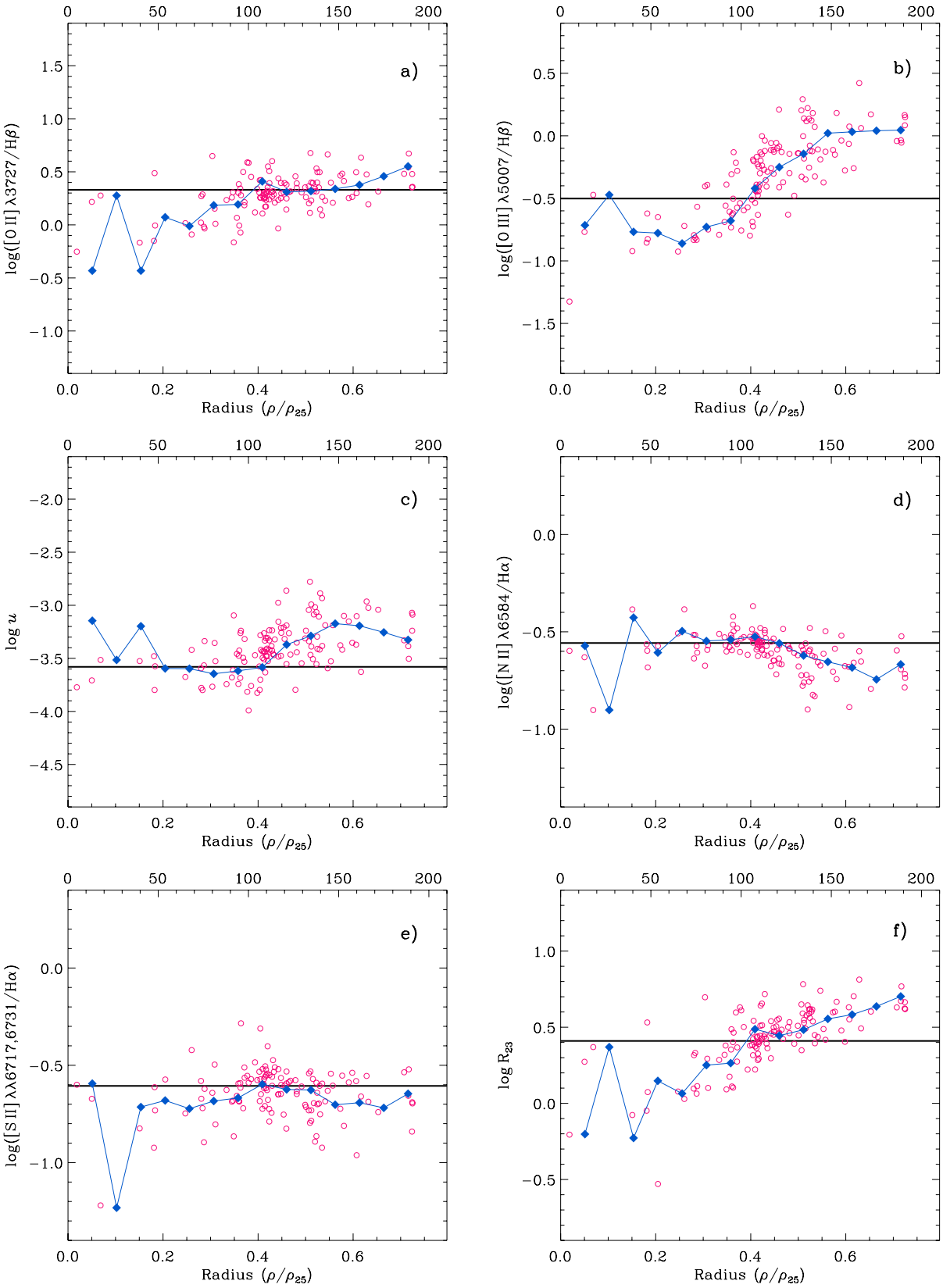

Figure 6.33: Radial variation of different line ratios and physical properties of NGC 628 for the $O_3 - limited$ sample (magenta circles) and the azimuthally-averaged spectra (blue diamonds). The deprojected radial position for the blue symbols has been normalised to the size of the optical disk at the 25 mag arcsec^{-2} isophote. The radial position of the red diamonds correspond to the projected outer radius of the corresponding annulus. The top values on the X-axes show the linear-projected galactocentric radius in arcsec. The horizontal lines in each diagram correspond to the values derived from the integrated spectrum of NGC 628.

mentioned, and a lower level of scatter. Panel f), showing the diagram of [N II]/[O II] vs. R_{23} of the $O_3 - limited$ sample presents a narrower correlation between these two line ratios, with a radial trend of increasing R_{23} with galactocentric distance. The radial spectra sits on the top of this tight correlation, with an evident outlier which, according to the colour tone, does not correspond to the same physical regions as the spectra of similar [N II]/[O II] ratios.

In conclusion, all diagrams are consistent with the physical trends previously seen in the analysis of the *fibre-by-fibre* sample, in terms of the lower oxygen values towards the inner regions of the galaxy, the narrow variation of the [N II]/Hα and [S II]/Hα along the galactocentric radius, and the [N II]/[O II] ratio being consistent with R_{23} values corresponding to the upper branch of the R_{23} relation.

Figure 6.33 shows the radial variations of a selection of line ratios and physical properties for the $O_3 - limited$ sample in a similar way as Figure 6.26 corresponding to the *fibre-by-fibre* analysis. As previously suggested by the diagnostic diagrams presented above, there is a lack of data points for the inner regions of the galaxy corresponding to normalised radius $\rho/\rho_{25} \lesssim 0.3$. The radial spectra in those regions were generated by very few spectra, or even only one spectrum. All radial trends show a similar behaviour to those presented in the *fibre-by-fibre* analysis for $\rho/\rho_{25} \gtrsim 0.4$. For those galactocentric radii, the radial average spectra of the $O_3 - limited$ sample show much smoother trends than in the *fibre-by-fibre* case. Similar conclusions to those presented previously can be drawn from the $O_3 - limited$ sample only for regions with $\rho/\rho_{25} \gtrsim 0.4$. In panel a), corresponding to the radial variation of [O II] λ3727/Hβ, an increase in the ratio can be inferred from the data, but there is no information in the inner regions to confirm a firm trend. A similar situation is seen in panels b), c), and d), corresponding to [O III] λ5007/Hβ, $\log u$ and [N II] λ6584/Hα, where the radial average spectra shows particularly a very defined trend for the outer regions. The case is slightly different for panel e), corresponding to [S II] $\lambda\lambda$6717,31/Hα, where the magenta data points do not show a trend as in the corresponding diagram of Figure 6.26. The same situation is reproduced for panel f), where the lack of data points in the inner regions banishes the nice trend shown by the radial average spectra for the outer regions. Interestingly, the line ratio values from the integrated spectrum coincide with all the trends at the same position as in the *fibre-by-fibre* case, i.e. for $\rho \sim 0.4\rho_{25}$.

The abundance gradients derived from the $O_3 - limited$ sample are shown in Figure 6.34 for the subset of abundance calibrators described in the previous section. The meaning of the different symbols and lines are similar to Figure 6.27 corresponding to abundance gradients of the *fibre-by-fibre* case. Despite the lower number of data points and the absence of spectra covering regions with galactocentric radius $\rho \lesssim 0.3\rho_{25}$, the abundance gradients $O_3 - limited$ sample look very similar to the ones derived for the *fibre-by-fibre* analysis. The scale offsets between the different calibrators are similar to the ones derived previously, which is not surprising, as the only real difference between the two analysis is the number of data points included in the final sample. The line ratios (and therefore, the derived abundances) are equal for the coincident spectra. Table 6.4 shows the derived gradients, the central oxygen and *characteristic* abundances for the analysis of the O_3 *limited* sample. Despite the lack of data points in the inner regions of the galaxy which might influence the derived slopes, the differences between the values presented in Table 6.4 and the corresponding figures from the *fibre-by-fibre* analysis shown in Table 6.3, are less than 0.1 dex for the M91, KK04 and ff–T_e relation methods, i.e. an extremely good agreement. Leaving aside the extreme case of the values derived through the PT05 method, the largest differences found between the two methods correspond to the $N2$ and $O3N2$ calibrators in terms of the derived slopes. In the case of $N2$, a shallow gradient can be inferred visually from the corresponding diagram, which was not the case for the same calibrator in the *fibre-by-fibre* analysis. In the case of $O3N2$, the main difference is found between the radial average spectra, for which

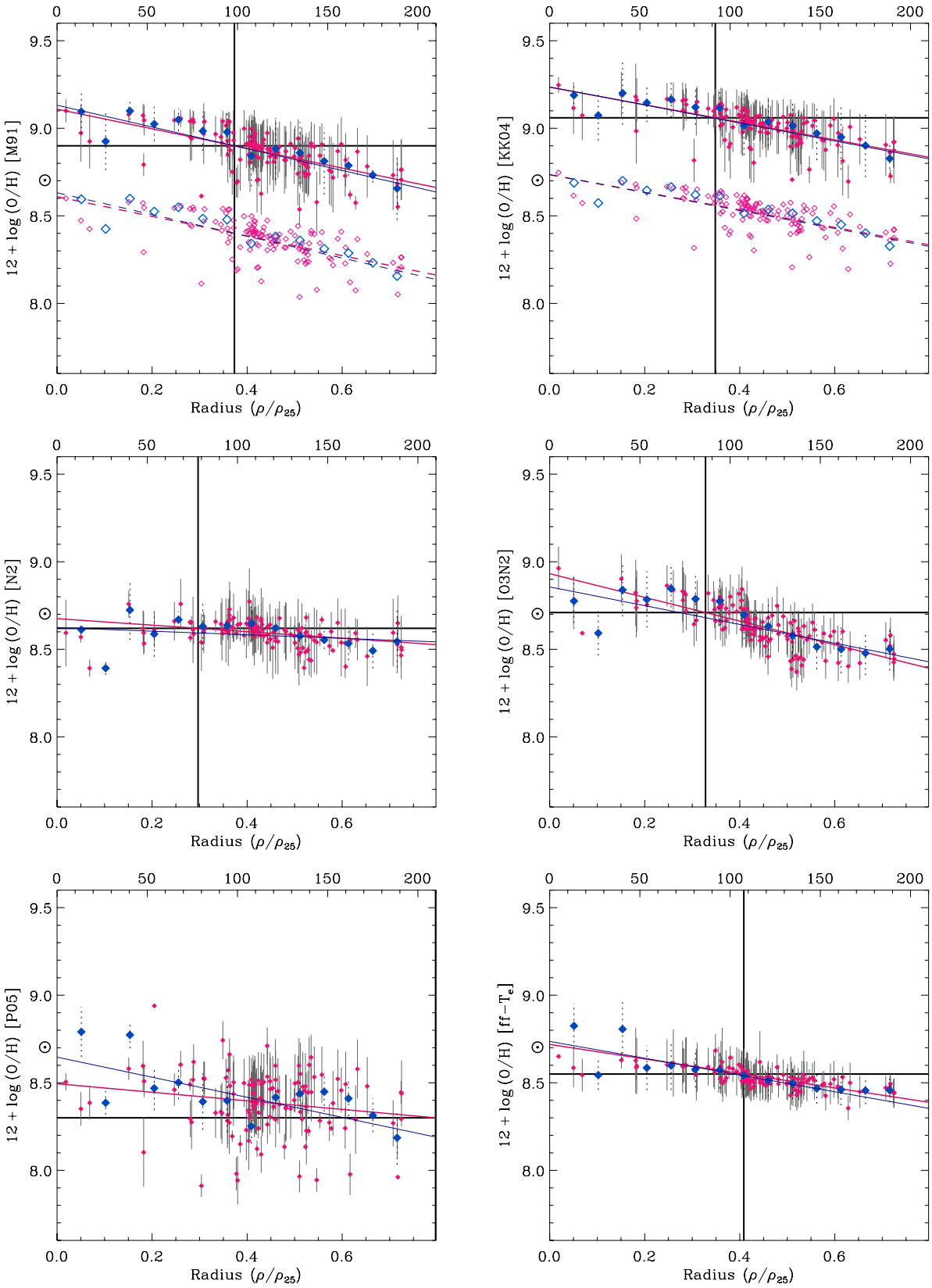

Figure 6.34: Radial abundance gradients derived for NGC 628 based on the $O_3 - limited$ analysis for different abundance diagnostics. In each plot, the magenta symbols correspond to the spectra of the final sample, the blue diamonds correspond to the azimuthally-averaged radial spectra. For the R_{23} calibrators, the open symbols correspond to an arbitrary offset of –0.5 dex. The top X-axis values correspond to the projected radii in arcsec for the radial average data. The assumed solar abundance is shown in the Y-axis. See the text for a full explanation.

RADIAL ABUNDANCE GRADIENTS FOR NGC 628: $O_3 - limited$ SAMPLE ANALYSIS

	M91		KK04		N2	
	O_3 sample	*Radial*	*O_3 sample*	*Radial*	*O_3 sample*	*Radial*
$12+\log(O/H)_{\rho=0}$	9.11 ± 0.03	9.13 ± 0.03	9.23 ± 0.02	9.24 ± 0.03	8.68 ± 0.02	8.62 ± 0.05
$12+\log(O/H)_{\rho=0.4\rho_{25}}$	8.88 ± 0.03	8.88 ± 0.03	9.03 ± 0.02	9.03 ± 0.03	8.60 ± 0.02	8.58 ± 0.05
$\log(O/H)_{(\mathrm{dex}\ \rho_{25}^{-1})}$	-0.56 ± 0.06	-0.62 ± 0.08	-0.50 ± 0.05	-0.51 ± 0.07	-0.19 ± 0.04	-0.10 ± 0.12
$\log(O/H)_{(\mathrm{dex\ kpc}^{-1})}$	-0.040 ± 0.005	-0.044 ± 0.006	-0.036 ± 0.004	-0.036 ± 0.005	-0.013 ± 0.003	-0.007 ± 0.008

	O3N2		PT05		ff–T_e	
	O_3 sample	*Radial*	*O_3 sample*	*Radial*	*O_3 sample*	*Radial*
$12+\log(O/H)_{\rho=0}$	8.93 ± 0.03	8.86 ± 0.05	8.49 ± 0.05	8.65 ± 0.07	8.72 ± 0.03	8.74 ± 0.04
$12+\log(O/H)_{\rho=0.4\rho_{25}}$	8.66 ± 0.03	8.64 ± 0.05	8.40 ± 0.05	8.42 ± 0.07	8.55 ± 0.03	8.54 ± 0.04
$\log(O/H)_{(\mathrm{dex}\ \rho_{25}^{-1})}$	-0.68 ± 0.06	-0.54 ± 0.12	-0.24 ± 0.12	-0.57 ± 0.18	-0.41 ± 0.07	-0.48 ± 0.10
$\log(O/H)_{(\mathrm{dex\ kpc}^{-1})}$	-0.048 ± 0.004	-0.038 ± 0.009	-0.017 ± 0.008	-0.041 ± 0.012	-0.029 ± 0.005	-0.034 ± 0.007

Table 6.4: Results from the oxygen abundance gradient analysis of NGC 628 based on the $O_3 - limited$ sample. The columns correspond to the different calibrators employed, showing the results from the selected fibres and the radial average spectra. The rows correspond to: the central abundance at galactocentric radius $\rho = 0$; the *characteristic* abundance at $\rho = 0.4\rho_{25}$; and the slope of the abundance gradients in dex ρ_{25}^{-1} and dex kpc^{-1}, respectively.

the gradient reported in Table 6.4 is –0.54 dex ρ_{25}^{-1}, while in the previous section the corresponding gradient was steeper (–0.66 dex ρ_{25}^{-1}). The oxygen central values agree within 0.1 dex for all cases (even for the PT05 calibrator). The abundances derived from the integrated spectrum match the gradient slopes at radius comparable to the case of the *fibre-by-fibre* analysis, consistent with $\rho \sim 0.4\rho_{25}$ for the M91, KK04 and ff–T_e methods. In the case of the *N*2 and *O*3*N*2 these radii are shifted towards lower values compared to the previous analysis. For the PT05 calibrator, the integrated value matches the main gradient for a radius larger than the values covered by the IFS data.

From the analysis of the diagnostic diagrams and the radial trends of the $O_3 - limited$ sample discussed above, we might conclude than the more restricted data selection provided spectra of better quality in terms of the spectral features than one might expect for well-defined regions. However, it was found that regions with low emission in oxygen were discarded from the final data sample. Given that the selection criteria considered a lower flux threshold than in the previous case, the flux limit cannot account for this effect. Therefore, the reason for the lack of these regions should be due to the selection criterion based on the [O III] ratio. In this particular case, regions with low emission in oxygen correspond to the inner parts of the galaxy, where the stellar population is more dominant in the observed spectra, and therefore, the errors in the measurement of the residual emission lines due to a deficient continuum subtraction during the SSP model fitting are larger (e.g. see Figure 6.35). For the outer regions of the galaxy, the contribution of the stellar population is lower, and therefore, it is easier to recover the proper [O III] ratio from the derived residual spectrum. However, in a region where the stellar population is more dominant and the emission lines are weak, the derived [O III] ratio from the residual spectrum might not be close to the theoretical ratio, but nevertheless, the total flux of these lines and their line ratios are representative of the physical conditions of the gas in that particular region. The fact that the inclusion of spectra with "non-physical" [O III] line ratios in the *fibre-by-fibre* sample produced well-defined trends (although with some level of scatter) in those weak oxygen (inner) regions may support this idea.

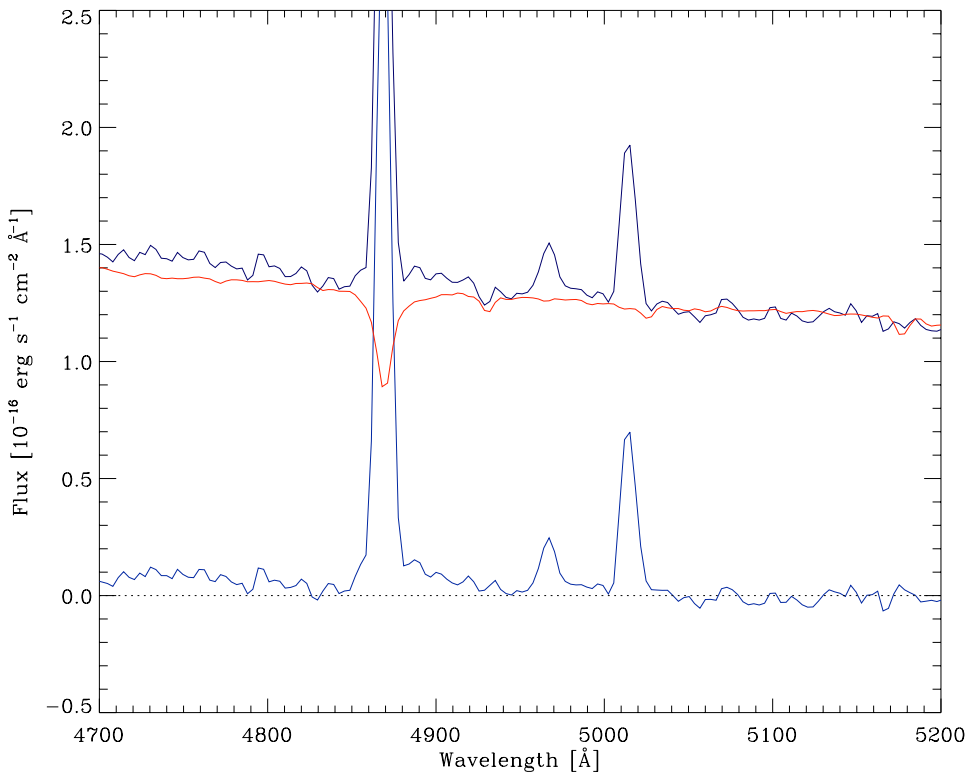

Figure 6.35: Example of a region with low emission in [O III] and a deficient SSP continuum subtraction (red line). Note that the SSP fit does not trace accurately the observed continuum (dark blue), leading to deviations from the theoretical [O III] λ5007/λ4959 ratio on the residual spectrum (light blue).

Furthermore, all the trends previously described in the *fibre-by-fibre* case were confirmed by the analysis of the $O_3 - limited$ sample, with the drawback that the trends were limited to those regions with enough data points, i.e. for $\rho/\rho_{25} \gtrsim 0.4$. It could be argued that an advantage of the use of the $O_3 - limited$ sample resides on narrower and clearer trends derived for the different line ratios, diagnostic diagrams and physical properties of the galaxy. Although this is true in some cases, it was found that by lowering the flux threshold, many regions were included with line indices not consistent with well-behaved H II regions, as it can be seen in panels c) and d) of Figure 6.32, producing different trends. Given the low number of spectra selected by this method, many spatial regions on the galaxy included few spectra from which the azimuthally-averaged radial spectra could be derived. In some cases, for a given annulus, only one spectrum would fall in that region. Therefore, the radial average spectra did not prove to be a better indicator compared with the *fibre-by-fibre* case, in terms of describing the radial trends of the line ratios and physical properties of the galaxy.

Despite the absence of selected spectra in the inner regions of the galaxy, the abundance gradients, central oxygen values and *characteristic* abundances derived from the $O_3 - limited$ sample show a extremely good level of agreement compared with the *fibre-by-fibre* case. The fact that we obtained almost identical values of these properties using the "physically-selected" sample, and that the abundances derived (especially from the few fibres in the inner regions) show the same correlation than in the previous case, might imply that the oxygen abundances calculated using the *fibre-by-fibre* sample are valid, and may support the idea that the derived oxygen line intensities of fibres with "non-physical" [O III] ratios are still representative of the physical conditions of those regions, and that the deviation of the [O III] line ratio from the theoretical one, might be due to the subtraction of the stellar continuum model. From the comparison of Table 6.3 and

Table 6.4 showing the abundance gradients parameters of both analysis, calibrators employing all the three strong oxygen lines, i.e. based on R_{23} (M91, KK04) or a modified version of this indicator, like the ff–T_e method, seem to be better behaved, showing practically the same values for all the properties. On the other hand, the PT05 indicator shows the same level of scatter for both analysis, reflecting that in the first case, the dispersion was not due to the inclusion of "non-physical" regions. Therefore, it is possible that that the PT05 calibrator does not represent an appropriate method for abundance determination in a *point-by-point* basis.

6.3.3 Method III: H II REGION CATALOGUE

Traditionally, spectroscopic studies of nearby galaxies have been performed by targeting a number of (bright) H II regions over the surface of the galaxy, placing long-slits and/or fibres of different apertures on top the selected regions, and integrating the flux over that aperture. The classical chemical abundance diagnostics based on the observation of strong emission lines ratios (e.g. R_{23}), were conceived as empirical methods describing the physical properties of these large, spatially-integrated, and individually defined H II regions. The calibration of these metallicity indicators were performed by using grids of photoionization models for a given range of metallicities and ionization parameters (e.g. M91, KK04), and therefore, are not based on observational data alone. Given the large parameter space under investigation, these calibrations have generally assumed assumed spherical or plane-parallel geometries without considering the effects of the distribution of gas, dust and multiple, non-centrally located ionizing sources. These geometrical effects may affect the temperature and ionization structure of the regions.

It has been argued that the geometrical distribution of ionization sources may partly account for the large scatter in metallicities derived using model-calibrated empirical methods (Ercolano et al., 2007, hereafter EBS07). According to recent results based on 3D photoionization models with various spatial distributions of the ionizing sources, for intermediate to high metallicities, models with fully distributed configurations of stars display lower ionization parameters than their fully concentrated counterparts. The implications of this effect varies depending on the sensitivity of the metallicity indicator to the ionization parameter (EBS07).

Generally speaking, results derived from the use of the empirical metallicity indicators should be considered within a statistical framework, as the error due to intrinsic temperature fluctuations and chemical inhomogeneities on a single region may be very large, even when the temperature of the region can be directly determined (e.g. Peimbert, 1967; García-Rojas et al., 2006; Ercolano et al., 2007). The analyses performed using the previous two methods were based on assuming that the spectra of individual fibres would contain enough information (after applying the selection criteria) in order to derive the physical properties of the region sampled by the individual fibre aperture. However, as shown by Figure 6.24, which displays the spatial distribution of spaxels in the *fibre-by-fibre* analysis, the selected fibres trace morphologically complex regions, which do not resemble the classical picture of well-defined spherical H II regions. Some of the most prominent emitting regions are embedded in giant H II complexes without an established geometrical centre, and most importantly, as shown in section 6.1, regions which would be considered as individual H II regions in classical terms, show variations on their emission line intensities from fibre-to-fibre. Therefore, are we observing real point-to-point variations of the physical properties within a region? i.e. the different measured line ratios are reflecting a real distribution of the ionizing sources, gas content, dust extinction and ionization structure within these regions?, or the line intensity variations are just spurious effects due to the relatively low signal-to-noise of those emitting regions?.

The results presented in the previous sections considered somewhat smaller apertures than the typically employed in order to derive the physical properties of the classical H II regions. An important question that we might raise at this point is: how valid are the results derived from the use of strong line calibrators applied on a point-to-point (fibre-to-fibre) basis, compared to the co-added spectrum of a larger, classically well-defined H II region?. In order to answer this and other questions, and at the same time perform a robust 2D spectroscopic analysis of the galaxy sample, a third analysis method was envisaged, based on considering "classical" H II regions as the source of analysable spectra.

For each galaxy of the sample, a number of H II regions was identified and classified by hand, based on the Hα emission line maps of each galaxy and on the *diffuse* plus *fibre-by-fibre* spatial distribution of fibres, as shown in Figure 6.24 for the case of NGC 628. The selection of the fibres considered to belong to an individual H II region was performed following a purely geometrical principle, i.e. fibres located within the same region, which seemed to be geometrically connected, were considered as a single H II region. This criterion might be relatively subjective, but "classical" H II regions in other spectroscopic studies were chosen following the same principle, e.g. by selecting the more prominent regions in Hα narrow band images.

The actual mechanism in order to generate the H II region catalogue for each galaxy was the following:

1. A group of fibres is identified by eye as an individual H II region from the *sub-mosaic* extracted from the *clean*–residual mosaic, corresponding to the *diffuse* plus the *fibre-by-fibre* samples. The positions and IDs of the selected fibres are stored and associated to the corresponding H II region. The fibre selection mechanism was based on two different methods: 1) by choosing the fibres individually by hand, following the morphological structure of the selected H II region; and 2) by considering all the fibres within a pre-established circular aperture centered at an arbitrary position, which might not coincide with the centre of any specific fibre. In the first case, the associated "location" of the H II region corresponds to centre of the first selected fibre, which was chosen to coincide nearly with the geometrical centre of the group of fibres considered as a H II region. In the second case, the location of the H II region corresponds to centre of the circular aperture, which was also chosen to coincide with the geometrical centre of the H II region. In the case of the circular aperture, different diameters were tested until the encompassed fibres would correspond to the visually selected region.

2. Once the positions and IDs of the fibres corresponding to a given H II region are identified in the *sub-mosaic* described above, the fibres corresponding to the same positions and IDs are recovered from the *clean*–observed mosaic, i.e. the RSS file before performing the SSP model subtraction. The spectra belonging to those fibres are co-added, obtaining a single spectrum corresponding to the selected H II region.

3. The integrated H II region spectrum is fitted by a linear combination of SSP templates by exactly the same procedure as described before, in order to decouple the contribution of the stellar population. Once the model of the underlying stellar population was derived, this is subtracted from the original spectrum, obtaining a *residual* H II region spectrum.

4. Individual emission line fluxes are measured from the residual spectrum by fitting single Gaussian functions as explained previously, obtaining a set of emission line intensities for each H II region.

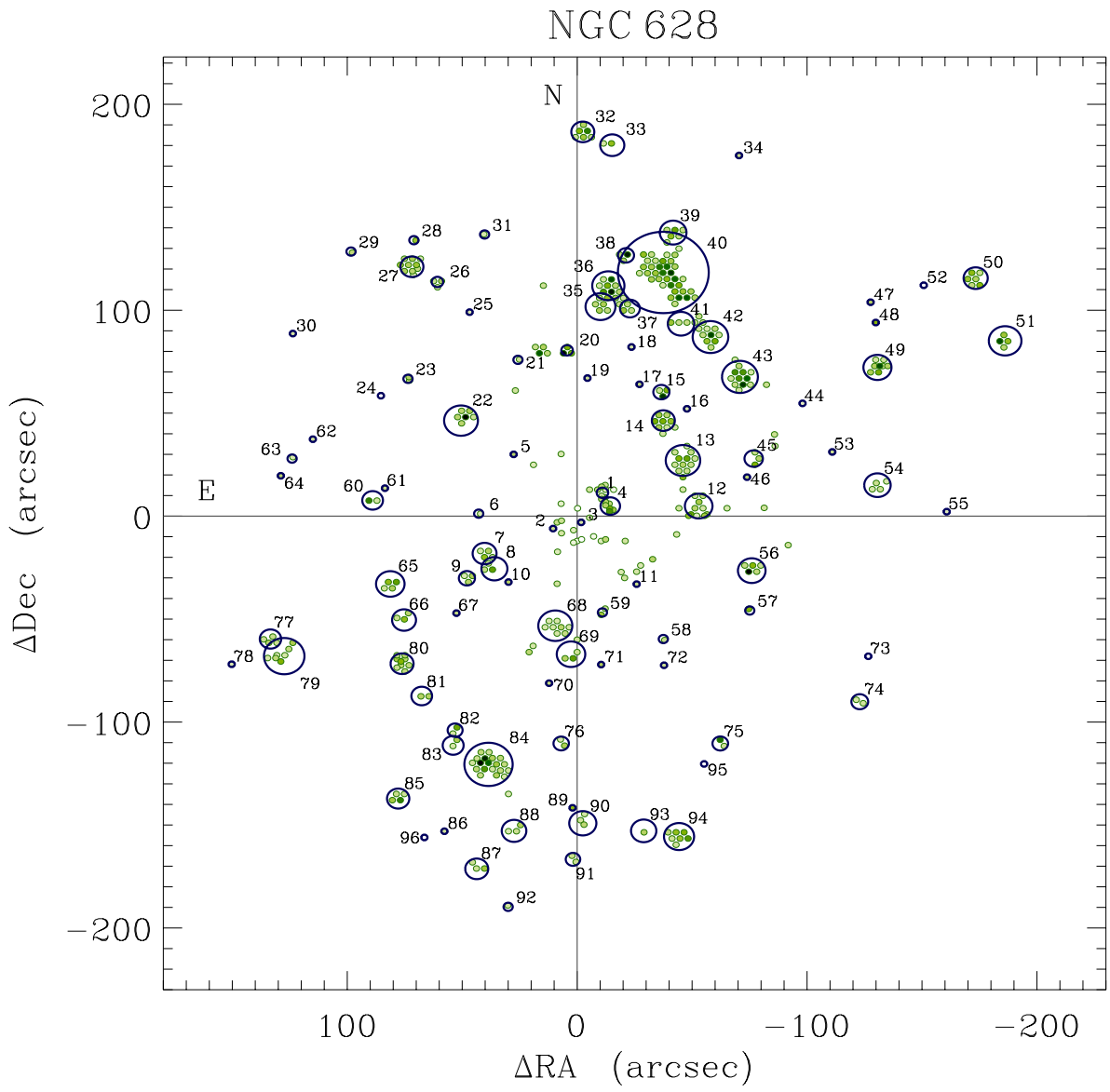

Figure 6.36: Spatial location and identification of the selected H II regions for NGC 628. The background fibres correspond to the *fibre-by-fibre* sample, with colour intensities scaled to the flux of the Hα emission line. The circles correspond to the real or equivalent aperture diameter, as explained in the text.

5. The process is repeated for each group of fibres identified as a single H II region, until the whole surface of the galaxy mosaic is covered.

A total of 108 H II regions were selected following the procedure described above. Similar quality selection criteria as in the case of the *fibre-by-fibre* analysis were applied to the residual spectra of the catalogue. Eleven spectra did not satisfy the first criteria (Hβ and [O III] λ4959 greater than zero), and therefore the number of H II regions was reduced to 97. Only one of these regions presented a non-finite value for the derived c(Hβ) and was therefore discarded. All the 96 remaining spectra fulfill the third selection criteria, i.e. a flux threshold in the observed line intensity of Hβ equals to 5×10^{-16} erg s^{-1} cm^{-2}, and the detectability of the [O II] λ3727 line

Figure 6.36 shows the final sample of 96 selected H II regions for NGC 628. The fibres displayed in this figure correspond to the *fibre-by-fibre* sample shown in Figure 6.24. The *diffuse* sample was not included

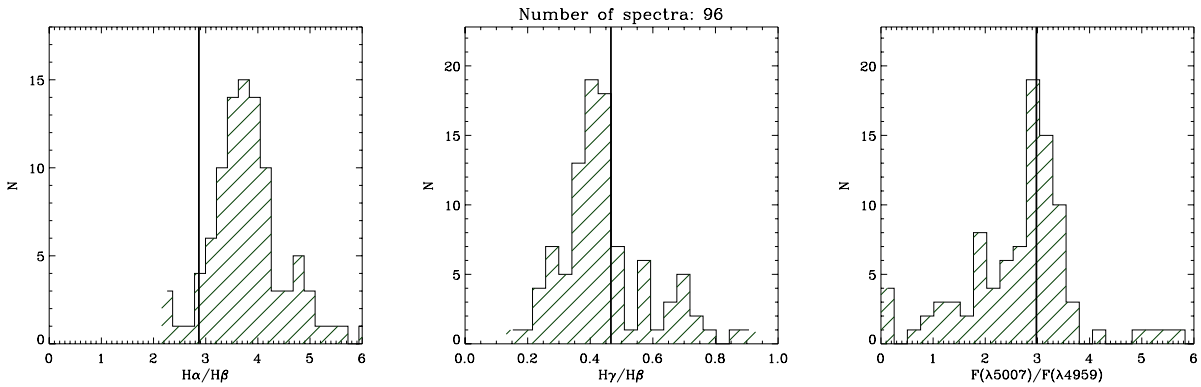

Figure 6.37: Selection criteria histograms for the final H II region catalogue of NGC 628. In each panel, the vertical lines correspond to the theoretical values of the given line ratio.

for the sake of clarity. The circles define the selected H II regions for this galaxy. The numbers next to the circles correspond to the internal identification of the H II region in this dissertation. The diameter of the circles correspond to: 1) an "equivalent aperture" in the case where the H II region was selected by choosing individual fibres by hand, e.g. region N628–40, at $(\Delta\alpha, \Delta\delta) \sim$ (–40,130); 2) to the real diameter of the circular aperture when the selected H II region was chosen on this basis. Note that some fibres in Figure 6.36 are not associated with any H II region (especially in the central region of the galaxy), the reason for this is that, by individual inspection of those fibres, they were not considered with enough signal-to-noise, and/or not to be representative of a well defined H II region. Note also that many H II regions are consistent with a single fibre. In those cases, the regions surrounding the fibres did not show spectra with significant signal; therefore, they were not considered as their inclusion would only add noise to the integrated spectrum. In Appendix D, I include the internal identification, coordinates, offsets, extraction method, equivalent/real aperture diameter (in arcsec and pc), and the number of extraction fibres for each selected H II region of NGC 628.

Figure 6.37 shows the quality-check histograms of the Hα/Hβ, Hγ/Hβ, and [O III] λ5007/λ4959 line ratios for the final H II region sample. As in the previous cases, the vertical lines show the theoretical values for these ratios. The Hα/Hβ histogram shows a similar behaviour to the $O_3 - limited$ case, i.e. a distribution of values consistent with a physical reddening, with Hα/Hβ ratios greater than the theoretical value. A very small tail of values lower than the theoretical ratio is found in this distribution. The peak of Hα/Hβ occurs for values $\sim$3.8. Similarly, the Hγ/Hβ ratio histogram shows the expected distribution for a well behaved sample of reddened spectra, with most ratios being lower or similar to the theoretical value. The tail of higher theoretical recombination values is much smaller than in the previous cases as shown in their corresponding figures. The [O III] λ5007/λ4959 ratio histogram shows a distribution highly centered at the theoretical value, with a long tail of smaller derived ratios. As explained previously, the reason of this "non-physical" [O III] values may reside in the errors introduce by the SSP fitting and posterior subtraction, specially for regions with weak emission in the [O III] lines. In general, the quality-check histograms for the H II region sample imply a well-behaved "physical" set of spectra, consistent in average with a low level of extinction.

In Figure 6.38 I present a comparison of the *diffuse* sample (grey symbols) and the values obtained from the H II region catalogue for the Hα/Hβ, Hγ/Hβ, and [O III] λ5007/λ4959 ratios as a function of the observed flux (green diamonds). As in similar figures presented before, the horizontal lines correspond to

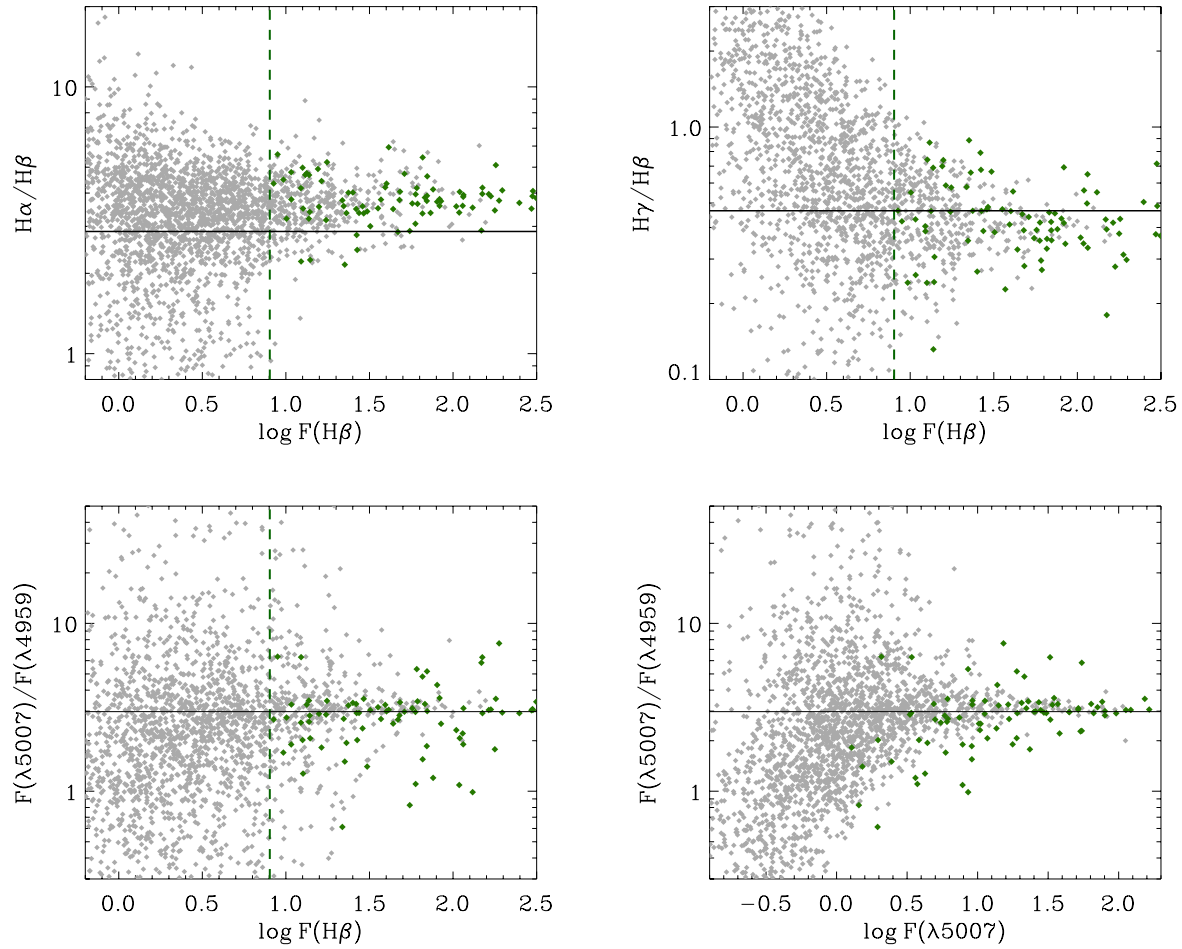

Figure 6.38: Hα/Hβ, Hγ/Hβ and [O III] λ5007/λ4959 ratios as a function of observed flux in Hβ and F(λ5007) for the analysis of the H II regions sample for NGC 628. Grey symbols correspond to the *diffuse* sample of the first analysis method, and are included for comparison purposes. Green symbols to the position of the H II regions described in this section. The horizontal lines correspond to the theoretical values for each ratio. The vertical dashed lines stand for the chosen flux threshold in Hβ.

the theoretical values of these ratios. The top panels show the distribution of the Balmer ratios as a function of Hβ, the Hα/Hβ ratio shows that the position of most of the H II regions in this diagram correspond to the region consistent with a "physical" reddening, i.e. values above the theoretical line with few spectra below. The Hγ/Hβ diagram shows an opposite trend, as expected, with the majority of the spectra corresponding to reddened values below the theoretical line. The [O III] ratio diagrams show what it can be inferred from the histograms shown in Figure 6.37, i.e. that the majority of the spectra are located near the theoretical value (especially for the brightest H II regions), with some level of scatter concentrated mainly for lower ratios. The inclusion of the *diffuse* sample was made for purely comparison purposes. It can be seen that the H II regions are located in regions of these plots which are coincident with the positions of the *fibre-by-fibre* sample, although the observed fluxes are in general higher, considering that the spectra of the H II regions were integrated from a certain number of fibres.

After the quality of the derived spectra was confirmed, we proceeded to correct the measured emission line intensities by extinction in order to derive the physical properties from this new sample. Given that, in general, the signal-to-noise of the H II regions was higher than in the individual spectra obtained from the *fibre-by-fibre* or the $O_3 - limited$ samples, we explore the possibility to obtain the logarithmic extinction

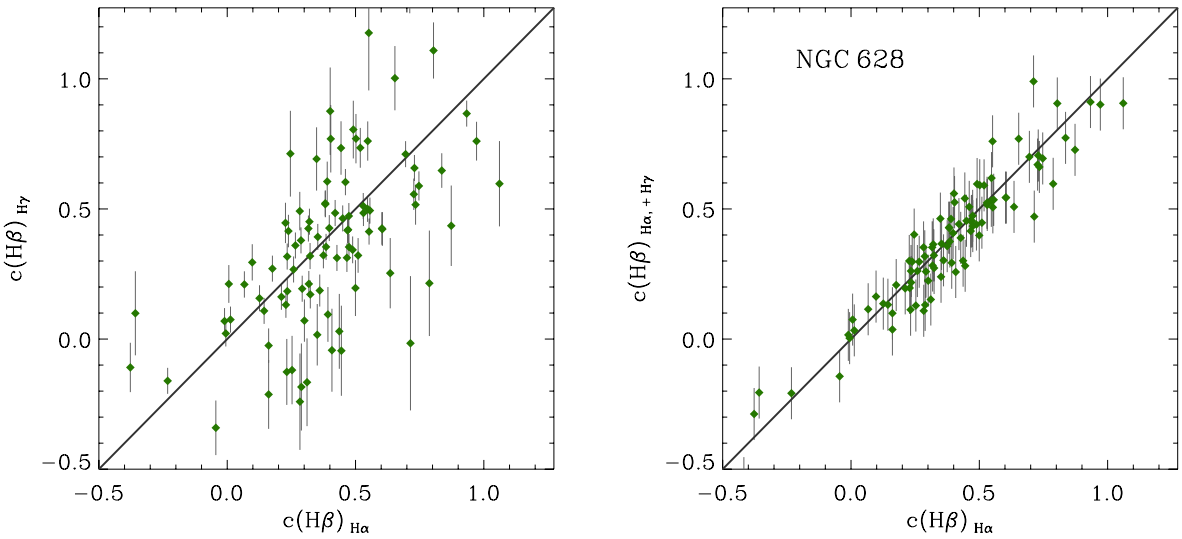

Figure 6.39: Comparison between different methods to obtain the logarithmic extinction coefficient value, c(Hβ). Left-panel: c(Hβ) values obtained independently by using the Hα/Hβ and Hγ/Hβ line ratios. Right-panel: c(Hβ) values calculated by using jointly the Hα/Hβ and Hγ/Hβ line ratios, as a function of the values derived solely by the Hα/Hβ ratio, as explained in Appendix B.

coefficient c(Hβ), using both the Hα/Hβ and Hγ/Hβ line ratios. In the left-panel of Figure 6.39 we show the comparison between the c(Hβ) values obtained by using each Balmer ratio independently, i.e. the X-axis corresponds to the c(Hβ) derived by using only the Hα/Hβ ratio as in the previous analysis, these values are labeled c(H$\beta)_{H\alpha}$. The Y-axis correspond to values derived solely by using the Hγ/Hβ ratio, labeled as c(H$\beta)_{H\gamma}$. The line represents equality of the two values.

The derived c(H$\beta)_{H\alpha}$ and the c(H$\beta)_{H\gamma}$ values agree (within the errors) for a reduced number of regions, however most of the values differ by a considerable amount. Typically, the determination of the c(Hβ) is performed by using a set of Balmer ratios, and not performed individually (expect in the case when only the Hα/Hβ ratio is reliable). The right-panel of Figure 6.39 shows the comparison between the c(Hβ) derived by using jointly the Hα/Hβ and Hγ/Hβ ratios, labeled as c(H$\beta)_{H\alpha+H\gamma}$, and the c(H$\beta)_{H\alpha}$ values. The details on the prescriptions in order to determine the different c(Hβ) values are presented in Appendix B, here it is only important to mention that during the determination of this value when using both line ratios, the Hα/Hβ ratio is given a higher weight in the calculation, and therefore the correlation shown in this panel is expected. However, as the inclusion of Hγ/Hβ ratios with good signal-to-noise would in theory provide better constrains on the value of the extinction coefficient, the c(H$\beta)_{H\alpha+H\gamma}$ values were adopted in order to correct the line intensities of the H II region catalogue for interstellar reddening. As in previous cases, the extinction law of Cardelli et al. (1989) with a total to selective extinction ratio $R_V = 3.1$ was adopted for the interstellar reddening correction. Formal errors were derived by propagating in quadrature the uncertainty in the flux calibration, the statistical error of the line emission fluxes and the error in the c(Hβ) term. Note that most of the adopted c(H$\beta)_{H\alpha+H\gamma}$ values correspond to positive (physical) corrections, with four outliers showing moderate negative values.

Figure 6.40 and Figure 6.41 show the diagnostic diagrams and radial trends derived from the H II region catalogue of NGC 628. Comparison of these plots with the corresponding diagrams presented previously show that, in general terms, all trends are exactly reproduced, with the difference being the lower level of

scatter in the case of the H II region catalogue diagrams. As in the previous similar plots, lighter colours in Figure 6.40 correspond to inner regions in the galaxy, darker tones to outer parts. Panel a) shows a clear trend of increasing oxygen intensity for both [O II] and [O III] species as a function of radius. Contrary to the case of the $O_3 - limited$ sample, H II regions with values log([O III] λ5007/Hβ) lower than –1 are present, both in the H II region sample (green symbols), and in the radial average spectra sample (reddish diamonds), obtained after co-adding successive annulus of 10 arcsec in an azimuthally radial way, as in the previous cases. The trends of panels b), c) and f) show much narrower correlations than in the case of the previous methods, extending to relatively low ratios of [O II] λ5007/Hβ and $\log R_{23}$, i.e. corresponding to the innermost regions of the galaxy. Panel d) of the same figure shows still a lot of scatter for both the H II regions and the radial average, reflecting the problems of the correct measurement of the [O I] λ6300 line due to sky residuals. The $\log O_{32}$ vs. $\log R_{23}$ relation shown in panel e) presents the same inferred trend as in the case of the *fibre-by-fibre* case, but regions with high $\log O_{32}$ (> 0) are absent in the H II region sample, while in the *fibre-by-fibre* and O_3 cases, the same zone in the diagram contained many regions, presumably corresponding to spectra of low signal-to-noise. The [N II]/[O II] ratio obtained from the H II regions sample confirms that all the spectra are consistent with R_{23} values corresponding to the upper branch of the O/H vs. R_{23} relation.

The radial trends shown in Figure 6.41 are consistent with the derived previously, especially for the case of the *fibre-by-fibre* analysis, where spectra of the inner regions of the galaxy ($\rho \lesssim 0.3\rho_{25}$) were included by the selection criteria. In the case of the H II region catalogue, the number of regions sampling this zone is low, but they are enough to indicate the trends of all the line ratios and to produce reliable radial-averaged spectra, contrary to the case of the $O_3 - limited$ sample where spectra in those regions were basically absent. Furthermore, the scatter in the inner regions has been reduced compared to the similar *fibre-by-fibre* plots. For radii $\rho > 0.4\rho_{25}$, the trends for all three different methods are practically identical, with a lower level of scatter for the H II regions sample. The position of the H II regions cover practically all radii from the inner regions of the galaxy (where the closest H II region to the centre is located at $\rho/\rho_{25} \sim 0.01$), to the outer parts (where the H II region with the largest radius is $\rho/\rho_{25} \sim 0.72$). However there is a gap between $\rho/\rho_{25} \sim 0.05$ and 0.15 where no H II regions are found.

The derived abundance gradients for the H II region catalogue of NGC 628 are shown in Figure 6.42, using the same calibrators are in the previous two methods. In each panel, the green symbols correspond to the oxygen abundance derived for each H II region, the red diamonds show the abundance obtained for the radial average spectra. The green and red straight lines stand for the least-squares linear fit to the corresponding the data. As in the previous cases, the M91 and KK04 diagrams show also an arbitrary offset of –0.5 dex from the derived abundance (open symbols). Direct comparison with the abundance gradients obtained from the *fibre-by-fibre* and $O_3 - limited$ samples show an extremely good agreement in terms of the derived slopes and central abundances for each calibrator. Table 6.5 shows the values derived from the abundance gradient fitting. The central oxygen values at $\rho = 0$ are in agreement within 0.1 dex with the values obtained previously. However, in general terms, the slopes derived from the H II regions sample are slightly steeper than the *fibre-by-fibre* and the $O_3 - limited$ case by ~ 0.05 dex ρ_{25}^{-1}, except in the case of the ff-T_e method, for which the H II region gradient is shallower than the obtained in the previous cases.

The scatter of the PT05 method is still present for the H II region sample, although to a less extend than in the previous cases. The abundance derived from the integrated spectrum matches the H II region abundance of each calibrator for a radius $\rho \sim 0.4\rho_{25}$ for all methods, except PT05 where the equality occurs at $\rho \sim 0.7\rho_{25}$. The $N2$ calibrator, did not show this behaviour previously, which follows the same

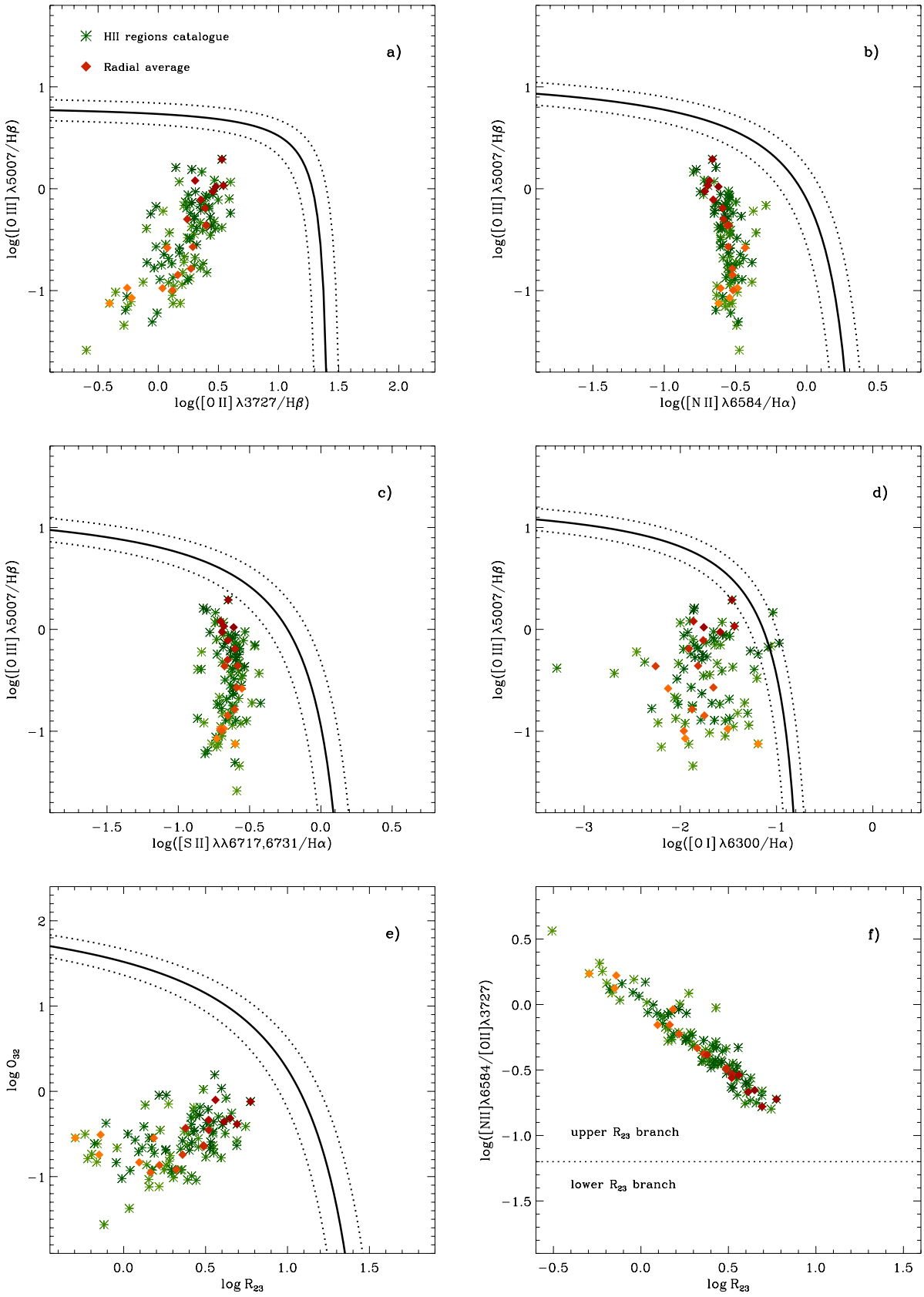

Figure 6.40: Diagnostic diagrams for NGC 628 corresponding to the selected H II regions catalogue (green symbols), the filled diamonds correspond to the azimuthally-averaged radial values. Lighter tones correspond to inner regions of the galaxy, darker colours to increasing galactocentric distance.

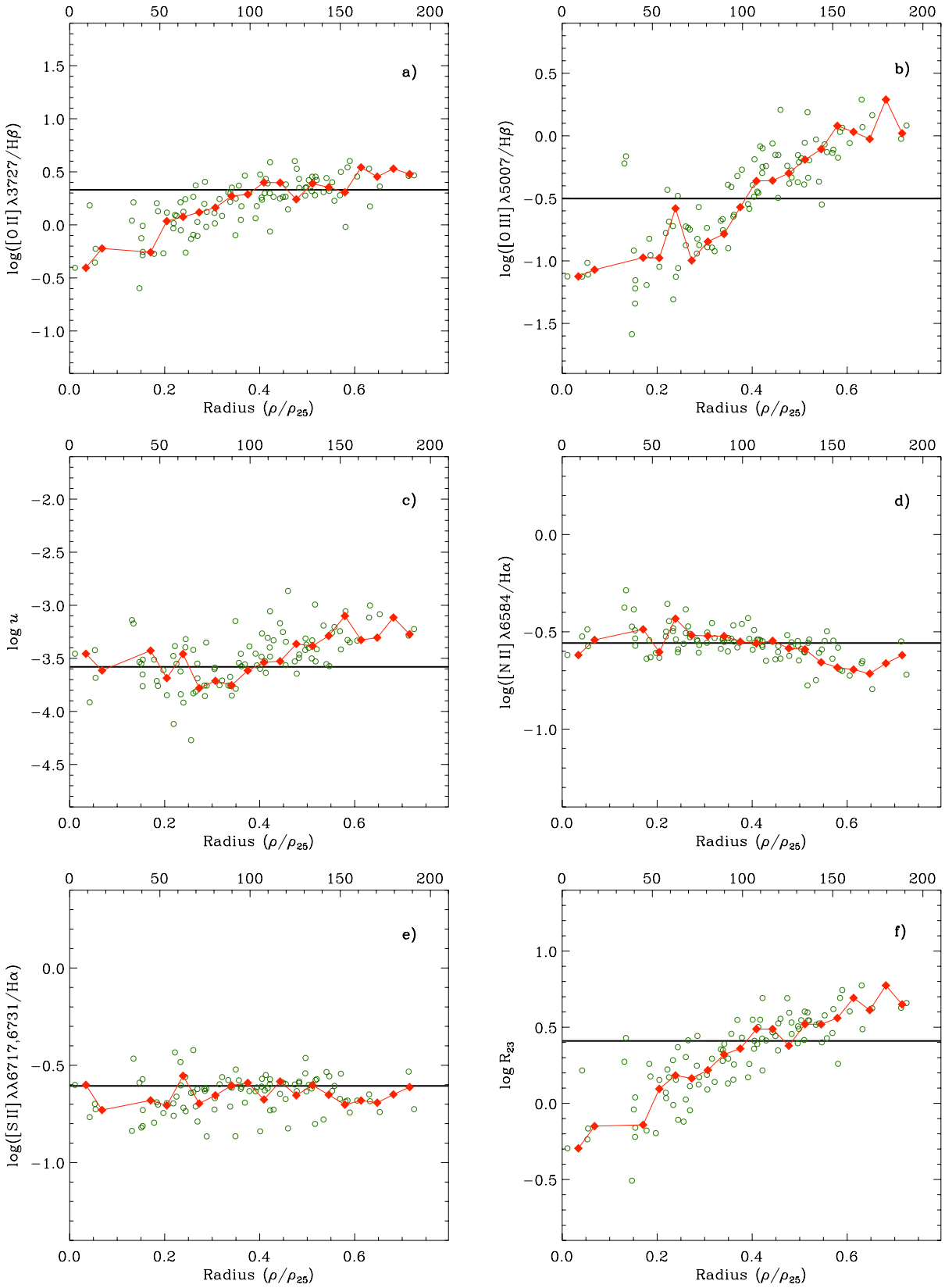

Figure 6.41: Radial variation of different line ratios and physical properties of NGC 628 for the H II regions catalogue (green circles) and the azimuthally-averaged spectra (red diamonds). The deprojected radial position for the blue symbols has been normalised to the size of the optical disk at the 25 mag arcsec^{-2} isophote. The radial position of the red diamonds correspond to the projected outer radius of the corresponding annulus. The top values on the X-axes show the linear-projected galactocentric radius in arcsec. The horizontal lines in each diagram correspond to the values derived from the integrated spectrum of NGC 628.

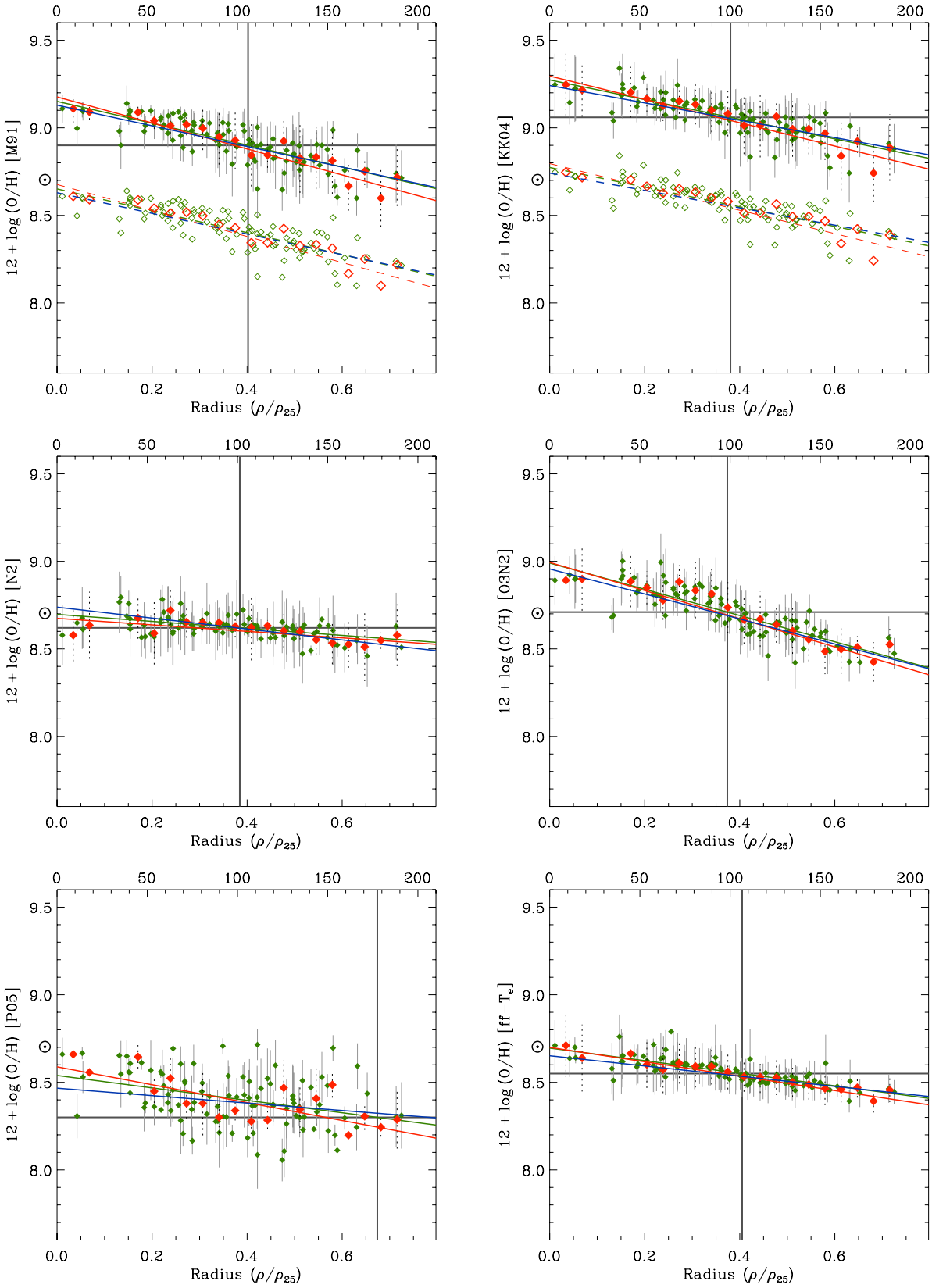

Figure 6.42: Radial abundance gradients derived for NGC 628 based on the selected H II regions catalogue. In each plot, the green symbols correspond to the spectra of the H II regions, the red diamonds correspond to the azimuthally-averaged radial spectra as explained in the text. For the R_{23} calibrators, the open symbols correspond to an arbitrary offset of –0.5 dex. See the text for a full explanation regarding the different linear fittings to the data.

RADIAL ABUNDANCE GRADIENTS FOR NGC 628: H II REGION CATALOGUE ANALYSIS

	M91			KK04		
	H II regions	*Radial*	*Bright sample*	*H II regions*	*Radial*	*Bright sample*
$12+\log(O/H)_{\rho=0}$	9.15 ± 0.02	9.18 ± 0.02	9.13 ± 0.04	9.27 ± 0.02	9.30 ± 0.02	9.24 ± 0.03
$12+\log(O/H)_{\rho=0.4\rho_{25}}$	8.90 ± 0.02	8.88 ± 0.02	8.89 ± 0.04	9.05 ± 0.02	9.03 ± 0.02	9.04 ± 0.03
$\log(O/H)_{(\mathrm{dex}\ \rho_{25}^{-1})}$	-0.62 ± 0.05	-0.74 ± 0.06	-0.59 ± 0.09	-0.56 ± 0.04	-0.67 ± 0.06	-0.50 ± 0.07
$\log(O/H)_{(\mathrm{dex\ kpc}^{-1})}$	-0.044 ± 0.004	-0.053 ± 0.004	-0.042 ± 0.007	-0.040 ± 0.003	-0.047 ± 0.004	-0.036 ± 0.005
	O3N2			N2		
	H II regions	*Radial*	*Bright sample*	*H II regions*	*Radial*	*Bright sample*
$12+\log(O/H)_{\rho=0}$	8.70 ± 0.01	8.67 ± 0.02	8.70 ± 0.06	8.99 ± 0.02	8.99 ± 0.03	8.95 ± 0.07
$12+\log(O/H)_{\rho=0.4\rho_{25}}$	8.62 ± 0.01	8.60 ± 0.02	8.61 ± 0.06	8.69 ± 0.02	8.67 ± 0.03	8.67 ± 0.07
$\log(O/H)_{(\mathrm{dex}\ \rho_{25}^{-1})}$	-0.20 ± 0.03	-0.19 ± 0.05	-0.23 ± 0.13	-0.75 ± 0.05	-0.80 ± 0.06	-0.70 ± 0.16
$\log(O/H)_{(\mathrm{dex\ kpc}^{-1})}$	-0.014 ± 0.002	-0.013 ± 0.004	-0.016 ± 0.010	-0.053 ± 0.004	-0.057 ± 0.005	-0.049 ± 0.011
	PT05			ff–T_e		
	H II regions	*Radial*	*Bright sample*	*H II regions*	*Radial*	*Bright sample*
$12+\log(O/H)_{\rho=0}$	8.54 ± 0.04	8.59 ± 0.05	8.46 ± 0.10	8.70 ± 0.01	8.70 ± 0.01	8.65 ± 0.02
$12+\log(O/H)_{\rho=0.4\rho_{25}}$	8.40 ± 0.04	8.38 ± 0.05	8.38 ± 0.10	8.55 ± 0.01	8.54 ± 0.01	8.54 ± 0.02
$\log(O/H)_{(\mathrm{dex}\ \rho_{25}^{-1})}$	-0.36 ± 0.09	-0.51 ± 0.11	-0.20 ± 0.23	-0.36 ± 0.03	-0.41 ± 0.03	-0.30 ± 0.05
$\log(O/H)_{(\mathrm{dex\ kpc}^{-1})}$	-0.025 ± 0.006	-0.036 ± 0.008	-0.014 ± 0.017	-0.026 ± 0.002	-0.029 ± 0.002	-0.021 ± 0.004

Table 6.5: Results from the oxygen abundance gradient analysis of NGC 628 based on the H II region sample. The columns correspond to the different calibrators employed, for each case the results from the H II regions and the radial average are presented. The rows correspond to: the central abundance at galactocentric radius $\rho = 0$; the *characteristic* abundance at $\rho = 0.4\rho_{25}$; and the slope of the abundance gradients in dex ρ_{25}^{-1} and dex kpc^{-1}, respectively.

trend. Leaving aside the results from PT05, the R_{23} calibrators (M91, KK04) present a higher level of scatter compared for example, to the gradient derived with the ff-T_e method. The slopes obtained by the R_{23} methods and *O3N2* are similar within the errors, while the (shallower) slopes derived from the *N2* and ff-T_e methods are comparable, with *N2* being again the flattest gradient.

The linear fits shown in Figure 6.42 are based on a relatively large number of H II regions, considering that typical spectroscopic studies are performed with a handful of H II regions from which previous abundance gradients have been derived. For example, in the case of NGC 628, FGW98 obtained an abundance gradient extending to $\rho \sim 1.8\rho_{25}$ by using 6 H II regions observed by these authors (two of them within the radii of the PINGS mosaic), and by adding 7 H II regions analysed previously by McCall et al. (1985) (all of them within the range of observed H II regions of this work), for a total of 13 regions. By using the M91 calibrator, they derived a gradient $12+\log(O/H) = 9.08 - (0.73 \pm 0.12)\rho/\rho_{25}$, which is consistent with gradients obtained in this work using the same calibrator, i.e. $12+\log(O/H) = 9.15 - (0.62 \pm 0.05)\rho/\rho_{25}$ for the H II regions, and $12+\log(O/H) = 9.18 - (0.74 \pm 0.06)\rho/\rho_{25}$ based on the radial average spectra. In both cases, the gradients were found by a linear (uniformly weighted) least-squares procedure. Zaritsky et al. (1994) also determined an abundance gradient based on 7 inner regions, however using a weighted linear least-squares fit, obtaining a slope $-(0.96 \pm 0.32)\rho/\rho_{25}$.

As stated by many studies, (e.g. Diaz, 1989), most of the H II regions observed in external galaxies fall under the category of *Giant Extragalactic H II regions* (GEHR). These correspond to very large H II regions

with dimensions up to 1 kpc, and with a substantial number of ionizing stars. Being such extended regions, the nebulae would include zones of different physical conditions, gas in different degrees of ionization and different amounts of reddening. Therefore, the observations of these regions would lead to systematic errors of the total derived abundance, if the latter is inferred from calibrators based on photoionization models which fail to provide adequate ionization correction factors[2] (ICF), and/or if they do not consider the 3D geometrical distribution of the ionizing sources.

As suggested by Ercolano et al. (2007), if compact clusters (corresponding to small H II regions) and loose associations (i.e. GEHRs or H II complexes) are randomly distributed throughout a given galaxy, the systematics errors due to spatial physical variations within a nebula would only cause a larger scatter in the observed metallicities at a given radius, and given a sufficient number statistics, they would not affect the measured metallicity gradient. However, if the distribution of compact clusters and large associations are somewhat dependent on the galactocentric radius, then the systematic errors may introduce a bias on the measured galactic metallicity gradient, if the abundances are obtained from strong line methods calibrated with models which do not reproduce the observed excitation of these large H II regions.

One way of assessing this issue is by comparing the results from metallicity indicators based on photoionization models (e.g. M91, KK04), and those based on purely empirical methods (e.g. $O3N2$). As discussed above, different calibrators show different trends and similarities among them, the most evident at the moment consists of slightly steeper slopes calculated by photoionization-based models, compared to the empirical methods.

However, as described above, most spectroscopic works have obtained abundance gradients by observing only a few, large and bright H II regions over the surface of the galaxies. The fact that we benefit from a nearly complete coverage of small and large H II regions observed over the surface of the galaxy, give us the possibility to explore the systematics between different ways of obtaining the abundance gradients. One possibility is to select different sets of spectra in order to explore variations and systematics of the derived abundance gradients. This has been partially done, by considering the three different analysis methods discussed so far. Nevertheless, the H II region catalogue offer us the possibility to discriminate between H II regions of different brightness and sizes, therefore we can simulate for example, the abundance gradient determination based only on a few bright H II regions of a galaxy, like performed in most "classical" studies, and compare the results with the abundance gradients obtained from the full distribution of H II regions.

For doing so, we chose 15 large (and bright) H II regions from the catalogue of NGC 628, distributed over a good range of galactocentric distances, and selected from the four quadrants of the galaxy as defined in Figure 6.36. They correspond to the regions: N628–12, 13, 22, 27, 32, 40, 42, 43, 50, 51, 56, 79, 80, 84 and 94. The minimum galactocentric distance of these sample is $\rho/\rho_{25} \sim 0.18$, and the maximum is $\rho/\rho_{25} \sim 0.7$. As the derived gradients using these regions may be biased by their somewhat arbitrary selection, a statistical approach was followed in order to derive the abundance gradients from the *bright* H II region subsample. Eight regions were extracted randomly from the sample of 15 large/bright regions; the abundance gradients were then calculated from this reduced number of regions. The process was repeated over 50 times for each abundance calibrator. The final gradients, central oxygen and characteristic abundances were derived from the mean values of the 50 realizations.

These numbers are shown in Table 6.5, corresponding to the columns marked as *Bright sample*. The average linear fit of this exercise is shown in Figure 6.42 as a blue line on each of the abundance gradient

[2]The ratios between the total abundances of the various elements and the abundance in a single state of ionization.

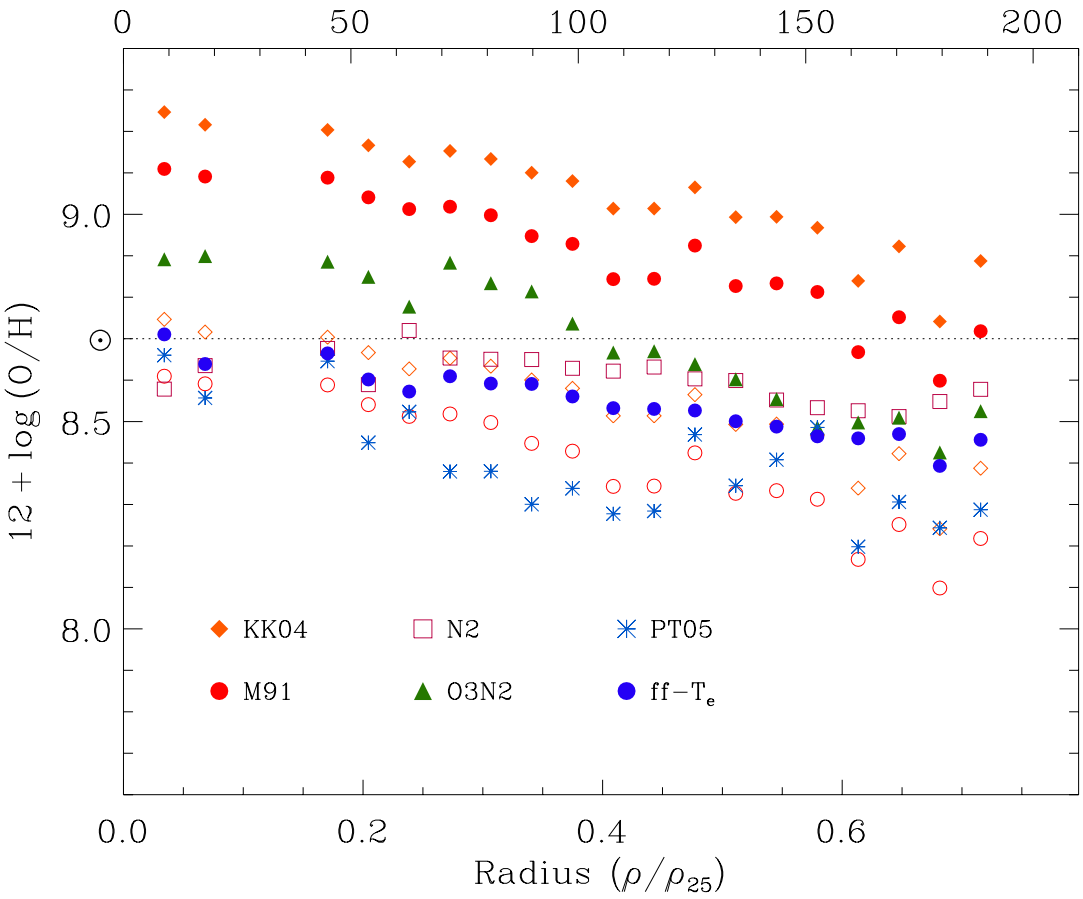

Figure 6.43: Comparison of the derived abundance gradients for NGC 628 using the H II region catalogue. The different symbols correspond to the radial average spectra values for each abundance calibrator. The open orange diamonds and red circles correspond to the arbitrary offset of –0.5 dex for the KK04 and M91 calibrators respectively. The horizontal dashed line corresponds to the oxygen solar value. The top X-axis values correspond to the projected radii in arcsec.

plots. The trends of these linear fits and the values shown in Table 6.5 suggest that, the abundance gradients of NGC 628 derived from the subsample of *large* and *bright* H II regions show systematically *shallower* slopes and *lower* central oxygen abundances, compared to the abundance gradients obtained from the full catalogue of H II regions. This results is true for all calibrators, except *N*2, for which the inverse trend is true, i.e. the *bright* subsample produces steeper gradients, with a higher central oxygen abundance. The determination of the abundance gradients using the *bright* H II region sample was repeated by changing the number of randomly selected regions in each step of the procedure in the range between 5 and 12 regions. The derived abundance gradient values resulted in exactly similar trends than the one discussed above, with variations in the central oxygen abundance of the order of ± 0.02 dex, but still showing flatter gradients than the full catalogue gradients. Note that the *characteristic* abundances are similar to within 0.02 dex for all the different determinations for each calibrator.

Although this trend is present in most of the abundance calibrators, the actual difference in slopes and central abundances are relatively low, i.e. of the order of ± 0.1 dex on both the oxygen abundance at $\rho = 0$, and the gradient in terms of the optical radius (dex/ρ_{25}). The generalization of this result (and their implications) will be addressed in the following sections, when applying the same exercise to the rest of the galaxies considered for this chapter.

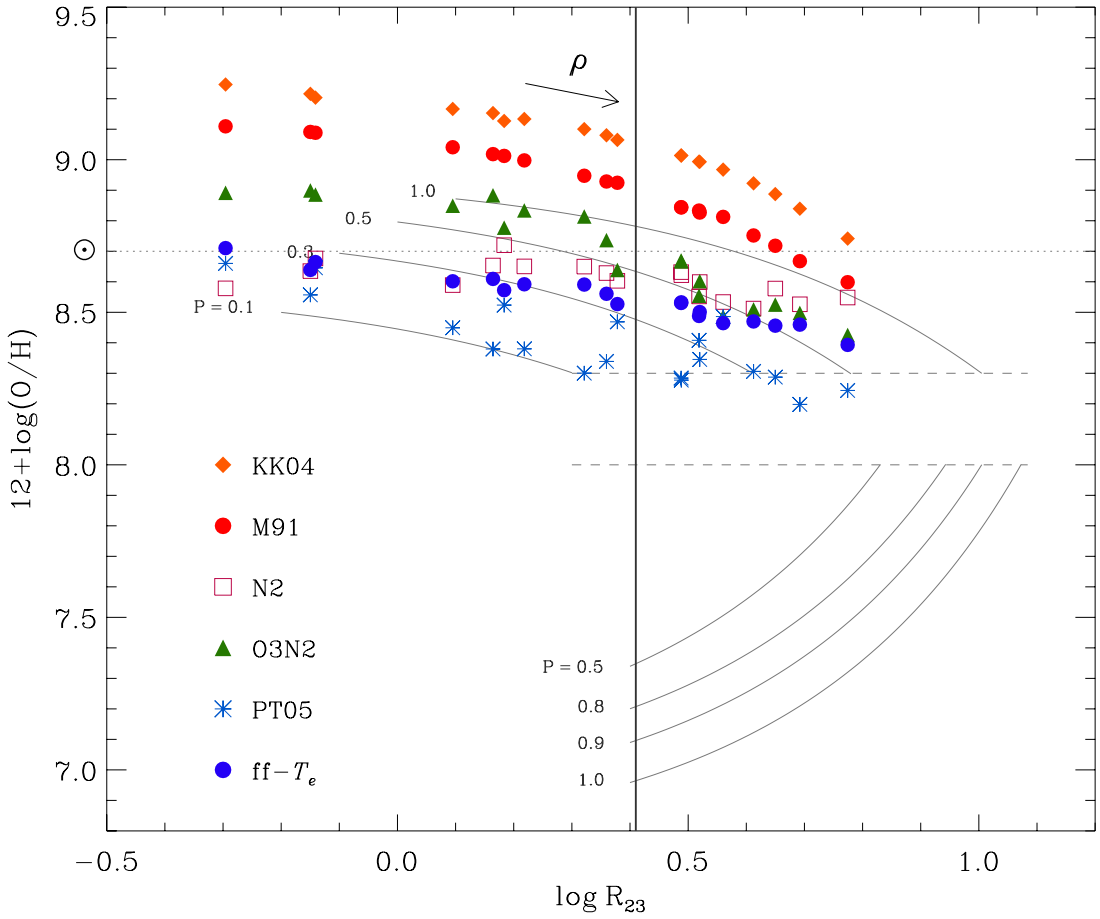

Figure 6.44: 12 + log(O/H) vs. log R_{23} diagram for the radial average spectra extracted from the H II region catalogue of NGC 628. The solid lines correspond to predictions of the empirical calibrations in both branches for different values of the excitation parameter P. The horizontal dashed lines show the transition zone between the two R_{23} branches. The arrow shows direction of increasing galactocentric radius. The vertical line shows the value of log R_{23} derived from the integrated spectrum of NGC 628.

Figure 6.44 shows the O/H vs. R_{23} relation for the radial average spectra obtained from the H II region catalogue sample. This representation was chosen instead of the full catalogue so that the trends of the different calibrators could be noticed. This plot can be compared to the previously derived for the *fibre-by-fibre* sample. The R_{23} methods show exactly the same trend as before, consistent with higher values of the derived oxygen abundance, followed by the $O3N2$, the ff–T_e method and the PT05 calibrator, in decreasing order of the derived abundances for a given value of R_{23}. The $O3N2$ calibrator shows practically the same trend as before, with slightly higher oxygen abundances derived for lower values of R_{23}. The opposite is true for the ff–T_e and PT05 methods, for which the derived abundances are lower than in the *fibre-by-fibre* case for log $R_{23} < 0.0$. The reason for this behaviour may be due to the higher signal-to-noise of the H II regions from which the average spectra is constructed, resulting in more consistent line ratios and derived abundances. The ff–T_e method shows a smooth, nearly linear trend as a function of log R_{23}, consistent with subsolar values (dotted horizontal line), except at the innermost region of the galaxy. As in Figure 6.28, the vertical line corresponds to the R_{23} value derived from the integrated spectrum of NGC 628, and the arrow shows the direction of increasing galactocentric radius. The PT05 presents the most scatter among the different calibrators, with many radial points falling into the transition zone between the two R_{23} branches. The high

level of scatter, and the systematic low values of the derived oxygen abundances using the PT05 calibrator are present in all the different analysis methods employed in this work. This might confirm the fact that the PT05 calibrator does not seem to be an appropriate method for the type of spectral data presented in this study.

DISCUSSION

Three different methods have been applied in order to study the 2D spectroscopic properties of NGC 628. The first two considered the spectra contained in single fibres to be representative of the physical conditions of those regions sampled by the fibre aperture. Different selection criteria were applied in both methods, seeking for only those regions with meaningful spectral features. These criteria reduced the number of analysable spectra to considerable amount, compared with the large number of fibres contained in the full IFS mosaic. The selection criteria of the first method, the *fibre-by-fibre* analysis, proved to select regions with good quality spectra from which different physical properties of the galaxy were derived, although with a high level of scatter. From the analysis of this sample, consistent line-ratios radial trends and oxygen abundance gradients were obtained. The analysis of the $O_3 - limited$ sample confirmed the results of the previous analysis, although the selection criteria reduced even more the number of analysable spectra, and discarded regions of low emission in oxygen, corresponding to the innermost parts of the galaxy. The third method consisted in creating a catalogue of H II regions by co-adding fibres corresponding to the same morphological regions. The analysis based on these spectra resulted in similar trends than the previous two samples, but with a much reduced scatter and clearer trends in the distribution of line ratios and abundance gradients.

Six different abundance calibrators were employed in order to derive the oxygen abundance of the individual spectra. The R_{23} methods (M91, KK04) resulted in more robust determinations in all three analysis methods, but with systematically high (and probably unrealistic) values of the derived abundances. From the empirical methods, the ff–T_e method stands as the best-behaved calibrator, following the trends marked by the R_{23} methods, at least in terms of the derived abundance gradients, as it can be noticed by the comparing the arbitrary offsets of the R_{23} methods and the results of the ff–T_e method. Leaving aside the results from the PT05 method, the $O3N2$ calibrator provides the steepest slope in all three different analysis, contrary to the case of the $N2$ indicator, which resulted in the flattest gradients among the different calibrators. For all three different methods, some calibrators suggest a flattening of the abundance gradient for the inner regions of the galaxy, although the few number of data points may preclude any firm conclusion. This possibility and their implications will be addressed in the next sections. The behaviour of all the three different calibrators can be compared in Figure 6.43, showing the abundance gradients derived from the radial average spectra obtained from the H II region catalogue sample.

The different values of the oxygen abundance derived from the integrated spectrum for each calibrator, equal the abundance gradient at galactocentric radius consistent with $\rho \sim 0.4\rho_{25}$, confirming for this galaxy previous results obtained for other objects, i.e. that the integrated abundance of a normal disk galaxy correlates with the *characteristic* gas-phase abundance measured at $\rho = 0.4\rho_{25}$. Furthermore, a "classical" abundance gradient determination was performed by selecting large and bright H II regions, the results are consistent (within the errors) with the values derived from the analysis of the full H II region distribution, although a systematic slightly flatter slope was found in most calibrators. Another conclusion deduced from

this section is that the "non-physical" [O III] λ5007/λ4959 ratios found in the final samples of the *fibre-by-fibre* and H II region catalogues is due to the errors introduced by the continuum subtraction of a SSP model to the data, especially to regions of weak emission in the [O III] lines. Therefore, although the [O III] ratio may not be close to the theoretical value, the sum of their flux, and especially the values of their derived line ratios, are representative of the physical conditions and metallicity abundance of those particular regions.

The consistency between the results from the *fibre-by-fibre* sample and the H II region catalogue is somewhat surprising. However, this result would contribute to reaffirm the robustness of the results obtained from strong-line methods applied to individual regions sampled by the fibre aperture, to the integrated spectra of a whole galaxy. On the other hand, the higher level of scatter found in the *fibre-by-fibre* analysis may be just reflecting statistical variations due to spectra of relatively low signal-to-noise compared with the integrated spectra of the H II regions catalogue. Nevertheless, the aperture of the PPAK fibres is relatively large compared with typical widths employed in long-slit spectroscopy ($\sim$ 1–3 arcsec), this combined with the quality selection criteria applied to the spectral samples, may reflect that the observed dispersion in the derived line ratios and chemical abundances might be due to real variations of these properties through as single H II region. In that case, it would mean that the observations are spatial and aperture dependent, as the analysis of the variations of the line ratios of the H II region FGW 1058E presented in section 6.1 suggests. If the latter possibility is true, then the scatter seen in the results of the *fibre-by-fibre* sample might be a combination of both, the geometrical distribution of the physical properties on a single region, which is reflected in the point-by-point observed spectra, and the statistical variations due to the intrinsic signal-to-noise of the data.

The rest of the galaxies considered in this chapter will be analysed in their 2D spectroscopic properties by using a combination of the methods presented in this section. However, given the practical limitations in terms on the content and extension that this dissertation might include, the study of these galaxies will be restricted to presenting their general physical properties and their abundance gradients, in a similar way to NGC 628. More detailed studies regarding the 2D distribution of the physical and chemical properties of the galaxies will be discussed in section 7.4, as future work.

6.4 NGC 1058

The chosen methodology to the rest of the galaxies consist on analysing the 2D distribution of their properties by comparing the results from the *fibre-by-fibre* method to those derived by a selected number of H II regions. Both methods are the extreme cases of the data selection, and by not restricting the sample to only those "physical" regions, (with Balmer and [O III] ratios close to their theoretical ratios), we can consider regions of weak oxygen emission. The comparison between the *raw* and *refined* samples, corresponding to the *fibre-by-fibre* and H II regions, can provide an idea of the errors and systematics arising when considering multiple spectra distributed over the surface of the galaxy.

In the case of NGC 1058, the *clean* residual mosaic consists of 3976 fibres, after applying the selection criteria of the *fibre-by-fibre* analysis this number reduces to 2370, for those fibres with detection in Hβ and [O III] λ4959; 2358 fibres after discarding fibres with non-finite values of c(Hβ) and 806 spectra after the third selection criteria, with a flux threshold of 5×10^{-16} erg s^{-1} cm^{-2}, corresponding to $\sim$ 20% of the number of fibres in the *clean* mosaic and $\sim$ 10% of the total number of observed fibres in the original mosaic. At the assumed distance of this galaxy (10.6 Mpc), the aperture of one fibre would correspond to a physical scale of 138.3 pc.

The top three rows of Figure 6.45 show the distribution of the control line ratios for the selection criteria

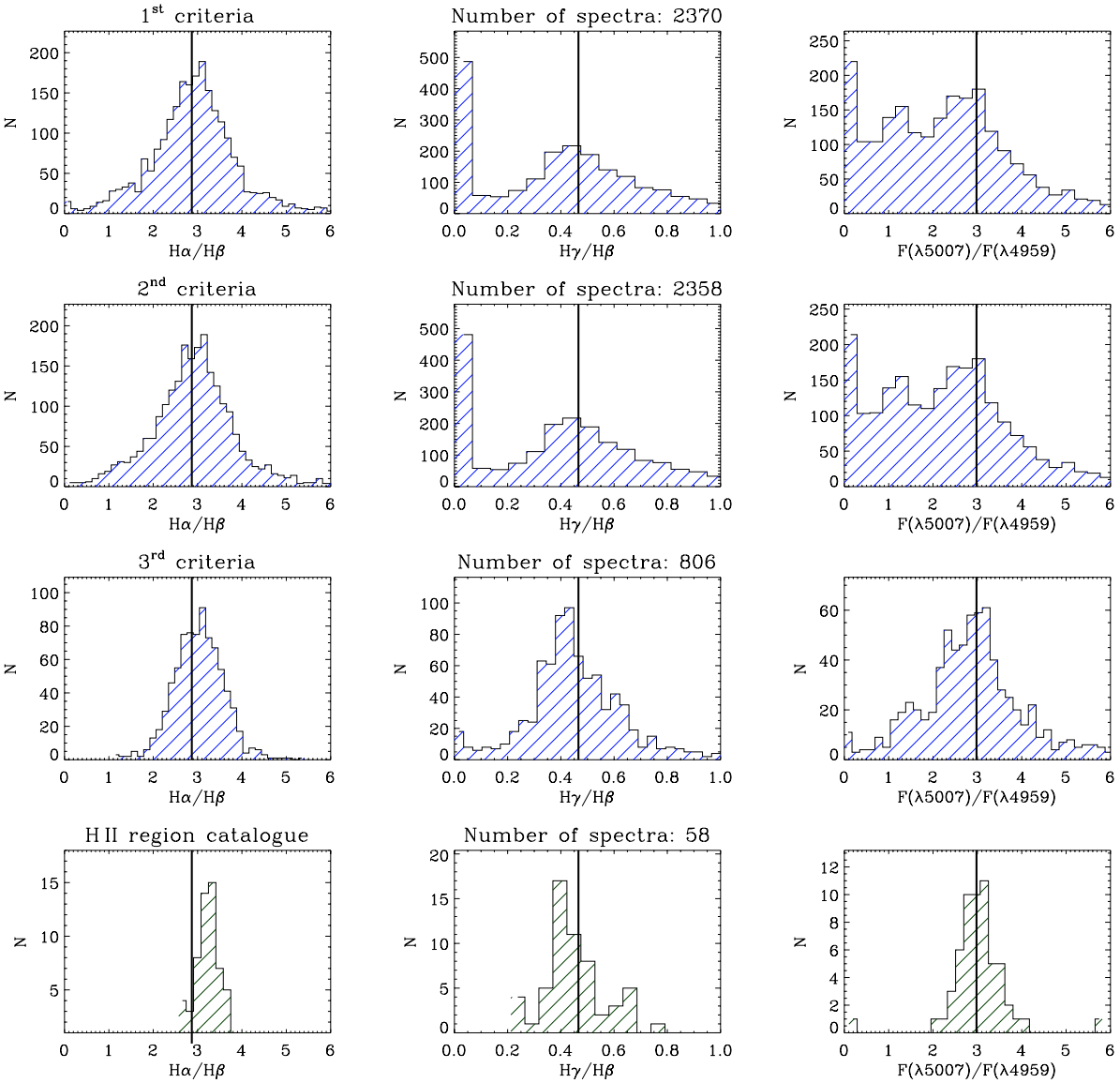

Figure 6.45: Selection criteria histograms for NGC 1058. The top three rows correspond to the *fibre-by-fibre* analysis, the bottom row to the H II region catalogue. In each panel, the vertical line correspond to the theoretical value of the given line ratio.

steps of the *fibre-by-fibre* analysis. The Hα/Hβ ratio for the final sample shows a distribution centered at the theoretical value, with a tail of higher ratios consistent with reddened spectra, and a somewhat higher number of values corresponding to a negative extinction, compared to NGC 628. A similar behaviour is shown by the Hγ/Hβ ratio, with most values lying near to the theoretical value of being consistent with lower ratios (reddened spectra). The distribution of the [O III] ratio is well centered at the theoretical value, but with long tails of lower and higher values, nearly equally distributed.

On the other hand, Figure 6.46 shows the 58 selected H II regions for NGC 1058, with their identification number and the equivalent or real extraction apertures drawn. The distribution of the overlapping fibres due to the dithering observation was considered when co-adding the fibres corresponding to a single region. The basic information of the selected catalogue can be found in Appendix D. Figure 6.46 shows a distribution of H II regions concentrated in the centre of the galaxy, with some prominent outlying regions. The dotted-line circle corresponds to the optical radius of the galaxy, ρ_{25}. The regions N1058–58 and 26 correspond to the

FGW 1058E and FGW 1058H regions discussed in section 6.1. Three outlying H II regions were selected with $\rho > 1.5\rho_{25}$. The bottom row of Figure 6.45 shows the histograms of the H II region catalogue. The line ratios show a narrower distribution compared to the final *fibre-by-fibre* sample, as expected. The Hα/Hβ distribution presents practically no values lower than the theoretical ratio. The [O III] ratio distribution shows a nearly Gaussian distribution is well centered at the theoretical value. From these histograms, we can corroborate than the quality of the final spectra in both samples is of a good level, within the limitations of the residual subtraction method. The values of the Hα/Hβ ratio are consistent with a lower average extinction, compared to the case of NGC 628. Figure 6.47 shows examples of radial average spectra of NGC 1058 extracted from the *fibre-by-fibre* sample, in arbitrary flux units, with galactocentric radius increasing from the bottom to the top of the figure. On the other hand, Figure 6.48 shows examples of three H II regions of NGC 1058 with different intrinsic signal-to-noise. For each H II region, the left panel corresponds to the observed integrated spectrum within the aperture and the SSP fit model overlaid, the right panel shows the residual spectrum from which the emission line intensities were calculated.

The observed line intensities were corrected by interstellar reddening following the procedure outlined before for NGC 628. For the *fibre-by-fibre* sample, the c(Hβ) term was derived solely from the Hα/Hβ ratio, while for the H II region catalogue, the Hγ/Hβ ratio was also considered in the determination. Figure 6.49 shows three diagnostic diagrams comparing the location of the spectra for the different samples. As in similar previous figures, the lighter tones correspond to spectra belonging to the inner regions of the galaxy, and darker colours to the outer parts. The positions of the azimuthally-average radial spectra, obtained by co-adding the spectra within consecutive annulus of 5 arcsec is shown as reddish diamonds on top of the main data for both samples. The top panels correspond to the [O III] λ5007/Hβ vs. [O II] λ3727/Hβ diagnostic diagrams, on the left-panel the plot corresponding to the *fibre-by-fibre* sample, on the right-panel the H II region catalogue is presented. Both samples show the same trend, although with a very different level of scatter. Both the [O II] and [O III] increase with galactocentric radius, as shown by the lower values of both ratios corresponding to lighter tones, but in different proportions. The value of [O III]/Hβ ratio varies more than one order of magnitude, while the value of the [O II] λ3727/Hβ ratio increases ~ 0.5 dex with increasing galactocentric distance. For bot cases, all the spectra are within the boundaries of starburst ionization, although for the outer regions, the line ratios lie very close to the transition zone.

The middle-panels of Figure 6.49 show the [O III] λ5007/Hβ vs. [N II] λ6584/Hα ratio diagrams. Again, the plots suggest the same trend with different scatter. The variation of [O III] with radius was discussed previously, but the [N II]/Hα ratio shows a nearly constant value consistent with [N II]/Hα $\sim$ –0.5, with a decrease of almost one order of magnitude for the outermost regions of the galaxy. Note that the radial average spectra follow basically the same trend for both samples. The bottom-panels show the [N II]/[O II] vs. logR_{23} diagrams. We find a negative correlation of these indicators, however, the scatter is considerably higher than in the case of NGC 628. As shown by the diagram corresponding to the H II regions sample, the inner regions of NGC 1058 present a good range of R_{23} values consistent with a [N II]/[O II] ratio $\sim$ –0.3. Most of the data points are located in the upper branch inferred from this diagram. However, the outermost regions of the galaxy are located at the transition between the two branches, and therefore we would have to consider both solutions of the R_{23} relation for those regions.

Figure 6.50 shows the radial trends for a selected number of properties of both samples. As in the diagnostic diagrams, the left column correspond to the *fibre-by-fibre* sample, the right column to the H II region catalogue. Given the large number of data points within $\rho/\rho_{25} \lesssim 1$ for the *fibre-by-fibre* sample, the X-axes of their corresponding diagrams are shown in logarithmic scale for the sake of clarity. The top panels cor-

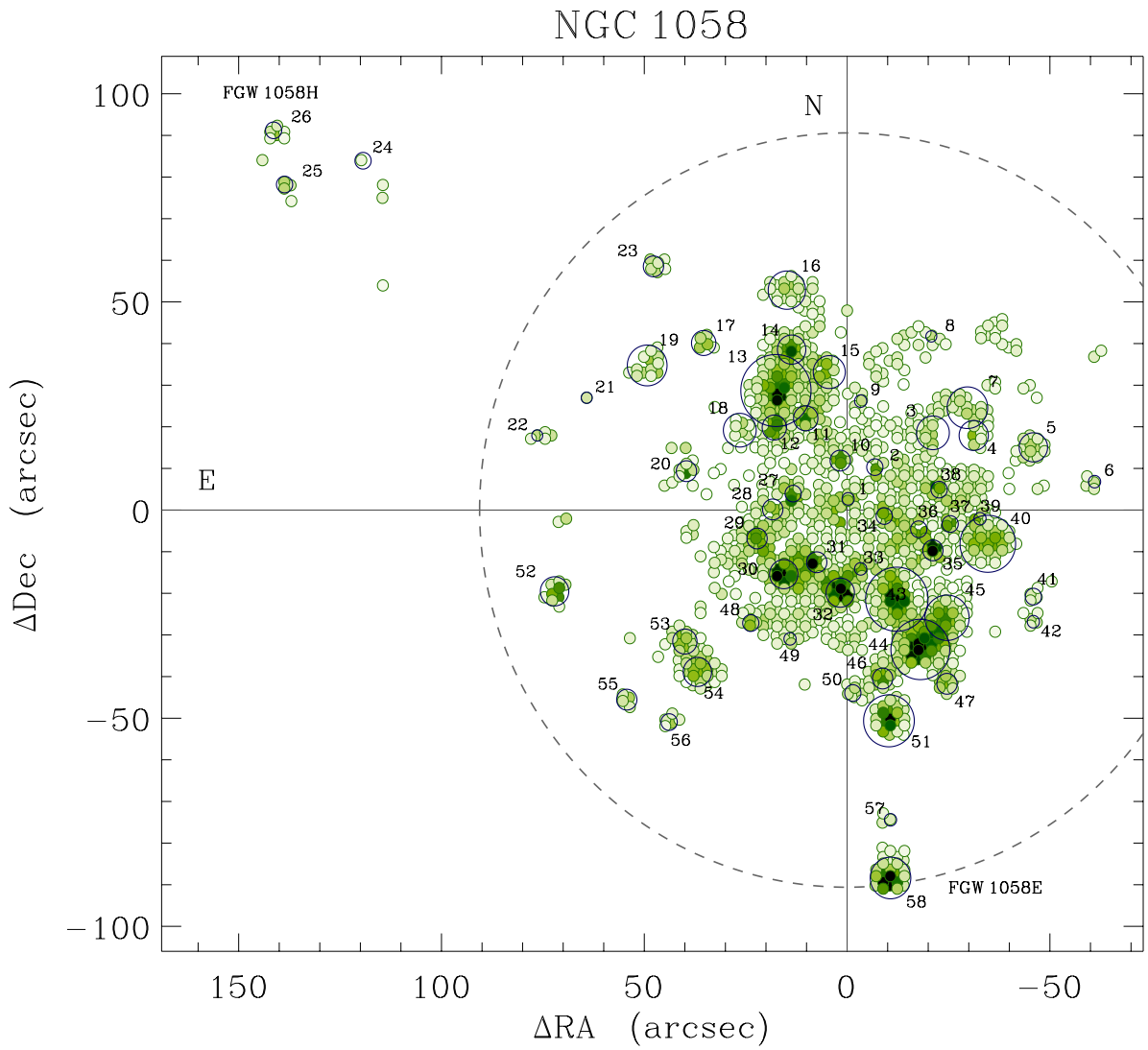

Figure 6.46: Spatial location and identification of the selected H II regions for NGC 1058. The background fibres correspond to the *fibre-by-fibre* sample, with colour intensities scaled to the flux of the Hα emission. The circles correspond to an equivalent aperture radius. The dotted-line circle corresponds to the isophotal radius ρ_{25}. The H II regions discussed in section 6.1 are labeled respectively.

respond to the radial variation of R_{23}, which aside being an indicator of metallicity, by its definition, it also represents a measure of the variation of the [O II] λ3727/Hβ and [O III] λ4959,λ5007/Hβ ratios. As seen in the previous diagnostic diagrams, the larger variation with galactocentric radius corresponds to [O III] , with a smaller contribution of [O II] . The increasing value of R_{23} with respect to the radius, and considering that the R_{23} values for the inner regions of the galaxy correspond to the upper branch of the R_{23} relation, imply a decreasing abundance gradient as a function of radius. However, for values of $\rho/\rho_{25} > 1$, the R_{23} ratio stops to increase, and the outer regions show a constant value consistent with $\log R_{23} \sim 0.8$, corresponding to the transition region between the two branches of the R_{23} relation. The value of R_{23} derived from the integrated spectrum matches the point-to-point radial variation at $\rho/\rho_{25} \sim 0.5$, for both cases. The absence of regions between $1.0 < \rho/\rho_{25} < 1.7$ makes difficult to infer a clear trend from the edge of the optical radius of the galaxy to these outlying regions.

The middle-plots correspond to the radial variation of the ionization parameter, which given its definition in Equation 5.4, reflects the variation of the [O II]/[O III] ratio. Both samples show a higher ionization at the

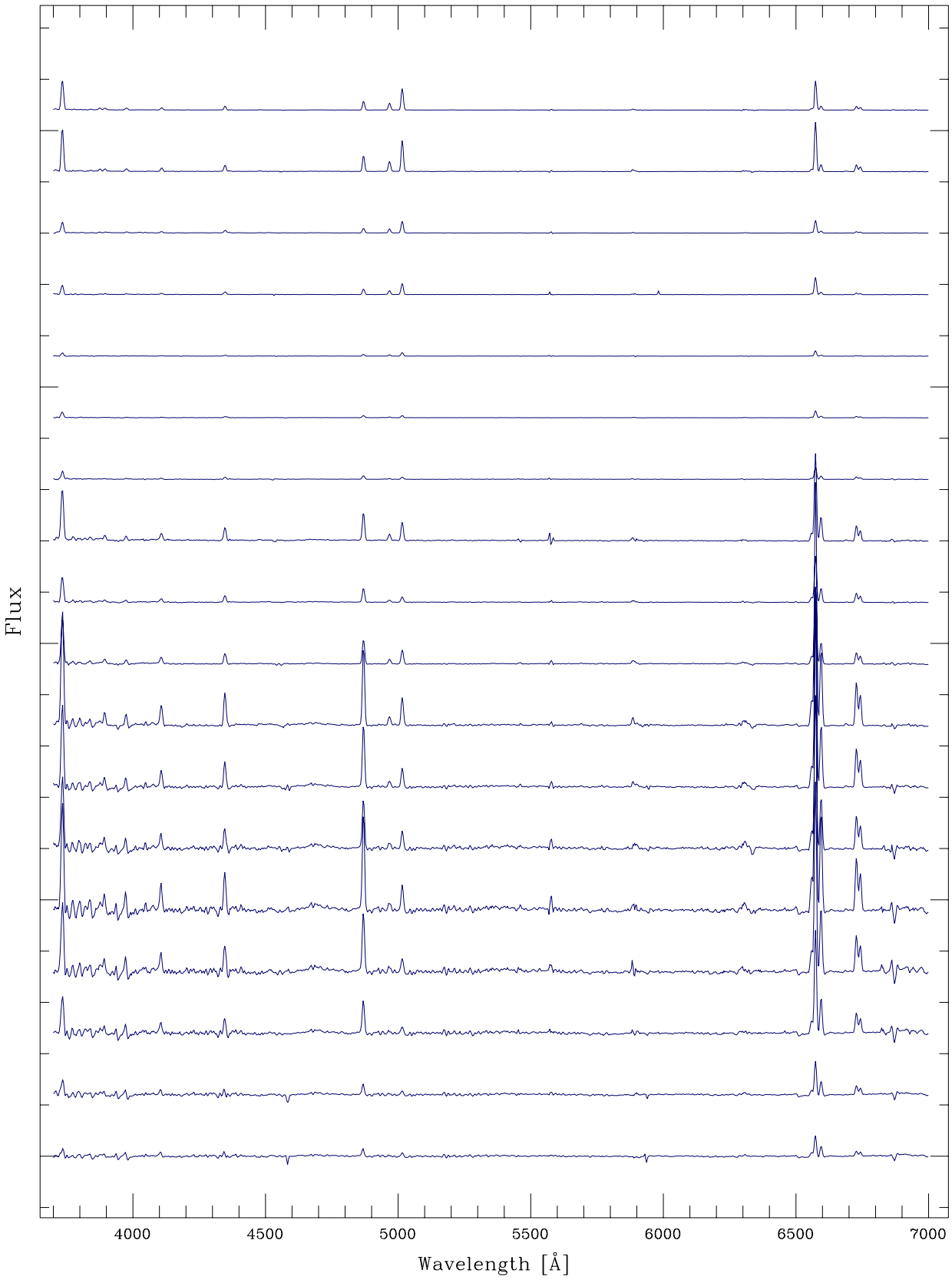

Figure 6.47: Radial average spectra of NGC 1058 extracted from the *fibre-by-fibre* sample, in arbitrary flux units. The galactocentric radius increases from the bottom to the top of the figure.

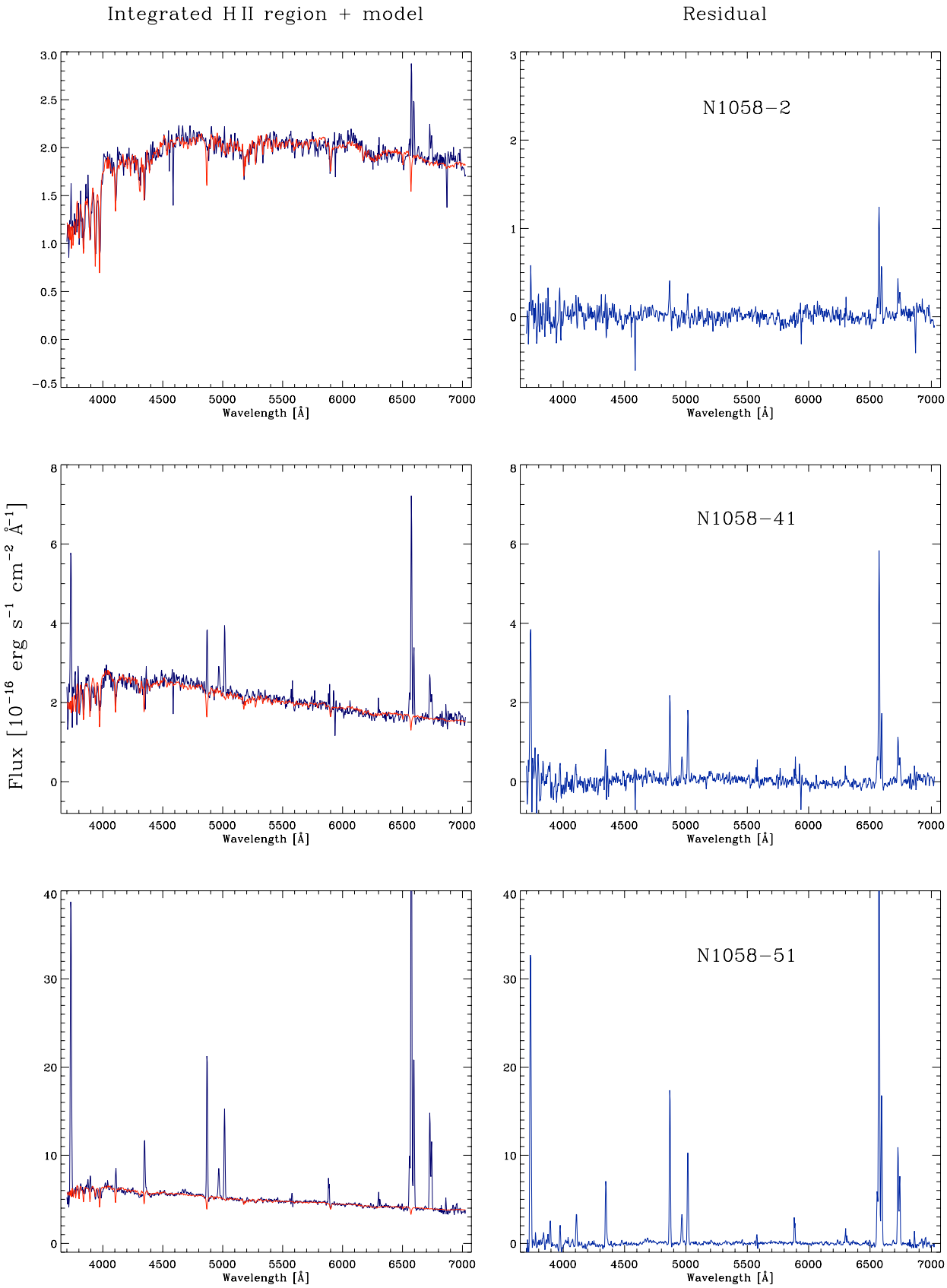

Figure 6.48: Examples of spectra of NGC 1058 extracted from the H II region catalogue. The left column corresponds to the observed integrated spectrum, plus the SSP fit model overlaid as a red line, the right column shows the residual spectrum. The label corresponds to the ID of the H II region.

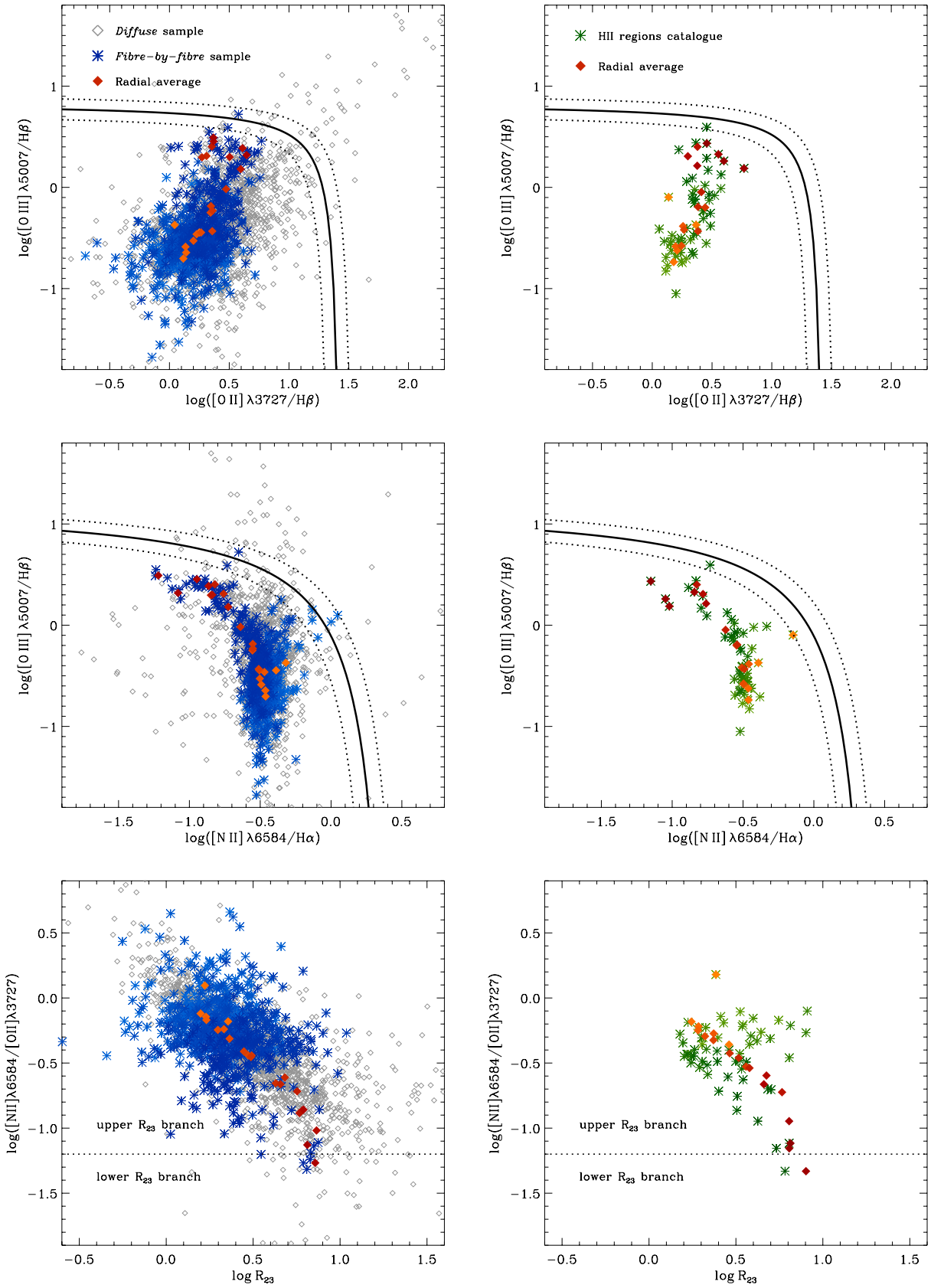

Figure 6.49: Diagnostic diagrams for NGC 1058. The left column correspond to the *fibre-by-fibre* sample, the right column to the H II region catalogue. The filled-diamonds correspond to the azimuthally-averaged radial values. Lighter/darker tones correspond to inner/outer regions of the galaxy, in terms of the galactocentric radius.

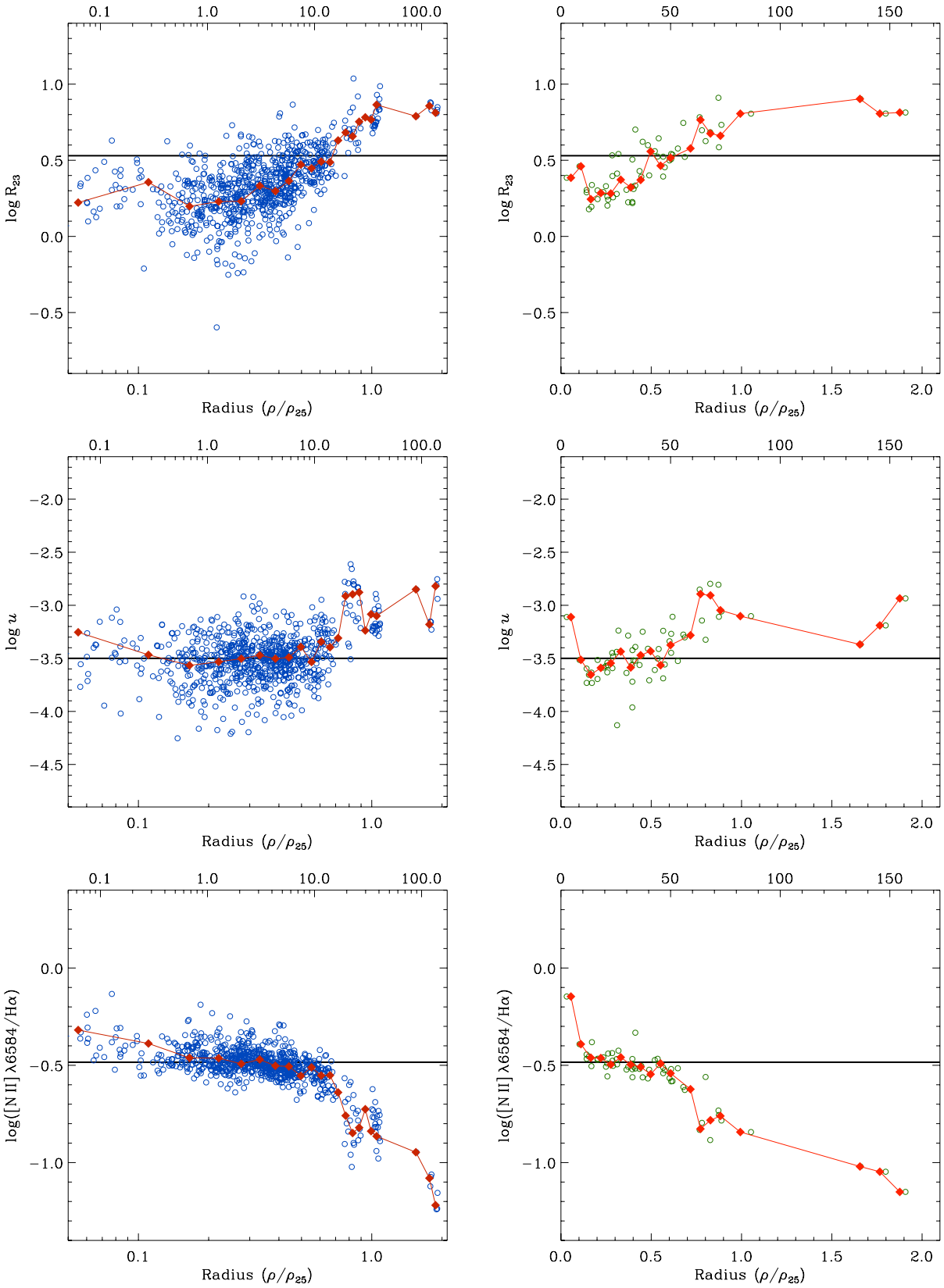

Figure 6.50: Radial variation of selected physical properties of NGC 1058. The left column correspond to the *fibre-by-fibre* sample, the right column to the H II region catalogue. In both cases, the position of the circles correspond to the deprojected galactocentric radius, normalised to the optical size of the galaxy. Note that in the left-panels, the X-axis is in logarithmic scale, while for the H II regions the scale is linear. The top X-axes values correspond to the projected size in arcsec. The horizontal lines correspond to the values derived from the integrated spectrum of the galaxy.

very central region of the galaxy, then falling to nearly constant but mildly increasing values of $\log u$ for $\rho/\rho_{25} < 0.8$, with a high peak for regions located near the optical size radius. The outlying regions present also a high value of ionization, consistent with values $\log u \sim -2.8$, compared to values of $\log u \sim -3.5$ found for most regions of the galaxy within the optical radius, reason for which the ionization parameter derived from the integrated spectrum correspond to this latter value. The bottom-panels correspond to the variation of the [N II] λ5484/Hα ratio, tracing the changes in the local ionization. This ratio decreases with galactocentric distance with a nearly constant slope until regions $\rho/\rho_{25} \sim 0.7$, falling drastically for exactly the same regions for which the ionization parameter increases, with even lower values for the outlying regions at $\rho/\rho_{25} > 1.5$. The behaviour is similar for both samples. The value derived from the integrated spectrum is consistent with values found between 0.2 and 0.5 normalised radius, as expected given the high distribution of values in this region. The radial distribution found for both the ionization parameter and the N_2H_α ratio imply that the ionization is much stronger for those regions at $\rho/\rho_{25} \gtrsim 1.0$.

The radial abundance gradients for NGC 1058 are shown in Figure 6.51 for a selected number calibrators chosen from the six previously employed in the analysis of NGC 628. From the category of the R_{23} methods, both the M91 and KK04 show very similar trends in the derived oxygen abundances, with a small offset between the two calibrators, being the KK04 higher; this last indicator was chosen from the group of R_{23} methods. From the category of the index-empirical, monotonic methods, the $O3N2$ method was chosen, mainly because the abundance gradients derived from this calibrator resemble more those derived through the R_{23} methods, as the $N2$ seemed to determine very flat gradients. The PT05 was discarded as previous analysis showed a pronounced scatter of the derived metallicities. The ff–T_e method was the last considered metallicity indicator.

The top panels of Figure 6.51 show the abundance gradients obtained by using the KK04 calibrator. As in previous figures, the left-panel corresponds to the *fibre-by-fibre* sample, the right-panel to the H II region catalogue. The red diamonds correspond to the results from the radial average spectra obtained for each sample. As shown by the [N II]/[O II] diagrams in Figure 6.49, the inner parts of the galaxy correspond to values of R_{23} belonging to the upper branch of the relation. However, as galactocentric distance increases, the spectra falls into the transition zone between the two branches. Analysis of the emission line ratios as a function of deprojected radius showed that, for regions with normalised radius $\rho/\rho_{25} \gtrsim 0.9$ in both samples, there is an ambiguity on the determination of the oxygen abundance due to the bi-modality of R_{23}. This effect is shown in the top-panels of Figure 6.51, where for regions at $\rho/\rho_{25} \gtrsim 0.9$ the oxygen abundances corresponding to the two branches are displayed for each single region, connected with a vertical line. For both samples, the dashed-lines correspond to a linear least-squares fit to only those points lying within $\rho = 0.9\rho_{25}$.

The selection of the upper or lower branch for these outlying H II regions has important consequences, as the determination of galactic abundance gradients to extended galactocentric distances can provide strong constrains for chemical evolution models of galaxies. In the case of the *fibre-by-fibre* sample, the inner regions ($\rho/\rho_{25} < 0.9$) show a well-defined and steep gradient extending to nearly the size of the optical radius. For the regions extending beyond this limit, the choice of the upper branch abundances, either traced by the individual regions or the radial average spectra, would be consistent with the gradient of the inner regions of the galaxy (i.e. the slopes defined by the dotted-lines). However, if the lower branch metallicity values are selected, then the abundance gradient of NGC 1058 would show a break in metallicity of $\sim$ 0.5 dex, decreasing abruptly from values of nearly solar abundance at the optical radius, to a flat gradient with an abundances 1/3 solar for the outermost regions of the galaxy. In the case of the H II regions sample,

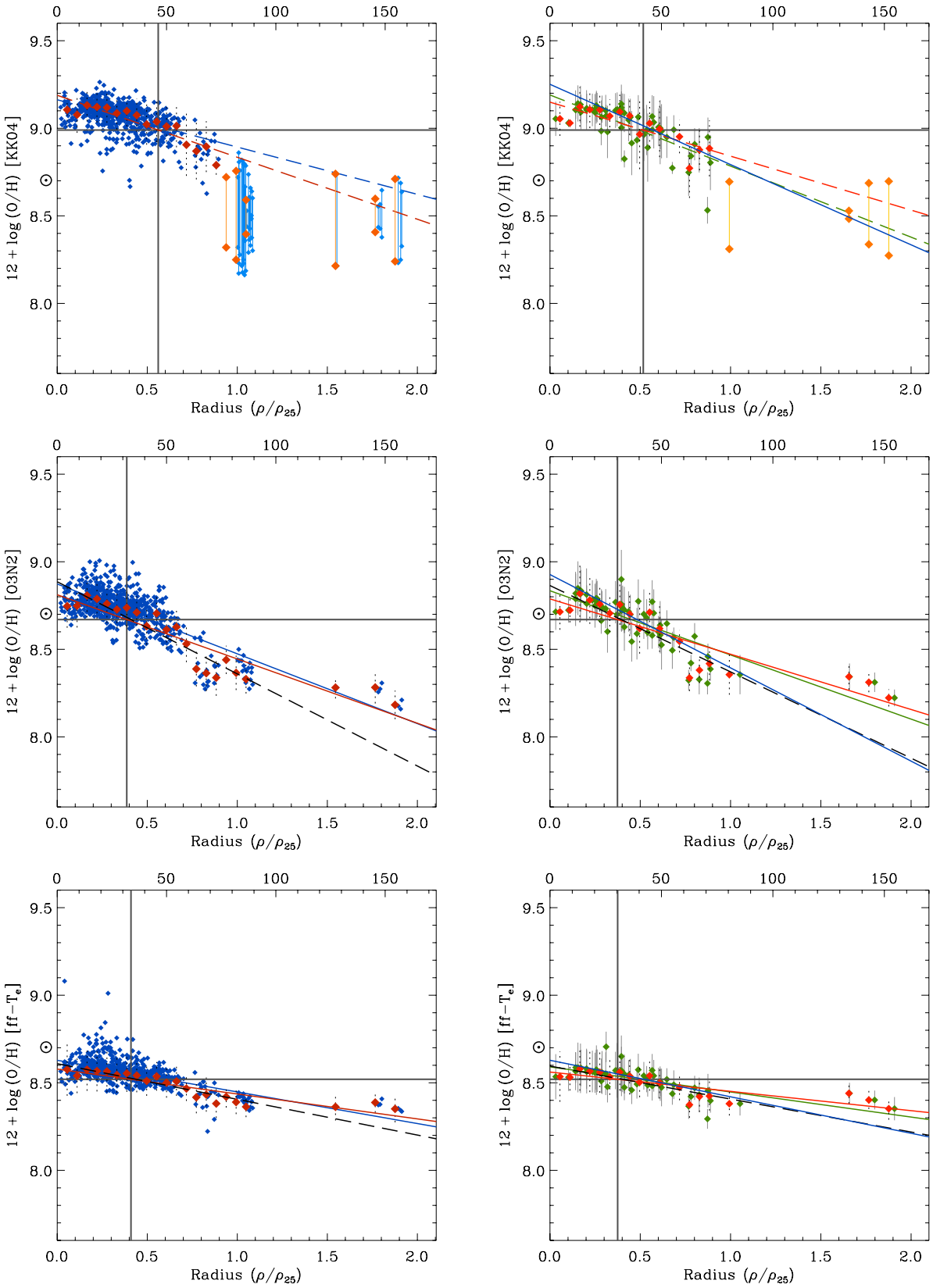

Figure 6.51: Radial abundance gradients for NGC 1058. The left column correspond to the *fibre-by-fibre* sample, the right column to the H II region catalogue. The red diamonds correspond to the radial average spectra obtained from each sample. The thick lines correspond to a linear least-squares fit to the corresponding data. The dashed-lines indicate the fit to only those pointings lying within the optical radius. The horizontal line corresponds to the metallicity value derived from the integrated spectrum, the vertical line to the intersection of this abundance with the radial average fit.

RADIAL ABUNDANCE GRADIENTS FOR NGC 1058

	KK04: *fibre-by-fibre*		KK04: H II region catalogue		
	All sample	*Radial*	*H II regions*	*Radial*	*Bright sample*
$12+\log(O/H)_{\rho=0}$	9.17 ± 0.01	9.19 ± 0.02	9.19 ± 0.03	9.15 ± 0.03	9.25 ± 0.04
$12+\log(O/H)_{\rho=0.4\rho_{25}}$	9.05 ± 0.01	9.05 ± 0.02	9.03 ± 0.03	9.03 ± 0.03	9.07 ± 0.04
$\log(O/H)_{(\text{dex } \rho_{25}^{-1})}$	-0.30 ± 0.02	-0.35 ± 0.05	-0.41 ± 0.05	-0.31 ± 0.06	-0.46 ± 0.06
$\log(O/H)_{(\text{dex kpc}^{-1})}$	-0.058 ± 0.003	-0.076 ± 0.010	-0.088 ± 0.011	-0.066 ± 0.013	-0.099 ± 0.014
	O3N2: *fibre-by-fibre*		O3N2: H II region catalogue		
	All sample	*Radial*	*H II regions*	*Radial*	*Bright sample*
$12+\log(O/H)_{\rho=0}$	8.87 ± 0.01	8.81 ± 0.03	8.83 ± 0.02	8.79 ± 0.03	8.93 ± 0.04
$12+\log(O/H)_{\rho=0.4\rho_{25}}$	8.71 ± 0.01	8.66 ± 0.03	8.69 ± 0.02	8.66 ± 0.03	8.71 ± 0.04
$\log(O/H)_{(\text{dex } \rho_{25}^{-1})}$	-0.40 ± 0.01	-0.37 ± 0.04	-0.37 ± 0.03	-0.32 ± 0.04	-0.53 ± 0.08
$\log(O/H)_{(\text{dex kpc}^{-1})}$	-0.086 ± 0.003	-0.079 ± 0.008	-0.079 ± 0.007	-0.068 ± 0.008	-0.115 ± 0.016
	ff–T_e: *fibre-by-fibre*		ff–T_e: H II region catalogue		
	All sample	*Radial*	*H II regions*	*Radial*	*Bright sample*
$12+\log(O/H)_{\rho=0}$	8.63 ± 0.01	8.58 ± 0.01	8.59 ± 0.01	8.56 ± 0.02	8.63 ± 0.02
$12+\log(O/H)_{\rho=0.4\rho_{25}}$	8.56 ± 0.01	8.52 ± 0.01	8.53 ± 0.01	8.52 ± 0.02	8.55 ± 0.02
$\log(O/H)_{(\text{dex } \rho_{25}^{-1})}$	-0.18 ± 0.01	-0.14 ± 0.02	-0.14 ± 0.02	-0.11 ± 0.02	-0.21 ± 0.03
$\log(O/H)_{(\text{dex kpc}^{-1})}$	-0.039 ± 0.002	-0.031 ± 0.003	-0.031 ± 0.004	-0.024 ± 0.004	-0.045 ± 0.006

Table 6.6: Results from the oxygen abundance gradient analysis of NGC 1058. Each block corresponds to a different calibrator, the columns are separated according to the different analysed samples. The rows correspond to: the central abundance at galactocentric radius $\rho = 0$; the *characteristic* abundance at $\rho = 0.4\rho_{25}$; and the slopes of the abundance gradients in units dex ρ_{25}^{-1} and dex kpc^{-1} respectively.

four individual regions were selected with $\rho/\rho_{25} > 0.9$, the choice of the R_{23} branch for these regions determine the global shape of the gradient. Again, selecting the upper branch for all these regions would be nearly consistent with the gradient derived for the radial average spectra (red dotted line). Selecting the lower branch metallicities would imply a break in the gradient with a flat distribution consistent with abundances $\sim$ 1/3 solar. However, (as it is also the case in the *fibre-by-fibre* sample), selecting the upper branch values for regions $\rho/\rho_{25} \sim 1.0$ and the lower branch metallicities for the outermost regions, would be consistent with the steeper gradient derived from the inner H II regions (green dotted-line). The blue line corresponds to the "bright" H II regions fitting introduced previously for NGC 628. The selected regions were N1058–5, 13, 16, 19, 30, 32, 40, 43, 44, 51, 52 and 58, from which the abundance gradient was calculated based on 6 regions randomly extracted over 100 realizations, as explained before. The "bright" sample fitting results in a steeper gradient than the derived from the full H II region sample and the radial average spectra. Contrary to previous cases, an arbitrary offset of the R_{23} has not been drawn for the sake of clarity.

The middle-panels of Figure 6.51 show the abundance gradients obtained after the *O3N2* method. Given that this calibrator is a monotonic function of the oxygen abundance, it does not suffer from the degeneracy of R_{23}, although it is limited by its sensitivity to the ionization. For both samples, inner regions at $\rho/\rho_{25} < 0.7$ are consistent with a steep gradient. However, for regions beyond $\rho = 0.7\rho_{25}$, the gra-

dient presents a break, dropping to nearly constant values 0.2 dex below the trend implied by the inner regions. The outermost regions beyond $\rho = 1.5\rho_{25}$ show even a lower metallicity consistent with values of 12 +log(O/H) = 8.3. The thick lines in each plot correspond to the linear fit of all the data, the black dotted-line indicates the fit to only those regions of the radial average sample within the optical radius ρ_{25}. The results from this calibrator support the idea of a break in the metallicity gradient of NGC 1058, with a bimodal chemical distribution consisting of a steep internal gradient for regions within the optical radius, with a discontinuity $\rho/\rho_{25} \sim 0.8$, and a shallower gradient for regions with larger galactocentric radius. In the case of the H II region catalogue, the linear fit to the"bright" sample (blue line) produces a steeper fit than the resulting from considering all the regions of the sample (which is expected since the outmost "bright" region is located at $\rho/\rho_{25} \sim 1.0$). On the other hand, the bottom-panels corresponding to the ff–T_e abundance determination, show a different picture. In the case of the *fibre-by-fibre* sample, for regions up to $\rho/\rho_{25} \sim 1.1$, the abundance gradient is consistent with a single, continuous, distribution with negative slope. Then, the metallicity distribution is consistent with a flat gradient with oxygen values 12 +log(O/H) = 8.4. No break in the metallicity gradient is seen from this sample and calibrator. In the case of the H II regions catalogue, a very similar behaviour is present, however there might be a small break on the oxygen abundance at $\rho/\rho_{25} \sim 0.8$ and then a flat gradient corresponding to 12 +log(O/H) = 8.4. An interesting feature present in both samples and in all calibrators is the break of metallicity at the innermost regions of the galaxy, i.e. $\rho/\rho_{25} \lesssim 0.15$. While in the case of NGC 628 the inner regions show a flattening of the metallicity gradient, in the case of NGC 1058 the analysis suggests a small discontinuity and a different central oxygen abundance that the suggested by the simple extrapolation of the outer gradient.

The horizontal lines in all the diagrams corresponds to the metallicity value derived from the integrated spectrum, the vertical line to the intersection of this abundance with the radial average fit. In the case of the KK04, the intersection occurs for radius $\rho/\rho_{25} \sim 0.5$, while for the other calibrators, the coincidence occurs at $\rho/\rho_{25} \sim 0.4$. The values of the derived gradients, central and characteristic oxygen abundances are presented in Table 6.6. The radial abundance variations discussed above show the importance of the outermost regions on determining the real chemical distribution and gradient slope for this galaxy. In the first case, the ambiguity on the abundance determination due to the degeneracy of R_{23} leave us with two possibilities: 1) the radial abundance gradient of NGC 1058 is consistent with a log–linear relationship; 2) the abundance gradient shows a discontinuity at $\rho/\rho_{25} \sim 0.9$, with a flat gradient for larger radii. In the second case, the $O3N2$ calibrator suggests a break in the abundance gradient, but of lower extend than the implied by KK04, with a shallow, almost flat gradient for radii larger than $\rho/\rho_{25} \sim 0.8$. The last considered calibrator suggests a log-linear relationship for radii $\rho/\rho_{25} \lesssim 1.1$, changing to flat distribution without a discontinuity.

Pilyugin (2003) has suggested that the observed bends in the abundance gradient of a galaxy can be an artificial effect as a result of the incorrect choice of the R_{23} branch from a certain galactocentric distance, or as due to a bend in the radial trend of the ionization. In the case of NGC 1058, we demonstrated above that the choice of different R_{23} branches can lead to different interpretations of the gradient. On the other hand, NGC 1058 does show a bend in the radial trend of the ionization for $\rho/\rho_{25} \sim 0.9$ (see Figure 6.50). As the $O3N2$ calibrator is very sensible to this parameter, the gradient "break" suggested by this indicator may be an artifact produced by the drastic change in the ionization for the outer regions. However, all three different calibrators suggest a bi-modality of the chemical radial distribution, possibly consistent with a flat gradient for radii larger than the optical radius. Recently, Bresolin et al. (2009) observed a flat oxygen abundance gradient and a drop in abundance beyond the ρ_{25} isophotal radius of M83. The result was confirmed by a

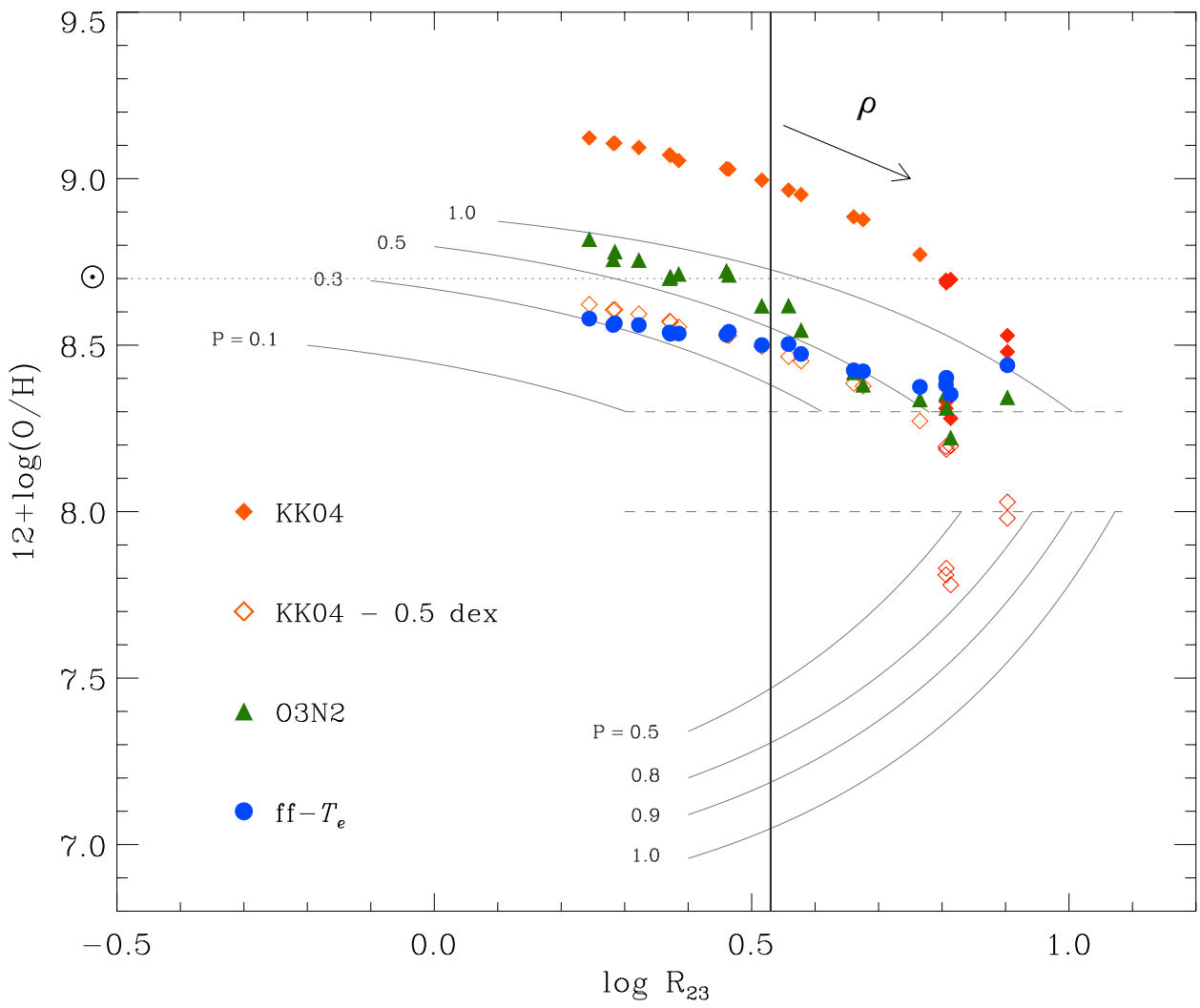

Figure 6.52: 12 + log(O/H) vs. log R_{23} diagram for the H II region radial average spectra of NGC 1058 for the selected metallicity indicators. The arrow shows the direction of increasing galactocentric radius. For the four outermost regions of the KK04 calibrator (red-diamonds), the low-branch values are also drawn. Note the agreement between the KK04 offset and the ff–T_e values. The vertical line shows the value of log R_{23} derived from the integrated spectrum.

wide range of abundance indicators and tests considering the impact of different ionizations at larger radii. The definite existence and interpretation of these features is still a matter of debate. In the case of NGC 1058, the given intrinsic errors in the abundance determination by using strong line methods the low number of observed outer regions, it might not be possible to assess yet the existence and significance of these features.

A previous abundance gradient determination of this galaxy was performed by FGW98, considering 8 H II regions, 4 of them with $\rho/\rho_{25} > 1.0$, employing the lower-branch calibration of R_{23} for these outer regions. They found a gradient consistent with a log–linear relationship with a slope –0.55 ± 0.11 dex ρ_{25}^{-1}. By assuming the same choice of the R_{23} branch for those regions, the slope derived from this work is –0.48 ± 0.05 dex ρ_{25}^{-1}. On the other hand, the gradient obtained by FGW98 using only those regions within the optical radius was –0.30 ± 0.14 dex ρ_{25}^{-1}, while the result from this work is –0.31 ± 0.06 dex ρ_{25}^{-1}, based in the radial average spectra of the H II regions.

Figure 6.52 shows the O/H vs. R_{23} relation for the radial average values obtained from the H II region catalogue. The vertical line corresponds to the value of R_{23} derived from the integrated spectrum. Increasing

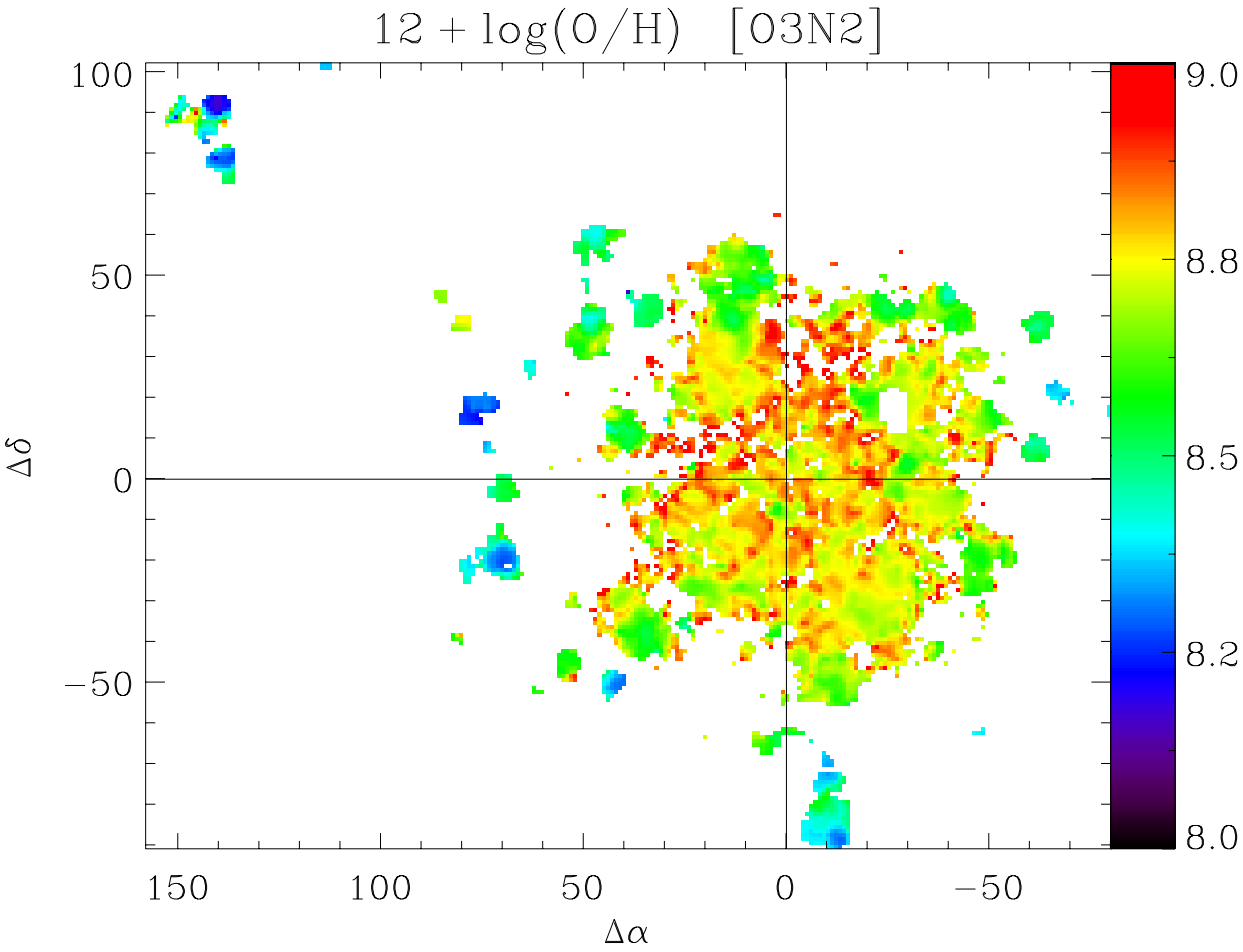

Figure 6.53: Oxygen abundance map of NGC 1058 derived by applying the *O3N2* calibrator to the emission line maps of the galaxy.

values of R_{23} correspond to increasing galactocentric distance, as indicated by the arrow. A notorious drop of the oxygen value is seen for the *O3N2* calibrator for $\log R_{23} > 0.6$. The four outlying regions with ambiguous R_{23} branches are shown as red diamonds for the KK04 case. An arbitrary –0.5 dex is also shown for the KK04 calibration. Note that the upper branch of this offset coincides nearly with the O/H values derived from the ff–T_e relation. Finally, in Figure 6.53 I present the oxygen abundance map of NGC 1058 derived from the *O3N2* calibrator. The map reflects the pattern shown by the previous abundance gradient plots. The most metal deficient regions are clearly identified at the outer part of the galaxy, including the outlying regions at the top-left corner. The average value of the oxygen abundance derived from this map is $12 + \log(\mathrm{O/H}) = 8.71 \pm 0.15$, which is in agreement with the value obtained from the integrated spectrum (8.67 ± 0.11).

Discussion

A spectroscopic analysis of NGC 1058 based on the IFS observations of this dissertation has been presented in this section. A combined methodology based on point-by-point spectra and selected H II regions was employed in order to describe the main physical parameters of the galaxy. In general, both samples are

consistent in a statistical basis, with a much lower level of scatter corresponding to the H II region sample, as expected. Azimuthally-averaged radial spectra was extracted from consecutive annulus of 5 arcsec for both samples, the distribution of the emission line ratios, metal content and ionization traced by these spectra follows the trends of the corresponding samples to a very good extent, and can be considered completely representative of the radial distribution of physical properties of the galaxy.

From the analysis of the radial variation of the physical properties it was found that the strength of the [O II] and (especially) [O III] emission lines increases with galactocentric radius, consistent with R_{23} values corresponding to the upper branch for the majority of the inner regions, but with outlying regions falling into the ill-defined transition zone between the branches of the R_{23} relation. The degree of ionization is nearly constant over the whole surface of the galaxy with a sharp increase for $\rho/\rho_{25} \gtrsim 0.8$. The radial distribution of the chemical abundance was derived using three different calibrators. Given the ambiguity on the R_{23} values for the outlying regions, no definite gradient was obtained from the KK04 indicator, however a small drop of the metallicity is seen for the innermost regions of the galaxy. The use of the $O3N2$ method showed features of a multi-modality in the chemical gradient, but in the case of the outer regions it is probably a fictitious effect due to the raise of the ionization and the sensitivity of this indicator to this parameter, however the break in metallicity for the innermost regions is also derived through this method. The ff–T_e relation suggested a log–linear relationship for the inner optical disk of the galaxy, and a flat gradient for larger radii based on the *fibre-by-fibre* sample. The flat outer gradient is more evident by using the H II regions sample, from which a discontinuity in the metallicity at the lowest galactocentric radius is present, consistent with a fall in the derived abundance of ~ 0.5 dex. The lack of observed H II regions (especially at the outskirts of this galaxy) prevented any firm conclusion regarding the true nature of the metallicity gradient, although the analysis of NGC 1058 shows evidence of a non-linear *multi-modal* abundance gradients, giving support to recent observational results that suggest the existence of a multiple components of the abundance gradients of spiral galaxies. This possibility will be discussed further after considering the analysis of NGC 3184, in the next section. As a consistency test, the derived gradients were compared with previously published works, by making the same assumptions in terms of galactocentric baselines and R_{23} branches, finding an excellent agreement.

6.5 NGC 3184

NGC 3184 is the second largest object of the sample, the *clean* mosaic of this galaxy consists of 3645 fibres, number which might seem low considering the large area covered by the observations; however, the observations for this galaxy were performed in non-dithering mode, and with non-optimum observing conditions, reducing the number of reasonable good quality spectra. At the assumed distance of this galaxy (11.1 Mpc), the physical size of the aperture of one PPAK fibre corresponds to 144.7 pc. Figure 6.54 shows the sample selection histograms for this galaxy and the number of fibres selected after each criteria step. In the case of the *fibre-by-fibre* sample (top-three panels), after the first selection criteria (detection of Hβ and [O III] λ4959) the number of fibres was reduced to 1923; 1861 spectra showed finite values of the derived c(Hβ) (second selection criteria), and only 290 fibres were selected after applying the Hβ flux limit cut (8 $\times 10^{-16}$ erg s^{-1} cm^{-2}), corresponding to only $\sim 8\%$ of the number of fibres in the *clean* mosaic, and $\sim 5\%$ of the total number of observed spectra.

The Hα/Hβ ratio histograms of the first two selection criteria show a broad distribution centered at the theoretical value, however, the flux cut eliminates most of the spectra with values lower than ~ 3, yielding

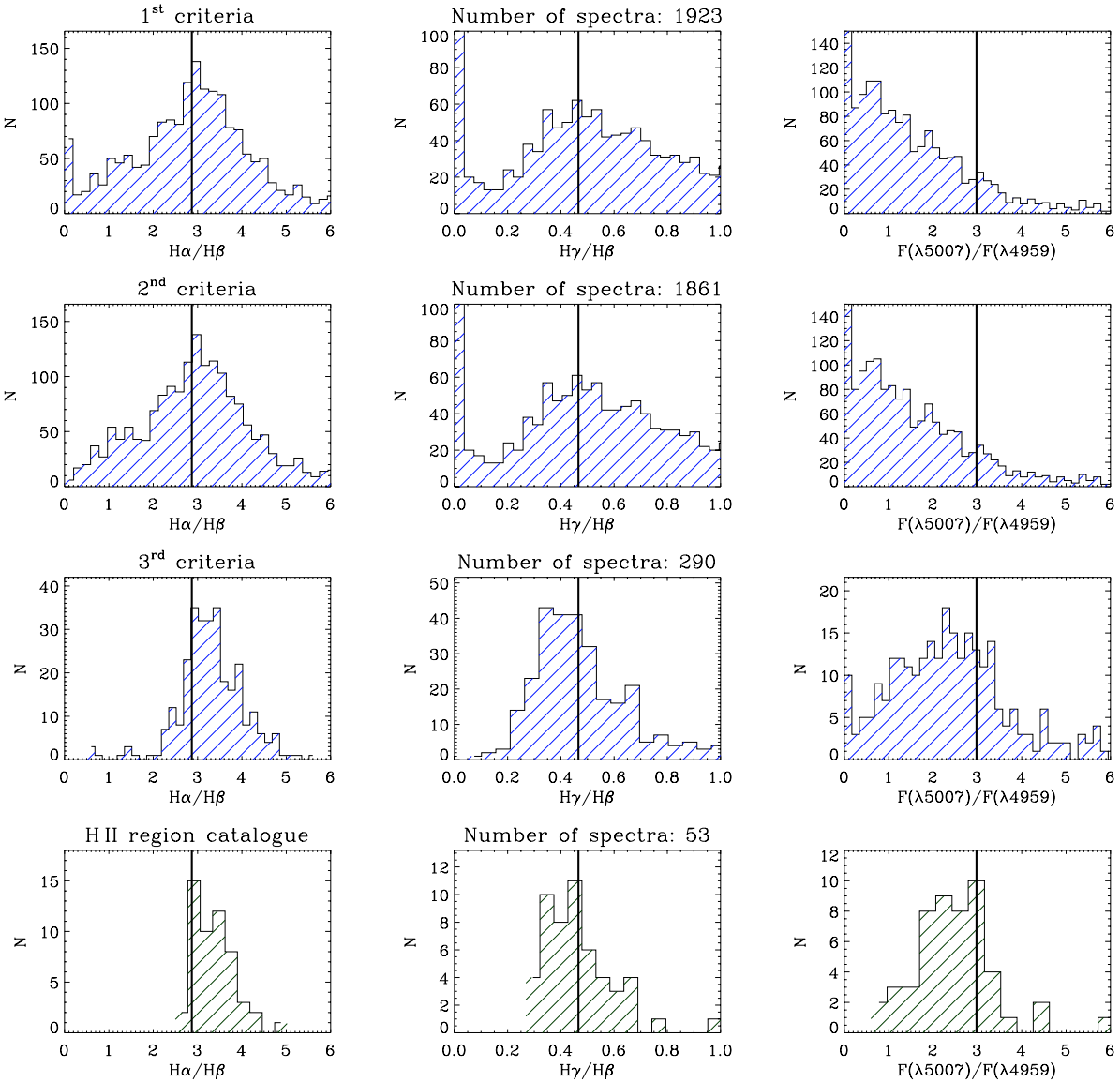

Figure 6.54: Selection criteria histograms for NGC 3184. Top three rows correspond to the *fibre-by-fibre* analysis, the bottom row to the H II region catalogue. In each panel, the vertical line correspond to the theoretical value of the given line ratio.

a distribution consistent with physical reddened spectra, with a small tail of values below 3. The Hγ/Hβ ratio histograms show a large number of spectra consistent with nearly null Hγ values. After the flux threshold has been applied, the distribution is consistent with that of the Hα/Hβ ratio. The [O III] ratio histograms show a large number of values lower than the theoretical one, even for the final sample. A preliminary visual inspection of the data reveals that most of the galaxy spectra present very weak emission in the [O III] lines, even for the outer regions of the galaxy. Therefore, the large distribution of [O III] ratios measured below the theoretical ratio can be explained due to the errors introduced by the automated stellar continuum subtraction.

The second spectral sample consists of the H II region catalogue selected for this galaxy. A total number of 53 H II regions were selected from the *clean* mosaic of NGC 3184. Figure 6.55 shows the spatial distribution of these regions, with their identification number and the equivalent/real extraction apertures. The coordinates, offsets, sizes and number of fibres co-added for each H II region can be found in Appendix D.

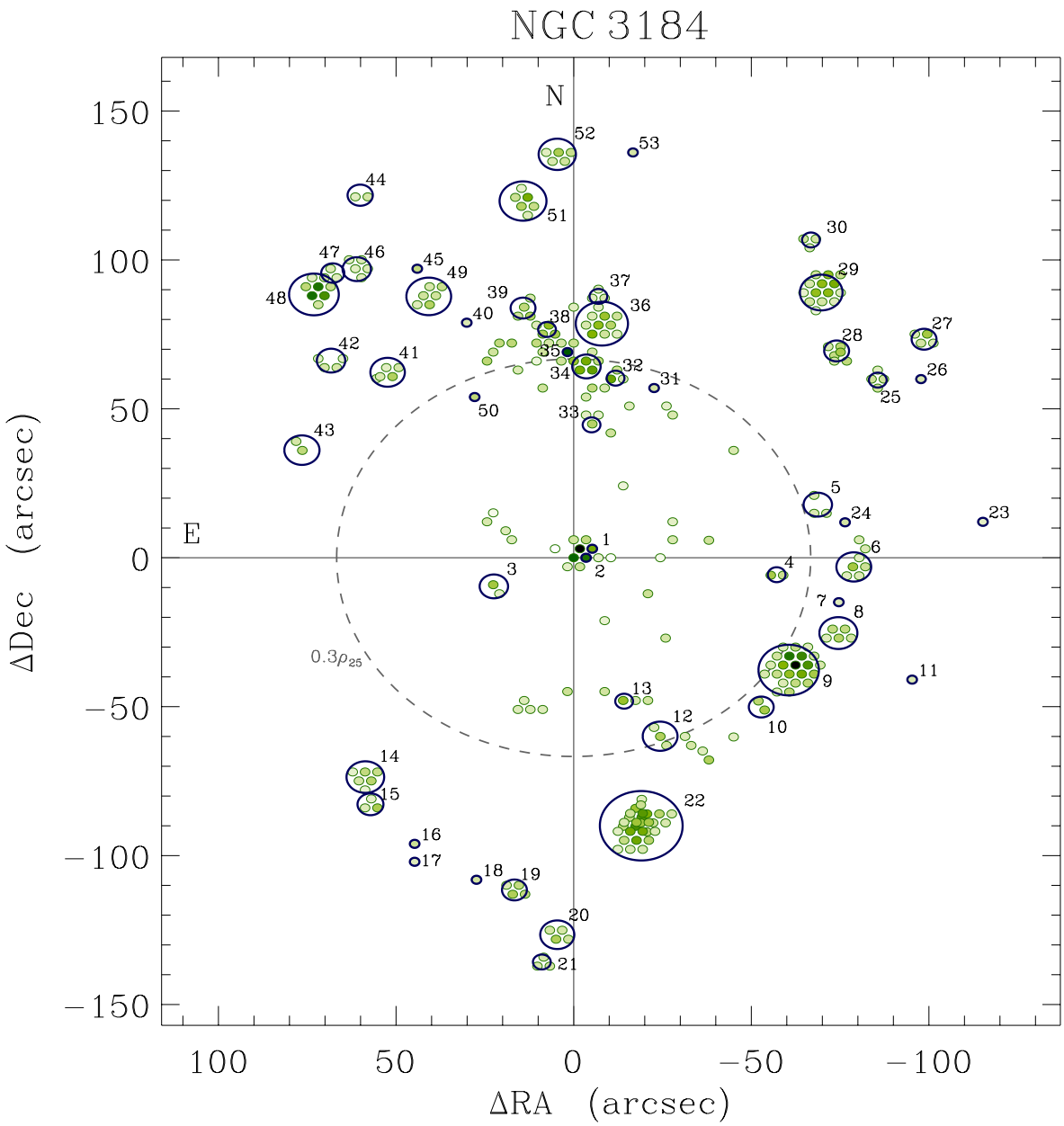

Figure 6.55: Spatial location and identification of the selected H II regions for NGC 3184. The background fibres correspond to the *fibre-by-fibre* sample, with colour intensities scaled to the flux of the Hα emission. The circles correspond to an equivalent aperture radius. The dotted-line circle corresponds to the radius $\rho = 0.3\rho_{25}$, discussed in the text.

The distribution of the H II regions follows practically the spiral arms of the galaxy, only three regions with significant signal-to-noise were found in the central part of the galaxy. The background fibres drawn in Figure 6.55 correspond to the final *fibre-by-fibre* sample, as in previous cases. Although there are many fibres in the intra-arms regions, individual inspection of the spectra contained in those fibres did not show enough signal-to-noise to be considered as well-defined H II region.

The bottom panels of Figure 6.54 show the distribution of the control line ratios for the H II region catalogue sample. The Hα/Hβ histograms shows practically no spectra with values lower than the theoretical ratio, and it is consistent with a reddened spectral sample. The Hγ/Hβ ratio shows also a well-behaved distribution, with some spectra corresponding to a non-physical extinction, as it could be expected given

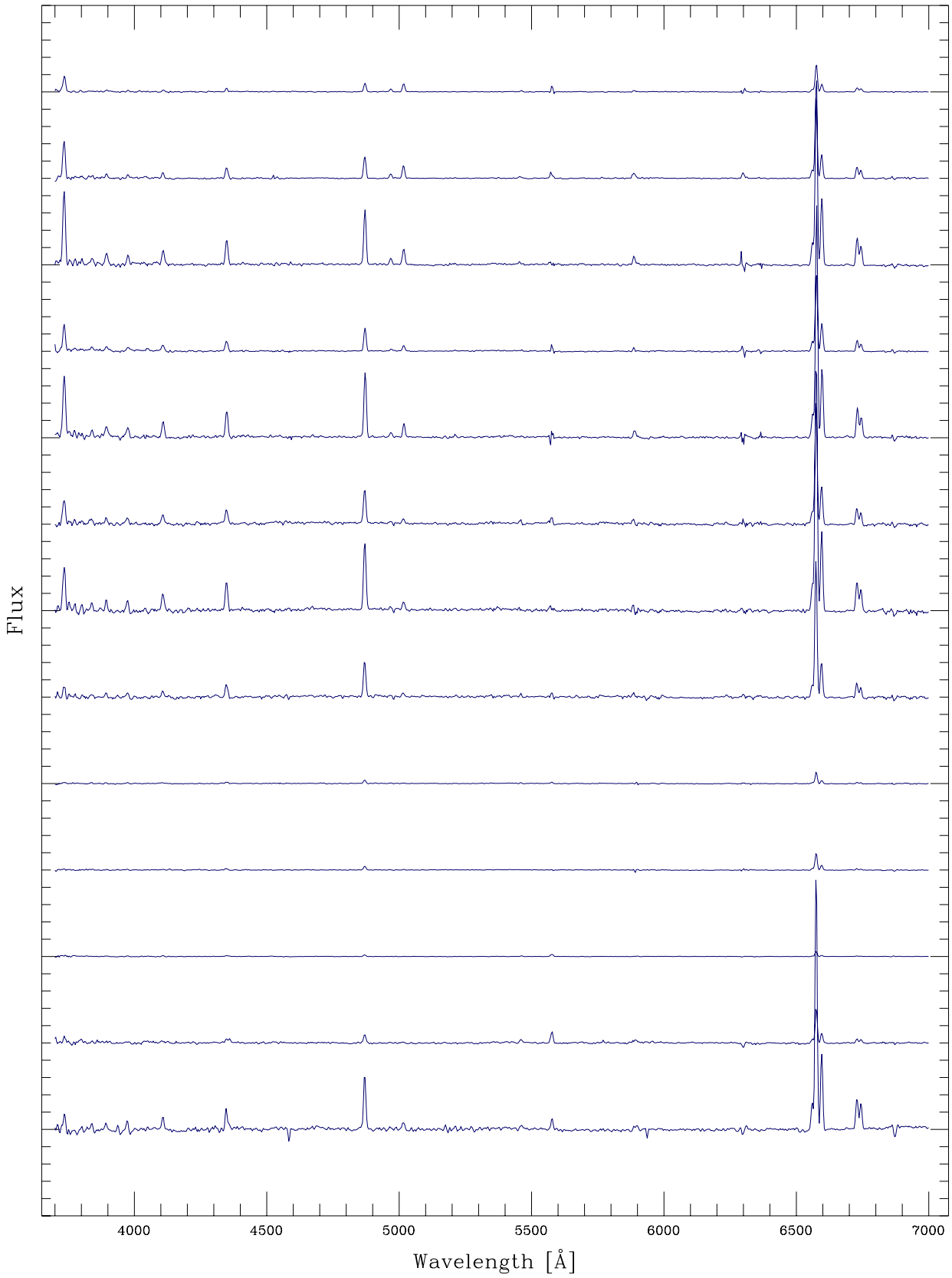

Figure 6.56: Radial average spectra of NGC 3184 extracted from the *fibre-by-fibre* sample, in arbitrary flux units. The galactocentric radius increases from the bottom to the top of the figure.

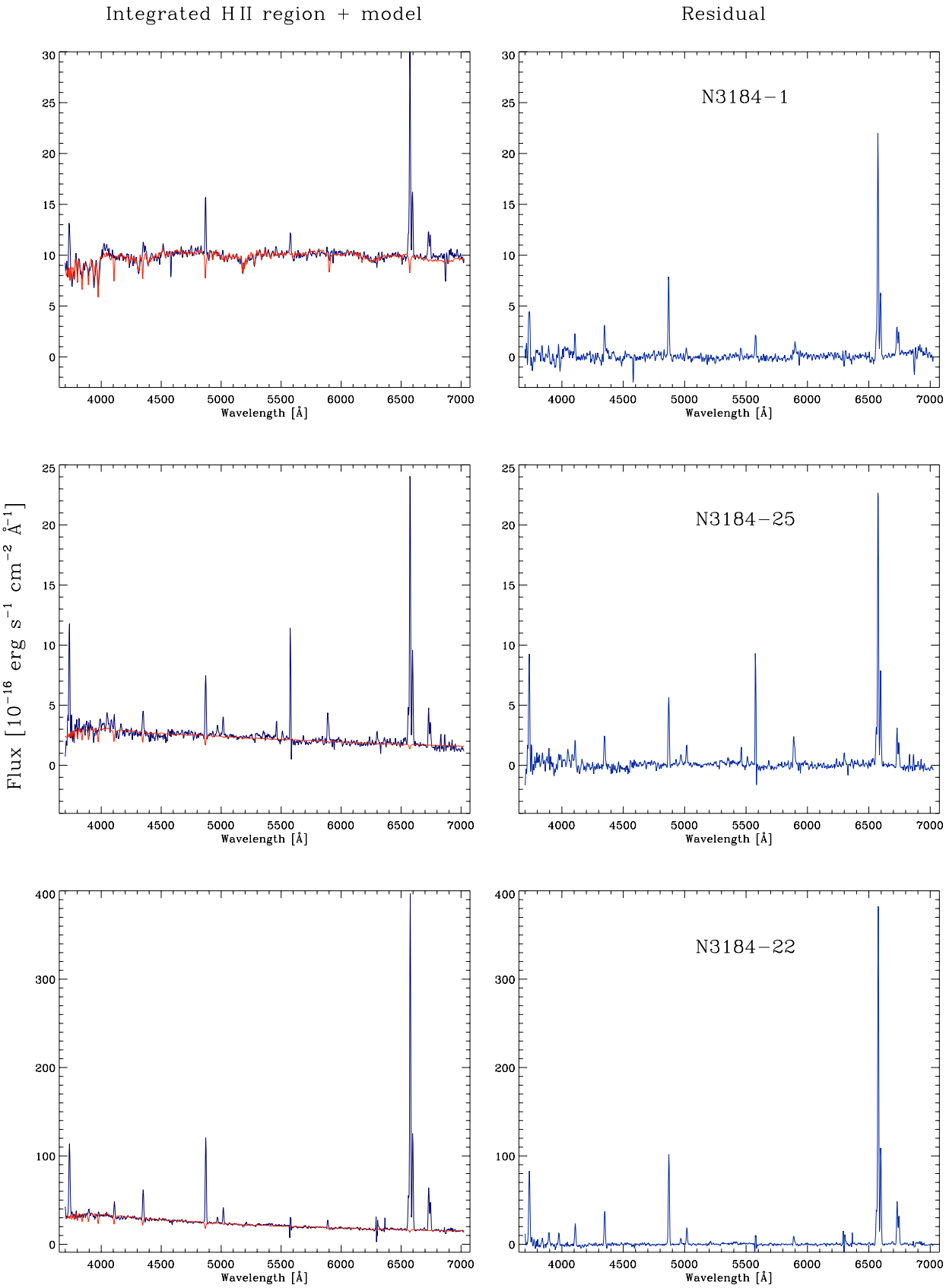

Figure 6.57: Examples of spectra of NGC 3184 extracted from the H II region catalogue. The left column corresponds to the observed integrated spectrum, plus the SSP fit model overlaid as a red line, the right column shows the residual spectrum. The label corresponds to the ID of the H II region.

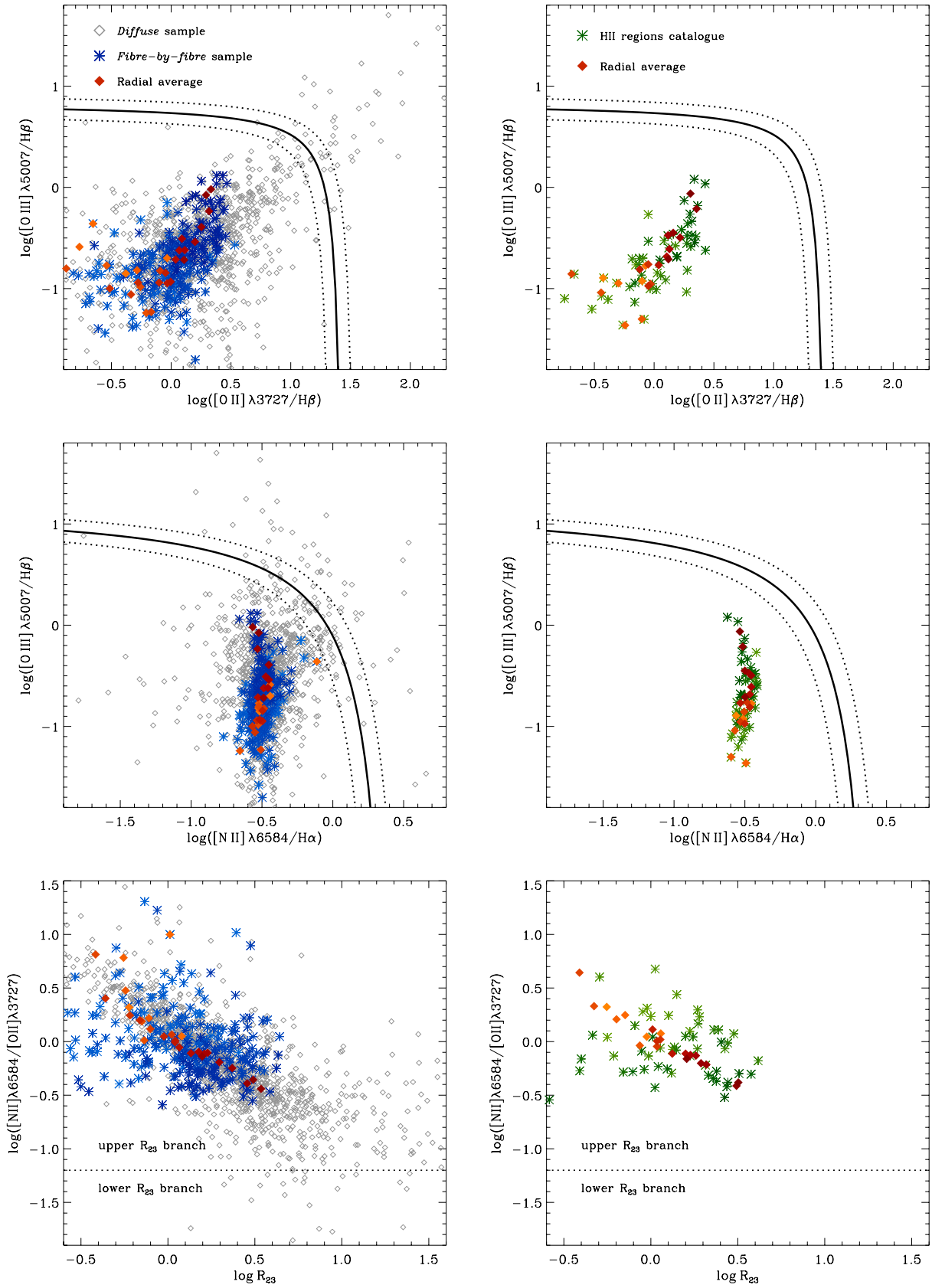

Figure 6.58: Diagnostic diagrams for NGC 3184. The left column correspond to the *fibre-by-fibre* sample, the right column to the H II region catalogue. The filled-diamonds correspond to the azimuthally-averaged radial values. Lighter/darker tones correspond to inner/outer regions of the galaxy, in terms of the galactocentric radius.

the low strength of the line and the problems with the continuum subtraction. In the case of the [O III] ratio, the distribution is concentrated at the theoretical value and at lower values, for the reasons given above. Figure 6.56 shows examples of radial average spectra of NGC 3184 extracted from the *fibre-by-fibre* sample, in arbitrary flux units, with galactocentric radius increasing from the bottom to the top of the figure. On the other hand, Figure 6.57 shows examples of three H II regions of intrinsically different signal-to-noise. For each H II region, the left panel corresponds to the observed integrated spectrum within the aperture and the SSP fit model overlaid, the right panel shows the residual spectrum from which the emission line intensities were calculated.

Figure 6.58 shows the selected diagnostic diagrams for NGC 3184, based on the the reddening corrected spectra of both samples. As in previous cases, the lighter colours correspond to spectra belonging to the inner regions of the galaxy, and darker tones to the outer parts. Azimuthally-averaged radial spectra were obtained for both samples by co-adding the spectra within consecutive annulus of 5 arcsec. The results from these spectra are shown as full reddish diamonds on top of the main data for both samples. The [O III]/Hβ vs. [O II]/Hβ plots show that low values of these ratios are consistent with the inner regions of the galaxy, the strength of both the [O II] and [O III] lines increase with galactocentric distance, although the log([O II]/Hβ) and log([O III]/Hβ) ratios are consistent with values lower than ~ 0.0 and 0.5 respectively, across the whole surface of the galaxy. As in the case of NGC 628, inner regions are consistent with a nearly constant value of log([O III]/Hβ) $\sim$ –1.0, which is more evident in the H II region catalogue sample. Both line ratios show variations of more than one order of magnitude between the sampled regions.

The middle-panels of Figure 6.58 present the [O III]/Hβ vs. [N II]/Hα diagnostic diagrams. The increase of [O III]/Hβ discussed previously is evident in this diagram, but both the *fibre-by-fibre* and H II regions samples show the same nearly constant value of the [N II]/Hα ratio across the galaxy, consistent with log([N II]/Hα) $\sim$ –0.5, a very small decrement of this ratio is seen for the outermost regions of the galaxy. The [N II]/[O II] vs. R_{23} diagrams in the bottom panels of the same figure show that the R_{23} values of all the spectra in both samples are consistent with the upper branch of the R_{23} relation. The individual data points in both samples show some level of scatter, but still consistent with a negative correlation between [N II]/[O II] and R_{23}, this latter increasing in value with galactocentric radius. On the other hand, the radial trends are consistent with a very narrow linear correlation correlation for both samples, with minimum values of the log([N II]/[O II]) ratio $\sim$ –0.5, well above the threshold limit between the upper and lower branch defined by this relation. As in the previous cases, the trends showed by the diagnostic diagrams of the *fibre-by-fibre* sample and those of the H II region catalogue are comparable, with larger scatter for the former case.

Figure 6.59 shows the radial variation of the R_{23} indicator (top-panels), ionization parameter $\log u$ (middle-panels) and the [N II] λ6584/Hα ratio (bottom-panels) for NGC 3184. As mentioned before, few regions in both samples (especially for the H II region catalogue) are found for regions within $\rho/\rho_{25} \lesssim 0.2$, therefore the trends for those very inner regions are subject to a low-number statistics. In the case of the R_{23} indicator, the *fibre-by-fibre* sample is consistent with a flat distribution up to $\rho/\rho_{25} \sim 0.3$ (with a lot of scatter), where it then raises up to the values $\log R_{23} \sim 0.5$. A similar trend is shown by the H II region catalogue. The value of R_{23} derived from the integrated spectrum matches the point-by-point variation at $\rho/\rho_{25} \sim 0.45$ in both cases. As suggested by the [N II]/[O II] diagnostic diagram, the values of R_{23} correspond to the upper branch of the relation, therefore, the increase of R_{23} as a function of radius is consistent with a negative metallicity gradient, as expected.

In the case of the *fibre-by-fibre* sample, the panel corresponding to the radial variation of the ionization

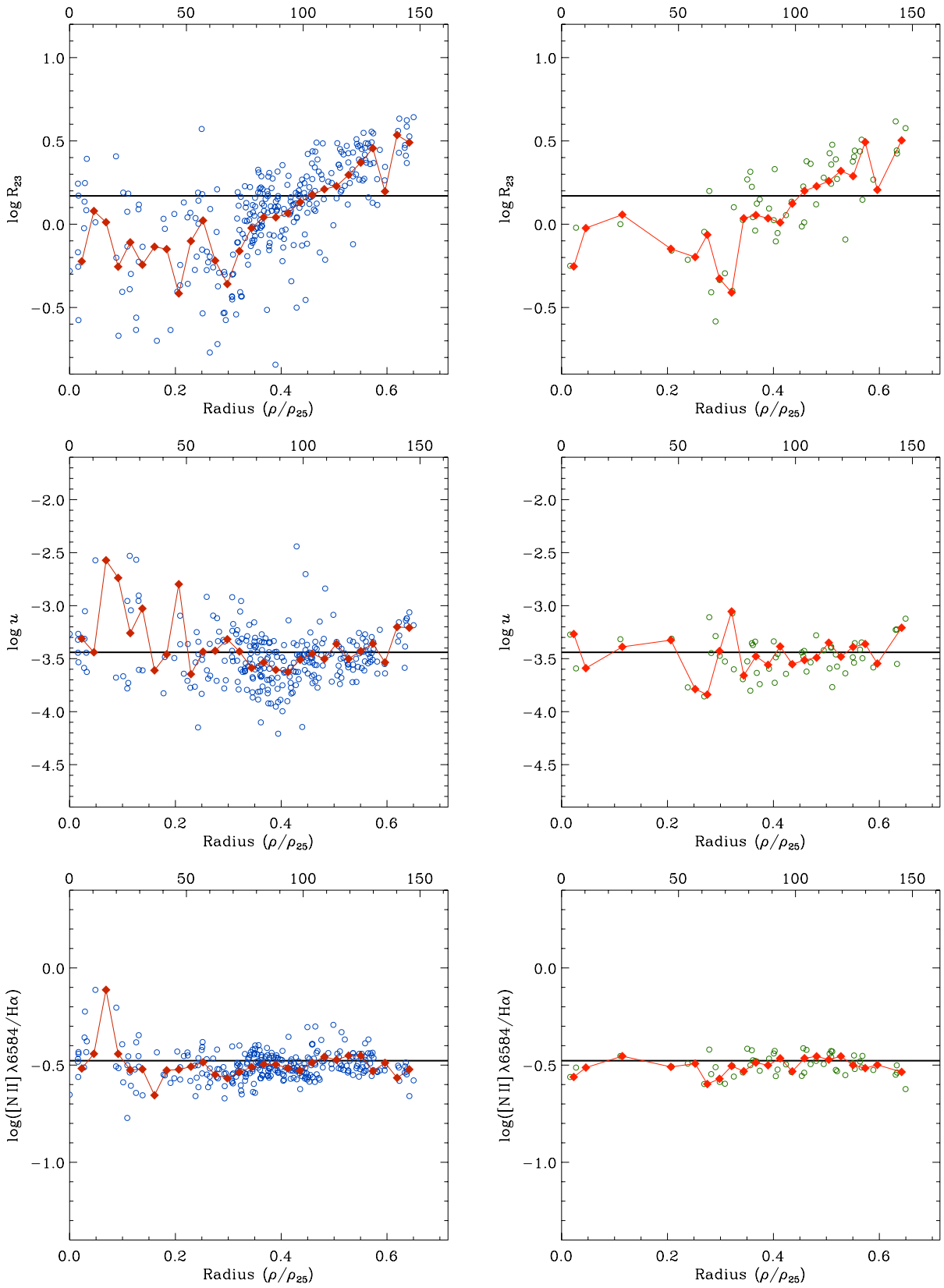

Figure 6.59: Radial variation of selected physical properties of NGC 3184. The left column correspond to the *fibre-by-fibre* sample, the right column to the H II region catalogue. In both cases, the position of the circles correspond to the deprojected galactocentric radius, normalised to the optical size of the galaxy. The top X-axes values correspond to the projected size in arcsec. The horizontal lines correspond to the values derived from the integrated spectrum of the galaxy.

parameter shows a lot of scatter for the inner regions, with probably slightly higher values of the ionization for $\rho/\rho_{25} \sim 0.2$, dropping to a constant value for larger radii, equivalent to $\log u \sim -3.5$. In the case of the H II region catalogue, the selected innermost regions are consistent with an ionization parameter constant along the different radii covered by the data, showing a much lower level of scatter. The integrated value of the ionization parameter is consistent with this flat distribution. The panels corresponding to the radial variation of the N_2H_α ratio show a very similar picture, a completely flat distribution for all radii in both samples. Therefore, the radial distributions of both the ionization parameter and the N_2H_α ratio imply a constant ionization over the surface of the galaxy, without prominent changes at any galactocentric radius $\rho/\rho_{25} \lesssim 0.6$.

Given that the IFS observations of NGC 3184 only cover regions within $0.7\rho_{25}$, we can just analyse the inner abundance gradient of the galaxy. This is presented for the different selected metallicity indicators in Figure 6.60. The top-panels show the gradients derived by the KK04 calibrator, with the *fibre-by-fibre* sample in the left-panel, and the H II region catalogue in the right-panel. The red diamonds correspond to the results from the radial average spectra obtained for each sample. As implied by the previous diagrams, the radial metallicity distribution is consistent with negative gradient. The majority of the sampled regions in both cases are located between $0.25 \lesssim \rho/\rho_{25} \lesssim 0.65$, showing a steep declining gradient. However, for regions $\rho/\rho_{25} \lesssim 0.3$, there seems to be a flattening of the gradient, with even a possible change of sign. This effect is clearly seen in the open-symbol data shown on the same diagram, corresponding to an arbitrary offset of –0.5 dex to the KK04 calibration. This "break" in the metallicity gradient is also present in the data corresponding to the H II region catalogue (top-right panel).

A similar behaviour is found by using the $O3N2$ indicator, where the steep "outer" gradient changes to a flat distribution for $\rho/\rho_{25} \lesssim 0.3$, consistent with a constant value $12 + \log(\mathrm{O/H}) \sim 8.85$, in both samples. The scenario is different for the ff-T_e method, the left-bottom panel of Figure 6.60 shows the gradient derived from the *fibre-by-fibre* sample. A similar steep "outer" gradient is present for radii greater than $\rho/\rho_{25} \gtrsim 0.3$, with a very narrow trend, considering that this sample is more prone to scatter due to the relatively low signal-to-noise of the data. However, the picture changes for the inner radii, at $\rho \sim 0.3\rho_{25}$, the metallicity values derived for the located at this radius show a large scatter, raising to values greater than $12 + \log(\mathrm{O/H}) \sim 9.1$. The reason for these high variations in the abundance determination may reside in the intrinsic signal-to-noise of the data. Nevertheless, inner regions are still consistent (in average) with a flat gradient $12 + \log(\mathrm{O/H}) \sim 8.6$. A similar trend is shown by the H II region sample. Two H II regions (one radial data point) are clearly outliers, coinciding with the region of high scatter of the previous sample. A flat, even decreasing gradient with diminishing radius could be inferred from the inner regions, *except* that for the existence of the innermost H II region of the sample, which shows a higher abundance and it is consistent with the general trend of the "outer" gradient.

Due to the existence of radial abundance gradients in the discs of spiral galaxies, it is assumed that the maximum oxygen abundance is found at the centres of these objects. NGC 3184 had been classified as one of the oxygen-richest galaxies, with a central oxygen abundance $(\mathrm{O/H})_{\rho_0} = 9.55$ (Z94) and 9.50 (van Zee et al., 1998, using a modified version of the M91 calibrator). These high central oxygen values were derived given the very steep gradients found in those studies for this galaxy, corresponding to –0.92 and –0.78 dex ρ_{25}^{-1}, respectively. Pilyugin et al. (2006) obtained $(\mathrm{O/H})_{\mathrm{ff}}$ abundances for this galaxy from a compilation of those published spectra, deriving an oxygen central abundance $(\mathrm{O/H})_{\rho_0} = 8.73$, with a much shallower slope, –0.42 dex ρ_{25}^{-1}. These authors argue that the previously derived high values of the central abundances in spiral galaxies are an artifact due to the non-reliability of empirical abundance calibrators

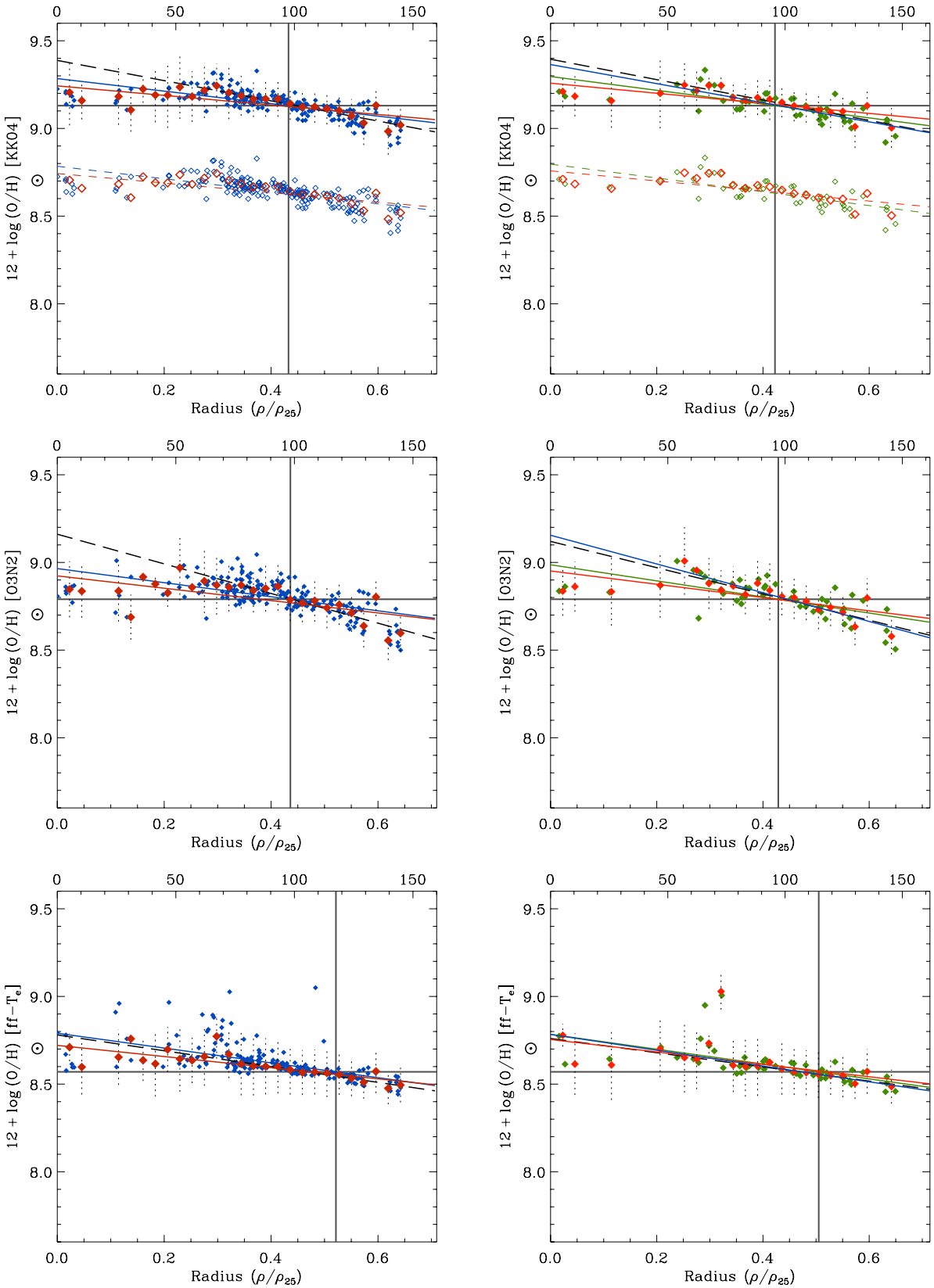

Figure 6.60: Radial abundance gradients for NGC 3184. Similar colour-coding as previous abundance diagrams. The thick lines correspond to a linear least-squares fit to the corresponding data. The black dashed-lines indicate the fit to only those pointings beyond $\rho = 0.3\rho_{25}$. The blue lines correspond to the "bright" sample fitting. The horizontal line corresponds to the metallicity value derived from the integrated spectrum, the vertical line to the intersection of this abundance with the radial average fit. For the KK04 calibrator, the open circles correspond to an arbitrary offset of –0.5 dex.

RADIAL ABUNDANCE GRADIENTS FOR NGC 3184

	KK04: *fibre-by-fibre*		KK04: H II region catalogue		
	All sample	*Radial*	*H II regions*	*Radial*	*Bright sample*
$12+\log(O/H)_{\rho=0}$	9.28 ± 0.01	9.24 ± 0.02	9.30 ± 0.02	9.26 ± 0.02	9.36 ± 0.09
$12+\log(O/H)_{\rho=0.4\rho_{25}}$	9.14 ± 0.01	9.13 ± 0.02	9.14 ± 0.02	9.14 ± 0.02	9.15 ± 0.09
$\log(O/H)_{(\text{dex } \rho_{25}^{-1})}$	-0.36 ± 0.03	-0.27 ± 0.05	-0.39 ± 0.06	-0.29 ± 0.06	-0.54 ± 0.17
$\log(O/H)_{(\text{dex kpc}^{-1})}$	-0.030 ± 0.002	-0.023 ± 0.004	-0.033 ± 0.005	-0.024 ± 0.005	-0.046 ± 0.015
	O3N2: *fibre-by-fibre*		O3N2: H II region catalogue		
	All sample	*Radial*	*H II regions*	*Radial*	*Bright sample*
$12+\log(O/H)_{\rho=0}$	8.96 ± 0.02	8.92 ± 0.03	8.99 ± 0.03	8.95 ± 0.04	9.16 ± 0.13
$12+\log(O/H)_{\rho=0.4\rho_{25}}$	8.80 ± 0.02	8.78 ± 0.03	8.80 ± 0.03	8.80 ± 0.04	8.83 ± 0.13
$\log(O/H)_{(\text{dex } \rho_{25}^{-1})}$	-0.40 ± 0.04	-0.35 ± 0.09	-0.46 ± 0.07	-0.38 ± 0.10	-0.82 ± 0.25
$\log(O/H)_{(\text{dex kpc}^{-1})}$	-0.034 ± 0.004	-0.030 ± 0.007	-0.038 ± 0.006	-0.032 ± 0.008	-0.069 ± 0.021
	ff–T_e: *fibre-by-fibre*		ff–T_e: H II region catalogue		
	All sample	*Radial*	*H II regions*	*Radial*	*Bright sample*
$12+\log(O/H)_{\rho=0}$	8.79 ± 0.02	8.72 ± 0.02	8.78 ± 0.03	8.75 ± 0.05	8.78 ± 0.06
$12+\log(O/H)_{\rho=0.4\rho_{25}}$	8.62 ± 0.02	8.59 ± 0.02	8.61 ± 0.03	8.61 ± 0.05	8.60 ± 0.06
$\log(O/H)_{(\text{dex } \rho_{25}^{-1})}$	-0.42 ± 0.04	-0.32 ± 0.05	-0.42 ± 0.08	-0.35 ± 0.13	-0.45 ± 0.11
$\log(O/H)_{(\text{dex kpc}^{-1})}$	-0.035 ± 0.004	-0.027 ± 0.005	-0.036 ± 0.006	-0.030 ± 0.011	-0.038 ± 0.009

Table 6.7: Results from the oxygen abundance gradient analysis of NGC 3184. Each block corresponds to a different calibrator, the columns are separated according to the different analysed samples. The rows correspond to: the central abundance at galactocentric radius $\rho = 0$; the *characteristic* abundance at $\rho = 0.4\rho_{25}$; and the slopes of the abundance gradients in units dex ρ_{25}^{-1} and dex kpc^{-1} respectively.

based on photoionization models in the high-metallicity regime, and that there is an upper limit to the oxygen abundance in spiral galaxies consistent with $12+\log(O/H) \sim 8.75$.

However, all previous published spectra for this galaxy (including early observations by McCall et al. 1985), did not include observations of regions with galactocentric radius $\rho < 0.3\rho_{25}$. The data presented in this dissertation sample for the first time the innermost regions of this galaxy. The thick colour lines in each diagram correspond to a least-squares linear fit to the data, considering all the regions of the corresponding sample (as in previous cases). The black dotted-lines correspond to the linear fit of the data, but considering only those regions with radii greater than $0.3\rho_{25}$. In the case of the KK04 calibrator, this "outer" fit is consistent with a high central oxygen abundance $12+\log(O/H) \sim 9.4$ (in both samples), with a much steeper gradient than those derived from the individual data points and/or the radial average spectra. The arbitrary offset in both samples suggest that the maximum oxygen abundance is consistent with a solar value.

The effect of the steep "outer" gradient is more obvious in the case of the *O3N2* calibrator, where the $(O/H)_{\rho_0}$ abundance is consistent with values $12+\log(O/H) \sim 9.15$, while the derived oxygen abundance of the innermost regions is ~ 8.85, the linear fits result in slightly higher abundances given the weight in the fit of the the outer regions. Given the high sensitivity of this indicator to the ionization parameter, it could be argued that the change of the metallicity gradient in the inner regions is due to a change in the ionization conditions for $\rho < 0.3\rho_{25}$. However, the diagrams corresponding to the H II region sample in Figure 6.59

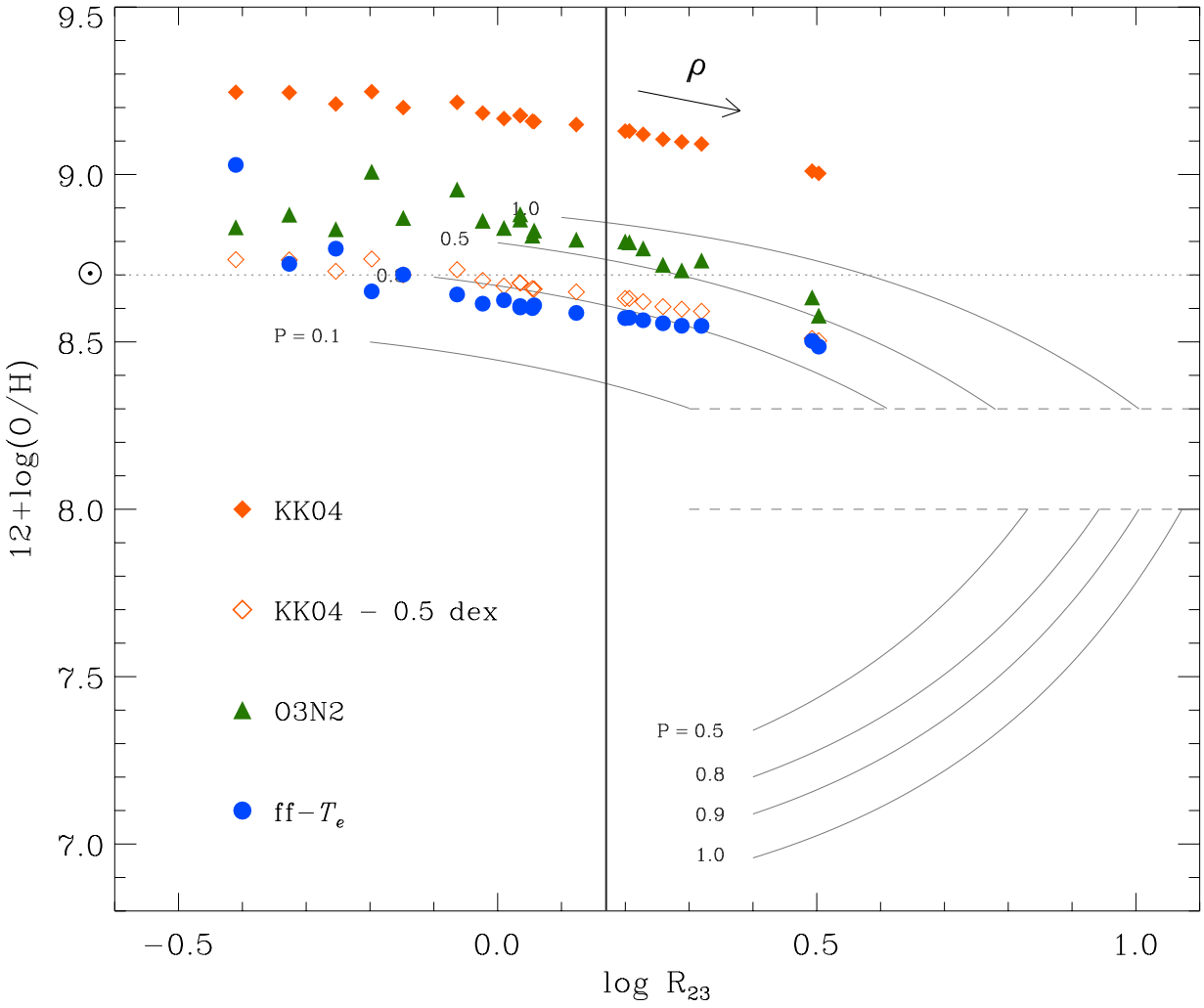

Figure 6.61: 12 + log(O/H) vs. log R_{23} diagram for the H II region radial average spectra of NGC 3184 for the selected metallicity indicators. The arrow shows the direction of increasing galactocentric radius (except for the outlying point of the ff–T_e relation, as explained in the text). The vertical line shows the value of log R_{23} derived from the integrated spectrum.

shows that both the ionization parameter and the [N II] λ6584/Hα ratio remain basically constant for all values of galactocentric radius, and therefore, the break in metallicity is not due to a change in the ionization conditions of the inner regions.

Figure 6.55, corresponding to the spatial distribution of the H II regions in NGC 3184, shows as a dotted-line the $0.3\rho_{25}$ radius for this galaxy, and the H II regions (and fibres of the first sample) within this area. As it can be seen, all the bright H II regions of NGC 3184 are located at galactocentric distances larger than the $0.3\rho_{25}$ radius, and that the regions within this area are small and faint. A similar exercise, as in previous cases, consisting on determining the abundance gradient from a sample of "bright" H II regions, was performed to NGC 3184 by selecting randomly 6 regions from a sample of 12 "bright" H II regions (all with galactocentric radius greater than $0.3\rho_{25}$), over 100 realizations, as explained before. The "bright" sample correspond to the regions: N3184–8, 9, 14, 20, 22, 27, 29, 36, 48, 49, 51 and 52. The blue thick line in the H II region sample abundance gradients of Figure 6.60 corresponds to the average fit from this simulation. As it can be noticed, the fit is almost coincident with black-dotted line for the KK04 calibrator (corresponding to a high central oxygen abundance), and results in a steeper gradient for the *O3N2* calibrator. However

in the case of the ff–T_e method, the agreement between the four fits (individual data points, radial average, "outer" and "bright" samples) is remarkable. Table 6.7 shows the parameters derived from the abundance gradient analysis of NGC 3184. Taking the radial average of the H II region sample as a base, the metallicity gradient derived for this galaxy using the ff–T_e method is $12+\log(\mathrm{O/H}) = 8.75\,(\pm 0.05)$ –$0.35\,(\pm 0.13)\rho$, which can be compared to the $(\mathrm{O/H})_{\mathrm{ff}}$ gradient mentioned above, derived by Pilyugin et al. (2006). The oxygen abundances derived from the integrated spectrum of this galaxy are shown as horizontal lines in each gradient diagram. They match the radial distributions of the metallicity at $\rho \sim 0.45\rho_{25}$ for the KK04 and *O*3*N*2 calibrators, while in the case of the ff–T_e method, the equality is shifted to slightly larger radii, consistent with $\rho \sim 0.5\rho_{25}$.

Figure 6.61 shows the O/H vs. R_{23} relation displaying the data points of the radial average spectra of the H II regions sample. The KK04 calibrator lies on the top of all the calibrators, with a decreasing trend with higher values of R_{23}, corresponding to increasing values of the galactocentric radius. The points belonging to the *O*3*N*2 calibrator are located in between the KK04 and ff–T_e methods, showing a flattening of the increasing trend in metallicity with decreasing values of R_{23}, consistent with the break of the abundance gradient. The ff–T_e method shows a nearly linear relationship of the metallicity with R_{23}, except for the outlier at $12+\log(\mathrm{O/H}) \sim 9.0$, which corresponds to the radial data point at $\rho/\rho_{25} \sim 0.3$. Note the very good agreement in terms of the trend and oxygen abundance between the values of the ff–T_e method with the offset values of the KK04 indicator. The vertical line corresponds to the R_{23} value derived from the integrated spectrum of NGC 3184.

The 2D abundance map of NGC 3184 derived from the *O*3*N*2 calibrator is presented in Figure 6.62. Outer regions show a lower metallicity than the central part of the galaxy, consistent with the abundance gradient discussed before. Although there seems to be some level of structure within a given region, the high values display at the edges of these regions are an artifact of the interpolation scheme. However, the lower values found at the centre of the galaxy are consistent with the bimodality of the abundance gradient, i.e. a flat distribution of metallicities for regions within $\rho/\rho_{25} \sim 0.3$. The average oxygen abundance derived from the map is $12+\log(\mathrm{O/H}) = 8.82 \pm 0.14$, in agreement with the integrated value, i.e. 8.79 ± 0.13.

Discussion

A spectroscopic analysis of NGC 3184 based on the 2D PINGS observations has been performed in this section, employing the *fibre-by-fibre* and H II region catalogue samples. Both analysis show the same trends in terms of the radial variations of emission line ratios and physical properties of the galaxy, with higher scatter for the former case. Azimuthally-averaged radial spectra was extracted from consecutive annulus of 5 arcsec (for those regions were spectra is found) from both samples. The results from these sub-samples is completely consistent with the results of the individual spectra. The emission from the [O II] and [O III] lines increases with galactocentric radius, with a somewhat constant trend for the inner regions of the galaxy, from the [N II]/[O II] diagram, the corresponding R_{23} values are consistent with the upper branch of the R_{23} relation, which is expected as this object has been considered one of the most metal rich observed galaxies. The degree of ionization does not show variations over the surface of the galaxy covered by the IFS observations, a higher level of scatter is found in the inner regions, which is more evident from the *fibre-by-fibre* sample, although from the results of the H II regions sample the inner regions are consistent with the constant values found for larger radii.

The abundance gradient analysis of this galaxy considered for the first time inner regions within $\rho/\rho_{25} \sim$

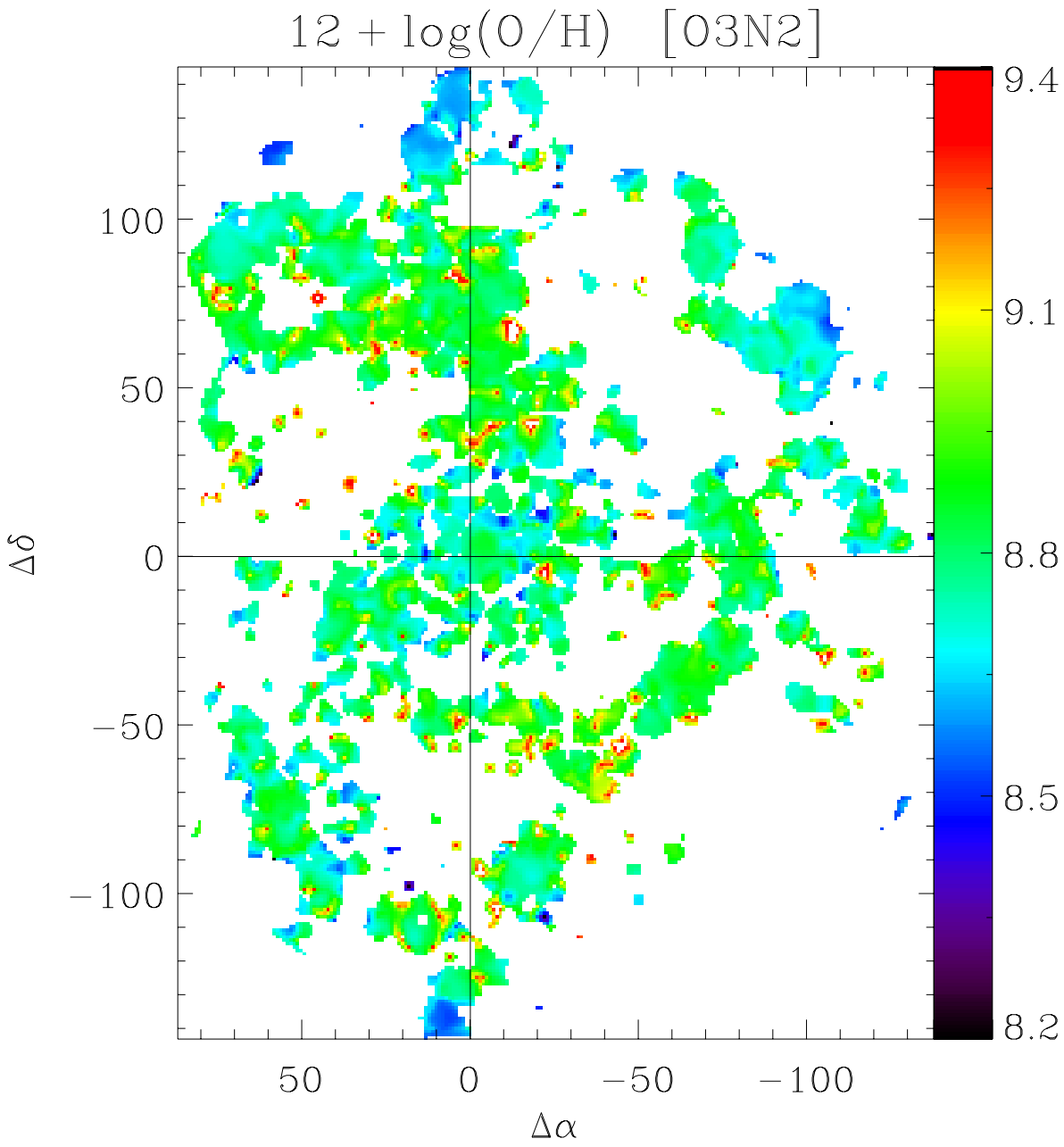

Figure 6.62: Oxygen abundance map of NGC 3184 derived by applying the *O3N2* calibrator to the emission line maps of the galaxy.

0.3, contrary to previous studies which targeted H II regions with larger galactocentric radius. All the different metallicity indicators suggest a bimodality of the abundance gradient, with an "outer" steep gradient, consistent with previous results, for radii larger than $\rho/\rho_{25} \sim 0.3$, and an "inner" flat gradient for smaller radii. Although the low number of observed H II regions in this part of the galaxy, and the large errors associated with the empirical determination of abundances in the high metallicity regime might preclude any firm conclusion, the results from the abundance gradient analysis of NGC 3184 brings support to the idea put forward by Pilyugin et al. (2006), i.e. that there is an upper limit to the oxygen abundance in spiral galaxies consistent with $12 + \log(\mathrm{O/H}) \sim 8.75$, despite the steep slopes derived for some metal-rich galaxies. The outermost observed regions for NGC 3184 in the literature correspond to radii $\rho/\rho_{25} \sim 0.85$ (Pilyugin et al., 2004), if there exist a break in the abundance gradient for regions with much larger radii (like in the

case of NGC 1058 or M83), then the abundance gradient of NGC 3184 (and probably of the metal-richest galaxies), may show a *trimodality* in their chemical abundance distribution, consistent with a flat–steep–flat gradient, with increasing galactocentric distance.

6.6 NGC 3310

All the previous galaxies analysed can be classified as normal, late-type, nearly face-on, isolated spirals. However, from all the galaxies in the PINGS sample, NGC 3310 stands out given its remarkable morphological and physical properties. NGC 3310 has been classified as a peculiar spiral galaxy, it was included in the catalogue of interacting galaxies by Vorontsov-Velyaminov (1977) and in the Atlas of Peculiar Galaxies by Arp (1966). It is likely that NGC 3310 collided with a smaller galaxy, triggering a large burst of star formation. As shown previously in section 6.2, the central part of the galaxy shows a prominent ~ 20 arcsec diameter ring of luminous giant H II regions, surrounding the bright compact nucleus. A large number of clusters of newly formed stars are visible as bright diffuse objects that trace the spiral arms of the galaxy.

The observation of NGC 3310 was performed in dithering mode, therefore the spectroscopic data samples all the area covered by the mosaic. At the assumed distance of the galaxy (17.5 Mpc, Terry et al. 2002), one PPAK fibre corresponds to a physical size of 227.6 pc. During the data reduction of NGC 3310, the sky-fibres corresponding to each observed position were employed in order to subtract the contribution of the sky-emission to the observed spectra. As part of the meticulous sky-subtraction process described in chapter 4, each sky-fibre was visually checked in the case that any bright foreground or background object would fall into those fibres, causing a contamination of the derived sky-spectrum. In the case of NGC 3310, several of these sky-fibres presented spectra corresponding to typical H II regions, extending up to ~ 120 arcsec (i.e. 10.1 kpc) from the nucleus of NGC 3310, especially towards the south-east part of the galaxy. Given the significance of these outlying regions in terms of describing the abundance gradient of the galaxy, we decided to include these regions for the spectroscopic analysis of NGC 3310. These regions were not considered in the emission line maps of section 6.2 as the large blank areas between these outliers and the main mosaic of the galaxy produced interpolation errors.

An alternative version of the *clean* mosaic for NGC 3310 was generated including the sky-fibres mentioned above. Given that the galaxy presents a very high surface brightness, with many spectra consisting of strong emission lines and a weak stellar continuum, the derived residual spectra resulted in a large number of fibres fulfilling the selection criteria. Figure 6.63 shows the quality selection histograms for NGC 3310. Spectra with detection of Hβ and [O III] λ4959 accounted for 2367 fibres from the original mosaic, after discarding one fibre with non-finite values of the extinction coefficient (second criterion), and then by applying the third selection criteria of the *fibre-by-fibre* sample, i.e. the flux cut in Hβ corresponding to 10×10^{-16} erg s^{-1} cm^{-2}, and detection of [O II] λ3727, 434 spectra were finally selected. This number corresponds to $\sim 17\%$ of the *clean* mosaic and $\sim 15\%$ of the total number of observed spectra for NGC 3310. The first three rows of Figure 6.63 show the selection step histograms for the *fibre-by-fibre* sample, the final spectra reflects an excellent quality, with practically all values of the Balmer ratios consistent with a physical extinction, and a very narrow distribution of the [O III] ratio centered at the theoretical value.

In the case of the H II region catalogue, a slightly different selection procedure was adopted. Since most of the galaxy emission is concentrated in a dense central region of the mosaic, circular extractions of ~ 3 arcsec in diameter were employed to cover most of the central pointing of the galaxy. For outer regions, an approach similar to previous cases was adopted, i.e. by selecting regions morphologically associated, with

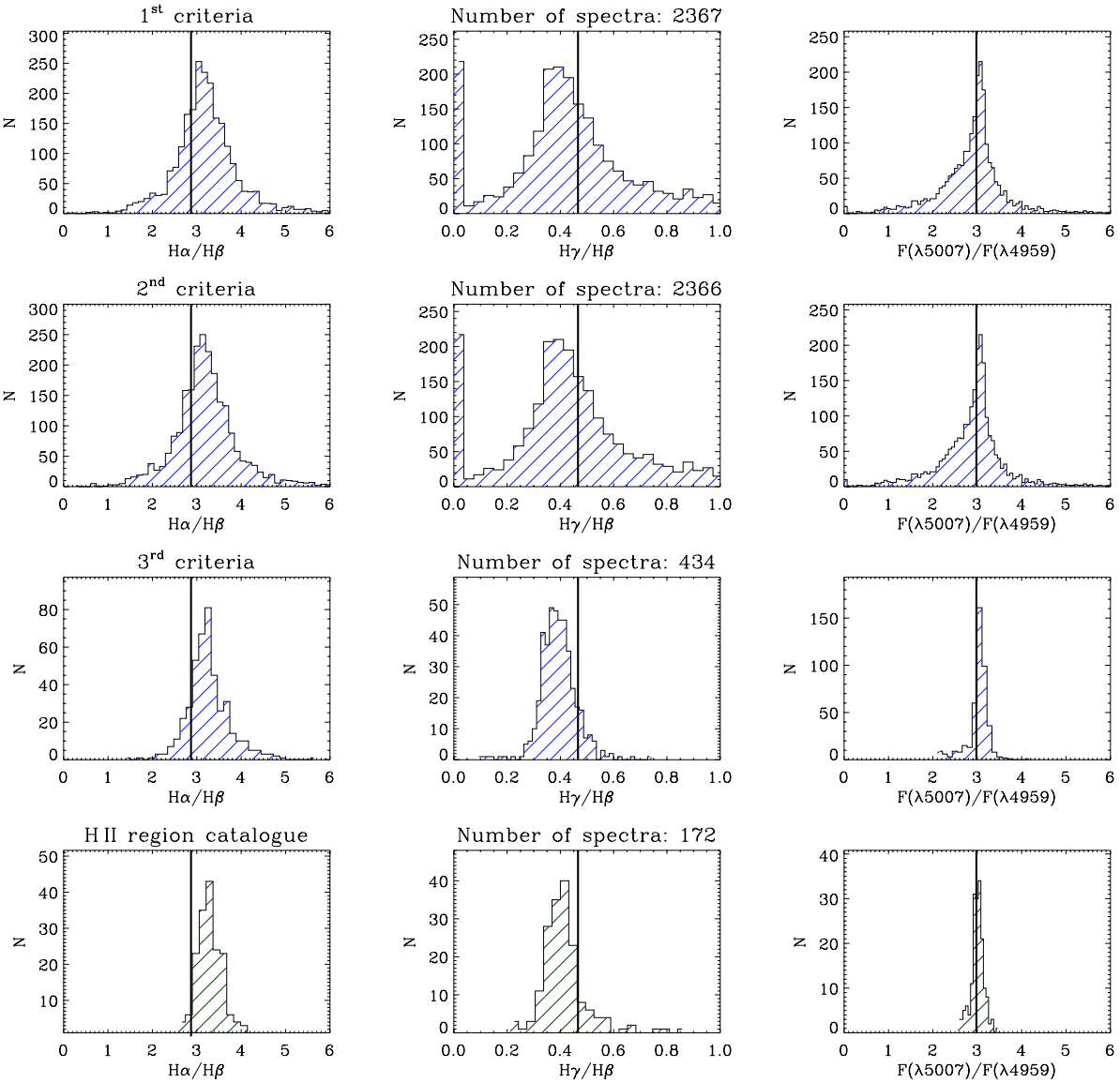

Figure 6.63: Selection criteria histograms for NGC 3310. Top three rows correspond to the *fibre-by-fibre* analysis, the bottom row to the H II region catalogue. In each panel, the vertical line correspond to the theoretical value of the given line ratio.

different aperture sizes. A total of 172 H II regions were selected for this sample. The distribution of the overlapping fibres due to the dithering observation was considered when co-adding the fibres corresponding to a single region. The spatial position of the selected H II regions is shown in Figure 6.64, with the fibres corresponding to the *fibre-by-fibre* sample as a background. The dotted-line circle corresponds to the optical radius of the galaxy, i.e. $\rho_{25} = 92.7$ arcsec. The outlying regions of NGC 3310 are clearly seen in this figure, corresponding to the position of the sky fibres of the PPAK pointings. Figure 6.65 shows a close-up of the central region of NGC 3310 for a better identification of the inner selected H II regions. The coordinates, size and other basic information of the selected catalogue can be found in Appendix D.

The bottom panels of Figure 6.63 show the histograms corresponding to the H II region catalogue, as in the case of the *fibre-by-fibre* sample, the Balmer ratios show an exceptional good behaviour, with somewhat a lower number of fibres corresponding to non-physical extinctions for the Hα/Hβ ratio. The [O III] ratio distribution is also very narrow, and well-centered at the theoretical value. Given the high surface brightness

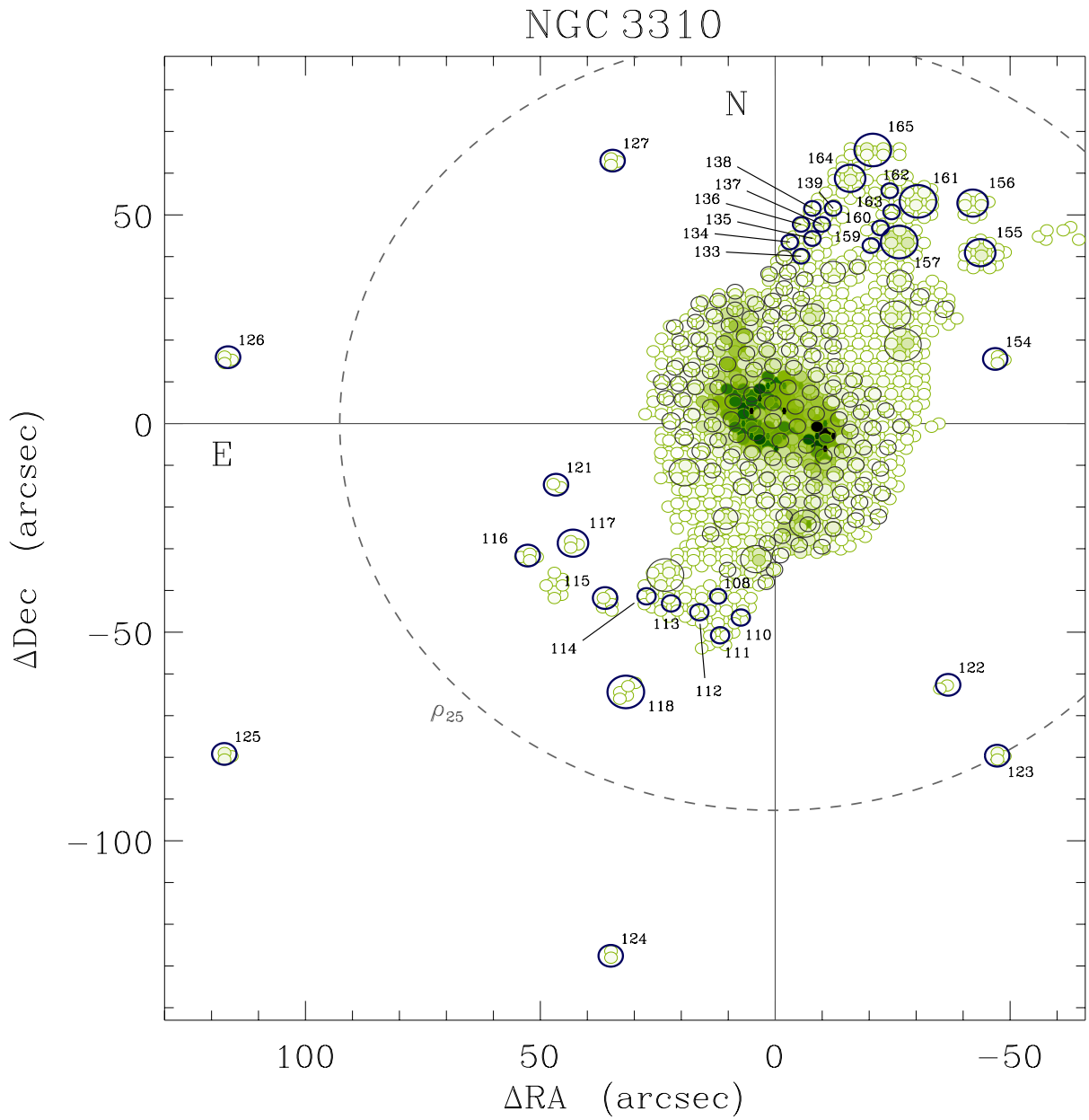

Figure 6.64: Spatial location and identification of the selected H II regions for NGC 3310. The background fibres correspond to the *fibre-by-fibre* sample, with colour intensities scaled to the flux of the Hα emission. The circles correspond to an equivalent aperture radius. The dotted-line circle corresponds to the optical radius ρ_{25}. Only the outer regions are labelled for the sake of clarity. The identification of the central regions can be found in Figure 6.65.

of this galaxy, the spectroscopic mosaic of NGC 3310 stands out as the object with the best signal-to-noise of the whole sample. Considering the high strength and large equivalent width of all the bright emission lines, combined with the weak stellar continua in most of the mosaic, the emission line intensities measured from the residual spectra are derived quite accurately, given that the errors introduced by the continuum subtraction are practically negligible. For this reason, the derived line ratios are completely consistent with "physical" regions, especially in the case of the [O III] ratio.

Figure 6.66 shows examples of individual fibre spectra of NGC 3310 in arbitrary flux units, separated in the spectra belonging to the central region (bottom panel) and external regions (top panel), with galacto-

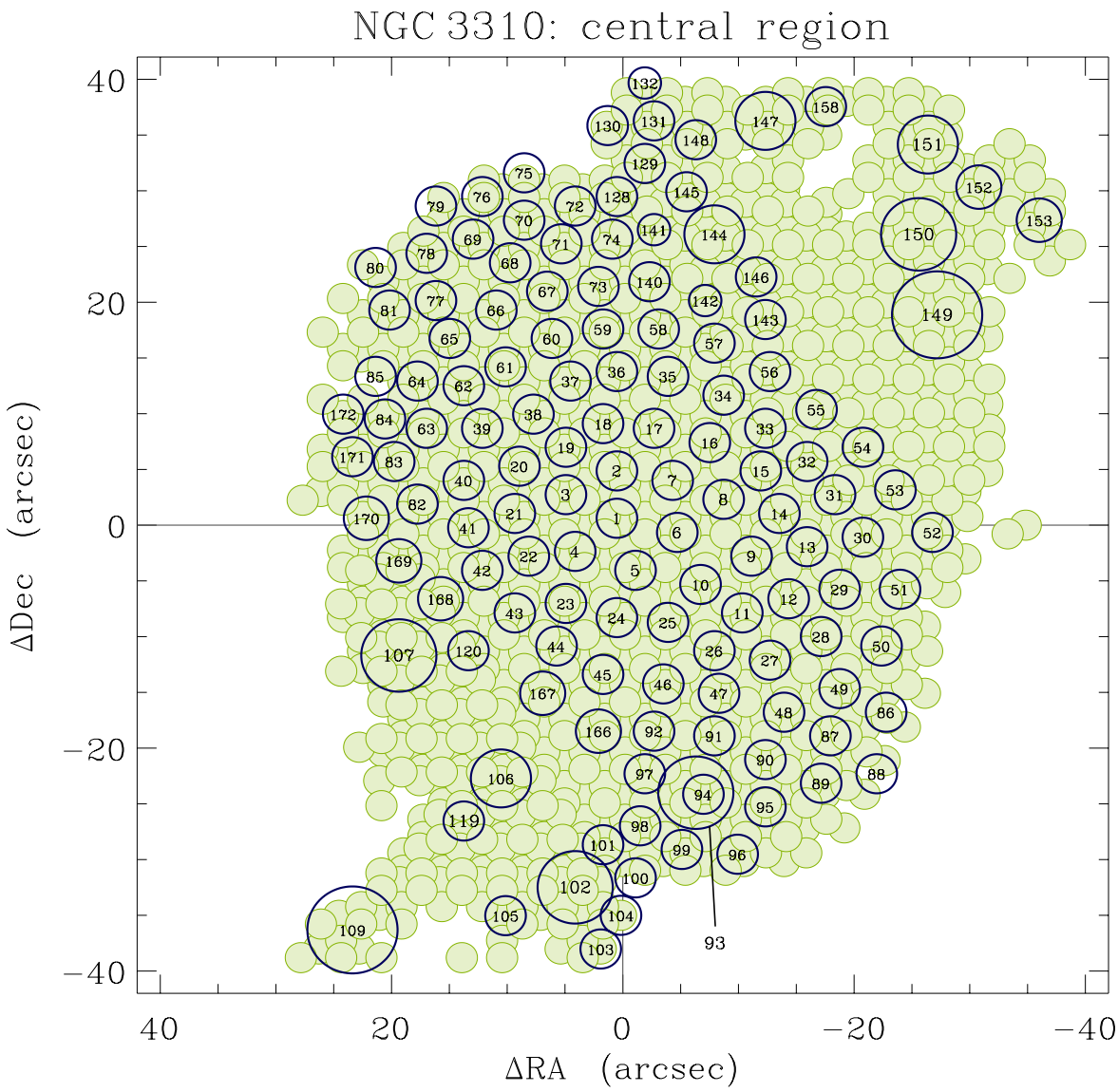

Figure 6.65: Same as Figure 6.64, but showing only the central region of the galaxy. The fibres are not scaled to the Hα intensity levels for the sake of clarity. Note that the region N3310–94 is embedded into the region N3310–93, see explanation in the text.

centric radius increasing from the bottom to the top on both panels. On the other hand, Figure 6.67 shows examples of three H II regions with different signal-to-noise. For each H II region, the left panel corresponds to the observed integrated spectrum within the aperture and the SSP fit model overlaid, the right panel shows the residual spectrum from which the emission line intensities were calculated. As for the rest of the galaxies, the observed intensities were corrected by interstellar reddening following the procedure outlined before, i.e. for the *fibre-by-fibre* sample, the c(Hβ) term was derived solely from the Hα/Hβ ratio, while for the H II region catalogue, the Hγ/Hβ ratio was also considered in the determination.

Figure 6.68 shows the diagnostic diagrams for NGC 3310, with the same symbology and colour coding as the previous cases. Azimuthally-average radial spectra were obtained by co-adding the fibres/H II regions located within consecutive annulus of 5 arcsec. These spectra is shown as reddish diamonds on top of the main data for both samples. The [O III] λ5007/Hβ vs. [O II] λ3727/Hβ diagnostic diagrams show a very concentrated locus consistent with values log(λ5007/Hβ) $>$ 0.0 for both samples, and log(λ3727/Hβ) $>$ 0.0

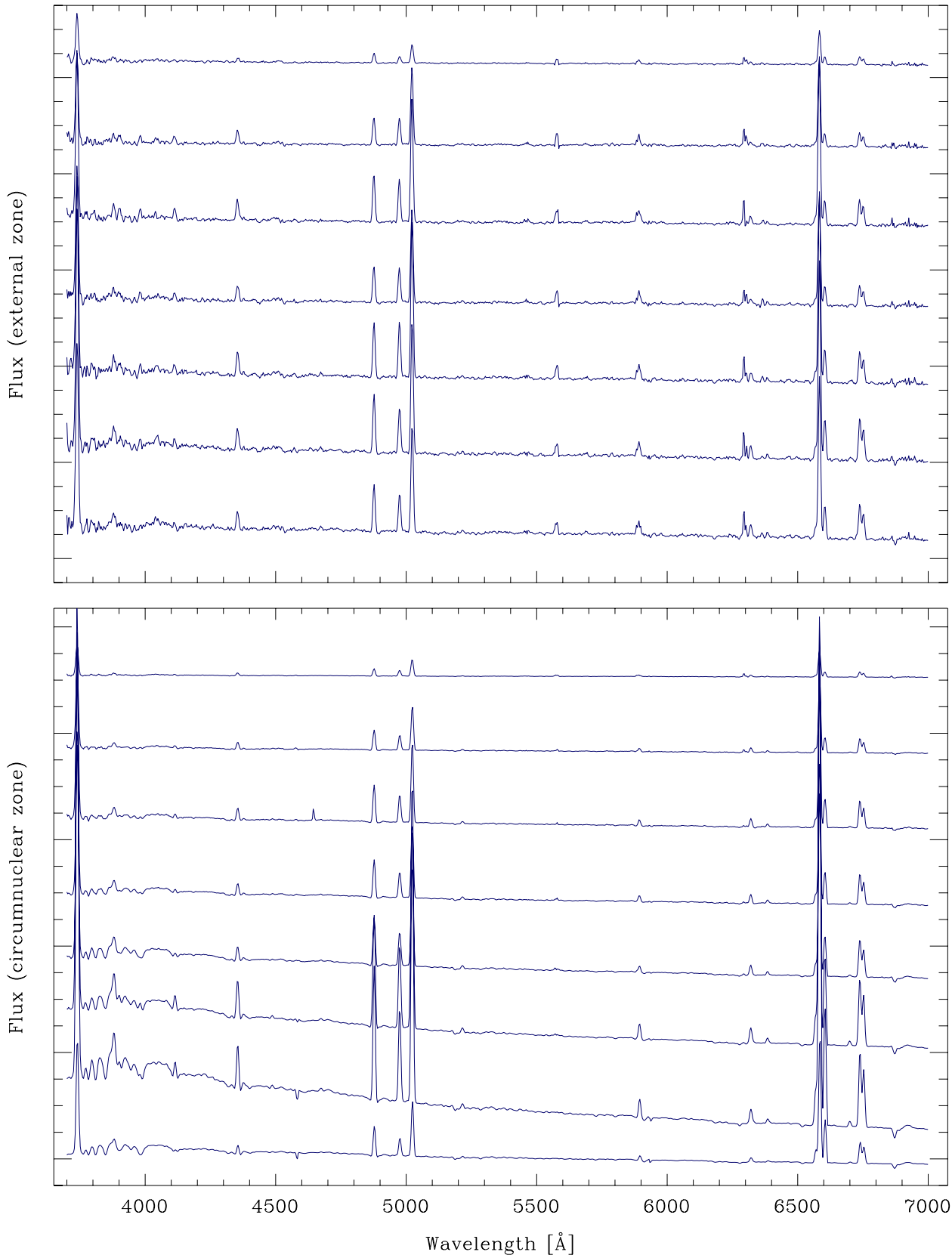

Figure 6.66: Examples of individual fibre spectra of NGC 3310 in arbitrary flux units, divided between spectra of the circumnuclear zone (bottom) and the external zone (top). The galactocentric radius increases from the bottom to the top on both panels.

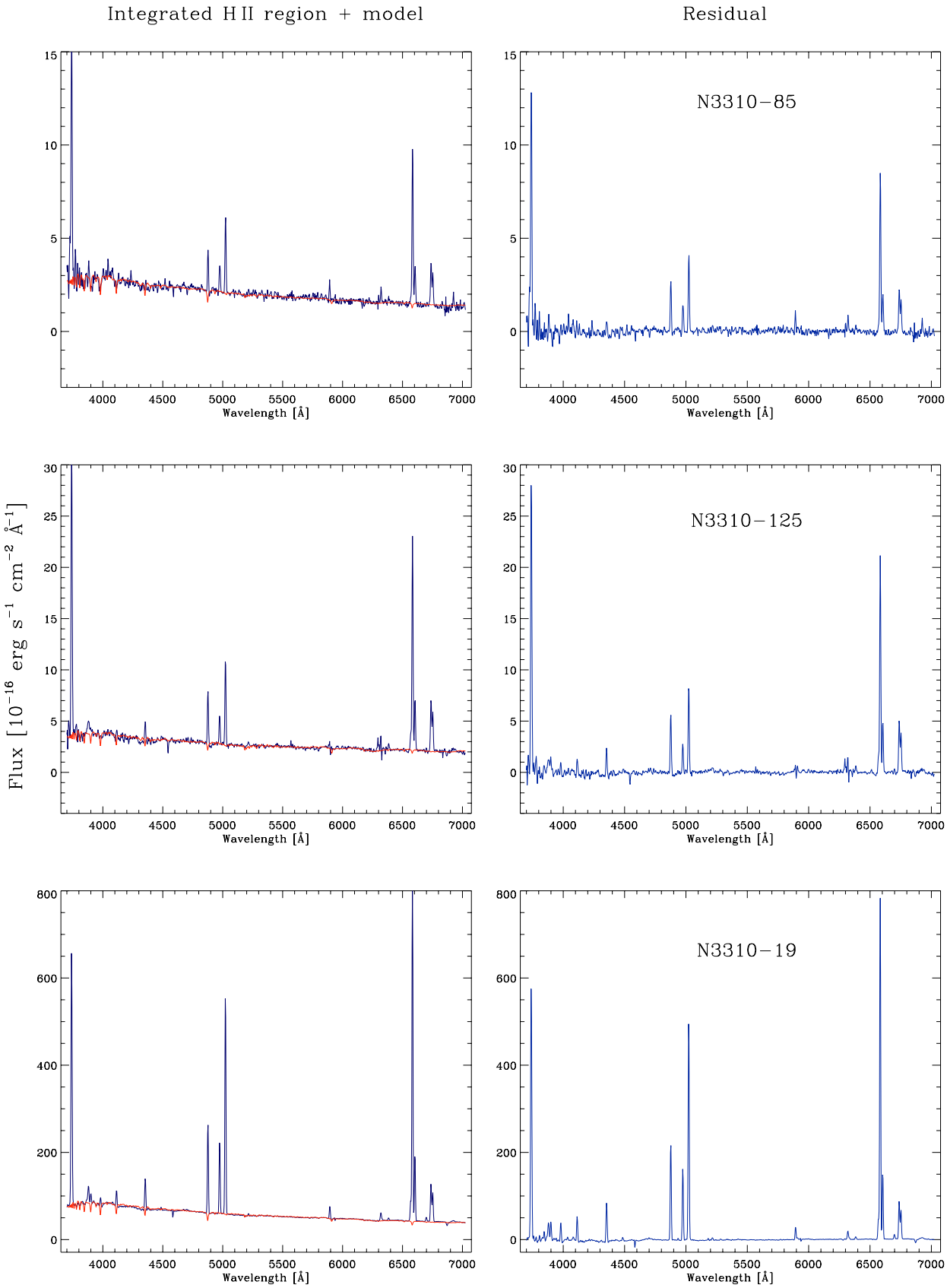

Figure 6.67: Examples of spectra of NGC 3310 extracted from the H II region catalogue. The left column corresponds to the observed integrated spectrum, plus the SSP fit model overlaid as a red line, the right column shows the residual spectrum. The label corresponds to the ID of the H II region.

and > 0.5 for the *fibre-by-fibre* and H II region samples, respectively; i.e. very high values of these ratios approaching the transition zone for other types of ionization. The radial trend suggests a nearly constant value of [O II] λ3727/Hβ ~ 0.5 for the inner regions, and a decrement of this ratio for the outer regions of the galaxy, with the [O III] λ5007/Hβ increasing for all galactocentric distances. This trend is contrary to the previously shown by the other galaxies, where both line ratios increase their values as a function or radius.

The middle-panels show the [O III] λ5007/Hβ vs. [N II] λ6584/Hα ratio diagrams, which again, show a totally different trend than the rest of "normal" spiral galaxies. In this case, the [N II]/Hβ ratio decreases with galactocentric distance, opposite to the nearly constant value log(N II]/Hβ) $\sim$ –0.5 for all radii shown in previous cases. This trend would suggest that the degree of the ionization decreases with galactocentric distance for NGC 3310. The location of the spectra on these diagrams is also very near the transition zone consistent with starburst ionization. The bottom-panels of the same figure show the [N II]/[O II] vs. logR_{23} diagrams. The *fibre-by-fibre* sample spans from values of $N_2O_2 \sim$ –0.5 to –1.15, i.e. approaching the boundary between the upper and lower branch of the R_{23} relation. The H II region catalogue shows a much narrower range of values, but also approaching the transition between the branches, especially for the outermost regions of the galaxy. Interestingly, most of the spectra are consistent with a nearly constant value of log$R_{23} \sim 0.8$, as it is particularly obvious from the radial average spectra in both samples. Given the proximity of the large radii spectra to the transition between the R_{23} branches, both solutions were considered for the abundance analysis of those regions.

Figure 6.69 shows the deprojected radial distributions of R_{23}, the ionization parameter log$u$, and N_2H_α for both spectral samples. It is important to note that the scale on the X-axes differ from one sample to another, in the case of the *fibre-by-fibre* sample, all diagrams display only those regions within $\rho \sim 0.8\rho_{25}$, while in the diagrams corresponding to the H II region catalogue, the X-axes extend to the whole range of observed galactocentric radius, i.e. $\rho \sim 1.7\rho_{25}$. The reason of the different scales resides on the large number of data points within $\rho/\rho_{25} \lesssim 0.7$ for the *fibre-by-fibre* sample, this choice was made to display in a clearer way the radial trends of the inner regions of the galaxy. The trends of the outermost regions are presented by using the higher signal-to-noise H II region catalogue, although the *fibre-by-fibre* sample follows exactly the same patterns. The vertical dotted-line in the H II regions diagrams show the radial boundary described by the *fibre-by-fibre* sample in the left-panels.

The top panels corresponds to the radial distribution of R_{23}, as inferred previously by the N_2O_2 vs. R_{23} diagnostic diagram, this indicator shows a very narrow range of values, but it is consistent with a slight increase as a function of radius. This trend is conserved for the outlying regions, as seen in the H II regions diagram, reaching values log$R_{23} \sim 0.95$, i.e. a difference of 0.15 dex with respect to the lower logR_{23} value at the centre of the galaxy. The R_{23} value derived from the integrated spectrum is consistent with the innermost regions of the galaxy (i.e. $\rho/\rho_{25} \sim 0.2$). The middle-diagrams correspond to the radial variation of log$u$, the ionization parameter. Both distributions are consistent with lower (nearly constant) values of the ionization for the inner regions of the galaxy ($\rho/\rho_{25} < 0.4$), and higher values with some level of scatter for those regions approaching $\rho/\rho_{25} \sim 0.8$. However, there seems to be a discontinuity of the ionization trend, for the outlying regions the ionization decreases to a flat distribution, with values even lower than those found at the innermost part of the galaxy, the outermost H II region showing a value of log$u \sim -3.5$. The log$u$ value derived from the integrated spectrum is again consistent with radial values at $\rho/\rho_{25} \sim 0.2$, The bottom-panels, showing the distribution of the [N II] λ5484/Hα ratio, show a steep decrement of this ratio as a function of galactocentric radius for radii $\rho/\rho_{25} < 0.8$ in both samples, however, just as the previous

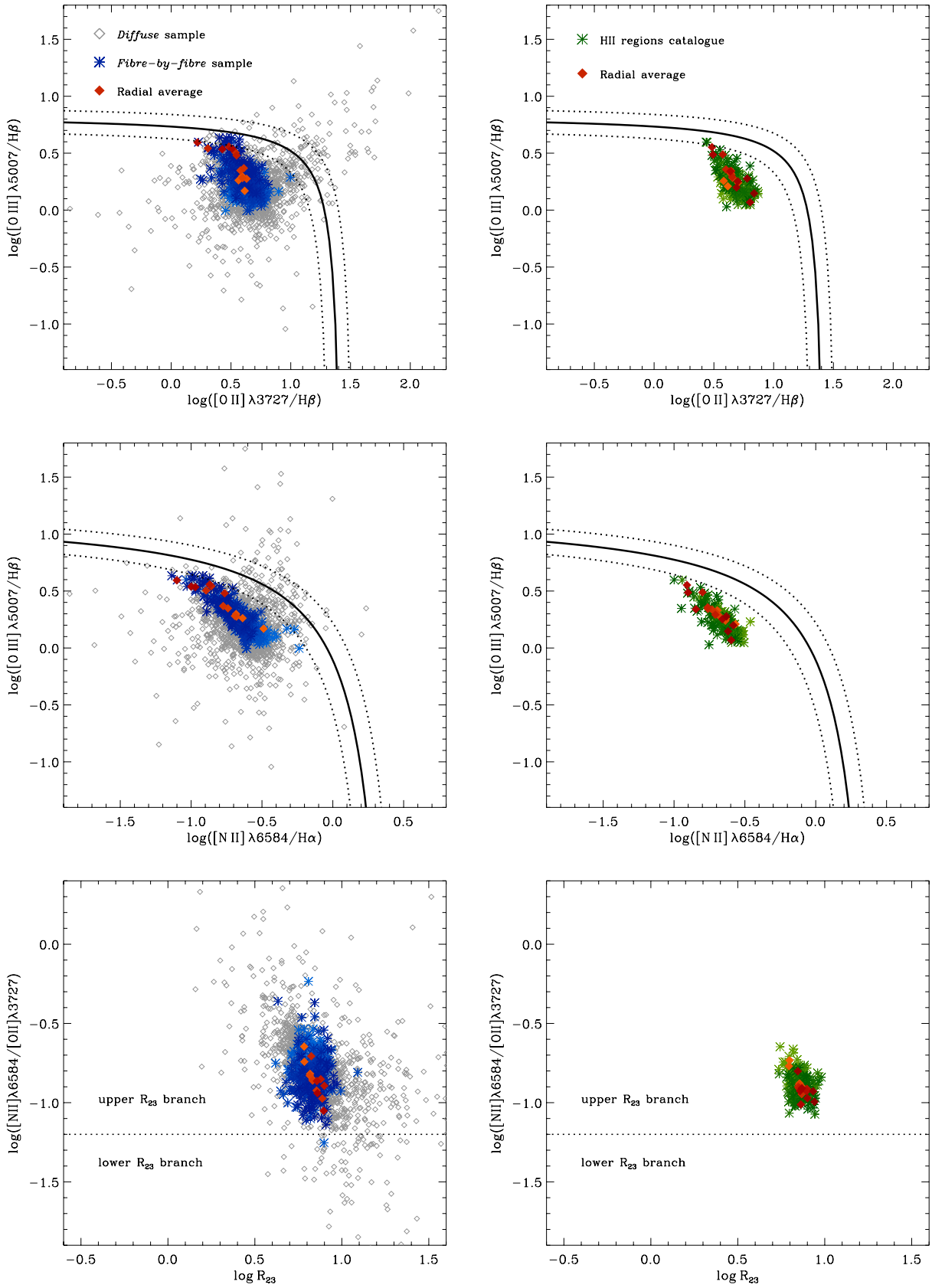

Figure 6.68: Diagnostic diagrams for NGC 3310. The left column correspond to the *fibre-by-fibre* sample, the right column to the H II region catalogue. The filled-diamonds correspond to the azimuthally-averaged radial values. Lighter/darker tones correspond to inner/outer regions of the galaxy, in terms of the galactocentric radius.

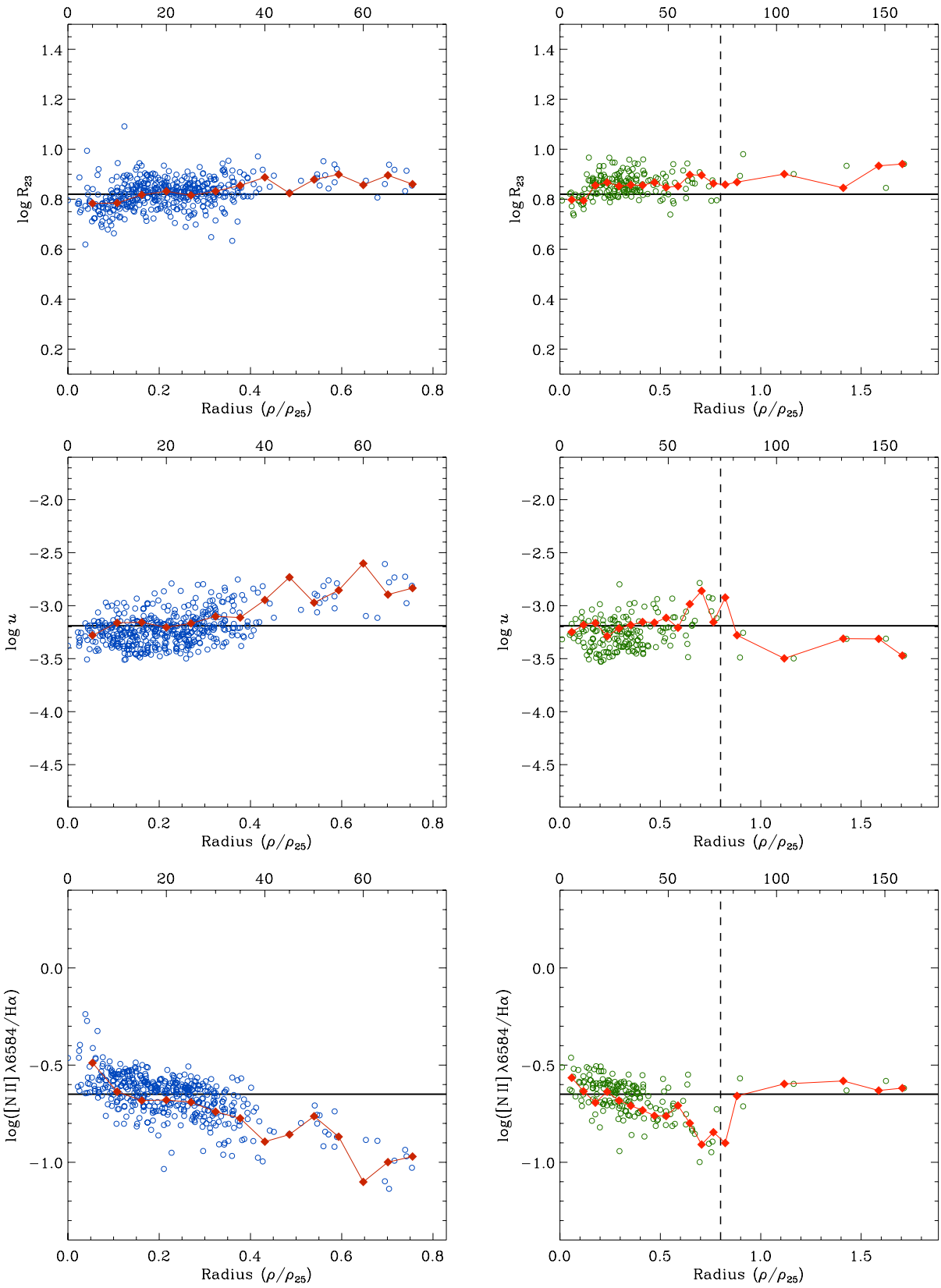

Figure 6.69: Radial variation of selected physical properties of NGC 3310. Equivalent colour-coding and axes units as previous similar figures. For the sake of clarity, the X-axes of the two samples have different scales, the H II region catalogue diagrams extend to the full baseline of the observed regions. The vertical dotted line in the right-panels marks the region showed by the left-panels. The horizontal lines correspond to the values derived from the integrated spectrum of the galaxy.

case, there is a break at $\rho/\rho_{25} \sim 0.8$ at which the N_2H_α value increases $\sim$0.4 dex, and remains nearly constant at a value $N_2H_\alpha \sim -0.6$ for the outlying regions of the galaxy. The value of this ratio derived from the integrated spectrum is consistent with an even lower galactocentric radius than the previous two cases, matching the radial distribution at $\rho/\rho_{25} \sim 0.1$.

The bimodality of the radial variation of the ionization parameter and the N_2H_α ratio is puzzling, considering that the R_{23} distribution does not show this break. This discontinuity suggests that outlying regions at radii larger than $\rho/\rho_{25} \sim 1.5$ present the same ionization conditions than the innermost regions of the galaxy, which is surprising given the high level of star formation and extreme conditions of the perinuclear region of NGC 3310.

The radial abundance gradients for this galaxy are presented in Figure 6.70 for the selected metallicity indicators. As in previous figures, the left-panel corresponds to the *fibre-by-fibre* sample, the right-panel to the H II region catalogue. In addition, a new sample is presented on each panel as black-star symbols, corresponding to the *direct* abundance determinations performed for a number of regions where the temperature-sensitive [O III] λ4363 line was detected and measured accurately. The combination of the high signal-to-noise of the observed spectra, and the larger redshift of NGC 3310 ($z \sim 0.0033$) compared with the rest of the galaxies discussed in this chapter, made possible to detect the [O III] λ4363 line for several H II regions. The larger value of the redshift prevented contamination of the strong Hg λ4358 sky-line, that strongly affects any attempt to measure the emission of this key diagnostic line. According to the [O III] λ4363 detection simulation explained in subsection 6.1.1, at the redshift of NGC 3310, the minimum observed flux of the λ4363 line to be considered with a significant detection is F(λ4363) $\gtrsim 2.14 \times 10^{-16}$ erg s^{-1} cm^{-2}. The automated emission line fitting process considers the possible detection of this line, creating a subsample of spectra for which the λ4363 measured intensity fulfils the flux threshold criterion. Only those H II regions for which, 1) the observed intensity was above the minimum flux, and 2) the *total* error[3] in the measured line was below 20% were considered.

Individual visual inspection followed this selection criteria, only those H II regions where the presence of the [O III] λ4363 was evident were considered. A total of 26 H II regions with significant detection of [O III] λ4363 were selected. The flux intensity measurement of the λ4363 line (and the rest of the diagnostic lines) was performed from the *observed* spectrum, not the residual one. The reason being that, given the weakness of this line, the measurement of this line in the residual spectrum would suffer from large errors due to the subtraction of the SSP model continuum, considering the vicinity of the Hγ absorption line in this particular spectral region. The physical conditions of the gas, total and ionic abundances were derived following the prescriptions outlined by Pagel et al. (1992) and Pérez-Montero & Díaz (2003) for the *direct* method of abundance determination, which are explained in detailed in Appendix C. The region identification, electron temperature, density and ionic abundances of these regions are presented in Table 6.9. As a side comment, the *Jumbo* H II region discussed in section 6.1 corresponds to the N3310–9 H II region of Table 6.9.

The top panels of Figure 6.70 show the abundance gradients obtained through the R_{23}–based KK04 calibrator. As in the case of Figure 6.69, the scales of the X–axes differ between the *fibre-by-fibre* sample and the H II region catalogue diagrams, the former showing only those regions within $\rho/\rho_{25} < 0.8$ for the sake of clarity. The vertical dotted-line in the right-panel marks the radius at which the discontinuity in the ionization conditions occurs, which is also coincident with the boundary of the X–axis of the left-panel. The

[3] Including the statistical errors and the uncertainty due to the flux calibration.

red diamonds correspond to the results from the radial average spectra obtained for each sample (except for the *direct* abundances). Error bars are only drawn for the radial average spectra in each sample, and the points corresponding to the *direct* abundances in the left-panel. Hereafter, those parts of the galaxy for which $\rho/\rho_{25} < 0.8$ will be referred as the "inner" region, while for larger radii they will be called the "outer" region. Both samples show a large scatter in the inner region, but consistent with a negative abundance gradient with a central oxygen abundance near the solar value. For regions $0.1 \lesssim \rho/\rho_{25} \lesssim 0.4$, the variations in metallicities due to the scatter are of the order of ± 0.5 dex. The decreasing metallicity as a function of radius is more evident by the trends traced by the radial average spectra for both the inner and outer regions.

However, from the discontinuity radius on, the R_{23} values of the selected regions enter into the ill-defined zone between the two branches of the relation. The right-panel of the KK04 indicator shows the oxygen abundances determined from both branches connected by a vertical line. Given the ambiguity on the metallicity abundance for these outer regions, a reliable gradient cannot be derived by including the regions in the outer part of the galaxy. The thick colour lines in both diagrams stand for the linear least-squares fit corresponding to each sample, but considering only those points within the discontinuity radius. In the case of the *fibre-by-fibre* sample both fits agree in terms of the central abundance and slopes, however, in the case of the H II region catalogue the fit corresponding to the radial average spectra (red line) shows a steeper gradient and higher central abundance than the fit corresponding to the H II region sample (green line). If we assume that the outer region follows the same linear gradient than inner part of NGC 3310, without any break, discontinuity or flattening of the gradient, then the radial average fit is consistent with the H II regions at $0.8 < \rho/\rho_{25} < 1.0$ belonging to the upper branch of R_{23}, and to the outermost regions belonging to the lower branch.

The position of the regions with *direct* abundances confirm the well-known offset of the strong abundance indicators based on photoionization models. However, they can be compared with the arbitrary –0.5 dex offset of the abundance derived from the radial average spectra, shown as open-red diamonds in both panels of the KK04 calibrator. In the left panel, both solutions of the R_{23} branches are included for the outlying regions. The black-dotted line corresponds to the linear fit of the regions with *direct* abundances. In general terms, there is a very good agreement between the fit of the *direct* abundances and the offset of the KK04 radial average, especially for the H II region sample. However, given that the *direct* abundances were obtained only for a narrow range of galactocentric radius in the inner region of the galaxy, they cannot be used to infer the radial trend of the metallicity beyond the discontinuity radius. In the case of the *fibre-by-fibre* sample, the derived integrated abundance matches the radial distribution for $\rho/\rho_{25} \sim 0.25$, however for the H II region sample, the equality occurs practically at $\rho/\rho_{25} \sim 0.0$.

The middle-panels of Figure 6.70 show the abundance gradient derived by applying the $O3N2$ calibrator. The inner region is consistent with a clear negative gradient in both samples, although the scatter is lower than in the previous case. For the *fibre-by-fibre* sample, both the point-by-point and the radial-average spectra fits show a very similar gradient, with practically the same slope consistent with a central oxygen abundance $12 + \log(\mathrm{O/H}) \sim 8.5$. However, the abundance values derived through the $O3N2$ calibrator show an offset of ~ 0.3 dex and a steeper slope than those determined through the *direct* method. The picture for the outer region is completely different compared to the KK04 indicator. Beyond the discontinuity radius, the derived abundances show an upturn, and then a flat distribution consistent with values $12 + \log(\mathrm{O/H}) \sim 8.5$, i.e. similar abundances that the innermost regions of NGC 3310 derived through this indicator. The odd behaviour of this abundance gradient can be explained by the high sensitivity of $O3N2$ with the ionization

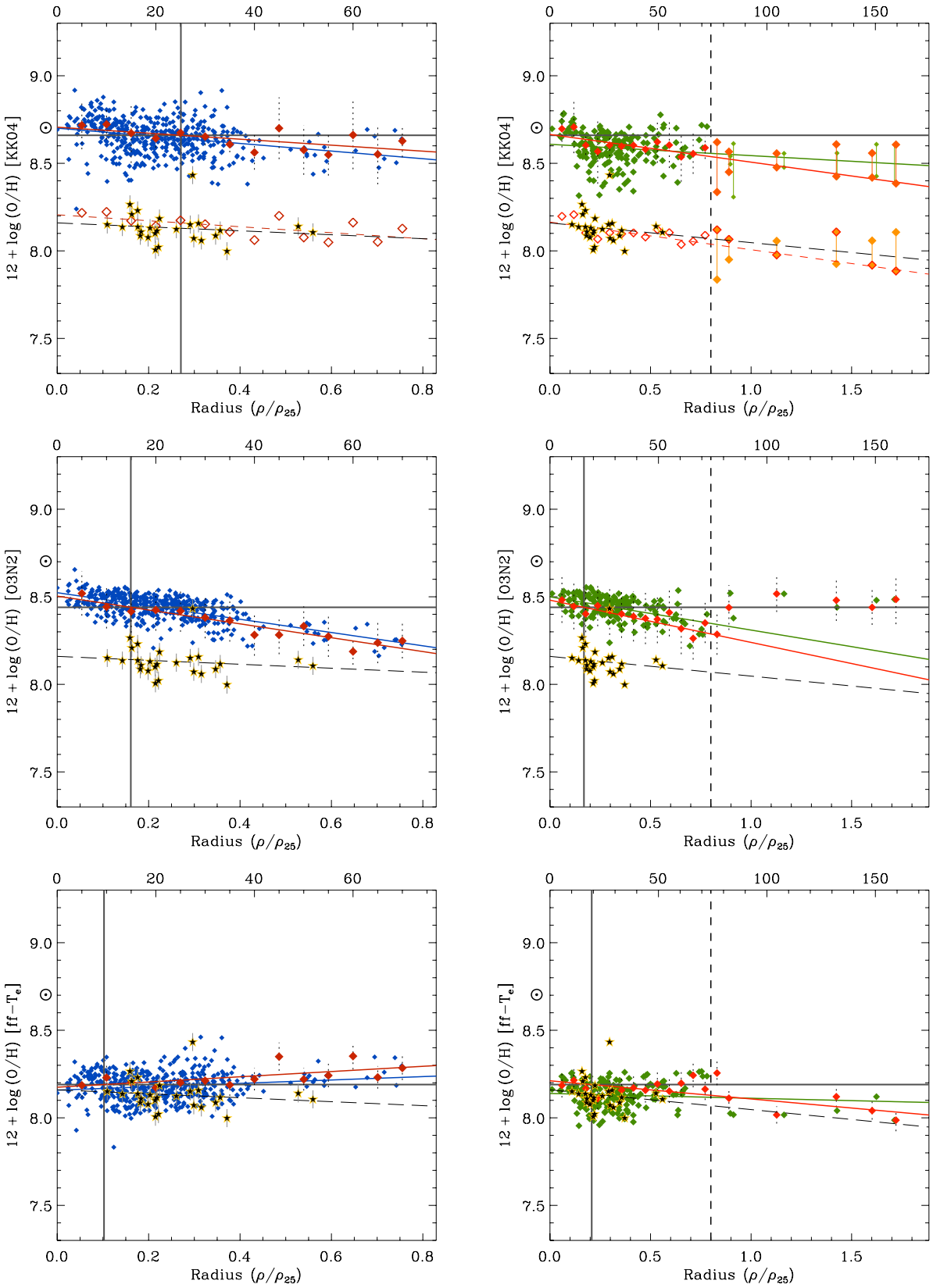

Figure 6.70: Radial abundance gradients for NGC 3310. Equivalent colour-coding and axes units as previous similar figures. The vertical dotted-line in the right-panels marks the region sampled by the left-panels. The black stars stand for *direct* abundances obtained for those regions with [O III] λ4363. The thick lines correspond to a linear least-squares fit to the corresponding data. The KK04 diagrams show the lower and upper oxygen values for $\rho/\rho_{25} > 0.8$, and a –0.5 dex offset of the radial average spectra. The horizontal line corresponds to the metallicity value derived from the integrated spectrum, the vertical line to the intersection of this abundance with the radial average fit.

RADIAL ABUNDANCE GRADIENTS FOR NGC 3310

		KK04: *fibre-by-fibre*		KK04: H II region catalogue	
	Direct method	*All sample*	*Radial*	*H II regions*	*Radial*
$12+\log(O/H)_{\rho=0}$	8.16 ± 0.05	8.70 ± 0.01	8.71 ± 0.03	8.61 ± 0.02	8.66 ± 0.02
$12+\log(O/H)_{\rho=0.4\rho_{25}}$	8.11 ± 0.05	8.61 ± 0.01	8.64 ± 0.03	8.58 ± 0.02	8.60 ± 0.02
$\log(O/H)_{(\text{dex } \rho_{25}^{-1})}$	-0.11 ± 0.08	-0.22 ± 0.04	-0.17 ± 0.06	-0.06 ± 0.05	-0.16 ± 0.05
$\log(O/H)_{(\text{dex kpc}^{-1})}$	-0.014 ± 0.021	-0.028 ± 0.005	-0.022 ± 0.007	-0.008 ± 0.006	-0.020 ± 0.007

	O3N2: *fibre-by-fibre*		O3N2: H II region catalogue	
	All sample	*Radial*	*H II regions*	*Radial*
$12+\log(O/H)_{\rho=0}$	8.52 ± 0.01	8.50 ± 0.02	8.50 ± 0.01	8.48 ± 0.02
$12+\log(O/H)_{\rho=0.4\rho_{25}}$	8.37 ± 0.01	8.35 ± 0.02	8.42 ± 0.01	8.38 ± 0.02
$\log(O/H)_{(\text{dex } \rho_{25}^{-1})}$	-0.38 ± 0.02	-0.40 ± 0.04	-0.19 ± 0.03	-0.24 ± 0.04
$\log(O/H)_{(\text{dex kpc}^{-1})}$	-0.049 ± 0.003	-0.051 ± 0.005	-0.024 ± 0.003	-0.031 ± 0.005

	ff–T_e: *fibre-by-fibre*		ff–T_e: H II region catalogue	
	All sample	*Radial*	*H II regions*	*Radial*
$12+\log(O/H)_{\rho=0}$	8.16 ± 0.01	8.17 ± 0.03	8.14 ± 0.01	8.21 ± 0.02
$12+\log(O/H)_{\rho=0.4\rho_{25}}$	8.20 ± 0.01	8.23 ± 0.03	8.13 ± 0.01	8.17 ± 0.02
$\log(O/H)_{(\text{dex } \rho_{25}^{-1})}$	0.10 ± 0.03	0.15 ± 0.06	-0.03 ± 0.02	-0.10 ± 0.03
$\log(O/H)_{(\text{dex kpc}^{-1})}$	0.012 ± 0.004	0.019 ± 0.007	-0.003 ± 0.003	-0.013 ± 0.004

Table 6.8: Results from the oxygen abundance gradient analysis of NGC 3310, separated for the different calibrators and the different analysed samples, including the *direct* abundances. The rows correspond to: the central abundance at galactocentric radius $\rho = 0$; the *characteristic* abundance at $\rho = 0.4\rho_{25}$; and the slopes of the abundance gradients in units dex ρ_{25}^{-1} and dex kpc^{-1} respectively. All gradients are calculated considering only those points in the inner region of the galaxy ($\rho/\rho_{25} < 0.8$), except for the ff–T_e H II region catalogue, where all galactocentric distances are considered.

parameter. The steeper slope in the inner region compared to the *direct* abundances is reflecting the also steep radial variation of the [N II] λ6584/Hα ratio observed in Figure 6.69, but this variation is due mostly to the radial gradient of the ionization parameter, and therefore, the large variations of the [N II] λ6584/Hα ratio are not due mainly to a change in metallicity, but to variations in the ionization, producing a steeper slope. The nearly constant value of R_{23} shown in Figure 6.69, and the shallow gradient derived through the KK04 calibrator give support to this idea.

In the case of the outer region, the upturn in metallicity can be explained by the discontinuity of the ionization parameter and the N_2H_α ratio as discussed before. The break of the ionization at large radii produces a large increase in the N_2H_α ratio, reaching similar values than those found at the centre of the galaxy, causing the $O3N2$ indicator to yield high metallicities for this outer regions. Again, the trend marked by R_{23} and the KK04 calibrator support the fact that the $O3N2$ upturn in the metallicity at the outer regions is an artifact, due to the dependency of this indicator on the ionization parameter. Given that the metallicities of the outer regions cannot be considered reliable, the linear fits shown on each diagram correspond only to those points within the discontinuity radius. For the H II region sample, the radial average fit shows a steeper slope than the regression corresponding to the H II regions, but with a similar central abundance. The values

of the integrated abundances match the radial distributions for $\rho/\rho_{25} \sim 0.15$ in both samples.

The bottom panels of Figure 6.70 show the abundance gradient determined through the ff–T_e relation. For mere consistency with the prescriptions employed in the *direct* determination, a minor modification in the ff–T_e method was implemented. The electron temperature of the low-ionization zone, $t_2 \equiv t([\mathrm{O\,II}])$ was determined by applying the $t_2 - t_3$ relation of Pérez-Montero & Díaz (2003), instead of the parametric version of Pilyugin (2007), see Appendix C for more details. Both samples show the same behaviour for the inner region, i.e. a nearly flat distribution of the metallicities, with a level of scatter compared to the KK04 calibrator. For consistency with the previous calibrators, the linear fit of the *fibre-by-fibre* sample (left-panel) was performed using only the data of the inner region. However, given the high concentration of data points in the innermost regions ($\rho/\rho_{25} < 0.4$) and the few points at $\rho/\rho_{25} \sim 0.7$ consistent with relatively high metallicities, the linear fits of both the point-by-point and radial average spectra show a fictitious inverse gradient, with decreasing metallicity with lower galactocentric radius, contrary to the trend traced by the *direct* abundances.

Nevertheless, the metallicity abundance determined through the ff–T_e relation coincides, at the general level, to the values obtained through the *direct* method. The good agreement between both methods is clearly seen in the bottom-right panel of Figure 6.70 showing the abundance gradient derived from the H II region catalogue of NGC 3310, where the *direct* abundances overlap the abundances derived through the ff–T_e method at the inner region. This sample shows a flat distribution of metallicities for regions with lower radii than the discontinuity radius, but for the outer regions, the metallicity distribution is consistent with a negative gradient, in agreement with the trend observed in the KK04 determination, by considering the outer regions at the lower branch of the R_{23} relation. Note however, that the gradient is not continuous but it shows a break at a distance coincident with the ionization discontinuity radius discussed before, reproducing the same behaviour as NGC 1058, in terms that, an abrupt change in the ionization coincides with a sudden change in the metallicity at the outer regions of the galaxy. The linear fits in the H II region sample consider all the regions extending up to $\rho/\rho_{25} \sim 1.7$, the radial average fit (red line) shows a steeper slope than the H II regions regression (green line), but in agreement with the gradient of the *direct* abundances (black dotted-line). A comparison between the abundances derived through the *direct* method and the ff–T_e relation is presented in Table 6.9. The value of the integrated abundance matches both samples at $\rho/\rho_{25} \sim 0.1$. The derived values of the abundance gradient analysis for NGC 3310 are shown in Table 6.8 for all the calibrators discussed above, including the *direct* abundances. The "bright" sample exercise was not performed on this galaxy given its peculiar morphology.

Previous determinations of the gas-phase metallicity of this galaxy have been performed, in particular, Pas93 analysed optical and IR spectra for six H II regions located at the circumnuclear region and the spiral arms, including the nucleus and the *Jumbo* H II region. They obtained *direct* abundances by using four temperature-sensitive lines (including [O III] λ4363 in the optical). The total oxygen abundances derived by these authors are in the range $8.13 \leqslant 12 + \log(\mathrm{O/H}) \leqslant 8.47$, which are in complete agreement with the *direct* abundances derived in this work. Taking the specific sample of the *Jumbo* H II region (N3310–9 in this work), Pas93 obtained $12 + \log(\mathrm{O/H}) = 8.21$, $12 + \log(\mathrm{N/H}) = 6.92$, and $t_3 \equiv t([\mathrm{O\ III}]) = 1.04$ (derived from the [O III] λ4363 line) in units of 10^4 K; the corresponding values from this study (Table 6.9) are: $12 + \log(\mathrm{O/H}) = 8.27$, $12 + \log(\mathrm{N/H}) = 7.11$ and $t_3 = 1.09$, i.e. showing an agreement within 0.1 dex for the total abundances and a difference of 500 K in the derived electron temperature. However, from the abundance gradient analysis discussed above, we cannot account for the high oxygen value derived by these authors for the nuclear region of the galaxy, $12 + \log(\mathrm{O/H}) = 9.0$. If that value is true, it would imply a

Direct METHOD: RESULTS

		Direct method					ff–T_e method		
H II region	I(λ4363)	t_3	O^+/H^+	O^{++}/H^+	O/H	N/H	t_3	O/H	N/H
9	2.20 (0.34)	1.09	8.07	7.82	8.27 (0.05)	7.11 (0.03)	1.11	8.24 (0.07)	7.13 (0.01)
11	2.18 (0.33)	1.13	8.08	7.70	8.23 (0.05)	7.08 (0.03)	1.14	8.22 (0.07)	7.14 (0.01)
12	3.20 (0.49)	1.35	8.01	7.45	8.11 (0.05)	6.97 (0.03)	1.29	8.12 (0.06)	7.12 (0.01)
13	2.70 (0.52)	1.40	7.93	7.30	8.02 (0.05)	7.05 (0.03)	1.12	8.21 (0.06)	7.28 (0.01)
14	3.24 (0.49)	1.48	8.04	7.26	8.11 (0.05)	7.05 (0.03)	1.14	8.20 (0.07)	7.23 (0.01)
19	2.08 (0.32)	1.12	7.96	7.70	8.15 (0.05)	7.14 (0.03)	1.04	8.29 (0.07)	7.24 (0.01)
20	2.89 (0.39)	1.25	7.99	7.58	8.14 (0.05)	7.06 (0.03)	1.20	8.18 (0.07)	7.17 (0.01)
26	4.12 (0.62)	1.58	8.08	7.24	8.14 (0.05)	6.99 (0.03)	1.24	8.15 (0.07)	7.15 (0.01)
38	2.86 (0.43)	1.29	8.12	7.49	8.21 (0.05)	7.06 (0.03)	1.26	8.14 (0.07)	7.16 (0.02)
39	4.47 (0.60)	1.46	8.04	7.42	8.13 (0.05)	7.05 (0.03)	1.14	8.22 (0.07)	7.20 (0.01)
40	3.74 (0.52)	1.28	7.88	7.64	8.08 (0.05)	6.98 (0.03)	1.09	8.26 (0.07)	7.12 (0.01)
41	4.64 (0.77)	1.64	8.02	7.21	8.09 (0.05)	7.07 (0.03)	1.12	8.23 (0.06)	7.26 (0.01)
47	3.90 (0.74)	1.42	7.88	7.42	8.01 (0.05)	6.94 (0.03)	1.17	8.20 (0.07)	7.14 (0.01)
60	3.43 (0.48)	1.38	8.00	7.43	8.10 (0.05)	7.00 (0.03)	1.20	8.18 (0.07)	7.16 (0.02)
61	3.18 (0.46)	1.38	8.11	7.39	8.18 (0.05)	7.02 (0.03)	1.29	8.12 (0.06)	7.14 (0.02)
67	3.59 (0.48)	1.41	8.03	7.40	8.12 (0.05)	6.99 (0.03)	1.24	8.15 (0.06)	7.14 (0.01)
68	3.83 (0.54)	1.53	8.10	7.26	8.16 (0.05)	6.98 (0.03)	1.23	8.15 (0.06)	7.13 (0.01)
71	3.45 (0.51)	1.44	7.98	7.34	8.07 (0.05)	6.99 (0.03)	1.19	8.17 (0.07)	7.17 (0.01)
93	2.03 (0.28)	1.07	7.88	7.82	8.15 (0.05)	7.09 (0.03)	1.08	8.26 (0.07)	7.15 (0.01)
94	1.93 (0.29)	0.94	8.03	8.22	8.43 (0.05)	7.22 (0.03)	1.10	8.27 (0.07)	7.08 (0.01)
95	3.24 (0.51)	1.18	7.81	7.76	8.09 (0.05)	7.06 (0.03)	1.13	8.24 (0.06)	7.15 (0.01)
96	3.91 (0.56)	1.32	7.78	7.59	8.00 (0.05)	7.00 (0.03)	1.05	8.29 (0.07)	7.20 (0.01)
101	3.90 (0.65)	1.40	7.93	7.46	8.06 (0.05)	6.93 (0.03)	1.15	8.21 (0.07)	7.11 (0.01)
102	3.07 (0.44)	1.19	7.89	7.73	8.12 (0.05)	6.93 (0.03)	1.20	8.19 (0.07)	7.01 (0.01)
137	4.95 (0.91)	1.52	8.05	7.39	8.14 (0.05)	6.91 (0.03)	1.22	8.18 (0.07)	7.05 (0.01)
157	4.55 (0.62)	1.28	7.87	7.73	8.11 (0.05)	7.01 (0.03)	1.17	8.23 (0.07)	7.10 (0.01)

Table 6.9: Results from the *direct* abundance method. The first column corresponds to the ID of the H II region; the second column to the extinction corrected intensity of the [O III] λ4363 line, normalized by Hβ (in units $100\times$I(λ4363)/Hβ); the following 5 columns correspond to the results of the *direct* method, the electronic temperature $t_3 \equiv t([\mathrm{O\ III}])$ in units 10^4 K, the ionic and total abundances are in units $12+\log(\mathrm{Z/H})$. The results from the ff–T_e method for the same regions are presented for comparison purposes.

change in the metallicity of ~ 0.9 dex, i.e. a factor of 8 from the perinuclear regions to the nuclear zone within less than 1 kpc. Contrary to Pas93, the spatial sampling presented in this work near (and including the nucleus), is consistent with a central oxygen metallicity $12+\log(\mathrm{O/H}) \sim 8.3$, which seems more reasonable considering the flat gradient of the central zone of NGC 3310.

During the selection process of the H II region catalogue of NGC 3310, some regions showed strong variations from point-to-point within a relatively small physical area. One example corresponds to the region N3310–93, located at $(\Delta\alpha, \Delta\delta) \sim (-8, -25)$ in Figure 6.65. Despite that, from the morphological point of view, N3310–93 seemed to be a well-defined, compact region, it showed large variations on the strengths of its emission lines (particularly oxygen) from fibre-to-fibre, in a very reduced area. Therefore, in order to study the small scale variations of the gas emission and physical properties, a smaller H II region, N3310–94, was extracted within the larger N3310–93, at the position of the fibre with the largest variation on the emission line intensities. Figure 6.71 shows the spectra of both regions, in the case of the larger N3310–93, the strength of the [O II] λ3727 line is comparable with that of the [O III] λ5007 line, while for N3310–94, the [O II] line is much weaker, comparable in strength with the [O III] λ4959 line. Furthermore, in N3310–94, the λ5007 line is of the same order of intensity as the Hα. The distribution of the *direct*

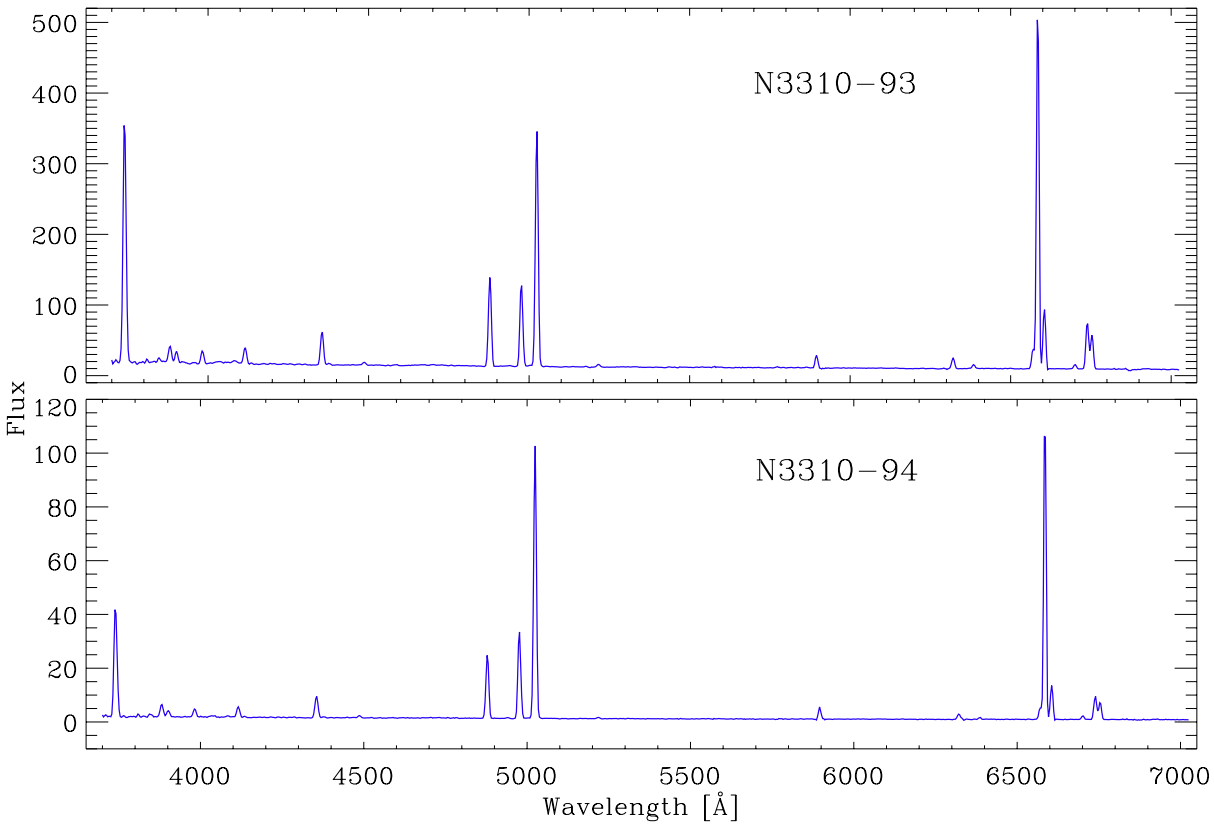

Figure 6.71: Variations on the observed spectra between the H II regions N3310–93 and N3310–94, located at a similar position but extracted a with different integration aperture.

abundances in Figure 6.70 shows an "outlying" H II region consistent with metallicity $12+\log(\mathrm{O/H}) = 8.43$ at $\rho/\rho_{25} \sim 0.3$, this region corresponds to N3310–94. The derived metallicity for N3310–93 is 8.15, i.e. a difference of ~ 0.3 dex (a factor of 2) in the derived abundance, merely by a small change in the extraction aperture of the spectra.

The compact N3310–94 region shows more contribution from the O^{++}/H^{+} to the total oxygen abundance, contrary to N3310–93 where the contribution from the lower ionization state is slightly higher (see Table 6.9). The ionization parameter also shows a considerable variation, with the compact N3310–94 region consistent with higher ionization ($\log u = -2.8$) than N3310–93 ($\log u = -3.03$). The logarithmic extinction coefficient c(Hβ) also varies depending on the integration aperture, for the larger N3310–93, c(Hβ) = 0.33, while for the compact N3310–94, c(Hβ) = 0.54. In the scenario of a classical two-zone model of ionization structure of a H II region, the inner zone presents a higher level of ionization and therefore the contribution from the O^{++} ion is more prominent. For larger Strömgren volumes the ionization drops, and therefore the contribution from the O^{+} ion is more significant to the total oxygen abundance. The fact that we observe more contribution from O^{++} in the inner N3310–94 region (and higher $\log u$), and that the contribution from the O^{+} ion becomes more important for the larger area covered by N3310–93 (with a lower integrated value of $\log u$), is consistent with the classical two-zone ionization structure described above. Therefore, the observed variations of the physical parameters between the areas cover by these two regions, may be reflecting an intrinsic internal structure within what would be considered classically a single H II region. This gives support to the idea previously discussed in section 6.1, that for relatively resolved H II regions, the observed line ratios and derived parameters are aperture dependent.

DISCUSSION

In this section, I presented the spectroscopic analysis of NGC 3310 based on two samples with the best quality and signal-to-noise found in the PINGS observations. The serendipitous discovery of H II regions in the fibres sampling the sky emission allowed to extend the baseline of the observations to normalised radius up to $\rho/\rho_{25} \sim 1.7$. Previous spectroscopic observations of this galaxy had only targeted the very bright perinuclear region of NGC 3310, therefore this study presents the first spectra extending to the spiral arms and tidal debris of this peculiar galaxy. The information provided by the diagnostic diagrams of the analysed regions show that the ionization is consistent with a thermal continuum, but approaching the boundaries of other types of ionization. The emission of the [O III] and [N II] lines present important changes as a function of galactocentric radius, especially for the latter specie. The value of R_{23} shows a flat and narrow distribution over the whole area of the galaxy, with values corresponding in general to the upper branch, but reaching the transition zone for the outer regions of the galaxy.

A striking feature is found on the radial variation of the ionization parameter (and the O_2H_α ratio), where a discontinuity is present at $\rho/\rho_{25} \sim 0.8$, after a constant increase of $\log u$ from the inner regions, corresponding to a decline in the ionization parameter of ~ 0.5 dex, reaching even lower values than those present in the innermost zone of the galaxy. This break is also seen in the O_2H_α ratio, translated to an upturn and flat distribution of this value from the discontinuity radius. This break of the ionization causes the $O3N2$ calibrator to produce a fictitious upturn in the metallicity gradient for the outer regions of the galaxy. The KK04 and ff-T_e methods are consistent with a flat central gradient, and lower metallicity values for the outermost regions, with a possible small break at the discontinuity radius. For a number of H II regions the determination of the oxygen abundance through the *direct* method was possible, due to the detection and accurate measurement of the [O III] λ4363 line. The derived *direct* abundances are in agreement with the –0.5 dex offset of the KK04 calibrator and the metallicity values derived from the ff–T_e method.

The fact that the outermost regions of the galaxy present the same level of ionization than the innermost parts is intriguing. Given the suspected merging history of this galaxy (Kregel & Sancisi, 2001), this trend might reflect that the interaction process proceeded in a way that these outlying regions correspond to debris from an accreted disk or a smaller interacting object, with ionization properties resembling those of the nuclear region of the galaxy. Furthermore, the fact that the outermost regions were discovered in a serendipitous way through the random location of the sky-fibres, may suggest that the outlying regions of NGC 3310 present a considerable level of recent star formation, that might be underestimated given the high brightness of the central region of the galaxy. In fact, the different values derived from the integrated spectrum of NGC 3310 equal the radial distribution at very inner regions, reflecting the high weight of the nuclear zone of the galaxy to the total integrated spectrum

Evidence of aperture-dependence on the measured emission line ratios and physical properties of H II regions was found for a peculiar region of this galaxy. The fact that we find a difference of ~ 0.3 dex in the derived *direct* oxygen metallicity within the same H II region, brings support to the idea that large H II regions might present either, intrinsic abundance inhomogeneities and/or large temperature fluctuations (e.g. Peimbert & Costero, 1969; Peimbert et al., 2004), that yield different chemical abundances measured from collisionally excited lines, as a function of the integration aperture and position.

7

Conclusions and future work

The emergence of a new generation of instrumentation, i.e. multi-object and integral field spectrometers with large fields of view, capable of performing emission-line surveys based on samples of hundreds of spectra in a 2D context, are allowing us to test, confirm, and extend the previous body of results from small-sample studies based on typical long-slit spectroscopy, while at the same time open up a new frontier of studying the 2D structure and intrinsic dispersion of the physical and chemical properties of the disks of nearby spiral galaxies.

The project developed in this dissertation represent the first endeavour to obtain full 2D coverage of the disks of a sample of spiral galaxies in the nearby universe. The semi-continuous coverage spectra provided by the imaging spectroscopy technique employed in this dissertation, allowed us to study the small and intermediate linear scale variation in line emission and the gas chemistry for a selected number of galaxies of the observed sample.

7.1 PINGS and the IFS of nearby galaxies

The PPAK IFS Nearby Galaxies Survey: PINGS, was a carefully devised observational project, designed to construct 2D spectroscopic mosaics of 17 nearby galaxies in the optical wavelength range. The sample includes different galaxy types, including normal, lopsided, interacting and barred spirals with a good range of galactic properties and star forming environments, with multi-wavelength public data. The spectroscopic data set comprises more than 50 000 individual spectra, covering an observed area of nearly 100 arcmin^2, an observed surface without precedents by an IFS study.

I have assessed very carefully all sources of errors and uncertainties found during the intrinsically complex reduction of the IFS observations. This complexity was further deepened considering the large spectroscopic sample produced by the mosaicing of the galaxies, for which the observations were performed at different stages, even spanning for periods of years. In this respect, I contributed importantly to improve the standard pipeline procedure for the PPAK spectroscopic data, improvements that can be applied to any simi-

lar integral-field observation and/or data reduction. In particular, new reduction methods were developed for the key steps that represent the main sources of error of any IFS observation: sky-subtraction and flux calibration. Thanks to these new techniques, I obtained the most accurate possible residual minimization and spectrophotometric calibration, within the limits imposed by the instrumentation. Therefore, I contribute not only to develop a reliable reduction pipeline, but to defining a self-consistent methodology in terms of observation, data reduction and analysis for the kind of IFS surveys as presented in this dissertation, as well as a whole new set of visualization and analysis software that will be made public in the near future.

Despite all the complexities involved in the observations, data reduction and analysis, the PINGS project proved to be feasible. In less than a three-years period, it was possible to build a comprehensive sample of galaxies with a good range of galactic properties and available multi-wavelength ancillary data, maximising both the original science goals of the project and the possible archival value of the survey. In fact, the science case of the PINGS project was the inspiration for the proposed Calar Alto observatory legacy survey, known as CALIFA (Calar Alto Large Integral Field Area Survey), which aims to observe a statistically complete sample of ~ 1000 galaxies in the local universe.

A comprehensive comparison of extracted spectra from the PINGS sample to previously published data was performed. This exercise helped to test the accuracy of the astrometry, the flux calibration, and the quality of the sky-subtraction. All comparisons showed a very good agreement in terms of the flux intensity level and spectral features, errors are within the uncertainties expected for this kind of spectroscopic data, i.e. of the order of 20%. At note of caution must be mentioned though, as slightly larger differences were found for wavelengths shorter than ~ 4000 Å, due to the exponential fall in sensitivity of the CCD detector. The scientific analysis of this dissertation comprises the study of the integrated properties of the ionized gas of the whole PINGS sample, and a detailed 2D study of the physical and chemical abundance distribution derived from the emission line spectra of four selected galaxies of the sample. The conclusions drawn from these analyses are presented in the following sections.

7.2 Integrated properties

Integrated spectra of the PINGS sample was obtained by co-adding all the fibres within a given galaxy mosaic. For a number of objects, their integrated spectra presented in this dissertation was obtained for the first time, while for the rest of the sample, the obtained spectra covered a much larger area than previous studies. In particular, the integrated spectrum of NGC 628 represents the nearby galaxy with the widest area covered by any spectroscopic means. Multi-SSP template modelling was performed in order to decouple the contribution to the spectrum of the stellar populations and the ionized gas. A full set of emission lines were detected and measured in each case from the residual spectrum after the stellar continuum subtraction, allowing an abundance analysis based on a suite of strong-line calibrators.

The ionization and excitation properties of the derived spectra were analysed by means of diagnostic diagrams, which confirm the thermal radiation nature of the ionization sources of the detected emission lines. The validity of the determination of the integrated chemical composition of a galaxy, through the analysis of global emission line spectra, was confirmed. Large offsets between the different empirical methods were found, the R_{23} methods based on photoionization modelling providing higher values of the derived abundances. The most stable and reliable abundance determination seems to be provided by the ff–T_e relation, although this technique seems to vary very little from a mean oxygen value. If an arbitrary negative offset is applied to the R_{23}-based indicators, their oxygen abundances seem to be consistent with infra-solar values,

in agreement with other empirical indices. All the derived abundances through the R_{23} method were obtained from the upper-branch of this relation. It was found that the validity of the abundance determination depends mainly on the chosen calibrator used to derived the chemical composition, and to a second order, on the SSP fitting decouple.

Despite the well-known offsets between the abundance determinations, all the empirical methods agree in the metallicity sequence of the galaxies. The object with the higher integrated metallicity content is NGC 3184, galaxy which previous studies of individual H II regions pointed as one of the oxygen-richest objects known in the nearby universe. The metallicity sequence is followed by NGC 1637, NGC 628, NGC 4625, NGC 6701, NGC 1058, NGC 7770, NGC 7771 and NGC 2976 within a range of $\sim$ 0.2 dex in metallicity, depending on the calibrator considered. The most metal-deficient galaxies correspond to NGC 5474 and NGC 3310, with a difference of $\sim$ 0.5 dex (a factor of 3) with respect to NGC 3184. The integrated properties derived in this dissertation were compared to the resolved properties of the selected galaxies for which a 2D analysis was performed.

7.3 Spatially resolved properties

Four galaxies of the PINGS sample were selected in order to perform a 2D spectroscopic analysis of their gas chemistry. They correspond to NGC 628, NGC 1058, NGC 3184 and NGC 3310, i.e. four of the largest and best covered objects of the sample. A similar decoupling technique as in the integrated spectra case was applied in order to subtract the stellar continuum underlying the nebular emission lines. The goodness of the continuum fitting was assess through a statistical approach, followed by an individual inspection and correction of those fibres flagged as bad fittings. Emission line intensities were measured from the residual spectra of the galaxy mosaics. During this process, special attention was paid in order to avoid an over-automatization of the method that could lead to errors in the derived physical parameters from the resultant spectra. Although, given the large amount of data, some problems might be expected for individual fibres, pointings or regions, or in the derived quantities from the measured line intensities. However, all the quality checks performed to the data (and the results derived from them) suggest that the methodology implemented in this dissertation is very advantageous for a statistical and comparative study, and when dealing with a large number of spectra.

Spatially-resolved maps of the emission line intensities and physical properties of the selected galaxies were derived for each of the four selected galaxies. Contrary to previous attempts to perform a 2D wide-field analysis based on narrow-band (or Fabry-Perot) imaging, which only allowed a basic analysis of the physical parameters and/or required assumptions on the line ratios included within individual filters (e.g. Hα), the emission line maps presented in this dissertation were constructed from individual (deblended) emission lines at any discrete spatial location of the galaxies, where enough signal-to-noise was found. This fact allowed to investigate the point-to-point variation of the physical properties over a considerable area on the surface of each galaxy. Extinction, ionization, and metallicity-sensitive indicators maps were derived from reddening corrected emission line maps. In general, they show that the ionized gas in these spiral galaxies exhibits a complex structure, morphologically associated with the star forming regions located along the spiral arms.

The distribution of the extinction varies considerably from galaxy to galaxy, but it shows no systematic dependence on galactocentric radius or excitation. The ionization maps show different behaviours depending on the galaxy, but consistent in general with higher values of the ionization parameter found at the outer

parts of the galaxies. On the other hand, the maps corresponding to the metallicity indicators show spatial variations corresponding to abundance gradients, consistent with higher values of metallicity at the centres of the galaxies, and lower values at the outer parts, although the galactocentric variation of these indicators (the gradient slope) changes from object to object. Some particularly interesting regions and trends were found by comparing different maps corresponding to different physical properties for each of the selected galaxies. It was found that the average values of all the considered physical parameters in the maps agree, within the errors, to the same values derived from the integrated spectrum of each galaxy.

Although the derived emission line maps proved to be useful in describing the general 2D properties of the selected galaxies, the conclusions raised from them were based on general trends that depend, to a certain level, on the interpolation scheme applied in order to derive the pixel-resolved maps. It was found that more robust conclusions can only be drawn by analysing individual regions of a given galaxy, or by co-adding spectra of regions with the same physical properties and comparing the results in the 2D context. This approach was followed in order to study the spatially-resolved spectroscopic properties of the selected galaxies. However, the spectroscopic dataset presented in this dissertation poses a challenge, regarding the correct methodology in order to handle and analyse, in a homogeneous and meaningful way, the full dataset.

The analysis of NGC 628 was taken as a case study in order to explore three different methodologies, taking into account the signal-to-noise of the data, the 2D spatial coverage, the physical sense of the derived results, and the final number of analysed spectra. The proposed methods differ mainly in the way to select a subsample of spectra from the IFS mosaics, from which a spectroscopic analysis can be later performed. Given that, in average, the aperture of each PPAK fibre of the selected galaxies would correspond to a physical size of $\sim$ 150 pc, two of the methods considered the spectra contained in single fibres to be representative of the physical conditions of the regions sampled by the fibre aperture. Different selection criteria were applied in both methods, seeking for only those regions with meaningful spectral features. The selection criteria of the first method, the *fibre-by-fibre* analysis, proved to select regions with good quality spectra from which different physical properties of the galaxy were derived, although with a high level of scatter. The second method was based on considering only those fibres with "physical" features in their spectra. This latter method reduced considerably the number of analysable spectra, and discarded regions of low (but meaningful) emission. The third method consisted in creating a catalogue of "classical" H II regions from a purely geometrical principle, i.e. by co-adding (by visual selection) fibres considered to belong to the same morphological region.

A combination of these methods was used in order to perform the 2D spectroscopic analysis of the selected galaxies. The locus of the selected spectra was explored by employing typical diagnostic diagrams of reddening corrected emission line ratios. In all the galaxies, the selected spectra were consistent with emission produced by ionization of a thermal continuum, i.e. hot OB stars. However, each galaxy showed different trends in terms of the location and the radial trends of the data points. The radial variation of the R_{23} metallicity indicator, the ionization parameter and the [N II] λ6584/Hα ratio were also analysed, showing in all cases clear, but different gradients, depending on each galaxy. A suite of strong-line metallicity indicators were employed in order to derive the oxygen abundance of each galaxy as a function of the galactocentric radius, i.e. their abundance gradients. For each of the considered spectral samples, azimuthally-averaged radial spectra were extracted from successive rings centered at the origin reference point on each galaxy. A similar analysis was performed to these data and the results compared with the point-to-point trends of the original samples. The galaxies presented different trends, some of them depending on a given metallicity calibrator, the overall conclusions regarding the radial distribution of the chemical abundances for the

selected galaxies are discussed thereinafter. General results inferred from the 2D spectroscopic analysis performed to the selected galaxies are the following:

1. Despite the large quantity of spectra contained in the observed mosaic of a single galaxy, the final number of fibres containing analysable spectra of enough signal-to-noise for a spectroscopic study of the ionized gas represents only a reduced percentage of the total number of fibres contained in the full IFS mosaic. In some cases, less than 10% of the total area sampled by the IFU observations is considered of sufficient quality.

2. The "non-physical" [O III] λ5007/λ4959 line ratios found in the final samples of the *fibre-by-fibre* and H II region catalogues are due to errors introduce by the continuum subtraction of the SSP models to the data, the effect is especially important in regions of weak emission in the [O III] lines (e.g. the centres of the galaxies). Therefore, although the [O III] ratio may not be close to the theoretical value, the combination of their derived line ratios are still representative of the physical conditions and metallicity abundance.

3. The comparison between the results derived from the *fibre-by-fibre* sample and those of the H II region catalogue show that, the selection criteria applied to the former case resulted in regions than follow, in statistical basis, exactly the same patterns and trends, provided by the more "refined" H II region sample, although with a larger level of scatter.

4. The analysis based on the radial average spectra resulted in similar trends than the previous two samples, but with a much reduced scatter and clearer trends in the distribution of line ratios and abundance gradients.

Some implications of the above results are discussed in the following sections.

7.3.1 Aperture and spatial dependence of the metallicity estimations

In subsection 6.3.3, I raised several questions regarding the reliability of the results derived from a point-to-point (fibre-to-fibre) basis, compared to the co-added spectrum of a larger, classically well-defined H II region. As discussed in this dissertation, it has been argued that several factor may prevent an accurate determination of the chemical abundance of a H II region, some of them related to the intrinsic geometrical structure of the emitting region, e.g. the existence of electron temperature fluctuations, the presence of chemical inhomogeneities, the geometrical distribution of the ionization sources, the possible depletion of oxygen on dust grains, etc. If true, some or all of these effects may account for the large scatter seen in the determination of metallicities, even if the electron temperature can be estimated directly from the spectra.

The 2D character of the PINGS data allow us to study the small-scale variation of the spectra within a given emitting area. In section 6.1, I performed an analysis of the variation of some emission line ratios as a function of integration aperture for a bright H II region of NGC 1058. From this exercise, it was found that the values of the emission line ratios measured using different extraction apertures vary considerably as a function of the aperture size, and that the scatter of the central value is larger than the statistical error in the measurements, reflecting that this might in fact be a physical effect. Another particularly striking example of the aperture-dependence of the measured emission line ratios and physical properties of H II regions is discussed in the spectroscopic analysis of NGC 3310, regarding the evident difference in the observed spectra and subsequent determination of the physical properties of the H II regions N3310–93 and 94, located

at a similar position, but extracted with a different integration aperture. The *direct* abundance measured in both regions differ by $\sim$ 0.3 dex, i.e a factor of 2 in metallicity within a region of $\sim$ 500 pc. A possible combination of the physical scenarios mentioned above could explain this discrepancy, however, the observations might be reflecting an intrinsic internal structure within what would be considered classically a single H II region.

Coming back to the point of the reliability of the results derived from the analysis based on a point-by-point basis, a plausible explanation of the high level of scatter found in the *fibre-by-fibre* analysis may be statistical variations due to spectra that, despite the quality selection criteria, are of relatively low signal-to-noise compared with the integrated spectra of the H II regions catalogue In this scenario, the line intensity variations would be just reflecting spurious effects due to the relatively weakness of those emitting regions.

On the other hand, if we take as a premise that for a sufficiently large H II region, the emission line measurements are aperture and spatial dependent, i.e. that the light is emitted under different physical conditions, by gas in different degrees of ionization, and modified by different amounts of reddening (and therefore providing different elemental ionic abundances), the scatter seen in the *fibre-by-fibre* analysis may be due to the intrinsic distribution of the ionizing sources, gas content, dust extinction and ionization structure within a given region, i.e. we would be sampling real point-to-point variations of the physical properties within a H II region. Two factors may give support to this hypothesis; first, the high level of consistency between the results from the *fibre-by-fibre* sample and the H II region catalogue in the spectroscopic analysis of the four selected galaxies. Second, the fact that the aperture of the PPAK fibres is relatively large compared with typical widths employed in long-slit spectroscopy ($\sim$ 1–3 arcsec), and therefore, at the assumed distances of the selected galaxies, each fibre samples regions larger than 100 pc, i.e. a physical size which in principle, would subtend a large enough volume of ionized gas capable of emitting a detectable, physical spectrum. These factors combined with the fact that the *fibre-by-fibre* sample was selected after applying a relatively strict quality selection criteria, may suggest that, *in the scenario of intrinsic physical and geometrical variations in an emitting nebula*, the observed dispersion in the derived line ratios and chemical abundances might be due to real variations of these properties within a single H II region.

If to some extent this last possibility is true, then a reasonable scenario may include a combination of both effects, i.e. that the scatter seen in the results of the *fibre-by-fibre* sample compared to the H II region catalogue is due to the contribution of both, the geometrical distribution of the physical properties on a single region, and the statistical variations due to the intrinsically low signal-to-noise of the observed spectra. From the analysis and results presented in this dissertation, I found evidence to support the idea that the measurements of emission lines, of a "classical" H II region, are not only aperture, but spatial dependent; and therefore, the derived physical parameters and metallicity content may significantly depend on the morphology of the region, on the slit/fibre position, on the extraction aperture and on the signal-to-noise of the observed spectrum.

7.3.2 Multi-modality of the abundance gradients of spiral galaxies

The abundance analysis for the selected galaxies was performed based on a variety of diagnostic techniques using reddening corrected spectra. Thanks to the nearly complete coverage of H II regions observed over the surface of the galaxies, I was able to explore (to a first order), the systematics of the derived abundance gradients by employing different sets of spectra and/or H II regions, covering different ranges of galactocentric radii. It was found that, in general, the derived slopes from the main samples (i.e. *fibre-by-fibre* and

H II regions) and those derived through the radial average samples are equivalent within the errors. For the largest objects of the selected galaxies, NGC 628 and NGC 3184, the IFS data covered only regions within $\rho/\rho_{25} \sim 0.7$, while for NGC 1058 and NGC 3184 the baseline extended up to radii $\rho/\rho_{25} \sim 1.7$. Despite the difference in the sampled regions, the 2D coverage of the PINGS data allowed to analyse regions that had not been considered in previous studies.

In the case of NGC 1058 and NGC 3310, the ambiguity on the selection of the R_{23} branch for the outlying regions prevented a definite determination of the gradient from the KK04 indicator. However, by comparing the results from different metallicity indicators, a general trend could be derived. Both galaxies show a flattening of the abundance gradient for large galactocentric radius, with probable a small discontinuity of the metallicity gradient of NGC 1058. The radial trends of NGC 3310 show a striking discontinuity in the ionization parameter, probably due to a recent merging episode, this drastic change in the ionization provokes an incorrect determination of the abundance gradient derived through the $O3N2$ indicator. This and other examples presented in this dissertation endorse the fact that, when deriving metallicity gradients of a given galaxy, several calibrators should be used and compared in order to provide a robust conclusion of the general trends. Furthermore, during the abundance analysis of NGC 3310, 26 H II regions were found with a reliable detection of the temperature-sensitive [O III] λ4363 line, allowing to perform a *direct* abundance determination. The metallicities derived from these regions coincide with previously published determinations of the circumnuclear region of this galaxy, and they agree with the derived abundance gradient of this galaxy.

In the case of NGC 628, NGC 1058 and especially NGC 3184, the data presented in this dissertation sample for the first time the emission of the ionized gas from the innermost regions of these galaxies. In all cases, the presence of these regions helped to determined in a better way the real trend of their metallicity gradients for these very low galactocentric radius. In the case of NGC 3184, the inclusion of these regions has a notorious effect in the final derived gradient of the galaxy, where the inner regions ($\rho < 0.3\rho_{25}$) present a *break* from the very steep "outer" gradient derived for regions with larger radii. All the metallicity indicators employed suggest a change in the gradient consistent with a flat distribution from $\rho/\rho_{25} \lesssim 0.3$. Previous studies of individual H II regions on NGC 3184 determined that this galaxy is one of the oxygen-richest objects in the nearby universe, although those results were derived assuming that the maximum value of the oxygen abundance is reached at galactocentric radius equals to zero, by extrapolating the trends observed in the outer parts of the galaxy disk.

A similar effect is found for the innermost regions of NGC 628 and NGC 1058, although the trends are less robust than in the case of NGC 3184. The derived parameters from the abundance gradients were compared with previously published works, making some assumptions in terms of the R_{23} branch employed for the outer regions of the galaxies, or by matching the galactocentric baseline of the observed H II regions from which the gradients were derived. In all cases, I found an excellent agreement, especially comparing the linear slope of the regressions.

An interesting common result found in all the selected galaxies is that, regardless the use of the metallicity calibrator, the abundance derived through the integrated spectrum of a given galaxy correlates with the spatially-resolved H II region abundance gradient for a normalised radius $\rho/\rho_{25} \sim 0.4$, i.e. the abundance inferred from the integrated spectrum of a galaxy is representative of the *characteristic* abundance of a galaxy. This trend was previously indicated by Moustakas & Kennicutt (2006a) for a different sample of galaxies. In this dissertation, I confirmed this correlation for the selected galaxies presented in chapter 6, extending the number of metallicity calibrators that show a similar trend. Figure 7.1 displays the character-

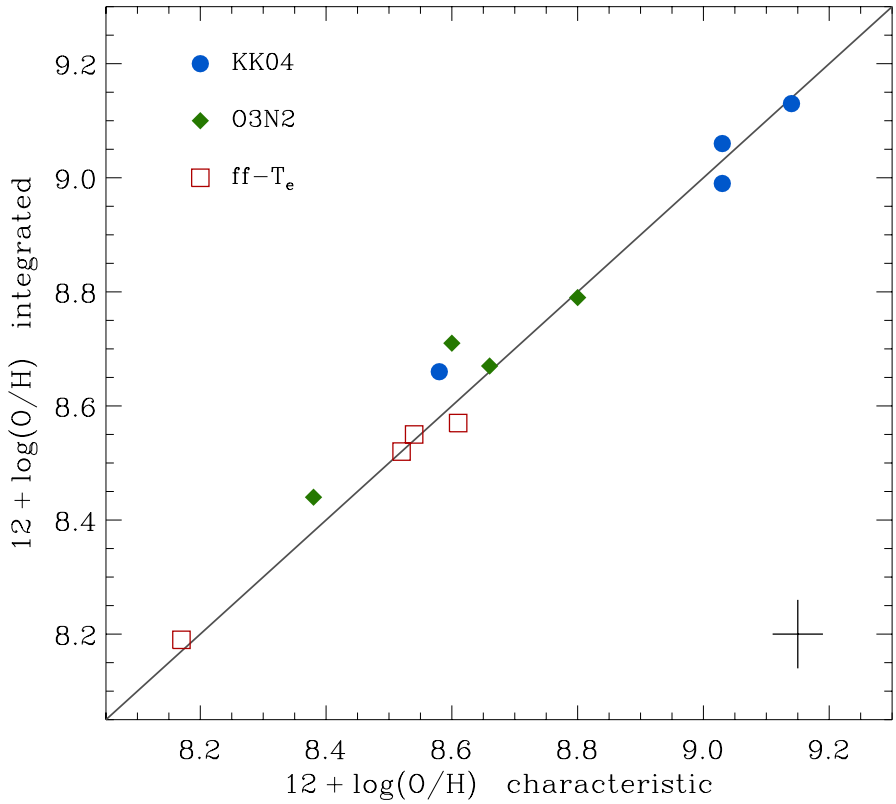

Figure 7.1: Characteristic vs. integrated oxygen abundance for the analysed galaxies of this dissertation. The results from different metallicity indicators are shown with different symbols. The values of the characteristic abundance correspond to those obtained from the radial average spectra of the H II regions catalogue in each galaxy. The mean uncertainty on the derived abundances is shown on the bottom-right corner of the figure.

istic vs. integrated oxygen abundance derived from the four selected galaxies, by using different abundance indicators. The values of the characteristic abundance correspond to those obtained from the radial average spectra of the H II regions catalogue in each galaxy. The values derived after the *O3N2* indicator show more deviations from this relation, the reason being that in general, the abundance gradient derived by this calibrator corresponded to steeper slopes than the rest of the metallicity indicators.

Despite the low number of observed H II regions in the innermost and outermost parts of the galaxy sample, and that the large errors associated with the empirical determination of chemical abundances might prevent any firm conclusion, the results from the abundance gradient analysis of the selected galaxies show features that indicate a multi-modality of the abundance gradients, contrary to the classic scenario of a well-behaved smooth linear negative gradient throughout all galactocentric distances. In this dissertation, evidence for the flattening of the abundance gradients for inner galactocentric radii was found for the "normal" spirals NGC 628, NGC 1058 and especially for NGC 3184. In addition to that, regions beyond the isophotal radius of NGC 1058 and NGC 3310 presented a flat distribution of metallicities, with a possible discontinuity in the case of NGC 1058.

The combination of these results might suggest that the radial abundance distribution of spiral galaxies show the existence of a *bi-* or even *tri-modality* in their chemical abundance distribution, consistent with a flat–steep–flat gradient, with increasing galactocentric distance, with important implications in terms of the

chemical evolution of galaxies. The abundance gradients of some spiral galaxies (including the Milky Way) show a complex behaviour that cannot be explained by a linear relation of the abundance (in logarithmic scales) with galactocentric radius (e.g. Daflon & Cunha, 2004; Zaritsky et al., 1994). These observation have motivated several studies from the theoretical side, suggesting a variety of scenarios consistent with non-linear gradients of the gas-phase metallicity across the disks of spiral galaxies. Some scenarios include the formation of minima and/or plateaus in the gradients near the corotation radius via a selective action of the star-formation, due to the lack of strong spiral shock waves (e.g. Mishurov et al., 2002; Acharova et al., 2005); in this picture, the temporal migration of the corotation resonance may produce either plateaus or minima in the inner radial abundance distribution.

The possible flattening in the abundance gradients have also been investigated by numerical hydrodynamic codes, predicting that the non-axisymmetric gravitational field of spiral stellar densities produce strong cyclones and anticyclones near the corotation. The gas flow induced by these features produce a flattening of the radial abundances profiles near corotation, after a few revolution periods of the galaxy (Vorobyov, 2006). N-body simulations of the dynamics of cold molecular clouds (Sellwood & Binney, 2002; Sellwood & Preto, 2002) also show a development of cyclonic and anti-cyclonic motions at corotation and predict the flattening of any metallicity gradients within the spiral disc. The development of plateaus in the abundance gradient at small and large galactocentric distances is also predicted by chemodynamical models (e.g. Samland et al., 1997) that consider the evolution of a galaxy with different stellar components and a multiphase interstellar medium. The non-linear, flat trends can be reproduce by inside-out scenarios of galaxy formation in which a spiral galaxy is built up via gas infall, and in which the timescale for the formation of the disk increases with galactocentric distance.

A generalization of the results obtained for the selected galaxies regarding the multi-modality of the radial abundance distribution might be premature. However, the results of this dissertation indicate the existence of non-linear abundance gradients in normal spiral galaxies, consistent with a flattening in the innermost and outermost parts of the galactic discs. Furthermore, the study of NGC 3184 and the multi-modality of the abundance gradients brings support to the idea put forward by Pilyugin et al. (2006), that there exists a physical upper limit to the oxygen abundance in spiral galaxies, despite the steep slopes derived for some metal-rich galaxies. A robust conclusion on whether these trends are real awaits further chemical abundance studies in a larger number of similar systems. However, in this dissertation I have proven the powerful capabilities of 2D spectroscopic studies, as I was able to characterise for the first time, the chemical composition of the whole surface of a spiral galaxy in a 2D context, allowing a more realistic determination of the physical properties of the analysed galaxies.

7.4 Future work

Given the practical limitations in terms of the content and extension of this dissertation, the analysis was restricted to only four selected galaxies from the observed sample. Despite the large quantity of analysed spectra, the number of studied galaxies is not sufficiently large to address questions regarding correlations between the metallicity content and other properties of spiral galaxies, which provide indirect, but measurable insights to the nature of galaxy formation. Future plans include to perform similar and complementary analysis to the rest of the sample, in order to fully exploit the 2D nature of the spectroscopic data presented in this dissertation.

In this section I present an overview of the different studies that I wish to undertake in order to follow the

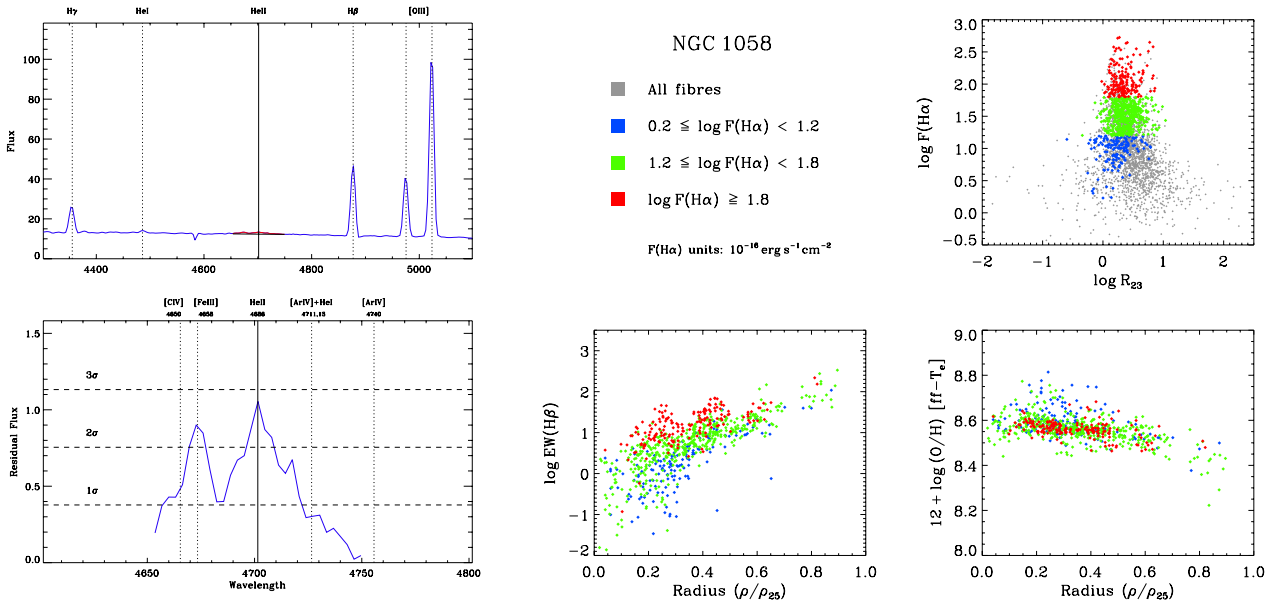

Figure 7.2: Left-panels: Wolf-Rayet features in the spectra of NGC 3310, corresponding to the "blue bump" at $\lambda\sim 4686$. Right panels: properties of H II region populations of NGC 1058, selected by applying discrete luminosity bins.

analysis previously described. Some of these exercises were actually carried out during the main analysis process of the thesis, but were left aside for a posterior, more careful investigation. Furthermore, more detailed studies on individual objects, regions and galaxies are being considered, always in the framework of the 2D distribution of the physical and chemical properties of the ionized gas.

- **Wolf-Rayet stellar population**. The Wolf-Rayet (WR) are hot, massive stars with a high rate of mass loss. They appear in the first stages of burst of star formation, lasting in average over a period of $\sim$ 5 Myr, being an excellent indicator of the age of the ionizing stellar population. The presence of WR stars can be identified by broad emission features or *bumps* in the spectra of H II regions, e.g. the "blue bump" centered at $\lambda\sim 4670$, due mainly by the broaden emission of the lines C IV λ4650, Fe III λ4658, and He II λ4686. To estimate the number of WR stars in an unresolved cluster the equivalent width of the blue bump or the ratio between this bump and the Hβ emission lines are used as diagnostics. I have identified several regions in the PINGS data showing features of WR populations. The left panels of Figure 7.2 show the spectrum of a H II region of NGC 3310, presenting a WR "blue bump" feature. The detection of the bump was performed by subtracting a local continuum in the spectral region of interest. We plan to estimate the number of WR stars from those regions in the PINGS sample showing features of this stellar population, in order to better characterise the ionizing stellar population of the H II region

- **Luminosity dependence of metallicity estimations**. Most spectroscopic studies to date for obvious reasons have preferentially targeted the brightest and highest surface brightness H II regions. The PINGS data provides a much fuller and more objective sampling of the H II region population, allowing a statistical study of the systematic dependences of the strong-line abundances on the size, luminosity, surface brightness an other properties of the H II regions. As an example, the right panels of Figure 7.2 show examples of the behaviour of different H II region populations of NGC 1058, selected by applying discrete luminosity bins. Clearly, different populations with varying intrinsic

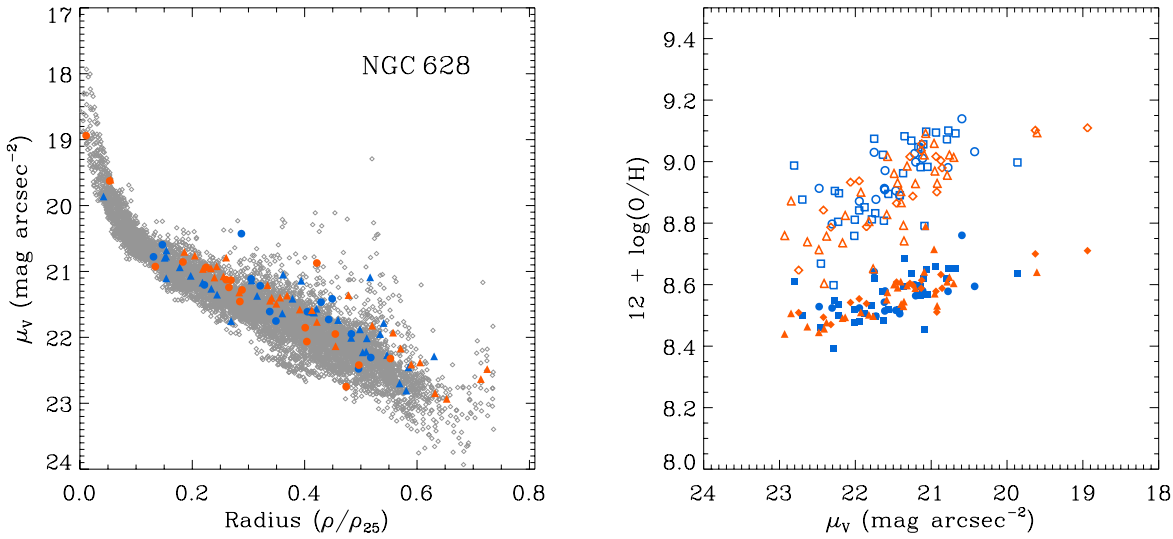

Figure 7.3: Left-panel: surface brightness profile of NGC 628 constructed from all the observed individual fibres in the IFS mosaic. The colour symbols overlaid correspond to the position and surface brightness of the integrated H II region catalogue, different colours and symbols correspond to H II regions located at different geometrical positions of the galaxy. Right-panel: Metallicity abundance from two calibrators (KK04, open symbols; ff–T_e closed symbols) as a function of the H II region surface brightness.

luminosity populate different regions of the galaxy, and show different behaviours in the emission line ratios. Other possible parameter that might be relevant in this context are the surface brightness and size of the H II regions. Left panel of Figure 7.3 shows the surface brightness profile of NGC 628 constructed from all the observed individual fibres in the IFS mosaic. The colour symbols overlaid correspond to the position and surface brightness of the integrated H II region catalogue, different colours and symbols correspond to H II regions located at different geometrical positions of the galaxy. On the right panel, the derived metallicity abundance from two calibrators (KK04, open symbols; ff–T_e closed symbols) as a function of the H II region surface brightness. From this approach, we aim to characterise the possible dependence of strong-line metallicity estimations on the intrinsic luminosity, size and/or surface brightness of the H II regions population.

- **Functional parameters of H II regions**. The features of the emission line spectrum of a H II region are controlled by three fundamental parameters: the shape of the ionizing continuum, related to the *effective temperature* of the ionizing source T_{eff}, the degree of ionization, related to the *ionization parameter u*, and the gas chemical composition, i.e. its *metallicity Z*. These so-called *functional parameters* can be derived from the observed spectra of H II regions by the measured line intensity ratios and translated into physical properties of the H II regions. We plan to study the functional parameters of the H II region catalogues derived in this dissertation in order to interpret these parameters in terms of the physical properties of the ionizing clusters.

- **Asymmetries in the physical properties of spiral galaxies**. The 2D spectroscopic view of a galaxy offer us the opportunity to test whether the metal abundance distributions in disks are axisymmetric, factor which is usually taken for granted in chemical evolution models, but one might expect strong deviations from symmetry in strongly lopsided, interacting or barred galaxies, which are subject to

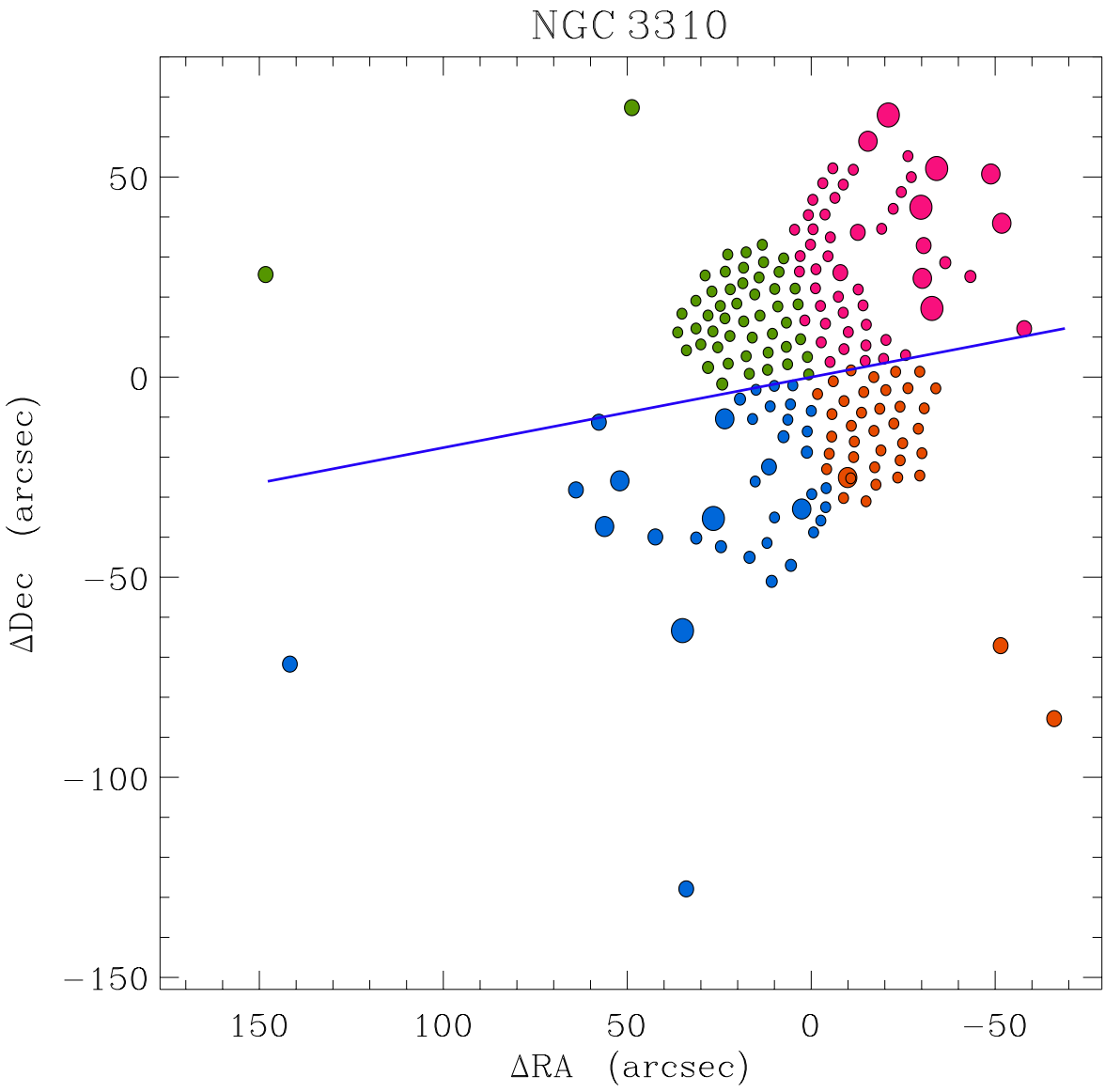

Figure 7.4: Spatial distribution of geometrically selected H II regions in NGC 3310.

large-scale gas flows. Furthermore, we plan to study the relation between abundances and dynamical features such as bar or rings, the influence of chemical enhanced regions and shocks. For example, Figure 7.4 shows the spatial distribution of the selected H II regions of NGC 3310. These regions have been grouped in different colours corresponding to their geometrical position with respect an arbitrary axis. For this galaxy in particular, as shown in this dissertation, the effects of tidal interactions may be relevant on the ionization properties on different portions of the galaxy. These studies will also consider differences in the arm versus intra-arm H II regions, possible asymmetries and morphological variations of the distribution of excitation and diffuse emission.

- **Aperture bias and the integrated spectra of galaxies**. Given the nature of the PINGS data set, the analysis of integrated spectra using different apertures for a given object would provide hints on how the aperture bias influences the determination of galactic properties and the consequences of this effect for the study of distant galaxies.

Other relevant investigations that might be performed by the full analysis of the PINGS sample are:

- To consider galactocentric normalizations other than the isophotal radius ρ_{25}, in order to investigate possible correlations with more physical or morphological related normalizations.
- To investigate the level of intrinsic scatter as a function of galactocentric radius in order to understand the efficiency and timescales for elemental mixing at any radii.
- To study how different mass functions, the size of H II regions and their spatial sampling affect measurements of metallicity and influence strong line calibrations.

In summary, given the richness of the PINGS observations, the data can be used in a variety of ways for many different studies and approaches, not only focusing on the properties of the ionized gas, but also considering the underlying stellar populations.

The future of 2D spectroscopy is very promising, as it may provide new insights into many topics regarding the growth and evolution of galaxies in the universe. However, there remains much work to do on determining the exact details that drive this evolution. The work presented in this dissertation has shed some light on the 2D properties of the gas content on a sample of spiral galaxies observed by means of imaging spectroscopy. This study, and the future planned investigations considered for the PINGS data sample, will hopefully contribute in a significant way to understand the nature of the physical and chemical properties of the gas phase in spiral galaxies.

Appendices

A

Multiple stellar population modelling

The spectral energy distribution (SED) of simple stellar populations (chemically homogeneous and coeval stellar systems) depends on a set of first principles (e.g. initial mass function, star formation rate, stellar isochrones, metallicity, etc.). From the, it is possible to generate synthetic stellar populations. This technique, known as evolutionary synthesis modeling (e.g. Tinsley, 1980), has been widely used to unveil the stellar population content of galaxies by reconciling the observed spectral energy distributions with those predicted by the theoretical framework. Unfortunately the variation of different physical quantities governing the evolution of stellar populations produce similar spectral features integrated light of those systems, leading to a situation in which the observational data is affected by undesirable degeneracies, like the widely known between age and metallicity (e.g. Oconnell, 1976; Aaronson et al., 1978; Worthey, 1994). However, the use of spectrophotometric calibrated spectra and the sampling of a wide wavelength range, as in the case of observed data in this dissertation, provides means to break the degeneracy and allows to derive reliable physical parameters by fitting the full spectral distribution with single-stellar populations (Cardiel et al., 2003).

On the other hand, the simple assumption that a single-stellar population describes well the SED of a galaxy is not valid for late-type galaxies. These objects present complex star formation histories, with different episodes of activity, of variable intensity and time scale. Therefore, in general, a single-stellar population does not reproduce well their stellar emission. A different technique, known as full-spectrum modeling, involving the linear combination of multiple stellar populations and the non-linear effects of dust extinction, has been developed to reconstruct their stellar populations (e.g. Fernandes et al., 2005; Ocvirk et al., 2006; Sarzi et al., 2006; Koleva et al., 2009; MacArthur et al., 2009). In general, these reconstructions require a wide wavelength range to probe the hot, young stars and the cool, old stars simultaneously. They also require the best spectrophotometric calibration to disentangle the effects of age, metallicity and dust extinction. Although different implementations of this technique have some differences, they are very similar in their basis, as described before. The extracted information from the multi stellar-population modelling differs in the different implementations. In some cases the luminosity (or mass) weight ages and metal-

licities are derived, based on the linear combination of different models (e.g. Sarzi et al., 2006). In other implementations the fraction of light (or mass) of different stellar populations (e.g. Stoklasová et al., 2009), or the fraction of light (or mass) that corresponds to old or young stellar populations (e.g. MacArthur et al., 2009) are derived.

For the particular analysis of this dissertation, it is required to model accurately the underlying continuum to get a good representation of the continuum in order to decouple it from the emission lines produced by the ionised gas. Therefore, even in the case that the combination of SSPs is strongly degenerated, and the model created has no physical meaning, it could be partially useful for this purpose.

The implementation of the multi stellar-population fitting technique used in this article is part of the FIT3D package (Sánchez et al., 2007b). This package allows to perform linear fits of a combination of SSPs, and non-linear ones of emission-lines plus an underlying stellar population. It also includes routines to extract the 2D distribution of the different derived parameters based on the analysis of the stellar population (age, metallicity, dust) and/or the analysis of the emission lines (flux intensity, systemic velocity and velocity dispersion). The basic steps performed by the fitting algorithm, spectrum by spectrum, are the following:

1. The program reads the input spectrum, determines the areas to be masked, and constructs the variance map. For the next steps, let us define G_i as the observed galaxy flux at wavelength λ_i, and N the number of elements of the masked spectrum.

2. The code reads the set of SSP template spectra, shifts them to the systemic velocity of the considered spectrum, convolves them to match its spectral resolution and velocity dispersion, and resamples them to its wavelength solution. Let us define F_{ji} as the flux of the i^{th} wavelength of the j^{th} template (once shifted, convolved and resampled), where M_0 is the total number of considered templates.

3. Next, it applies a certain dust extinction to the templates. The extinction law of Cardelli et al. (1989) was adopted, with a ratio of total to selective extinction of R_V =3.1 (Jenkins, 1987). Let us define $F_{ji}^{A_V}$ as the flux of the i^{th} wavelength of the j^{th} template, after applying the dust extinction corresponding to a certain extinction of A_V magnitudes.

4. At this point, it performs a linear least-square fitting of the input spectrum with the set of SSP templates, using a modified χ^2 as a merit function to be minimised, with the form:

$$\chi^2 = \frac{1}{N-M}\sum_{i=1}^{N} R_i^2, \tag{A.1}$$

where

$$R_i = w_i\Big(G_i - \sum_{j=1}^{M} a_j F_{ji}^{A_V}\Big). \tag{A.2}$$

In the above expression, w_i is the weight of the i^{th} pixel, defined as

$$w_i = \frac{1}{\sigma_i^2}, \tag{A.3}$$

where a_j is the coefficient of the j^{th} template in the final modelled spectrum, and M is the number of templates considered in the fitting procedure.

5. The code determines for which templates the fitting produces negative coefficients in the linear combination (i.e. $a_j < 0$). These templates will be excluded from the next iteration of the fitting procedure, that will be resumed in the step (3). At each iteration, M is decreased by the amount of excluded templates. This loop ends once all the coefficients are positive.

6. The modified χ^2 corresponding to the considered dust extinction is stored as $\chi^2_{A_V}$, and the fitting procedure is repeated again starting at the step (3), modifying the considered amount of dust and starting the procedure with the full set of templates (i.e. $M = M_0$, again). This loop ends once the dust extinction has covered a pre-defined range of possible values, that it is defined as an input parameter.

7. The best linear combination of templates and dust extinctions are selected based on the minimisation of the stored χ^2 parameters. The final modelled spectrum flux at λ_i is given by

$$S_i = \sum_{j=1}^{M} a_j F_{ji}^{A_V}, \tag{A.4}$$

   where in this case, only the M templates with positive coefficients a_j are considered, and A_V corresponds to that value which minimises $\chi^2_{A_V}$.

8. The luminosity-weighted age (H) and metallicity (Z) of the underlying stellar population is then derived by the formulae:

$$H = \sum_{j=1}^{M} a_j H_j, \tag{A.5}$$

   and

$$Z = \sum_{j=1}^{M} a_j Z_j, \tag{A.6}$$

   where H_j and Z_j are the corresponding age and metallicity of the j^{th} SSP template. These luminosity-weighted ages and metallicities should be considered as the *equivalent* ages and metallicities of the modeled stellar population, since they would match with the corresponding values if the population was composed by a single SSP.

By construction, the fitting algorithm is useful for masking out undesirable regions in the spectrum. As described in chapter 4, it is necessary to mask: (i) strong and variable night sky-line regions, (ii) regions affected by defects in the CCD (like dead columns) whose effect was not completely removed during the data reduction process, (iii) regions affected by telluric absorptions, not completely corrected during the flux calibration process, and (iv) emission line regions from ionised gas.

As mentioned before, for the purpose of this dissertation, the main goal of this fitting procedure is to provide with and accurate modelling of the underlying stellar population, and to derive a pure-emission line spectrum, given by

$$C_i = G_i - S_i. \tag{A.7}$$

A.1 SSP template library

As indicated by MacArthur et al. (2009), this kind of analysis is always limited by the template library, which comprises a discrete sampling of the SSP ages and metallicities. It would be desired for the stellar library to be as complete as possible, and non-redundant. However, this would require an exact match between the models and the data, which is not possible to achieve in general terms, and in particular if the stellar population comprises more than one SSP. As a suitable solution for the analysis presented in this work, the adopted SSP template library covers the widest possible range of ages and metallicities. These templates have already demonstrated to be useful for modelling the stellar population of a varied set of galaxies.

The SSP models were created using the GISSEL code (Bruzual & Charlot, 2003), assuming a Salpeter IMF Salpeter (1955), for different ages and metallicities. 72 models were created covering a discrete grid of 12 ages (5 Myr, 25 Myr, 100 Myr, 290 Myr, 640 Myr, 0.9 Gyr, 1.4 Gyr, 2.5 Gyr, 5 Gyr, 11 Gyr, 13 Gyr, and 17 Gyr), and 6 metallicities (Z =0.0001, 0.0004, 0.004, 0.008, 0.02 and 0.05). Figure A.1 shows the spectra of all the templates, grouped by their metallicity, and normalized to their flux at 5000 Å. The adopted library is similar in many aspects to the one proposed by MacArthur et al. (2009). Both libraries have a similar number of templates, although the latter library has a wider coverage of the ages and a more reduced coverage of the metallicities of the stellar populations.

There is a number of caveats when applying model SSPs to the integrated light of a star forming galaxy, which have been clearly identified by MacArthur et al. (2009). The most important one is to assume that the parameter space covered by the empirical library represents well that of the real data. However in general, libraries are based on stars in the solar neighborhood, and therefore it is not granted that they represent well the stellar populations in other galaxies (or even in other regions of our Galaxy). There are other potential problems related to the particular selected templates, since it is well known that the Bruzual & Charlot (2003) models have problems when dealing with the non-solar abundance ratios. Most of these problems are not particularly important in the context of the science case of this work, since the primary goal is to model the stellar population to analyse the ionised gas emission.

In addition, it is important to note that the treatment of the dust extinction may affect the resulting derived parameters (i.e. the equivalent age and metallicity of the stellar population). In this particular implementation of the analysis, the Cardelli et al. (1989) extinction law was adopted, which may not be the optimal solution to study the dust extinction in star-forming galaxies (e.g. Calzetti, 2001). MacArthur et al. (2009) adopted a completely different extinction law, based on the two-components dust model of Charlot & Fall (2000), which is particularly developed to model the dust extinction in star forming galaxies. Despite the conceptual differences between the two extinction laws, their actual shapes are very similar in the wavelength range covered by the data of this work.

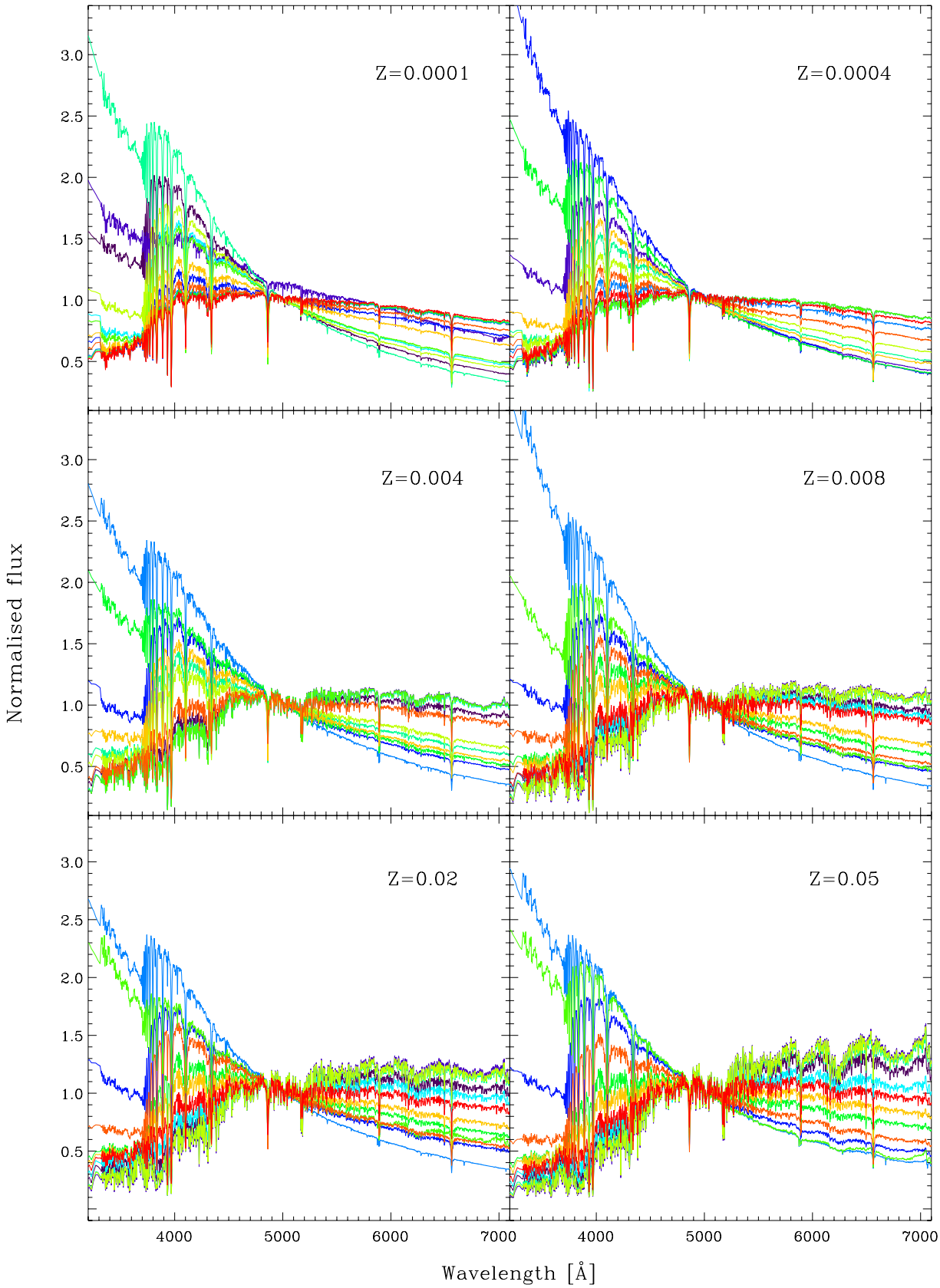

Figure A.1: Spectra of the 72 SSP templates used in the population synthesis fits. Metallicity increases from the top-left to the bottom-right. Different ages are represented by different colours. All the spectra are normalized to the flux at 5000 Å.

B

Interstellar reddening correction

Here I summarised the procedure employed in order to correct the line ratios of the observed spectra for interstellar reddening. First we consider the relation

$$F_\lambda = I_\lambda 10^{-0.4A_\lambda}, \tag{B.1}$$

where F_λ is the observed flux at the wavelength λ, I_λ is the intrinsic (unobscured) flux, and A_λ is the extinction (in magnitudes) at λ. Equation B.1 is equivalent to a flux passing through a medium of optical depth τ_λ

$$F_\lambda = I_\lambda e^{-\tau_\lambda}, \tag{B.2}$$

where $e^{-\tau_\lambda}$ is the extinction factor, and assuming that the interstellar extinction has the same wavelength dependence, $\tau_\lambda = Cf(\lambda)$, where $f(\lambda)$ can be obtained from a given extinction curve.

If we normalised Equation B.2 by the flux intensity of Hβ, and apply a base-10 logarithm, we obtain

$$\frac{F_\lambda}{F_{H\beta}} = \frac{I_\lambda}{I_{H\beta}} 10^{-c(H\beta)[f(\lambda)-f(H\beta)]}, \tag{B.3}$$

where $c = 0.434C$, and $c(H\beta)$ is the *reddening constant* or the *logarithmic extinction coefficient* at Hβ, i.e.

$$F_{H\beta} = I_{H\beta} 10^{-c(H\beta)}. \tag{B.4}$$

Given that, in the emission line spectra of normal H II regions the Balmer lines are strong and the line ratios are relative insensitive to the electron temperature, they can be used to determine the interstellar extinction with a rough estimation of the temperature. From Equations B.3 and B.4 we obtain

$$I_\lambda = F_\lambda 10^{c(H\beta)[1+g(\lambda)]}, \tag{B.5}$$

is the extinction corrected flux I_λ, where $g(\lambda) = f(\lambda) - f(H\beta)$.

On the other hand, the function $f(\lambda)$ can be determined from a given extinction law, classic examples from the literature are:

- Miller & Mathews (1972).
- Savage & Mathis (1979).
- Cardelli et al. (1989).

As in the case of Cardelli et al. (1989), these laws can be parametrised as

$$\zeta(\lambda, R_V) = \frac{A_\lambda}{A_V}, \tag{B.6}$$

where A_λ is the extinction (in magnitudes) at λ, A_V is the extinction in the visual, and R_V, the selective ratio of total to selective extinction, is given by

$$R_V = \frac{A_V}{E_{B-V}}, \tag{B.7}$$

where $E_{B-V} = A_B - A_V$ is the colour excess. Equating B.1 to B.5, and considering that $c(H\beta) = 0.4A_{H\beta}$, we obtain

$$g(\lambda) = \frac{A_\lambda}{A_{H\beta}} - 1 = \frac{\zeta(\lambda, R_V)}{\zeta(H\beta, R_V)} - 1. \tag{B.8}$$

Therefore, for a given value of R_V, we obtain

$$c(\lambda) = c(H\beta)\,(1 + g(\lambda)) = c(H\beta)\left(\frac{\zeta(\lambda)}{\zeta(H\beta)}\right), \tag{B.9}$$

thus, the intrinsic flux I_λ is given by

$$I_\lambda = F_\lambda 10^{c(\lambda)} = F_\lambda 10^{c(H\beta)\left(\frac{\zeta(\lambda)}{\zeta(H\beta)}\right)}. \tag{B.10}$$

Another way of estimating the extinction is by relating the visual extinction to the observed ratio of two lines. Given the relation

$$I_\lambda = F_\lambda 10^{0.4A_\lambda}, \tag{B.11}$$

where F_λ and I_λ are the observed and intrinsic fluxes respectively, we can relate the flux of two lines by

$$\frac{I_1}{I_2} = \frac{F_1}{F_2} 10^{0.4(A_1 - A_2)}, \tag{B.12}$$

applying the logarithm in both sides of the equation and rearranging

$$A_1 - A_2 = 2.5\left[\log\left(\frac{I_1}{I_2}\right) - \log\left(\frac{F_1}{F_2}\right)\right], \tag{B.13}$$

but considering that, for a given value of R_V, $A_\lambda = \zeta(\lambda)A_V$, the LHS of Equation B.13 becomes

$$A_1 - A_2 = A_V\,(\zeta_1 - \zeta_2)\,, \tag{B.14}$$

and therefore

$$A_V = 2.5\left[\frac{\log\left(I_1/I_2\right) - \log\left(F_1/F_2\right)}{\zeta_1 - \zeta_2}\right], \tag{B.15}$$

In the case of observed ratio of Hα and Hβ, Equation B.15 translates to

$$A_V = 2.5\left[\frac{\log\left(I_{H\alpha}/I_{H\beta}\right) - \log\left(F_{H\alpha}/F_{H\beta}\right)}{\zeta_{H\alpha} - \zeta_{H\beta}}\right]. \tag{B.16}$$

B.1 Determination of c(Hβ)

The logarithmic extinction coefficient, c(Hβ), was derived from measurements of the observed Balmer lines, and using the intrinsic values of the Balmer ratios for a canonical electronic density of $n_e = 100$ cm^{-3} and temperature $T_e = 10^4$ K, for the case-B recombination (Osterbrock & Ferland, 2006)

$$\frac{H\alpha}{H\beta} = 2.87 \tag{B.17}$$

$$\frac{H\gamma}{H\beta} = 0.466 \tag{B.18}$$

$$\frac{H\delta}{H\beta} = 0.158 \tag{B.19}$$

using these values and Equation B.3 we derive

$$c(H\beta)_{H\alpha} = \frac{\log(2.87) - \log\left(\frac{F_{H\alpha}}{F_{H\beta}}\right)}{f(H\alpha) - f(H\beta)}, \tag{B.20}$$

$$c(H\beta)_{H\gamma} = \frac{\log(0.466) - \log\left(\frac{F_{H\gamma}}{F_{H\beta}}\right)}{f(H\gamma) - f(H\beta)}, \tag{B.21}$$

$$c(H\beta)_{H\delta} = \frac{\log(0.158) - \log\left(\frac{F_{H\delta}}{F_{H\beta}}\right)}{f(H\delta) - f(H\beta)}. \tag{B.22}$$

Let us define $f'(\lambda) = f(\lambda) - f(H\beta)$, in this way, equations B.20, B.21 and B.22 define three points in a XY plane, where

$$\log\left(\frac{I_\lambda/I_{H\beta}}{F_\lambda/F_{H\beta}}\right) = c f'(\lambda), \tag{B.23}$$

represents a straight line of the form $y = mx$. For Hβ, $y = x = 0$. A least-square fitting was implemented considering the number of points available, i.e. if the Hγ, Hδ lines were reliable measured. The slope, m,

of this regression defines the value of c(Hβ). Note that when only Hα and Hβ are available, the fitting is equivalent to the c(Hβ) value obtained from Equation B.20.

Another possibility (not considered in this work), is to obtain a weighted-average for c(Hβ) from the values provided by equations B.20 to B.22 by using

$$c(H\beta) = \frac{2}{3}\left[c(H\beta)_{H\alpha} + \frac{1}{2}c(H\beta)_{H\gamma}\right] \tag{B.24}$$

when $H\alpha$, $H\beta$ and $H\gamma$ are available, and

$$c(H\beta) = \frac{3}{5}\left[c(H\beta)_{H\alpha} + \frac{1}{3}c(H\beta)_{H\gamma} + \frac{1}{3}c(H\beta)_{H\delta}\right] \tag{B.25}$$

when all these lines are available.

C

Chemical abundance diagnostics

Here I present the explicit expressions for the abundance estimators employed in this dissertation. They include the empirical (bright-lines) calibrators, and the equations involved in the *direct* method for chemical abundance determinations.

C.1 Empirical calibrators

C.1.1 The M91 calibrator

The M91 calibrator (McGaugh, 1991), corresponds to the family of R_{23} estimators, is based on detailed H II region models using the photoionization code Cloudy (Ferland et al., 1998). This calibrator takes into account a correction for the ionization parameter. The parametric expressions for the lower and upper branches for this calibrator given by Kobulnicky et al. (1999) were used in this study. They correspond to

$$12+\log(\mathrm{O/H})_{\mathrm{lower}} = 12-4.944+0.767x+0.602x^2-y(0.29+0.332x-0.331x^2), \quad \text{(C.1)}$$

$$\begin{aligned} 12+\log(\mathrm{O/H})_{\mathrm{upper}} &= 12-2.939-0.2x-0.237x^2-0.305x^3-0.0283x^4 \\ &\quad -y(0.0047-0.0221x-0.102x^2-0.0817x^3-0.00717x^4), \end{aligned} \quad \text{(C.2)}$$

where

$$x = \log R_{23} = \log\left(\frac{[\mathrm{O\,II}]\,\lambda3727+[\mathrm{O\,III}]\,\lambda4959+[\mathrm{O\,III}]\,\lambda5007}{\mathrm{H}\beta}\right), \quad \text{(C.3)}$$

$$y = \log O_{32} = \log\left(\frac{[\mathrm{O\,III}]\,\lambda4959+[\mathrm{O\,III}]\,\lambda5007}{[\mathrm{O\,II}]\,\lambda3727}\right). \quad \text{(C.4)}$$

The accuracy of the M91 calibrator is ~ 0.15 dex (Kewley & Ellison, 2008).

C.1.2 The Z94 calibrator

The Z94 calibrator (Zaritsky et al., 1994) is based on the R_{23} line ratio. This calibration was derived from the average of three previous calibrations by Edmunds & Pagel (1984), Dopita & Evans (1986) and McCall et al. (1985). Zaritsky et al. provided a polynomial fit that is only valid for the upper R_{23} branch

$$12+\log(\mathrm{O/H})_{\mathrm{upper}} = 9.265-0.33x-0.202x^2-0.207x^3-0.333x^4, \tag{C.5}$$

where $x = \log R_{23}$, as defined in Equation C.3. This calibration does not consider explicitly a solution for the ionisation parameter. The estimated accuracy of Z94 is equal to the difference between the different methods.

C.1.3 The KK04 calibrator

Kobulnicky & Kewley (2004) employed the stellar evolution and photoionization grids from Kewley & Dopita (2002) to produce an improved fit to the R_{23} calibration. They propose an iterative method which takes into account the ionisation parameter to produce an estimate of the metallicity. First, a guess value of the metallicity has to be provided depending on the R_{23} branch (previously determined from the [N II]/[O II] ratio), these nominal values (12+log(O/H)$_{lower}$ = 8.2 and 12+log(O/H)$_{upper}$ = 8.7) are used to calculate an ionization parameter q, i.e.

$$\begin{aligned}\log q \;=\; & \left\{32.81-1.153y^2+[12+\log(\mathrm{O/H})]\left(-3.396-0.025y+0.1444y^2\right)\right\} \\ & \mathrm{x}\left\{4.603-0.3119y-0.163y2+[12+\log(\mathrm{O/H})]\left(-0.48+0.0271y+0.02037y^2\right)\right\}^{-1}\end{aligned} \tag{C.6}$$

where

$$y = \log\left(\frac{[\mathrm{O\,III}]\,\lambda 5007}{[\mathrm{O\,II}]\,\lambda 3727}\right). \tag{C.7}$$

The initial resulting ionization parameter is used to derive an initial metallicity estimate depending on the R_{23} branch

$$12+\log(\mathrm{O/H})_{\mathrm{lower}} \;=\; 9.40+4.65x-3.17x^2-\log q\left(0.272+0.547x-0.513x^2\right), \tag{C.8}$$

$$\begin{aligned}12+\log(\mathrm{O/H})_{\mathrm{upper}} \;=\; & 9.72-0.777x-0.951x^2-0.072x^3-0.811x^4 \\ & -\log q\left(0.0737-0.0713x-0.141x^2+0.0373x^3-0.058x^4\right),\end{aligned} \tag{C.9}$$

where $x = \log R_{23}$, as defined in Equation C.3. Equations C.6 and C.8 (or C.9) are iterated until 12+log(O/H) converges. Few iterations are typically required to reach convergence.

C.1.4 The N2-index calibrator

The $N2$ index was first proposed by Storchi-Bergmann et al. (1994), it is defined as

$$N2 = \log\left(\frac{[\mathrm{N\,II}]\,\lambda 6584}{\mathrm{H}\alpha}\right). \tag{C.10}$$

This ratio is sensitive to the metallicity as measured by the oxygen abundance through a combination of two effects. As O/H decreases below solar, there is a tendency for the ionization to increase (either from the hardness of the ionizing spectrum or from the ionization parameter, or both), decreasing the ratio [N II]/[N III]; on the other hand, the N/O ratio decreases at the high-abundance end, due to the secondary nature of nitrogen. The relation between $N2$ and metallicity is single-valued and it is basically non-affected by the effects of reddening. Nevertheless, it has a high scatter associated to the functional parameters of the nebula (ionization parameter and ionizing radiation temperature) and to intrinsic N/O variations.

Following up earlier work, Denicoló et al. (2002) provided a linear fit valid in the regime $\sim$ –2.5 $\lesssim N2 \lesssim$ –0.5. The calibration is based on a fit to the relationship between the $N2$ index and metallicities obtained from T_e measurements, the M91 calibration and the empirical method proposed by Díaz & Pérez-Montero (2000) based on the sulfur lines. The Denicoló et al. calibration is given by a linear least-squares fit:

$$12 + \log(\mathrm{O/H}) = 9.12 + 0.73N2. \tag{C.11}$$

Pettini & Pagel (2004) revised this calibration with an updated database, finding a better fit by a third-order polynomial, which is given by

$$12 + \log(\mathrm{O/H}) = 9.37 + 2.03N2 + 1.26N2^2 + 0.32N2^3, \tag{C.12}$$

valid for –2.5 $< N2 <$ –0.3. The $N2$ metallicity values derived in this dissertation correspond to the average between the $N2$ metallicities obtained from equations C.11 and C.12. The estimated uncertainty of the derived metallicities is $\sim \pm$ 0.2 dex.

C.1.5 The O3N2-index calibrator

The O3N2 parameter was first introduced by Alloin et al. (1979), a slightly different definition was proposed by Pettini & Pagel (2004)

$$O3N2 = \log\left(\frac{[\mathrm{O\,III}]\,\lambda 5007/\mathrm{H}\beta}{[\mathrm{N\,II}]\,\lambda 6584/\mathrm{H}\alpha}\right), \tag{C.13}$$

considering only the [O III] λ5007 line in the numerator. This index is almost independent of reddening correction or flux calibration. The claimed advantage of this index with respect to $N2$ is that the inclusion of [O III] could be useful in the high metallicity regime where [N II] saturates but the strength of [O III] continues to decrease with increasing metallicity. This calibrator was mainly focus on determining metallicities for galaxies at high redshift, and suited to the analysis of data of only moderate signal-to-noise. Pettini & Pagel

(2004) fitted the observed relationship between this ratio and T_e based metallicities, obtaining monotonic relationship given by

$$12+\log(\mathrm{O/H}) = 8.73-0.32\cdot O3N2, \tag{C.14}$$

valid for $O3N2 < 2$, with an estimated accuracy of $\sim \pm 0.25$ dex.

C.1.6 The PT05 calibrator

This calibration (Pilyugin & Thuan, 2005) is based on an updated version of the Pilyugin (2001b) estimator, based on the relationship between R_{23} and T_e metallicities. This calibration includes and excitation parameter P that takes into account the effect of the ionisation parameter. The calibration has an upper branch calibration that is valid for T_e-based metallicities 12+log (O/H) > 8.25 and a lower branch calibration that is valid for T_e-based metallicities 12+log (O/H) < 8.0. PT05 give two parametrizations corresponding to the lower and upper branches of R_{23} given by

$$12+\log(\mathrm{O/H})_{\mathrm{lower}} = \frac{R_{23}+106.4+106.8P-3.40P^2}{17.72+6.60P+6.95P^2-0.302R_{23}}, \tag{C.15}$$

$$12+\log(\mathrm{O/H})_{\mathrm{upper}} = \frac{R_{23}+726.1+842.2P+337.5P^2}{85.96+82.76P+43.98P^2+1.793R_{23}}, \tag{C.16}$$

where

$$R_{23} = \frac{[\mathrm{O\,II}]\,\lambda3727+[\mathrm{O\,III}]\,\lambda4959+[\mathrm{O\,III}]\,\lambda5007}{\mathrm{H}\beta}, \tag{C.17}$$

$$P = \frac{([\mathrm{O\,III}]\,\lambda4959+[\mathrm{O\,III}]\,\lambda5007)/\mathrm{H}\beta}{R_{23}}. \tag{C.18}$$

Pilyugin & Thuan claim an accuracy of $\sim \pm 0.1$ dex for the PT05 calibration.

C.1.7 The ff–T_e method

The ff-T_e method is the combination of the flux-flux (or ff-relation) proposed by Pilyugin (2005), the t_2-t_3 relation between the O^+ and O^{++} zones electron temperatures for high-metallicity regions proposed by Pilyugin (2007), and an updated version of the T_e-based method for metallicity determination (Izotov et al., 2006). The ff-relation links the flux of the auroral line [O III] λ4363 to the total flux in the strong nebular lines [O II] λ3727 and [O III] λ4959, λ5007. This relation is metallicity-dependent at low metallicities, but becomes independent at metallicities higher than 12+log(O/H) $\sim$ 8.25, i.e. the regime of high-metallicity H II regions. Using this relation, an inferred value of the [O III] λ4363 line can be derived, which translates to an electronic temperature of the high-ionisation zone $t_3 \equiv t([\mathrm{O\ III}])$.

The t_2-t_3 relation proposed by Pilyugin (2007) is based on the relationship between the ratio of nebular to auroral nitrogen line intensities, which is believed to be a better indicator of the electron temperature t_2 in the O^+ low-ionisation zone of H II regions. This relation takes into account the effects of the excitation

parameter P. This temperature, coupled with the t_3 obtained via the ff-relation, are used together with the strong-line intensity ratios in order to derive the chemical abundance using the revised T_e direct method by (Izotov et al., 2006).

The following notations are defined:

$$R = \frac{[\mathrm{O\,III}]\,\lambda 4363}{\mathrm{H}\beta}, \tag{C.19}$$

$$R_2 = \frac{[\mathrm{O\,II}]\,\lambda 3727}{\mathrm{H}\beta}, \tag{C.20}$$

$$R_3 = \frac{[\mathrm{O\,III}]\,\lambda 4959 + [\mathrm{O\,III}]\,\lambda 5007}{\mathrm{H}\beta}, \tag{C.21}$$

$$R_{23} = R_2 + R_3. \tag{C.22}$$

With these definitions, the excitation parameter P can be expressed as

$$P = \frac{R_3}{R_2 + R_3}. \tag{C.23}$$

THE FF RELATION

The ff relation is defined as the relationship between the flux R in the auroral line and the total flux R_{23} in the strong nebular lines through a relation of the type

$$\log R = a + b \log R_{23}, \tag{C.24}$$

but since $R_{23} = R_3/P$, the ff relation can be also expressed in the form $R = f(R_3, P)$. This last relation was parametrised by Pilyugin et al. (2006) in the following way

$$\log R = -4.151 - 3.118 \log P + 2.958 \log R_{23} - 0.680 (\log P)^2. \tag{C.25}$$

From this equation, a ratio of the nebular [O III] $\lambda 4363$ line to Hβ is obtained, and therefore, a value of the electron temperature T_e can be derived.

ADOPTED T_e EQUATIONS

For abundance determination in a H II region, a two-zone model for the temperature structure is usually adopted. Izotov et al. (2006) published a set of equations for the determination of oxygen abundance in the context of such a model. The electron temperature t_3 within the [O III] zone, in units of 10^4 K, is given by

$$t_3 = \frac{1.432}{\log(R_3/R) - \log C_T}, \tag{C.26}$$

where

$$C_T = \left(8.44 - 1.09t_3 + 0.5t_3^2 - 0.08t_3^3\right) v, \quad \text{(C.27)}$$

$$v = \frac{1 + 0.0004x_3}{1 + 0.044x_3}, \quad \text{(C.28)}$$

and

$$x_3 = 10^{-4} n_e t_3^{-1/2}. \quad \text{(C.29)}$$

As for the ionic abundances, they are derived from the following equations:

$$12 + \log(\mathrm{O}^{++}/\mathrm{H}^{+}) = \log R_3 + 6.20 + \frac{1.251}{t_3} - 0.55\log t_3 - 0.014t_3, \quad \text{(C.30)}$$

$$12 + \log(\mathrm{O}^{+}/\mathrm{H}^{+}) = \log R_2 + 5.961 + \frac{1.676}{t_2} - 0.40\log t_2 - 0.034t_2 + \log\left(1 + 1.35x_2\right), \quad \text{(C.31)}$$

where

$$x_2 = 10^{-4} n_e t_2^{-1/2}, \quad \text{(C.32)}$$

and n_e is the electron density in cm^{-3}. The total oxygen abundance is derived from

$$\frac{\mathrm{O}}{\mathrm{H}} = \frac{\mathrm{O}^{+}}{\mathrm{H}^{+}} + \frac{\mathrm{O}^{++}}{\mathrm{H}^{+}}. \quad \text{(C.33)}$$

THE $t_2 - t_3$ RELATION

The electron temperature t_2 of the [O II] zone is usually determined from an equation which relates t_2 to t_3, derived by fitting H II region models. Several versions of this $t_2 - t_3$ relation have been proposed (e.g. Campbell et al., 1986; Pagel et al., 1992; Izotov et al., 1997; Deharveng et al., 2000; Oey & Shields, 2000)

Pilyugin (2007) suggested that there is no one-to-one correspondence between t_2 and t_3, and that instead the $t_2 - t_3$ is a function of the excitation parameter P. Based on this idea, Pilyugin suggested a $t_2 - t_3$ relation of the form

$$\frac{1}{t_2} = 0.41\frac{1}{t_3} - 0.34P + 0.81. \quad \text{(C.34)}$$

which is the $t_2 - t_3$ relation used for the ff–T_e method. According to the formulation described above, the combination of all these methods solves the problem of the determination of the electron temperatures in high-metallicity H II regions, where faint auroral lines are not detected. However, the abundances determined through this method rely on the validity of the classic T_e method, which has been questioned for

the high-metallicity regime in a number of studies by comparisons with H II region photoionization models (Stasińska, 2005).

The oxygen abundances derived in this dissertation using the so-called ff–T_e method, are based on the equations C.26 through C.34, using a canonical electron density value of $n_e = 100$ cm^{-3}.

C.2 The *direct* method for abundance determination

The classic prescriptions for a direct abundance determination rely on the detection and reliable measurement of the [O III] λ4363 auroral line (or other auroral lines). The pseudo-direct determination performed in this dissertation uses the t_3 temperature derived through the ff-relation as characteristic of the O^{++} region. The determination of other physical conditions of the gas (t_2, n_e) and the ionic abundances are obtained using the procedures outlined by Pagel et al. (1992) and Pérez-Montero & Díaz (2003), including the nitrogen abundance.

Density

Electronic densities were calculated from the $R_{S\,II}$ parameter, defined as

$$R_{S2} = \frac{[\mathrm{S\,II}]\,\lambda 6717}{[\mathrm{S\,II}]\,\lambda 6731}, \tag{C.35}$$

using the relation

$$n([\mathrm{S\,II}]) = 10^3 \cdot \frac{a_0(t) R_{S2} + a_1(t)}{b_0(t) R_{S2} + b_1(t)}, \tag{C.36}$$

where

$$\begin{aligned} a_0(t) &= 2.21 - 1.3/t_3 - 1.25t + 0.23t_3^2, \\ a_1(t) &= -3.35 + 1.94/t_3 + 1.93t - 0.36t_3^2, \\ b_0(t) &= -4.33 + 2.33/t + 2.72t_3 - 0.57t_3^2, \\ b_1(t) &= 1.84 - 1/t - 1.14t_3 + 0.24t_3^2. \end{aligned}$$

In those cases where this relation yielded negative vales, a value of n_e = 10 cm^{-3} was assumed.

The t_2 temperature

When the [O II] λ3727, λ3729 and [O II] λ7319, λ7330 lines are available, the t_2 temperature can be obtained from the R_{O2} parameter defined as

$$R_{O2} = \frac{[\mathrm{O\,II}]\,\lambda 3727, \lambda 3729}{[\mathrm{O\,II}]\,\lambda 7319, \lambda 7330}. \tag{C.37}$$

However, as no information was available for the [O II] λ7319, λ7330 doublet, the t_2 temperature was determined from a fit to photoionization models taking into account the dependency of the electronic temperature:

$$t_2 = \frac{1.2 + 0.002 n_e + \frac{4.2}{n_e}}{t_3^{-1} + 0.08 + 0.003 n_e + \frac{2.5}{n_e}}, \tag{C.38}$$

where t_2 is expressed in units of 10^4 K.

IONIC ABUNDANCES

The ionic abundances were calculated based on the functional forms provided by Pagel et al. (1992). In the following relations, the electron temperature t is in units of 10^4 K and n_e is the electron density.

The chemical abundance of O^+ can be determined from the intensity of the [O II] λ3727 line:

$$12 + \log\left(\frac{O^+}{H^+}\right) = \log\left(\frac{[O\,II]\,\lambda 3727}{H\beta}\right) + 5.992 + \frac{1.583}{t_2} - 0.681 \cdot \log t_2 + \log\left(1 + 0.00023\right) n_e, \tag{C.39}$$

while, for the O^{++} abundance, the [O III] λ4959, λ5007 lines are used:

$$12 + \log\left(\frac{O^{++}}{H^+}\right) = \log\left(\frac{[O\,III]\,\lambda 4959 + [O\,III]\,\lambda 5007}{H\beta}\right) + 6.144 + \frac{1.251}{t_3} - 0.55 \cdot \log t_3. \tag{C.40}$$

The total oxygen abundance is obtained assuming that

$$\frac{O}{H} = \frac{O^+}{H^+} + \frac{O^{++}}{H^+}. \tag{C.41}$$

given that, by the charge-exchange reactions, the relative fractions of oxygen and neutral hydrogen, $O^0/O = H^0/H$ are similar.

The N^+ abundance was derived from the intensities of the [N II] λ6548 and λ6584 lines, using the electronic temperature corresponding to the region of low-ionization t_2:

$$12 + \log\left(\frac{N^+}{H^+}\right) = \log\left(\frac{[N\,II]\,\lambda 6548 + [N\,II]\,\lambda 6584}{H\beta}\right) + 6.273 + \frac{0.894}{t_2} - 0.592 \cdot \log t_2. \tag{C.42}$$

The total abundance of nitrogen was derived using the widely used assumption that

$$\frac{N}{O} = \frac{N^+}{O^+}, \tag{C.43}$$

where the value of O/H is derived from the [O II] relation of Equation C.39.

D

H II region catalogues

In this appendix, I present the basic information of the H II region catalogues of the galaxy sample presented in chapter 6. For each of the four selected galaxies, their corresponding tables include the number identification (ID), as shown in the H II region maps of each galaxy (i.e. NGC 628: Figure 6.36; NGC 1058: Figure 6.46; NGC 3184: Figure 6.55; NGC 3310: Figure 6.64 and Figure 6.65). The Right Ascension and Declination of the central reference point of each H II region (in sexagesimal and degree units), for the 2000 equinox. The offsets of each region, in arcsec, with respect to the reference central point of the IFS mosaic, as reported in Table 3.1, in the standard configuration with north-east positive. The "Method" column correspond to the extraction method employed during the selection of the H II region, **A** stands for an *aperture* extraction (i.e. a circular aperture of given size in arcsec), and **M** stands for *manual* extraction (i.e. fibres selected by hand). The column corresponding to the "Aperture" values shows the real (aperture) or equivalent (manual) extraction aperture diameter in arcsec. The "Size" column corresponds to the physical size of the H II region in parsecs, at the assumed distance to the galaxy. Finally, the last column correspond to the total number of fibres from which the spectrum of the H II region was extracted.

H II REGION CATALOGUE: NGC 628

ID	RA	Dec	RA	Dec	ΔRA	ΔDec	Method	Aperture	Size	Fibres
1	$01^h\ 36^m\ 41.0^s$	$15°\ 47^m\ 13.5^s$	24.1709	15.7871	−11.0	11.3	A	5.0	224	12
2	$01^h\ 36^m\ 42.5^s$	$15°\ 46^m\ 56.1^s$	24.1771	15.7822	10.4	−6.0	M	2.7	121	1
3	$01^h\ 36^m\ 41.7^s$	$15°\ 46^m\ 59.1^s$	24.1736	15.7831	−1.8	−3.0	M	2.7	121	1
4	$01^h\ 36^m\ 40.8^s$	$15°\ 47^m\ 07.0^s$	24.1699	15.7853	−14.4	4.9	M	8.5	381	3
5	$01^h\ 36^m\ 43.7^s$	$15°\ 47^m\ 32.1^s$	24.1821	15.7923	27.6	30.0	M	2.7	121	1
6	$01^h\ 36^m\ 44.8^s$	$15°\ 47^m\ 03.3^s$	24.1865	15.7843	42.8	1.2	A	4.0	179	5
7	$01^h\ 36^m\ 44.6^s$	$15°\ 46^m\ 43.9^s$	24.1857	15.7789	40.3	−18.2	M	10.4	466	4
8	$01^h\ 36^m\ 44.3^s$	$15°\ 46^m\ 36.6^s$	24.1845	15.7768	36.0	−25.5	M	11.3	507	2
9	$01^h\ 36^m\ 45.1^s$	$15°\ 46^m\ 32.0^s$	24.1879	15.7755	48.0	−30.2	A	7.0	314	7
10	$01^h\ 36^m\ 43.9^s$	$15°\ 46^m\ 30.1^s$	24.1827	15.7750	29.9	−32.0	M	2.7	121	1
11	$01^h\ 36^m\ 40.0^s$	$15°\ 46^m\ 29.1^s$	24.1666	15.7747	−25.9	−33.0	M	2.7	121	1
12	$01^h\ 36^m\ 38.1^s$	$15°\ 47^m\ 07.0^s$	24.1588	15.7853	−52.9	4.9	A	12.0	538	18
13	$01^h\ 36^m\ 38.6^s$	$15°\ 47^m\ 29.1^s$	24.1608	15.7914	−46.0	27.0	A	15.0	673	27
14	$01^h\ 36^m\ 39.2^s$	$15°\ 47^m\ 48.5^s$	24.1633	15.7968	−37.5	46.4	A	10.0	448	13
15	$01^h\ 36^m\ 39.2^s$	$15°\ 48^m\ 02.3^s$	24.1635	15.8007	−36.6	60.2	A	7.0	314	8
16	$01^h\ 36^m\ 38.5^s$	$15°\ 47^m\ 54.2^s$	24.1603	15.7984	−47.8	52.1	M	2.7	121	1
17	$01^h\ 36^m\ 39.9^s$	$15°\ 48^m\ 06.1^s$	24.1663	15.8017	−27.1	64.0	M	2.7	121	1
18	$01^h\ 36^m\ 40.1^s$	$15°\ 48^m\ 24.2^s$	24.1673	15.8067	−23.6	82.1	M	2.7	121	1
19	$01^h\ 36^m\ 41.5^s$	$15°\ 48^m\ 09.2^s$	24.1728	15.8025	−4.5	67.0	M	2.7	121	1
20	$01^h\ 36^m\ 42.1^s$	$15°\ 48^m\ 22.6^s$	24.1754	15.8063	4.4	80.5	A	5.0	224	4
21	$01^h\ 36^m\ 43.6^s$	$15°\ 48^m\ 18.0^s$	24.1815	15.8050	25.7	75.9	A	4.0	179	5
22	$01^h\ 36^m\ 45.3^s$	$15°\ 47^m\ 48.5^s$	24.1887	15.7968	50.5	46.4	M	14.7	659	6
23	$01^h\ 36^m\ 46.9^s$	$15°\ 48^m\ 08.8^s$	24.1953	15.8024	73.6	66.7	A	4.0	179	6
24	$01^h\ 36^m\ 47.7^s$	$15°\ 48^m\ 00.6^s$	24.1987	15.8002	85.3	58.5	M	2.7	121	1
25	$01^h\ 36^m\ 45.0^s$	$15°\ 48^m\ 41.2^s$	24.1876	15.8114	46.8	99.1	A	2.7	121	1
26	$01^h\ 36^m\ 46.0^s$	$15°\ 48^m\ 55.8^s$	24.1916	15.8155	60.8	113.7	A	5.0	224	4
27	$01^h\ 36^m\ 46.8^s$	$15°\ 49^m\ 03.2^s$	24.1948	15.8176	71.9	121.1	A	10.0	448	13
28	$01^h\ 36^m\ 46.7^s$	$15°\ 49^m\ 16.1^s$	24.1946	15.8211	71.0	134.0	A	4.0	179	4
29	$01^h\ 36^m\ 48.6^s$	$15°\ 49^m\ 10.6^s$	24.2025	15.8196	98.4	128.5	A	4.0	179	3
30	$01^h\ 36^m\ 50.4^s$	$15°\ 48^m\ 30.8^s$	24.2098	15.8085	123.7	88.7	A	2.7	121	1
31	$01^h\ 36^m\ 44.6^s$	$15°\ 49^m\ 18.9^s$	24.1857	15.8219	40.3	136.8	A	4.0	179	2
32	$01^h\ 36^m\ 41.6^s$	$15°\ 50^m\ 08.7^s$	24.1734	15.8358	−2.5	186.6	A	10.0	448	12
33	$01^h\ 36^m\ 40.7^s$	$15°\ 50^m\ 02.2^s$	24.1697	15.8340	−15.3	180.1	M	10.5	471	3
34	$01^h\ 36^m\ 36.9^s$	$15°\ 49^m\ 57.3^s$	24.1538	15.8326	−70.4	175.1	M	2.7	121	1
35	$01^h\ 36^m\ 41.1^s$	$15°\ 48^m\ 43.8^s$	24.1712	15.8122	−10.1	101.7	M	13.0	583	6
36	$01^h\ 36^m\ 40.8^s$	$15°\ 48^m\ 54.0^s$	24.1702	15.8150	−13.6	111.9	M	14.0	628	8
37	$01^h\ 36^m\ 40.2^s$	$15°\ 48^m\ 42.9^s$	24.1675	15.8119	−23.0	100.8	M	8.6	386	3
38	$01^h\ 36^m\ 40.3^s$	$15°\ 49^m\ 08.8^s$	24.1680	15.8191	−21.2	126.6	A	7.0	314	7
39	$01^h\ 36^m\ 38.9^s$	$15°\ 49^m\ 19.8^s$	24.1620	15.8222	−41.8	137.7	M	11.6	520	5
40	$01^h\ 36^m\ 39.2^s$	$15°\ 49^m\ 00.4^s$	24.1633	15.8168	−37.5	118.3	M	39.5	1773	32
41	$01^h\ 36^m\ 38.7^s$	$15°\ 48^m\ 35.5^s$	24.1611	15.8099	−45.2	93.4	M	11.5	516	3
42	$01^h\ 36^m\ 37.8^s$	$15°\ 48^m\ 29.1^s$	24.1574	15.8081	−58.0	87.0	M	15.5	695	9
43	$01^h\ 36^m\ 36.9^s$	$15°\ 48^m\ 09.7^s$	24.1537	15.8027	−70.8	67.6	M	15.6	700	11
44	$01^h\ 36^m\ 35.0^s$	$15°\ 47^m\ 56.9^s$	24.1458	15.7991	−98.0	54.8	M	2.7	121	1
45	$01^h\ 36^m\ 36.5^s$	$15°\ 47^m\ 30.1^s$	24.1519	15.7917	−76.8	27.9	A	8.0	359	9
46	$01^h\ 36^m\ 36.7^s$	$15°\ 47^m\ 21.0^s$	24.1528	15.7892	−73.9	18.9	M	2.7	121	1
47	$01^h\ 36^m\ 32.9^s$	$15°\ 48^m\ 46.0^s$	24.1373	15.8128	−127.6	103.9	M	2.7	121	1
48	$01^h\ 36^m\ 32.8^s$	$15°\ 48^m\ 36.1^s$	24.1366	15.8100	−129.9	94.0	M	2.7	121	1
49	$01^h\ 36^m\ 32.7^s$	$15°\ 48^m\ 14.3^s$	24.1364	15.8040	−130.6	72.2	M	12.2	547	11
50	$01^h\ 36^m\ 29.8^s$	$15°\ 48^m\ 57.7^s$	24.1241	15.8160	−173.3	115.6	M	10.5	471	7
51	$01^h\ 36^m\ 28.9^s$	$15°\ 48^m\ 27.2^s$	24.1204	15.8076	−186.1	85.1	M	14.2	637	7
52	$01^h\ 36^m\ 31.3^s$	$15°\ 48^m\ 54.2^s$	24.1306	15.8151	−150.8	112.1	M	2.7	121	1
53	$01^h\ 36^m\ 34.1^s$	$15°\ 47^m\ 33.3^s$	24.1421	15.7926	−111.0	31.2	M	2.7	121	1
54	$01^h\ 36^m\ 32.7^s$	$15°\ 47^m\ 17.1^s$	24.1364	15.7881	−130.6	15.0	M	11.5	516	4
55	$01^h\ 36^m\ 30.6^s$	$15°\ 47^m\ 04.3^s$	24.1277	15.7845	−160.8	2.2	M	2.7	121	1

continues on next page

Table D.1: H II regions NGC 628: Part 1.

H II REGION CATALOGUE: NGC 628

ID	RA	Dec	RA	Dec	ΔRA	ΔDec	Method	Aperture	Size	Fibres
continued from previous page										
56	$01^h\ 36^m\ 36.5^s$	$15°\ 46^m\ 35.6^s$	24.1522	15.7766	−75.9	−26.5	M	12.0	538	5
57	$01^h\ 36^m\ 36.6^s$	$15°\ 46^m\ 16.3^s$	24.1524	15.7712	−75.1	−45.8	A	4.0	179	4
58	$01^h\ 36^m\ 39.2^s$	$15°\ 46^m\ 02.4^s$	24.1633	15.7673	−37.5	−59.7	A	4.0	179	3
59	$01^h\ 36^m\ 41.0^s$	$15°\ 46^m\ 15.3^s$	24.1709	15.7709	−11.0	−46.8	A	4.0	179	4
60	$01^h\ 36^m\ 47.9^s$	$15°\ 47^m\ 09.8^s$	24.1998	15.7860	89.0	7.7	M	9.0	404	4
61	$01^h\ 36^m\ 47.6^s$	$15°\ 47^m\ 15.7^s$	24.1982	15.7877	83.6	13.6	M	2.7	121	1
62	$01^h\ 36^m\ 49.7^s$	$15°\ 47^m\ 39.5^s$	24.2073	15.7943	114.9	37.4	M	2.7	121	1
63	$01^h\ 36^m\ 50.4^s$	$15°\ 47^m\ 30.1^s$	24.2099	15.7917	124.0	27.9	A	4.0	179	3
64	$01^h\ 36^m\ 50.7^s$	$15°\ 47^m\ 21.7^s$	24.2113	15.7894	128.9	19.6	A	2.7	121	1
65	$01^h\ 36^m\ 47.4^s$	$15°\ 46^m\ 29.2^s$	24.1976	15.7748	81.3	−32.9	M	12.4	556	5
66	$01^h\ 36^m\ 47.0^s$	$15°\ 46^m\ 11.7^s$	24.1958	15.7699	75.3	−50.5	M	10.4	466	4
67	$01^h\ 36^m\ 45.4^s$	$15°\ 46^m\ 15.0^s$	24.1893	15.7708	52.5	−47.1	M	2.7	121	1
68	$01^h\ 36^m\ 42.4^s$	$15°\ 46^m\ 08.9^s$	24.1768	15.7691	9.5	−53.2	M	14.8	664	8
69	$01^h\ 36^m\ 42.0^s$	$15°\ 45^m\ 55.1^s$	24.1749	15.7653	2.7	−67.1	M	12.4	556	5
70	$01^h\ 36^m\ 42.6^s$	$15°\ 45^m\ 41.0^s$	24.1776	15.7614	12.2	−81.1	M	2.7	121	1
71	$01^h\ 36^m\ 41.1^s$	$15°\ 45^m\ 50.0^s$	24.1711	15.7639	−10.4	−72.1	M	2.7	121	1
72	$01^h\ 36^m\ 39.2^s$	$15°\ 45^m\ 49.7^s$	24.1632	15.7638	−37.8	−72.4	M	2.7	121	1
73	$01^h\ 36^m\ 33.0^s$	$15°\ 45^m\ 54.1^s$	24.1375	15.7650	−126.6	−68.1	M	2.7	121	1
74	$01^h\ 36^m\ 33.3^s$	$15°\ 45^m\ 32.0^s$	24.1386	15.7589	−122.9	−90.1	M	7.3	327	4
75	$01^h\ 36^m\ 37.5^s$	$15°\ 45^m\ 11.7^s$	24.1561	15.7533	−62.3	−110.4	M	6.8	305	2
76	$01^h\ 36^m\ 42.3^s$	$15°\ 45^m\ 11.7^s$	24.1761	15.7533	6.9	−110.4	M	6.7	300	2
77	$01^h\ 36^m\ 51.0^s$	$15°\ 46^m\ 02.4^s$	24.2126	15.7673	133.4	−59.7	M	9.3	417	4
78	$01^h\ 36^m\ 52.2^s$	$15°\ 45^m\ 50.2^s$	24.2175	15.7639	150.3	−71.9	M	2.7	121	1
79	$01^h\ 36^m\ 50.6^s$	$15°\ 45^m\ 54.1^s$	24.2109	15.7650	127.4	−68.0	M	17.6	790	8
80	$01^h\ 36^m\ 47.1^s$	$15°\ 45^m\ 50.4^s$	24.1961	15.7640	76.2	−71.7	A	10.0	448	18
81	$01^h\ 36^m\ 46.5^s$	$15°\ 45^m\ 34.8^s$	24.1936	15.7597	67.6	−87.3	M	9.0	404	2
82	$01^h\ 36^m\ 45.5^s$	$15°\ 45^m\ 18.2^s$	24.1894	15.7550	53.1	−103.9	M	6.5	291	2
83	$01^h\ 36^m\ 45.5^s$	$15°\ 45^m\ 10.8^s$	24.1897	15.7530	53.9	−111.3	M	9.1	408	2
84	$01^h\ 36^m\ 44.5^s$	$15°\ 45^m\ 01.6^s$	24.1852	15.7504	38.5	−120.6	M	21.0	942	19
85	$01^h\ 36^m\ 47.2^s$	$15°\ 44^m\ 45.0^s$	24.1966	15.7458	77.8	−137.2	M	9.7	435	4
86	$01^h\ 36^m\ 45.8^s$	$15°\ 44^m\ 29.1^s$	24.1908	15.7414	57.7	−153.0	M	2.7	121	1
87	$01^h\ 36^m\ 44.8^s$	$15°\ 44^m\ 10.8^s$	24.1867	15.7363	43.7	−171.3	M	10.0	448	4
88	$01^h\ 36^m\ 43.7^s$	$15°\ 44^m\ 29.3^s$	24.1820	15.7415	27.5	−152.8	M	10.7	480	3
89	$01^h\ 36^m\ 41.9^s$	$15°\ 44^m\ 40.5^s$	24.1747	15.7446	2.0	−141.6	M	2.7	121	1
90	$01^h\ 36^m\ 41.6^s$	$15°\ 44^m\ 33.0^s$	24.1734	15.7425	−2.5	−149.1	M	11.8	529	4
91	$01^h\ 36^m\ 41.9^s$	$15°\ 44^m\ 15.4^s$	24.1746	15.7376	1.8	−166.7	M	6.3	282	2
92	$01^h\ 36^m\ 43.9^s$	$15°\ 43^m\ 52.4^s$	24.1828	15.7312	30.0	−189.7	A	4.0	179	2
93	$01^h\ 36^m\ 39.8^s$	$15°\ 44^m\ 29.3^s$	24.1657	15.7415	−28.9	−152.8	M	11.0	493	4
94	$01^h\ 36^m\ 38.7^s$	$15°\ 44^m\ 26.5^s$	24.1613	15.7407	−44.3	−155.6	M	13.1	588	8
95	$01^h\ 36^m\ 38.0^s$	$15°\ 45^m\ 01.8^s$	24.1582	15.7505	−55.2	−120.3	M	2.7	121	1
96	$01^h\ 36^m\ 46.4^s$	$15°\ 44^m\ 26.1^s$	24.1933	15.7406	66.4	−156.0	M	2.7	121	1

Table D.2: H II regions NGC 628: Part 2.

H II REGION CATALOGUE: NGC 1058

ID	RA	Dec	RA	Dec	ΔRA	ΔDec	Method	Aperture	Size	Fibres
1	$02^h\ 43^m\ 30.0^s$	$37°\ 20^m\ 31.2^s$	40.8751	37.3420	−0.2	2.7	A	3.0	153	6
2	$02^h\ 43^m\ 29.5^s$	$37°\ 20^m\ 38.8^s$	40.8728	37.3441	−6.8	10.3	A	4.0	204	9
3	$02^h\ 43^m\ 28.3^s$	$37°\ 20^m\ 47.1^s$	40.8678	37.3464	−21.1	18.6	M	8.1	414	4
4	$02^h\ 43^m\ 27.4^s$	$37°\ 20^m\ 46.4^s$	40.8643	37.3462	−31.2	17.9	M	7.2	368	5
5	$02^h\ 43^m\ 26.2^s$	$37°\ 20^m\ 43.6^s$	40.8592	37.3454	−45.9	15.1	A	7.0	358	21
6	$02^h\ 43^m\ 24.9^s$	$37°\ 20^m\ 35.3^s$	40.8539	37.3431	−61.0	6.8	A	3.0	153	7
7	$02^h\ 43^m\ 27.6^s$	$37°\ 20^m\ 53.1^s$	40.8648	37.3481	−29.7	24.6	M	10.0	512	6
8	$02^h\ 43^m\ 28.3^s$	$37°\ 21^m\ 10.2^s$	40.8679	37.3528	−20.8	41.7	A	2.7	138	3
9	$02^h\ 43^m\ 29.8^s$	$37°\ 20^m\ 54.7^s$	40.8740	37.3485	−3.3	26.2	A	3.0	153	7
10	$02^h\ 43^m\ 30.2^s$	$37°\ 20^m\ 40.4^s$	40.8758	37.3446	1.7	11.9	A	5.0	256	14
11	$02^h\ 43^m\ 30.9^s$	$37°\ 20^m\ 50.5^s$	40.8788	37.3474	10.2	22.0	A	6.0	307	19
12	$02^h\ 43^m\ 31.6^s$	$37°\ 20^m\ 48.3^s$	40.8815	37.3468	17.9	19.8	A	6.0	307	17
13	$02^h\ 43^m\ 31.5^s$	$37°\ 20^m\ 57.2^s$	40.8813	37.3492	17.5	28.7	M	17.3	885	33
14	$02^h\ 43^m\ 31.2^s$	$37°\ 21^m\ 07.0^s$	40.8800	37.3520	13.7	38.5	A	7.0	358	21
15	$02^h\ 43^m\ 30.4^s$	$37°\ 21^m\ 01.7^s$	40.8767	37.3505	4.4	33.2	M	7.9	404	6
16	$02^h\ 43^m\ 31.3^s$	$37°\ 21^m\ 21.3^s$	40.8804	37.3559	14.9	52.8	M	9.2	471	10
17	$02^h\ 43^m\ 33.0^s$	$37°\ 21^m\ 08.6^s$	40.8876	37.3524	35.4	40.1	A	6.0	307	12
18	$02^h\ 43^m\ 32.3^s$	$37°\ 20^m\ 47.7^s$	40.8844	37.3466	26.5	19.2	M	8.1	414	6
19	$02^h\ 43^m\ 34.2^s$	$37°\ 21^m\ 03.2^s$	40.8924	37.3509	49.3	34.7	M	9.8	501	11
20	$02^h\ 43^m\ 33.4^s$	$37°\ 20^m\ 37.9^s$	40.8890	37.3438	39.6	9.4	A	5.0	256	13
21	$02^h\ 43^m\ 35.4^s$	$37°\ 20^m\ 55.5^s$	40.8976	37.3487	64.2	27.0	M	2.7	138	1
22	$02^h\ 43^m\ 36.5^s$	$37°\ 20^m\ 46.4^s$	40.9019	37.3462	76.4	17.9	M	2.7	138	1
23	$02^h\ 43^m\ 34.1^s$	$37°\ 21^m\ 27.0^s$	40.8919	37.3575	47.7	58.5	A	5.0	256	11
24	$02^h\ 43^m\ 40.1^s$	$37°\ 21^m\ 52.4^s$	40.9169	37.3646	119.3	83.9	A	4.0	204	2
25	$02^h\ 43^m\ 41.7^s$	$37°\ 21^m\ 46.7^s$	40.9237	37.3630	138.7	78.2	A	4.0	204	8
26	$02^h\ 43^m\ 41.9^s$	$37°\ 21^m\ 59.7^s$	40.9246	37.3666	141.4	91.2	A	4.0	204	11
27	$02^h\ 43^m\ 31.2^s$	$37°\ 20^m\ 32.5^s$	40.8798	37.3424	13.3	4.0	A	4.0	204	8
28	$02^h\ 43^m\ 31.6^s$	$37°\ 20^m\ 28.7^s$	40.8816	37.3413	18.3	0.2	A	5.0	256	13
29	$02^h\ 43^m\ 31.9^s$	$37°\ 20^m\ 21.7^s$	40.8830	37.3394	22.2	−6.8	A	5.0	256	15
30	$02^h\ 43^m\ 31.4^s$	$37°\ 20^m\ 13.1^s$	40.8807	37.3370	15.6	−15.4	A	7.0	358	20
31	$02^h\ 43^m\ 30.7^s$	$37°\ 20^m\ 16.0^s$	40.8778	37.3378	7.5	−12.5	A	5.0	256	13
32	$02^h\ 43^m\ 30.2^s$	$37°\ 20^m\ 08.7^s$	40.8758	37.3357	1.7	−19.8	A	7.0	358	21
33	$02^h\ 43^m\ 29.8^s$	$37°\ 20^m\ 14.4^s$	40.8740	37.3373	−3.3	−14.1	A	3.0	153	7
34	$02^h\ 43^m\ 29.3^s$	$37°\ 20^m\ 27.1^s$	40.8720	37.3409	−9.1	−1.4	A	4.0	204	9
35	$02^h\ 43^m\ 28.3^s$	$37°\ 20^m\ 18.8^s$	40.8678	37.3386	−21.1	−9.7	A	5.0	256	16
36	$02^h\ 43^m\ 28.6^s$	$37°\ 20^m\ 23.9^s$	40.8690	37.3400	−17.7	−4.6	A	4.0	204	9
37	$02^h\ 43^m\ 27.9^s$	$37°\ 20^m\ 25.2^s$	40.8663	37.3403	−25.4	−3.3	A	4.0	204	10
38	$02^h\ 43^m\ 28.1^s$	$37°\ 20^m\ 33.4^s$	40.8673	37.3426	−22.7	4.9	A	4.0	204	9
39	$02^h\ 43^m\ 27.3^s$	$37°\ 20^m\ 26.4^s$	40.8638	37.3407	−32.8	−2.1	A	3.0	153	7
40	$02^h\ 43^m\ 27.1^s$	$37°\ 20^m\ 20.4^s$	40.8631	37.3390	−34.7	−8.1	M	13.7	701	20
41	$02^h\ 43^m\ 26.2^s$	$37°\ 20^m\ 07.7^s$	40.8592	37.3355	−45.9	−20.8	A	4.0	204	10
42	$02^h\ 43^m\ 26.2^s$	$37°\ 20^m\ 01.7^s$	40.8592	37.3338	−45.9	−26.8	A	3.0	153	4
43	$02^h\ 43^m\ 29.0^s$	$37°\ 20^m\ 07.1^s$	40.8709	37.3353	−12.2	−21.4	M	15.4	788	20
44	$02^h\ 43^m\ 28.5^s$	$37°\ 19^m\ 55.0^s$	40.8689	37.3320	−18.0	−33.5	M	14.5	742	21
45	$02^h\ 43^m\ 28.0^s$	$37°\ 20^m\ 02.6^s$	40.8666	37.3341	−24.6	−25.9	M	10.9	558	15
46	$02^h\ 43^m\ 29.3^s$	$37°\ 19^m\ 48.0^s$	40.8721	37.3300	−8.8	−40.5	A	5.0	256	12
47	$02^h\ 43^m\ 28.0^s$	$37°\ 19^m\ 46.8^s$	40.8666	37.3297	−24.6	−41.7	A	5.0	256	15
48	$02^h\ 43^m\ 32.0^s$	$37°\ 20^m\ 01.4^s$	40.8835	37.3337	23.8	−27.1	A	4.0	204	9
49	$02^h\ 43^m\ 31.2^s$	$37°\ 19^m\ 57.6^s$	40.8801	37.3327	14.1	−30.9	A	3.0	153	8
50	$02^h\ 43^m\ 29.9^s$	$37°\ 19^m\ 44.5^s$	40.8747	37.3290	−1.4	−44.0	A	4.0	204	10
51	$02^h\ 43^m\ 29.2^s$	$37°\ 19^m\ 37.9^s$	40.8716	37.3272	−10.3	−50.6	M	12.5	640	16
52	$02^h\ 43^m\ 36.1^s$	$37°\ 20^m\ 09.0^s$	40.9004	37.3358	72.1	−19.5	A	7.0	358	17
53	$02^h\ 43^m\ 33.4^s$	$37°\ 19^m\ 56.9^s$	40.8892	37.3325	40.0	−31.6	A	6.0	307	16
54	$02^h\ 43^m\ 33.1^s$	$37°\ 19^m\ 49.6^s$	40.8881	37.3304	36.9	−38.9	A	7.0	358	22
55	$02^h\ 43^m\ 34.6^s$	$37°\ 19^m\ 43.0^s$	40.8942	37.3286	54.3	−45.5	A	5.0	256	12
56	$02^h\ 43^m\ 33.7^s$	$37°\ 19^m\ 37.6^s$	40.8905	37.3271	43.9	−50.9	A	4.0	204	9
57	$02^h\ 43^m\ 29.2^s$	$37°\ 19^m\ 14.1^s$	40.8715	37.3206	−10.7	−74.4	A	3.0	153	6
58	$02^h\ 43^m\ 29.2^s$	$37°\ 19^m\ 00.1^s$	40.8715	37.3167	−10.7	−88.4	A	10.0	512	25

Table D.3: H II regions NGC 1058.

H II REGION CATALOGUE: NGC 3184

ID	RA	Dec	RA	Dec	ΔRA	ΔDec	Method	Aperture	Size	Fibres
1	$10^h\ 18^m\ 16.6^s$	$41°\ 25^m\ 29.7^s$	154.5691	41.4249	−5.2	3.0	M	2.7	144	1
2	$10^h\ 18^m\ 16.7^s$	$41°\ 25^m\ 26.7^s$	154.5697	41.4241	−3.5	0.0	M	2.7	144	1
3	$10^h\ 18^m\ 19.0^s$	$41°\ 25^m\ 17.1^s$	154.5794	41.4214	22.5	−9.6	A	8.0	428	7
4	$10^h\ 18^m\ 12.0^s$	$41°\ 25^m\ 21.0^s$	154.5499	41.4225	−57.1	−5.7	A	5.0	268	4
5	$10^h\ 18^m\ 10.9^s$	$41°\ 25^m\ 44.6^s$	154.5456	41.4290	−68.7	17.8	A	8.0	428	7
6	$10^h\ 18^m\ 10.0^s$	$41°\ 25^m\ 23.6^s$	154.5418	41.4232	−78.8	−3.1	M	9.8	525	10
7	$10^h\ 18^m\ 10.4^s$	$41°\ 25^m\ 11.8^s$	154.5434	41.4199	−74.6	−14.9	M	2.7	144	1
8	$10^h\ 18^m\ 10.4^s$	$41°\ 25^m\ 01.4^s$	154.5434	41.4171	−74.5	−25.3	M	10.7	573	12
9	$10^h\ 18^m\ 11.7^s$	$41°\ 24^m\ 49.0^s$	154.5486	41.4136	−60.5	−37.7	A	17.0	911	15
10	$10^h\ 18^m\ 12.4^s$	$41°\ 24^m\ 36.6^s$	154.5515	41.4102	−52.8	−50.1	M	7.0	375	4
11	$10^h\ 18^m\ 08.6^s$	$41°\ 24^m\ 45.8^s$	154.5357	41.4127	−95.3	−40.9	M	2.7	144	1
12	$10^h\ 18^m\ 14.9^s$	$41°\ 24^m\ 26.8^s$	154.5620	41.4074	−24.3	−59.9	M	9.8	525	10
13	$10^h\ 18^m\ 15.8^s$	$41°\ 24^m\ 38.6^s$	154.5658	41.4107	−14.2	−48.2	A	5.0	268	4
14	$10^h\ 18^m\ 22.3^s$	$41°\ 24^m\ 13.1^s$	154.5928	41.4036	58.7	−73.6	M	10.6	568	12
15	$10^h\ 18^m\ 22.1^s$	$41°\ 24^m\ 03.9^s$	154.5922	41.4011	57.2	−82.8	M	7.3	391	5
16	$10^h\ 18^m\ 21.0^s$	$41°\ 23^m\ 50.7^s$	154.5876	41.3974	44.8	−96.1	M	2.7	144	1
17	$10^h\ 18^m\ 21.0^s$	$41°\ 23^m\ 44.6^s$	154.5876	41.3957	44.8	−102.1	M	2.7	144	1
18	$10^h\ 18^m\ 19.5^s$	$41°\ 23^m\ 38.6^s$	154.5812	41.3941	27.4	−108.1	M	2.7	144	1
19	$10^h\ 18^m\ 18.5^s$	$41°\ 23^m\ 35.2^s$	154.5772	41.3931	16.7	−111.5	A	7.0	375	5
20	$10^h\ 18^m\ 17.5^s$	$41°\ 23^m\ 20.2^s$	154.5727	41.3889	4.6	−126.6	M	9.6	514	8
21	$10^h\ 18^m\ 17.8^s$	$41°\ 23^m\ 11.0^s$	154.5743	41.3864	9.0	−135.7	A	5.0	268	4
22	$10^h\ 18^m\ 15.4^s$	$41°\ 23^m\ 56.7^s$	154.5640	41.3991	−19.0	−90.0	M	23.3	1248	17
23	$10^h\ 18^m\ 06.8^s$	$41°\ 25^m\ 38.8^s$	154.5284	41.4274	−115.2	12.1	M	2.7	144	1
24	$10^h\ 18^m\ 10.3^s$	$41°\ 25^m\ 38.6^s$	154.5427	41.4274	−76.4	11.9	M	2.7	144	1
25	$10^h\ 18^m\ 09.4^s$	$41°\ 26^m\ 26.4^s$	154.5393	41.4407	−85.6	59.7	A	5.0	268	4
26	$10^h\ 18^m\ 08.4^s$	$41°\ 26^m\ 26.7^s$	154.5348	41.4408	−97.8	60.0	M	2.7	144	1
27	$10^h\ 18^m\ 08.3^s$	$41°\ 26^m\ 40.1^s$	154.5345	41.4445	−98.6	73.4	A	7.0	375	5
28	$10^h\ 18^m\ 10.5^s$	$41°\ 26^m\ 36.2^s$	154.5436	41.4434	−74.0	69.4	A	7.0	375	5
29	$10^h\ 18^m\ 10.9^s$	$41°\ 26^m\ 55.8^s$	154.5452	41.4488	−69.7	89.1	A	12.0	643	9
30	$10^h\ 18^m\ 11.1^s$	$41°\ 27^m\ 13.4^s$	154.5463	41.4537	−66.8	106.7	A	5.0	268	4
31	$10^h\ 18^m\ 15.0^s$	$41°\ 26^m\ 23.7^s$	154.5626	41.4399	−22.6	57.0	M	2.7	144	1
32	$10^h\ 18^m\ 16.0^s$	$41°\ 26^m\ 27.0^s$	154.5667	41.4408	−11.8	60.3	A	5.0	268	4
33	$10^h\ 18^m\ 16.6^s$	$41°\ 26^m\ 11.3^s$	154.5692	41.4365	−5.0	44.6	A	5.0	268	4
34	$10^h\ 18^m\ 16.7^s$	$41°\ 26^m\ 31.0^s$	154.5697	41.4419	−3.6	64.2	A	8.0	428	7
35	$10^h\ 18^m\ 17.2^s$	$41°\ 26^m\ 35.8^s$	154.5717	41.4433	1.8	69.1	M	2.7	144	1
36	$10^h\ 18^m\ 16.3^s$	$41°\ 26^m\ 45.3^s$	154.5681	41.4459	−7.9	78.6	M	14.7	787	12
37	$10^h\ 18^m\ 16.4^s$	$41°\ 26^m\ 54.5^s$	154.5685	41.4485	−7.0	87.8	A	5.0	268	4
38	$10^h\ 18^m\ 17.7^s$	$41°\ 26^m\ 43.4^s$	154.5738	41.4454	7.5	76.6	A	5.0	268	4
39	$10^h\ 18^m\ 18.3^s$	$41°\ 26^m\ 50.6^s$	154.5763	41.4474	14.3	83.8	A	7.0	375	5
40	$10^h\ 18^m\ 19.7^s$	$41°\ 26^m\ 45.6^s$	154.5822	41.4460	30.1	78.9	M	2.7	144	1
41	$10^h\ 18^m\ 21.7^s$	$41°\ 26^m\ 29.0^s$	154.5904	41.4414	52.4	62.3	M	9.7	519	8
42	$10^h\ 18^m\ 23.1^s$	$41°\ 26^m\ 32.9^s$	154.5963	41.4425	68.3	66.2	A	8.0	428	6
43	$10^h\ 18^m\ 23.8^s$	$41°\ 26^m\ 02.9^s$	154.5994	41.4341	76.5	36.1	M	9.9	530	8
44	$10^h\ 18^m\ 22.4^s$	$41°\ 27^m\ 28.5^s$	154.5933	41.4579	60.1	121.7	M	7.1	380	5
45	$10^h\ 18^m\ 21.0^s$	$41°\ 27^m\ 03.8^s$	154.5873	41.4510	44.0	97.0	M	2.7	144	1
46	$10^h\ 18^m\ 22.5^s$	$41°\ 27^m\ 03.6^s$	154.5937	41.4510	61.1	96.9	A	8.0	428	7
47	$10^h\ 18^m\ 23.1^s$	$41°\ 27^m\ 02.3^s$	154.5962	41.4506	67.8	95.6	M	6.5	348	4
48	$10^h\ 18^m\ 23.5^s$	$41°\ 26^m\ 55.1^s$	154.5981	41.4486	73.1	88.4	M	14.0	750	10
49	$10^h\ 18^m\ 20.7^s$	$41°\ 26^m\ 54.5^s$	154.5861	41.4485	40.8	87.8	M	12.6	675	11
50	$10^h\ 18^m\ 19.5^s$	$41°\ 26^m\ 20.7^s$	154.5814	41.4391	27.9	54.0	M	2.7	144	1
51	$10^h\ 18^m\ 18.3^s$	$41°\ 27^m\ 26.5^s$	154.5763	41.4574	14.3	119.8	M	13.2	707	12
52	$10^h\ 18^m\ 17.5^s$	$41°\ 27^m\ 42.2^s$	154.5727	41.4617	4.6	135.4	M	10.5	562	9
53	$10^h\ 18^m\ 15.6^s$	$41°\ 27^m\ 42.8^s$	154.5648	41.4619	−16.7	136.1	M	2.7	144	1

Table D.4: H II regions NGC 3184.

H II REGION CATALOGUE: NGC 3310

ID	RA	Dec	RA	Dec	ΔRA	ΔDec	Method	Aperture	Size	Fibres
1	$10^h\ 38^m\ 45.9^s$	$53°\ 30^m\ 12.9^s$	159.6914	53.5036	0.5	0.6	A	3.5	295	4
2	$10^h\ 38^m\ 45.9^s$	$53°\ 30^m\ 17.2^s$	159.6914	53.5048	0.5	4.9	A	4.4	369	5
3	$10^h\ 38^m\ 46.4^s$	$53°\ 30^m\ 15.1^s$	159.6935	53.5042	4.9	2.7	A	5.3	443	6
4	$10^h\ 38^m\ 46.4^s$	$53°\ 30^m\ 10.0^s$	159.6931	53.5028	4.1	−2.3	A	3.5	295	4
5	$10^h\ 38^m\ 45.8^s$	$53°\ 30^m\ 08.3^s$	159.6907	53.5023	−1.1	−4.1	A	4.4	369	5
6	$10^h\ 38^m\ 45.4^s$	$53°\ 30^m\ 11.7^s$	159.6890	53.5032	−4.7	−0.6	A	3.5	295	4
7	$10^h\ 38^m\ 45.4^s$	$53°\ 30^m\ 16.3^s$	159.6892	53.5045	−4.3	4.0	A	4.4	369	5
8	$10^h\ 38^m\ 44.9^s$	$53°\ 30^m\ 14.6^s$	159.6871	53.5041	−8.7	2.3	A	5.3	443	6
9	$10^h\ 38^m\ 44.6^s$	$53°\ 30^m\ 09.5^s$	159.6860	53.5026	−11.1	−2.8	A	3.5	295	4
10	$10^h\ 38^m\ 45.1^s$	$53°\ 30^m\ 07.0^s$	159.6881	53.5019	−6.7	−5.3	A	3.5	295	4
11	$10^h\ 38^m\ 44.7^s$	$53°\ 30^m\ 04.4^s$	159.6864	53.5012	−10.3	−7.9	A	5.3	443	6
12	$10^h\ 38^m\ 44.3^s$	$53°\ 30^m\ 05.7^s$	159.6845	53.5016	−14.3	−6.6	A	5.3	443	6
13	$10^h\ 38^m\ 44.1^s$	$53°\ 30^m\ 10.4^s$	159.6838	53.5029	−15.9	−1.9	A	6.1	517	7
14	$10^h\ 38^m\ 44.4^s$	$53°\ 30^m\ 13.4^s$	159.6849	53.5037	−13.5	1.0	A	4.4	369	5
15	$10^h\ 38^m\ 44.6^s$	$53°\ 30^m\ 17.2^s$	159.6856	53.5048	−11.9	4.9	A	5.3	443	6
16	$10^h\ 38^m\ 45.0^s$	$53°\ 30^m\ 19.7^s$	159.6877	53.5055	−7.5	7.4	A	3.5	295	4
17	$10^h\ 38^m\ 45.6^s$	$53°\ 30^m\ 21.0^s$	159.6899	53.5058	−2.7	8.7	A	3.5	295	4
18	$10^h\ 38^m\ 46.1^s$	$53°\ 30^m\ 21.4^s$	159.6920	53.5060	1.7	9.1	A	4.4	369	5
19	$10^h\ 38^m\ 46.4^s$	$53°\ 30^m\ 19.3^s$	159.6935	53.5054	4.9	7.0	A	4.4	369	5
20	$10^h\ 38^m\ 46.9^s$	$53°\ 30^m\ 17.6^s$	159.6954	53.5049	8.9	5.3	A	4.4	369	5
21	$10^h\ 38^m\ 46.9^s$	$53°\ 30^m\ 13.4^s$	159.6956	53.5037	9.3	1.0	A	4.4	369	5
22	$10^h\ 38^m\ 46.8^s$	$53°\ 30^m\ 09.5^s$	159.6950	53.5026	8.1	−2.8	A	3.5	295	4
23	$10^h\ 38^m\ 46.4^s$	$53°\ 30^m\ 05.3^s$	159.6935	53.5015	4.9	−7.0	A	4.4	369	5
24	$10^h\ 38^m\ 45.9^s$	$53°\ 30^m\ 04.0^s$	159.6914	53.5011	0.5	−8.3	A	3.5	295	4
25	$10^h\ 38^m\ 45.5^s$	$53°\ 30^m\ 03.6^s$	159.6894	53.5010	−3.9	−8.7	A	3.5	295	4
26	$10^h\ 38^m\ 45.0^s$	$53°\ 30^m\ 01.1^s$	159.6875	53.5003	−7.9	−11.3	A	3.5	295	4
27	$10^h\ 38^m\ 44.5^s$	$53°\ 30^m\ 00.2^s$	159.6853	53.5001	−12.7	−12.1	A	3.0	252	3
28	$10^h\ 38^m\ 44.0^s$	$53°\ 30^m\ 02.3^s$	159.6832	53.5006	−17.1	−10.0	A	4.4	369	5
29	$10^h\ 38^m\ 43.8^s$	$53°\ 30^m\ 06.6^s$	159.6825	53.5018	−18.8	−5.8	A	3.5	295	4
30	$10^h\ 38^m\ 43.6^s$	$53°\ 30^m\ 11.2^s$	159.6815	53.5031	−20.8	−1.1	A	4.4	369	5
31	$10^h\ 38^m\ 43.8^s$	$53°\ 30^m\ 15.1^s$	159.6826	53.5042	−18.4	2.7	A	4.4	369	5
32	$10^h\ 38^m\ 44.1^s$	$53°\ 30^m\ 18.0^s$	159.6838	53.5050	−15.9	5.7	A	8.8	739	10
33	$10^h\ 38^m\ 44.5^s$	$53°\ 30^m\ 21.0^s$	159.6855	53.5058	−12.3	8.7	A	7.0	591	8
34	$10^h\ 38^m\ 44.9^s$	$53°\ 30^m\ 24.0^s$	159.6871	53.5067	−8.7	11.7	A	5.3	443	6
35	$10^h\ 38^m\ 45.5^s$	$53°\ 30^m\ 25.7^s$	159.6894	53.5071	−3.9	13.4	A	4.4	369	5
36	$10^h\ 38^m\ 45.9^s$	$53°\ 30^m\ 26.1^s$	159.6914	53.5072	0.5	13.8	A	3.5	295	4
37	$10^h\ 38^m\ 46.4^s$	$53°\ 30^m\ 25.2^s$	159.6933	53.5070	4.5	12.9	A	3.5	295	4
38	$10^h\ 38^m\ 46.8^s$	$53°\ 30^m\ 22.3^s$	159.6948	53.5062	7.7	10.0	A	3.5	295	4
39	$10^h\ 38^m\ 47.3^s$	$53°\ 30^m\ 21.0^s$	159.6969	53.5058	12.1	8.7	A	5.3	443	6
40	$10^h\ 38^m\ 47.4^s$	$53°\ 30^m\ 16.3^s$	159.6976	53.5045	13.8	4.0	A	6.1	517	7
41	$10^h\ 38^m\ 47.4^s$	$53°\ 30^m\ 12.1^s$	159.6974	53.5034	13.4	−0.2	A	3.5	295	4
42	$10^h\ 38^m\ 47.3^s$	$53°\ 30^m\ 08.3^s$	159.6969	53.5023	12.1	−4.1	A	7.0	591	8
43	$10^h\ 38^m\ 46.9^s$	$53°\ 30^m\ 04.4^s$	159.6956	53.5012	9.3	−7.9	A	4.4	369	5
44	$10^h\ 38^m\ 46.5^s$	$53°\ 30^m\ 01.5^s$	159.6939	53.5004	5.7	−10.8	A	4.4	369	5
45	$10^h\ 38^m\ 46.1^s$	$53°\ 29^m\ 58.9^s$	159.6920	53.4997	1.7	−13.4	A	5.3	443	6
46	$10^h\ 38^m\ 45.5^s$	$53°\ 29^m\ 58.1^s$	159.6896	53.4995	−3.5	−14.2	A	5.3	443	6
47	$10^h\ 38^m\ 45.0^s$	$53°\ 29^m\ 57.2^s$	159.6873	53.4992	−8.3	−15.1	A	3.0	252	3
48	$10^h\ 38^m\ 44.3^s$	$53°\ 29^m\ 55.5^s$	159.6847	53.4988	−13.9	−16.8	A	5.3	443	6
49	$10^h\ 38^m\ 43.8^s$	$53°\ 29^m\ 57.7^s$	159.6825	53.4993	−18.8	−14.7	A	3.5	295	4
50	$10^h\ 38^m\ 43.4^s$	$53°\ 30^m\ 01.5^s$	159.6808	53.5004	−22.4	−10.8	A	5.3	443	6
51	$10^h\ 38^m\ 43.2^s$	$53°\ 30^m\ 06.6^s$	159.6800	53.5018	−24.0	−5.8	A	3.5	295	4
52	$10^h\ 38^m\ 42.9^s$	$53°\ 30^m\ 11.7^s$	159.6787	53.5032	−26.8	−0.6	A	3.5	295	4
53	$10^h\ 38^m\ 43.2^s$	$53°\ 30^m\ 15.5^s$	159.6802	53.5043	−23.6	3.2	A	4.4	369	5
54	$10^h\ 38^m\ 43.6^s$	$53°\ 30^m\ 19.3^s$	159.6815	53.5054	−20.8	7.0	A	5.3	443	6
55	$10^h\ 38^m\ 44.0^s$	$53°\ 30^m\ 22.7^s$	159.6834	53.5063	−16.8	10.4	A	5.3	443	6

continues on next page

Table D.5: H II regions NGC 3310: Part 1.

H II REGION CATALOGUE: NGC 3310

ID	RA	Dec	RA	Dec	ΔRA	ΔDec	Method	Aperture	Size	Fibres
continued from previous page										
56	$10^h\ 38^m\ 44.5^s$	$53°\ 30^m\ 26.1^s$	159.6853	53.5072	−12.7	13.8	A	6.1	517	7
57	$10^h\ 38^m\ 45.0^s$	$53°\ 30^m\ 28.6^s$	159.6875	53.5080	−7.9	16.3	A	4.4	369	5
58	$10^h\ 38^m\ 45.5^s$	$53°\ 30^m\ 29.9^s$	159.6898	53.5083	−3.1	17.6	A	3.5	295	4
59	$10^h\ 38^m\ 46.1^s$	$53°\ 30^m\ 29.9^s$	159.6920	53.5083	1.7	17.6	A	5.3	443	6
60	$10^h\ 38^m\ 46.6^s$	$53°\ 30^m\ 29.1^s$	159.6941	53.5081	6.1	16.8	A	3.5	295	4
61	$10^h\ 38^m\ 47.0^s$	$53°\ 30^m\ 26.5^s$	159.6959	53.5074	10.1	14.2	A	4.4	369	5
62	$10^h\ 38^m\ 47.4^s$	$53°\ 30^m\ 24.8^s$	159.6976	53.5069	13.8	12.5	A	5.3	443	6
63	$10^h\ 38^m\ 47.8^s$	$53°\ 30^m\ 21.0^s$	159.6991	53.5058	17.0	8.7	A	3.5	295	4
64	$10^h\ 38^m\ 47.9^s$	$53°\ 30^m\ 25.2^s$	159.6995	53.5070	17.8	12.9	A	3.5	295	4
65	$10^h\ 38^m\ 47.6^s$	$53°\ 30^m\ 29.1^s$	159.6982	53.5081	15.0	16.8	A	3.5	295	4
66	$10^h\ 38^m\ 47.1^s$	$53°\ 30^m\ 31.6^s$	159.6963	53.5088	10.9	19.3	A	4.4	369	5
67	$10^h\ 38^m\ 46.6^s$	$53°\ 30^m\ 33.3^s$	159.6943	53.5093	6.5	21.0	A	3.0	252	3
68	$10^h\ 38^m\ 47.0^s$	$53°\ 30^m\ 35.9^s$	159.6958	53.5100	9.7	23.5	A	3.5	295	4
69	$10^h\ 38^m\ 47.3^s$	$53°\ 30^m\ 38.0^s$	159.6973	53.5105	12.9	25.7	A	3.5	295	4
70	$10^h\ 38^m\ 46.8^s$	$53°\ 30^m\ 39.7^s$	159.6952	53.5110	8.5	27.4	A	4.4	369	5
71	$10^h\ 38^m\ 46.5^s$	$53°\ 30^m\ 37.6^s$	159.6937	53.5104	5.3	25.2	A	6.1	517	7
72	$10^h\ 38^m\ 46.4^s$	$53°\ 30^m\ 40.9^s$	159.6931	53.5114	4.1	28.6	A	3.5	295	4
73	$10^h\ 38^m\ 46.1^s$	$53°\ 30^m\ 33.7^s$	159.6922	53.5094	2.1	21.4	A	3.5	295	4
74	$10^h\ 38^m\ 46.0^s$	$53°\ 30^m\ 38.0^s$	159.6916	53.5105	0.9	25.7	A	3.5	295	4
75	$10^h\ 38^m\ 46.8^s$	$53°\ 30^m\ 43.9^s$	159.6952	53.5122	8.5	31.6	A	3.0	252	3
76	$10^h\ 38^m\ 47.3^s$	$53°\ 30^m\ 41.8^s$	159.6969	53.5116	12.1	29.5	A	5.3	443	6
77	$10^h\ 38^m\ 47.7^s$	$53°\ 30^m\ 32.5^s$	159.6988	53.5090	16.2	20.1	A	3.5	295	4
78	$10^h\ 38^m\ 47.8^s$	$53°\ 30^m\ 36.7^s$	159.6991	53.5102	17.0	24.4	A	5.3	443	6
79	$10^h\ 38^m\ 47.7^s$	$53°\ 30^m\ 40.9^s$	159.6988	53.5114	16.2	28.6	A	3.5	295	4
80	$10^h\ 38^m\ 48.3^s$	$53°\ 30^m\ 35.4^s$	159.7012	53.5098	21.4	23.1	A	4.4	369	5
81	$10^h\ 38^m\ 48.2^s$	$53°\ 30^m\ 31.6^s$	159.7006	53.5088	20.2	19.3	A	4.4	369	5
82	$10^h\ 38^m\ 47.9^s$	$53°\ 30^m\ 14.2^s$	159.6995	53.5039	17.8	1.9	A	4.4	369	5
83	$10^h\ 38^m\ 48.1^s$	$53°\ 30^m\ 18.0^s$	159.7004	53.5050	19.8	5.7	A	3.5	295	4
84	$10^h\ 38^m\ 48.2^s$	$53°\ 30^m\ 21.8^s$	159.7008	53.5061	20.6	9.5	A	4.4	369	5
85	$10^h\ 38^m\ 48.3^s$	$53°\ 30^m\ 25.7^s$	159.7012	53.5071	21.4	13.4	A	3.5	295	4
86	$10^h\ 38^m\ 43.3^s$	$53°\ 29^m\ 55.5^s$	159.6806	53.4988	−22.8	−16.8	A	5.3	443	6
87	$10^h\ 38^m\ 43.9^s$	$53°\ 29^m\ 53.4^s$	159.6828	53.4982	−18.0	−18.9	A	3.5	295	4
88	$10^h\ 38^m\ 43.4^s$	$53°\ 29^m\ 50.0^s$	159.6810	53.4972	−22.0	−22.3	A	3.5	295	4
89	$10^h\ 38^m\ 44.0^s$	$53°\ 29^m\ 49.2^s$	159.6832	53.4970	−17.1	−23.1	A	3.5	295	4
90	$10^h\ 38^m\ 44.5^s$	$53°\ 29^m\ 51.3^s$	159.6855	53.4976	−12.3	−21.0	A	4.4	369	5
91	$10^h\ 38^m\ 45.0^s$	$53°\ 29^m\ 53.4^s$	159.6875	53.4982	−7.9	−18.9	A	3.5	295	4
92	$10^h\ 38^m\ 45.6^s$	$53°\ 29^m\ 53.8^s$	159.6899	53.4983	−2.7	−18.5	A	3.5	295	4
93	$10^h\ 38^m\ 45.2^s$	$53°\ 29^m\ 48.3^s$	159.6883	53.4968	−6.3	−24.0	A	12.3	1035	14
94	$10^h\ 38^m\ 45.1^s$	$53°\ 29^m\ 48.2^s$	159.6880	53.4967	−7.0	−24.1	M	3.0	252	1
95	$10^h\ 38^m\ 44.5^s$	$53°\ 29^m\ 47.0^s$	159.6855	53.4964	−12.3	−25.3	A	6.1	517	7
96	$10^h\ 38^m\ 44.8^s$	$53°\ 29^m\ 42.8^s$	159.6866	53.4952	−9.9	−29.5	A	3.5	295	4
97	$10^h\ 38^m\ 45.7^s$	$53°\ 29^m\ 50.0^s$	159.6903	53.4972	−1.9	−22.3	A	7.0	591	8
98	$10^h\ 38^m\ 45.7^s$	$53°\ 29^m\ 45.3^s$	159.6905	53.4959	−1.5	−27.0	A	3.0	252	3
99	$10^h\ 38^m\ 45.3^s$	$53°\ 29^m\ 43.2^s$	159.6888	53.4953	−5.1	−29.1	A	5.3	443	6
100	$10^h\ 38^m\ 45.8^s$	$53°\ 29^m\ 40.7^s$	159.6907	53.4946	−1.1	−31.6	A	3.0	252	2
101	$10^h\ 38^m\ 46.1^s$	$53°\ 29^m\ 43.6^s$	159.6920	53.4955	1.7	−28.7	A	6.1	517	7
102	$10^h\ 38^m\ 46.4^s$	$53°\ 29^m\ 39.8^s$	159.6931	53.4944	4.1	−32.5	A	14.0	1183	16
103	$10^h\ 38^m\ 46.1^s$	$53°\ 29^m\ 34.3^s$	159.6921	53.4929	1.9	−38.0	A	3.0	252	1
104	$10^h\ 38^m\ 45.9^s$	$53°\ 29^m\ 37.3^s$	159.6913	53.4937	0.2	−35.0	A	3.0	252	1
105	$10^h\ 38^m\ 47.0^s$	$53°\ 29^m\ 37.3^s$	159.6959	53.4937	10.1	−35.0	A	3.0	252	3
106	$10^h\ 38^m\ 47.1^s$	$53°\ 29^m\ 49.6^s$	159.6961	53.4971	10.5	−22.7	A	13.2	1109	15
107	$10^h\ 38^m\ 48.1^s$	$53°\ 30^m\ 00.6^s$	159.7003	53.5002	19.4	−11.7	A	17.5	1479	20
108	$10^h\ 38^m\ 47.3^s$	$53°\ 29^m\ 30.9^s$	159.6969	53.4919	12.1	−41.4	A	5.3	443	6
109	$10^h\ 38^m\ 48.5^s$	$53°\ 29^m\ 36.0^s$	159.7021	53.4933	23.4	−36.3	A	14.0	1183	16
110	$10^h\ 38^m\ 46.7^s$	$53°\ 29^m\ 25.8^s$	159.6946	53.4905	7.3	−46.5	A	3.5	295	4

continues on next page

Table D.6: H II regions NGC 3310: Part 2.

H II REGION CATALOGUE: NGC 3310

ID	RA	Dec	RA	Dec	ΔRA	ΔDec	Method	Aperture	Size	Fibres
continued from previous page										
111	$10^h\ 38^m\ 47.2^s$	$53°\ 29^m\ 21.6^s$	159.6967	53.4893	11.7	−50.7	A	5.3	443	6
112	$10^h\ 38^m\ 47.7^s$	$53°\ 29^m\ 27.1^s$	159.6988	53.4909	16.2	−45.2	A	6.1	517	7
113	$10^h\ 38^m\ 48.4^s$	$53°\ 29^m\ 29.2^s$	159.7016	53.4914	22.2	−43.1	A	6.1	517	7
114	$10^h\ 38^m\ 49.0^s$	$53°\ 29^m\ 30.9^s$	159.7040	53.4919	27.4	−41.4	A	5.3	443	6
115	$10^h\ 38^m\ 49.9^s$	$53°\ 29^m\ 30.5^s$	159.7081	53.4918	36.2	−41.8	A	6.1	517	7
116	$10^h\ 38^m\ 51.8^s$	$53°\ 29^m\ 40.7^s$	159.7158	53.4946	52.7	−31.6	A	7.0	591	8
117	$10^h\ 38^m\ 50.7^s$	$53°\ 29^m\ 43.6^s$	159.7113	53.4955	43.0	−28.7	A	11.4	961	13
118	$10^h\ 38^m\ 49.5^s$	$53°\ 29^m\ 08.0^s$	159.7061	53.4856	31.8	−64.3	A	9.7	813	11
119	$10^h\ 38^m\ 47.4^s$	$53°\ 29^m\ 45.8^s$	159.6976	53.4960	13.8	−26.5	A	8.8	739	10
120	$10^h\ 38^m\ 47.4^s$	$53°\ 30^m\ 01.1^s$	159.6974	53.5003	13.4	−11.3	A	5.3	443	6
121	$10^h\ 38^m\ 51.1^s$	$53°\ 29^m\ 57.7^s$	159.7130	53.4993	46.7	−14.7	A	10.5	887	12
122	$10^h\ 38^m\ 41.8^s$	$53°\ 29^m\ 09.7^s$	159.6740	53.4860	−36.8	−62.6	A	3.0	252	3
123	$10^h\ 38^m\ 40.6^s$	$53°\ 28^m\ 52.7^s$	159.6691	53.4813	−47.2	−79.6	A	3.5	295	4
124	$10^h\ 38^m\ 49.8^s$	$53°\ 28^m\ 04.8^s$	159.7076	53.4680	35.0	−127.6	A	3.5	295	4
125	$10^h\ 38^m\ 59.0^s$	$53°\ 28^m\ 53.1^s$	159.7460	53.4814	117.3	−79.2	A	3.5	295	4
126	$10^h\ 38^m\ 58.9^s$	$53°\ 30^m\ 28.2^s$	159.7456	53.5078	116.5	15.9	A	3.0	252	3
127	$10^h\ 38^m\ 49.8^s$	$53°\ 31^m\ 15.3^s$	159.7074	53.5209	34.6	63.0	A	3.5	295	4
128	$10^h\ 38^m\ 45.9^s$	$53°\ 30^m\ 41.8^s$	159.6914	53.5116	0.5	29.5	A	4.4	369	5
129	$10^h\ 38^m\ 45.7^s$	$53°\ 30^m\ 44.8^s$	159.6903	53.5124	−1.9	32.5	A	6.1	517	7
130	$10^h\ 38^m\ 46.0^s$	$53°\ 30^m\ 48.2^s$	159.6918	53.5134	1.3	35.8	A	3.5	295	4
131	$10^h\ 38^m\ 45.6^s$	$53°\ 30^m\ 48.6^s$	159.6899	53.5135	−2.7	36.3	A	3.5	295	4
132	$10^h\ 38^m\ 45.7^s$	$53°\ 30^m\ 52.0^s$	159.6903	53.5144	−1.9	39.7	A	4.4	369	5
133	$10^h\ 38^m\ 45.3^s$	$53°\ 30^m\ 52.4^s$	159.6886	53.5146	−5.5	40.1	A	5.3	443	6
134	$10^h\ 38^m\ 45.5^s$	$53°\ 30^m\ 55.8^s$	159.6898	53.5155	−3.1	43.5	A	3.0	252	3
135	$10^h\ 38^m\ 45.0^s$	$53°\ 30^m\ 56.7^s$	159.6875	53.5157	−7.9	44.3	A	3.5	295	4
136	$10^h\ 38^m\ 45.3^s$	$53°\ 31^m\ 00.0^s$	159.6886	53.5167	−5.5	47.7	A	3.5	295	4
137	$10^h\ 38^m\ 44.8^s$	$53°\ 31^m\ 00.0^s$	159.6866	53.5167	−9.9	47.7	A	3.5	295	4
138	$10^h\ 38^m\ 45.0^s$	$53°\ 31^m\ 03.9^s$	159.6875	53.5177	−7.9	51.5	A	3.0	252	3
139	$10^h\ 38^m\ 44.5^s$	$53°\ 31^m\ 03.9^s$	159.6855	53.5177	−12.3	51.5	A	5.3	443	6
140	$10^h\ 38^m\ 45.6^s$	$53°\ 30^m\ 34.2^s$	159.6901	53.5095	−2.3	21.8	A	3.5	295	4
141	$10^h\ 38^m\ 45.6^s$	$53°\ 30^m\ 38.8^s$	159.6899	53.5108	−2.7	26.5	A	5.3	443	6
142	$10^h\ 38^m\ 45.1^s$	$53°\ 30^m\ 32.5^s$	159.6879	53.5090	−7.1	20.1	A	7.9	665	9
143	$10^h\ 38^m\ 44.5^s$	$53°\ 30^m\ 30.8^s$	159.6855	53.5085	−12.3	18.5	A	9.7	813	11
144	$10^h\ 38^m\ 45.0^s$	$53°\ 30^m\ 38.4^s$	159.6875	53.5107	−7.9	26.1	A	15.8	1331	18
145	$10^h\ 38^m\ 45.3^s$	$53°\ 30^m\ 42.2^s$	159.6886	53.5117	−5.5	29.9	A	8.8	739	10
146	$10^h\ 38^m\ 44.6^s$	$53°\ 30^m\ 34.6^s$	159.6858	53.5096	−11.5	22.3	A	6.1	517	7
147	$10^h\ 38^m\ 44.5^s$	$53°\ 30^m\ 48.6^s$	159.6855	53.5135	−12.3	36.3	A	7.9	665	9
148	$10^h\ 38^m\ 45.2^s$	$53°\ 30^m\ 46.9^s$	159.6883	53.5130	−6.3	34.6	A	3.5	295	4
149	$10^h\ 38^m\ 42.8^s$	$53°\ 30^m\ 31.2^s$	159.6785	53.5087	−27.2	18.9	A	16.7	1405	19
150	$10^h\ 38^m\ 43.0^s$	$53°\ 30^m\ 38.4^s$	159.6793	53.5107	−25.6	26.1	A	12.3	1035	14
151	$10^h\ 38^m\ 42.9^s$	$53°\ 30^m\ 46.5^s$	159.6789	53.5129	−26.4	34.2	A	6.1	517	7
152	$10^h\ 38^m\ 42.4^s$	$53°\ 30^m\ 42.6^s$	159.6768	53.5118	−30.8	30.3	A	4.4	369	5
153	$10^h\ 38^m\ 41.9^s$	$53°\ 30^m\ 39.7^s$	159.6744	53.5110	−36.0	27.4	A	4.4	369	5
154	$10^h\ 38^m\ 40.6^s$	$53°\ 30^m\ 27.8^s$	159.6693	53.5077	−46.8	15.5	A	8.8	739	10
155	$10^h\ 38^m\ 41.0^s$	$53°\ 30^m\ 53.3^s$	159.6708	53.5148	−43.6	40.9	A	12.3	1035	14
156	$10^h\ 38^m\ 41.2^s$	$53°\ 31^m\ 05.1^s$	159.6716	53.5181	−42.0	52.8	A	12.3	1035	14
157	$10^h\ 38^m\ 42.9^s$	$53°\ 30^m\ 55.8^s$	159.6789	53.5155	−26.4	43.5	A	14.0	1183	16
158	$10^h\ 38^m\ 43.9^s$	$53°\ 30^m\ 49.9^s$	159.6830	53.5139	−17.5	37.5	A	5.3	443	6
159	$10^h\ 38^m\ 43.6^s$	$53°\ 30^m\ 55.0^s$	159.6817	53.5153	−20.4	42.6	A	3.0	252	3
160	$10^h\ 38^m\ 43.4^s$	$53°\ 30^m\ 59.2^s$	159.6808	53.5164	−22.4	46.9	A	3.0	252	3

continues on next page

Table D.7: H II regions NGC 3310: Part 3.

H II REGION CATALOGUE: NGC 3310

ID	RA	Dec	RA	Dec	ΔRA	ΔDec	Method	Aperture	Size	Fibres
continued from previous page										
161	$10^h\ 38^m\ 42.5^s$	$53°\ 31^m\ 05.6^s$	159.6770	53.5182	−30.4	53.2	A	16.7	1405	19
162	$10^h\ 38^m\ 43.2^s$	$53°\ 31^m\ 08.1^s$	159.6798	53.5189	−24.4	55.8	A	4.4	369	5
163	$10^h\ 38^m\ 43.1^s$	$53°\ 31^m\ 03.0^s$	159.6796	53.5175	−24.8	50.7	A	5.3	443	6
164	$10^h\ 38^m\ 44.1^s$	$53°\ 31^m\ 11.1^s$	159.6838	53.5197	−15.9	58.8	A	13.2	1109	15
165	$10^h\ 38^m\ 43.6^s$	$53°\ 31^m\ 17.9^s$	159.6815	53.5216	−20.8	65.6	A	10.5	887	12
166	$10^h\ 38^m\ 46.1^s$	$53°\ 29^m\ 53.8^s$	159.6922	53.4983	2.1	−18.5	A	4.4	369	5
167	$10^h\ 38^m\ 46.7^s$	$53°\ 29^m\ 57.2^s$	159.6944	53.4992	6.9	−15.1	A	5.3	443	6
168	$10^h\ 38^m\ 47.7^s$	$53°\ 30^m\ 05.7^s$	159.6986	53.5016	15.8	−6.6	A	7.9	665	9
169	$10^h\ 38^m\ 48.1^s$	$53°\ 30^m\ 09.1^s$	159.7003	53.5025	19.4	−3.2	A	7.9	665	9
170	$10^h\ 38^m\ 48.4^s$	$53°\ 30^m\ 12.9^s$	159.7016	53.5036	22.2	0.6	A	5.3	443	6
171	$10^h\ 38^m\ 48.5^s$	$53°\ 30^m\ 18.5^s$	159.7021	53.5051	23.4	6.1	A	3.0	252	3
172	$10^h\ 38^m\ 48.6^s$	$53°\ 30^m\ 22.3^s$	159.7025	53.5062	24.2	10.0	A	5.3	443	6

Table D.8: H II regions NGC 3310: Part 4.

BIBLIOGRAPHY

Aaronson M., Cohen J. G., Mould J., et al., 1978, ApJ, 223, 824 A

Acharova I. A., Lépine J. R. D., Mishurov Y. N., 2005, Mon. Not. R. Astron. Soc., 359, 819 7.3.2

Afflerbach A., Churchwell E., Werner M. W., 1997, Astrophysical Journal v.478, 478, 190 1.3, 1.3.1

Aller L. H., 1984, Physics of Thermal Gaseous Nebulae, 112 1.2

Allington-Smith J. R., Content R., Haynes R., 1998, Proc. SPIE Vol. 3355, 3355, 196 2.2, 2.2

Alloin D., Collin-Souffrin S., Joly M., et al., 1979, A&A, 78, 200 2, C.1.5

Appleton P. N., Xu K. C., Reach W., et al., 2006, ApJ, 639, L51 3.4.12

Arp H., 1966, Astrophysical Journal Supplement, 14, 1 6.6

Arribas S., Carter D., Cavaller L., et al., 1998, Proc. SPIE Vol. 3355, 3355, 821 2.2

Arribas S., Mediavilla E., García-Lorenzo B., et al., 1999, A&AS, 136, 189 4.2.3

Bacon R., Copin Y., Monnet G., et al., 2001, MNRAS, 326, 23 2.2, 2.3.1

Baldwin J. A., Phillips M. M., Terlevich R., 1981, Astronomical Society of the Pacific, 93, 5 5.2.4

Balkowski C., Bottinelli L., Chamaraux P., et al., 1974, The Formation and Dynamics of Galaxies: Proceedings from IAU Symposium no. 58 held in Canberra, 58, 237 3.4.12

Batcheldor D., Axon D., Merritt D., et al., 2005, ApJS, 160, 76 2.3.1

Benn C., Talbot G., Bacon R., 2003, The Newsletter of the Isaac Newton Group of Telescopes (ING Newsl.), 7, 21 2.2

Blanc G. A., Heiderman A., Gebhardt K., et al., 2009, ApJ, 704, 842 2.3.2

Bresolin F., Ryan-Weber E., Kennicutt R. C., et al., 2009, ApJ, 695, 580 6.4

Bruzual G., Charlot S., 2003, Mon. Not. R. Astron. Soc., 344, 1000 5.2.1, A.1

Burbidge E. M., Burbidge G. R., 1965, ApJ, 142, 634 5.2.4

Calzetti D., 1997, Astronomical Journal v.113, 113, 162 5.2.3

Calzetti D., 2001, PASP, 113, 1449 5.2.3, A.1

Campbell A., Terlevich R., Melnick J., 1986, MNRAS, 223, 811 C.1.7

Cappellari M., Bacon R., Bureau M., et al., 2006, Mon. Not. R. Astron. Soc., 366, 1126 2.3.1

Cardelli J. A., Clayton G. C., Mathis J. S., 1989, ApJ, 345, 245 5.2.3, 6.1, 6.2.2, 6.3.1, 6.3.3, 3, A.1, B

Cardiel N., Gorgas J., Sánchez-Blázquez P., et al., 2003, A&A, 409, 511 A

Castellanos M., Díaz A. I., Terlevich E., 2002, Mon. Not. R. Astron. Soc., 329, 315 5.2.4

Charlot S., Fall S. M., 2000, ApJ, 539, 718 A.1

Chemin L., Balkowski C., Cayatte V., et al., 2006, Mon. Not. R. Astron. Soc., 366, 812 2.3.1

Chilingarian I., Prugniel P., Sil'Chenko O., et al., 2005, Near-fields cosmology with dwarf elliptical galaxies, p. 105 2.3.1

Chornock R., Filippenko A. V., Li W., et al., 2007, CBET, 1036, 1 4.2.6

Colless M., Dalton G., Maddox S., et al., 2001, Mon. Not. R. Astron. Soc., 328, 1039 1, 5.1

Daflon S., Cunha K., 2004, ApJ, 617, 1115 7.3.2

Davidson K., Kinman T. D., Friedman S. D., 1989, AJ, 97, 1591 1.1.1

de Paz A. G., Madore B. F., Boissier S., et al., 2005, ApJ, 627, L29 3.4.7

de Vaucouleurs G., de Vaucouleurs A., Corwin H. G., et al., 1991, Third Reference Catalogue of Bright Galaxies (RC3) 3.1, 3.2

de Zeeuw P. T., Bureau M., Emsellem E., et al., 2002, Mon. Not. R. Astron. Soc., 329, 513 2.3.1

Deharveng L., Peña M., Caplan J., et al., 2000, Mon. Not. R. Astron. Soc., 311, 329 C.1.7

Denicoló G., Terlevich R., Terlevich E., 2002, MNRAS, 330, 69 5.3.1, 1, 5.8, C.1.4
Diaz A. I., 1989, IN: Evolutionary phenomena in galaxies (A90-31743 13-90). Cambridge and New York, p. 377 6.3.3
Diaz A. I., 1994, 1. IAC-RGO Meeting: Violent star formation - from 30 Doradus to QSOs, p. 105 5.2.4
Díaz A. I., Castellanos M., Terlevich E., et al., 2000, Mon. Not. R. Astron. Soc., 318, 462 5.2.4
Díaz A. I., Pérez-Montero E., 2000, Mon. Not. R. Astron. Soc., 312, 130 6.2.2, C.1.4
Diaz A. I., Terlevich E., Pagel B. E. J., et al., 1987, MNRAS, 226, 19 1.1.1, 5.3.1, 6.2.2
Diaz A. I., Terlevich E., Vilchez J. M., et al., 1991, MNRAS, 253, 245 5.2.4
Dinerstein H. L., 1990, IN: The interstellar medium in galaxies; Proceedings of the 2nd Teton Conference, 161, 257 1
Dopita M. A., 1981, ApJ, 246, 65 1.1.1
Dopita M. A., 1990, IN: The interstellar medium in galaxies; Proceedings of the 2nd Teton Conference, 161, 437 1.4
Dopita M. A., Evans I. N., 1986, ApJ, 307, 431 1.3, 2, C.1.2
Dopita M. A., Fischera J., Sutherland R. S., et al., 2006, ApJS, 167, 177 6.2.2
Dopita M. A., Kewley L. J., Heisler C. A., et al., 2000, ApJ, 542, 224 6.2.2
Drozdovsky I. O., Karachentsev I. D., 2000, A&AS, 142, 425 3.2
Eastman R. G., Schmidt B. P., Kirshner R., 1996, ApJ, 466, 911 3.2
Edmunds M. G., Pagel B. E. J., 1984, MNRAS, 211, 507 2, C.1.2
Emsellem E., Cappellari M., Peletier R. F., et al., 2004, Mon. Not. R. Astron. Soc., 352, 721 2.3.1
Ercolano B., Bastian N., Stasińska G., 2007, Mon. Not. R. Astron. Soc., 379, 945 6.3.3, 6.3.3
Evans I. N., 1986, ApJ, 309, 544 1.3
Falco E. E., Kurtz M. J., Geller M. J., et al., 1999, PASP, 111, 438 3.2
Falcón-Barroso J., Bacon R., Bureau M., et al., 2006, Mon. Not. R. Astron. Soc., 369, 529 2.3.1
Ferguson A. M. N., Gallagher J. S., Wyse R. F. G., 1998, AJ, 116, 673 3.4.2, 6.1, 6.1, 6.1, 6.2.1
Ferland G. J., Korista K. T., Verner D. A., et al., 1998, PASP, 110, 761 1, C.1.1
Fernandes R. C., Mateus A., Sodré L., et al., 2005, MNRAS, 358, 363 5.2.1, A
Fevre O. L., Vettolani G. P., Maccagni D., et al., 1998, Proc. SPIE Vol. 3355, 3355, 8 2.2
Filippenko A. V., 1982, PASP, 94, 715 4.2.3
Fisher K. B., Huchra J. P., Strauss M. A., et al., 1995, ApJS, 100, 69 3.2
Fukugita M., Shimasaku K., Ichikawa T., 1995, PASP, 107, 945 4.1.10
Galianni P., Burbidge E. M., Arp H., et al., 2005, ApJ, 620, 88 3.4.12
Gallagher S. C., Charlton J. C., Hunsberger S. D., et al., 2001, AJ, 122, 163 3.4.12
Ganda K., Falcón-Barroso J., Peletier R. F., et al., 2006, Mon. Not. R. Astron. Soc., 367, 46 2.5
García-Rojas J., Esteban C., Peimbert M., et al., 2006, Mon. Not. R. Astron. Soc., 368, 253 1.2, 6.3.3
Garnett D. R., 2002, ApJ, 581, 1019 1.4, 3.1
Garnett D. R., Shields G. A., 1987, ApJ, 317, 82 1.3
Hawley S. A., 1978, ApJ, 224, 417 1.3.1
Haynes M. P., van Zee L., Hogg D. E., et al., 1998, AJ, 115, 62 3.2
Hendry M. A., Smartt S. J., Maund J. R., et al., 2005, MNRAS, 359, 906 3.2
Hickson P., de Oliveira C. M., Huchra J. P., et al., 1992, ApJ, 399, 353 3.2
Hinshaw G., Weiland J. L., Hill R. S., et al., 2009, The Astrophysical Journal Supplement, 180, 225 6.3.1
Hodge P., Lee M. G., Kennicutt R. C., 1989, Astronomical Society of the Pacific, 101, 640 1.1.1

Hodge P. W., Kennicutt R. C., 1983, AJ, 88, 296 1.1.1
Hodge P. W., Wright F. W., 1967, SAO Publications, 4699, 1 1.1.1
Hodge P. W., Wright F. W., 1977, Research supported by the National Science Foundation Seattle 1.1.1
Hoopes C. G., Walterbos R. A. M., Bothun G. D., 2001, ApJ, 559, 878 5.3
Israel F. P., Goss W. M., Allen R. J., 1975, A&A, 40, 421 1.1.1
Izotov Y. I., Stasińska G., Meynet G., et al., 2006, A&A, 448, 955 5.3.2, C.1.7, C.1.7
Izotov Y. I., Thuan T. X., 2004, ApJ, 602, 200 6.1.1
Izotov Y. I., Thuan T. X., Lipovetsky V. A., 1997, Astrophysical Journal Supplement v.108, 108, 1 C.1.7
Jarrett T. H., Chester T., Cutri R., et al., 2003, AJ, 125, 525 3.2
Jenkins E. B., 1987, IN: Interstellar processes; Proceedings of the Symposium, 134, 533 3
Jenkins L. P., Roberts T. P., Ward M. J., et al., 2005, Mon. Not. R. Astron. Soc., 357, 109 5.2.3
Karachentsev I. D., Dolphin A. E., Geisler D., et al., 2002, A&A, 383, 125 3.2
Karachentsev V. E., Karachentsev I. D., Lebedev V. S., 1988, BULL. SPECIAL ASTROF.OBS. NORTH CAUCASUS V. 26, 26, 42 5.2.3
Kehrig C., Vílchez J. M., Sánchez S. F., et al., 2008, A&A, 477, 813 2.6, 2.3.2
Kelz A., Roth M. M., 2006, NewAR, 50, 355 1.5, 2.2, 2.2.1, 2.4, 3.4
Kelz A., Verheijen M. A. W., Roth M. M., et al., 2006, PASP, 118, 129 4.1.3
Kennicutt R. C., 1983, ApJ, 272, 54 5.3
Kennicutt R. C., 1984, ApJ, 287, 116 1.1.1
Kennicutt R. C., 1988, ApJ, 334, 144 1.1.1
Kennicutt R. C., 1992, ApJS, 79, 255 5.1
Kennicutt R. C., 1998, ARA&A, 36, 189 5.2.3
Kennicutt R. C., Armus L., Bendo G., et al., 2003, PASP, 115, 928 3.2, 4.1.10, 1
Kennicutt R. C., Edgar B. K., Hodge P. W., 1989, ApJ, 337, 761 1.1.1
Kennicutt R. C., Garnett D. R., 1996, ApJ, 456, 504 1.3, 2.3.2, 5.3.1
Kennicutt R. C., Keel W. C., Blaha C. A., 1989, Astronomical Journal (ISSN 0004-6256), 97, 1022 3
Kennicutt R. C., Lee J. C., Funes S. J., et al., 2008, ApJS, 178, 247 5.3
Kent S. M., 1981, Astronomical Society of the Pacific, 93, 554 3.4.12
Kewley L. J., Dopita M. A., 2002, ApJS, 142, 35 5.2.4, 5.3.1, 5.3.2, C.1.3
Kewley L. J., Dopita M. A., Sutherland R. S., et al., 2001, ApJ, 556, 121 5.24, 5.2.4, 6.3.1
Kewley L. J., Ellison S. L., 2008, ApJ, 681, 1183 1.2, 5.3.1, 5.3.2, C.1.1
Kinman T. D., 1984, Astronomy with Schmidt-type Telescopes. Proceedings of the 78th. Colloquium of the International Astronomical Union, p. 409 1.1.1
Kniazev A. Y., Pustilnik S. A., Grebel E. K., et al., 2004, ApJS, 153, 429 1.2
Kobulnicky H. A., Kennicutt R. C., Pizagno J. L., 1999, ApJ, 514, 544 5.3, 5.3.2, C.1.1
Kobulnicky H. A., Kewley L. J., 2004, ApJ, 617, 240 5.3.1, 5.8, C.1.3
Kobulnicky H. A., Zaritsky D., 1999, ApJ, 511, 118 1
Koleva M., Prugniel P., Bouchard A., et al., 2009, A&A, 501, 1269 5.2.1, A
Kregel M., Sancisi R., 2001, A&A, 376, 59 3.4.6, 6.6
Lamareille F., Mouhcine M., Contini T., et al., 2004, Mon. Not. R. Astron. Soc., 350, 396 6.3.1
Leonard D. C., Filippenko A. V., Li W., et al., 2002, AJ, 124, 2490 3.2
Liang Y. C., Yin S. Y., Hammer F., et al., 2006, ApJ, 652, 257 5.3.1
Lu N. Y., Hoffman G. L., Groff T., et al., 1993, ApJS, 88, 383 3.2

MacArthur L. A., González J. J., Courteau S., 2009, Mon. Not. R. Astron. Soc., 395, 28 5.2.1, A, A.1
McCall M. L., Rybski P. M., Shields G. A., 1985, ApJS, 57, 1 1.1.1, 3.4.5, 2, 6.1.1, 6.2.1, 6.2.2, 6.2.2, 6.2.4, 6.3.3, 6.5, C.1.2
McGaugh S. S., 1991, ApJ, 380, 140 5.3.1, 5.8, C.1.1
Maeder A., Lequeux J., Azzopardi M., 1980, A&A, 90, L17 1.1.1
Magrini L., Vílchez J. M., Mampaso A., et al., 2007, A&A, 470, 865 1.2
Marcum P. M., O'Connell R. W., Fanelli M. N., et al., 2001, ApJS, 132, 129 5.3
Marquez I., Moles M., Masegosa J., 1996, A&A, 310, 401 3.4.10
Martin P., Roy J.-R., 1994, ApJ, 424, 599 3.1, 3.4.10
Mathis J. S., 1985, ApJ, 291, 247 1.3
Matteucci F., Francois P., 1989, MNRAS, 239, 885 1.4
Miller J. S., Mathews W. G., 1972, ApJ, 172, 593 B
Mishurov Y. N., Lépine J. R. D., Acharova I. A., 2002, ApJ, 571, L113 7.3.2
Moustakas J., Kennicutt R. C., 2006a, ApJ, 651, 155 5.3.2, 5.3.3, 6.3.1, 7.3.2
Moustakas J., Kennicutt R. C., 2006b, ApJS, 164, 81 2.3.2, 4.1.10, 2, 5.1, 5.1.2, 5.1.4, 5.1.5, 5.1.7, 5.1.8, 5.3.3
Nakano S., Kushida R., 1999, IAU Circ., 7329, 1 3.4.5
Navasardyan H., Benetti S., Harutyunyan A., et al., 2008, CBET, 1325, 1 4.2.6
Nishiura S., Shimada M., Ohyama Y., et al., 2000, AJ, 120, 1691 3.2
Nordgren T. E., Chengalur J. N., Salpeter E. E., et al., 1997, Astronomical Journal v.114, 114, 77 3.4.11
Oconnell R. W., 1976, ApJ, 206, 370 A
Ocvirk P., Pichon C., Lançon A., et al., 2006, Mon. Not. R. Astron. Soc., 365, 46 5.2.1, A
Oey M. S., Kennicutt R. C., 1993, ApJ, 411, 137 6.2.1
Oey M. S., Shields J. C., 2000, ApJ, 539, 687 C.1.7
Oke J. B., 1990, AJ, 99, 1621 4.1.8
Osterbrock D. E., Ferland G. J., 2006, Astrophysics of gaseous nebulae and active galactic nuclei 1, 1.2, 5.2.3, 5.2.3, 6.1, 6.3.1, B.1
Pagel B. E. J., 1985, IN: ESO Workshop on Production and Distribution of C, N, O in HII regions, 21, 155 1.3
Pagel B. E. J., 1986, IN: Highlights of astronomy. Volume 7 - Proceedings of the Nineteenth IAU General Assembly, 7, 551 1.1.1
Pagel B. E. J., 1997, Nucleosynthesis and chemical evolution of galaxies 1.2
Pagel B. E. J., Edmunds M. G., Blackwell D. E., et al., 1979, MNRAS, 189, 95 5.3.1
Pagel B. E. J., Edmunds M. G., Smith G., 1980, MNRAS, 193, 219 5.3.1
Pagel B. E. J., Simonson E. A., Terlevich R. J., et al., 1992, MNRAS, 255, 325 5.3.2, 6.1.1, 6.6, C.1.7, C.2, C.2
Pasquini L., Avila G., Blecha A., et al., 2002, The Messenger (ISSN 0722-6691), 110, 1 2.2
Pastoriza M. G., Dottori H. A., Terlevich E., et al., 1993, MNRAS, 260, 177 6.1, 6.1
Peimbert M., 1967, ApJ, 150, 825 6.3.3
Peimbert M., Costero R., 1969, Boletín de los Observatorios de Tonantzintla y Tacubaya Vol. 5, 5, 3 6.6
Peimbert M., Peimbert A., Ruiz M. T., et al., 2004, ApJS, 150, 431 6.6
Pérez-Montero E., Díaz A. I., 2003, MNRAS, 346, 105 5.3.2, 6.6, 6.6, C.2
Pérez-Montero E., Díaz A. I., 2005, MNRAS, 361, 1063 1, 5.3.1

Petersen L., Gammelgaard P., 1996, A&A, 308, 49 6.2.2
Pettini M., Pagel B. E. J., 2004, MNRAS, 348, L59 5.3.1, 1, 2, 5.8, 6.2.2, C.1.4, C.1.5, C.1.5
Pilyugin L. S., 2001a, A&A, 369, 594 5.3.1
Pilyugin L. S., 2001b, A&A, 374, 412 5.3.2, C.1.6
Pilyugin L. S., 2003, A&A, 397, 109 6.4
Pilyugin L. S., 2005, A&A, 436, L1 5.3.2, C.1.7
Pilyugin L. S., 2007, Mon. Not. R. Astron. Soc., 375, 685 5.3.2, 6.6, C.1.7, C.1.7
Pilyugin L. S., Contini T., Vílchez J. M., 2004, A&A, 423, 427 5.3, 5.3.2
Pilyugin L. S., Thuan T. X., 2005, ApJ, 631, 231 5.3.1, 5.8, 5.3.3, 5.3.3, C.1.6, C.1.6
Pilyugin L. S., Thuan T. X., Vílchez J. M., 2006, Mon. Not. R. Astron. Soc., 367, 1139 5.3.2, 6.5, 6.5, 6.5, 7.3.2, C.1.7
Pilyugin L. S., Vílchez J. M., Contini T., 2004, A&A, 425, 849 6.5
Pipher J. L., Helfer H. L., Herter T., et al., 1984, ApJ, 285, 174 1.3.1
Roberts M. S., Hogg D. E., Schulman E., 2001, Gas and Galaxy Evolution, 240, 294 3.4.3
Rosolowsky E., Simon J. D., 2008, ApJ, 675, 1213 1.3, 1.3, 2.3.2, 3.1
Roth M. M., Kelz A., Fechner T., et al., 2005, PASP, 117, 620 1.5, 2.2, 3.4
Roy J.-R., Walsh J. R., 1988, MNRAS, 234, 977 2.3.2
Rubin R. H., Simpson J. P., Erickson E. F., et al., 1988, ApJ, 327, 377 1.3.1
Saha A., Thim F., Tammann G. A., et al., 2006, ApJS, 165, 108 3.2
Salpeter E. E., 1955, ApJ, 121, 161 5.2.1, A.1
Samland M., Hensler G., Theis C., 1997, Astrophysical Journal v.476, 476, 544 7.3.2
Sánchez S. F., 2004, AN, 325, 167 4.1
Sánchez S. F., 2006, AN, 327, 850 4, 4.1, 4.1.3, 4.2.3
Sánchez S. F., Aceituno J., Thiele U., et al., 2007, PASP, 119, 1186 3.4, 4.1.8, 4.1.8, 4.2.1, 4.2.1
Sánchez S. F., Cardiel N., Verheijen M. A. W., et al., 2007a, Mon. Not. R. Astron. Soc., 376, 125 5.2.1
Sánchez S. F., Cardiel N., Verheijen M. A. W., et al., 2007b, A&A, 465, 207 2.3.2, 2.7, A
Sánchez S. F., García-Lorenzo B., Jahnke K., et al., 2006, AN, 327, 167 5.2.1, 5.2.2, 6.2.1
Sandin C., Schönberner D., Roth M. M., et al., 2008, A&A, 486, 545 4.2.3
Sarzi M., Falcón-Barroso J., Davies R. L., et al., 2006, Mon. Not. R. Astron. Soc., 366, 1151 2.3.1, 5.2.1, A
Savage B. D., Mathis J. S., 1979, In: Annual review of astronomy and astrophysics. Volume 17. (A79-54126 24-90) Palo Alto, 17, 73 B
Scott P., Asplund M., Grevesse N., et al., 2009, ApJ, 691, L119 6.3.1
Scowen P. A., Hester J. J., Gallagher J. S., et al., 1996, BAAS, 189, 1360 2.3.2
Searle L., 1971, ApJ, 168, 327 1.3
Searle L., Sargent W. L. W., 1972, ApJ, 173, 25 1.4
Sellwood J. A., Binney J. J., 2002, Monthly Notice of the Royal Astronomical Society, 336, 785 7.3.2
Sellwood J. A., Preto M., 2002, Disks of Galaxies: Kinematics, 275, 281 7.3.2
Sharp R., Team T. A., 2006, Anglo-Australian Observatory Newsletter, 110, 24 2.2
Shaver P. A., McGee R. X., Newton L. M., et al., 1983, MNRAS, 204, 53 1.3.1
Shields G. A., 1974, ApJ, 193, 335 1.3
Shields G. A., Tinsley B. M., 1976, ApJ, 203, 66 1.3
Skillman E. D., 1985, ApJ, 290, 449 1.1.1
Skillman E. D., Kennicutt R. C., Hodge P. W., 1989, ApJ, 347, 875 3.1

Smith D. A., Herter T., Haynes M. P., et al., 1999, ApJ, 510, 669 3.4.11, 5.2.3, 5.2.3, 5.2.3
Springob C. M., Haynes M. P., Giovanelli R., et al., 2005, ApJS, 160, 149 3.2
Stasińska G., 2005, A&A, 434, 507 5.3.2, C.1.7
Stoklasová I., Ferruit P., Emsellem E., et al., 2009, A&A, 500, 1287 A
Storchi-Bergmann T., Calzetti D., Kinney A. L., 1994, ApJ, 429, 572 1, C.1.4
Storey P. J., Zeippen C. J., 2000, Mon. Not. R. Astron. Soc., 312, 813 5.2.3, 6.1, 1, 6.3.1
Strömgren B., 1939, ApJ, 89, 526 1.1
Terlevich R., Melnick J., 1981, MNRAS, 195, 839 1.1.1
Terry J. N., Paturel G., Ekholm T., 2002, A&A, 393, 57 3.2, 6.6
Theureau G., Bottinelli L., Coudreau-Durand N., et al., 1998, A&AS, 130, 333 3.2
Thilker D. A., Walterbos R. A. M., Braun R., et al., 2002, AJ, 124, 3118 5.3.2
Tielens A. G. G. M., 2005, The Physics and Chemistry of the Interstellar Medium 1
Tinsley B. M., 1980, FCPh, 5, 287 A
Torres-Peimbert S., Peimbert M., Fierro J., 1989, ApJ, 345, 186 1.3, 1.3, 1.4
Tremonti C. A., Heckman T. M., Kauffmann G., et al., 2004, ApJ, 613, 898 3.1, 5, 5.1
Valenti S., Elias-Rosa N., Taubenberger S., et al., 2008, ApJ, 673, L155 4.2.6
van Dokkum P. G., 2001, PASP, 113, 1420 4.1.1
van Zee L., Salzer J. J., Haynes M. P., et al., 1998, AJ, 116, 2805 6.2.4, 6.5
Veilleux S., Osterbrock D. E., 1987, Astrophysical Journal Supplement Series (ISSN 0067-0049), 63, 295 5.2.4
Verheijen M. A. W., Bershady M. A., Andersen D. R., et al., 2004, AN, 325, 151 1.5, 3.4
Vila-Costas M. B., Edmunds M. G., 1992, MNRAS, 259, 121 1.3.1, 3.1
Vilchez J. M., Pagel B. E. J., 1988, MNRAS, 231, 257 1.3
Vilchez J. M., Pagel B. E. J., Diaz A. I., et al., 1988, MNRAS, 235, 633 1.3
Vorobyov E. I., 2006, Mon. Not. R. Astron. Soc., 370, 1046 7.3.2
Vorontsov-Velyaminov B. A., 1977, Astron. Astrophys., 28, 1 6.6
Willick J. A., Courteau S., Faber S. M., et al., 1997, ApJS, 109, 333 3.2
Woods D. F., Geller M. J., Barton E. J., 2006, AJ, 132, 197 3.2
Worthey G., 1994, ApJS, 95, 107 A
York D. G., Adelman J., Anderson J. E., et al., 2000, AJ, 120, 1579 1, 5.1
Young J. S., Allen L., Kenney J. D. P., et al., 1996, Astronomical Journal v.112, 112, 1903 5.3
Zaritsky D., Kennicutt R. C., Huchra J. P., 1994, ApJ, 420, 87 3.1, 5.3.1, 5.8, 6.3.3, 7.3.2, C.1.2